CORTICAL MAPS: DATA AND MODELS

EDITED BY: Nick Swindale and Geoffrey Goodhill
PUBLISHED IN: Frontiers in Neuroinformatics, Frontiers in Neuroanatomy and Frontiers in Systems Neuroscience

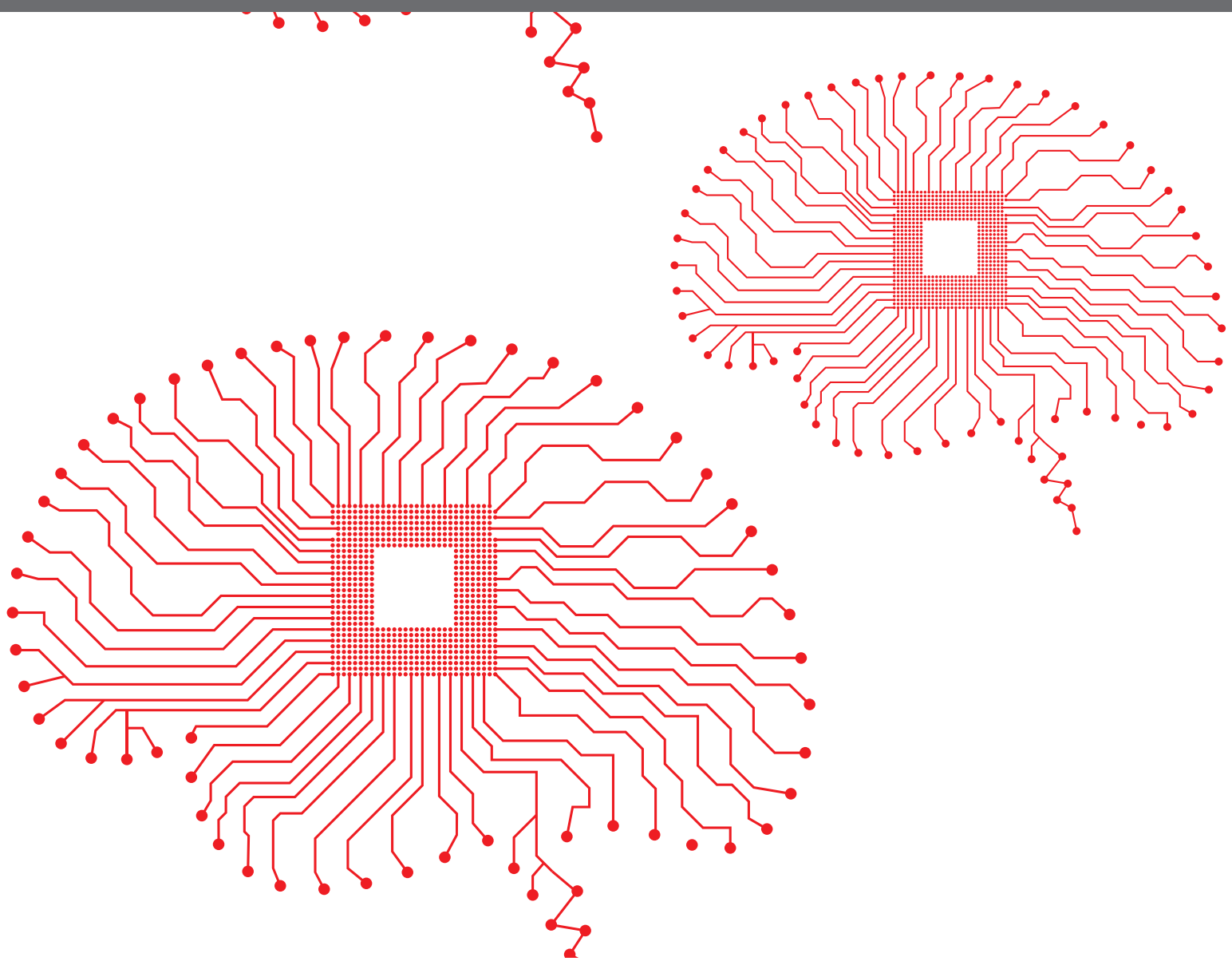

frontiers Research Topics

ISSN 1664-8714
ISBN 978-2-88976-544-7
DOI 10.3389/978-2-88976-544-7

About Frontiers

Frontiers is more than just an open-access publisher of scholarly articles: it is a pioneering approach to the world of academia, radically improving the way scholarly research is managed. The grand vision of Frontiers is a world where all people have an equal opportunity to seek, share and generate knowledge. Frontiers provides immediate and permanent online open access to all its publications, but this alone is not enough to realize our grand goals.

Frontiers Journal Series

The Frontiers Journal Series is a multi-tier and interdisciplinary set of open-access, online journals, promising a paradigm shift from the current review, selection and dissemination processes in academic publishing. All Frontiers journals are driven by researchers for researchers; therefore, they constitute a service to the scholarly community. At the same time, the Frontiers Journal Series operates on a revolutionary invention, the tiered publishing system, initially addressing specific communities of scholars, and gradually climbing up to broader public understanding, thus serving the interests of the lay society, too.

Dedication to Quality

Each Frontiers article is a landmark of the highest quality, thanks to genuinely collaborative interactions between authors and review editors, who include some of the world's best academicians. Research must be certified by peers before entering a stream of knowledge that may eventually reach the public - and shape society; therefore, Frontiers only applies the most rigorous and unbiased reviews.
Frontiers revolutionizes research publishing by freely delivering the most outstanding research, evaluated with no bias from both the academic and social point of view. By applying the most advanced information technologies, Frontiers is catapulting scholarly publishing into a new generation.

What are Frontiers Research Topics?

Frontiers Research Topics are very popular trademarks of the Frontiers Journals Series: they are collections of at least ten articles, all centered on a particular subject. With their unique mix of varied contributions from Original Research to Review Articles, Frontiers Research Topics unify the most influential researchers, the latest key findings and historical advances in a hot research area! Find out more on how to host your own Frontiers Research Topic or contribute to one as an author by contacting the Frontiers Editorial Office: frontiersin.org/about/contact

CORTICAL MAPS: DATA AND MODELS

Topic Editors:
Nick Swindale, University of British Columbia, Canada
Geoffrey Goodhill, The University of Queensland, Australia

Citation: Swindale, N., Goodhill, G., (2022). Cortical Maps: Data and Models. Lausanne: Frontiers Media SA. doi: 10.3389/978-2-88976-544-7

Table of Contents

frontiers | Frontiers in Neuroinformatics

EDITORIAL
published: 17 June 2022
doi: 10.3389/fninf.2022.954042

Editorial: Cortical Maps: Data and Models

Nicholas V. Swindale[1]* *and Geoffrey J. Goodhill*[2,3]

[1] Department of Ophthalmology and Visual Sciences, University of British Columbia, Vancouver, BC, Canada, [2] Departments of Developmental Biology and Neuroscience, Washington University in St. Louis, St. Louis, MO, United States, [3] Queensland Brain Institute and School of Mathematics and Physics, The University of Queensland, St Lucia, QLD, Australia

Keywords: cortical maps, topographic maps, somatotopic maps, tonotopic maps, columns, orientation maps

Editorial on the Research Topic

Cortical Maps: Data and Models

In our original solicitation for papers on the topic of cortical maps, we posed a number of currently unanswered questions. How widespread are maps in the cortex? Are there, for example, ordered representations of speech-related properties in Broca's area? Are there maps of some kind in frontal cortical areas? To what extent are map details dependent on innate, genetically programmed mechanisms, or on patterns of neural activity resulting from sensory experiences and motor behaviors? Despite the interest they have aroused, might maps be epiphenomena with no real function (Horton and Adams, 2005)? These issues, among others, are addressed by the articles in this collection. They range from reviews (Grossberg, Ibbotson and Jung, and Sereno), modeling studies (Grossberg, Tanaka et al.), descriptive advances in the classification of pathways and areas (Johnson et al., Wojtasik et al., and Choi et al.) and experimental and modeling studies of critical period plasticity (Tanaka et al., Thomas et al.).

Sereno et al. address the issue of the ubiquity of maps by showing that the most basic kinds of topographic map: retinotopic, somatotopic and tonotopic, cover half the cortical surface in humans. The authors also point out that patchy local connectivity has been found in many cortical areas, including those where the evidence for topographic maps is limited or lacking. Patchy local connections seem a very strong indicator of fine scale columnar organization of functional properties, given that connected sets of neurons are likely to share functional properties. Hence even if some types of map are absent in some species, maps and columns in general appear to be ubiquitous features of cortical organization. The article by Grossberg shows how maps and columns may enable computations based on canonical wiring rules such as Gaussian, or difference of Gaussian, interactions mediated in the space of the cortex by branching axons. Rules of this nature have the consequence of reducing the developmental demands on the axonal wiring involved—not just the lengths of the wires but in making fewer demands on genetic instructions. More importantly, Grossberg's article provides a valuable summary of almost half a century of modeling work done by himself and his colleagues. The various models unite low-level facts of cortical anatomy and physiology with cognitive operations in a way that is rarely attempted. The models are ambitious but they provide a firm foundation for future tests and development that may be exceedingly valuable.

As Grossberg's article makes clear, maps provide a context which makes studying the functions that are carried out in them much easier. The existence of maps has also made many developmental processes more accessible to study: for example the dramatic change in the widths of ocular dominance stripes demonstrated by Hubel et al. (1977) following monocular deprivation was surely

OPEN ACCESS

Edited and reviewed by:
Sean L. Hill,
University of Toronto, Canada

***Correspondence:**
Nicholas V. Swindale
swindale@mail.ubc.ca

Received: *26 May 2022*
Accepted: *06 June 2022*
Published: *17 June 2022*

Citation:
Swindale NV and Goodhill GJ (2022) Editorial: Cortical Maps: Data and Models. Front. Neuroinform. 16:954042. doi: 10.3389/fninf.2022.954042

much more informative than the corresponding change in the shape of the ocular dominance histogram. Maps have also highlighted and simplified the understanding of critical periods in development, since structural map plasticity is often a key indicator of these periods. Two papers in the collection deal with this problem. Thomas et al. study the consequences of auditory map plasticity induced by rearing rat pups in an environment where a continuous 7 KHz tone was audible, resulting in an increase in the area of the map devoted to that frequency. There is evidence that this kind of alteration may contribute to conditions such as tinnitus and sensitivity to loud sounds. Tanaka et al. combine modeling and experimentation to study plasticity of orientation maps. The maps have a critical period and in general the experimental and modeling data agree beautifully well.

Like many previous modelers, Tanaka et al. employ stimulation with oriented gratings to produce correlated activity in cortical neurons which then leads to the development of an orientation map. Until recently, this might have been considered an unrealistic assumption as there is good evidence that orientation selectivity and orientation maps are present at birth in monkeys (Wiesel and Hubel, 1974) as well as shortly after birth in visually deprived cats (Crair et al., 1998) and it has been presumed that visual stimulation can only occur after birth, and if the eyes are open. However it is becoming clear that environmental visual stimulation can occur *in utero* (Del Giudice, 2011) and that the human fetus, whose eyes open before birth, is responsive to visual stimuli (Reid et al., 2017). If this is true for humans, it is likely to be even more so for other mammals, who do not wear clothes and have very much thinner uterine and abdominal walls. So the assumption that vision (beyond the limited patterns provided by retinal waves) cannot be present before birth, and which has colored work on map development for decades, may be wrong.

Comparative studies of maps in different species almost always seem to be illuminating, especially since maps have been studied in only a handful of species. The article by Ibbotson and Jung reviews the factors that might determine the presence or absence of ordered orientation maps. Although phylogeny is currently the best predictor, an alternative, more directly related to visual system function, is the ratio of central and peripheral ganglion cell densities. This idea is consistent with existing data as well as more recent findings that the agouti (a large rodent) lacks maps (Ferreiro et al., 2021) and that wallabies have them (Jung, 2020).

Finally, an important aspect of work on maps involves the description of new areas and making the descriptions accessible. Three articles in the collection address this issue. Sereno et al. provide a downloadable annotation and parcellation of 115 human cortical areas with topological maps in the FreeSurfer *fsaverage* surface. Johnson et al. provide a DTI atlas for the cat available at https://ecommons.cornell.edu/handle/1813/58775.2 Four new cytoarchitectonically defined areas of human orbitofrontal cortex are described by Wojtasik et al. and are available at a number of sites given in the article.

AUTHOR CONTRIBUTIONS

NVS wrote the text which was revised in response to comments and suggestions by GJG. Both authors have approved the final version.

ACKNOWLEDGMENTS

The editors thank the authors for their valuable contributions to this topic and hope that the collection will inspire continued research into the developmental origins, functional significance and species diversity of cortical maps.

REFERENCES

Crair, M. C., Gillespie, D. C., and Stryker, M. P. (1998). The role of visual experience in the development of columns in cat visual cortex. *Science* 279, 566–570. doi: 10.1126/science.279.5350.566

Del Giudice, M. (2011). Alone in the dark? Modeling the conditions for visual experience in human fetuses. *Dev. Psychobiol.* 53, 214–219. doi: 10.1002/dev.20506

Ferreiro, D. N., Conde-Ocazionez, S. A., Patriota, J. H. N., Souza, L. C., Oliveira, M. F., Wolf, F., et al. (2021). Spatial clustering of orientation preference in primary visual cortex of the large rodent agouti. *iScience* 24, 101882. doi: 10.1016/j.isci.2020.101882

Horton, J. C., and Adams, D. L. (2005). The cortical column: a structure without a function. *Phil. Trans, R. Soc. B* 360, 837–862. doi: 10.1098/rstb.2005.1623

Hubel, D. H., Wiesel, T. N., and LeVay, S. (1977). Plasticity of ocular dominance columns in monkey striate cortex. *Phil. Trans. R. Soc. B* 278, 131–163. doi: 10.1098/rstb.1977.0050

Jung, Y. J. (2020). *Functional organisation of the tammar wallaby visual cortex* (Ph.D. thesis). University of Melbourne. Availale online at: http://hdl.handle.net/11343/268025

Reid, V., Dunn, K., Young, R. J., Amu, J., Donovan, T., and Reissland, N. (2017). The human fetus preferentially engages with face-like vsual stimuli. *Curr. Biol.* 27, 1825–1828. doi: 10.1016/j.cub.2017.05.044

Wiesel, T. N., and Hubel, D. H. (1974). Ordered arrangement of orientation columns in monkeys lacking visual experience. *J. Comp. Neurol.* 158, 307–318. doi: 10.1002/cne.901580306

Conflict of Interest: The authors declare that the research was conducted in the absence of any commercial or financial relationships that could be construed as a potential conflict of interest.

frontiers in Systems Neuroscience

ORIGINAL RESEARCH
published: 23 October 2019
doi: 10.3389/fnsys.2019.00055

Evidence of Hyperacusis in Adult Rats Following Non-traumatic Sound Exposure

Maryse E. Thomas[1,2], *Gerson D. Guercio*[3,4], *Kristina M. Drudik*[1] *and Étienne de Villers-Sidani*[1,2]*

[1]Montreal Neurological Institute, McGill University, Montreal, QC, Canada, [2]Centre for Research on Brain, Language and Music, Montreal, QC, Canada, [3]Department of Psychiatry, University of Minnesota Medical School, Minneapolis, MN, United States, [4]Biomedical Sciences Institute, Federal University of Rio de Janeiro, Rio de Janiero, Brazil

Manipulations that enhance neuroplasticity may inadvertently create opportunities for maladaptation. We have previously used passive exposures to non-traumatic white noise to open windows of plasticity in the adult rat auditory cortex and induce frequency-specific functional reorganizations of the tonotopic map. However, similar reorganizations in the central auditory pathway are thought to contribute to the generation of hearing disorders such as tinnitus and hyperacusis. Here, we investigate whether noise-induced reorganizations are accompanied by electrophysiological or behavioral evidence of tinnitus or hyperacusis in adult Long-Evans rats. We used a 2-week passive exposure to moderate-intensity (70 dB SPL) broadband white noise to reopen a critical period for spectral tuning such that a second 1-week exposure to 7 kHz tone pips produced an expansion of the 7 kHz frequency region in the primary auditory cortex (A1). We demonstrate for the first time that this expansion also takes place in the ventral auditory field (VAF). Sound exposure also led to spontaneous and sound-evoked hyperactivity in the anterior auditory field (AAF). Rats were assessed for behavioral evidence of tinnitus or hyperacusis using gap and tone prepulse inhibition of the acoustic startle response. We found that sound exposure did not affect gap-prepulse inhibition. However, sound exposure led to an improvement in prepulse inhibition when the prepulse was a 7 kHz tone, showing that exposed rats had enhanced sensorimotor gating for the exposure frequency. Together, our electrophysiological and behavioral results provide evidence of hyperacusis but not tinnitus in sound-exposed animals. Our findings demonstrate that periods of prolonged noise exposure may open windows of plasticity that can also be understood as windows of vulnerability, potentially increasing the likelihood for maladaptive plasticity to take place.

Keywords: tonotopic map, maladaptive plasticity, tinnitus, hyperacusis, GPIAS, PPI, sound exposure, auditory cortex

Edited by:
Nick Swindale,
The University of British Columbia, Canada

Reviewed by:
Yoshinao Kajikawa,
Nathan Kline Institute for Psychiatric Research, United States
Todd M. Mowery,
New York University, United States

***Correspondence:**
Étienne de Villers-Sidani
etienne.de-villers-sidani@mcgill.ca

Received: *09 July 2019*
Accepted: *03 October 2019*
Published: *23 October 2019*

Citation:
Thomas ME, Guercio GD, Drudik KM and de Villers-Sidani É (2019) Evidence of Hyperacusis in Adult Rats Following Non-traumatic Sound Exposure. Front. Syst. Neurosci. 13:55. doi: 10.3389/fnsys.2019.00055

INTRODUCTION

As recent decades of neuroscience research have revealed the brain's lifelong capacity for plastic change (Hofer et al., 2006; de Villers-Sidani and Merzenich, 2011), the goal of reopening critical periods (CPs) in order to stimulate learning and recovery in adulthood has become an important area of study. Researchers have already demonstrated the ability to reopen CPs in the auditory

(Reed et al., 2011; Zhou et al., 2011; Blundon et al., 2017), visual (Pizzorusso et al., 2002; He et al., 2006; Harauzov et al., 2010), and somatosensory domains (Chung et al., 2017) in animal models. And steps have even been taken in humans, as the histone-deacetylase inhibitor, valproate, was found to reopen a CP for absolute pitch in adult non-musicians (Gervain et al., 2013). The inevitable quest for lifelong adaptability, however, should not be undertaken without considering the potential risks of opening windows of vulnerability on the brain.

One such vulnerability is the opportunity for maladaptive plasticity, which refers to structural or functional nervous system changes that disrupt normal function. Dysplastic symptoms such as hyperexcitation, altered neural connectivity, and topographic reorganizations can interfere with perceptual discrimination (O'Reilly et al., 2019), cause hypersensitivities or phantom percepts (Flor et al., 2001; Costigan et al., 2009; De Ridder et al., 2011), and contribute to chronic pain (Kuner and Flor, 2016). In the central auditory system, maladaptive plasticity is thought to underlie the generation of auditory disorders including chronic tinnitus and hyperacusis, the uncomfortable sensations of ringing in the ears and sound hypersensitivity. These potentially debilitating conditions usually emerge late in life comorbid with hearing loss and affect between 6% to 15% of the general population (Brozoski and Bauer, 2016). Although the exact neural underpinnings of tinnitus and hyperacusis remain elusive, their frequent co-occurrence with hearing loss points to the reduction of auditory inputs as a potential trigger for plasticity in spatially-defined regions of the auditory pathway (Eggermont and Roberts, 2004; Roberts et al., 2010; Langers et al., 2012). In animal models, tinnitus has primarily been associated with expanded representations of mid-to-high frequency regions, hypersynchronization, increased spontaneous firing, and increased burst firing in structures including the cochlear nucleus, inferior colliculus, and auditory cortex (Eggermont and Roberts, 2004; Roberts et al., 2010). Hyperacusis has been related to increased gain in the central auditory pathway in animal models detectable *via* higher spontaneous firing rates and sound-evoked potentials (Sun et al., 2012; Aazh et al., 2014; Hickox and Liberman, 2014). At present, some evidence links spontaneous and sound-evoked hyperactivity to tinnitus or hyperacusis in humans (Adjamian et al., 2009; Gu et al., 2010), but neuroimaging studies have yet to demonstrate macroscopic tonotopic reorganization in patients with tinnitus (Langers et al., 2012; Elgoyhen et al., 2015), illustrating that much remains to be understood in the etiology of both conditions.

Tinnitus has been tentatively linked to lifetime environmental noise exposure (Holgers and Pettersson, 2005; Guest et al., 2017; Moore et al., 2017). In adult rats and cats, prolonged moderate-intensity sound exposures have been shown to produce strong experience-dependent plasticity altering tonotopic organization and auditory excitability (Pienkowski and Eggermont, 2009; Pienkowski et al., 2011; Zhou et al., 2011; Zheng, 2012). We have previously demonstrated that 2 weeks of passive exposure to moderate-intensity white noise can reopen windows of CP-like plasticity in the adult rat auditory cortex (Thomas et al., 2018). We confirmed CP plasticity with a second passive exposure to pure tones that led to the expansion of the corresponding frequency region in the primary auditory cortex (A1). The perceptual consequences of this map expansion are incompletely understood and differ based on the mode of induction, with primarily sound-driven—as opposed to neuromodulatory-driven—expansions impairing discrimination for the exposure frequency (Han et al., 2007; Eggermont, 2013; Froemke et al., 2013). Based on the common phenotype of map expansion in both sound-exposed animals and animals with tinnitus, we wondered if the sound exposure used in our previous study could have imparted our rats with tinnitus or another auditory disorder.

In the present study, we investigated the possibility that cortical map expansion could be indicative of maladaptive plasticity in sound-exposed animals. To this end, we induced 7 kHz map expansion in female adult Long Evans rats using continuous exposure to moderate-intensity (70 dB SPL) broadband white noise for 2 weeks followed by 7 kHz tone pips for 1 week. We hypothesized that this exposure would lead to specific maladaptive plasticity in cortical regions that preferentially respond to 7 kHz accompanied by behavioral evidence of hyperacusis or tinnitus as measured by prepulse inhibition (PPI) and gap-prepulse inhibition (GPIAS) of the acoustic startle reflex, respectively. We documented the effects of exposure on electrophysiological response properties in the A1, anterior auditory field (AAF), and ventral auditory field (VAF). We found evidence of hyperactivity in the AAF of exposed animals consistent with hyperacusis, which was supported by an improvement in PPI when the prepulse was a 7 kHz pure tone. We did not find electrophysiological or behavioral evidence of tinnitus. Our findings indicate that although non-traumatic white noise exposure can open windows of plasticity on the brain, these can also be understood as windows of vulnerability that may increase the likelihood for maladaptive plasticity to occur.

MATERIALS AND METHODS

The experimental procedures used in this study were approved by the Montreal Neurological Institute Animal Care Committee and follow the guidelines of the Canadian Council on Animal Care.

Sound Exposure

Female 3- to 4-month-old Long-Evans rats were housed in sound-attenuated chambers under a 12 h light/dark cycle and given *ad libitum* access to food and water. Rats were assigned to either the naive or sound exposure condition. Naive rats (N = 23) had no acoustic manipulation of their environment (background sound level 40 dB SPL). Exposed rats (N = 25) were passively exposed to 70 dB SPL (decibels sound pressure level, RMS) continuous white noise for 2 weeks immediately followed by a 1-week exposure to trains of 7 kHz tone pips. From each group, 12 rats were used for behavioral testing (12 Naïve-BEH and 12 Exposed-BEH) while the remaining rats (11 Naive and 13 Exposed) were used for electrophysiological recordings. To reduce the number of animals sacrificed for this study, the electrophysiological data for the Exposed group came from

combining two groups of noise + 7 kHz-exposed animals that underwent slightly different 7 kHz exposures. Four rats came from Thomas et al. (2018) and were exposed to 7 kHz pure tones. The other nine rats were exposed to 7 kHz tone pip clouds consisting of pure tones of random frequencies within a $\frac{1}{4}$ octave range centered on 7.6 kHz (ranging between 7 and 8.3 kHz). Other than tone frequencies, all other properties of the tone exposures were the same. The noise and tone pips were generated using custom MATLAB scripts (The MathWorks, Inc., Natick, MA, USA) and played through an Ultralite-mk3 Hybrid Interface (MOTU Inc., Cambridge, MA, USA) with sampling at 192 kHz. The noise stimuli were amplified to a free-field sound level calibrated so that the average stimulus intensity measured in the center of the chamber was 70 dB SPL. Tones were 50 ms in duration (5 ms onset and offset ramps) and delivered in trains of five pips per second. The interval between each train of tones was a random duration generated from a normal distribution with a mean of 2.5 s. The tone pips were amplified to an intensity of 65 dB SPL measured in the center of the chamber. All stimuli were played 24 h per day for the duration of the exposure periods.

Electrophysiological Recordings

Electrophysiological recordings of the left auditory cortex were performed under isoflurane anesthesia in a shielded soundproof recording chamber. Rats were pre-medicated with dexamethasone (0.2 mg/kg, i.m.) to minimize brain edema. Anesthesia was induced with ketamine/xylazine/acepromazine (63/13/1.5 mg/kg, i.p.) followed by continuous delivery of isoflurane 1% in oxygen *via* endotracheal intubation and mechanical ventilation. Heart rate and blood oxygen saturation were monitored with a pulse oximeter. Body temperature was monitored with a rectal probe and maintained at 37°C with a homeothermic blanket system. Rats were held by the orbits in a custom-designed head holder leaving the ears unobstructed. The cisterna magna was drained of cerebrospinal fluid to further minimize cerebral edema. To access the auditory cortex, the left temporalis muscle was reflected, the skull over the auditory cortex was removed, and the dura was resected. Once exposed, the cortex was maintained under a thin layer of silicone oil to prevent desiccation. Acoustic stimuli were delivered in a free field manner to the right ear through a calibrated speaker. Cortical responses were recorded with a high-impedance 64-channel tungsten microelectrode array (Tucker-Davis Technologies, TDT, Alachua, FL, USA) lowered to a depth of 600–900 μm (layers 4/5). The electrode wires (33 μm diameter) were arranged in an 8 × 8 grid orthogonal to the cortex spaced 375 μm apart with row separation of 500 μm. To maximize recording density, neural responses were consecutively recorded from multiple positions within each rat. The stereotaxic location of each position relative to the first was noted in order to accurately reconstruct auditory maps during offline analysis. Extracellular multi-unit responses were obtained, amplified, and filtered (0.3–5 kHz) using a TDT RZ2 processor. The TDT OpenEx software package was used to generate acoustic stimuli, monitor cortical activity online, and store data for offline analysis.

Acoustic Stimulation

Frequency-intensity receptive fields were constructed using neuronal responses to a range of frequency-intensity combinations of pure tones. Sixty-six frequencies (0.75–70 kHz; 0.1 octave increments; 25 ms duration; 5 ms ramps) were presented at eight sound intensities (0–70 dB SPL; 10 dB increments) at a rate of one tone per second with three repetitions and in random presentation order. The characteristic frequency (CF) and threshold of a cortical site were defined, respectively, as the frequency and intensity at the tip of the V-shaped tuning curve derived from peri-stimulus time histograms (PSTHs). For flat-peaked tuning curves or tuning curves with multiple peaks, the CF was defined as the frequency with the lowest threshold and the strongest firing rate. Response bandwidths 20 dB above the threshold of tuning curves (BW20) were measured for all sites. The onset latency, defined as the time in ms when the PSTH first exceeded mean baseline firing rate by 2.5 standard deviations, was also measured for each cortical site. The CF, threshold, BW20, and latencies were first determined by an automated custom MATLAB routine and then manually verified by an experimenter blind to the identity of the experimental groups. Cortical sites were identified as belonging to A1, AAF, VAF, or posterior auditory field (PAF) based on published functional characteristics of each field (Polley et al., 2007). These were reversal of tonotopic gradients, onset latencies, threshold, and PSTH morphologies (**Supplementary Figure S1**). To generate tonotopic maps, Voronoi tessellation was performed using custom MATLAB scripts to create tessellated polygons with electrode penetration sites at their centers.

Neural Synchrony

The degree of neural synchronization in the auditory cortex was computed from recordings of spontaneous neural activity that were at least 5 min long. Recordings with apparent burst suppression were not included in analyses. Burst suppression was characterized by periods of high spontaneous firing alternating with periods of no activity determined through visual inspection of the raster plots and continuous average firing rate. If a portion of any recording was deemed to have burst suppression, the recording was rejected. The average coefficient of variation (CV) of the inter-spike interval—a measure of burstiness—corresponded well with our classification of burst suppression, as the mean CV was significantly higher for recordings identified as having burst suppression (mean = 3.45, SD = 0.15) than those that were not [mean = 1.86, SD = 0.07; mixed-effects one-way analysis of variance (ANOVA) $F_{(1,48.13)} = 93.34$, $p < 0.0001$, $n = 2{,}070$ units within 53 positions and 24 rats]. Offline spike sorting was performed using TDT OpenSorter software to isolate single unit activity based on an automated Bayesian sorting algorithm. The success of the spike sorting algorithm was assessed by inspecting the number of refractory period violations for all identified clusters (**Supplementary Figure S2**). The fraction of spikes that fell within a 2 ms refractory period was calculated and it was found that 36.1% of all clusters had zero refractory period violations and 96.9% of all clusters had two or fewer violations per 100 spikes (**Supplementary Figure S2A**). An average of 1.63 units was

identified per electrode channel. Example histograms of the interspike interval and the autocorrelation of spike times for representative units are presented in **Supplementary Figure S2B**, displaying a dearth of spikes occurring within the refractory period. In addition, the percentage of refractory period violations did not differ between experimental groups (**Supplementary Figure S2C**). These results indicate that there are a relatively small number of false-positive classifications present in the data, which are unlikely to affect experimental outcomes. Measures of synchronization were computed from binary spike events detected from A1 units in separate channels. Cross-correlograms were computed by counting the number of spike coincidences for pairs of spike trains for time lags of −500 to 500 ms with 1 ms bin size and normalized by dividing each bin by the square root of the product of the number of total discharges in each spike train (Eggermont, 1992).

Behavioral Testing

Behavioral testing took place during the day at the Glen Site of the McGill University Health Centre. At the end of the exposure period, each Naïve-BEH animal was randomly assigned to a pair with one Exposed-BEH animal. Once paired, the rats were transported in their original cages to a loading area by cart. There, they were transferred to a vehicle and driven to the Glen Site, approximately 25 min away. The rats were again transported to a holding area adjoining the behavioral testing facility by cart where they were acclimatized for a minimum of 2 h. Rats remained covered for all of the steps above until they reached the holding area. The paired rats then underwent behavioral testing simultaneously in order of pairing (two rats were tested at a time). This procedure took place twice, with six animals from each group tested on each day. All behavioral data were collected in sound-attenuating chambers. Sounds were delivered from a free-field speaker and rats were free to roam the chamber. The acoustic startle response was measured using the LE 118–8 Startle and Fear Interface (Panlab, Barcelona, Spain). The startle pulse was a white noise burst (120 dB SPL, 40 ms) for both GPIAS and PPI. For GPIAS, rats were acclimatized for 3 min in a pure tone background that was either 3.5 kHz or 7 kHz (65 dB SPL), followed by four randomly interleaved no-gap and gap (30 ms) trials (intertrial interval 12–30 s). During the gap trials, the gap preceded the pulse by 60 ms. This procedure was performed three times, and startle activity for the no-gap and gap trials were averaged across a total of 12 trials each. For PPI, rats were acclimatized for 3 min in a white noise background (65 dB SPL). The subsequent experimental protocol consisted of 10 trials each of no stimulus, the startle pulse alone, and two prepulse frequencies (3.5 or 7 kHz, 20 ms, 75 dB SPL) presented 60 ms before the startle pulse, in pseudorandom order (intertrial interval 12–30 s). The startle activity for the no stimulus, startle pulse, 3.5 kHz prepulse, and 7 kHz prepulse trials were averaged across the 10 trials. We calculated prepulse inhibition of the startle response using the formula: %PPI = 100 − (startle response for prepulse trials/startle response for startle pulse alone trials) × 100. We calculated gap-prepulse inhibition of the startle response with the formula: %GPIAS = 100 − (startle response for gap trials/startle response for no-gap trials) × 100.

Statistical Analyses

For all statistical analyses, results are reported in parentheses including test name, statistic, and number of data points per level of nested data. Linear mixed-effects models (Reed and Kaas, 2010; Aarts et al., 2014) were used to analyze data collected through nested experimental designs (e.g., for synchronization analyses: neuron pair nested within recording position nested within rat). For these models, recording position nested within rat ID were included as random effects. A matched pairs design using paired *t*-tests was employed to analyze behavioral data in order to control for potential confounding effects of transport, handling, waiting, and testing times on the acoustic startle response (Geyer and Swerdlow, 1998; Longenecker and Galazyuk, 2012). Accordingly, the effect size calculated by Cohen's dav is reported for behavioral results (Lakens, 2013). Analyses were conducted using MATLAB and JMP 13 (SAS Institute, Cary, NC, USA). The mixed-effect test results are reported with the degrees of freedom denominator approximated for normal data using the Kenward-Roger adjustment. Unless otherwise stated, Tukey's test evaluated at an alpha level of 0.05 was used for all *post hoc* comparisons. Where applicable, back-transformed means derived from statistical models were plotted in figures. Where results are not shown in figures, means ± standard error are reported in the text.

RESULTS

Electrophysiological Correlates of Sound Exposure

We documented the effects of 2 weeks of passive exposure to white noise followed by 1 week of 7 kHz tone pip exposure on electrophysiological response properties in 13 rats (Exposed Group) and compared them to 11 rats that were housed in a standard acoustic environment (Naïve Group; **Figure 1A**). CF tonotopic maps were reconstructed from the left auditory cortex under isoflurane anesthesia using *in vivo* multiunit responses to presentations of tone pips of various frequencies and intensities (**Figure 1B**). Responsive sites were classified as belonging to A1, AAF, VAF, or PAF based on the published functional characteristics of each field (Polley et al., 2007; Profant et al., 2013), specifically reversal of tonotopic gradients, onset latencies, threshold, and PSTH morphologies (**Supplementary Figure S1**). Using functional properties alone, we were not able to distinguish VAF from the fifth rat auditory field, suprarhinal auditory field (SRAF), so any presumed VAF or SRAF site was classified under the common label of VAF. In addition, we did not conduct analyses on the data we obtained from PAF due to the difficulty of assigning a CF to most PAF units, which have broad and noisy tuning curves. For each animal, we determined whether we obtained full or partial A1, AAF, and VAF maps. A full map was defined by having low, medium, and high frequency regions as well as a reversal of the tonotopic gradient on one border and non-auditory sites on the opposite border. In **Figure 1B**, the representative CF maps from each group were selected for having

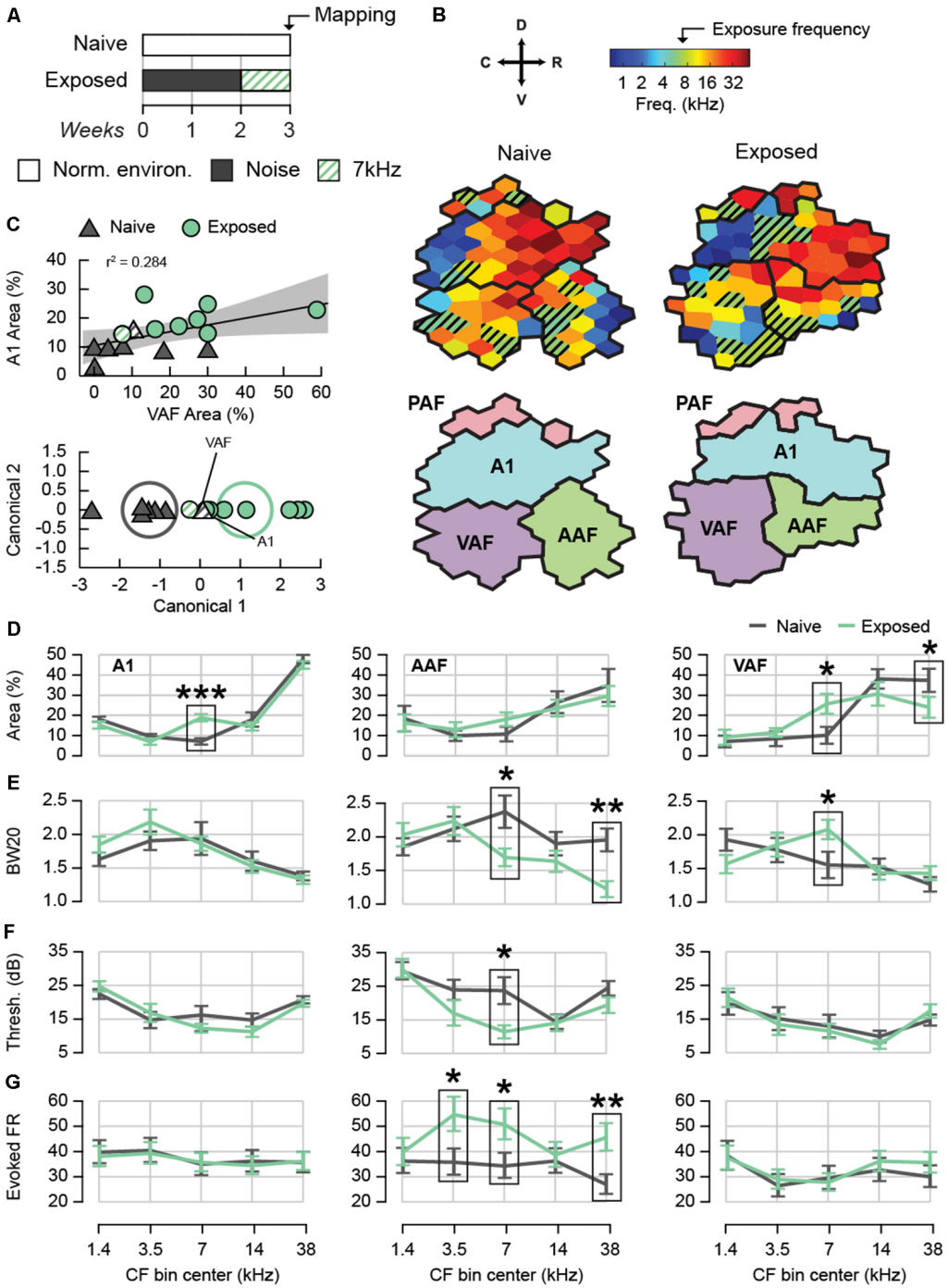

FIGURE 1 | Effect of sound exposure on cortical tuning and tone-evoked activity. **(A)** Sound exposure protocol. Naïve rats were housed in a normal acoustic environment while exposed rats were passively exposed to 2 weeks of moderate-intensity broadband white noise followed by 1 week of 7 kHz tone pips. **(B)** An example characteristic frequency (CF) map from each experimental group containing all auditory fields. Hatched sites represent those with a CF of 7 kHz $\pm \frac{1}{2}$ octave. **(C)** Top: correlation between the percent A1 area and percent VAF area with a CF of 7 kHz $\pm \frac{1}{2}$ octave. Shaded region represents 95% confidence of fit for the regression. Bottom: canonical plot of the linear discriminant analysis based on the percent of A1 and VAF area with a CF of 7 kHz $\pm \frac{1}{2}$ octave. Rats were automatically classified as either naïve or exposed; hatched points identify rats that were misclassified. Ellipses represent the 95% confidence region for the true mean of each group. **(D)** Average map area with CF in five frequency bins. Only full auditory fields were used for map percentages. **(E)** Average BW20 for receptive fields with CF in five frequency bins. **(F)** Average cortical threshold for receptive fields with CF in five frequency bins. **(G)** Average tone-evoked firing rate for units with CF in five frequency bins. $^{*}p < 0.05$, $^{**}p < 0.01$, $^{***}p < 0.001$. Error bars represent standard error of the mean (SEM). A1, primary auditory field; AAF, anterior auditory field; VAF, ventral auditory field; PAF, posterior auditory field. See **Table 1** for number of rats, recording positions, and cortical sites per auditory field and group.

TABLE 1 | Summary of data.

					Sites/Units per CF bin					
	Group	**Field**	**Rats**	**Positions**	**1.4**	**3.5**	**7**	**14**	**38**	**Total**
All data	Naive	A1	10	22	55	29	21	52	155	312
		AAF	11	22	31	16	19	35	50	151
		VAF	10	18	15	15	17	48	52	147
		PAF	10	17	-	-	-	-	-	69
		All	**11**	**24**						**679**
	Exposed	A1	13	30	47	29	67	59	187	389
		AAF	11	23	23	17	27	31	43	141
		VAF	13	27	19	21	46	62	47	195
		PAF	11	21	-	-	-	-	-	105
		All	**13**	**30**						**830**
Full fields only	Naïve	A1	10	21	53	28	21	52	136	290
		AAF	7	16	22	15	18	32	44	131
		VAF	7	12	11	13	12	43	42	121
		PAF	5	10	-	-	-	-	-	49
		All	**11**	**24**						**591**
	Exposed	A1	9	19	47	21	59	47	141	315
		AAF	8	19	23	17	25	27	37	129
		VAF	9	19	17	20	41	49	39	166
		PAF	8	18	-	-	-	-	-	99
		All	**13**	**30**						**709**
Sorted units	Naïve	A1	10	19	77	32	34	77	197	417
		AAF	11	19	33	23	18	29	65	168
		VAF	9	15	17	17	17	62	76	189
		PAF	10	17	-	-	-	-	-	110
		All	**11**	**20**						**884**
	Exposed	A1	13	25	76	36	90	80	263	545
		AAF	11	18	28	17	28	36	45	154
		VAF	13	22	25	33	62	91	59	270
		PAF	10	18	-	-	-	-	-	164
		All	**13**	**25**						**1,133**

Number of rats and recording positions from which data were obtained for each auditory field and experimental group. Number of cortical sites (or units, for sorted data) per CF bin in each field. PAF units were not assigned CFs.

full maps of each field. **Table 1** lists the number of cortical sites obtained for each auditory field and experimental group for both full and partial maps.

We first compared the degree of 7 kHz map expansion between exposed and naïve animals (**Figures 1B–D**). Using full field maps only, we calculated the percentage of map area with CFs in five frequency bins with centers at approximately 1.4, 3.5, 7, 14, and 38 kHz. The range of each bin was 1 octave except for the first and last bin, which were 1.7 and 1.8 octaves respectively. The bins were defined in relation to 7 kHz in order to maximize specificity for the middle bins while covering the full range of recorded CFs. In A1, as expected, we observed a significantly greater percentage of map area tuned to 7 kHz for the Exposed group (two-way ANOVA with Group and Bin as factors. Interaction $F_{(4,4)} = 5.30$, $p = 0.0007$ followed by simple main effects for 7 kHz $F_{(1,85)} = 16.94$, $p < 0.0001$, $n = 19$ rats). This over-representation was not compensated by a consistent under-representation in another frequency bin as no other simple main effect was significant ($F_{(1,85)} \leq 1.41$, all $p \geq 0.2387$). In AAF, we detected no difference in map area for any frequency bin (two-way ANOVA with Group and Bin as factors. Interaction: $F_{(4,4)} = 0.55$, $p = 0.6965$, $n = 15$ rats), whereas in VAF we observed a significant over-representation of the 7 kHz frequency bin for exposed animals, as well as a significant decrease in map area in the highest frequency bin (two-way ANOVA with Group and Bin as factors. Interaction $F_{(4,4)} = 2.96$, $p = 0.0257$ followed by simple main effects for 7 kHz $F_{(1,70)} = 5.85$, $p = 0.0182$ and 38 kHz $F_{(1,70)} = 4.30$, $p = 0.0418$, $n = 16$ rats). No other frequency bin was significantly changed (simple main effects $F_{(1,70)} \leq 1.33$, all $p \geq 0.2521$). To ensure that we did not oversample the 7 kHz frequency region in the Exposed group, we compared the average distance between each site and its nearest neighbor from full field maps. We observed no significant differences in nearest-neighbor distance between Naïve and Exposed animals in any frequency bin for any field, confirming that differences in frequency representation were not due to differences in sampling (mixed-effects two-way ANOVAs with Group and Bin as factors. A1: mean distance Naïve = 323.72 ± 6.82 μm, Exposed = 326.21 ± 7.14 μm, Interaction $F_{(4,579)} = 1.00$, $p = 4060$. Main effect of Group $F_{(1,17.26)} = 0.06$, $p = 0.8038$, $n = 605$ sites

within 19 rats. AAF: mean distance Naïve = 336.20 ± 11.56 μm, Exposed = 329.73 ± 10.77 μm, Interaction $F_{(4,246.8)} = 1.04$, $p = 0.3863$. Main effect of Group $F_{(1,13.31)} = 0.17$, $p = 0.6887$, $n = 260$ sites within 15 rats. VAF: mean distance Naïve = 355.58 ± 11.85 μm, Exposed = 338.55 ± 10.09 μm, Interaction $F_{(4,269.5)} = 1.73$, $p = 0.1445$. Main effect of Group $F_{(1,14.9)} = 1.20$, $p = 0.2911$, $n = 287$ sites within 16 rats). The above results document for the first time that noise-induced CP plasticity extends to A1 and VAF, but not AAF.

It is possible that not every sound-exposed rat will exhibit CP-like plasticity. However, if 7 kHz map expansion is a reliable indicator, it could be used to distinguish rats that show phenotypic CP plasticity from those that do not. We explored this possibility using a linear discriminant analysis to test the hypothesis that exposed and naive rats could be distinguished based on a linear combination of the 7 kHz percent map areas in more than one auditory field (**Figure 1C**). Only animals with full maps in both A1 and VAF were included (7 Naïve and 8 Exposed). The 7 kHz percent map area in A1 and VAF were positively correlated, $r = 0.53$, $p = 0.0408$, $n = 15$ rats (**Figure 1C**, top). This is in contrast to A1 and AAF, $r = 0.09$, $p = 0.8068$, $n = 10$ rats, and VAF and AAF, $r = 0.22$, $p = 0.5964$, $n = 8$ rats, which were not significantly correlated. The canonical function resulting from the linear discriminant analysis was statistically significant (canonical correlation = 0.79, Wilks' Lambda = 0.38, $F_{(2,12)} = 9.68$, $p = 0.0031$, $n = 15$ rats, **Figure 1C**, bottom). Reclassification of the rats based on the new canonical variable using leave-one-out cross-validation was successful: 88.10 ± 1.2% of the rats were correctly classified into their exposure condition. The canonical function was positively correlated with both 7 kHz percent map area in A1, $r = 0.99$, $p < 0.0001$, $n = 15$ rats, and VAF, $r = 0.66$, $p = 0.0069$, $n = 15$ rats. This result was approximately equivalent to performing a linear discriminant analysis using the 7 kHz percent map area in A1 alone and better than using VAF alone. When including only A1, the canonical function was significant (canonical correlation = 0.77, Wilks' Lambda = 0.41, $F_{(1,17)} = 24.15$, $p = 0.0001$, $n = 19$ rats), cross-validated reclassification led to 89.47 ± 0.41% correct classification. When including only VAF, the canonical function was also significant but less successful (canonical correlation = 0.53, Wilks' Lambda = 0.72, $F_{(1,14)} = 5.38$, $p = 0.0360$, $n = 16$ rats). Cross-validated reclassification led to 71.25 ± 1.4% correct classification. These results show that the degree of map expansion is relatively consistent within each animal; rats with high map expansion in A1 are likely to have high map expansion in VAF. This characteristic also allows rats that have undergone sound exposure to be classified with high accuracy, suggesting that degree of map expansion is a reliable indicator of CP plasticity whether taking into account only A1 or A1 and VAF together.

To establish the electrophysiological correlates of 7 kHz map expansion, we continued to compare neural response properties in five CF bins using data from both full and partial maps. We predicted that the 7 kHz-tuned neurons of exposed animals would show additional evidence of plasticity. We compared the receptive field bandwidth 20 dB above threshold (BW20), a measure of response specificity, in each auditory field (**Figure 1E**). In A1, we observed no significant change in BW20 following exposure for any CF bin (mixed-effects two-way ANOVA with Group and Bin as factors. Interaction $F_{(4,687.7)} = 1.10$, $p = 0.3545$. Main effect of Group $F_{(1,70.18)} = 0.26$, $p = 0.6093$, $n = 701$ sites within 52 positions and 23 rats). In AAF we found significantly narrower BW20s for the 7 kHz and 38 kHz bins (mixed-effects two-way ANOVA with Group and Bin as factors. Interaction $F_{(4,278.1)} = 3.32$, $p = 0.0113$ followed by simple main effects for 7 kHz $F_{(1,194.5)} = 6.25$, $p = 0.0132$ and 38 kHz $F_{(1,127.9)} = 11.94$, $p = 0.0007$. No other CF bin was significant $F_{(1,160.3–234.5)} \leq 1.42$, all $p \geq 0.2360$, $n = 292$ sites within 47 positions and 22 rats). In VAF, on the other hand, we observed broader BW20s for the 7 kHz bin (mixed-effects two-way ANOVA with Group and Bin as factors. Interaction $F_{(4,327.1)} = 2.74$, $p = 0.0288$, followed by simple main effects for 7 kHz $F_{(1,242.8)} = 5.42$, $p = 0.0207$. No other CF bin was significant $F_{(1,121.5–278.7)} \leq 2.78$, all $p \geq 0.0966$, $n = 342$ sites within 45 positions and 23 rats). These differences demonstrate a reduction in tuning specificity for VAF neurons tuned to 7 kHz following sound exposure and an increase in specificity for AAF neurons tuned to 7 kHz and 38 kHz.

Cortical thresholds measure a neuron's sensitivity to low intensity sounds and can provide an approximate estimate of hearing thresholds. We compared the average cortical thresholds of neurons in each CF bin between experimental groups (**Figure 1F**). We observed no group differences in A1 or VAF for any CF bin (mixed-effects two-way ANOVAs with Group and Bin as factors A1: Interaction $F_{(4,657)} = 1.28$, $p = 0.2761$. Main effect of Group $F_{(1,49.79)} = 0.01$, $p = 0.9190$, $n = 701$ sites within 52 positions and 23 rats. VAF: interaction $F_{(4,310.9)} = 0.71$, $p = 0.5867$. Main effect of Group $F_{(1,43.54)} = 0.02$, $p = 0.8924$, $n = 342$ sites within 45 positions and 23 rats). In AAF, however, we found that average thresholds were significantly lower for the 7 kHz bin (mixed-effects two-way ANOVA with Group and Bin as factors. Interaction $F_{(4,255.6)} = 2.41$, $p = 0.0494$ followed by simple main effects for 7 kHz ($F_{(1,124.8)} = 4.70$, $p = 0.0320$. No other CF bin was significant $F_{(1,67.93–156.3)} \leq 2.28$, $p \geq 0.1334$, $n = 292$ sites within 47 positions and 22 rats). These results show that after sound exposure, AAF became more sensitive to the 7 kHz frequency. Importantly, the cortical thresholds of the Exposed group were either the same or lower than Naïve for all fields, demonstrating that the exposure intensities were non-traumatic and did not cause any apparent hearing loss. Taken together, the changes in BW20 and cortical thresholds observed in sound-exposed animals may highlight differences in the receptive field properties of AAF and VAF. VAF neurons tend to have narrow tuning curves with low thresholds while AAF neurons tend to have broad tuning curves with relatively high thresholds. Plasticity following sound exposure appears to have reduced these field-specific qualities for 7 kHz-tuned neurons.

Sound-evoked firing rates are elevated in hyperacusis (Sun et al., 2012; Aazh et al., 2014; Hickox and Liberman, 2014). We compared the tone-evoked firing rate between exposed

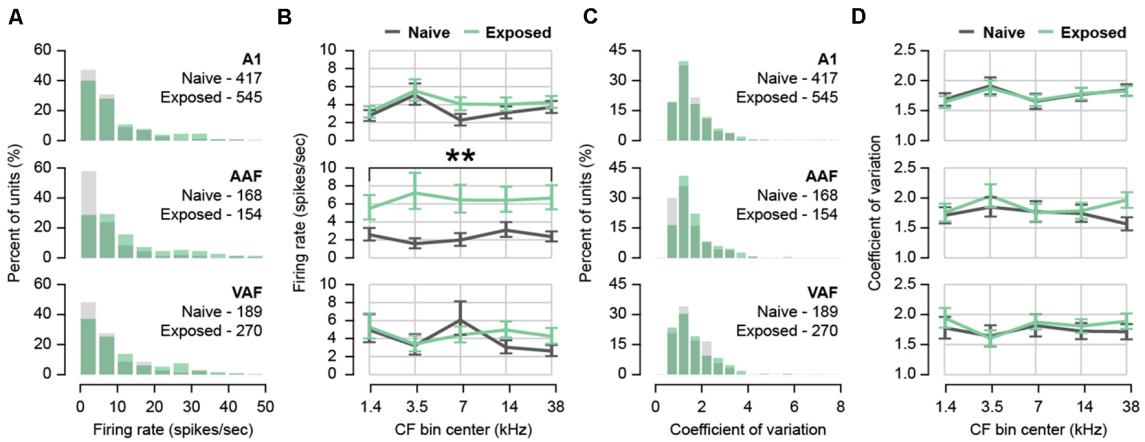

FIGURE 2 | Effect of sound exposure on spontaneous firing rate and burst firing. **(A)** Histogram of firing rates for each auditory field. N units per field and group in inset. **(B)** Back-transformed mean firing rate with CF in five frequency bins for each auditory field. **(C)** Histogram of coefficient of variation (CV) for each auditory field. N units per field and group in inset. **(D)** Back-transformed mean CV in five frequency bins for each auditory field. $^{**}p < 0.01$. Error bars represent SEM. A1, primary auditory field; AAF, anterior auditory field; VAF, ventral auditory field. See **Table 1** for number of rats, recording positions, and units per auditory field and group.

and naive animals (**Figure 1G**). The average firing rate in response to the full range of tonal stimuli (66 frequencies presented at eight intensities) was considered. The rate was computed from the number of spikes counted between 8 and 58 ms after tone presentation minus the number of spikes counted in the 50 ms preceding tone presentation. As could be expected, firing rate was positively correlated with sound intensity, $r = 0.11$, $p < 0.0001$, $n = 7{,}093$ observations. We also found that onset latency was negatively correlated with firing rate, $r = -0.20$, $p < 0.0001$, $n = 7{,}093$ observations, possibly because a fixed epoch window resulted in less spikes being counted for sites with later latencies. We did not observe a significant difference in onset latency between naïve and exposed animals for any field (mixed effects two-way ANOVAs with Group and Bin as factors. A1: Interaction $F_{(4,678.3)} = 1.74$, $p = 0.1403$. Main effect of Group $F_{(1,64.63)} = 0.39$, $p = 0.5325$, $n = 701$ sites within 52 positions and 23 rats. AAF: interaction $F_{(4,253.2)} = 1.74$, $p = 0.1414$. Main effect of Group $F_{(1,34.73)} = 3.00$, $p = 0.0920$, $n = 292$ sites within 47 positions and 22 rats. VAF: interaction $F_{(4,317.9)} = 0.13$, $p = 0.9698$. Main effect of Group $F_{(1,37.34)} = 0.09$, $p = 0.7683$, $n = 342$ units within 45 positions and 23 rats). As a result, we performed two-way ANCOVAs with intensity and latency as covariates to determine whether the tone-evoked firing rate differed between experimental groups controlling for these two variables. We did not find a significant difference between groups for any CF bin in A1 or VAF (mixed effects two-way ANCOVAs with Group and Bin as factors. A1: interaction $F_{(4,3662)} = 0.35$, $p = 0.8456$. Main effect of Group $F_{(1,50.68)} = 0.01$, $p = 0.9073$, $n = 3{,}697$ observations within 52 positions and 23 rats. VAF: interaction $F_{(4,1937)} = 1.38$, $p = 0.2393$. Main effect of Group $F_{(1,40.82)} = 0.10$, $p = 0.7516$, $n = 1{,}965$ observations within 45 positions and 23 rats). In AAF, however, we observed a significantly higher tone-evoked firing rate for the 3.5 kHz, 7 kHz, and 38 kHz bins (mixed effects two-way ANCOVAs with Group and Bin as factors. Interaction $F_{(4,1398)} = 9.02$, $p < 0.0001$ followed by simple main effects for 3.5 kHz $F_{(1,60.06)} = 4.39$, p 0.0403, 7 kHz $F_{(1,67.83)} = 4.99$, $p = 0.0288$, and 38 kHz $F_{(1,47.66)} = 8.03$, $p = 0.0067$. No other CF bins were significant $F_{(1,51.18-60.75)} \leq 0.23$, both $p \geq 0.63$, $n = 1{,}431$ observations within 47 positions and 22 rats) For all of the ANCOVAs above, intensity ($F_{(1,1383-3646)} \geq 35.56$, all $p \leq 0.0001$) and latency ($F_{(1,1406-3666)} \geq 78.36$, all $p \leq 0.0001$) remained significant factors. These results show that after sound exposure, tone-evoked firing rate was greater within AAF for neurons tuned to a broad range of frequencies.

Tinnitus and hyperacusis are associated with higher spontaneous firing rates (Wang et al., 2011; Kaltenbach, 2011), and tinnitus in particular is associated with more burst firing in the auditory pathway including the auditory thalamus (Kalappa et al., 2014) and auditory cortex (Syka and Rybalko, 2000; Noreña and Eggermont, 2003). From 5-min-long recordings of spontaneous activity during silence, we computed the spontaneous firing rate and inter-spike intervals (ISIs) of single-unit activity (**Figure 2**). Each sorted unit was assigned an auditory field and CF based on sound-evoked responses in the same recording position resulting in a total of 1,743 units from A1, AAF, and VAF combined. The number of units included in each auditory field and group is listed in **Table 1**. Because the distribution of firing rates was positively skewed (**Figure 2A**), we applied a natural logarithmic transform before statistical analyses. Back-transformed means are plotted in **Figure 2B**. The average spontaneous firing rates of our naïve animals were as follows: A1 = 5.33 ± 0.33, AAF = 4.77 ± 0.58, VAF = 5.67 ± 0.57 spikes/second. After sound exposure, we did not observe any difference in spontaneous firing rates in A1 or VAF regardless of CF bin (mixed effects two-way ANOVAs with Group and Bin as factors. A1: Interaction $F_{(4,932.2)} = 0.85$, $p = 0.4951$. Main effect of Group $F_{(1,40.85)} = 1.04$, $p = 0.3134$, $n = 962$ units within 44 positions and 23 rats. VAF: Interaction $F_{(4,442.9)} = 1.65$, $p = 0.1596$. Main effect of Group

$F_{(1,37.86)} = 0.34$, $p = 0.5626$, $n = 459$ units within 37 positions and 22 rats). In AAF, on the other hand, sound exposure led to a significant and uniform increase in firing rate for all CF bins (mixed effects two-way ANOVA with Group and Bin as factors. Interaction $F_{(4,304.7)} = 1.06$, $p = 0.3759$. Main effect of Group $F_{(1,39.57)} = 14.67$, $p = 0.0004$, $n = 322$ units within 37 positions and 22 rats). The increased spontaneous firing rate in AAF indicates strong, tuning-independent hyperactivity resulting from sound exposure.

The ISI coefficient of variation (CV) was used to estimate the bursting activity of auditory neurons. This measure was obtained by dividing the standard deviation of each unit's ISI distribution by its mean (Longenecker and Galazyuk, 2016). A high CV indicated more irregular spiking intervals, suggestive of bursting. Again, the distribution of CVs was positively skewed (**Figure 2C**) so a natural logarithmic transform was applied before statistical analyses and back-transformed means are plotted in **Figure 2D**. We did not observe any difference in the average CV of any field after sound exposure (mixed effects two-way ANOVAs with Group and Bin as factors. A1: Interaction $F_{(4,932.3)} = 0.07$, $p = 0.9908$. Main effect of Group $F_{(1,39.63)} = 0.01$, $p = 0.9126$, $n = 962$ units within 44 positions and 23 rats. AAF: Interaction $F_{(4,306.8)} = 1.40$, $p = 0.2325$. Main effect of Group $F_{(1,36.99)} = 0.78$, $p = 0.3842$, $n = 322$ units within 37 positions and 22 rats. VAF: Interaction $F_{(4,433.8)} = 0.32$, $p = 0.8627$. Main effect of Group $F_{(1,33)} = 0.30$, $p = 0.5886$, $n = 459$ units within 37 positions and 22 rats). From this, we concluded that burst firing was unchanged in the auditory cortex following sound exposure.

Tinnitus has also been associated with hypersynchronization in animal models. Hypersynchronization typically appears immediately after noise trauma in a frequency-specific manner (Eggermont and Roberts, 2004) and is evidence of increased connectivity, either thalamocortical or corticocortical, between neurons. To assess whether the Exposed group displayed hypersynchronization, we calculated normalized cross-correlograms between single-unit pairs recorded in silence (**Figure 3**). From the 1,743 units detected above, we identified 16,441 unit pairs in separate channels. We limited our analysis to pairs with a peak between −150 and 150 ms, falling within approximately ±2.3 standard deviations of the mean peak, resulting in a total of 14,008 unit pairs for all fields. **Figure 3A** shows histograms of the cross-correlogram peak lag times demonstrating that peaks tend to fall near 0 ms and **Figure 3B** shows the average cross-correlogram for all pairs in each field. The peak value of the cross-correlogram tended to decrease with greater inter-unit distance, $r = -0.24$, $p < 0.0001$, $n = 14{,}008$ pairs, as well as greater ΔCF, $r = -0.24$, $p < 0.0001$, $n = 14{,}008$ pairs. Distance and ΔCF were positively related, $r = 0.42$, $p < 0.0001$, $n = 14{,}008$ pairs. As a result, we performed mixed-effects two-way ANCOVAs with distance as a covariate to determine whether the peak correlation coefficient differed between exposure groups while controlling for differences in inter-unit distance (**Figure 3C**). As the distribution of peaks was positively skewed, we multiplied the data, originally on a 0–1 scale, by 100 and applied a natural logarithmic transform before statistical analyses. In **Figure 3C**, the difference between back-transformed group means for each CF bin combination is depicted by a heatmap. The interaction was significant for A1, AAF, and VAF (mixed effects two-way ANCOVAs with Group and Combined CF Bin as factors and Distance as covariate: A1 $F_{(24,9632)} = 5.35$, $p < 0.0001$, AAF $F_{(24,1407)} = 2.16$, $p = 0.0009$, VAF $F_{(24,2730)} = 1.88$, $p = 0.0060$). The simple main effect of Group was evaluated over each level of Combined CF Bin and the significant comparisons are outlined in bold on the heatmap in **Figure 3C**. Distance remained a significant covariate in each ANCOVA (A1 $F_{(1,9650)} = 358.29$, $p < 0.0001$, AAF $F_{(1,1406)} = 47.43$, $p < 0.0001$, VAF $F_{(1,2740)} = 47.48$, $p < 0.0001$). From the heatmaps, we observed few significant differences in synchronization strength. Sound-exposed A1 and VAF tended to have shorter cross-correlograms for most frequency combinations, with peak values being significantly smaller for low-to-medium frequency combinations only. In AAF, differences with respect to naïve animals were less consistent. Only synchronization between unit pairs where both units had CFs in the 38 kHz bin was significantly greater.

The strength of synchronization can also be estimated by the width of the cross-correlogram, with wider functions representing greater synchronization at longer lag times. The width at half-height of each peak was compared between exposure groups as a function of CF bin (**Figure 3D**). Width could not be computed for 38 pairs for which the function did not dip below half-height, resulting in 13,970 analyzed pairs. Width was found to weakly but significantly increase with inter-unit distance, $r = 0.03$, $p = 0.0009$, $n = 13{,}970$ pairs, and ΔCF, $r = 0.03$, $p = 0.0013$, $n = 13{,}970$. However, distance did not remain significant when included as a covariate for any field (mixed effects two-way ANCOVAs with Group and Combined CF Bin as factors and Distance as covariate. Effect of Distance: A1 $F_{(1,9651)} = 0.22$, $p = 0.6381$, AAF $F_{(1,1403)} = 0.003$, $p = 0.9545$, VAF $F_{(1,2739)} = 0.41$, $p = 0.5239$). As a result, we removed the covariate and performed mixed-effects two-way ANOVAs. The interaction was significant for A1, AAF, and VAF (mixed effects two-way ANOVA with Group and Combined CF Bin as factors: A1 $F_{(24,9499)} = 4.12$, $p < 0.0001$, AAF $F_{(24,1422)} = 2.60$, $p < 0.0001$, VAF $F_{(24,2741)} = 1.67$, $p = 0.0214$). The simple main effect of Group was evaluated over each level of Combined CF Bin and the significant comparisons are outlined in bold on the heatmap in **Figure 3D**. In the heatmaps, we observed clear wider cross-correlograms in the sound-exposed A1, AAF, and VAF. In A1, this trend showed units in low-to-mid frequency bins having wider cross-correlograms with units in the highest frequency bins. In AAF, almost every frequency bin combination tended to have wider cross-correlograms, with significant differences in the mid-to-high frequency combinations, and notably with the 7 kHz bin showing the greatest increase in width. Interestingly, VAF showed an opposite trend, where only the lowest frequency bins had significantly wider cross-correlograms when paired with the highest frequency bins. The mid-range bins, including 7 kHz, showed either no change in width or a slight decrease in width for VAF.

A greater average cross-correlogram width could result from either more pairs with broad cross-correlograms or more pairs with off-centered peaks. To investigate the contribution of pairs with off-centered peaks to the wider cross-correlograms we

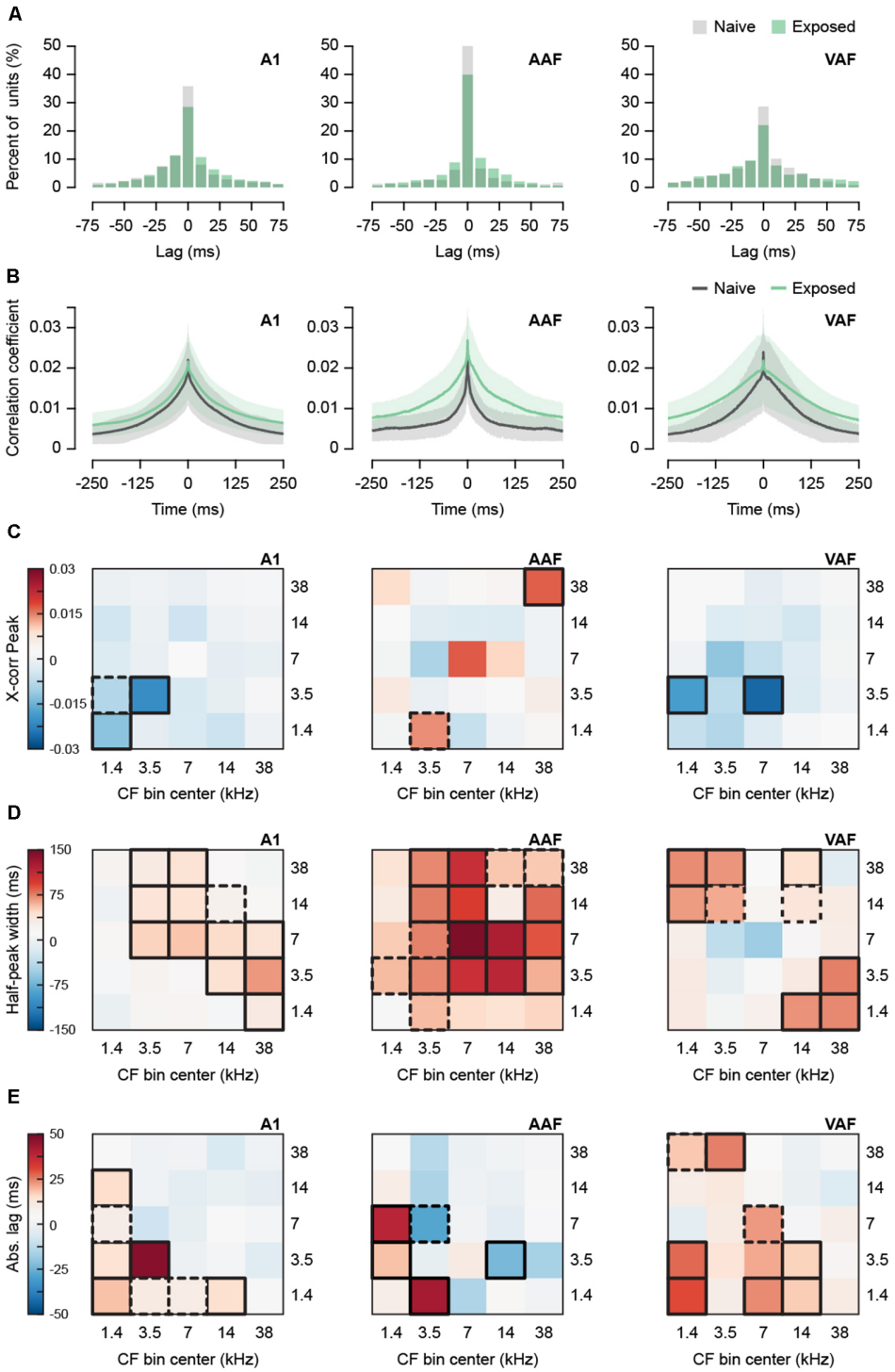

FIGURE 3 | Effect of sound exposure on spontaneous synchronization. **(A)** Histogram of lag times of the peak of the cross-correlogram for all recorded unit pairs in A1, AAF, and VAF. Data for lag times outside −75 and 75 are not shown. **(B)** Average cross-correlogram for all unit pairs detected in separate channels in A1, AAF, and VAF. Shaded region represents SEM. **(C)** Subtracted (Exposed—Naïve) difference between average peak correlation coefficient for unit pairs with CF in five frequency bins. **(D)** Subtracted (Exposed—Naïve) difference between average half-peak width for unit pairs with CF in five frequency bins. **(E)** Subtracted (Exposed—Naïve) difference between average time lag in absolute values of the peak of the cross-correlogram. Bolded boxes are significant with $p < 0.05$. Dashed boxes represent p-values < 0.10. A1, primary auditory field; AAF, anterior auditory field; VAF, ventral auditory field; CF, characteristic frequency. N unit pairs per auditory field and group: Naïve A1 3,614; AAF 746; VAF 1,092. Exposed A1 6,116; AAF 733; VAF 1,707. See **Table 1** for number of rats, recording positions, and units per auditory field and group.

observed in each field, we conducted mixed-effects two-way ANCOVAs with distance as a covariate on the absolute lag of the peak of the cross-correlogram (**Figure 3E**). Distance was positively correlated with absolute lag, $r = 0.23$, $p < 0.0001$ $n = 14{,}008$ pairs. The interaction between exposure group and CF bin was significant for A1, AAF, and VAF (mixed effects two-way ANCOVA with Group and Combined CF Bin as factors and Distance as covariate: A1 $F_{(24,9499)} = 4.12$, $p < 0.0001$, AAF $F_{(24,1422)} = 2.60$, $p < 0.0001$, VAF $F_{(24,2741)} = 1.67$, $p = 0.0214$). The simple main effect of Group was evaluated over each level of Combined CF Bin and the significant comparisons are outlined in bold on the heatmap in **Figure 3E**. Distance remained a significant covariate for all three fields (A1 $F_{(1,9679)} = 305.61$, $p < 0.0001$, AAF $F_{(1,1427)} = 7.50$, $p = 0.0062$, VAF $F_{(1,2748)} = 45.29$, $p < 0.0001$). The heatmaps revealed mostly increases in absolute lag for the Exposed group, suggestive of a greater number of off-centered peaks. However, in A1 and AAF, the CF bins with greater absolute lag did not correspond with those that showed the broadest widths in **Figure 3D**. This suggests that a greater number of broadly synchronized unit pairs contribute to the wider cross-correlograms in these fields. In VAF, some CF bins with wider cross-correlograms corresponded with bins that also had greater absolute lag, indicating a mixed contribution between broader synchronization and off-centered peaks.

Behavioral Correlates of Sound Exposure

A common behavioral measure for detecting tinnitus in rodents is gap-prepulse inhibition of the acoustic startle response (GPIAS), in which a short silent gap within a background sound carrier reduces the magnitude of a rodent's involuntary startle to a subsequent loud noise burst (Brozoski and Bauer, 2016). Impaired GPIAS is considered evidence of tinnitus in rodents, meaning that the gap is less effective at reducing the startle response, possibly because the presence of tinnitus interferes with the ability to hear silence. This test is usually accompanied by a similar measure called prepulse inhibition (PPI) of the acoustic startle response. PPI has been proven useful in characterizing hyperacusis and hypoacusis, since a short tonal stimulus will either enhance or dampen inhibition of the startle response in rodents with hyper- or hypoacusis, respectively (Carlson and Willott, 1996; Turner and Parrish, 2008; Turner and Larsen, 2016; Pienkowski, 2018). To investigate whether sound exposure could have altered these behavioral measures, we performed GPIAS and PPI testing on two additional groups of naïve (Naïve-BEH, $N = 12$) and exposed (Exposed-BEH, $N = 12$) rats.

We found that the Exposed-BEH group did not differ from Naïve-BEH in GPIAS (**Figure 4**). A schematic of the behavioral protocol for GPIAS is presented in **Figure 4A**. We hypothesized that a deficit in inhibition of the acoustic startle response would be specific to the 7 kHz exposure frequency. To test this, we performed testing in the presence of either a 7 kHz pure tone background or a 3.5 kHz pure tone background with the order of testing counterbalanced between pairs. First, we confirmed that the magnitude of the response to the startle pulse alone was not significantly different between groups for either pure tone condition (7 kHz: two-tailed paired t-test $t_{(11)} = -0.81$, $p = 0.4372$, Cohen's dav −0.32; 3.5 kHz: two-tailed paired t-test $t_{(11)} = -0.08$, $p = 0.9371$, Cohen's dav −0.03, $n = 12$ pairs, **Figures 4B,C**, bottom left). Next, we computed the percent reduction in the startle response when the startle pulse was preceded by a silent gap. We found that the average reduction in startle did not differ between groups for either the 7 kHz (one-tailed paired t-test $t_{(11)} = -0.45$ $p = 0.3303$, Cohen's dav −0.22, $n = 12$ pairs, **Figure 4B**) or the 3.5 kHz (one-tailed paired t-test $t_{(11)} = 0.44$ $p = 0.6656$, Cohen's dav 0.20, $n = 12$ pairs, **Figure 4C**) condition. From these results, we concluded that sound exposure did not lead to behavioral evidence of tinnitus in any frequency tested.

We observed an enhancement in PPI for the Exposed-BEH group when the prepulse was a 7 kHz tone (**Figure 5**). A schematic of the behavioral protocol for PPI is presented in **Figure 5A**. Of note, a magnified response to the startle pulse alone is also sometimes taken as evidence of hyperacusis (Chen et al., 2013), but we hypothesized that an improvement in inhibition of the acoustic startle response would be specific to the 7 kHz exposure frequency. As a result, we performed PPI testing using either a 7 kHz or 3.5 kHz pure tone prepulse with the order of 7 kHz prepulse, 3.5 kHz prepulse, and no prepulse trials randomly interleaved within a single testing session. Testing took place in the presence of a 65 dB white noise background. We observed that the magnitude of the response to the startle pulse alone was not significantly different between groups (paired t-test $t_{(11)} = -0.21$, $p = 0.8343$, Cohen's dav −0.09, $n = 12$ pairs, **Figure 5B**, bottom left). Next, we compared the average percent reduction in the startle response when the startle pulse was preceded by a prepulse tone. We found that the average reduction in startle was significantly greater for the Exposed-BEH group when the prepulse was a 7 kHz tone (one-tailed paired t-test $t_{(11)} = 2.69$ $p = 0.0105$, Cohen's dav 0.63, $n = 12$ pairs, **Figure 5B**) but not when the prepulse was a 3.5 kHz tone (one-tailed paired t-test $t_{(11)} = 0.66$ $p = 0.2621$, Cohen's dav 0.29, $n = 12$ pairs, **Figure 5C**) condition. Our positive findings remained significant when adjusting the alpha value to account for three comparisons using either the Bonferroni or Holms-Bonferroni correction (both $\alpha = 0.0167$). From these results, we concluded that Exposed-BEH exhibited behavioral evidence of hyperacusis for the 7 kHz frequency.

DISCUSSION

Passive exposure to moderate-intensity broadband white noise can be used to open a CP window for frequency tuning in the adult rat auditory cortex, allowing for subsequent frequency-specific reorganization of the tonotopic map. This phenomenon could have profound implications for plasticity-based neurotherapeutics that aim to improve learning and memory or treat disorders of plasticity through non-invasive means. However, frequency-specific tonotopic map expansions and regional changes in excitability have also been described as symptoms of tinnitus and hyperacusis in animal models, leading us to wonder whether noise exposure could increase the risk of developing one or both of these disorders. In the present investigation, we extended previous studies by examining the effects of noise and tone pip exposure on secondary

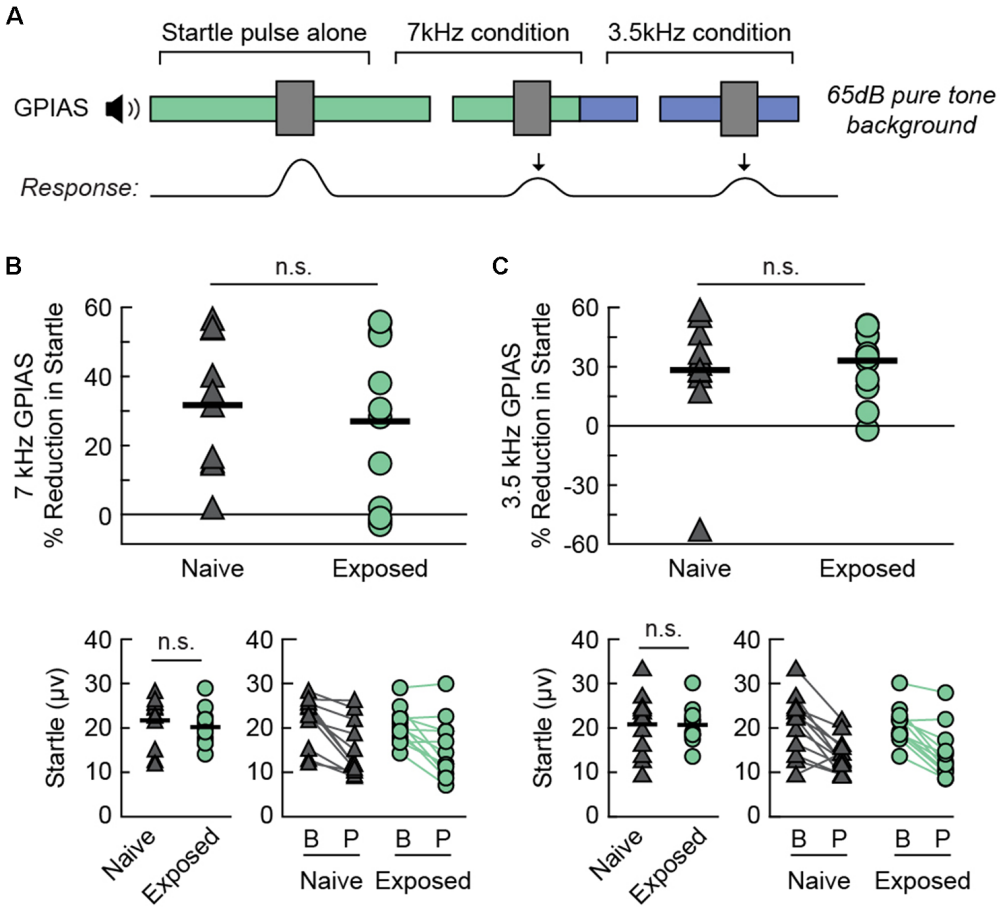

FIGURE 4 | Sound exposed rats demonstrate no change in GPIAS. **(A)** A schematic drawing of the behavioral protocol. Testing takes place in the presence of a 65 dB SPL continuous pure tone (3.5 or 7 kHz). A 30 ms silent gap prepulse preceding the startle sound (40 ms white noise burst, 120 dB SPL) reduces the magnitude of the acoustic startle response. **(B)** Percent GPIAS (Top), baseline startle response (Bottom Left), and comparison of startle response between Baseline (B) and Prepulse (P) trials (Bottom Right) in the presence of a 7 kHz pure tone background. Lines connect responses from the same animal. **(C)** Percent GPIAS (Top), baseline startle response (Bottom Left), and comparison of startle response between Baseline (B) and Prepulse (P) trials (Bottom Right) in the presence of a 3.5 kHz pure tone background. Lines connect responses from the same animal. Ns, not significant. *N* rats per group: 12 Naive, 12 Exposed. GPIAS, Gap-Prepulse Inhibition of the Acoustic Startle response.

auditory fields and carried out novel experiments to determine whether sound-exposed animals display evidence of tinnitus or hyperacusis.

As in previous studies (Zhou et al., 2011; Thomas et al., 2018), we observed map expansion in the A1 of adult rats passively exposed to moderate-intensity broadband white noise followed by tone pips with no elevation in cortical thresholds. We also showed for the first time that a CP-like window is also opened in VAF as demonstrated by map expansion in this field accompanied by broader receptive field bandwidths for 7 kHz-tuned neurons. Apart from map expansion, however, we observed few changes in spontaneous activity or auditory processing in the A1 and VAF of exposed animals. In contrast, we observed strong evidence of hyperactivity in AAF, where there was no map expansion. This included an overall increased spontaneous firing rate, stronger tone-evoked firing rates and narrower receptive field bandwidths for a range of frequencies, and a lower cortical threshold for 7 kHz-tuned neurons. Despite changes in AAF affecting multiple iso-frequency bands, the band corresponding to 7 kHz showed changes consistent with heightened sensitivity in all of our measures. Our behavioral results also pointed to enhanced sensorimotor gating for the 7 kHz frequency, since exposed rats had improved PPI when the prepulse was a 7 kHz pure tone. Taken together, our findings point to hyperacusis for the 7 kHz frequency in sound-exposed animals.

We expected hypersynchronization to accompany map expansion given the close link between receptive field overlap and neural synchronization (Noreña and Eggermont, 2006; Eggermont, 2007; Kilgard et al., 2007). However, we did not observe clear hypersynchronization in any field. The absence of this relationship could be due to the unique manner in which noise induces plasticity. Noise exposure on its own produces lasting desynchronization with shorter cross-correlogram peaks

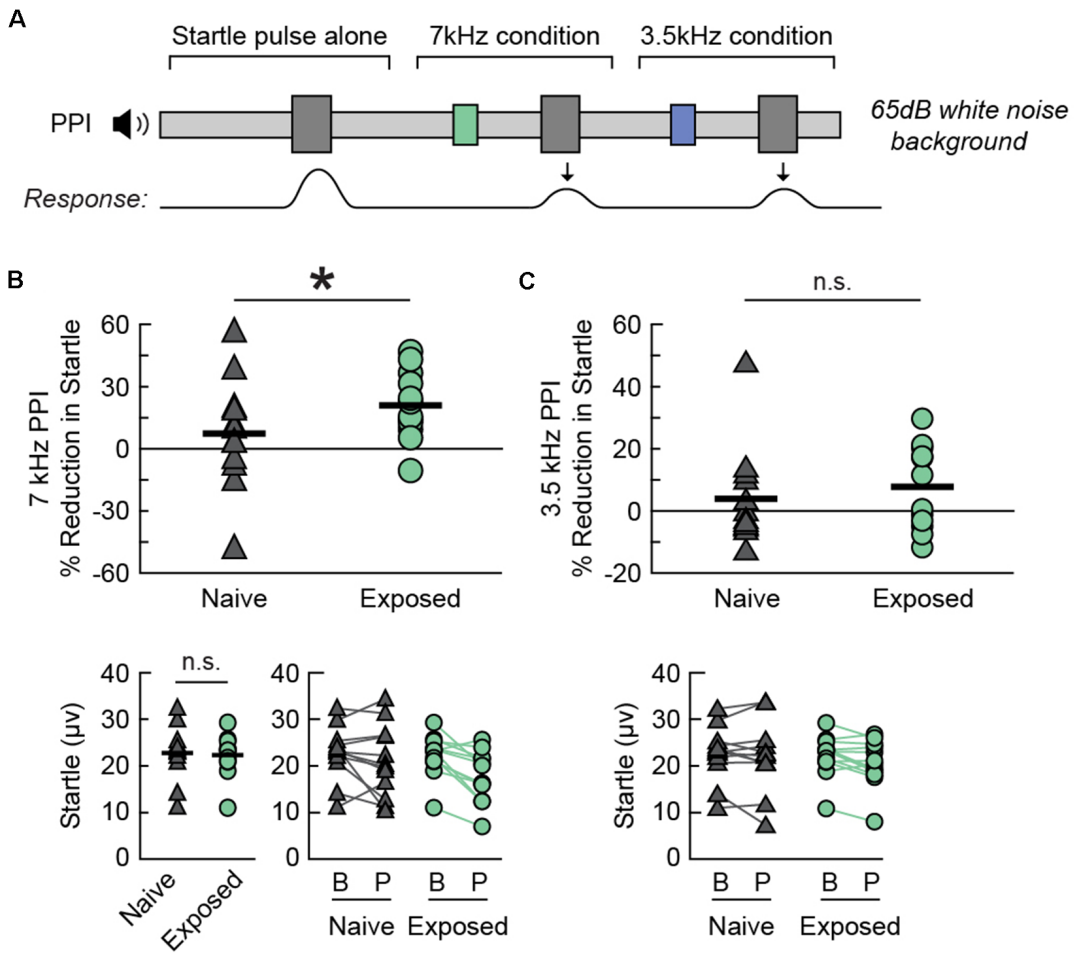

FIGURE 5 | Sound exposed rats demonstrate a frequency-specific enhancement in PPI. **(A)** A schematic drawing of the behavioral protocol. Testing takes place in the presence of a continuous 65 dB SPL background noise. A 20 ms tone pip (3.5 or 7 kHz, 75 dB SPL) preceding the startle sound (40 ms white noise burst, 120 dB SPL) reduces the magnitude of the acoustic startle response. **(B)** Percent PPI (Top), baseline startle response (Bottom Left), and comparison of startle response between Baseline (B) and Prepulse (P) trials (Bottom Right) when the prepulse is a 7 kHz tone. Lines connect responses from the same animal. **(C)** Percent PPI (Top) and comparison of startle response between Baseline (B) and Prepulse (P) trials (Bottom) when the prepulse is a 3.5 kHz tone. Lines connect responses from the same animal. Note that the same baseline startle values were used for computing PPI in **(B,C)**. $^*p < 0.05$, ns, not significant. *N* rats per group: 12 Naive, 12 Exposed. PPI, Prepulse Inhibition of the acoustic startle response.

in A1 (Zhou et al., 2011; Kamal et al., 2013; Thomas et al., 2018). The prevalence of lower peaks and broader cross-correlogram widths observed in A1 and VAF could be consistent with these earlier findings, assuming partial recovery of desynchronization potentially hastened by tone pip exposure. The broader widths that we observed in AAF centered on 7 kHz are likely the combined result of greater disinhibition and increased firing, since secondary effects independent of connectivity can also affect the width of the cross-correlogram. These include firing patterns intrinsic to each neuron, such as burst firing, and global oscillations (Eggermont and Smith, 1996; Nowak and Bullier, 2005). Although cross-correlograms were normalized with respect to firing rate and significant differences in burst firing measured by CV were not observed, a higher firing rate could increase the impact of secondary effects on cross-correlogram width. Clear evidence of disinhibition or changes in firing were not observed in A1 or VAF in the present study, therefore assumptions about the origin of broader cross-correlogram widths beyond residual effects of noise exposure remain speculative.

The role of the auditory cortex in generating tinnitus and hyperacusis has not been fully established. Although changes in neural activity related to hearing loss begin in the auditory nerve and cochlear nucleus, individuals with clinically normal audiograms can also report these percepts, and electrophysiological signatures of each condition have been reported in cortex in animal models. In addition, studies have primarily identified A1 and the auditory thalamus (medial geniculate body, MGB) as sites of experience-dependent plasticity following non-traumatic passive sound exposures (Pienkowski and Eggermont, 2011; Lau et al., 2015; Pienkowski, 2018), revealing a possible mechanism by which passive

experience could lead to changes in auditory processing in the absence of hearing loss. Here, we observed a significant difference between the electrophysiological response properties of A1 and AAF following noise exposure that may suggest a causal role for AAF in the generation of hyperacusis. Whereas A1 has been studied extensively in the context of passive sound exposure, much less is known about how AAF adapts to such experiences. Sparse findings demonstrate asymmetric plasticity in each field despite both receiving direct inputs from the ventral MGB and displaying similar tone-evoked response properties (Polley et al., 2007). Takahashi et al. (2006) found that A1 responses of juvenile mice were more potentiated than those of AAF following exposure to an amplitude-modulated tone for 4–5 weeks but did not observe an over-representation of the exposure frequency in either field. A recent study documented differences in parvalbumin positive (PV+) interneuron and peri-neuronal net (PNN) densities in A1 and AAF following 70 dB SPL broadband noise exposure in mice during the first month of life (Reinhard et al., 2019). Noise exposure decreased the density of PNNs in A1 but not AAF, showing that inhibitory elements can be differently regulated across these two fields. Given the preliminary nature of our study, further studies should be undertaken to understand the potential mechanisms by which AAF could contribute to hyperacusis.

The sound exposure paradigm used to induce 7 kHz map expansion consisted of two distinct components: white noise exposure and 7 kHz tone pip exposure. On its own, chronic exposure to moderate-intensity white noise has been shown to lead to tonotopic disorganization, broadened receptive field bandwidths, decreased neural synchronization, and disrupted temporal processing. These plastic changes develop whether the noise is present for 2 weeks (Thomas et al., 2018), 6–8 weeks (Zhou et al., 2011; Kamal et al., 2013), or on a 10-h-per-day schedule (Zhou and Merzenich, 2012). As long as the noise is broadband, its effects are non-frequency-specific as illustrated by comparison with band-limited noise exposure (de Villers-Sidani et al., 2008). In the present study, the most prominent electrophysiological measure that was affected in a non-frequency-specific manner was the increased spontaneous firing rate in AAF, and it is possible that this change was driven primarily by white noise exposure. Exposure to non-traumatic white noise has been scarcely studied in the context of PPI or GPIAS, especially in contrast to traumatic noise exposures. One exception is a recent study that found that band-limited noise exposure did not produce either hyper- or hypoacusis in mice exposed for 3 months (Pienkowski, 2018).

Taken alone, exposure to pure tones has not been shown to induce strong cortical plasticity leading to map expansion or altered discrimination abilities for the exposure frequency in adult rodents (Zhou et al., 2011; Blundon et al., 2017). This is consistent with the view that the mature cortex is largely resistant to change based on passively experienced stimuli (Keuroghlian and Knudsen, 2007). However, extensive research performed in cat auditory cortex has shown convincingly that band-limited tone pip ensembles can lead to frequency-specific changes in auditory responsiveness after chronic exposure (Pienkowski and Eggermont, 2009, 2010; Pienkowski et al., 2011). Specifically, cortical regions tuned to the exposure frequency range show reduced responsiveness while cortical regions outside the exposure frequency range show increased responsiveness. This suggests that there could be detectable differences in the electrophysiological properties of the auditory cortex after tone pip exposure that could also alter behavioral responses to PPI or GPIAS. However, extrapolating from these results one would expect animals exposed to 7 kHz to display hypoacusis for this frequency. Consequently, we do not believe that tone pip exposure on its own would cause increased cortical sensitivity to 7 kHz.

A limitation of the present study is that in the interest of reducing the number of animals used, the electrophysiological data for the Exposed group came from combining two groups of sound-exposed animals that underwent slightly different 7 kHz exposures (i.e., 7 kHz tone pips vs. 7–8.3 kHz tone pip clouds, see "Materials and Methods" section). It is likely that these exposures would produce different electrophysiological signatures. For example, we would expect tone pip clouds to lead to map expansion for a broader frequency range. To account for this, we used relatively coarse ($\geq$1 octave) CF bins in our analysis so that the 7 kHz bin spanned 5–10 kHz and presumably encompassed all neurons that would have shifted their CFs to the exposure frequencies. However, the combined group contained a greater number of rats exposed to tone pip clouds (n = 9) than tone pips (n = 4), so it is possible that the average data is a better representation of the tone pip cloud exposure. The Exposed-BEH group, on the other hand, was not heterogeneous; every rat was exposed to the tone pip stimulus. As a result, the Exposed group used for electrophysiology is not a perfect analogue for the Exposed-BEH group. Furthermore, because the animals used for behavioral testing in our study were not the same animals that were used for electrophysiological recording, we were unable to correlate auditory response properties with PPI or GPIAS. This additionally prevents us from making any direct conclusions about cortical properties, such as degree of map expansion, that may have influenced inhibition of the acoustic startle response.

A second limitation is that classifying auditory fields based purely on functional characteristics will always result in an imperfect classification. It is possible that some cortical sites, especially those on borders with CF gradient reversals (such as A1 and AAF), were misclassified as being in neighboring fields. Of note, we were unable to distinguish VAF and SRAF based purely on functional properties and therefore pooled the data from these fields. These challenges are not unique to our study, and there is precedence for pooling VAF and SRAF with sparse datasets (Takahashi et al., 2011). Without accompanying anatomical tracer data or similar, conclusions about the response properties of any auditory field should only be drawn from multiple independent replications. Importantly, an experimenter blind to the identity of the experimental groups performed field classification for the present study. The average response properties reported for each field in **Supplementary Figure S1** are in strong agreement with the published literature on the adult rat auditory cortex (Polley et al., 2007; Profant et al., 2013).

Finally, stress is another factor that could have played a role in our results, as it is known to affect PPI (Guercio et al.,

2014). Importantly, chronic noise exposure, even at moderate intensities, is a known stressor for humans and animals and has a complex interplay with tinnitus, mostly exacerbating its symptoms (Eggermont, 2017a). The chronic sound exposures used in our study could have caused stress that could affect the acoustic startle response or PPI. The main argument against this, however, is that we did not observe differences in baseline startle response between exposed and unexposed animals. Furthermore, any stress-induced differences in PPI or GPIAS would likely not have been specific to the 7 kHz frequency.

In summary, our study examines the phenomenon of noise-induced map expansion and demonstrates that prolonged exposure to moderate-intensity noise could be considered a risk factor for hyperacusis in adulthood. Our results could have implications for noise levels presently deemed "safe" in occupational, private, and public settings (Pienkowski and Eggermont, 2012; Gourévitch et al., 2014; Eggermont, 2017b). Rather than suggesting that noise exposure should not be used for neurotherapeutic purposes, however, we would urge continued investigation into this subject. For one, sensorimotor gating measured by PPI is impaired in some neuropsychiatric disorders, most notably schizophrenia (Swerdlow et al., 2000; Swerdlow and Light, 2018). Noise-induced map expansion could thus be a way to target and reverse this specific preattentional deficit (Braff and Light, 2004). Additional candidate strategies to drive plasticity in a sensory-specific manner are vagus nerve stimulation paired with the presentation of pure tones (Engineer et al., 2011) and cognitive training programs designed to improve basic sensory processing (Cramer et al., 2011; Merzenich et al., 2014). Exciting or inhibiting specific brain areas through sensory experience is a more targeted and non-invasive means of driving plasticity than purely pharmaceutical strategies such as those presently used in the treatment of schizophrenia (Guercio et al., 2019) and dementia (Farlow and Cummings, 2007; Massoud and Léger, 2011). By focusing on "retuning" cortical maps, sensory deprivation or stimulation paradigms in other systems could potentially be developed to treat or reverse symptoms of sensory disorders such as phantom sensations or chronic pain (Flor et al., 2001; Tabot et al., 2015). Through both electrophysiological and behavioral measures, the results of our study suggest that map expansion induced by passive sound exposure opens windows of plasticity that can also be understood as windows of vulnerability. However, as our understanding of the rules that regulate plasticity and the opening and closure of CPs progress, our hope is that we will 1 day be able to harness them to treat a variety of brain disorders.

DATA AVAILABILITY STATEMENT

The datasets generated for this study can be obtained upon request from the study authors.

ETHICS STATEMENT

The animal study was reviewed and approved by Montreal Neurological Institute Animal Care Committee.

AUTHOR CONTRIBUTIONS

GG and EV-S designed the study. GG, KD and MT performed the experiments. GG and KD obtained the behavioral data. MT obtained the electrophysiological data, analyzed the data, and wrote the first draft of the manuscript. All authors contributed to manuscript revision, read, and approved the submitted version.

FUNDING

This research was supported by an operating grant from the Canadian Institutes of Health Research. The Centre for Research on Brain, Language and Music is funded by the government of Quebec *via* the Fonds de Recherche Nature et Technologies and Société et Culture. MT was supported by scholarships from the Natural Sciences and Engineering Research Council of Canada, the Centre for Research on Brain, Language and Music, and the Fonds de Recherche Nature et Technologies. GG was supported by a scholarship from Conselho Nacional de Desenvolvimento Científico e Tecnológico (CNPq-Brazil).

SUPPLEMENTARY MATERIAL

The Supplementary Material for this article can be found online at: https://www.frontiersin.org/articles/10.3389/fnsys.2019.00055/full#supplementary-material.

REFERENCES

Aarts, E., Verhage, M., Veenvliet, J. V., Dolan, C. V., and van der Sluis, S. (2014). A solution to dependency: using multilevel analysis to accommodate nested data. *Nat. Neurosci.* 17, 491–496. doi: 10.1038/nn.3648

Aazh, H., McFerran, D., Salvi, R., Prasher, D., Jastreboff, M., and Jastreboff, P. (2014). Insights from the first international conference on hyperacusis: causes, evaluation, diagnosis and treatment. *Noise Health* 16, 123–126. doi: 10.4103/1463-1741.132100

Adjamian, P., Sereda, M., and Hall, D. A. (2009). The mechanisms of tinnitus: perspectives from human functional neuroimaging. *Hear. Res.* 253, 15–31. doi: 10.1016/j.heares.2009.04.001

Blundon, J. A., Roy, N. C., Teubner, B. J. W., Yu, J., Eom, T.-Y., Sample, K. J., et al. (2017). Restoring auditory cortex plasticity in adult mice by restricting thalamic adenosine signaling. *Science* 356, 1352–1356. doi: 10.1126/science.aaf4612

Braff, D. L., and Light, G. A. (2004). Preattentional and attentional cognitive deficits as targets for treating schizophrenia. *Psychopharmacology* 174, 75–85. doi: 10.1007/s00213-004-1848-0

Brozoski, T. J., and Bauer, C. A. (2016). Animal models of tinnitus. *Hear. Res.* 338, 88–97. doi: 10.1016/j.heares.2015.10.011

Carlson, S., and Willott, J. F. (1996). The behavioral salience of tones as indicated by prepulse inhibition of the startle response: relationship to hearing loss and central neural plasticity in C57BL/6J mice. *Hear. Res.* 99, 168–175. doi: 10.1016/s0378-5955(96)00098-6

Chen, G., Lee, C., Sandridge, S. A., Butler, H. M., Manzoor, N. F., and Kaltenbach, J. A. (2013). Behavioral evidence for possible simultaneous induction of hyperacusis and tinnitus following intense sound exposure.

J. Assoc. Res. Otolaryngol. 14, 413–424. doi: 10.1007/s10162-013-0375-2

Chung, S., Jeong, J. H., Ko, S., Yu, X., Kim, Y. H., Isaac, J. T. R., et al. (2017). Peripheral sensory deprivation restores critical-period-like plasticity to adult somatosensory thalamocortical inputs. *Cell Rep.* 19, 2707–2717. doi: 10.1016/j.celrep.2017.06.018

Costigan, M., Scholz, J., and Woolf, C. J. (2009). Neuropathic pain: a maladaptive response of the nervous system to damage. *Annu. Rev. Neurosci.* 32, 1–32. doi: 10.1146/annurev.neuro.051508.135531

Cramer, S. C., Sur, M., Dobkin, B. H., O'Brien, C., Sanger, T. D., Trojanowski, J. Q., et al. (2011). Harnessing neuroplasticity for clinical applications. *Brain* 134, 1591–1609. doi: 10.1093/brain/awr039

De Ridder, D., Elgoyhen, A. B., Romo, R., and Langguth, B. (2011). Phantom percepts: tinnitus and pain as persisting aversive memory networks. *Proc. Natl. Acad. Sci. U S A* 108, 8075–8080. doi: 10.1073/pnas.1018466108

de Villers-Sidani, É., and Merzenich, M. M. (2011). "Lifelong plasticity in the rat auditory cortex: basic mechanisms and role of sensory experience," *Progress in Brain Research* (Vol. 191), eds A. M. Green, C. E. Chapman, J. F. Kalaska, and F. Lepore (Amsterdam: Elsevier), 119–131.

de Villers-Sidani, E., Simpson, K. L., Lu, Y.-F., Lin, R. C. S., and Merzenich, M. M. (2008). Manipulating critical period closure across different sectors of the primary auditory cortex. *Nat. Neurosci.* 11, 957–965. doi: 10.1038/nn.2144

Eggermont, J. J. (1992). Neural interaction in cat primary auditory cortex. Dependence on recording depth, electrode separation, and age. *J. Neurophysiol.* 68, 1216–1228. doi: 10.1152/jn.1992.68.4.1216

Eggermont, J. J. (2007). Correlated neural activity as the driving force for functional changes in auditory cortex. *Hear. Res.* 229, 69–80. doi: 10.1016/j.heares.2007.01.008

Eggermont, J. J. (2013). On the similarities and differences of non-traumatic sound exposure during the critical period and in adulthood. *Front. Syst. Neurosci.* 7:12. doi: 10.3389/fnsys.2013.00012

Eggermont, J. J. (2017a). "Animal models of stress and tinnitus," in *Tinnitus and Stress: An Interdisciplinary Companion for Healthcare Professionals*, eds A. Szczepek and B. Mazurek (Cham: Springer International Publishing), 77–94.

Eggermont, J. J. (2017b). Effects of long-term non-traumatic noise exposure on the adult central auditory system. Hearing problems without hearing loss. *Hear. Res.* 352, 12–22. doi: 10.1016/j.heares.2016.10.015

Eggermont, J. J., and Roberts, L. E. (2004). The neuroscience of tinnitus. *Trends Neurosci.* 27, 676–682. doi: 10.1016/j.tins.2004.08.010

Eggermont, J. J., and Smith, G. M. (1996). Neural connectivity only accounts for a small part of neural correlation in auditory cortex. *Exp. Brain Res.* 110, 379–391. doi: 10.1007/bf00229138

Elgoyhen, A. B., Langguth, B., De Ridder, D., and Vanneste, S. (2015). Tinnitus: perspectives from human neuroimaging. *Nat. Rev. Neurosci.* 16, 632–642. doi: 10.1038/nrn4003

Engineer, N. D., Riley, J. R., Seale, J. D., Vrana, W. A., Shetake, J. A., Sudanagunta, S. P., et al. (2011). Reversing pathological neural activity using targeted plasticity. *Nature* 470, 101–104. doi: 10.1038/nature09656

Farlow, M. R., and Cummings, J. L. (2007). Effective Pharmacologic Management of Alzheimer's Disease. *Am. J. Med.* 120, 388–397. doi: 10.1016/j.amjmed.2006.08.036

Flor, H., Denke, C., Schaefer, M., and Grüsser, S. (2001). Effect of sensory discrimination training on cortical reorganisation and phantom limb pain. *Lancet* 357, 1763–1764. doi: 10.1016/s0140-6736(00)04890-x

Froemke, R. C., Carcea, I., Barker, A. J., Yuan, K., Seybold, B. A., Martins, A. R. O., et al. (2013). Long-term modification of cortical synapses improves sensory perception. *Nat. Neurosci.* 16, 79–88. doi: 10.1038/nn.3274

Gervain, J., Vines, B. W., Chen, L. M., Seo, R. J., Hensch, T. K., Werker, J. F., et al. (2013). Valproate reopens critical-period learning of absolute pitch. *Front. Syst. Neurosci.* 7:102. doi: 10.3389/fnsys.2013.00102

Geyer, M. A., and Swerdlow, N. R. (1998). Measurement of startle response, prepulse inhibition, and habituation. *Curr. Protoc. Neurosci.* 3, 8.7.1–8.7.15. doi: 10.1002/0471142301.ns0807s03

Gourévitch, B., Edeline, J.-M., Occelli, F., and Eggermont, J. J. (2014). Is the din really harmless? Long-term effects of non-traumatic noise on the adult auditory system. *Nat. Rev. Neurosci.* 15, 483–491. doi: 10.1038/nrn3744

Gu, J. W., Halpin, C. F., Nam, E.-C., Levine, R. A., and Melcher, J. R. (2010). Tinnitus, diminished sound-level tolerance, and elevated auditory activity in humans with clinically normal hearing sensitivity. *J. Neurophysiol.* 104, 3361–3370. doi: 10.1152/jn.00226.2010

Guercio, G. D., Bevictori, L., Vargas-Lopes, C., Madeira, C., Oliveira, A., Carvalho, V. F., et al. (2014). D-serine prevents cognitive deficits induced by acute stress. *Neuropharmacology* 86, 1–8. doi: 10.1016/j.neuropharm.2014.06.021

Guercio, G. D., Thomas, M. E., Cisneros-Franco, J. M., Voss, P., Panizzutti, R., and de Villers-Sidani, E. (2019). Improving cognitive training for schizophrenia using neuroplasticity enhancers: lessons from decades of basic and clinical research. *Schizophr. Res.* 207, 80–92. doi: 10.1016/j.schres.2018.04.028

Guest, H., Munro, K. J., Prendergast, G., Howe, S., and Plack, C. J. (2017). Tinnitus with a normal audiogram: relation to noise exposure but no evidence for cochlear synaptopathy. *Hear. Res.* 344, 265–274. doi: 10.1016/j.heares.2016.12.002

Han, Y. K., Köver, H., Insanally, M. N., Semerdjian, J. H., and Bao, S. (2007). Early experience impairs perceptual discrimination. *Nat. Neurosci.* 10, 1191–1197. doi: 10.1038/nn1941

Harauzov, A., Spolidoro, M., DiCristo, G., De Pasquale, R., Cancedda, L., Pizzorusso, T., et al. (2010). Reducing intracortical inhibition in the adult visual cortex promotes ocular dominance plasticity. *J. Neurosci.* 30, 361–371. doi: 10.1523/JNEUROSCI.2233-09.2010

He, H.-Y., Hodos, W., and Quinlan, E. M. (2006). Visual deprivation reactivates rapid ocular dominance plasticity in adult visual cortex. *J. Neurosci.* 26, 2951–2955. doi: 10.1523/JNEUROSCI.5554-05.2006

Hickox, A. E., and Liberman, M. C. (2014). Is noise-induced cochlear neuropathy key to the generation of hyperacusis or tinnitus? *J. Neurophysiol.* 111, 552–564. doi: 10.1152/jn.00184.2013

Hofer, S. B., Mrsic-Flogel, T. D., Bonhoeffer, T., and Hübener, M. (2006). Lifelong learning: ocular dominance plasticity in mouse visual cortex. *Curr. Opin. Neurobiol.* 16, 451–459. doi: 10.1016/j.conb.2006.06.007

Holgers, K., and Pettersson, B. (2005). Noise exposure and subjective hearing symptoms among school children in Sweden. *Noise Health* 7, 27–37. doi: 10.4103/1463-1741.31635

Kalappa, B. I., Brozoski, T. J., Turner, J. G., and Caspary, D. M. (2014). Single unit hyperactivity and bursting in the auditory thalamus of awake rats directly correlates with behavioural evidence of tinnitus. *J. Physiol.* 592, 5065–5078. doi: 10.1113/jphysiol.2014.278572

Kaltenbach, J. A. (2011). Tinnitus: models and mechanisms. *Hear. Res.* 276, 52–60. doi: 10.1016/j.heares.2010.12.003

Kamal, B., Holman, C., and de Villers-Sidani, E. (2013). Shaping the aging brain: role of auditory input patterns in the emergence of auditory cortical impairments. *Front. Syst. Neurosci.* 7:52. doi: 10.3389/fnsys.2013.00052

Keuroghlian, A. S., and Knudsen, E. I. (2007). Adaptive auditory plasticity in developing and adult animals. *Prog. Neurobiol.* 82, 109–121. doi: 10.1016/j.pneurobio.2007.03.005

Kilgard, M. P., Vazquez, J. L., Engineer, N. D., and Pandya, P. K. (2007). Experience dependent plasticity alters cortical synchronization. *Hear. Res.* 229, 171–179. doi: 10.1016/j.heares.2007.01.005

Kuner, R., and Flor, H. (2016). Structural plasticity and reorganisation in chronic pain. *Nat. Rev. Neurosci.* 18, 20–30. doi: 10.1038/nrn.2016.162

Lakens, D. (2013). Calculating and reporting effect sizes to facilitate cumulative science: a practical primer for t-tests and ANOVAs. *Front. Psychol.* 4:863. doi: 10.3389/fpsyg.2013.00863

Langers, D. R. M., de Kleine, E., and van Dijk, P. (2012). Tinnitus does not require macroscopic tonotopic map reorganization. *Front. Syst. Neurosci.* 6:2. doi: 10.3389/fnsys.2012.00002

Lau, C., Zhang, J. W., McPherson, B., Pienkowski, M., and Wu, E. X. (2015). Long-term, passive exposure to non-traumatic acoustic noise induces neural adaptation in the adult rat medial geniculate body and auditory cortex. *Neuroimage* 107, 1–9. doi: 10.1016/j.neuroimage.2014.11.048

Longenecker, R. J., and Galazyuk, A. V. (2012). Methodological optimization of tinnitus assessment using prepulse inhibition of the acoustic startle reflex. *Brain Res.* 1485, 54–62. doi: 10.1016/j.brainres.2012.02.067

Longenecker, R. J., and Galazyuk, A. V. (2016). Variable effects of acoustic trauma on behavioral and neural correlates of tinnitus in individual animals. *Front. Behav. Neurosci.* 10:207. doi: 10.3389/fnbeh.2016.00207

Massoud, F., and Léger, G. C. (2011). Pharmacological Treatment of Alzheimer Disease. *Can. J. Psychiatry.* 56, 579–588. doi: 10.1177/070674371105601003

Merzenich, M. M., Van Vleet, T. M., and Nahum, M. (2014). Brain plasticity-based therapeutics. *Front. Hum. Neurosci.* 8:385. doi: 10.3389/fnhum.2014.00385

Moore, D. R., Zobay, O., Mackinnon, R. C., Whitmer, W. M., and Akeroyd, M. A. (2017). Lifetime leisure music exposure associated with increased frequency of tinnitus. *Hear. Res.* 347, 18–27. doi: 10.1016/j.heares.2016.10.030

Noreña, A. J., and Eggermont, J. J. (2003). Changes in spontaneous neural activity immediately after an acoustic trauma: implications for neural correlates of tinnitus. *Hear. Res.* 183, 137–153. doi: 10.1016/s0378-5955(03)00225-9

Noreña, A. J., and Eggermont, J. J. (2006). Enriched acoustic environment after noise trauma abolishes neural signs of tinnitus. *Neuroreport* 17, 559–563. doi: 10.1097/00001756-200604240-00001

Nowak, L. G., and Bullier, J. (2005). "Cross correlograms for neuronal spike trains: different types of temporal correlation in neocortex, their origin and significance," in *Time and the Brain*, ed. R. Miller (Amsterdam: Harwood Academic Publishers), 53–96.

O'Reilly, K. C., Perica, M. I., and Fenton, A. A. (2019). Synaptic plasticity/dysplasticity, process memory and item memory in rodent models of mental dysfunction. *Schizophr. Res.* 207, 22–36. doi: 10.1016/j.schres.2018.08.025

Pienkowski, M. (2018). Prolonged exposure of CBA/Ca mice to moderately loud noise can cause cochlear synaptopathy but not tinnitus or hyperacusis as assessed with the acoustic startle reflex. *Trends Hear.* 22:2331216518758109. doi: 10.1177/2331216518758109

Pienkowski, M., and Eggermont, J. J. (2009). Long-term, partially-reversible reorganization of frequency tuning in mature cat primary auditory cortex can be induced by passive exposure to moderate-level sounds. *Hear. Res.* 257, 24–40. doi: 10.1016/j.heares.2009.07.011

Pienkowski, M., and Eggermont, J. J. (2010). Intermittent exposure with moderate-level sound impairs central auditory function of mature animals without concomitant hearing loss. *Hear. Res.* 261, 30–35. doi: 10.1016/j.heares.2009.12.025

Pienkowski, M., and Eggermont, J. J. (2011). Cortical tonotopic map plasticity and behavior. *Neurosci. Biobehav. Rev.* 35, 2117–2128. doi: 10.1016/j.neubiorev.2011.02.002

Pienkowski, M., and Eggermont, J. J. (2012). Reversible long-term changes in auditory processing in mature auditory cortex in the absence of hearing loss induced by passive, moderate-level sound exposure. *Ear Hear.* 33, 305–314. doi: 10.1097/aud.0b013e318241e880

Pienkowski, M., Munguia, R., and Eggermont, J. J. (2011). Passive exposure of adult cats to bandlimited tone pip ensembles or noise leads to long-term response suppression in auditory cortex. *Hear. Res.* 277, 117–126. doi: 10.1016/j.heares.2011.02.002

Pizzorusso, T., Medini, P., Berardi, N., Chierzi, S., Fawcett, J. W., and Maffei, L. (2002). Reactivation of ocular dominance plasticity in the adult visual cortex. *Science* 298, 1248–1251. doi: 10.1126/science.1072699

Polley, D. B., Read, H. L., Storace, D. A., and Merzenich, M. M. (2007). Multiparametric auditory receptive field organization across five cortical fields in the albino rat. *J. Neurophysiol.* 97, 3621–3638. doi: 10.1152/jn.01298.2006

Profant, O., Burianová, J., and Syka, J. (2013). The response properties of neurons in different fields of the auditory cortex in the rat. *Hear. Res.* 296, 51–59. doi: 10.1016/j.heares.2012.11.021

Reed, A., Riley, J., Carraway, R., Carrasco, A., Perez, C., Jakkamsetti, V., et al. (2011). Cortical map plasticity improves learning but is not necessary for improved performance. *Neuron* 70, 121–131. doi: 10.1016/j.neuron.2011.02.038

Reed, J. L., and Kaas, J. H. (2010). Statistical analysis of large-scale neuronal recording data. *Neural Netw.* 23, 673–684. doi: 10.1016/j.neunet.2010.04.005

Reinhard, S. M., Abundez-Toledo, M., Espinoza, K., and Razak, K. A. (2019). Effects of developmental noise exposure on inhibitory cell densities and perineuronal nets in A1 and AAF of mice. *Hear. Res.* 381:107781. doi: 10.1016/j.heares.2019.107781

Roberts, L. E., Eggermont, J. J., Caspary, D. M., Shore, S. E., Melcher, J. R., and Kaltenbach, J. A. (2010). Ringing ears: the neuroscience of tinnitus. *J. Neurosci.* 30, 14972–14979. doi: 10.1523/JNEUROSCI.4028-10.2010

Sun, W., Deng, A., Jayaram, A., and Gibson, B. (2012). Noise exposure enhances auditory cortex responses related to hyperacusis behavior. *Brain Res.* 1485, 108–116. doi: 10.1016/j.brainres.2012.02.008

Swerdlow, N. R., Braff, D. L., and Geyer, M. A. (2000). Animal models of deficient sensorimotor gating: what we know, what we think we know, and what we hope to know soon. *Behav. Pharmacol.* 11, 185–204. doi: 10.1097/00008877-200006000-00002

Swerdlow, N. R., and Light, G. A. (2018). Sensorimotor gating deficits in schizophrenia: advancing our understanding of the phenotype, its neural circuitry and genetic substrates. *Schizophr. Res.* 198, 1–5. doi: 10.1016/j.schres.2018.02.042

Syka, J., and Rybalko, N. (2000). Threshold shifts and enhancement of cortical evoked responses after noise exposure in rats. *Hear. Res.* 139, 59–68. doi: 10.1016/s0378-5955(99)00175-6

Tabot, G. A., Kim, S. S., Winberry, J. E., and Bensmaia, S. J. (2015). Restoring tactile and proprioceptive sensation through a brain interface. *Neurobiol. Dis.* 83, 191–198. doi: 10.1016/j.nbd.2014.08.029

Takahashi, K., Hishida, R., Kubota, Y., Kudoh, M., Takahashi, S., and Shibuki, K. (2006). Transcranial fluorescence imaging of auditory cortical plasticity regulated by acoustic environments in mice. *Eur. J. Neurosci.* 23, 1365–1376. doi: 10.1111/j.1460-9568.2006.04662.x

Takahashi, H., Yokota, R., Funamizu, A., Kose, H., and Kanzaki, R. (2011). Learning-stage-dependent, field-specific, map plasticity in the rat auditory cortex during appetitive operant conditioning. *Neuroscience* 199, 243–258. doi: 10.1016/j.neuroscience.2011.09.046

Thomas, M. E., Friedman, N. H., Cisneros-Franco, J. M., Ouellet, L., and de Villers-Sidani, É. (2018). The prolonged masking of temporal acoustic inputs with noise drives plasticity in the adult rat auditory cortex. *Cereb. Cortex* 29, 1032–1046. doi: 10.1093/cercor/bhy009

Turner, J. G., and Larsen, D. (2016). Effects of noise exposure on development of tinnitus and hyperacusis: prevalence rates 12 months after exposure in middle-aged rats. *Hear. Res.* 334, 30–36. doi: 10.1016/j.heares.2015.11.004

Turner, J. G., and Parrish, J. (2008). Gap detection methods for assessing salicylate-induced tinnitus and hyperacusis in rats. *Am. J. Audiol.* 17, S185–S192. doi: 10.1044/1059-0889(2008/08-0006)

Wang, H., Brozoski, T. J., and Caspary, D. M. (2011). Inhibitory neurotransmission in animal models of tinnitus: maladaptive plasticity. *Hear. Res.* 279, 111–117. doi: 10.1016/j.heares.2011.04.004

Zheng, W. (2012). Auditory map reorganization and pitch discrimination in adult rats chronically exposed to low-level ambient noise. *Front. Syst. Neurosci.* 6:65. doi: 10.3389/fnsys.2012.00065

Zhou, X., and Merzenich, M. M. (2012). Environmental noise exposure degrades normal listening processes. *Nat. Commun.* 3:843. doi: 10.1038/ncomms1849

Zhou, X., Panizzutti, R., de Villers-Sidani, E., Madeira, C., and Merzenich, M. M. (2011). Natural restoration of critical period plasticity in the juvenile and adult primary auditory cortex. *J. Neurosci.* 31, 5625–5634. doi: 10.1523/JNEUROSCI.6470-10.2011

Conflict of Interest: The authors declare that the research was conducted in the absence of any commercial or financial relationships that could be construed as a potential conflict of interest.

frontiers in Neuroanatomy

ORIGINAL RESEARCH
published: 05 February 2020
doi: 10.3389/fnana.2020.00002

Cytoarchitectonic Characterization and Functional Decoding of Four New Areas in the Human Lateral Orbitofrontal Cortex

Magdalena Wojtasik[1], Sebastian Bludau[2], Simon B. Eickhoff[3,4], Hartmut Mohlberg[2], Fatma Gerboga[1], Svenja Caspers[2,5] and Katrin Amunts[1,2]*

[1]*Cécile and Oskar Vogt—Institute for Brain Research, Medical Faculty, Heinrich-Heine-University Düsseldorf, Düsseldorf, Germany,* [2]*Institute of Neuroscience and Medicine 1 (INM-1), Research Center Jülich, Jülich, Germany,* [3]*Institute of Neuroscience and Medicine 7 (INM-7), Research Center Jülich, Jülich, Germany,* [4]*Institut für Systemische Neurowissenschaften, Medizinische Fakultät, Heinrich-Heine Universität Düsseldorf, Düsseldorf, Germany,* [5]*Institute for Anatomy I, Medical Faculty, Heinrich-Heine-University Düsseldorf, Düsseldorf, Germany*

A comprehensive concept of the biological basis of reward, social and emotional behavior, and language requires a deeper understanding of the microstructure and connectivity of the underlying brain regions. Such understanding could provide deeper insights into their role in functional networks, and form the anatomical basis of the functional segregation of this region as shown in recent *in vivo* imaging studies. Here, we investigated the cytoarchitecture of the lateral orbitofrontal cortex (lateral OFC) in serial histological sections of 10 human postmortem brains by image analysis and a statistically reproducible approach to detect borders between cortical areas. Profiles of the volume fraction of cell bodies were therefore extracted from digitized histological images, describing laminar changes from the layer I/layer II boundary to the white matter. As a result, four new areas, Fo4–7, were identified. Area Fo4 was mainly found in the anterior orbital gyrus (AOG), Fo5 anteriorly in the inferior frontal gyrus (IFG), Fo6 in the lateral orbital gyrus (LOG), and Fo7 in the lateral orbital sulcus. Areas differed in cortical thickness, abundance and size of pyramidal cells in layer III and degree of granularity in layer IV. A hierarchical cluster analysis was used to quantify cytoarchitectonic differences between them. The 3D-reconstructed areas were transformed into the single-subject template of the Montreal Neurological Institute (MNI), where probabilistic maps and a maximum probability map (MPM) were calculated as part of the JuBrain Cytoarchitectonic Atlas. These maps served as reference data to study the functional properties of the areas using the BrainMap database. The type of behavioral tasks that activated them was analyzed to get first insights of co-activation patterns of the lateral OFC and its contribution to cognitive networks. Meta-analytic connectivity modeling (MACM) showed that functional decoding revealed activation in gustatory perception

OPEN ACCESS

Edited by:
Nick Swindale,
University of British Columbia, Canada

Reviewed by:
Carlos Avendaño,
Autonomous University of Madrid, Spain
Giorgio Innocenti,
Karolinska Institutet (KI), Sweden

****Correspondence:***
Magdalena Wojtasik
magdalena.wojtasik@hhu.de

Received: *07 November 2019*
Accepted: *17 January 2020*
Published: *05 February 2020*

Citation:
Wojtasik M, Bludau S, Eickhoff SB, Mohlberg H, Gerboga F, Caspers S and Amunts K (2020) Cytoarchitectonic Characterization and Functional Decoding of Four New Areas in the Human Lateral Orbitofrontal Cortex. Front. Neuroanat. 14:2. doi: 10.3389/fnana.2020.00002

in Fo4; reward and somesthetic perception in Fo5; semantic processing and pain perception in Fo6; and emotional processing and covert reading in Fo7. Together with existing maps of the JuBrain Cytoarchitectonic Atlas, the new maps can now be used as an open-source reference for neuroimaging studies, allowing to further decode brain function.

Keywords: lateral orbitofrontal cortex, BA47, human brain atlas, cytoarchitecture, maximum probability maps, meta-analytic connectivity modeling, JuBrain, BigBrain

INTRODUCTION

The lateral orbitofrontal cortex (lateral OFC) includes the cytoarchitectonically defined Brodmann area (BA) 47 (Brodmann, 1909). It seems to occupy a structurally variable part of the human brain (Chiavaras and Petrides, 2000). According to Brodmann, BA 47 spans over the lateral orbital gyrus (LOG) with extensions into the posterior parts of the ventrolateral frontal cortex and anterior parts of the inferior frontal gyrus (IFG; Brodmann, 1909). As known from previous studies, the macroanatomy itself is variable with respect to the sulcal and gyral patterns including interhemispheric differences (Chiavaras and Petrides, 2000; Chiavaras et al., 2001; Kringelbach and Rolls, 2004; Rodrigues et al., 2015; Rolls et al., 2015). In many cases, the OFC is composed of an "H"-shaped pattern of sulci, which is characterized by the lateral and medial orbital sulcus (LOS, MOS). They run parallel to each other, are separated by the anterior orbital gyrus (AOG), and connected through the transverse orbital sulcus (TOS). Other patterns have been described as well (Ono et al., 1990; Chiavaras et al., 2001; Rodrigues et al., 2015), but the relationship of the different sulcal patterns with the microstructure at the level of areas are not well understood.

Previous studies have shown that the lateral OFC could be divided into a different number of areas. The parcellation schemes became more complex and fine-grained over time (see **Figure 1**). Different approaches were applied to map the lateral OFC including histological techniques such as cytoarchitectonic analysis or the function-driven approach using the functional magnetic resonance imaging (fMRI) technique. The varying number of areas, their size and location were influenced by the different analysis techniques as well as intersubject variability in brain shape and size.

In addition, different conceptual approaches were applied to characterize the lateral OFC, and introduced, for example, subareas and transitions. The term "area 47/12" was first *postulated by* Öngür and Price (2000). Further studies took up this term (Petrides and Pandya, 2002; Öngür et al., 2003; Kringelbach and Rolls, 2004; Deng et al., 2017), and assigned it to one large area surrounding the LOG. In combination with the medial OFC, the designations 47 m for the medial OFC and 47l for the lateral OFC were postulated (Uylings et al., 2000, 2010). Further terms were introduced, which reflected the topography, i.e., 47 m for the medial frontal cortex and 47° for the OFC (Neubert et al., 2015). Recently, some areas in the medial OFC have been named after their topographic location, abbreviated and numbered consecutively. Research from our own group identified area Fo1 in the anterior gyrus rectus, Fo2 in the posterior gyrus rectus, and area Fo3 reaching from the inner medial orbital sulcus to the outer medial orbital sulcus, enclosing Fo1 and Fo2 laterally (Henssen et al., 2016). The analysis was based on cytoarchitecture, and considered changes in cell density and cell distribution, mainly in layers III, IV and V.

Functional analyses of the lateral OFC revealed that this region is involved in the processing of gustatory, olfactory or somatosensory rewarding stimuli but also the processing of emotional punishments, evaluating and updating the emotional status, maintaining social behavior, active retrieval of information, semantic processing, verb generation, processing of stimuli that have a coherent temporal structure, music listening, assigning value to certain things and events and decision-making (Papathanassiou et al., 2000; Levitin and Menon, 2003; Kringelbach and Rolls, 2004; Petrides, 2005; Campbell-Meiklejohn et al., 2012; Alluri et al., 2013; Liu et al., 2015; Neubert et al., 2015; Rolls et al., 2015; Hirose et al., 2016). Tasks that require quick responses while retrieving information from the long-term and working memory also showed activations in the lateral OFC. This region seems to create an interconnecting role between the frontal cortex and the hippocampus (Ross et al., 2013; Deng et al., 2017; Rudebeck and Rich, 2018). Another functional study separated the OFC into a medial and a lateral portion (Zald et al., 2014). The latter corresponded to BA 47 and co-activated with areas in the IFG and area BA 46/9 of the dorsomedial frontal cortex along with several subcortical structures, e.g., the amygdala, hippocampus and nucleus accumbens among others.

The present study provides a comprehensive cytoarchitectonic analysis of the human lateral OFC using a computerized approach to detect cytoarchitectonic borders between adjacent areas based on image analysis and statistical criteria (Schleicher et al., 1998, 1999, 2005), and provides cytoarchitectonic probabilistic maps in 3D reference space (Amunts and Zilles, 2015). The maps have been created based on the same methods as used for previous mapping studies of our group [most recent include, e.g., the parietal cortex (Richter et al., 2019), the motor cortex (Ruan et al., 2018), and the fusiform gyrus (Lorenz et al., 2017)], and allow to integrate them into a coherent atlas framework of the human brain. Meta-analytic connectivity modeling (MACM) was conducted to assess all task-based functional connectivities between the lateral OFC areas and their respective co-activated

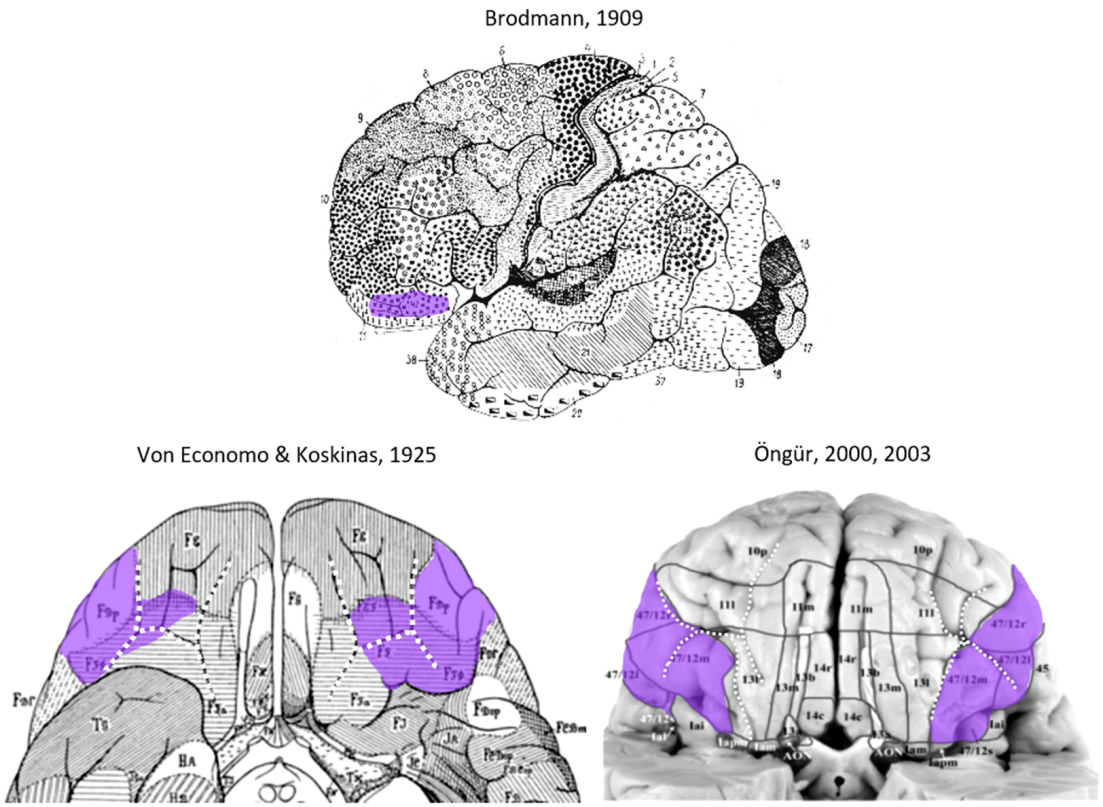

FIGURE 1 | Area 47 in the lateral orbitofrontal cortex (lateral OFC) in the human brain according to previous cytoarchitectonical analyses (Brodmann, 1909; von Economo and Koskinas, 1925; Von Economo, 1929; Öngür et al., 2003). The sulcal pattern is highlighted with white dotted lines. Images have been modified such that the sulcal patterns are highlighted with white dotted lines, and the approximate extent of Area 47 is labeled in purple.

cortical and subcortical brain regions in the same reference space. Their corresponding activation foci with the lateral OFC areas as seed regions were detected *via* the BrainMap database (Laird et al., 2009; Robinson et al., 2010). The present work aims to combine the structural peculiarity of the lateral OFC with its functional properties and to give a first insight into the cognitive networks in which the lateral OFC is integrated.

MATERIALS AND METHODS

Processing of Postmortem Brains

Ten brains (five females with age range of 59–86 years, and five males with age range of 30–75 years, mean age of 65, 8 years) were obtained from the body donor program of the Department of Anatomy at the University Hospital Düsseldorf of the Heinrich-Heine-University in accordance with legal requirements with no indications of neurologic or psychiatric diseases in clinical records. The postmortem delay did not exceed 24–36 h (**Table 1**). The brains were fixed in 4% buffered formalin (pH 7.4) or Bodian's fixative for at least 6 months. All brains underwent magnetic resonance imaging on a Siemens 1.5 Tesla scanner (Erlangen, Germany) using a T1-weighted 3D FLASH sequence (flip angle 40°, repetition time TR 40 ms, echo time TE 5 ms). Obtained images were used as an undistorted spatial reference for the 3D-reconstruction of the histological sections as previously described (Bludau et al., 2014).

Brains were embedded in paraffin and serially sectioned in the coronal plane on a large-scale microtome (thickness of 20 μm). Every 15th section (corresponding to a distance of 300 μm) was mounted on a glass slide covered with gelatin, stained for

TABLE 1 | List of postmortem brains used for cytoarchitectonic analysis.

Brain ID	Gender	Cause of death
pm1	Female	Bladder carcinoma
pm4	Male	Rectal cancer
pm5	Female	Cardiorespiratory insufficiency
pm8	Female	Kidney failure
pm9	Female	Generalized atherosclerosis, aortic valve stenosis, left heart insufficiency, basal ganglia infarction
pm11	Male	Heart attack
pm13	Male	Drowning
pm14	Female	Cardiorespiratory insufficiency, right-sided breast cancer
pm20	Male	Decompensated heart failure, respiratory insufficiency, prostate cancer, tumor anemia
pm21	Male	Bronchopneumonia, recurrence of Hodgkin's disease, deep vein thrombosis

cell bodies using a silver staining technique (Merker, 1983), and digitized on a flatbed scanner (resolution of 1,200 dpi). At least every 60th section was analyzed (distance between them of 1.200 μm).

Identification of Cytoarchitectonic Borders Based on the Grey Level Index (GLI)

The identification of cytoarchitectonic borders (**Supplementary Figure S1A**) was based on image analyses of rectangular regions of interests (ROIs) in every 60th histological section, and statistical criteria (Schleicher et al., 1998, 1999, 2005). ROIs were digitized with a CCD camera (Axiocam MRm, ZEISS, Germany), which was connected to a computer-controlled optical light microscope with motorized scanning stage (Axioplan 2 imaging, ZEISS, Germany). The Zeiss image analysis software Axiovision (version 4.6) allowed to scan the defined ROIs in a mosaic-like way with an in-plane resolution of 1.02 μm per pixel (**Supplementary Figure S1B**). GLI images were computed in adjacent square fields of 17 × 17 μm using in-house written MatLab scripts (The MathWorks, Inc., Natick, MA, USA) as a robust estimate of the volume fraction of cell bodies (Wree et al., 1982; Schleicher et al., 1986, 2005; **Supplementary Figure S1C**). The GLI is defined as an estimate of the local volume density of cellular structures that is influenced by section thickness (here 20 μm for all sections). The GLI measures the areal proportion as a numerical equivalent for the volume density (Schleicher et al., 1986). The GLI is the ratio of the area covered by image elements, which are darker than a given gray value threshold, to the entire area of the measuring field, which is of fixed size (Schleicher et al., 1986). The gray value threshold was set to the gray value of the boundary between the dark cellular image elements and the bright background by analyzing the gray value histogram of the image (Schleicher et al., 1986). The cortical ribbon was delineated by an outer contour (border between layer I and II) and an inner contour line (border between layer VI and white matter; **Supplementary Figure S1D**). Curvilinear traverses running perpendicular to the cortical layers from the outer to the inner contour were defined to calculate GLI profiles (**Supplementary Figure S1E**), and GLI values, reflecting the laminar changes in cytoarchitecture, were extracted along the traverses. GLI profiles were described by a 10-element feature vector consisting of the mean GLI value, the center of gravity in x- and y-direction, the standard deviation, kurtosis, skewness and the equivalent parameters of the profiles' first derivatives (Schleicher et al., 2005). Vectors of each profile were used to calculate the Mahalanobis distance (MD, Mahalanobis et al., 1949) between blocks of profiles. The MD is a measure for cytoarchitectonic dissimilarity between profiles. The larger the dissimilarity, the higher the MD, and vice versa. A Hotelling's T2 test with Bonferroni correction was applied to test for significance between differences of profiles. A predefined number of profiles was combined into a block, with a block size ranging from 12 to 30 profiles to increase robustness of the procedure. MDs were computed in a sliding window procedure for each profile position and every block size surrounding this position across the whole cortex in each ROI. If the MD reached a significant maximum at different block sizes at a certain profile position (**Supplementary Figure S1F**), a cytoarchitectonic border was assumed (**Supplementary Figures S1G,H**). Resulting areas were manually delineated in digitized high-resolution scans *via* the Section Tracer Online Tool developed in-house (**Supplementary Figure S1I**).

Hierarchical Cluster Analysis of Cytoarchitectonic Dissimilarities Between Cortical Areas

A hierarchical cluster analysis was performed to detect structural dissimilarities between the lateral OFC areas, and compared to the adjacent areas Fo3 (Henssen et al., 2016), Fp1 (Bludau et al., 2014) as well as area 45 as part of Broca's region (Amunts et al., 2004). Therefore, 15–20 consecutive profiles were extracted in three successive sections per area and hemisphere in each of the 10 brains at cortical locations where curvature and tangency had their lowest expanse. Each profile was represented by the 10-element feature vector, which enabled the analysis of linkage (Ward's method) and distance (Euclidean distance) between given areas to quantify their degree of dissimilarity. The Euclidean distance describes the distances between pairs of neighboring profiles, i.e., the differences in the shape of these profiles, without taking into account the variability within clusters of profiles (Schleicher et al., 1998, 1999). An in-house written script for MatLab (The MathWorks, Inc., Natick, MA, USA) was used for the calculation. A value of a high Euclidean distance indicated a low structural similarity (and a large degree of cytoarchitectonic difference), and vice versa, a low value indicated high similarity. Respective brains were pooled either by gender (male/female) or by hemisphere (left/right). A dendrogram visualized the hierarchical clustering of all analyzed cortical areas.

Probabilistic Cytoarchitectonic Maps in Stereotaxic Space and Maximum Probability Maps (MPMs)

The contour lines of the areas of the lateral OFC of all 10 brains were interactively traced onto 1,200 dpi high-resolution images of the histological sections, and 3D-reconstructed (Bludau et al., 2014). Spatially normalized areas of all 10 brains were transferred onto the T1-weighted, single-subject brain template of the Montreal Neurological Institute (MNI) "Colin27". This brain template was used as the anatomical reference brain (Holmes et al., 1998; Evans et al., 2012) and transferred to anatomical MNI space (Amunts et al., 2005). After the superimposition of the areas in reference space, probabilistic maps were calculated. They showed the percentage of location and size probability of a given area in each voxel in the reference brain, and were color-coded values from 10% (blue) to 100% (red). Subsequently, a maximum probability map (MPM) was calculated for the whole lateral OFC, where each voxel was assigned to the cytoarchitectonic area with the highest locational probability in this voxel (Eickhoff et al.,

2005). At borders of lateral OFC areas with unmapped or currently unknown areas (posteriorly adjacent cortex), the threshold for including a voxel into the MPM of each area was set to 0.4, resulting in a probability of 40% for each voxel to be assigned to a specific area (Eickhoff et al., 2005). The respective areal representations can be accessed and are available in the JuBrain Cytoarchitectonic Atlas[1] as well as the new BigBrain template of the HBP atlas[2], resembling an ultrahigh-resolution three-dimensional model of a human brain at nearly cellular resolution of 20 × 20 μm (Amunts et al., 2013) and the MNI template of the HBP human brain atlas[3]. In order to compare the data sets in the different template spaces, vector fields have been calculated based on a 400 μm isotropic down-sampled volume, to define a homeomorphic transformation between the BigBrain and the MNI space (Amunts et al., 2013).

Volumetric Analysis

Individual shrinkage factors were obtained for each postmortem brain (Amunts et al., 2007). The ratio of the fresh brain volume was therefore divided by its volume after histological processing, further multiplied with the mean specific density of 1.033 g/mm^3 (Zilles et al., 1988). Volume correction was obtained by calculation of areal proportions in each brain to enable the comparison between all brains due to their differing weight. A contrasting estimate was calculated between the means of grouped gender and hemispheres using in-house software written in MatLab (The MathWorks, Inc., Natick, MA, USA) as well as pair-wise permutation tests to detect significant differences of the volume proportion between the lateral OFC areas. The null distribution was estimated using Monte-Carlo simulation with a repetition of 1,000,000 iterations. The difference between all four areas was considered significant if the contrast estimate of the comparison exceeded 95% of the values under random distribution ($P < 0.05$).

Analysis of Macro Anatomical Pattern in an Extended Sample of Brains

Considering the significant intersubject variability in the sulcal and gyral pattern of the lateral OFC, we investigated the individual macroanatomy of the OFC on images of the basal and lateral views of 26 human postmortem brains of the JuBrain Cytoarchitectonic Atlas, which were used in the past years for mapping (for an overview, see Amunts and Zilles, 2015). The 10 postmortem brains used for the cytoarchitectonic mapping and analysis were part of this sample. Previous studies (Ono et al., 1990; Chiavaras et al., 2001; Rodrigues et al., 2015) proposed three or four different sulcal patterns, which we applied. This resulted in a classification of four types of patterns of sulci and gyri in the 52 hemispheres. The paths of the respective sulci of the orbitofrontal cortex (OFC) were traced in the histological sections of the brains and labeled in the ventral views of the images of the postmortem brains.

[1]https://jubrain.fz-juelich.de/apps/cytoviewer/cytoviewer.php
[2]https://bigbrain.humanbrainproject.org/
[3]https://www.humanbrainproject.eu/en/explore-the-brain/atlases/

Functional Decoding of Areas in the Lateral OFC

The BrainMap[4] database includes a large number of search criteria to limit the exploration for matching studies. On the experimental level, behavioral domains (BDs) and paradigm classes (PCs) enabled the specification of given experiments and the functional decoding of examined VOIs. Functional decoding of a given seed region involved the acquisition of all detectable functions by the over-representation of BDs and PCs in the experiments activating each VOI relative to the BrainMap database (Eickhoff et al., 2011). Studies with functional imaging data showing peak x-y-z-coordinates were explored using the following search criteria: normal mapping, activations only, using either fMRI or PET studies and only healthy subjects were included (Laird et al., 2011). This approach yielded a total number of 1,167 functional neuroimaging experiments at the time of analysis (**Supplementary Table S1**). No preselection of taxonomic categories had been conducted.

Functional characterization using BrainMap's metadata was visualized with bar graphs displaying all BDs and PCs for every examined VOI with their respective probability likelihood ratio, indicating activation in each area by a particular BD and PC using forward and reverse inference. The former approach describes the probability of the observation of activity in a brain region, given the knowledge of the psychological process, whereas reverse inference defines the probability of a psychological process being present, given the knowledge of activation in a particular brain region. The respective bar graphs were transformed into network diagrams.

Meta-analytic Connectivity Modeling on the Lateral OFC Areas

MACM was performed using the activation likelihood estimation (ALE) algorithm. It identified coincided whole-brain co-activation patterns from the neuroimaging study contingent of the BrainMap database as peak x-y-z coordinates in stereotaxic space for each lateral OFC seed region. Here, similarities in co-activation profiles of each VOI (Eickhoff et al., 2011) were extracted as activation foci from all matching neuroimaging studies showing potential functional co-activation and were displayed on the MNI ICBM 152 brain template. The MNI ICBM 152 reference space consists of brain scans from 152 different subjects. They were non-linearly registered in the MNI ICBM 152 coordinate system, and averaged. To establish a null-distribution reflecting a random spatial association between experiments, 10,000 permutations were calculated. All analyses were thresholded at an FWE-corrected threshold of $P < 0.05$ using the cluster-level FWE thresholding (Eickhoff et al., 2016).

In this context, we performed a conjunction analysis in which overlap of all four MACM co-activation maps was conducted. This allowed us to find out which brain regions were affected by all four lateral OFC areas. Additionally, contrast analyses were

[4]http://brainmap.org

performed on each of the co-activation maps of the four lateral OFC areas with two contrasting co-activation patterns at a time to demonstrate any differing functional connectivity between the two respective seed VOIs and to identify unique functions for each area per hemisphere (Eickhoff et al., 2011).

RESULTS

Cytoarchitecture of Areas Fo4–Fo7

The cytoarchitectonic analysis of the lateral OFC revealed four new areas (**Figure 2**): Fo4 was located at the AOG, lateral to area Fo3, which occupied the medial orbital gyrus and sulcus. Area Fo5 was spreading over the most anterior tip of the IFG, posterolateral to the frontomarginal sulcus (FMS) and ventrolateral to frontal polar area Fp1 (Bludau et al., 2014). Fo6 was encompassing the LOG following Fo5 posteriorly, and Fo7 was mostly occupying the lateral orbital sulcus and gyrus medial to Fo6, following Fo4 posteriorly; it did not exceed the TOS.

Each area had a specific cytoarchitecture. Layer II of area Fo4 (**Figure 3**) was thin and loosely occupied by granule cells. Layer III was broad as compared to the other layers, and loosely packed by pyramidal cells, especially in layer IIIa and IIIb. In addition, all cells showed a relatively uniform size, except for sublayer IIIc

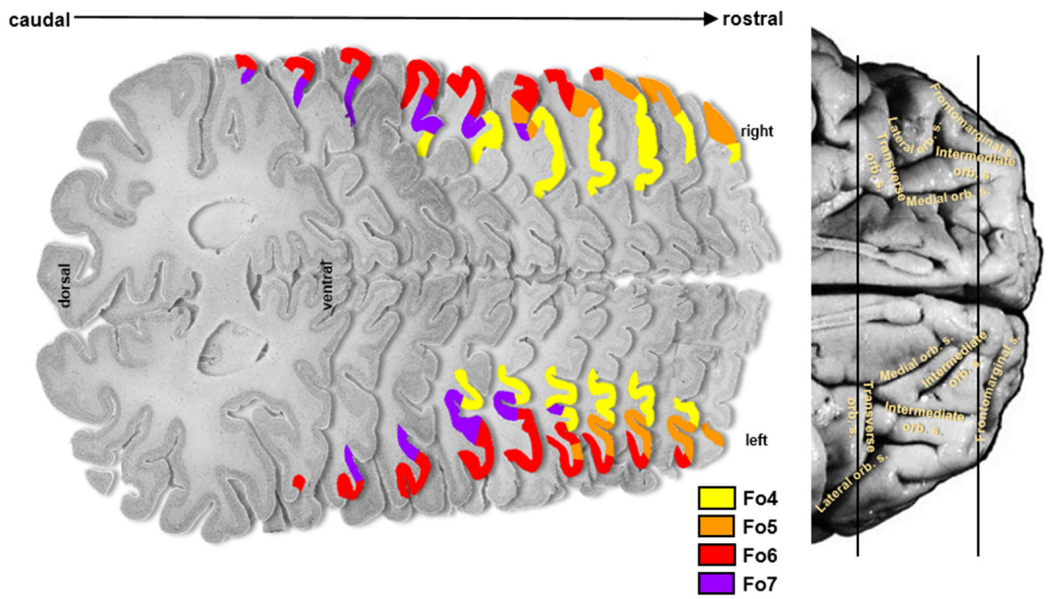

FIGURE 2 | Localization of cytoarchitectonical areas Fo4, Fo5, Fo6, and Fo7 in the lateral OFC in serial histological sections of brain pm8.

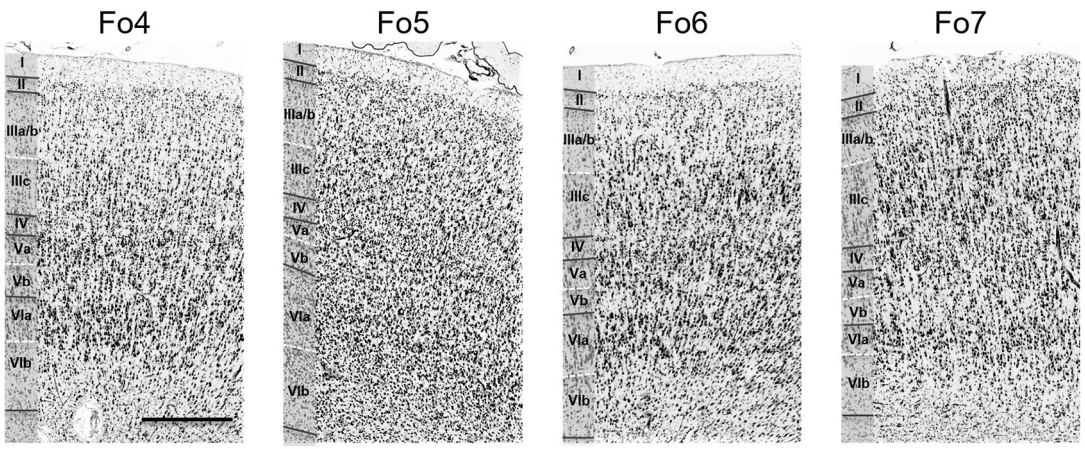

FIGURE 3 | Cytoarchitecture of areas Fo4–Fo7 in the lateral OFC. Roman numerals indicate cortical layer I to VI. Scale bar = 500 μm.

showing slightly larger pyramidal cells. The thin layer IV was almost dysgranular. Layer V showed rather small pyramidal cells, but bigger than in sublayer IIIc. It was subdivided into sublayers Va and Vb. Cells in sublayer VIa were bigger and more densely packed than in sublayer VIb. Layer VI showed a rather smooth transition to the white matter.

Layer II of area Fo5 was also thin but tended to be thicker than in Fo4, and more cell dense. Sublayers IIIa and b displayed small-sized pyramidal cells with an increased cell size towards sublayer IIIc (**Figure 3**). Layer III showed a moderate cell density with lower amounts of cells than in the adjacent layers. Layer IV was also thin, but broader than in Fo4 and more populated with granule cells. Sublayer Va contained some large pyramidal cells, and sublayer Vb was more densely occupied than the analogs sublayer in area Fo4 (**Figure 3**). Sublayer VIa showed a higher cell density than layer V. The cortex-white matter border was also not sharp.

Compared to area Fo5, area Fo6 (**Figure 3**) had a slightly broader, but less cell-dense layer II with no sharp border to sublayer IIIa. Layer III was also less cell-dense. It showed medium-sized pyramidal cells in sublayer IIIc, and a decreasing cell size going towards the outer layers IIIb and IIIa. In addition, it contained larger pyramidal cells than in layer III of Fo5. Layer IV was wider and better visible than in areas Fo4 and Fo5, and more densely packed than Fo4, but not Fo5. Sublayer Va revealed prominent pyramidal cells, close to layer IV. Sublayer Vb showed a lower cell density than in Fo4 and Fo5. Similar to Fo4, sublayer VIa of area Fo6 was more densely packed with cells, but, in contrast to Fo4, showed a clear cut border to the white matter.

Area Fo7 (**Figure 3**) showed a more pronounced laminar pattern than the other three areas. Fo7 was characterized by large pyramidal cells in layer IIIc and a high cell density. Layer II was broad and contained uniformly sized granule cells. It was followed by a broad and densely packed layer III. Sublayer IIIc contained many large pyramidal cells and also smaller cells in IIIa and b. The broad and cell dense layer IV was also entangled with cells from sublayers IIIc and Va. Sublayer Va also showed large pyramidal cells, but smaller than those of IIIc. Sublayer Vb was the least cell dense. As in area Fo6, the transition between cortex and white matter was also clear-cut.

An example of a cytoarchitectonic border between Fo6 and Fo7 is shown in **Figure 4**. Compared to Fo6, Fo7 was characterized by a wide and cell dense layer III. In addition, the internal granular and pyramidal layers were accentuated by higher cell densities and cortex width. The thickness of layer VI appeared to be narrower in Fo7 than Fo6 in cortical regions with the comparative angle of sectioning. At the same time, it was more cell dense in sublayer VIa and exhibited an even better visible border to the white matter in sublayer VIb than Fo6.

The anterior ramus of the horizontal fissure formed a macroscopical landmark of Fo6 to the adjacent area 46. Posteromedial parts of the LOG and the entire lateral orbital sulcus were inhabited by Fo7, which was following Fo4 on the AOG, in few cases separated by an intermediate sulcus, ending in the TOS and slowly being cornered medially and posteriorly by new areas of the posterolateral orbital region which are still to be delineated.

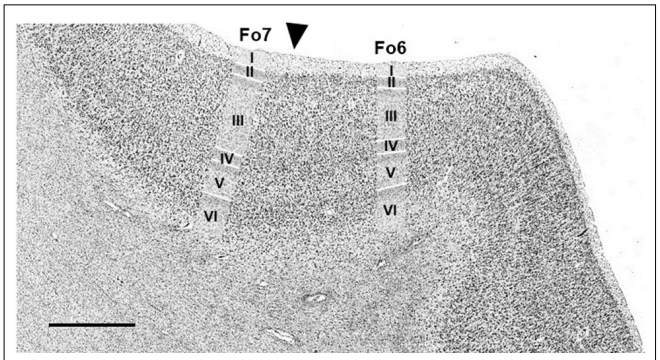

FIGURE 4 | Cytoarchitectonic border of Fo6 with Fo7 (black arrowhead). Scale bar = 1 mm.

Differentiation of Areas Fo4–Fo7 From Neighboring Areas

The direct neighboring areas were frontopolar area Fp1 (Bludau et al., 2014) at the lateral surface of the frontal pole, anteriorly to Fo4 and Fo5, and Fo3 (Henssen et al., 2016) in the medial OFC. Fo3 bordered medially to Fo4. Additional orbitofrontal areas were located posteriorly to Fo6 and Fo7, but their cytoarchitecture has not yet been analyzed in detail. Area 46 was found lateral to area Fo6, beyond the horizontal ramus of the lateral fissure (Rajkowska and Goldman-Rakic, 1995).

In most hemispheres, borders between areas Fp1 (Bludau et al., 2014) and Fo4 were found at the onset of the AOG, where Fo4 was following Fp1 posteriorly and was being medially cornered by Fo3 and laterally by Fo5 (**Figure 5**, upper panel). No clear macroscopical landmark was found between Fp1 and Fo4. Fo5 was located basolaterally to Fp1. Both areas shared borders in the most frontal part of the IFG right below the FMS (**Figure 5**, lower panel), which served as a macroscopical landmark separating both areas.

The medial orbital sulcus was associated as the macroscopical landmark between Fo3 (Henssen et al., 2016) and Fo4, with the latter area being located laterally to the sulcus. Borders between all cortical layers were better distinguishable in Fo4 than Fo3 (**Figure 6**).

The cytoarchitecture of these areas is summarized in **Table 2**. All areas were clearly separable from each other and exhibited distinct cytoarchitectonic characteristics representing true structural differences.

Hierarchical Cluster Analysis of Cytoarchitectonic Differences and Similarities in the Lateral OFC

The hierarchical cluster analysis of areas Fp1, Fo3, Fo4, Fo5, Fo6, Fo7 and area 45 as an additional area from the ventral prefrontal cortex revealed a twofold clustering of areas with area 45 of the IFG on one branch, and all the other areas

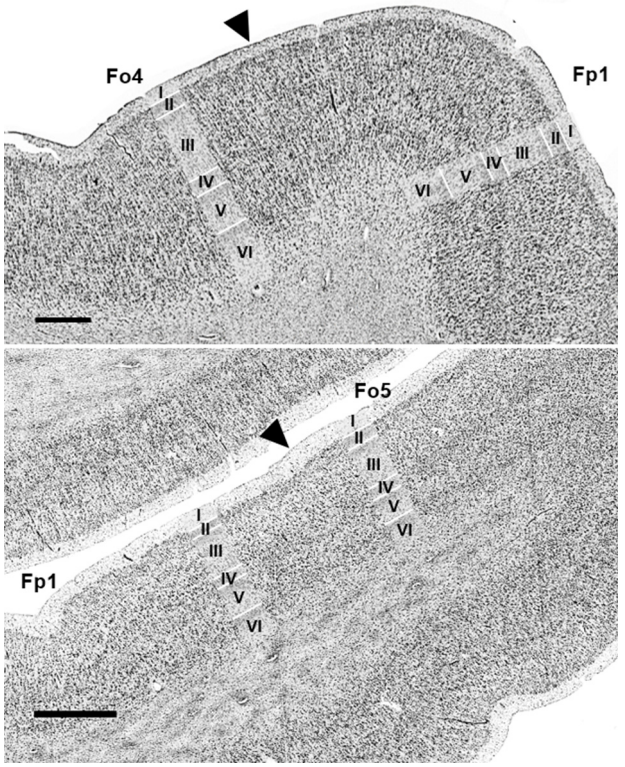

FIGURE 5 | Cytoarchitectonic borders of Fp1 with Fo4 (upper panel) and Fp1 with Fo5 (lower panel). Arrowheads indicate borders between areas. Scale bars = 1 mm. Images come from the BigBrain, a high-resolution whole-brain model of the human brain, which can be found at: https://bigbrain.humanbrainproject.org/ (Amunts et al., 2013).

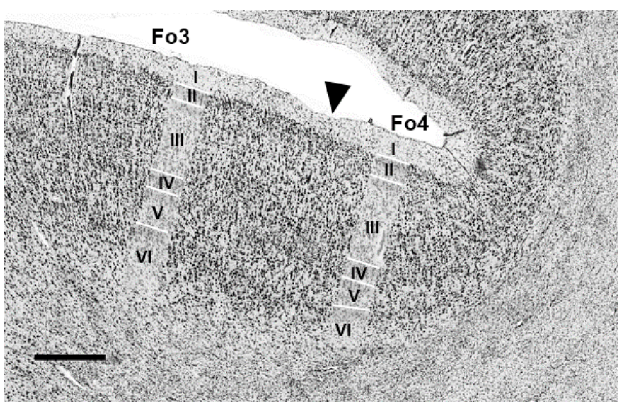

FIGURE 6 | Cytoarchitectonic border of Fo3 with Fo4 (indicated by black arrowhead). Scale bar = 1 mm.

on the second branch (**Figure 7**). Fp1 and Fo3 were separated from the four lateral OFC areas on a higher hierarchical level. Fo4 and Fo6 were structurally more similar to each other than to Fo5 and Fo7, which was already visible in the cytoarchitectonic analysis. Fo5 and Fo7 differed from Fo4 and Fo6 by a denser cortex and larger cells in sublayer IIIc. The areas of the lateral OFC showed rather low degrees of structural dissimilarity. An increased degree of structural dissimilarity was found between the lateral OFC areas and Fo3 and Fp1, respectively. Area 45 was quite different from the areas of the lateral OFC, mostly due to its very large pyramidal cells in layer IIIc, not found in any other area adjacent to the lateral OFC.

TABLE 2 | Cytoarchitectonic characteristics of areas Fo4–Fo7 in the lateral orbitofrontal cortex (lateral OFC) and neighboring areas.

Area	Cytoarchitectonic characteristics
Fp1	Sharp border between layers I, II and III
	Dense layers II and IIIc
	Considerably larger pyramids in deeper than in upper layer III
	Broader layer IV than Fp2
Fo3	Large pyramidal cells in layer IIIc
	Inner granular layer with higher cell density and more prominent in its anterior than posterior part
	Layer Va of Fo3 with higher cell density than the respective layer of Fo4
Fo4	Narrow cortex throughout the area
	Indistinct borders between layers II, III, IV and V
	Uniformly packed layer III
	Middle-sized pyramidal cells in layer Va
Fo5	Very large pyramidal cells in densely packed layer IIIc
	Broad layer III
	More dense layer IV and V than Fo4
Fo6	Decreasing cell size in layer III from deeper to upper part
	Broad and cell-dense layer IV
	Middle-sized pyramidal cells in layer Va
Fo7	All layers very densely packed
	Indistinct borders between layers II, III, IV and V
	Large pyramidal cells in a deeper part of broad layer III
	Broad layer II, IV and V
	Layer IV more cell dense than Fo4–Fo6

Descriptions for Fp1 and Fo3 adapted from Bludau et al. (2014) and Henssen et al. (2016), respectively.

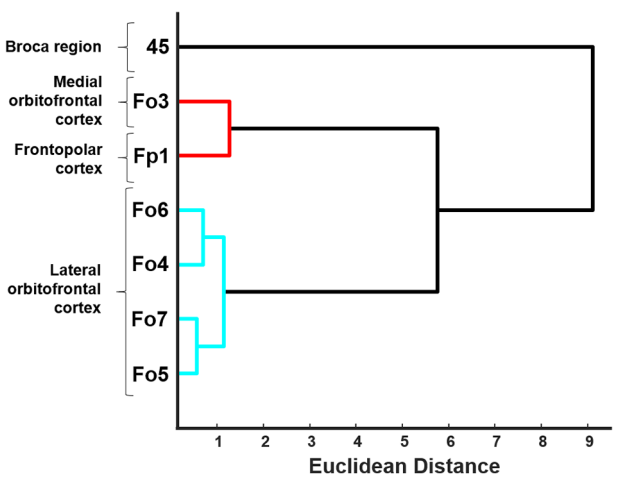

FIGURE 7 | Dendrogram of the hierarchical cluster analysis of areas Fo4–Fo7 of the lateral OFC, area Fo3 of the medial OFC (Henssen et al., 2016), area Fp1 of the frontal pole (Bludau et al., 2014) and area 45 of the Broca region (Amunts et al., 2004). Euclidean distance was used as an indicator of structural dissimilarity. Areas of the lateral OFC are building a distinguishably separate cluster and show structural differences compared to their neighboring adjacent areas.

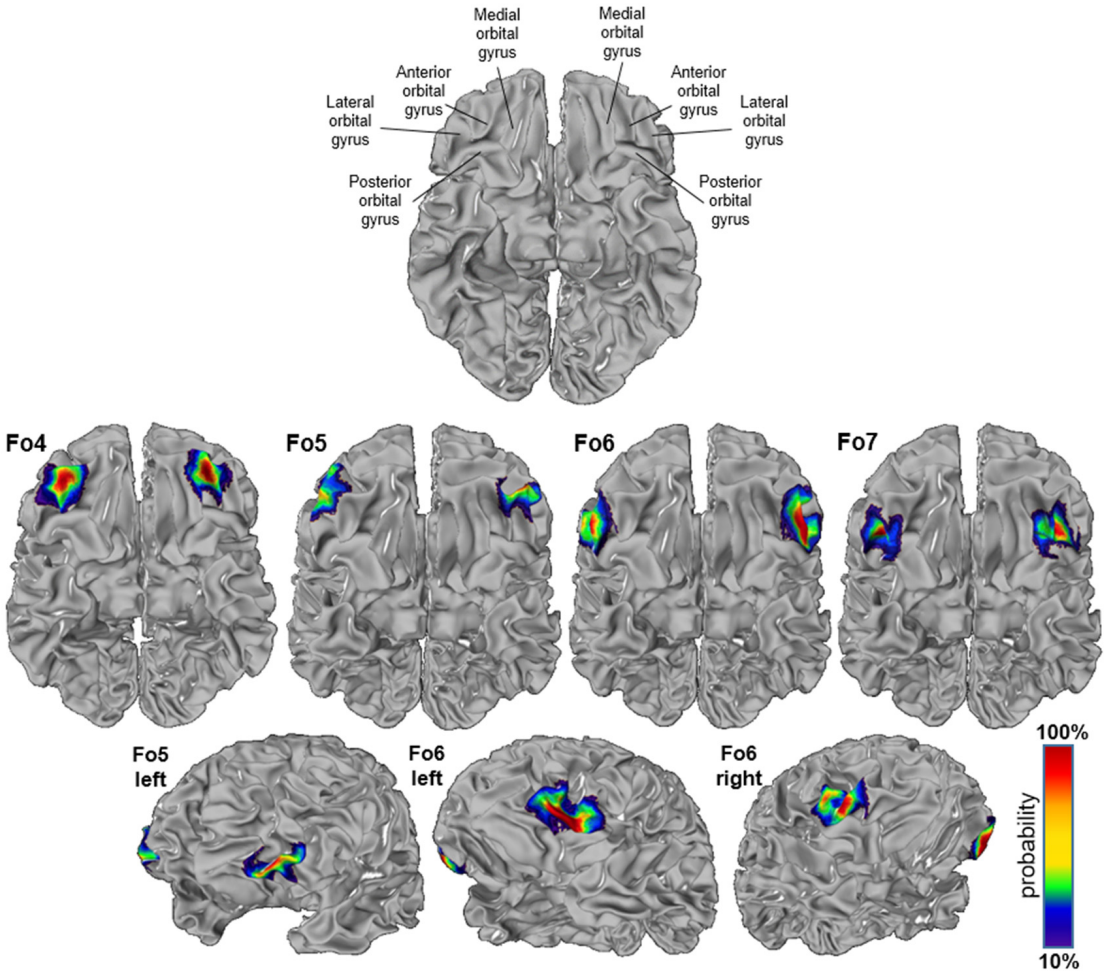

FIGURE 8 | Probability maps registered to the anatomical Montreal Neurological Institute (MNI) anatomical reference brain "Colin27"; inflated version (JuBrain atlas: https://jubrain.fz-juelich.de/apps/cytoviewer/cytoviewer.php. Ventral views of areas Fo4–Fo7 (upper panels) and lateral views of Fo5 and Fo6 (lower panels). The probability is color-coded (red = full overlap of all 10 brains, dark blue = only one brain).

Cytoarchitectonic 3D-Maps and Intersubject Variability in Space

The intersubject variability of the four lateral OFC areas was quantified, and shown as probabilistic maps in the anatomical MNI reference space (**Figure 8**). An inflated version of the JuBrain Cytoarchitectonic Atlas visualized the areas in the depths of the sulci. Fo4 occupied the AOG in all 10 brains (red area in the center). Fo5 was predominantly present in the most anterior part of the IFG and also reached into the lateral orbital sulcus and the FMS. Fo6 occupied the LOG and its medially adjacent lateral orbital sulcus with a rather low probability of being present in the horizontal ramus of the lateral sulcus. Fo7 was likely to be found in the lateral orbital sulcus, also inhabiting the medial half of the LOG, as well as the posterior part of the medial orbital sulcus. The coordinates of all analyzed areas were provided in **Table 3** for the MNI reference spaces MNI Colin27 and MNI ICBM 152.

The MPM of all four lateral OFC areas and their respective neighbors represented a non-overlapping portrayal of the occupying surface representations. Surface representations of the MPM showed the extent of the areas with respect to gyri and sulci (**Figure 9**). In addition, cytoarchitectonically delineated areas neighboring the lateral OFC, i.e., Fp1 and Fo3, as well as Fo1, Fo2, area 44 and area 45 were displayed.

The new maps are available and open for download at https://bigbrain.humanbrainproject.org/ using the DOIs: 10.25493/29G0-66F (for Fo4), 10.25493/HJMY-ZZP (for Fo5), 10.25493/34Q4-H62 (for Fo6), and 10.25493/3WEV-561 (for Fo7), and are free to share and adapt under the creative commons license agreement.

Volumes of Areas in the Lateral OFC

The volume of Fo5 was the smallest in this region, followed by Fo7, Fo4, and Fo6 as the largest area (**Supplementary Table S2**). The combined cortical volume of all lateral OFC areas for the left hemisphere was 3,111 $\pm$ 577 mm^3, and for the right

TABLE 3 | Center of gravity coordinates in MNI ICBM 152 space (upper panel) and anatomical MNI Colin27 space of continuous probability maps (lower panel) of all lateral OFC areas separated by hemisphere.

Area	Hemisphere	X	Y	Z
		Sagittal	Coronal	Horizontal
Center of gravity coordinates in MNI ICBM 152 space				
Fo4	Left	−28	53	−17
	Right	32	51	−16
Fo5	Left	−38	59	−10
	Right	44	55	−8
Fo6	Left	−45	39	−19
	Right	49	43	−15
Fo7	Left	−35	36	−10
	Right	38	37	−13
Center of gravity coordinates in anatomical MNI Colin 27 space of continuous probability maps				
Fo4	Left	−29	53	−10
	Right	32	48	−11
Fo5	Left	−37	56	−4
	Right	44	52	−1
Fo6	Left	−46	37	−11
	Right	49	37	−7
Fo7	Left	−35	34	−5
	Right	39	34	−8

hemisphere 3,126 ± 549 mm^3. Female brains had a volume of 3,075 ± 335 mm^3 in the left, and 3,133 ± 237 mm^3 in the right hemisphere. Male brains had a volume of 3,147 ± 796 mm^3 in the left, and 3,119 ± 788 mm^3 in the right hemisphere. All areal volumes were calculated for the shrinkage corrected brain volumes in each hemisphere. Using a permutation test, neither significant differences between the female and male brains, or left and right hemispheres were detected. The total cortical volume of all lateral OFC areas combined was 6,208 ± 492 mm^3 in females, and 6,268 ± 1,576 mm^3 in males. In both genders, the proportional distribution of left and right hemispheric lateral OFC was 49.5% and 50.5%, respectively, in females as well as 50.3% and 49.8%, respectively, in males.

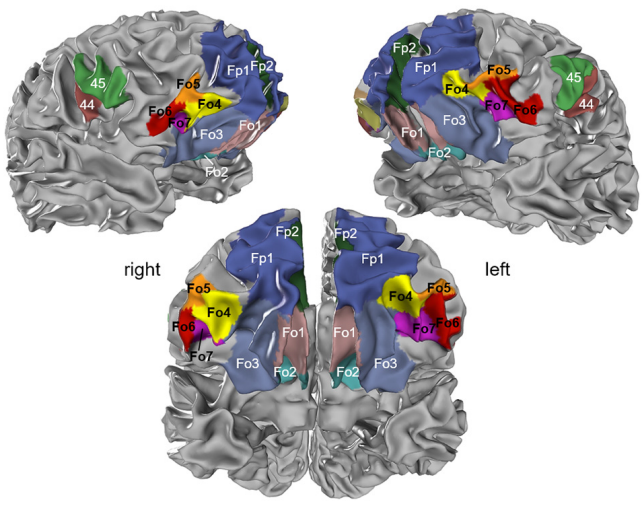

FIGURE 9 | Maximum probability map (MPM) of the four areas registered to the single subject MNI template "Colin27"; view of right (upper left panel) and left (upper right panel) hemispheres and basal view (lower panel) showing the non-overlapping surface representations of the respective areas. Maps can be viewed at http://www.fz-juelich.de/inm/inm-1/jubrain_cytoviewer, and are available at https://bigbrain.humanbrainproject.org/ for download.

Macroanatomical Patterns and Their Variability

The macroanatomy of the OFC included a variety of different patterns of gyri and sulci. The different patterns were investigated on images of the basal views of the 52 hemispheres. Four different sulcal pattern types (one with two subtypes) were found according to the *criteria of* Chiavaras and Petrides (2000) and Chiavaras et al. (2001) as well as Rodrigues et al. (2015; **Figure 10**). Sulcal patterns were rather similar between the hemispheres in 13 out of 26 brains. The other half showed more pronounced interhemispheric differences in sulcus patterns. Interhemispheric differences were found in the anterior and posterior orbital gyrus and the medial and LOG, respectively, based on the formations of the medial, lateral and TOS.

The first type of pattern was formed by a segmented medial orbital sulcus, which consisted of a rostral and a caudal portion (**Figure 10**, Type I). The lateral orbital sulcus formed one single segment, and the TOS connected the caudal portions of the medial and lateral orbital sulcus. Of the 52 hemispheres, four left and nine right hemispheres distributed this pattern type (see **Supplementary Figure S3**).

The second pattern type could be divided into two different subtypes. The first subtype resembled the shape of the letter "H". The medial and lateral orbital sulcus formed the two vertical "legs" and the TOS formed the connection between them. The AOG was separated from the posterior orbital gyrus (**Figure 10**, Type II). Additionally, an "X "-pattern subtype was found. It was characterized by a short and barely segmented AOG. The medial orbital gyrus was touching the LOG and a barely visible TOS connected the caudal portions of the former two sulci. In the more pronounced H-pattern the TOS was still relatively short, while in the X-pattern it almost completely disappeared. From all 52 hemispheres, 16 revealed the H-subtype in the left and 8 in the right hemisphere. Additionally, three out of 52 hemispheres showed the X-subtype in the left and right hemispheres, respectively.

The third pattern was characterized by a prominent TOS dividing the posterior orbital gyrus from all other gyri (**Figure 10**, Type III). Both, the medial and lateral orbital sulcus were separated into rostral and caudal parts and only the caudal sulci were connected through the TOS. Out of all examined hemispheres, only one demonstrated this type in the left and four in the right hemisphere.

The fourth pattern type was characterized by a continuous medial orbital sulcus and a fragmented lateral orbital sulcus, the counterpart of the first pattern type so to speak (**Figure 10**, Type IV). The length of the TOS varied but was longer than in the X-subtype of the second pattern. Of the 52 analyzed

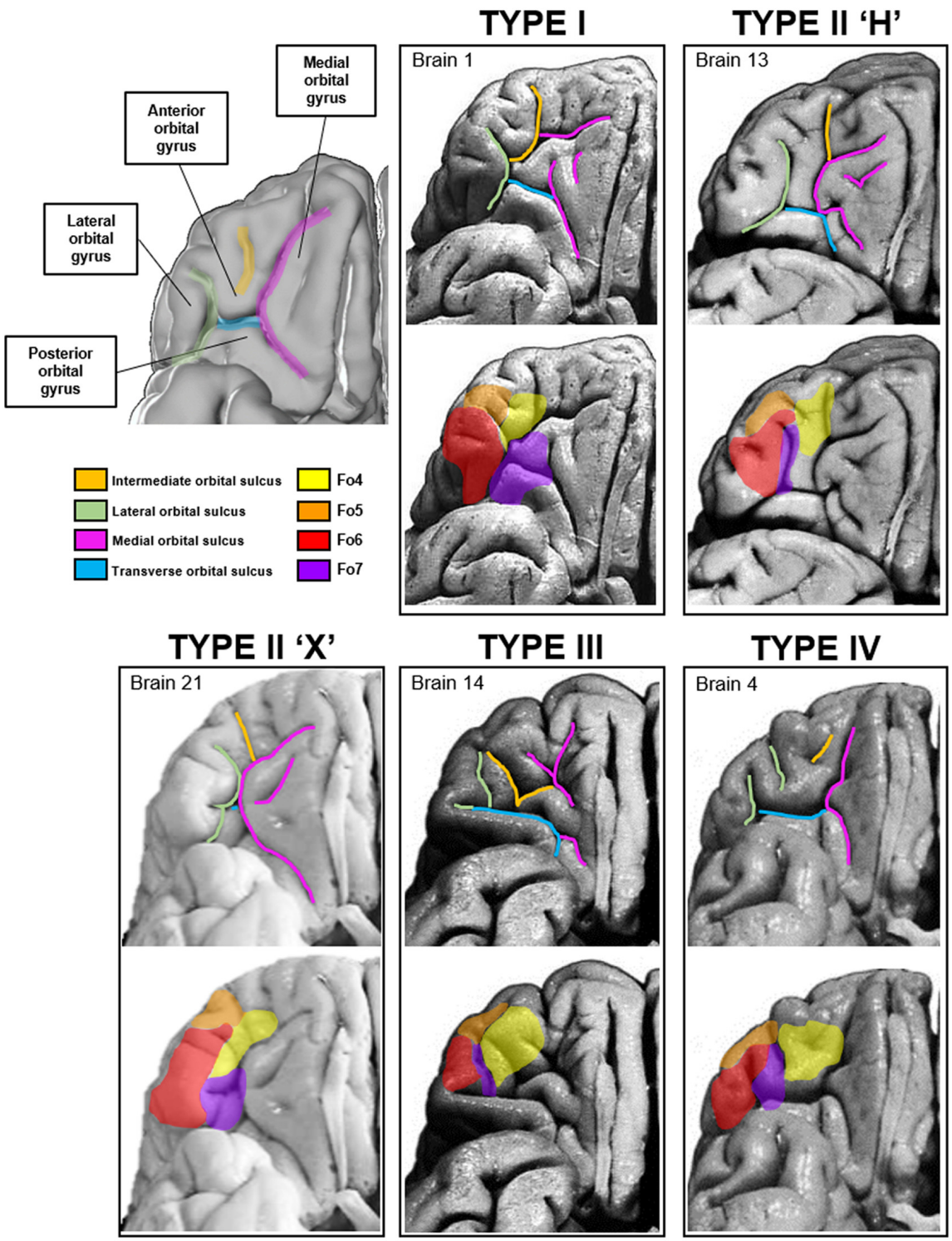

FIGURE 10 | Four types of sulci and gyri patterns in the medial and lateral orbitofrontal region of the right hemisphere have been described according to Ono, Chiavaras and Rodrigues (Ono et al., 1990; Chiavaras and Petrides, 2000; Chiavaras et al., 2001; Rodrigues et al., 2015). Localization of the respective areas differed between the four types according to the sulcal arrangements.

hemispheres, two left and five right hemispheres harbored the fourth pattern type.

Images of all brains are displayed in the supplementary material (**Supplementary Figure S2**).

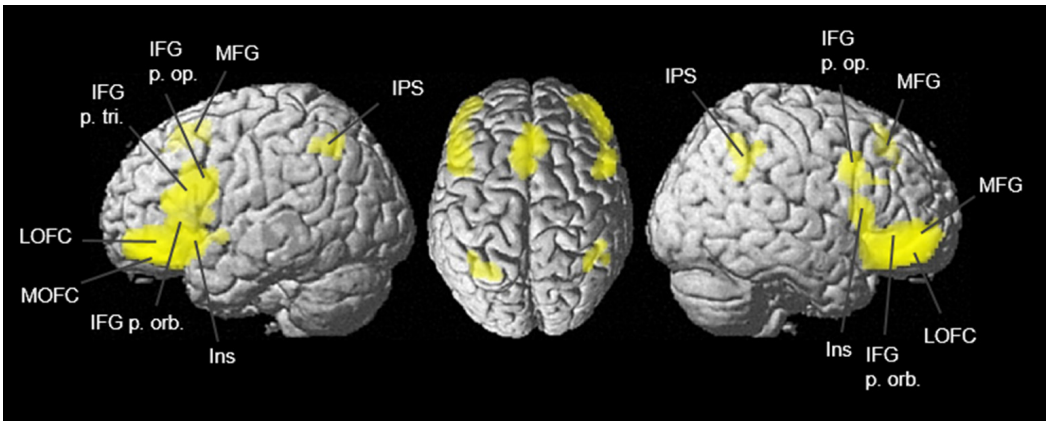

FIGURE 11 | Conjunction analysis of lateral OFC areas Fo4–Fo7 was calculated with meta-analytic connectivity modeling (MACM) and projected onto the MNI ICBM 152 reference brain (Eickhoff et al., 2009). Conjunctional representations of combined co-activation of all four lateral OFC areas revealed joint co-activations in the dorsomedial and dorsolateral prefrontal cortex, the Broca region, and the intraparietal sulcus. Due to imaging modality, subcortical co-activations are not displayed although present.

Coordinate-Based Meta-analysis of Functional Imaging Studies Reporting Activations in the Lateral OFC Areas

With MACM, conjunctional analysis enabled the detection of all co-activational patterns in each lateral OFC area in both hemispheres (**Figure 11**). All lateral OFC areas showed co-activational connectivity with Broca's region, the intraparietal sulcus, the dorsolateral prefrontal cortex as well as the Wernicke area. In addition, contrast analyses revealed differences in co-activation comparing two lateral OFC areas one at a time between the hemispheres (**Supplementary Figure S4**). All co-activation results were summarized in **Supplementary Table S3**.

Using the SPM Anatomy Toolbox (Eickhoff et al., 2005), co-activational clustering of the examined VOIs was connected with the cytoarchitectonically delineated areas of the JuBrain Cytoarchitectonic Atlas[5] (**Supplementary Tables S3, S4**). The eight co-activational clusters of Fo4 represented co-activations with hIP1 and hIP3 (Choi et al., 2006) in both hemispheres, left area 2 (Grefkes et al., 2001), left and right area Fp1 (Bludau et al., 2014) as well as area Fo3 (Henssen et al., 2016), and left area 44 (Amunts et al., 2004). Fo5 showed co-activation with hIP1, hIP2, hIP3, areas 44 and 45, Fp1, Fo3 and area 2, each in both hemispheres and right inferior parietal area PFm (Caspers et al., 2006, 2008). Fo6 revealed co-activational patterns with left areas 44 and 45, as well as being strongly connected with hIP1, hIP2, hIP3, right area PFm and right area PGa (Caspers et al., 2006, 2008). Different from the other three lateral OFC areas, Fo7 showed co-activation with left area s32 (Vogt et al., 2013), left area Fp2 (Bludau et al., 2014), right area Fo3, left amygdala (laterobasal and centromedial nucleus) and the CA1 region of the left hippocampus as well as left area 45 and the left hippocampal amygdaloid transition area (Amunts et al., 2005).

[5]https://jubrain.fz-juelich.de/apps/cytoviewer/cytoviewer.php

The analysis of BDs and PCs resulted in different area-specific task-related functionalities based on the neuroimaging studies of the BrainMap database (**Supplementary Figure S5** and **Table 4**). Hemispheric differences were detected in all four lateral OFC areas. Left Fo4 was involved in perceiving gustational input and taste. Left Fo5 had a strong bias towards reward processing and left Fo6 was activated during the processing of semantics in language-based tasks. Left Fo7 also showed activation in tasks concerning orthography, semantics, memory and gustational perception. The right Fo4 and Fo5 were co-activated while retrieving memory, right Fo5 and Fo6 share activities in the perception of touch, both comforting and painful. Also, activity while processing emotional behavior tasks was being observed in right Fo6, especially anger and disgust. Additionally, right Fo7 was active in face recognition tasks. Linking relationships between the four areas were also observed in other cognitive processes, e.g., areas Fo4, Fo5 and Fo7 were being activated in actions involving working memory. Areas Fo6 and Fo7 were active while conduction of tasks concerning attention as well as emotional induction.

DISCUSSION

In the present study, four new cytoarchitectonic areas, Fo4, Fo5, Fo6, and Fo7, of the lateral OFC were identified, analyzed and mapped in 10 human postmortem brains. Their variable location and extent were reflected in the cytoarchitectonic probabilistic maps in two reference spaces, the MNI Colin27 space and the MNI ICBM 152 space. Co-activations and functional specifics of these areas showed area-specific functional connectivities with other brain regions. BDs and PCs showed lateralization towards a rational left-hemispheric lateral OFC and an emotional right-hemispheric lateral OFC.

The macroanatomy of the OFC revealed a variety of gyral and sulcal patterns. The medial and lateral orbital sulcus were

TABLE 4 | Functional characterization of lateral OFC areas for each hemisphere, adapted from the BDPC characterization of the MACM analysis (Eickhoff et al., 2009).

Area	Functional contribution
Fo4 left	Gustational perception
	Working memory
Fo4 right	Reward processing
	Working memory
Fo5 left	Reward processing
	Language processing: phonology
	Working and Explicit memory
Fo5 right	Explicit memory
	Perception of physical pain
Fo6 left	Language processing: semantics
	Disgust, Anger
Fo6 right	Perception of physical pain
	Action inhibition
Fo7 left	Gustational perception
	Olfactory perception
	Language processing: orthography
	Memory
Fo7 right	Emotional processing
	Face recognition

connected through the TOS forming a bridge between the two former sulci. The TOS developed a distinct AOG and a visible separation of the posterior orbital gyrus from the other adjacent gyri. Several studies have identified similar shapes of sulci and gyri in the OFC and suggest a considerable interindividual variability. The *work by* Chiavaras and Petrides (2000) and Chiavaras et al. (2001) conducted an in-depth analysis of the orbital surface of the macaque and the human brain. Their work showed three different types of sulcal patterns based on the spatial variability in the OFC's anatomy, which could be partially applied to the data of the present study. The ontological development of the brain changed the course of the gyri and sulci in a considerable way. The different patterns could be explained by various genetic and environmental factors. Chi et al. (1977) defined an increasing mediolateral and caudorostral trend of the OFC's sulci, due to their varying chronology in the gestational formation. *According to Chi*, the lateral orbital sulcus is developing in the 32–35 weeks and the TOS later, at 36 weeks of gestation. All intermediate sulci emerge later at 40–44 weeks of gestation. Certain events, such as hereditary diseases caused by genetic mutations, metabolic disorders, environmental influences, etc., can influence the formation of the gyri and sulci in the fetal brain. *Chiavaras postulated* that sulci appearing early in gestation were more constant, whereas sulci appearing later were more variable (Chiavaras et al., 2001).

In addition, Rodrigues et al. (2015) have identified four different types of patterns of gyri and sulci in the OFC. Their patterning was supported by our discoveries, with the medial and lateral orbital sulcus being connected through a pronounced TOS or a complete separation of the sulci flowing into a less developed TOS. In contrast to Chiavaras and Petrides (2000), Rodrigues et al. (2015) extended their pattern detection by a fourth pattern, in which the lateral orbital sulcus was separated into rostral and caudal portions, but the medial orbital sulcus was longitudinally intact throughout the OFC region. Other authors also identified varying arrangements of sulci and gyri in the whole OFC. Earlier on, Ono et al. (1990) were able to find differing sulcal compositions. Inspecting the medial and lateral orbital sulcus, they postulated a division into anterior and posterior portions and found three different pattern types in the anterior parts of the OFC and four different types in the posterior OFC (Ono et al., 1990). More importantly, the number of sulci in the orbital region was also supported by our inspections. Ono et al. (1990) found three sulci ascending from the TOS which is analogous to our rostral portions of the medial and lateral orbital sulcus, as well as the intermediate orbital sulcus. In addition, two descending sulci were found posteriorly, which are equal to our caudal portions of the medial and lateral orbital sulcus. The classification of the sulci in the OFC also corresponded to that of the Automated Anatomical Labeling (AAL) atlas[6], which was based on data from Chiavaras and Petrides (2000) and Chiavaras et al. (2001) and is now available online in its third version (Rolls et al., 2015). *Rolls postulated* that the AOG was inhabited by area 11 l (lateral), and the LOG by area 47/12 (Rolls et al., 2015). The former designations are based on Brodmann (1909), Öngür and Price (2000) and Öngür et al. (2003).

Comparison to Previous OFC Maps and Methodical Limitations

von Economo and Koskinas (1925) delineated five areas in the OFC: F*Dp*, F*EF*, F*F*, F*Fa* and F*F*ϕ (Von Economo, 1929). Frontal areas F*Dp* and F*F*ϕ matched our delineated areas Fo5 and Fo6 in location and cytoarchitecture, respectively. The corresponding areal equivalent to area Fo4 was located in the F*EF* area. Furthermore, area F*F* extends topographically over the entire posterior orbital gyrus as well as the lateral orbital sulcus in which our Fo7 is located, but which does not exceed the TOS. Öngür and Price (2000) and Öngür et al. (2003) had identified four different areas in the lateral OFC, but just three matched our areas in location and structure, namely 47/12r in the rostral part of the lateral OFC corresponding to our area Fo5, the anterior part of 47/12 m analogous to our area Fo4, and 47/12l in the lateral parts of the ventral surface equivalent to our area Fo6. The reason for a missing locational or structural areal equivalent for area Fo7 was the fact that Öngür did not describe any areas hidden in the sulcal parts of the orbital surface. Nevertheless, their described laminar patterns were equal to our delineations of areas Fo4, Fo5 and Fo6. They found a sub laminated layer V and horizontal striations in layers III/IV in 47/12 m (Fo4), a granular layer IV in 47/12r (Fo5), and 47/12l (Fo6) being characterized by a stronger granular layer IV as well as large pyramidal cells in layer III, sharply demarcated layers and a sub laminated layer V (Öngür et al., 2003).

The identification of cytoarchitectonic areas of the lateral OFC was based on the Mahalanobis distance as a measure of cytoarchitectonic differences. Many studies of the past had identified boundaries between adjacent areas in a reproducible

[6]http://www.gin.cnrs.fr/en/tools/aal/

manner (Schleicher et al., 1998, 1999). It is less sensitive to gradual changes in the laminar pattern due to the integration of the covariance matrix changing at abrupt changes in cytoarchitecture between cortical areas (Schleicher et al., 1999; Morosan et al., 2001; Zilles et al., 2002). In order to consider differences in cortical geometry, the Mahalanobis distance was calculated for different block sizes of neighboring profiles (Schleicher et al., 1998). Borders were only accepted when the distance was significant for a large number of block sizes. Cortical regions, which were heavily tangentially cut, could not be analyzed by this method and were excluded (Amunts et al., 1999; Schleicher et al., 1999, 2000, 2005). Tangential sectioning of the cytoarchitecture represented a limitation to any type of analysis in 2D. However, alternative methods for cortical parcellation are under development, which use, for example, deep convolutional networks (Spitzer et al., 2018). In combination with high-resolution 3D models such as the Big Brain (Amunts et al., 2013), they open a new perspective to map the brain, independently on the angle of physical sectioning.

Functional Connectivity of the Lateral OFC Areas

In agreement with previous studies (Elliott et al., 2000), areas in the lateral OFC showed co-activational connectivity with areas of the association cortex, also receiving gustatory and olfactory input as well as projecting to the central part of the caudate nucleus (Öngür and Price, 2000), hypothalamus (Rolls, 2000), hippocampus, amygdala and cingulate cortex (Kringelbach and Rolls, 2004; Ross et al., 2013). We were able to confirm these connections and extend them by cytoarchitectonically delineated areas from the frontal and parietal lobe and parts of the limbic system.

For areas Fo4 and Fo5, we found co-activations in Fp1 (Bludau et al., 2014), hIP1, hIP2 and hIP3 (Choi et al., 2006; Scheperjans et al., 2008a,b) in both hemispheres. These connectivities could explain the functional contribution of Fo4 and Fo5 in memory and reward processing. Fp1 (Bludau et al., 2014), which is involved in working memory, planning and cognition, is in close proximity to Fo4 and Fo5, probably linked with the anterior OFC areas through association fibers. Areas hIP1-3 (Choi et al., 2006; Scheperjans et al., 2008a,b) are also active during working memory, both spatial and object memory are being processed here. Functional connectivity of Fo4 to Fo3 (Henssen et al., 2016) could explain Fo4's activity in gustational perception, possibly being a secondary gustational cortex region. The perception of pain with activity in the right areas Fo5 and Fo6 may also be explained by the functional connection to area PFm in the right inferior parietal lobule (Caspers et al., 2006, 2008). Attention reorientation, affective arousal and cognitive control were known functions of PFm and could explain the connection to right Fo5 and Fo6, which probably runs through the superior longitudinal fasciculus, since only the right PFm was activated. The pars orbitalis of the IFG is known to be activated in tasks which involve listening to music as well as in the processing of temporal coherence in music (Levitin and Menon, 2003). Semantics and musical structure tend to be related to each other (Levitin and Menon, 2003), what would explain the activations in the lateral OFC, especially area Fo6, in semantic tasks (Papathanassiou et al., 2000; Levitin and Menon, 2003; Amunts et al., 2004; Zald et al., 2014).

Additionally, areas 44 and 45 (Amunts et al., 2004) were co-activated with our areas Fo5, Fo6 and Fo7 in the left hemisphere, adding a language-processing role to them and broaden the knowledge of already known language-related cortical areas, as well as including a functional lateralization to the lateral OFC. Area 44 and 45 are known to be activated in verbal fluency tasks and left area 45 showed higher activation in semantic tasks (Amunts et al., 2004). According to Keller et al. (2009), it was assumed that the cytoarchitectonic differences and the different co-activation of areas 44 and 45 were also reflected in different functions. We can confirm this, although our areas of the lateral OFC are only partially different. We see similarities rather in areas that are not spatially adjacent. According to the hierarchical cluster analysis, Fo4 and Fo6 as well as Fo5 and Fo7 are structurally similar. We cannot confirm these similarities on the basis of their individual functions.

In contrast to the left hemispheric areas, right Fo5, Fo6 and Fo7 were more activated in emotion-driven cognitive processes, probably because of their connections to area s32 in the rectal gyrus (Vogt et al., 2013; Palomero-Gallagher et al., 2015), Fp2 (Bludau et al., 2014) in the medial frontal polar cortex, the hippocampus and the laterobasal and centromedial nuclei of the amygdala (Amunts et al., 2005). Area s32 is known to be activated in the processing of fear rather than sadness as well as in the processing of reward (Palomero-Gallagher et al., 2015), which corresponds to our activations in right Fo5. Area Fp2 was activated in social cognition and emotional processing (Bludau et al., 2014), which corresponded well with our functional discoveries for right areas Fo6 and Fo7. The hippocampus is well known in memory tasks (Amunts et al., 2005). Its CA1 region is activated in the processing of autobiographical and episodic memories among others (Bartsch et al., 2011), which was consistent with the functions of our right areas Fo5 and Fo6. Finally, the amygdala is mostly known to be involved in the processing of emotions, especially fear and fear conditioning (Sah et al., 2003). This connection gives the right area Fo6 more importance in the processing of fear and other negative emotions, such as anger. One possible connection between the amygdaloid nuclei and the orbital cortex could be the uncinated fasciculus, which was imaged and described elsewhere (Kier et al., 2004). The fasciculus extends into the superior, medial and inferior temporal gyrus as well as into the gyrus rectus, the medial and lateral orbital cortex and the orbital portion of the IFG (Kier et al., 2004). Possibly, the right Fo6 receives information with emotional content from the amygdaloid nuclei, which can then be analyzed to make decisions appropriate to the context. Actions may then be adapted accordingly. Also, a weak activation in the right pars orbitalis of the IFG was detected together with the adjacent anterior insula while listening to music (Levitin and Menon, 2003; Alluri et al., 2013). These activations do not need to be driven either by auditory or linguistic stimuli to process the temporal coherence of music (Levitin and Menon, 2003).

Our findings indicated that the anterior areas of the lateral OFC, areas Fo4 and Fo5, were both of importance in working and explicit memory, which already was reported in various studies (Rolls, 2000; Wallis, 2007; Rolls and Grabenhorst, 2008; Ross et al., 2013; Zald et al., 2014). Further, several studies reported the lateral OFC being activated in reward guided-behavior (Elliott et al., 2000; Rolls, 2000, 2004; Kringelbach and Rolls, 2004; Wallis, 2007; Rolls and Grabenhorst, 2008; Zald et al., 2014; Neubert et al., 2015; Cho et al., 2016; Dalton et al., 2016; Troiani et al., 2016; Rudebeck et al., 2017; Rudebeck and Rich, 2018), which could be corroborated in the present study for left area Fo5.

The lateral and posterior located areas Fo6 and Fo7 showed a more well-defined functional lateralization. Hence, processing language, especially semantics and orthography, in the left hemisphere with co-activations in the Broca region (Zald et al., 2014). The lateral OFC region is also activated in somatosensory and emotional processing, e.g., anger and disgust, in the right hemisphere with co-activations in the inferior parietal sulcus areas hIP1–hIP3 (Choi et al., 2006; Scheperjans et al., 2008a,b), as well as the amygdala, the hippocampus and the HATA region (Amunts et al., 2005). These observations were also reported in past studies (Kringelbach and Rolls, 2004; Nestor et al., 2013; Ross et al., 2013). According to Elliott et al. (2000), the right lateral OFC was associated with responses to angry faces but not to neutral faces, which corresponds well with our results with right area Fo6 being active while processing anger. All four examined lateral OFC areas seem to be involved in higher-order cognitive functions with a strong lateralization into rational task-based processing in the left hemisphere and the processing of emotionally charged behavior in the right hemisphere according to the results of the functional decoding (see also **Supplementary Figure S5** and **Table 4**).

CONCLUSION

The statistically reproducible cytoarchitectonical border detection in 10 postmortem brains allowed to identify four new cytoarchitectonically distinct areas Fo4, Fo5, Fo6, and Fo7. Probabilistic maps were computed demonstrating for the first time their different locational extent and interindividual variability. The functional meta-analysis of the lateral OFC assigned individual functions to its areas which revealed an interhemispheric lateralization. The processing of language and working memory revealed activations in the left hemisphere as opposed to the perception of gustational input, physical pain as well as emotional processing in the right hemisphere. The new maps of the areas in the lateral OFC were included in the publicly available JuBrain Cytoarchitectonic Atlas (DOI: 10.25493/8EGG-ZAR), furthermore they are available as separate downloads at the DOIs: 10.25493/29G0-66F (for Fo4), 10.25493/HJMY-ZZP (for Fo5), 10.25493/34Q4-H62 (for Fo6), and 10.25493/3WEV-561 (for Fo7). All maps are available in the MNI Colin27 and MNI ICBM 152 reference spaces. Since the lateral OFC was also natively mapped in the "BigBrain," all maps are available in the "BigBrain" space as well. The fact that the maps are offered in different reference spaces and thus also in different resolutions enables a specific and adapted use by a broad readership. The here presented new insights of the lateral OFC may provide a better understanding of its functional relevance and the new maps can now be used as an anatomical reference for *in vivo* mapping procedures.

DATA AVAILABILITY STATEMENT

All datasets generated for this study are included in the article/**Supplementary Material**.

ETHICS STATEMENT

Body donors gave written informed consent for the general use of postmortem tissue used in this study for aims of research and education. The usage is covered by a vote of the ethics committee of the medical faculty of the Heinrich Heine University Düsseldorf (#4863).

AUTHOR CONTRIBUTIONS

Cytoarchitectonic characterization, statistical border detection of the lateral OFC areas and statistics were performed and calculated by MW with support by KA and SC. KA designed the study. Prior lateral OFC analysis by FG was part of the analysis. Hierarchical cluster analysis was prepared by MW and calculated by SB. Volumetric analysis was estimated by HM and final calculations were made by MW and SB. Probabilistic maps and MPMs were calculated by HM, final adaptions of these maps were made by MW. Functional characterization was estimated by MW and MACM analysis was conducted by MW with support by SE. Discussion of results and writing were performed by all co-authors.

FUNDING

This project has received funding from the European Union's Horizon 2020 Research and Innovation Programme under Grant Agreement No. 785907 (HBP SGA2).

ACKNOWLEDGMENTS

We thank Prof. Karl Zilles and Prof. Rüdiger Seitz for their continuous input and support throughout the whole project time. Special thanks also go out to Julia Camilleri for her assistance and help.

SUPPLEMENTARY MATERIAL

The Supplementary Material for this article can be found online at: https://www.frontiersin.org/articles/10.3389/fnana.2020.00002/full#supplementary-material.

REFERENCES

Alluri, V., Toiviainen, P., Lund, T. E., Wallentin, M., Vuust, P., Nandi, A. K., et al. (2013). From vivaldi to beatles and back: predicting lateralized brain responses to music. *NeuroImage* 83, 627–636. doi: 10.1016/j.neuroimage.2013.06.064

Amunts, K., Armstrong, E., Malikovic, A., Hömke, L., Mohlberg, H., Schleicher, A., et al. (2007). Gender-specific left-right asymmetries in human visual cortex. *J. Neurosci.* 27, 1356–1364. doi: 10.1523/JNEUROSCI.4753-06.2007

Amunts, K., Kedo, O., Kindler, M., Pieperhoff, P., Mohlberg, H., Shah, N. J., et al. (2005). Cytoarchitectonic mapping of the human amygdala, hippocampal region and entorhinal cortex: intersubject variability and probability maps. *Anat. Embryol.* 210, 343–352. doi: 10.1007/s00429-005-0025-5

Amunts, K., Lepage, C., Borgeat, L., Mohlberg, H., Dickscheid, T., Rousseau, M. É., et al. (2013). BigBrain: an ultrahigh-resolution 3D human brain model. *Science* 340, 1472–1475. doi: 10.1126/science.1235381

Amunts, K., Schleicher, A., Bürgel, U., Mohlberg, H., Uylings, H. B. M., and Zilles, K. (1999). Broca's region revisited: cytoarchitecture and intersubject variability. *J. Comp. Neurol.* 412, 319–341. doi: 10.1002/(sici)1096-9861(19990920)412:2<319::aid-cne10>3.0.co;2-7

Amunts, K., Weiss, P. H., Mohlberg, H., Pieperhoff, P., Eickhoff, S. B., Gurd, J. M., et al. (2004). Analysis of neural mechanisms underlying verbal fluency in cytoarchitectonically defined stereotaxic space—the roles of Brodmann areas 44 and 45. *NeuroImage* 22, 42–56. doi: 10.1016/j.neuroimage.2003.12.031

Amunts, K., and Zilles, K. (2015). Architectonic mapping of the human brain beyond brodmann. *Neuron* 88, 1086–1107. doi: 10.1016/j.neuron.2015.12.001

Bartsch, T., Döhring, J., Rohr, A., Jansen, O., and Deuschl, G. (2011). CA1 neurons in the human hippocampus are critical for autobiographical memory, mental time travel, and autonoetic consciousness. *Proc. Natl. Acad. Sci. U S A* 108, 17562–17567. doi: 10.1073/pnas.1110266108

Bludau, S., Eickhoff, S. B., Mohlberg, H., Caspers, S., Laird, A. R., Fox, P. T., et al. (2014). Cytoarchitecture, probability maps and functions of the human frontal pole. *NeuroImage* 93, 260–275. doi: 10.1016/j.neuroimage.2013.05.052

Brodmann, K. (1909). *Vergleichende Lokalisationslehre der Großhirnrinde.* Leipzig: Verlag von Johann Ambrosius Barth.

Campbell-Meiklejohn, D. K., Kanai, R., Bahrami, B., Bach, D. R., Dolan, R. J., Roepstorff, A., et al. (2012). Structure of orbitofrontal cortex predicts social influence. *Curr. Biol.* 22, R123–R124. doi: 10.1016/j.cub.2012.01.012

Caspers, S., Eickhoff, S. B., Geyer, S., Scheperjans, F., Mohlberg, H., Zilles, K., et al. (2008). The human inferior parietal lobule in stereotaxic space. *Brain Struct. Funct.* 212, 481–495. doi: 10.1007/s00429-008-0195-z

Caspers, S., Geyer, S., Schleicher, A., Mohlberg, H., Amunts, K., and Zilles, K. (2006). The human inferior parietal cortex: cytoarchitectonic parcellation and interindividual variability. *NeuroImage* 33, 430–448. doi: 10.1016/j.neuroimage.2006.06.054

Chi, J. G., Dooling, E. C., and Gilles, F. H. (1977). Gyral development of the human brain. *Ann. Neurol.* 1, 86–93. doi: 10.1002/ana.410010109

Chiavaras, M. M., LeGoualher, G., Evans, A., and Petrides, M. (2001). Three-dimensional probabilistic atlas of the human orbitofrontal sulci in standardized stereotaxic space. *NeuroImage* 13, 479–496. doi: 10.1006/nimg.2000.0641

Chiavaras, M. M., and Petrides, M. (2000). Orbitofrontal sulci of the human and macaque monkey brain. *J. Comp. Neurol.* 422, 35–54. doi: 10.1002/(sici)1096-9861(20000619)422:1<35::aid-cne3>3.0.co;2-e

Cho, C., Smith, D. V., and Delgado, M. R. (2016). Reward sensitivity enhances ventrolateral prefrontal cortex activation during free choice. *Front. Neurosci.* 10:529. doi: 10.3389/fnins.2016.00529

Choi, H. J., Zilles, K., Mohlberg, H., Schleicher, A., Fink, G. R., Armstrong, E., et al. (2006). Cytoarchitectonic identification and probabilistic mapping of two distinct areas within the anterior ventral bank of the human intraparietal sulcus. *J. Comp. Neurol.* 495, 53–69. doi: 10.1002/cne.20849

Dalton, G. L., Wang, N. Y., Phillips, A. G., and Floresco, S. B. (2016). Multifaceted contributions by different regions of the orbitofrontal and medial prefrontal cortex to probabilistic reversal learning. *J. Neurosci.* 36, 1996–2006. doi: 10.1523/JNEUROSCI.3366-15.2016

Deng, W., Rolls, E. T., Ji, X., Robbins, T. W., Banaschewski, T., Bokde, A. L. W., et al. (2017). Separate neural systems for behavioral change and for emotional responses to failure during behavioral inhibition. *Hum. Brain Mapp.* 38, 3527–3537. doi: 10.1002/hbm.23607

Eickhoff, S. B., Bzdok, D., Laird, A., Roski, C., Zilles, K., and Fox, P. (2011). Co-activation patterns distinguish cortical modules, their connectivity and functional differentiation. *NeuroImage* 57, 938–949. doi: 10.1016/j.neuroimage.2011.05.021

Eickhoff, S. B., Laird, A. R., Grefkes, C., Wang, L. E., Zilles, K., and Fox, P. T. (2009). Coordinate-based activation likelihood estimation meta-analysis of neuroimaging data: a random-effects approach based on empirical estimates of spatial uncertainty. *Hum. Brain Mapp.* 30, 2907–2926. doi: 10.1002/hbm.20718

Eickhoff, S. B., Nichols, T. E., Laird, A. R., Hoffstaedter, F., Amunts, K., Fox, P. T., et al. (2016). Behavior, sensitivity, and power of activation likelihood estimation characterized by massive empirical simulation. *NeuroImage* 15, 70–85. doi: 10.1016/j.neuroimage.2016.04.072

Eickhoff, S. B., Stephan, K. E., Mohlberg, H., Grefkes, C., Fink, G. R., Amunts, K., et al. (2005). A new SPM toolbox for combining probabilistic cytoarchitectonic maps and functional imaging data. *NeuroImage* 25, 1325–1335. doi: 10.1016/j.neuroimage.2004.12.034

Elliott, R., Dolan, R. J., and Frith, C. D. (2000). Dissociable functions in the medial and lateral orbitofrontal cortex: evidence from human neuroimaging studies. *Cereb. Cortex* 10, 308–317. doi: 10.1093/cercor/10.3.308

Evans, A. C., Janke, A. L., Collins, D. L., and Baillet, S. (2012). Brain templates and atlases. *NeuroImage* 62, 911–922. doi: 10.1016/j.neuroimage.2012.01.024

Grefkes, C., Geyer, S., Schormann, T., Roland, P., and Zilles, K. (2001). Human somatosensory area 2: observer-independent cytoarchitectonic mapping, interindividual variability, and population map. *NeuroImage* 14, 617–631. doi: 10.1006/nimg.2001.0858

Henssen, A., Zilles, K., Palomero-Gallagher, N., Schleicher, A., Mohlberg, H., Gerboga, F., et al. (2016). Cytoarchitecture and probability maps of the human medial orbitofrontal cortex. *Cortex* 75, 87–112. doi: 10.1016/j.cortex.2015.11.006

Hirose, S., Osada, T., Ogawa, A., Tanaka, M., Wada, H., Yoshizawa, Y., et al. (2016). Lateral-medial dissociation in orbitofrontal cortex-hypothalamus connectivity. *Front. Hum. Neurosci.* 10:244. doi: 10.3389/fnhum.2016.00244

Hof, P. R., Mufson, E. J., and Morrison, J. H. (1995). Human orbitofrontal cortex: cytoarchitecture and quantitative immunohistochemical parcellation. *J. Comp. Neurol.* 359, 48–68. doi: 10.1002/cne.903590105

Holmes, C. J., Hoge, R., Collins, L., Woods, R., Toga, A. W., and Evans, A. C. (1998). Enhancement of MR images using registration for signal averaging. *J. Comput. Assist. Tomogr.* 22, 324–333. doi: 10.1097/00004728-199803000-00032

Keller, S. S., Crow, T., Foundas, A., Amunts, K., and Roberts, N. (2009). Broca's area: nomenclature, anatomy, typology and asymmetry. *Brain Lang.* 109, 29–48. doi: 10.1016/j.bandl.2008.11.005

Kier, E. L., Staib, L. H., Davis, L. M., and Bronen, R. A. (2004). MR imaging of the temporal stem: anatomic dissection tractography of the uncinate fasciculus, inferior occipitofrontal fasciculus and Meyer's loop of the optic radiation. *Am. J. Neuroradiol.* 25, 677–691.

Kringelbach, M. L., and Rolls, E. T. (2004). The functional neuroanatomy of the human orbitofrontal cortex: evidence from neuroimaging and neuropsychology. *Prog. Neurobiol.* 72, 341–372. doi: 10.1016/j.pneurobio.2004.03.006

Laird, A. R., Eickhoff, S. B., Fox, P. M., Uecker, A. M., Ray, K. L., Saenz, J. J., et al. (2011). The BrainMap strategy for standardization, sharing and meta-analysis of neuroimaging data. *BMC Res. Notes* 4:349. doi: 10.1186/1756-0500-4-349

Laird, A. R., Eickhoff, S. B., Kurth, F., Fox, P. M., Uecker, A. M., Turner, J. A., et al. (2009). ALE meta-analysis workfl ows *via* the BrainMap database: progress towards a probabilistic functional brain atlas. *Front. Neuroinform.* 3:23. doi: 10.3389/neuro.11.023.2009

Levitin, D. J., and Menon, V. (2003). Musical structure is processed in "language" areas of the brain: a possible role for Brodmann Area 47 in temporal coherence. *NeuroImage* 20, 2142–2152. doi: 10.1016/j.neuroimage.2003.08.016

Liu, H., Qin, W., Qi, H., Jiang, T., and Yu, C. (2015). Parcellation of the human orbitofrontal cortex based on gray matter volume covariance. *Hum. Brain Mapp.* 36, 538–548. doi: 10.1002/hbm.22645

Lorenz, S., Weiner, K. S., Caspers, J., Mohlberg, H., Schleicher, A., Bludau, S., et al. (2017). Two new cytoarchitectonic areas on the human mid-fusiform gyrus. *Cereb. Cortex* 27, 373–385. doi: 10.1093/cercor/bhv225

Mahalanobis, P. C., Majumdar, D. N., Yeatts, M. W. M., and Rao, C. R. (1949). Anthropometric survey of the united provinces, 1941: a statistical study. *Calcutta Stat. Assoc. Bull.* 9, 89–324.

Merker, B. (1983). Silver staining of cell bodies by means of physical development. *J. Neurosci. Methods* 9, 235–241. doi: 10.1016/0165-0270(83)90086-9

Morosan, P., Rademacher, J., Schleicher, A., Amunts, K., Schormann, T., and Zilles, K. (2001). Human primary auditory cortex: cytoarchitectonic subdivisions and mapping into a spatial reference system. *NeuroImage* 13, 684–701. doi: 10.1006/nimg.2000.0715

Nestor, P. G., Nakamura, M., Niznikiewicz, M., Thompson, E., Levitt, J. J., Choate, V., et al. (2013). In search of the functional neuroanatomy of sociality: MRI subdivisions of orbital frontal cortex and social cognition. *Soc. Cogn. Affect. Neurosci.* 8, 460–467. doi: 10.1093/scan/nss018

Neubert, F. X., Mars, R. B., Sallet, J., and Rushworth, M. F. S. (2015). Connectivity reveals relationship of brain areas for reward-guided learning and decision making in human and monkey frontal cortex. *Proc. Natl. Acad. Sci. U S A* 112, E2695–E2704. doi: 10.1073/pnas.1410767112

Öngür, D., Ferry, A. T., and Price, J. L. (2003). Architectonic subdivision of the human orbital and medial prefrontal cortex. *J. Comp. Neurol.* 460, 425–449. doi: 10.1002/cne.10609

Öngür, D., and Price, J. L. (2000). The organization of networks within the orbital and medial prefrontal cortex of rats, monkeys and humans. *Cereb. Cortex* 10, 206–219. doi: 10.1093/cercor/10.3.206

Ono, M., Kubik, S., and Abernathey, C. D. (1990). *Atlas of the Cerebral Sulci.* New York, NY: Georg Thieme Verlag.

Palomero-Gallagher, N., Eickhoff, S. B., Hoffstaedter, F., Schleicher, A., Mohlberg, H., Vogt, B. A., et al. (2015). Functional organization of human subgenual cortical areas: relationship between architectonical segregation and connectional heterogeneity. *NeuroImage* 115, 177–190. doi: 10.1016/j.neuroimage.2015.04.053

Papathanassiou, D., Etard, O., Mellet, E., Zago, L., Mazoyer, B., and Tzourio-Mazoyer, N. (2000). A common language network for comprehension and production: a contribution to the definition of language epicenters with PET. *NeuroImage* 11, 347–357. doi: 10.1006/nimg.2000.0546

Petrides, M. (2005). Lateral prefrontal cortex: architectonic and functional organization. *Philos. Trans. R. Soc. Lond. B Biol. Sci.* 360, 781–795. doi: 10.1098/rstb.2005.1631

Petrides, M., and Pandya, D. N. (2002). Comparative cytoarchitectonic analysis of the human and the macaque ventrolateral prefrontal cortex and corticocortical connection patterns in the monkey. *Eur. J. Neurosci.* 16, 291–310. doi: 10.1046/j.1460-9568.2001.02090.x

Rajkowska, G., and Goldman-Rakic, P. S. (1995). Cytoarchitectonic definition of prefrontal areas in the normal human cortex: II. Variability in locations of areas 9 and 46 and relationship to the Talairach coordinate system. *Cereb. Cortex* 5, 323–337. doi: 10.1093/cercor/5.4.323

Richter, M., Amunts, K., Mohlberg, H., Bludau, S., Eickhoff, S. B., Zilles, K., et al. (2019). Cytoarchitectonic segregation of human posterior intraparietal and adjacent parieto-occipital sulcus and its relation to visuomotor and cognitive functions. *Cereb. Cortex* 29, 1305–1327. doi: 10.1093/cercor/bhy245

Robinson, J. L., Laird, A. R., Glahn, D. C., Lovallo, W. R., and Fox, P. T. (2010). Meta-analytic connectivity modeling: delineating the functional connectivity of the human amygdala. *Hum. Brain Mapp.* 31, 173–184. doi: 10.1002/hbm.20854

Rodrigues, T. P., Rodrigues, M. A. S., Paz Dde, A., Costa, M. D. S., Centeno, R. S., Chaddad-Neto, F. E., et al. (2015). Orbitofrontal sulcal and gyrus pattern in human: an anatomical study. *Arq. Neuropsiquiatr.* 73, 431–435. doi: 10.1590/0004-282x20150048

Rolls, E. T. (2000). The orbitofrontal cortex and reward. *Cereb. Cortex* 10, 284–294. doi: 10.1093/cercor/10.3.284

Rolls, E. T. (2004). The functions of the orbitofrontal cortex. *Brain Cogn.* 55, 11–29. doi: 10.1016/S0278-2626(03)00277-X

Rolls, E. T., and Grabenhorst, F. (2008). The orbitofrontal cortex and beyond: from affect to decision-making. *Prog. Neurobiol.* 86, 216–244. doi: 10.1016/j.pneurobio.2008.09.001

Rolls, E. T., Joliot, M., and Tzourio-Mazoyer, N. (2015). Implementation of a new parcellation of the orbitofrontal cortex in the automated anatomical labeling atlas. *NeuroImage* 122, 1–5. doi: 10.1016/j.neuroimage.2015.07.075

Ross, R. S., LoPresti, M. L., Schon, K., and Stern, C. E. (2013). Role of the hippocampus and orbitofrontal cortex during the disambiguation of social cues in working memory. *Cogn. Affect. Behav. Neurosci.* 23, 900–915. doi: 10.3758/s13415-013-0170-x

Ruan, J., Bludau, S., Palomero-Gallagher, N., Caspers, S., Mohlberg, H., Eickhoff, S. B., et al. (2018). Cytoarchitecture, probability maps, and functions of the human supplementary and pre-supplementary motor areas. *Brain Struct. Funct.* 223, 4169–4186. doi: 10.1007/s00429-018-1738-6

Rudebeck, P. H., and Rich, E. L. (2018). Orbitofrontal cortex. *Curr. Biol.* 28, R1083–R1088. doi: 10.1016/j.cub.2018.07.018

Rudebeck, P. H., Saunders, R. C., Lundgren, D. A., and Murray, E. A. (2017). Specialized representations of value in the orbital and ventrolateral prefrontal cortex: desirability versus availability of outcomes. *Neuron* 95, 1208.e5–1220.e5. doi: 10.1016/j.neuron.2017.07.042

Sah, P., Faber, E. S. L., Lopez De Armentia, M., and Power, J. (2003). The amygdaloid complex: anatomy and physiology. *Physiol. Rev.* 83, 803–834. doi: 10.1152/physrev.00002.2003

Samara, Z., Evers, E. A. T., Goulas, A., Uylings, H. B. M., Rajkowska, G., Ramaekers, J. G., et al. (2017). Human orbital and anterior medial prefrontal cortex: intrinsic connectivity parcellation and functional organization. *Brain Struct. Funct.* 222, 2941–2960. doi: 10.1007/s00429-017-1378-2

Scheperjans, F., Eickhoff, S. B., Hömke, L., Mohlberg, H., Hermann, K., Amunts, K., et al. (2008a). Probabilistic maps, morphometry, and variability of cytoarchitectonic areas in the human superior parietal cortex. *Cereb. Cortex* 18, 2141–2157. doi: 10.1093/cercor/bhm241

Scheperjans, F., Hermann, K., Eickhoff, S. B., Amunts, K., Schleicher, A., and Zilles, K. (2008b). Observer-independent cytoarchitectonic mapping of the human superior parietal cortex. *Cereb. Cortex* 18, 846–867. doi: 10.1093/cercor/bhm116

Schleicher, A., Amunts, K., Geyer, S., Kowalski, T., Schormann, T., Palomero-Gallagher, N., et al. (2000). A stereological approach to human cortical architecture: identification and delineation of cortical areas. *J. Chem. Neuroanat.* 20, 31–47. doi: 10.1016/s0891-0618(00)00076-4

Schleicher, A., Amunts, K., Geyer, S., Kowalski, T., and Zilles, K. (1998). An observer-independent cytoarchitectonic mapping of the human cortex using a stereological approach. *Acta Stereologia* 17, 75–82.

Schleicher, A., Amunts, K., Geyer, S., Morosan, P., and Zilles, K. (1999). Observer-independent method for microstructural parcellation of cerebral cortex: a quantitative approach to cytoarchitectonics. *NeuroImage* 9, 165–177. doi: 10.1006/nimg.1998.0385

Schleicher, A., Palomero-Gallagher, N., Morosan, P., Eickhoff, S. B., Kowalsi, T., de Vos, K., et al. (2005). Quantitative architectural analysis: a new approach to cortical mapping. *Anat. Embryol.* 210, 373–386. doi: 10.1007/s00429-005-0028-2

Schleicher, A., Zilles, K., and Wree, A. (1986). A quantitative approach to cytoarchitectonics: software and hardware aspects of a system for the evaluation and analysis of structural inhomogeneities in nervous tissue. *J. Neurosci. Methods* 18, 221–235. doi: 10.1016/0165-0270(86)90121-4

Spitzer, H., Kiwitz, K., Amunts, K., Harmeling, S., and Dickscheid, T. (2018). "Improving cytoarchitectonic segmentation of human brain areas with self-supervised siamese networks," in *Lecture Notes in Computer Science (Including Subseries Lecture Notes in Artificial Intelligence and Lecture Notes in Bioinformatics), 11072 LNCS 2018*, eds A. Frangi, J. Schnabel, C. Davatzikos, C. Alberola-López and G. Fichtinger (Cham: Springer), 663–671.

Troiani, V., Dougherty, C. C., Michael, A. M., and Olson, I. R. (2016). Characterization of face-selective patches in orbitofrontal cortex. *Front. Hum. Neurosci.* 10:279. doi: 10.3389/fnhum.2016.00279

Uylings, H. B. M., Sanz-Arigita, E. J., de Vos, K., Pool, C. W., Evers, P., and Rajkowska, G. (2010). 3-D cytoarchitectonic parcellation of human

orbitofrontal cortex. *Psychiatry Res.* 183, 1–20. doi: 10.1016/j.pscychresns.2010.04.012

Uylings, H. B. M., Sanz Arigital, E., De Vos, K., Smeets, W. J. A. J., Pool, C. W., Amunts, K., et al. (2000). The importance of a human 3D database and atlas for studies of prefrontal and thalamic functions. *Prog. Brain Res.* 126, 357–368. doi: 10.1016/s0079-6123(00)26024-x

Vogt, B. A., Hof, P. R., Zilles, K., Vogt, L. J., Herold, C., and Palomero-Gallagher, N. (2013). Cingulate area 32 homologies in mouse, rat, macaque and human: cytoarchitecture and receptor architecture. *J. Comp. Neurol.* 521, 4189–4204. doi: 10.1002/cne.23409

Von Economo, C. (1929). Der zellaufbau der grosshirnrinde und die progressive cerebration. *Ergeb. Physiol.* 29, 83–128. doi: 10.1007/bf02322367

von Economo, C., and Koskinas, G. N. (1925). *Die Cytoarchitektonik der Hirnrinde des Erwachsenen Menschen*, Wien: Springer Verlag.

Wallis, J. D. (2007). Orbitofrontal cortex and its contribution to decision-making. *Annu. Rev. Neurosci.* 30, 31–56. doi: 10.1146/annurev.neuro.30.051606.094334

Wree, A., Schleicher, A., and Zilles, K. (1982). Estimation of volume fractions in nervous tissue with an image analyzer. *J. Neurosci. Methods* 6, 29–43. doi: 10.1016/0165-0270(82)90014-0

Zald, D. H., McHugo, M., Ray, K. L., Glahn, D. C., Eickhoff, S. B., and Laird, A. R. (2014). Meta-analytic connectivity modeling reveals differential functional connectivity of the medial and lateral orbitofrontal cortex. *Cereb. Cortex* 24, 232–248. doi: 10.1093/cercor/bhs308

Zilles, K., Armstrong, E., Schleicher, A., and Kretschmann, H. J. (1988). The human pattern of gyrification in the cerebral cortex. *Anat. Embryol.* 179, 173–179. doi: 10.1007/bf00304699

Zilles, K., Schleicher, A., Palomero-Gallagher, N., and Amunts, K. (2002). "Quantitative analysis of cyto- and receptor architecture of the human brain," in *Brain Mapping: The Methods*, eds A. W. Toga and J. C. Mazziotta (New York, NY: Academic Press), 573–602.

Conflict of Interest: The authors declare that the research was conducted in the absence of any commercial or financial relationships that could be construed as a potential conflict of interest.

frontiers in Neuroinformatics

REVIEW
published: 06 February 2020
doi: 10.3389/fninf.2020.00004

Developmental Designs and Adult Functions of Cortical Maps in Multiple Modalities: Perception, Attention, Navigation, Numbers, Streaming, Speech, and Cognition

*Stephen Grossberg**

Center for Adaptive Systems, Graduate Program in Cognitive and Neural Systems, Departments of Mathematics & Statistics, Psychological & Brain Sciences, and Biomedical Engineering, Boston University, Boston, MA, United States

This article unifies neural modeling results that illustrate several basic design principles and mechanisms that are used by advanced brains to develop cortical maps with multiple psychological functions. One principle concerns how brains use a *strip map* that simultaneously enables one feature to be represented throughout its extent, as well as an ordered array of another feature at different positions of the strip. Strip maps include circuits to represent ocular dominance and orientation columns, place-value numbers, auditory streams, speaker-normalized speech, and cognitive working memories that can code repeated items. A second principle concerns how feature detectors for multiple functions develop in topographic maps, including maps for optic flow navigation, reinforcement learning, motion perception, and category learning at multiple organizational levels. A third principle concerns how brains exploit a spatial gradient of cells that respond at an ordered sequence of different rates. Such a rate gradient is found along the dorsoventral axis of the entorhinal cortex, whose lateral branch controls the development of time cells, and whose medial branch controls the development of grid cells. Populations of time cells can be used to learn how to adaptively time behaviors for which a time interval of hundreds of milliseconds, or several seconds, must be bridged, as occurs during trace conditioning. Populations of grid cells can be used to learn hippocampal place cells that represent the large spaces in which animals navigate. A fourth principle concerns how and why all neocortical circuits are organized into layers, and how functionally distinct columns develop in these circuits to enable map development. A final principle concerns the role of Adaptive Resonance Theory top-down matching and attentional circuits in the dynamic stabilization of early development and adult learning. Cortical maps are modeled in visual, auditory, temporal, parietal, prefrontal, entorhinal, and hippocampal cortices.

Keywords: adaptive resonance theory, ocular dominance column, auditory stream, place-value number, speaker normalization, reinforcement learning, navigation, working memory

OPEN ACCESS

Edited by:
Nick Swindale,
University of British Columbia, Canada

Reviewed by:
Bruno Poucet,
Centre National de la Recherche Scientifique (CNRS), France
Peter Stratton,
University of Queensland, Australia

***Correspondence:**
Stephen Grossberg
steve@bu.edu

Received: *15 October 2019*
Accepted: *16 January 2020*
Published: *06 February 2020*

Citation:
Grossberg S (2020) Developmental Designs and Adult Functions of Cortical Maps in Multiple Modalities: Perception, Attention, Navigation, Numbers, Streaming, Speech, and Cognition. Front. Neuroinform. 14:4. doi: 10.3389/fninf.2020.00004

CORTICAL MAPS: A BASIC PRINCIPLE OF CORTICAL DESIGN

The editors of this *Frontiers* Research Topic, Nick Swindale and Geoffrey Goodhill, have posed several basic questions about cortical maps, notably concerning whether or not, despite being ubiquitous in advanced brains, they have functional significance. In particular, these authors wrote: "while maps seem to be ubiquitous in the primary sensory cortical areas, many questions about their significance remain. Might they simply be an epiphenomenon of development with no real functional significance? How widespread are maps in the cortex? For example are there maps of speech properties in Broca's area? Are there maps in the frontal cortex?...Orientation columns are also a puzzle, because it seems they can develop in the absence of natural visual stimulation but it is not clear how this could happen. Retinal waves may not have enough structure nor are they easy for models based on them to explain how matched preferences can develop in the two eyes. Their periodic structure has also been especially hard to capture."

This article proposes answers to all these questions. It does so by unifying a series of modeling studies that were carried out during the past 40 years by the author with multiple colleagues. The article focuses upon these research streams because, to the best of my knowledge, the resultant models, after multiple stages of development and refinement, come closer to principled theories of their large targeted databases than alternative models in the literature. These multiple stages of model evolution have accumulated and satisfied computational and experimental constraints that competing models have not, at least to the present time.

This theoretical approach tries to at least partially alleviate a general problem in modeling brain models of psychological phenomena: models that propose explanations of small neurobiological data sets often cannot survive under the weight of accumulating interdisciplinary constraints. For example, in modeling visual cortical development, several models may simulate small data sets about the simplest properties of simple and complex cells. Some analyses may even cast doubt on the existence of separate classes of simple and complex cells; e.g., Mechler and Ringach (2002). However, they may fail to show how the results of their analyses can support conscious visual perception, which is the evolutionary outcome of vision.

The perspective taken in this article is to be guided by all available evidence to attempt to construct a principled computational theory that is powerful enough to explain psychological and neurobiological data on multiple levels of organization, ranging from single-cell properties to organismic behaviors. Our own models have thus been shaped by the weight of both psychological and neurobiological constraints to provide accumulating evidence for the validity of their main design principles, mechanisms, circuits, and architectures. The article will also describe various alternative models as part of its exposition, and will use this review to compare and contrast them with the models that are its focus.

As noted above, the models that have emerged from this process of conceptual and mechanistic evolution suggest answers to all the questions in the first paragraph, in addition to others about cortical organization in general and cortical maps in particular, including the organization of cortical maps within the characteristic *layers* of all neocortical circuits. Previous articles from the author and his colleagues have shown how variations of the same canonical laminar cortical architecture can be used to explain and simulate neurobiological and psychological data about vision, speech and language, and cognitive information processing. The current article suggests how and why this laminar organization, sometimes called Laminar Computing, constrains how cortical maps form. Few, if any, alternative models of cortical map formation have considered how maps develop within and across this canonical cortical laminar architecture.

Within this unifying framework, the exposition proposes how a small number of design principles and mechanisms have been used in neural models to explain and unify the explanation of psychological and neurobiological data for brain functions as diverse as:

- visual retinogeniculate, thalamocortical, and corticocortical development, perception, attention, and categorization (Grossberg and Levine, 1975; Grossberg, 1975b, 1976a; Grunewald and Grossberg, 1998; Olson and Grossberg, 1998; Grossberg and Kelly, 1999; Grossberg and Raizada, 2000; Kelly and Grossberg, 2000; Grossberg and Williamson, 2001; Raizada and Grossberg, 2001, 2003; Grossberg and Grunewald, 2002; Grossberg and Seitz, 2003; Grossberg and Swaminathan, 2004; Cao and Grossberg, 2005, 2012; Markowitz et al., 2012);
- development of entorhinal grid cells and hippocampal place cells to support spatial navigation (Gorchetchnikov and Grossberg, 2007; Grossberg and Pilly, 2012, 2014; Mhatre et al., 2012; Pilly and Grossberg, 2012, 2013a,b, 2014);
- optic flow navigation by the dorsal, or Where. cortical stream (Cameron et al., 1998; Browning et al., 2009a,b; Elder et al., 2009);
- time cells for adaptively timed learning by the hippocampus (Grossberg and Schmajuk, 1989; Fiala et al., 1996; Franklin and Grossberg, 2017);
- analog and place-value numerical representations by the parietal and prefrontal cortices (Grossberg and Repin, 2003);
- auditory streaming (Cohen et al., 1995; Grossberg et al., 2004);
- auditory scene analysis and speaker normalization by the auditory cortex (Cohen et al., 1999; Grossberg et al., 2004; Ames and Grossberg, 2008);
- reinforcement learning by cognitive-emotional interactions within and between multiple brain regions (Grossberg, 1975a, 2018, 2019; Fiala et al., 1996);
- motion vector decomposition due to form-motion interactions across the ventral, or What, and the dorsal, or Where, cortical streams (Grossberg et al., 2011);
- linguistic, spatial, and motor working memories in the prefrontal cortex that can temporarily store event sequences with repeats (Grossberg et al., 1997;

Grossberg and Myers, 2000; Grossberg and Pearson, 2008; Grossberg and Kazerounian, 2011, 2016; Silver et al., 2012);
- and sequence categories, or list chunks, in the prefrontal cortex that can encode lists of variable length (Cohen and Grossberg, 1986, 1987; Grossberg and Myers, 2000; Kazerounian and Grossberg, 2014).

Given the number and functional diversity of the types of maps reviewed herein, the model summaries will primarily emphasize the main concepts used in their design. Key references to the broader literature will be included, but the archival articles contain many more.

Laminar Computing: From Infant Development to Adult Perception, Attention, and Cognition

One important theme describes an emerging computational neural theory of how the laminar circuits of neocortex develop. Indeed, it has long been known that all perceptual and cognitive neocortex seems to have six main layers of cells, in addition to characteristic sublaminae (Martin, 1989; Brodmann, 1909) and that these neocortical circuits integrate bottom-up, top-down, and horizontal interactions. Brodmann (1909) described more than 50 distinct areas of neocortex based on differences in the thickness of the layers, and the sizes and shapes of the neurons within them. How a shared laminar organization might support different behavioral functions of these specialized areas was not, however, clear until a series of articles about Laminar Computing started to explain them (e.g., Grossberg et al., 1997; Grossberg, 1999a; Grossberg and Raizada, 2000; Grossberg and Williamson, 2001).

This theory's original focus was on the development of the visual cortex. It soon became clear, however, that it has broad implications in other areas of psychology and neuroscience, for at least two reasons. First, emergent properties of the developed circuits simulated psychological and neurobiological data about adult visual perception, attention, and learning, including the basic perceptual processes of 2D and 3D boundary completion and surface filling-in. Second, related modeling studies showed how variations of the same laminar neocortical circuits can help to explain psychological and neurobiological data about adult speech, language, and cognitive information processing, notably about the organization of cognitive and motor working memories and learned sequence categories, also called chunks or plans. These laminar cortical models built upon non-laminar models of brain development that introduced their main design constraints and mechanisms, before additional insights showed how to embody them in laminar cortical circuits with a broader explanatory and predictive range.

Laminar Computing achieves three basic general properties of biological intelligence:

(1) self-stabilizing development and learning;
(2) seamless fusion of pre-attentive, automatic, bottom-up information processing with attentive, task-selective, top-down processing; and
(3) *analog coherence*; namely a solution of the binding problem for perceptual grouping without a loss of analog sensitivity.

In fact, the proposed solution of problem (1) implies solutions to problems (2) and (3). Thus, mechanisms that enable the visual cortex to develop and learn in a stable way impose key properties of adult visual information processing in such a way that there is no strict separation between preattentive processes, such as perceptual grouping, and task-selective attention. A family of models that unifies these themes is called LAMINART because it clarifies how mechanisms of Adaptive Resonance Theory, or ART, which had previously been predicted to occur in neocortex to help stabilize cortical development and learning (e.g., Grossberg, 1980, 1999b), are realized in identified laminar visual cortical circuits (e.g., Grossberg, 1999a). The following text clarifies these issues.

Feedforward and Feedback: Self-normalizing Circuits Trade Certainty Against Speed

Neocortex can achieve fast feedforward processing when input data are unambiguous (e.g., Thorpe et al., 1996). When multiple ambiguous alternatives exist in the data, processing automatically slows down. This happens because cortical computations are normalized, so that when multiple alternatives exist, each alternative becomes less active, thereby slowing down processing. Intracortical positive feedback loops contrast-enhance and choose the alternative, or alternatives, that are best supported by the data, while negative feedback suppresses weaker alternatives. As the chosen alternatives become more active, their processing speeds up and gives rise to output signals.

Such a system "runs as fast as it can," trading certainty against speed. Because laminar neocortex uses self-normalizing competition, cell activities can be interpreted as "real-time probabilities" and the process of contrast-enhancement as one of choosing the most likely alternatives. Laminar neocortical dynamics that are modeled by ART go beyond the capabilities of Bayesian decision-making models. Indeed, ART can learn about rare but important events, such as the first outbreak of a disease, for which no priors may exist. ART can do so without confusing the rare event with similar diseases, due to ART's ability to dynamically regulate the concreteness or abstractness of learned recognition categories using vigilance control (Carpenter and Grossberg, 1987a,b; Grossberg, 2017a). ART can also learn from small and nonstationary databases from which reliable probability estimates cannot be made. It does not need a statistical analysis to succeed.

Talking about statistics: although various ART models do exhibit properties of Bayesian statistics, some go beyond the capabilities of Bayesian classifiers; e.g., Williamson (1996, 1997). Various other ART properties that go beyond Bayesian ones will be described below. More generally, ART circuit designs can be derived from thought experiments whose hypotheses are ubiquitous properties of environments that we all experience (Grossberg, 1980). ART circuits emerge as solutions that satisfy multiple environmental constraints to which humans and other terrestrial animals have successfully adapted. This fact suggests

that ART designs may, in some form, have a property of *universality* that may be expected to eventually be embodied in all autonomous adaptive intelligent devices, whether biological or artificial.

Analog and Digital: Analog Coherence

Analog coherence combines the stability of digital computing with the sensitivity of analog computing. As noted above, making decisions in neural networks typically requires the action of recurrent on-center off-surround networks whose positive on-center feedback helps to choose a winner, while negative off-surround feedback suppresses weaker alternatives. These feedback interactions endow network decisions with useful properties of coherence, notably synchronization and persistence. However, incorrectly designed feedback networks may always allocate maximum activity to a winning cell population, no matter how weak the evidence is for that decision. Such winner-take-all decisions at early stages of processing could undermine the ability of later processing stages to properly weigh accumulating evidence for decision-making. Laminar recurrent on-enter off-surround networks embody the useful properties of coherence, while also allowing grouping strength to increase with the amount of evidence for it.

Adaptive Resonance Theory and the Stability-Plasticity Dilemma

In order to dynamically stabilize learning to prevent catastrophic forgetting, advanced brains use a particular kind of top-down feedback circuit that is said to obey the ART Matching Rule (**Figure 1**, top row, left column). Without the action of such a feedback circuit, new learning could rapidly erode memories of older learning. This is called the property of *catastrophic forgetting*, a property that is ubiquitous in most neural networks, including backpropagation and the Deep Learning algorithm built upon it. Adaptive Resonance Theory, or ART, which was introduced in 1976 (Grossberg, 1976a,b, 1980) and incrementally developed to the present, is a biological neural network that solves the catastrophic forgetting problem. I prefer to call this problem the *stability-plasticity dilemma* because it requires that fast learning, or *plasticity*, be possible, without also forcing fast forgetting or a loss of memory *stability*. ART solves the stability-plasticity dilemma while overcoming 17 computational problems of backpropagation and Deep Learning (Grossberg, 1988).

Top-down learned expectations and attentional focusing are needed to solve the stability-plasticity dilemma. In particular, the ART Matching Rule governs object attention in the brain (**Figure 1**, top row, left column). In an ART Matching Rule circuit, bottom-up feature signals can, by themselves, activate feature detectors (bottom layer of the figure). An activated recognition category (top layer of the figure) can, in turn, activate top-down learned expectation signals. The top-down signals define a modulatory on-center, off-surround network. The modulatory on-center cannot, by itself, activate its target cells to suprathreshold values. However, it can sensitize, or modulate, them in preparation for matching bottom-up signals. The off-surround can, by itself, inhibit its target cells. When bottom-up and top-down signals are both active at target cells, then two sources of excitatory signals and one source of inhibitory signals converge upon them, so that they can fire ("two against one"). Cells in the off-surround receive only one source of bottom-up excitatory signals and one source of top-down inhibitory signals, so they are suppressed ("one against one"). An attentional focus hereby forms across the matched cells.

When cells in the on-center of the ART Matching Rule fire, they can reactivate the bottom-up excitatory pathways that originally activated them. An excitatory feedback loop between the feature pattern and category layers is hereby closed. It triggers a *feature-category resonance* that synchronizes, amplifies, and prolongs system activity, focuses attention upon the feature pattern that is resonating, and supports conscious recognition of the resonating category and its feature pattern (**Figure 1**, top row, right column; Grossberg, 2017b). Such a resonance can trigger learning in the adaptive weights in active bottom-up pathways and top-down expectation pathways.

Thus, unlike artificial neural networks like backpropagation and Deep Learning that include only feedforward, or bottom-up connections, a biological theory like ART includes bottom-up and top-down connections in order to solve the stability-plasticity dilemma. ART also includes recurrent horizontal connections to choose the categories whose top-down expectations are matched against bottom-up signals.

ART is currently the most advanced cognitive and neural theory about how brains learn to attend, recognize, and predict objects and events in a changing world that includes unexpected events. This claim is supported by the fact that ART has explained and predicted more psychological and neurobiological data than other theories of how brains learn, and all the computational hypotheses upon which ART is based have been supported by subsequent psychological and neurobiological data. See Grossberg (2013, 2017a,b, 2018, 2019, 2020) for reviews.

Preattentive and Attentive Learning

In the LAMINART and 3D LAMINART models that develop ART to include cortical layers and identified cortical cells within them, both *inter*cortical and *intra*cortical feedback circuits obey the ART Matching Rule (e.g., Grossberg and Raizada, 2000). In particular, both intercortical and intracortical pathways share a key decision circuit in the deeper layers, between layers 6 and 4, of each cortical area (**Figure 1**, bottom row). In particular, the *inter*cortical circuits realize top-down attention, which can dynamically stabilize learning using a modulatory on-center, off-surround network from a higher cortical region to a lower one. For example, layer 6 in the cortical area V2 can attentionally prime processing in V1 *via* a circuit of this type. Here active cells in layer 6 in V2 send excitatory topographic signals to cells in layer 6 of V1, either directly or *via* layer 5 cells. The activated V1 cells, in turn, send signals to layer 4 in V1 *via* modulatory on-center, off-surround interactions. Taken together, these various signals realize an *intercortical, top-down, modulatory on-center, off-surround network*. The flow of signals from layer 6-to-6 and then back from layer 6-to-4 is said to embody *folded feedback*.

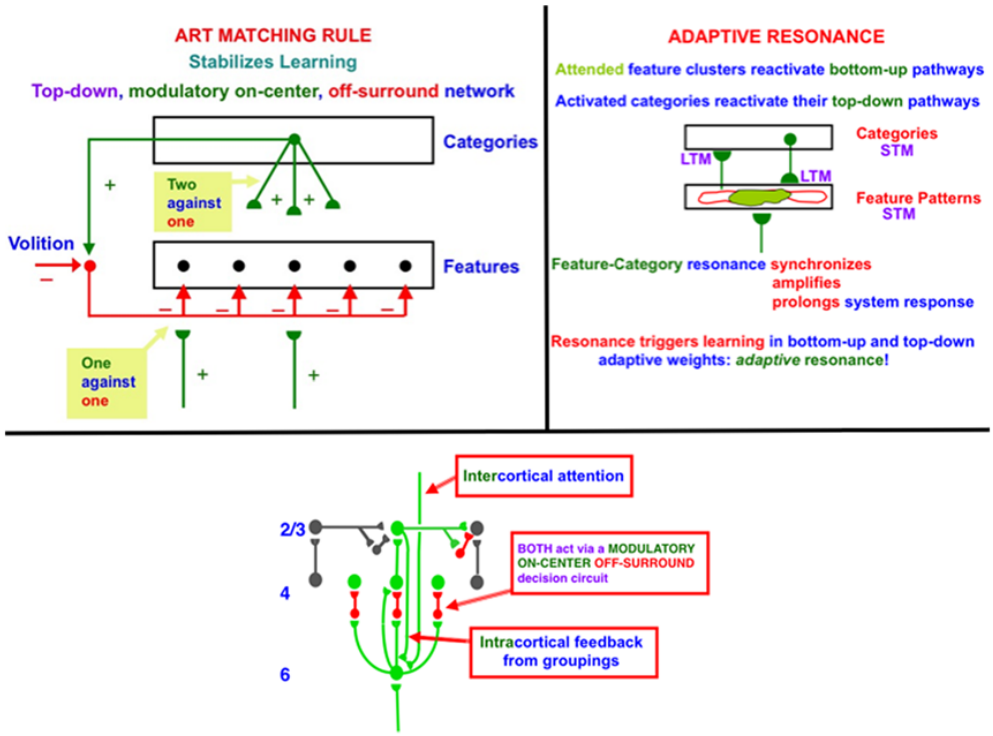

FIGURE 1 | (top row, left column) The ART Matching Rule governs object attention in the brain, notably the ventral, or What, cortical stream. Bottom-up feature signals can, by themselves, activate feature detectors (bottom layer of the figure). A recognition category (top layer of the figure) can activate top-down attentional signals. These top-down signals are carried by a modulatory on-center, off-surround network. The modulatory on-center cannot, by itself, activate its target cells to suprathreshold values, but it can sensitize, or modulate, them in preparation for matching bottom-up signals. The off-surround can, by itself, inhibit its target cells. When bottom-up and top-down signals are both active, then cells that receive two sources of excitatory signals and one source of inhibitory signals can fire ("two against one"), whereas cells in the off-surround are suppressed ("one against one"). (top row, right column) When cells in the on-center of the ART Matching Rule fire, they can reactivate the bottom-up excitatory pathways that originally activated them. An excitatory feedback loop between the feature pattern and category layers is hereby closed, leading to a *feature-category resonance*. (bottom row) A modulatory on-center, off-surround network from layer 6–4 is activated both by intercortical top-down attention and intracortical groupings in layer 2/3. The intercortical pathway supports top-down attention that obeys the ART Matching Rule. This intercortical pathway selects critical features that fall within its modulatory on-center, while inhibiting features that fall within its off-surround. The intracortical pathway enables a grouping to serve as its own attentional prime. It helps to choose a final grouping and to dynamically stabilize its own development. Because the intercortical and intracortical pathways include the same layer 6-to-4 modulatory on-center, off-surround decision network, attentive and preattentive constraints can cooperate and compete to choose the final grouping.

*Intra*cortical circuits help to dynamically stabilize the development of long-range horizontal connections that form *via* recurrent signals among cells in layer 2/3. In addition to these intralaminar recurrent interactions, interlaminar but intracortical signals help to stabilize development and learning among the layer 2/3 neurons. In particular, cells in layer 2/3 of V2 send excitatory signals to cells in layer 6 of V2. The activated V2 cells, in turn, send signals to layer 4 in V2 *via* modulatory on-center, off-surround interactions. This is the same example of folded feedback that realizes top-down attention. Here, however, it occurs within a cortical area in response to activation of horizontal cortical groupings that can form automatically and preattentively, or in the absence of attention.

Perceptual groupings are completions of boundaries in the interblob cortical stream. They include illusory contours, as well as groupings of 2D shading gradients and texture elements that support filling-in of brightnesses and colors to create 3D surface representations (Grossberg and Pessoa, 1998; Kelly and Grossberg, 2000). To emphasize the difference between intercortical and intracortical forms of attention, I like to say that "a preattentive grouping is its own attentional prime."

In summary, both the intercortical and intracortical circuits include the same layer 6-to-4 modulatory on-center, off-surround network of interactions. This shared network is said to be an *attention-preattention interface*. It is here that contextual constraints of preattentive grouping and task-related top-down attention come together to decide which from the set of possible groupings will be chosen in the current visual context.

ART MATCHING RULE SOLVES STABILITY-PLASTICITY DILEMMA *VIA* ATTENTION-PREATTENTION INTERFACE

As noted above, Adaptive Resonance Theory, or ART, uses top-down attention that obeys the ART Matching Rule to enable

advanced brains to solve the *stability-plasticity dilemma*, whereby our brains can rapidly learn throughout life, without also rapidly forgetting what they already know. Rapid brain *plasticity* can thus occur without losing the memory *stability* that prevents catastrophic forgetting. The generality of the stability-plasticity dilemma suggests that similar top-down mechanisms should occur between multiple cortical areas wherein self-stabilizing learning can occur.

What circuits does top-down attention modulate? Answering this question leads to the assertion that "a preattentive grouping is its own attentional prime," as well as to an understanding of how solving problem (1) above also solves problems (2) and (3). This is because one of the most important types of circuits that top-down attention modulates during vision is the perceptual groupings that form due to interactions among long-range horizontal connections in layer 2/3. With perceptual groupings in mind, it can readily be seen that an improper solution to the stability-plasticity problem could easily lead to an *infinite regress*, because perceptual groupings can form automatically and preattentively before providing a neural substrate upon which higher-level attentional processes can act. But how can a preattentive grouping develop in a stable way, before the higher-order attentional processes can develop with which to stabilize them? In particular, how can long-range horizontal connections in layer 2/3 of cortical area V1 develop before they can be modulated by top-down attention from cortical area V2? If such preattentive mechanisms cannot deliver reliable signals to the higher cortical areas, then any top-down signals from these higher areas may be of little use in stabilizing their own development.

I called this the *attention-preattention interface problem* because the laminar cortical circuits include layers (the *interface*) where both preattentive and attentive mechanisms can come together, notably layers 6-to-4 in **Figure 1** (bottom row), to help determine which of several possible "preattentive" groupings will be chosen.

The existence of this kind of cortical interface within multiple intercortical and intracortical feedback loops clarifies why distinguished scientists have debated for decades about the distinction between preattentive and attentive processes, as illustrated by some descendants of the great vision scientists Hermann von Helmholtz (von Helmholtz, 1866, 1962), who emphasized top-down interactions that were a precursor of current Bayesian concepts, and Gaetano Kanizsa (Kanizsa, 1955, 1974, 1976), who emphasized bottom-up and horizontal interactions. As illustrated by **Figure 1** (bottom row), all three types of processes—bottom-up, horizontal, and top-down—interact strongly using shared decision circuits within the attention-preattention interface.

WHY DOES NOT THE DEVELOPMENT OF PREATTENTIVE GROUPINGS VIOLATE THE ART MATCHING RULE?

The fact that "a preattentive grouping is its own attentional prime" solves a challenging problem for perceptual groupings, such as illusory contours, that can generate suprathreshold responses over positions that do *not* receive bottom-up inputs. They, therefore, seem to violate the ART Matching Rule, which asserts that, in order for cortical learning to be stable, only cells that get bottom-up activation should be able to fire to suprathreshold levels. That is one reason why circuits that embody the ART Matching Rule can only modulate the activities of the cells in their on-centers. How, then, can the horizontal connections that generate perceptual groupings maintain themselves in a stable way? Why are they not washed away whenever an illusory contour forms across positions that do not receive a bottom-up input? The answer is now clear: At *every* position where an illusory contour forms, the preattentive grouping is its own attentional prime, so that development and learning at that position are dynamically stabilized by the same modulatory on-center, an off-surround circuit that attention can use to stabilize learning. The current analysis hereby proposes an answer to this question that clarifies how perceptual grouping, attention, development, and adult perceptual learning are intimately bound together within the laminar circuits of the visual cortex.

INFANT DEVELOPMENT AND ADULT LEARNING USE SIMILAR LAWS: A UNIVERSAL DEVELOPMENTAL CODE

This conclusion illustrates an even broader generalization: both psychological and neurobiological data support the idea that the neural laws that regulate infant development and adult learning in grouping and attentional circuits are the same. Supportive data include the fact that the horizontal connections that support perceptual grouping in cortical areas like V1 and V2 develop through a learning process that is influenced by visual experience (Callaway and Katz, 1990; Löwel and Singer, 1992; Antonini and Stryker, 1993). It is also known that many developmental and learning processes, including those that control horizontal cortical connections, are stabilized dynamically, and can be reactivated by lesions and other sources of cortical imbalance (Gilbert and Wiesel, 1992; Das and Gilbert, 1995) in order to relearn the environmental statistics to which the new cortical substrate is exposed.

More generally, adult learning often seems to use the same types of mechanisms as the infant developmental processes upon which it builds (Kandel and O'Dell, 1992). This was one of the guiding themes behind early ART predictions from the 1970s about how brain circuits that form during infant development can support later learning that refines and builds upon them. For example, two articles that were published back-to-back in the 1978 annual volume of *Progress in Theoretical Biology* developed this theme. One article is called Communication, Memory, and Development (Grossberg, 1978b), a title that underscores the article's proposal that all cellular tissues, both inside and outside brains, embody a universal developmental code whose mathematical laws are often formally the same as those that control later learning, albeit possibly realized by different physical mechanisms;

e.g., directed growth of connections during development vs. learned tuning of synaptic connections during adult learning. The other article is called A Theory of Human Memory: Self-organization and Performance of Sensory-motor Codes, Maps, and Plans (Grossberg, 1978a), a title that summarizes the article's goal of discussing various learning processes that occur after infant development. This article included contributions to ART. Both articles laid theoretical foundations for many additional model developments during the subsequent decades.

LAMINART CIRCUITS FOR DEVELOPMENT AND ADULT PREATTENTIVE GROUPING AND ATTENTION

The LAMINART model proposes how horizontal and interlaminar connections develop in cortical areas V1 and V2, after which they support adult perceptual grouping and attention. During the development of perceptual groupings, initially there is crude clustering of weak horizontal connections until patterned visual input occurs after eye opening. Visual input strengthens and refines these connections while doubling the projection range of long-range horizontal connections in layer 2/3 (**Figure 2**, top image). These horizontal connections also double their length in the model's layer 2/3 (**Figure 2**, bottom image) between iso-orientation columns, preferentially along each cell's preferred orientation, leading to cells that exhibit other experimentally reported properties, such as length summation and appropriate responses to surround stimuli, as well as the temporal sequencing and relative amounts by which different V1 laminae develop orientation selectivity.

During development, random or visual inputs from lateral geniculate nucleus (LGN) excite cells in layer 4 (**Figure 3A**) which in turn activate cells in layer 2/3 (**Figure 3B**), where the horizontal connections self-organize between cells responding to different orientations and locations according to correlational and competitive growth rules (**Figure 3C**). This developmental process results in a network of long-range horizontal excitatory connections between layer 2/3 model pyramidal cells, along with shorter-range disynaptic inhibitory connections mediated by layer 2/3 model smooth stellate cells.

Such a network supports inward perceptual grouping between two or more approximately collinear and like-oriented boundary inducers, but not outward grouping from a single inducer. This property is called the *bipole grouping rule*. Form-sensitive scenic boundaries are hereby completed. The existence of bipole cells was predicted in Grossberg (1984) and simulated in a series of articles beginning with Grossberg and Mingolla (1985). The first neurophysiological evidence for bipole cells was reported in cortical area V2 by von der Heydt et al. (1984).

As noted above, boundary signals from layer 2/3 feedback to layer 4 *via* layer 6, which sends on-center excitation and adaptive off-surround inhibition to layer 4 (**Figure 3C**). The model develops V2 connections using similar rules, but with larger spatial scales.

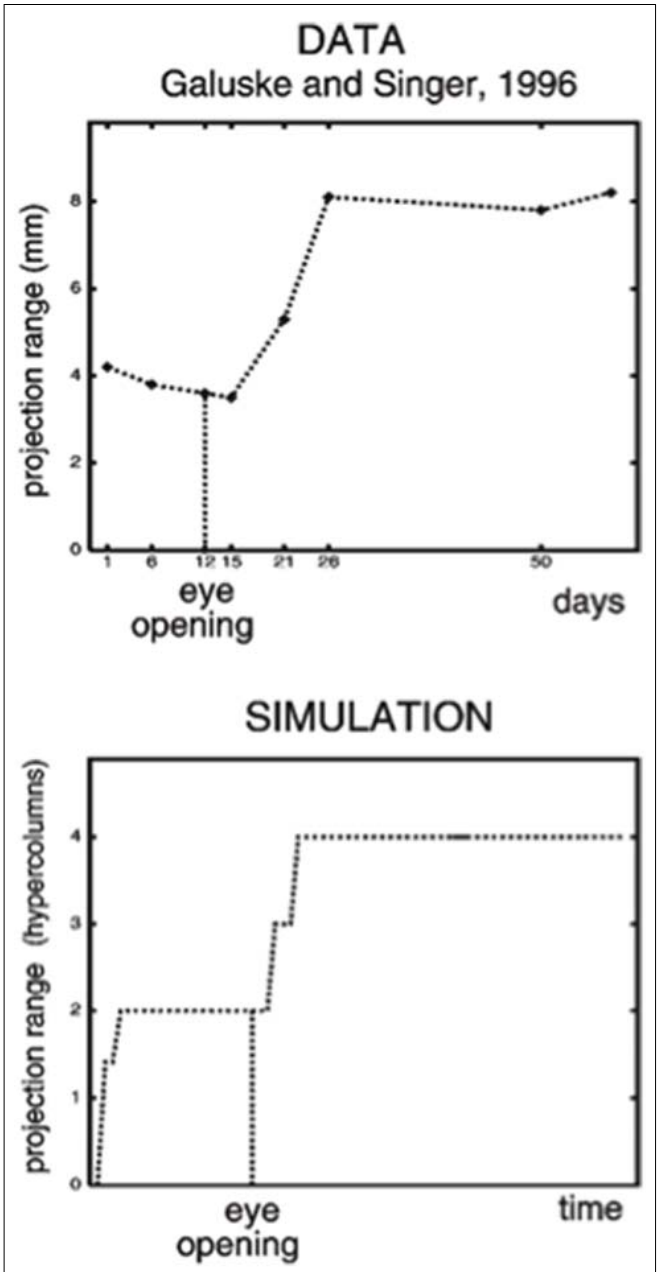

FIGURE 2 | (Top image) The projection range of pyramidal cells in cat visual cortex doubles after eye opening [adapted from Galuske and Singer (1996)]. (Bottom image) The same thing happens during model development [reprinted with permission from Grossberg and Williamson (2001)].

BALANCED EXCITATION AND INHIBITION ENABLE BOTH GROUPING AND ATTENTION CIRCUITS TO DEVELOP

The LAMINART model clarifies how the excitatory and inhibitory connections that occur in these circuits can develop by maintaining a balance between excitation and inhibition. The growth of long-range excitatory horizontal connections

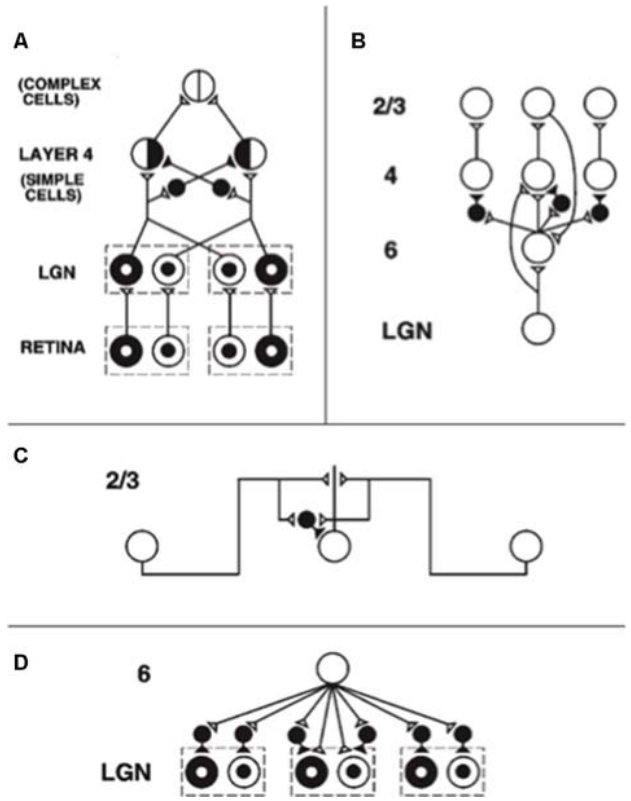

FIGURE 3 | The adult network of retinal, lateral geniculate nucleus (LGN), and cortical V1 neurons to which the developmental model converges. **(A)** Feedforward circuit from the retina to LGN to cortical layer 4: retinal ON cells have an on-center off-surround organization (white disk surrounded by black annulus). Retinal OFF cells have an off-center on-surround organization (black disk surrounded by white annulus). LGN ON and OFF cells receive feedforward ON and OFF cell inputs from the retina, which activate excitatory inputs to layer 4 oriented simple cell receptive fields. Like-oriented layer 4 simple cells with opposite contrast polarities compete before generating half-wave rectified outputs that are pooled at complex cells, which can thus respond to both polarities. **(B)** Cortical feedback loop between layers 6, 4, and 2/3: LGN activates layer 6 and layer 4 cells. Layer 6 cells excite layer 4 cells with a narrow on-center and inhibit them using layer 4 inhibitory interneurons within a broader off-surround. Layer 4 cells then excite layer 2/3 cells, which send excitatory feedback signals back to layer 6 cells *via* layer 5 (not shown). Layer 2/3 can hereby activate the layer 6-to-4 modulatory on-center, off-surround network. **(C)** Horizontal interactions in layer 2/3 support perceptual grouping: Layer 2/3 complex pyramidal cells monosynaptically excite one another *via* horizontal connections, primarily on their apical dendrites, and inhibit one another *via* disynaptic inhibition *via* model smooth stellate cells. **(D)** Top-down corticogeniculate feedback from layer 6: Layer 6 cells send topographic excitatory signals to LGN ON and OFF cells and broadly distributed inhibitory signals *via* LGN inhibitory interneurons. The feedback signals pool outputs over all cortical orientations and are delivered equally to ON and OFF cells [reprinted with permission from Grossberg and Williamson (2001)].

between layer 2/3 pyramidal cells is balanced against that of short-range disynaptic interneuronal connections. Within the attention-preattention interface that is shared by both grouping and attentional pathways, the growth of excitatory on-center connections from layer 6-to-4 is balanced against that of inhibitory interneuronal off-surround connections.

These balanced connections have been shown through theorems and computer simulations in Grossberg and Williamson (2001) to develop properly using a combination of outstar (Grossberg, 1968, 1971) and instar [Grossberg, 1976a, 1980 (Appendix)] learning laws. The names of these learning laws reflect the anatomies in which they occur (**Figure 4**). In an outstar, when a "source cell" in the center of the outstar (green disk) is activated, it sends a sampling signal along all of its axons to the synapses at their ends, which are drawn in **Figure 4** as hemidisks. In these synapses, adaptive weights, or long term memory (LTM) traces, begin learning whenever a sampling signal is active. The LTM traces can increase to match large postsynaptic activities or decrease to match small ones. Through time, these LTM traces learn a time-average of the activities of the cells that they abut whenever their sampling signal is active. In this way, an outstar can learn a time-averaged *spatial pattern* of activities of the cells in its border. In different specialized circuits, these spatial patterns can represent a wide range of specific patterns, ranging from top-down cognitive expectations to motor synergies.

The anatomy of an instar differs from that of an outstar by reversing the direction of the signal flow in its axons. This is the *duality* property of instar and outstar in **Figure 4**. Thus, in an instar, the cell that triggers learning receives signals from all the cells in the instar border. When it is activated, this cell triggers learning in all LTM traces within its abutting synapses. The pattern, or vector, of all these LTM traces, hereby becomes more parallel to the time-averaged pattern of all the input signals that they experience when the sampling cell is active. After learning occurs, input patterns that are more parallel to the LTM vector more vigorously activate their shared postsynaptic cell.

This tuning process supports the learning of recognition categories in self-organizing maps (SOM) and ART networks, among many others. In such networks, multiple sampling cells compete. The cells that are almost parallel to the current input pattern have the highest activation and win the competition. In this way, such a network's input patterns selectively activate the recognition categories that best represent them.

The development of grouping and attentional circuits in laminar neocortical networks is yet another of the applications where outstar and instar learning are valuable. *Instar* learning helps to tune the growth and selectivity of excitatory horizontal connections in layer 2/3, whereas *outstar* learning helps to tune how inhibitory interneurons balance excitation in layers 4 and 2/3 (Grossberg and Williamson, 2001).

Outstars and instars are typically used in rate-based neural networks. There has been substantial progress since their introduction in showing how their activation and learning laws can be embedded in spiking networks with detailed biophysical and biochemical interpretations, including a method for transforming any rate model that uses membrane equations into an equivalent spiking model (e.g., Fiala et al., 1996; Cao and Grossberg, 2012; Pilly and Grossberg, 2013b). This rich theme of work on learning will not be further discussed herein.

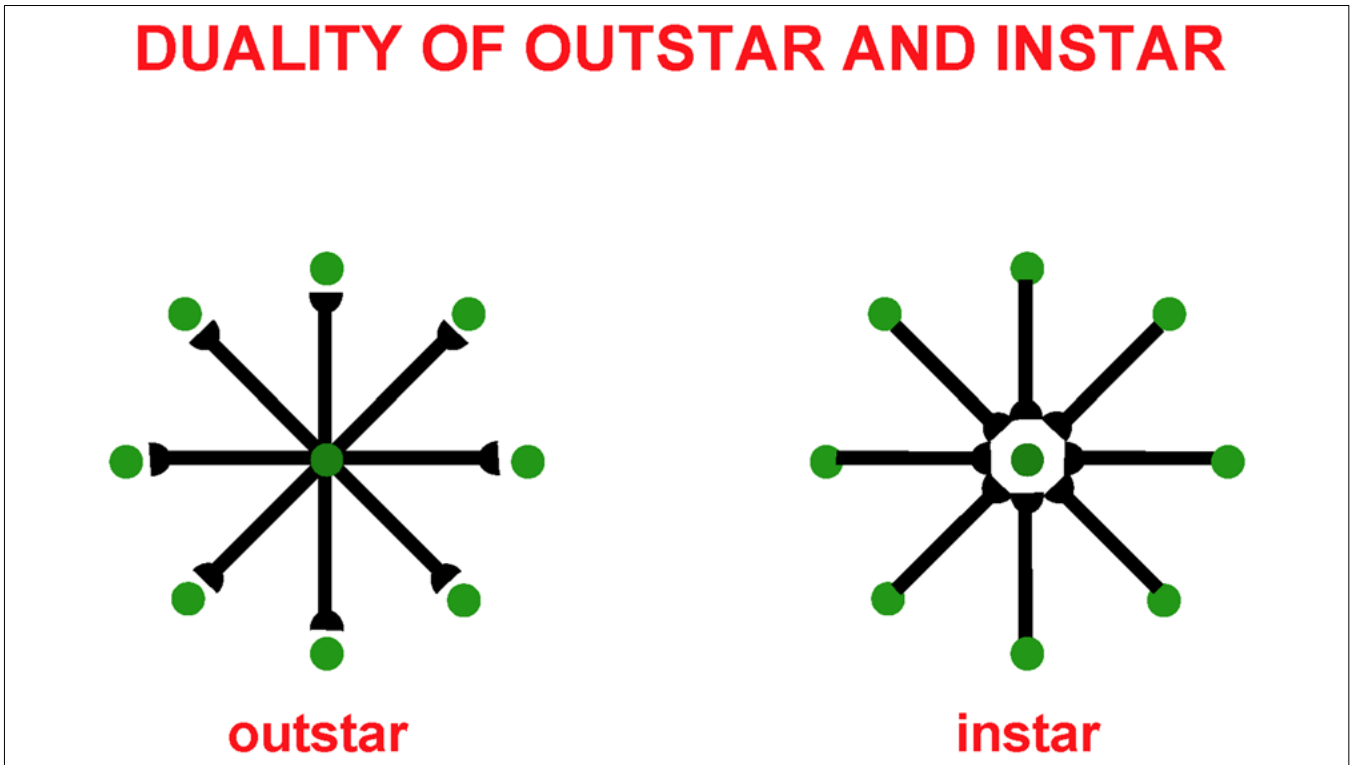

FIGURE 4 | Instar and outstar networks can both learn spatial patterns of activity from the network of cells that they sample. When the source cell of an outstar is active, its adaptive weights sample and learn a time-average of the activities in the outstar's border cells. The outstar can then read-out the net spatial pattern of activity that it learned across the border cells. When the source cell of an instar is active, its abutting adaptive weights learn a time-average of the axonal signals that they gate from sampled cells. This tuning process makes the source cell fire more selectively to activity patterns across the sampled cells that match it. The source cell functions like a recognition category for that, and similar, activity patterns.

BALANCED SIGNALS SUPPORT SPARSE AND VARIABLE SPIKING AS WELL AS RAPID SYNCHRONIZATION

The balance between excitatory and inhibitory interactions helps to explain the observed sparseness and variability in the number and temporal distribution of spikes emitted by cortical neurons (Shadlen and Newsome, 1998; van Vreeswijk and Sompolinsky, 1998). This kind of spiking does not efficiently activate neurons, but may provide background activation that helps to maintain homeostatic plasticity during periods of rest (Turrigiano, 1999). Given this inefficiency, how do neurons ever fire efficiently? A property of such balanced networks, at least when they are properly designed using neuronal membrane equations that include automatic gain control by shunting interactions (e.g., Grossberg, 2013), is that, when they are driven with external inputs, their activities are rapidly amplified and synchronized, thereby achieving efficient processing (e.g., Grossberg and Williamson, 2001; Grossberg and Versace, 2008).

The LAMINART model hereby suggests that a balance between excitation and inhibition in multiple cortical layers ensures several useful properties: stable development and learning by cortical circuits, perceptual grouping and attention, a baseline of inputs during resting states to support homeostatic plasticity, and rapid, efficient, and synchronous processing of input patterns during performance.

Various other authors have also emphasized a role for balanced excitation and inhibition, including in the development of map properties such as orientation tuning in primary visual cortex (Mariño et al., 2005) and frequency tuning in primary auditory cortex (Sun et al., 2010).

HOW DOES THE CORTICAL MAP DEVELOP IN THE LAMINAR CORTEX OF CORTICAL AREA V1?

The above results do not yet explain how the development of cortical maps in cortical area V1 may occur, how this development may be coordinated across cortical layers to form cortical columns (Hubel and Wiesel, 1974), or how maps form that coordinate inputs from both eyes. In particular, in cortical area V1, cells tuned to orientation and ocular dominance are found within its map (Blasdel, 1992a,b; Crair et al., 1997a,b; Hübener et al., 1997). The V1 map is, however, only one of many in the brain. Topographically organized maps in functional columns have been found in visual (Tootell

et al., 1982, 1998; Duffy et al., 1998), auditory (Komiya and Eggermont, 2000; Stanton and Harrison, 2000), somatosensory (Dykes et al., 1980; Grinvald et al., 1986; Wallace and Stein, 1996) and motor (Nieoullon and Rispal-Padel, 1976; Munoz et al., 1991; Chakrabarty and Martin, 2000) thalamic and cortical areas. An important task in understanding the brain, and in building computational models thereof, is to explain the organizational principles and mechanisms whereby such maps develop and are coordinated between interacting cortical columns. The cortical map in V1 will be discussed first as a prototype for maps in other modalities.

Early neural models proposed how maps of orientation (OR), ocular dominance (OD), and related properties may develop in V1 (e.g., von der Malsburg, 1973; Grossberg, 1975b, 1976a; Willshaw and von der Malsburg, 1976; Swindale, 1980, 1992; Kohonen, 1982; Linsker, 1986a,b,c; Miller et al., 1989; Rojer and Schwartz, 1990; Olson and Grossberg, 1998). These models showed how the spontaneous activity that occurs before eye opening, when it interacts with associative learning and competitive interactions, can generate maps with properties similar to those found *in vivo*. However, these results did not explain how cortical columns develop the consistent tuning for orientation and ocular dominance that is observed along with vertical penetrations across multiple cortical layers (Hubel and Wiesel, 1974). This was a significant challenge for models because the orientation maps in layers 4 and 6, as well as the crude clustering in layers 2/3 and 5, begin to develop before interlaminar connections within V1 exist with which to coordinate their formation across layers (Callaway and Katz, 1992). These initial preferences are, moreover, preserved and refined in response to patterned vision after eye opening (Callaway and Katz, 1990, 1991). It was thus an urgent question to explain how these initially shared properties across cortical layers could be coordinated without interlaminar connections that arise within the cortex itself.

Grossberg and Seitz (2003) proposed that this coordination is realized by the cortical subplate (Rakic, 1976; Luskin and Shatz, 1985; Allendoerfer and Shatz, 1994; Ghosh and Shatz, 1994; Ghosh, 1995; McAllister, 1999). The subplate exists transiently as a kind of extra deep layer of V1 where it receives thalamocortical connections at an early stage of development. These connections wait for weeks before innervating layer 4. During that time, the subplate sends vertical connections throughout the developing cortical plate (Ghosh and Shatz, 1993; McConnell et al., 1994). The critical developmental role of the subplate was also illustrated by the fact that its ablation prevents the formation of cortical cells tuned to orientation (Kanold et al., 2003) and ocular dominance maps (Ghosh and Shatz, 1992).

Grossberg and Seitz (2003) modeled how a cortical map develops within the subplate, and sends signals topographically through the cortical layers. These topographic subplate signals act as teaching signals whereby the early consistent tuning for orientation and ocular dominance across layers is achieved, even before interlaminar connections within V1 exist. The subplate's interlaminar topographic signals also activate the growth of topographic interlaminar pathways within the cortex that support cortical columns.

WHY IS THE SUBPLATE NEEDED FOR CORTICAL DEVELOPMENT?

This overview raises the question of why the subplate is needed, given that there are successful models of cortical map development that do not require a subplate. Grossberg and Seitz (2003) proposed that the subplate ensures the development of topographically precise cortical columns that coordinate the activities of cells in multiple cortical layers, as in **Figure 1** (bottom row). The subplate avoids a serious problem that was shown to occur in a laminar model of cortical development without a subplate. Without a subplate to guide the topographic growth of interlaminar connections, long-range horizontal connections in layer 2/3, among others, caused correlations across multiple cortical positions, resulting in interlaminar connections distributed broadly across the network, rather than in topographical cortical columns. A major reduction in the spatial resolution of cortical representations was hereby caused. Such a cortex could not represent the orientations and eye of origin from a sufficient number of retinal positions to provide adequate visual acuity using cortical maps.

The subplate hereby resolves a design tension between the need to provide adequate visual acuity using topographic cortical columns that can learn to become selective to different visual features, and the need to enable long-range horizontal processes like perceptual grouping to occur. Because earlier models of V1 map development included neither cortical layers nor long-range cortical interactions, this problem did not occur in them.

STM, MTM, AND LTM IN CORTICAL MAP DEVELOPMENT

As in earlier models of cortical development, the Grossberg and Seitz (2003) subplate model proposed that subplate circuits embody a source of noisy input, a bandpass filter, and normalization across model cells. Moreover, all model cortical layers realize bandpass filter and normalization properties, which arise naturally in the networks of on-center off-surround interactions between cells that obey membrane, or shunting, equations (Grossberg, 1973, 1976a, 1980, 2013). As noted above, such networks can balance cell cooperation and competition and thereby enable network neurons to remain sensitive to the relative size of inputs whose total size may vary greatly through time.

When these networks include recurrent interactions, they can also contrast enhance their cell responses to input patterns while normalizing them. In particular, contrast enhancement amplifies cell activities in response to their small initial inputs due to the small size of bottom-up adaptive weights before development occurs. The contrast-enhanced activities enable development to occur efficiently by helping to choose the cell population, or small set of populations, that receive the largest inputs. These winning

cells can then drive instar learning in the LTM traces within the synapses that abut them, and thereby tune the adaptive filters that learn the cortical map.

The above comments invoke short term memory (STM) traces, or cell activations, as well as LTM traces, or adaptive weights, in map development. No less important are medium-term memory (MTM) traces, or habituative transmitter gates (Grossberg, 1976a, 1980), which also occur in so-called depressing synapses (Abbott et al., 1997) and dynamic synapses (Tsodyks et al., 1998). MTM traces occur in the subplate and in the subsequently developing cortical layers. These transmitters gate, or multiply, the axonally-mediated signals between cells and habituate in an activity-dependent way.

MTM traces overcome a serious problem that could impede development in their absence; namely, they prevent the cells that first win the competition from persistently dominating network dynamics thereafter, due to the fact that their LTM traces have become larger. Because the STM signal in a pathway is multiplied both by LTM *and* MTM traces before a net signal activates target cells, the increasing size of the LTM trace can be offset by the decreasing size of the corresponding MTM trace when a given STM signal has been active for a while. After the MTM traces recover, the larger LTM traces can again help to choose winning cells in response to input patterns that their LTM vector best matches.

TEMPORAL ORGANIZATION OF STAGES IN CORTICAL MAP DEVELOPMENT

Spontaneous Retinal Waves Drive the Development of Retina-to-LGN and LGN-to-Subplate Connections

The model's initial circuit contains the retina, LGN and subplate (**Figure 5A**). Several types of data support the hypothesis that this circuit is monocular: Neurophysiological recordings in area 17 of kittens show that, at eye opening, the majority of cells respond only to contralateral eye inputs (Albus and Wolf, 1984). In young ferrets, LGN activity is largely unchanged when ipsilateral inputs from the retina are cut (Weliky and Katz, 1997). In addition, there exists an early bias of oriented OFF cell activity in the retina (Wong and Oakley, 1996) and the kitten cortex (Albus and Wolf, 1984) before eye opening. Accordingly, the model contains only OFF ganglion cells at this stage of development.

Spontaneous activity arising in the retina drives the development of model feedforward and feedback connections between the LGN and the subplate. After development, the pattern of feedforward connections to a given subplate cell and the feedback connections from that cell share the same axis of elongation (Murphy et al., 1999).

Markowitz et al. (2012) have additionally modeled how spontaneous retinal activity in the form of retinal waves can drive retinogeniculate map development before the LGN connects to the subplate. This study simulates how suitably defined retinal waves guide the connections from each eye into distinct LGN layers A and A1, while these connections also develop in topographic registration. The details of this model can be found in the article.

Development of Ocular Dominance Columns

The next steps in model development clarify how pathways from both eyes are coordinated during development to form ocular dominance columns in the subplate (**Figure 5B**). First, connections from the contralateral eye develop a monocular cortical map with orientation columns to the subplate. Activity from the ipsilateral eye begins subsequently, and uses the scaffold of the contralateral eye map, abetted by interocular correlated activity due to processing of the same visual inputs, to create a binocular map with ocular dominance columns. In this way, the ipsilateral eye inherits the orientation map of the contralateral eye, just as receptive fields of the cortical layers will subsequently inherit properties of the subplate.

A Subplate Map Is Taught to the Other Cortical Layers

After the subplate forms, it guides map formation in the cortical layers. In the model, each cortical layer develops separately. This property is consistent with the fact that, *in vivo*, learning in layer 2/3 occurs after layer 4 has developed its orientation map (Callaway and Katz, 1992; Galuske and Singer, 1996). The development of layer 4 is guided by topographic afferents from the subplate as afferents from the LGN begin to develop into layer 4 (**Figure 5C**). The endogenous retinal activity enables layer 4 inputs from the subplate to teach developing connections from the LGN into layer 4. The layer 4 LTM traces stabilize as a map similar to that found in the subplate is learned. Maps of ocular dominance and orientation tuning also form in layer 6 (**Figure 5E**) at a time and manner similar to the developing map in layer 4, as will be explained more fully below.

Development of the horizontal connections in layer 2/3 (**Figure 5D**) begins when subplate inputs reach this layer. *in vivo*, these subplate inputs are carried by axons that terminate in the marginal zone (Ghosh, 1995) where layer 2/3 cell dendrites occur (Callaway, 1998). In the model, long-range horizontal connections between layer 2/3 cells develop in response to lateral correlations within the subplate inputs. Recurrent signals within these developing layer 2/3 connections amplify the subplate-activated correlations, leading to refinement of the specificity of connections. The subplate inputs to layer 2/3 are the same as those to layer 4, but in layer 2/3 lateral connections develop instead of connections from the LGN. The horizontal connections in layer 5 are proposed to develop in a similar manner to those of layer 2/3.

Development of Interlaminar Connections

After maps develop in each of the cortical layers, interlaminar connections grow (Callaway and Katz, 1992). In the model, layer 6-to-4 and layer 4-to-2/3 connections develop (**Figure 5E**). They do so vertically through the cortical layers because the subplate provides the same teaching input to each of them. These vertical interlaminar connections support the dynamics of adult cortical

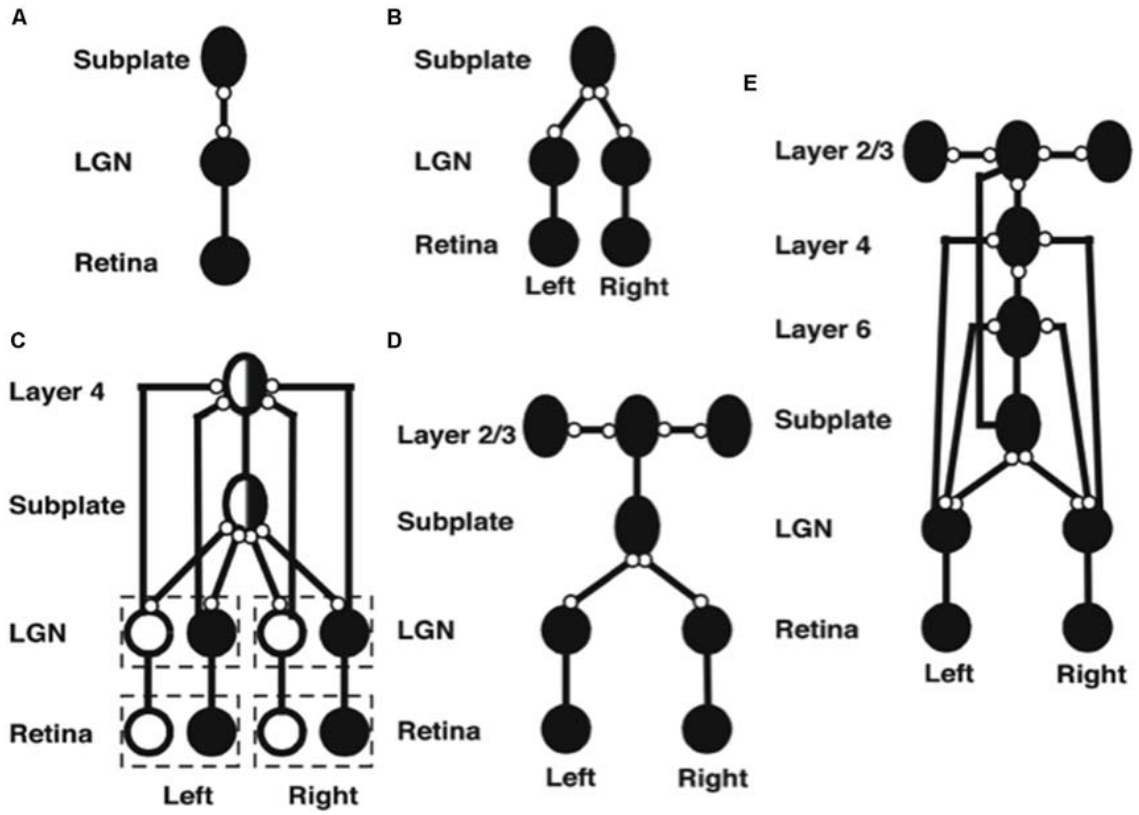

FIGURE 5 | Stages of model development (black circles denote OFF receptive fields, white circles denote ON receptive fields, ovals denote orientationally tuned cells, lines ending in open circles denote adaptive connections, lines ending without circles denote non-adaptive connections). **(A)** Monocular subplate circuit: spontaneous activity in retinal OFF cells activates the LGN, which in turn activates the subplate. Feedforward adaptive weights from the LGN to the subplate and feedback adaptive weights from the subplate to the LGN develop a map of oriented receptive fields. **(B)** Binocular subplate circuit: inputs from the second eye activate, leading to learning of a map of ocular dominance in the subplate that is superimposed on the existing orientation map. **(C)** Binocular layer 4 circuit: the ocular dominance and orientation maps in the subplate are taught to layer 4. Retinal ganglion ON cells activate and correlated retinal inputs help to segregate ON and OFF subfields in layer 4. **(D)** Layer 2/3 circuit: clusters of horizontal connections develop in layer 2/3, driven by the correlations in subplate inputs. **(E)** Fully developed model: Layer 6 develops connections to and from the LGN. Then interlaminar connections develop from layer 6 to layer 4, and from layer 4 to layer 2/3. After the subplate and its connections are removed, model maps remain stable [reprinted with permission from Grossberg and Seitz (2003)].

columns. Poorer correlations between cortical layers developed in the absence of subplate teaching signals.

Development of the Layer 6 Map and Subplate Atrophy

Layer 6 develops a map from the LGN that is topographically similar to the map in layer 4 using the same subplate inputs as layer 4 does. Layer 6 also develops a set of top-down connections to the LGN (**Figures 3D**, **5E**), which are similar to those from the subplate to the LGN (**Figures 5D,E**).

The subplate is a transient structure that atrophies after the cortical maps and interlaminar cortical connections form. In the model, after the layer 6 connections form, the subplate is removed. Simulations without the subplate demonstrate that the developed cortical architecture is stable. Grossberg and Seitz (2003) also simulated more subtle factors that influence cortical development, such as the role of BDNF (Ghosh and Shatz, 1994; Cabelli et al., 1995, 1997; Berardi and Maffei, 1999).

Development of ON and OFF Regions in Simple Cell Receptive Fields

As noted above, during early development, oriented cells found in the cortex are monocular and dominated by OFF inputs. During normal development, layer 4 simple cells quickly develop distinct ON and OFF input fields (Albus and Wolf, 1984). In contrast, dark rearing of the ferret causes convergence of ON and OFF signals to LGN cells (Akerman et al., 2002). How distinct but spatially correlated ON and OFF subfields develop is clarified by their properties in response to visual inputs (Schiller, 1992). After the eyes open, the mean firing rates of ON and OFF retinal cells equalizes. Moreover, their activities become anti-correlated because, when an ON cell is active, the OFF cell at that location is hyperpolarized and spatially neighboring OFF cells are active, due to the organization of these cells in on-center off-surround networks within each cell type, and opponent, or competitive, interactions between cell types at each position. Such a network is called a *double opponent* network. These anti-correlated activities across position help to drive selective learning of ON cell inputs

to the ON subfield of a simple cell's receptive field, and OFF cell inputs to the OFF subfield of the cell (**Figure 5C**).

Additional properties are needed to explain how, at each position, a pair of simple cells with oppositely polarized ON and OFF subfields develop. An answer can be found in the properties of the LGN double opponent networks of ON cells and OFF cells. In addition to their fast STM interactions, such networks also include MTM habituative transmitter gates in the opponent circuits whereby ON and OFF cells interact at each position. Such a network is called a *gated dipole field* (Grossberg, 1980). Its individual ON and OFF opponent cells at each position are said to form a *gated dipole*. Grossberg (1972a,b) showed how the offset of a sustained input to an ON cell in a gated dipole can cause an antagonistic rebound that transiently activates the corresponding OFF cell (**Figure 6**).

Grunewald and Grossberg (1998) have simulated the dynamics of antagonistic rebounds between LGN ON and OFF cells that interact within gated dipole fields during the development of simple cells that are also organized into ON and OFF cell pairs. Suppose that a visual input has activated ON and OFF inputs to an LGN cell, which in turn activates a cortical cell whose orientation and contrast polarity begin to develop into a simple cell with the same orientation and contrast polarity preference. When that visual input turns off, its developing simple cell also shuts off. As a result, antagonistic rebounds in the LGN ON and OFF cells cause LGN OFF and ON cells to transiently turn on, at the same time as the opponent cell of the developing simple cell also turns on. This opponent cell can then begin to learn how to become a simple cell, but one that responds to an opposite polarity input with the same orientation in the same position. When such an opposite polarity input later turns on at this position, this prior partial development give the opposite polarity cell an advantage in winning the competition with other cells. Its development as an opposite polarity cell with the same orientation and position can hereby continue. In this way, opponent pairs of simple cells with like orientation and opposite contrast polarity selectivity can develop in the same position.

Development of Complex Cells: How Anti-correlated Simple Cells Input to a Complex Cell

The development of opposite polarity simple cells with the same orientation preference at each position sets the stage for the development of complex cells. Complex cells pool inputs from pairs of like-oriented simple cells at the same position but with opposite contrast polarities; that is, with ON-OFF and OFF-ON receptive subfields across position (Hubel and Wiesel, 1962; Movshon et al., 1978). As a result, when one of the simple cells that inputs to a complex cell is active, the simple cell with the opposite contrast polarity preference at that position is silent. Their activities are anti-correlated. How does a complex cell learn to get activated by pairs of anti-correlated simple cells?

An answer follows from the previous discussion of how opposite polarity simple cells develop. In particular, suppose that a simple cell with a given contrast polarity is activated, and starts learning to activate a complex cell. When that simple cell turns off, its opposite polarity simple cell turns on due to a rapid antagonistic rebound. If the previously activated complex cell stays active during this rebound period, it can begin to become correlated with the simple cells of both contrast polarity preferences. Then, just as in the development of opposite polarity simple cells, this initial advantage of the opposite polarity simple cell in activating the complex cell will give it a competitive advantage in response to later inputs that directly turn it on, so that its opposite polarity learning can continue. Grunewald and Grossberg (1998) have simulated the development of complex cells using this kind of dynamics. That article, as well as Grossberg and Grunewald (2002), also simulates how these complex cells develop with a prescribed binocular disparity preference, which is known to occur *in vivo* (Ohzawa et al., 1990). They also simulated development of the top-down connections from complex cells in V1 to the LGN that carry out a matching process *via* the ART Matching Rule, which dynamically stabilizes both bottom-up and top-down learning (Varela and Singer, 1987; Sillito et al., 1994).

3D LAMINART: BINOCULAR VISUAL PROCESSING BY LAMINAR CORTICAL CIRCUITS

The above discussion noted that complex cells in V1 receive binocular inputs, but not how this occurs within laminar cortical circuits in a way that can support binocular vision, including boundary grouping in depth. The 3D LAMINART model proposes and simulates key properties of the anatomical, neurophysiological, and perceptual properties of the brain networks that support vision, including how complex cells in layer 2/3 of V1 become binocular, indeed disparity selective, as well as of how simple, complex, hypercomplex, and bipole cells in cortical areas V1, V2, and beyond support binocular vision (**Figure 7**; Grossberg and Howe, 2003; Grossberg, 2003; Grossberg and Swaminathan, 2004; Yazdanbakhsh and Grossberg, 2004; Cao and Grossberg, 2005, 2012; Grossberg and Yazdanbakhsh, 2005; Berzhanskaya et al., 2007; Bhatt et al., 2007; Grossberg et al., 2008; Léveillé et al., 2010). The present overview will just summarize how the model proposes that complex cells develop to represent disparity-sensitive properties within the laminar cortical circuits in V1.

Disparity-Selective Complex Cells in Layer 2/3 of V1

As noted above, complex cells pool inputs from opposite polarity simple cells with similarly oriented receptive fields. Complex cells can hereby respond all along an object's boundary even if its contrast polarity with respect to the background reverses as the boundary is traversed. Layer 2/3 is known to implement this kind of contrast-invariant boundary detection (e.g., Hubel and Wiesel, 1962; Poggio, 1972; Katz et al., 1989; Alonso and Martinez,

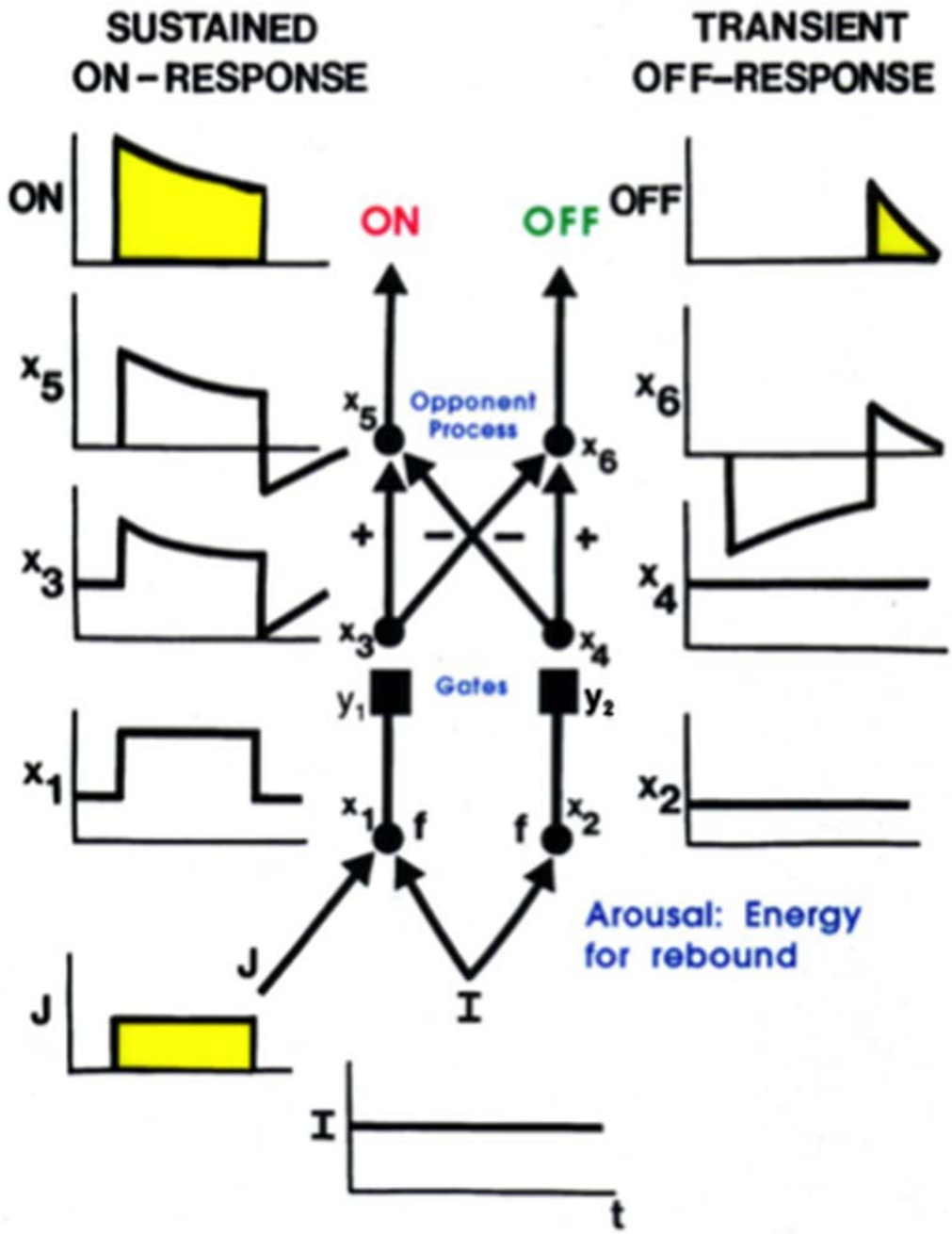

FIGURE 6 | A gated dipole opponent network can generate a transient antagonistic rebound from its OFF channel in response to offset of a sustained input (J) to its ON channel. This can happen because a nonspecific, tonically active, arousal input (I) equally energizes both the ON and OFF channels. The phasic input J to the ON channel habituates its transmitter gate (y_1) and thus its net output after competition occurs between the ON and OFF channels (see sustained ON-response in yellow). When J shuts off, the net input to the OFF channel is larger than that to the ON channel, because both ON and OFF channels are now driven by the same arousal input I, but the ON channel gate (y_1) is more habituated than the OFF channel gate (y_2). An antagonistic rebound then occurs in the OFF channel. The rebound is transient (see transient OFF-response in yellow) because it gradually causes an equal amount of habituation to occur in the transmitter gates of both the ON and OFF channels.

1998). It is also known that monocular, polarity-selective simple cells exist in layer 4 (Hubel and Wiesel, 1962, 1968; Schiller et al., 1976; Callaway, 1998). These properties raise the question: How do the monocular, polarity-selective simple cells in layer 4 get transformed into binocular, disparity-selective, contrast-invariant complex cells in layer 2/3?

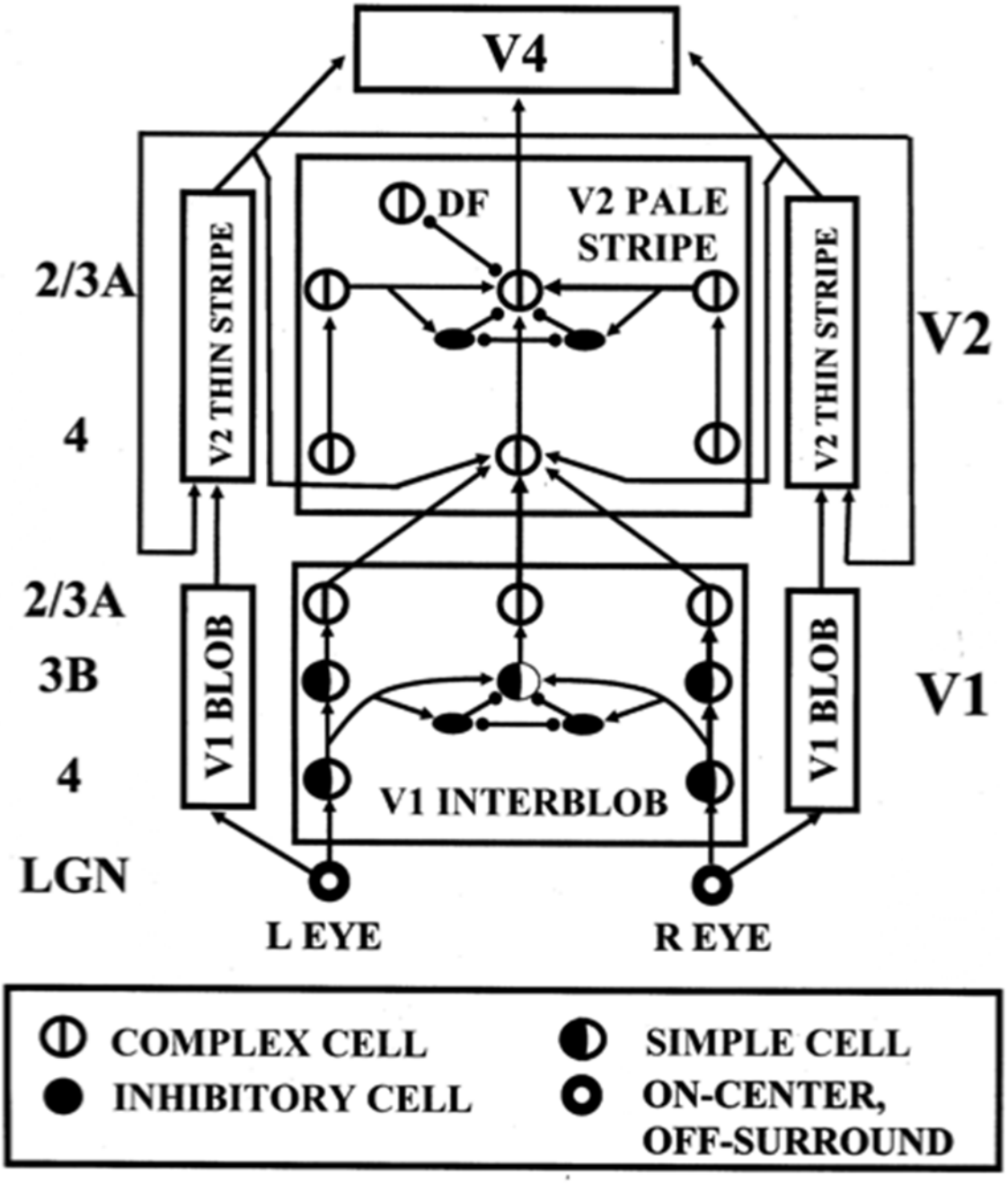

FIGURE 7 | The 3D LAMINART model circuit diagram. The model consists of a (V1 Interblob)—(V2 Pale Stripe)—V4 boundary stream which computes 3D perceptual groupings, and a (V1 Blob)—(V2 Thin Stripe)—V4 surface stream which computes 3D surface representations of lightness, color, and depth. The two processing streams interact to overcome their complementary deficiencies (Grossberg, 2000) and create consistent 3D boundary and surface percepts. Note the binocular interaction in layer 3B of spatially displaced inputs from monocular left and right eye simple cells with the same polarity in layer 4, before opposite polarity binocular simple cells input to complex cells in layer 2/3A [reprinted with permission from Cao and Grossberg (2005)].

Grossberg and Howe (2003) proposed that this occurs in two stages (**Figure 7**): first, pairs of same-polarity, like-oriented, *monocular* simple cells, that respond to opposite eyes at nearby positions in layer 4, input to same-polarity, like-oriented, *binocular* simple cells at an intermediate position in layer 3B. These binocular simple cells respond selectively to a narrow range of binocular disparities. This processing stage clarifies how inputs from the two eyes binocularly fuse cells that are sensitive to the same polarity, but not to opposite contrast polarities (Julesz, 1971; Poggio and Poggio, 1984; Read et al., 2002). This *same*

sign property is one of several that help to guarantee that only monocular cell responses from the left and right eyes that arise from the same object can be binocularly fused. These binocular simple cells can develop from their monocular simple cell inputs using properties of SOM that were summarized above.

Second, pairs of *opposite-polarity*, like-oriented, binocular simple cells at the same position in layer 3B learn to input to *contrast-invariant*, like-oriented, binocular complex cells in layer 2/3 using the above adaptive filtering and rebound properties. These hypotheses are supported by facts such as: layer 4 cells output to layer 3B, but not to layer 2/3 (Callaway, 1998); layer 3B projects heavily to layer 2/3 (Callaway, 1998); and layer 2/3 contains a large number of binocular and complex cells (Poggio, 1972). These complex cells can develop using the properties of opponent rebounds that were summarized above.

This summary does not go into multiple subtleties that are explained in the archival modeling articles, such as the slight differences in the orientation preferences of monocular simple cells of opposite eyes that are activated by viewing an object boundary in-depth, and that is fused at binocular simple cells.

Alternative Models of V1 Complex Cells

Various alternative models of complex cells have been proposed. For example, Tao et al. (2004) have suggested a model of the neuronal dynamics in the input layer 4Cα of LGN output signals to cortical area V1. They propose to explain how both simple and complex cell responses are found in this layer, and that "through a balance of strong recurrent excitation and inhibition this model yields complex responses in those cells with relatively little LGN drive." Chance et al. (1999) have proposed that phase-specific outputs of excitatory simple cells drive cells that are coupled together in an excitatory recurrent network. In particular, these authors propose that "local recurrent connections. . .are responsible for the spatial-phase invariance of complex-cell responses. . .neurons exhibit simple-cell responses when recurrent connections are weak and complex-cell responses when they are strong, suggesting that simple and complex cells are the low- and high-gain limits of the same basic cortical circuit" (p. 277).

These models are underconstrained in the sense that they do not explain how critical properties, such as the binocular disparity-selective responding of complex cells is realized. They also do not explain how monocular simple cells and binocular complex cells are proposed to support 3D figure-ground separation and both 3D boundary and surface perception. These accomplishments of the visual cortex have been modeled as part of the 3D LAMINART model, whose model cell types and interlaminar interactions have been supported by multiple anatomical, neurophysiological, and psychophysical experiments (e.g., Grossberg and Raizada, 2000; Raizada and Grossberg, 2001, 2003; Grossberg and Swaminathan, 2004; Cao and Grossberg, 2005, 2012, 2014, 2018; Fang and Grossberg, 2009; Grossberg, 2016a). These articles also provide comparative discussions of other models of visual cortex that do not attempt to explain such data; e.g., Raizada and Grossberg (2003, Section 7).

As noted above, one motivation for these models is the fact that both simple and complex cell properties can be recorded in cortical layer 4. There are several possible reasons for this fact, due to both bottom-up and top-down influences, all of them consistent with the theoretical perspective taken in this article. A bottom-up explanation would note that, just as there may be varying degrees of ocular dominance across cells in the V1 cortical map (LeVay et al., 1978; Kara and Boyd, 2009), if only due to the statistical nature of map development, so too may there be gradients of polarity-selective vs. polarity-pooling bottom-up interactions there. A top-down explanation would note that complex cells in layer 2/3 of V1 feed back to simple cells in layer 4 of V1, thereby mixing, albeit with a brief temporal delay, their polarity-invariant properties with the polarity-specific properties of simple cells. Sorting out these various possibilities would benefit from more detailed statistical analyses of both experiments and models of V1 cortical development.

HOMOLOGS OF OCULAR DOMINANCE COLUMNS IN OTHER DEVELOPING CORTICAL MODALITIES: STRIP MAPS

The preceding sections focused on models of visual cortical development and architecture because psychological and neurobiological studies of vision were some of the earliest ones made and because they enjoy one of the largest interdisciplinary databases in science. Other neural models of cortical development have shown that several modalities use variants of the same design principles and mechanisms that support visual cortical development. The following text reviews and unifies some highlights of their properties.

Strip Maps in Multiple Modalities

A key property is that all the maps exploit variations of how a single ocular dominance column can be used to represent multiple orientations of images that excite an eye at a given position. In all the other examples that will now be summarized, a strip of cells represents a given property that is also used to represent an ordered series of changes in another property. Such a design is accordingly called a *strip map*. A strip map provides enough cortical representational space for the ordered values of the second property to be represented in a map that also codes the first property. Examples include how cortical maps develop to represent the following kinds of information: place-value numbers, auditory streams, speaker-normalized speech, and cognitive working memories that can store repeated items; e.g., ABACBD. These maps occur in both the ventral What cortical stream and the dorsal Where cortical stream, and at multiple levels of the cortical hierarchy.

Development of Place-Value Numbers and Numerical Comparisons

Both animals and humans are capable of representing and comparing numerical quantities. This competence is supported by a spatial map in the inferior parietal cortex that represents small numbers in order of increasing size (Dehaene et al., 1996; Pinel et al., 1999; Piazza et al., 2004). Rhesus monkeys are also known to represent the numerosities 1–9 on an ordinal scale (Brannon and Terrace, 1998, 2000). Only humans,

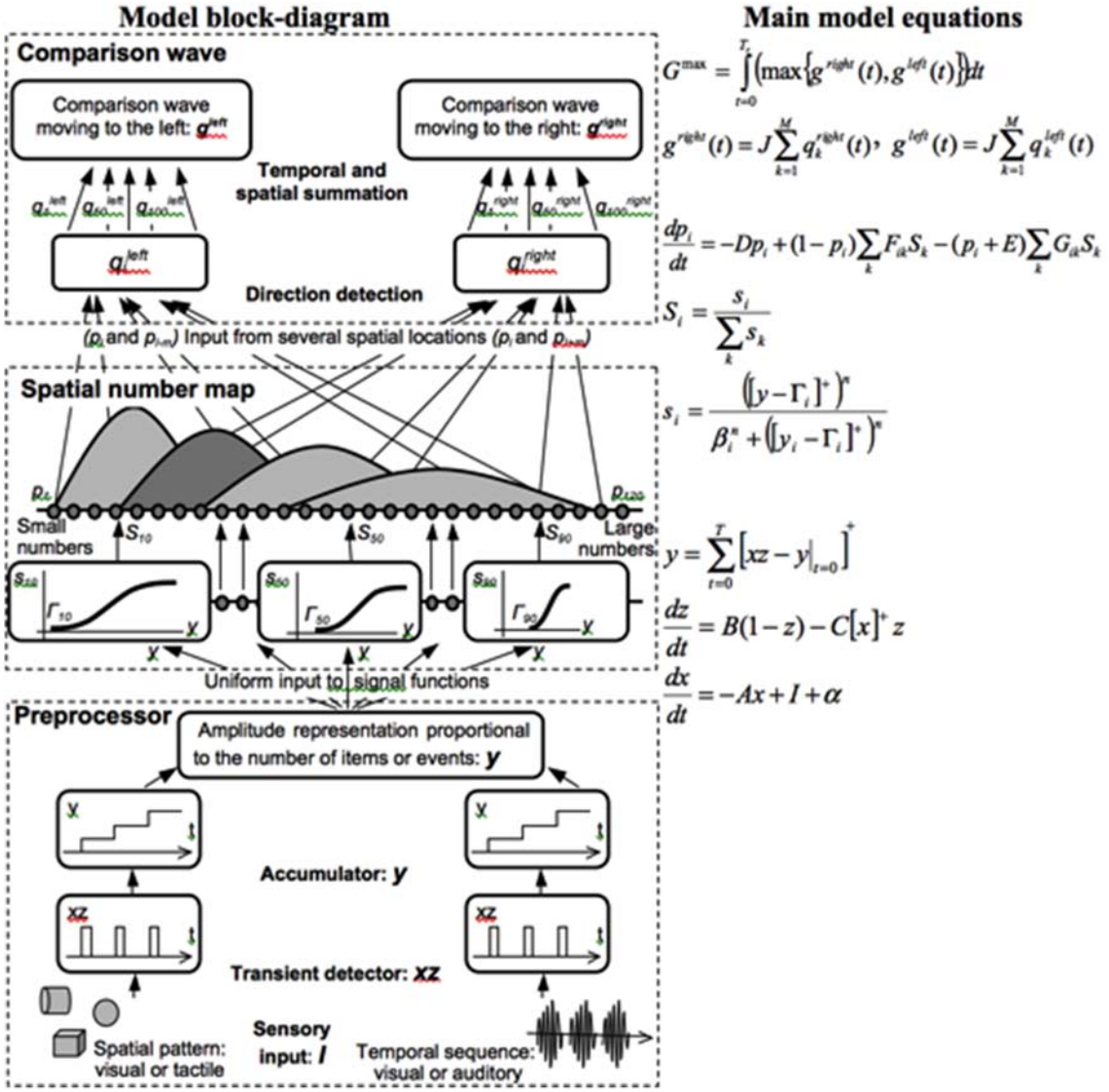

FIGURE 8 | Processing stages of the SpaN model. Preprocessor: For each sensory input increments the activity of the integrator y. Integrator activity uniformly activates the spatial number map. Spatial number map: Each activity p_i receives the output S_i that is activated by the integrator input y. The signal functions s_i that give the rise to S_i has increasing thresholds and slopes at each successive map cell i. Examples for cells 10, 50, and 100 are shown on the diagram. Each pattern p_i "bump" on the spatial number map represents the analog numerical map value of increasing numbers of inputs in a sequence. Comparison wave: see the archival article for details [reprinted with permission from Grossberg and Repin (2003)].

however, have evolved multi-digit place-value number systems whereby much larger numbers can be represented by such a map. Grossberg and Repin (2003) proposed a neural model that is called the Spatial Number Network, or SpaN model (**Figure 8**), to explain and simulate how small numbers are represented in an ordered spatial map in the inferior parietal cortex of the Where cortical processing stream. Multi-digit place-value numerical representations are proposed to develop through learned associations between categorical language representations in the What cortical processing stream and the Where spatial representation. For example, learned language categories that symbolize separate digits, such as "one," "two," "three," etc., as well as place markers like "ty," "hundred," "thousand," etc., are together associated through learning with the spatial locations of the Where spatial representation. The model that realizes this expanded numerical capability is called the Extended SpaN, or EspaN, model.

As noted in **Figure 9A**, each numerical representation in the primary analog number map is expanded into a strip map that provides enough representational space for the learning of place-value numbers. Such a strip is a kind of *numerical hypercolumn*. A number that activates a given analog numerical representation in the primary number map can also activate the entire strip corresponding to that numerical representation.

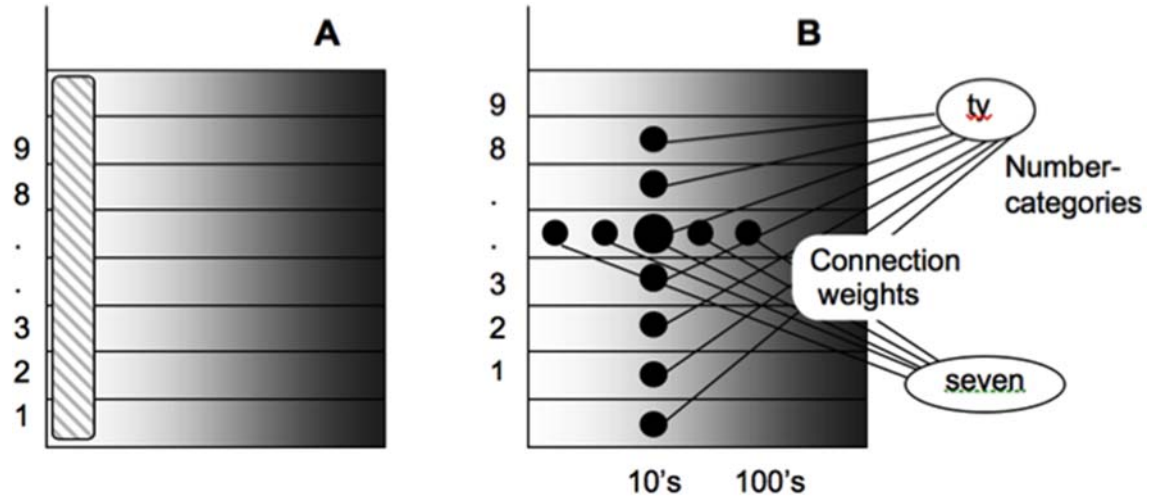

FIGURE 9 | Summary of how place-value numbers are learned *via* What-to-Where interstream information fusion. **(A)** The striped vertical area on the left denotes the primary analog number map in the Where cortical stream. Horizontal strips respond to the same numbers as the corresponding cells in the primary map. **(B)** How What-to-Where associations activate a spatial representation of the number *seven-ty* in the strip that corresponds to *seven* in the primary number map. Sizes of the solid circles encode activities of cells in the strip map. Convergent associations from language representations of "seven" and "ty" maximally activate the cells representing "seventy" [reprinted with permission from Grossberg and Repin (2003)].

For example, the number "seven" would send inputs to its entire strip (**Figure 9B**). Different place values, such as "ty," "hundred," "thousand," and so on, initially send broadly distributed adaptive signals to the entire strip map. After unsupervised learning, they can activate different positions within each strip, with numbers like "seven," "seventy," and "seven hundred" being represented in progressively more distant positions from the primary number map. This ordering emerges from how the learning spontaneously develops when the entire strip map also includes competitive interactions both within and across strips. Grossberg and Repin (2003) hereby demonstrated how a place-value number system develops as an emergent property of What-to-Where interstream information fusion. Piazza et al. (2007) have provided additional experimental fMRI support of this conception by reporting "a magnitude code common to numerosities and number symbols in human intraparietal cortex."

This summary will not detail the large body of psychophysical and neurobiological data that these models have explained. In particular, the model quantitatively simulates error rates in quantification and numerical comparison tasks, and reaction times for number priming and numerical assessment and comparison tasks. The dynamics of numerical comparison are encoded in activity pattern changes within this spatial map that cause a "directional comparison wave" with properties that mimic data about numerical comparisons, such as the Number Size Effect and the Number Distance Effect (Dehaene, 1997). To clarify how these mechanisms may have arisen through evolution—that is, to explain "where numbers come from"—Grossberg and Repin (2003) noted that these mechanisms are specializations of neural mechanisms that had earlier been used to model data about motion perception, attention shifts, and target tracking, an explanation which clarifies how numerical representations may have evolved from more primitive functions that are known to occur in the cortical Where processing stream, and how inputs to the parietal numerical representation arise.

Development of Auditory Streams and the Cocktail Party Problem

Auditory communication often takes place in an environment with multiple sound sources simultaneously active, as when we talk to a friend at a crowded noisy party. Despite this fact, we can often track our friend's conversation, even though harmonics from other speakers' voices may overlap those of our friend's voice. Such a conversation is possible because the auditory system can often separate multiple overlapping sound sources into distinct mental objects, or auditory streams. This process has been called *auditory scene analysis* (Bregman, 1990) and enables our brains to solve what is called the *cocktail party problem*.

Many models of auditory scene analysis have been proposed since Bregman's seminal book. Some of them apply classical engineering methods, such as Independent Component Analysis, to separate independent sources of activity from recorded mixtures of acoustic sources; e.g., Brown et al. (2001). This particular method works if the sources are non-Gaussian signals that are statistically independent of each other. If N sources are present, then at least N observations (e.g., microphones) are needed to recover them[1] Models of auditory scene analysis vary considerably in their biological plausibility and their ability to detect and track auditory streams without external supervision. An issue of particular importance is whether and

[1]https://en.wikipedia.org/wiki/Independent_component_analysis

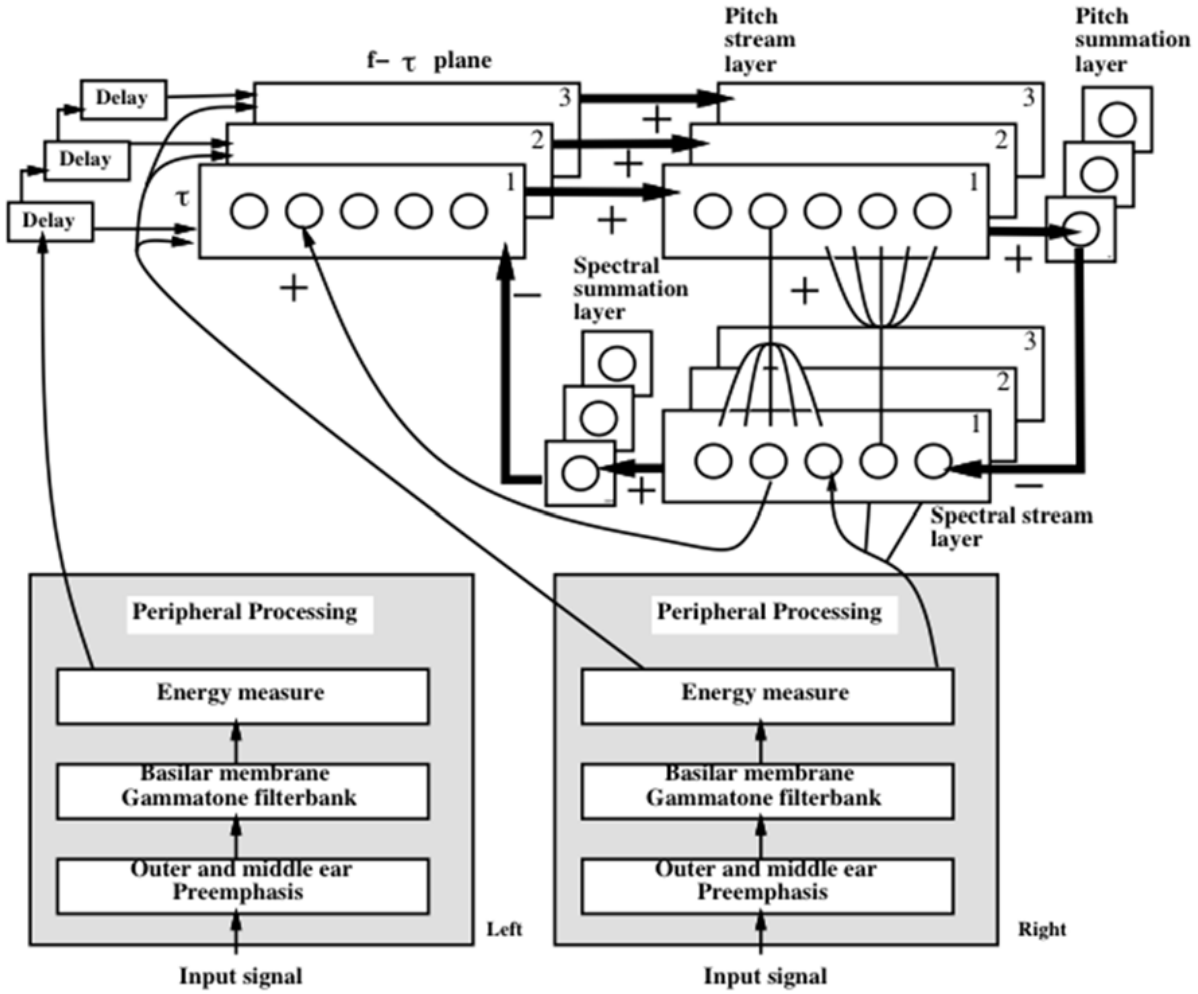

FIGURE 10 | The ARTSTREAM model explains and simulates key data about how auditory scene analysis occurs by combining pitch and source direction information. Multiple auditory streams (labeled 1, 2, 3) can emerge within strip maps that are perpendicular to the primary spectral representation within the spectral stream layer. Spectral-pitch resonances develop between the spectral stream layer and the pitch stream layer to track each acoustic source. These are denoted by the bottom-up and top-down filters with branching pathways between these layers, combined with top-down lateral inhibition *via* the pitch summation layer to realize the ART Matching Rule. Interactions of the ART Matching Rule and asymmetric competition mechanisms in cortical strip maps explain how a source selects the consistent frequencies in its own stream while separating other acoustic signals into another stream. Signals from both ears combine to compute source direction, which also helps to identify a source [adapted with permission from Grossberg et al. (2004)].

how source separation occurs when the auditory signals are significantly occluded by noise. See Szabó et al. (2016) for a recent review.

Grossberg et al. (2004) introduced the ARTSTREAM neural network model of auditory scene analysis to explain how auditory scene analysis can be achieved by applying basic ART principles and mechanisms in the auditory domain, notably the ART Matching Rule for attentional focusing and resonant conscious awareness, and how it can be used to select and complete multiple auditory streams in noise (**Figure 10**). To separate multiple auditory streams, the ARTSTREAM model uses variations of the strip maps that represent place-value numbers (**Figure 9**). These ART and strip map designs together provide a secure biological foundation for ARTSTREAM by suggesting how auditory scene analysis may have emerged during evolution by exploiting widely used brain mechanisms and circuits, while also ensuring that its representations may be incrementally learned in real-time, without experiencing catastrophic forgetting, even in response to noisy and nonstationary acoustical environments.

In the ARTSTREAM model, multiple stages of auditory preprocessing generate a spatial map of tonotopically ordered sound frequencies in log-polar coordinates. This map is often called a *spectral representation*. In order to carry out an auditory scene analysis, a brain uses its spectral representation to learn representations of the pitch of a sound and its spatial location (Bregman, 1990). The front end of the ARTSTREAM model accordingly uses the SPINET, or Spatial PItch NETwork, of Cohen et al. (1995; see gray boxes in **Figure 10**) to model how the pitch representations arise and simulate

many data about pitch perception to support its proposed neural mechanisms.

Using its spectral, pitch, and location representations, ARTSTREAM can track several auditory streams simultaneously. These several requirements build upon a strip map that extends the spectral representation to enable multiple streams to be represented, just as the EspaN model enables place-value numbers to be represented. In the ARTSTREAM strip map, when a sound frequency activates its primary spectral representation, it also activates the entire strip of cells that encode that sound frequency, in much the same way that ordered representations of small numbers in the primary number map expand their representations into strips that can represent place-value numbers. In **Figure 10**, the anatomical substrate of each stream in the *spectral stream layer* is denoted by a different integer (1, 2, 3). Each stream includes a complete copy of the spectral representation. The strips are perpendicular to the streams, and redundantly represent each different frequency in all the streams.

A stream in the model forms as a result of a *spectral-pitch resonance* that emerges during feedback interactions between the spectral representation of a sound source in the strip map and a representation of its pitch in the pitch stream layer (**Figure 10**). This pitch representation is a learned recognition category, much like any such category in an ART network. The following processing steps illustrate model dynamics:

First, a sound is transformed into a spatial pattern of frequency-specific activations across the spectral stream layer (**Figure 10**). These frequencies typically activate the harmonics of a sound's pitch, at least for the sonorant types of sounds that have a pitch, such as vowels, due to the way in which such sounds are processed in the cochlea. Each frequency activates its entire strip. The cells that are activated by these sound frequencies then send bottom-up signals through an adaptive filter. Because the harmonics of the sound's pitch are active, this filter is sometimes called a *harmonic sieve* (Duifhuis et al., 1982; Scheffers, 1983).

Output signals from this filter activate a subset of cells within the pitch stream layer (**Figure 10**) before these cells compete to choose the most active cell population. Because such a cell selectively responds to the harmonics of a pitch, it is called a *pitch category*. A chosen pitch category, in turn, activates a top-down expectation that obeys the ART Matching Rule. Because the top-down expectation obeys the ART Matching Rule, spectral components are selected if they match harmonics of the active pitch category, and are suppressed if they do not. In this way, noise is suppressed that would otherwise occlude processing the pitch's spectral components. Reciprocal bottom-up and top-down excitatory signals then resonate between the spectral and pitch stream layers. Such a resonance provides the temporal coherence that allows one voice or instrument to be tracked through a noisy environment that contains multiple active sound sources.

A proper balance of cooperation and competition is needed to choose multiple streams while suppressing noise. Asymmetric intrastrip competition is stronger from the primary spectral representation to other positions on its strip, than conversely; that is, from stream 1 to streams 2 and 3. Interstrip competition also occurs, and is regulated by active top-down expectations that obey the ART Matching Rule.

The intrastrip competition enables the primary spectral representation (labeled 1 in **Figure 10**) to win the competition for generating the first spectral-pitch resonance. It hereby becomes the first stream to be active. The harmonic components that resonate with the chosen pitch category can also use the asymmetric intrastrip competition to inhibit these components at other strip positions that are distal to the primary spectral representation (labeled 2 and 3 in **Figure 10**).

In contrast, the frequencies that are inhibited in the primary stream by pitch-activated top-down signals that obey the ART Matching Rule cannot inhibit themselves at positions distal to the primary spectral representation. These uninhibited frequencies can then activate the bottom-up filter at positions distal to the primary spectral representation (e.g., in stream 2), so that another pitch category can be chosen, and can begin to resonate with a subset of spectral stream cells, thereby creating another spectral-pitch resonance within stream 2. And so on, thereby enabling several spectral-pitch resonances to simultaneously represent several auditory streams. These specialized versions of Adaptive Resonance Theory, or ART, mechanisms also clarify how spatial location cues can help to disambiguate two sound sources with similar spectral cues (see the $f - \tau$ plane in **Figure 10**).

Auditory Continuity Illusion, Separation of Intersecting Frequency Sweeps, and Scale Illusion

The ARTSTREAM model simulates data from streaming experiments, such as how the *auditory continuity illusion* occurs, during which a tone is perceived to continue through a noise burst even if the tone is not present during the noise; how a tone sweeping upwards in frequency creates a bounce percept by grouping with a downward sweeping tone due to proximity in frequency, even if noise replaces the tones at their intersection point; and how the scale illusion of Deutsch occurs (Deutsch, 1975), whereby downward and upward scales presented alternately to the two ears are regrouped based on frequency proximity, leading to a bounce percept.

ARTSTREAM would need to be further developed to explain more complex streaming data. ARTSTREAM models only a single scale of sustained detectors, or detectors of a given size that respond to sounds with sustained energy across time in particular frequencies. Grossberg et al. (2004) noted that preprocessing by detectors of multiple scales that are sensitive to transient sounds are needed, in addition to sustained detectors, to fully explain data about how frequency sweeps are separated, as well as other acoustic signals with rapidly changing frequencies. Parallel interacting streams of sustained and transient cells are also used to explain data about how speech and language sounds are represented at higher levels of brain processing (e.g., Cohen and Grossberg, 1997; Boardman et al., 1999). The circuit properties that give rise to these transient cells can also be used to guide the design of transient cells at earlier processing stages.

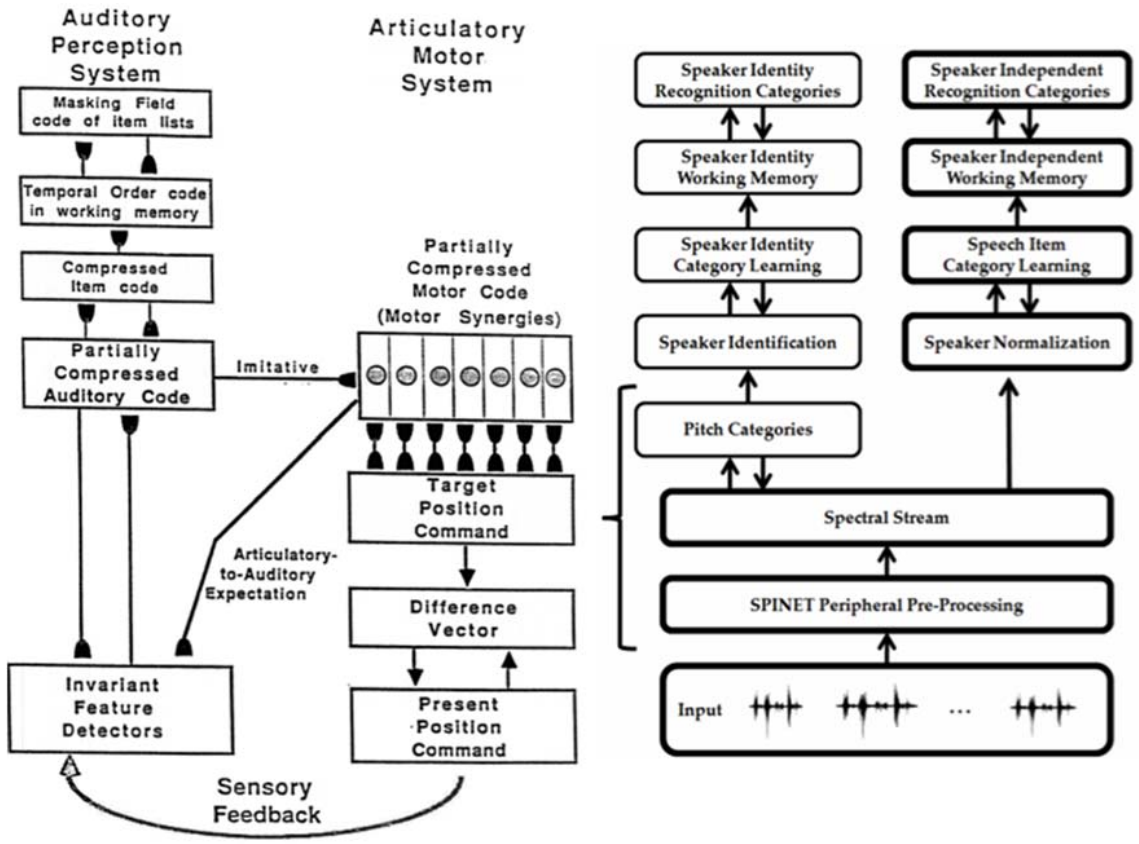

FIGURE 11 | (left architecture) An auditory-to-articulatory feedback loop enables babbled sounds to activate learning in an imitative map that is later used to learn to reproduce the sounds of other speakers. The invariant feature detectors include preprocessing by speaker normalization circuits. An articulatory-to-auditory expectation renders learning possible by making the auditory and motor data dimensionally consistent [reproduced with permission from Cohen et al. (1988)]. (right architecture) Parallel streams in the ARTSPEECH model learn speaker-independent speech and language meaning, including a mechanism for speaker normalization (right cortical stream), and for learning speaker-dependent vocalic qualities (left cortical stream) [reproduced with permission from Ames and Grossberg (2008)].

For present purposes, the main point is that multiple auditory streams and their spectral-pitch resonances build upon strip maps, abetted by intrastrip and interstrip competitive interactions, just as in the case of place-value numbers.

Development of Speaker Normalization and Language by Circular Reactions

Different speakers—such as young children, women, and men—utter language utterances in different frequency ranges. Despite this variability, we can all understand each other's language utterances without having to separately learn language meanings for each different frequency range that any speaker might use. The transformation of individual speaker frequency ranges into a format that can be understood in a speaker-invariant way is called *speaker normalization*. Various engineering approaches to speaker normalization have been proposed; e.g., Joy et al. (2018). The biological neural model that is proposed below again uses ART, strip maps, and asymmetric competitive interactions to achieve speaker normalization, and is moreover homologous to the model used for auditory streaming.

Speaker normalization is essential for babies to learn language from adult speakers, since their parents' spoken frequencies differ from those that the baby can *babble*. Babies babble simple sounds during a critical period of their development. They also hear their own babbled sounds and learn to associate the heard sounds with the motor commands that they used to make them. This feedback loop between speaking and hearing is called a circular reaction (Piaget, 1963).

How do babies use these relatively simple learned associations to learn the more complex language utterances of adult speakers? By converting all speech sounds into a frequency-normalized format, including the sounds that the baby babbled, speaker normalization enables sounds from adult caretakers to be filtered by the speaker-normalized map that was learned during babbling, and to thereby enable the baby to begin to imitate heard sounds as part of its own language productions. This kind of map is accordingly called an *imitative map* (**Figure 11**, left panel).

The NormNet model of Ames and Grossberg (2008) simulates speaker normalization to generate a pitch-independent representation of speech sounds, while also preserving information about speaker identity in a parallel cortical

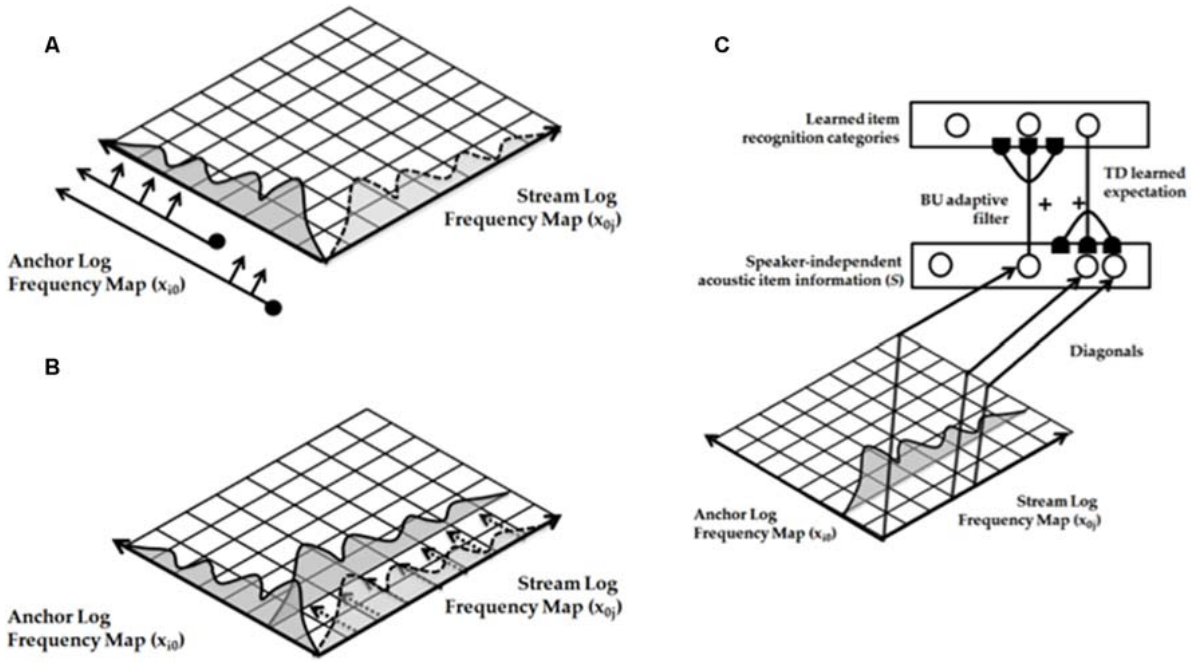

FIGURE 12 | (A) Anchor Map and Stream Map: these strip maps are organized so that their strips overlap each other. Both maps receive the spectral representation, in log frequency coordinates, from the streamed sound. **(B)** Coincidence detection: chosen by asymmetric competition, the winning Anchor Frequency Coding Cell triggers coincidence detection along its Anchor Frequency Strip, which also receives spectral inputs from the Stream Map. Activations of the Stream Map are thereby translated into the Anchor Frequency Strip. **(C)** Speaker-independent spectral representation: summation of activities along each diagonal strip creates a speaker-independent spectral representation, which is then fed into an ART network that learns to categorize it [adapted with permission from Ames and Grossberg (2008)].

stream (**Figure 11**, right panel). The model exploits the fact that auditory streams form before the stage where speaker normalization occurs. In this way, our brains can normalize the frequencies of a single attended voice after it is segregated in a stream.

Remarkably, both auditory streaming and speaker normalization in the model uses multiple strip representations and asymmetric competitive interactions (**Figure 12**), thereby suggesting that these two circuits, with their strikingly different functions, arose from similar neural designs.

In the auditory cortex of both humans and other mammals, multiple tonotopic maps exist that contain strips of cells called iso-frequency contours that respond to a specific best frequency (Merzenich and Brugge, 1973; Imig et al., 1977; Morel and Kaas, 1992; Morel et al., 1993; Hackett et al., 1998; Kaas and Hackett, 1998, 2000; Formisano et al., 2003; Rauschecker and Tian, 2004; Petkov et al., 2006). NormNet assumes that two identical tonotopic strip maps occur with perpendicular, or at least overlapping, orientations (**Figure 12A**). These maps are called the Anchor Log Frequency Map (Anchor Map) and the Stream Log Frequency Map (Stream Map). Both the Anchor Map and Stream Map are activated by a speech sound, which is assumed to have already been segregated into an auditory stream by processes such as those modeled by ARTSTREAM.

Due to this spatial format, activations in these strips intersect. Asymmetric competition occurs between frequencies in the Anchor Map to choose the cell with the lowest active frequency in the speech sound, which typically has the greatest spectral energy (**Figure 12A**). This cell is called the *anchor frequency coding cell*. While the anchor frequency coding cell wins the asymmetric competition, it inhibits activations corresponding to higher frequencies in the Anchor Map. Coincidence detection between the perpendicular strips determines which cells will next be activated. In particular, only cells in the Stream Map that receive acoustic inputs and that intersect the strip of the anchor frequency coding cell will be activated (**Figure 12B**). In other words, such coincidences occur in the strip corresponding to the Anchor Frequency of the Anchor Map and all the active strips corresponding to spectral activations in the Stream Map.

These coincidences are registered by diagonally connected strips that transform the Anchored Stream into a speaker-normalized representation *S* (**Figure 12C**). In particular, each cell in the *S* field sums inputs from all cells within diagonal stripes that cross the maps. This speaker-normalized representation then triggers the learning of speaker-normalized recognition categories. In Ames and Grossberg (2008), category learning is carried out by a fuzzy ARTMAP network with default parameters (Carpenter et al., 1992).

NormNet was tested by simulating how its normalized speech items are categorized and stably remembered by ART circuits. The simulated acoustic inputs were synthesized steady-state

vowels from the Peterson and Barney (1952) vowel database and achieved accuracy rates similar to those achieved by human listeners.

Development of Item-Order-Rank Working Memories

Essentially all higher-order biological intelligence requires that *sequences* of previously experienced items or events be used to determine subsequent thoughts, decisions, and actions. Working memory temporarily stores such sequences until they are performed or used to trigger learning and LTM of sequence categories, or *list chunks*, with which to control future behaviors. Due to its importance of working memory in controlling intelligent choices and predictions in complex situations, the psychological and neurobiological study and modeling of working memory has been very active for decades; e.g., Miller et al. (1960), Atkinson and Shiffrin (1968), Baddeley and Hitch (1974), Baddeley (2010) and Constantinidis and Klingberg (2016). As with all the kinds of models reviewed in this book, these models vary greatly in their biological plausibility and in their ability to support learning. For example, in the pioneering Atkinson and Shiffrin (1968) model, previously stored items move from one storage slot to the next as a new item is stored. Such a model faces both conceptual and empirical problems. For example, it cannot explain the ubiquitous bowed curves that are found in working memory data (see below) and it cannot learn list chunks.

Multiple working memories are used to temporarily store sequences of linguistic, spatial, and motor items, among others, such as sequences of words, navigational goals, and arm movement commands. It is explained below why all working memories are realized by a similar kind of recurrent neural network, despite their different functions. Another important property of working memories is that they can store repeated items, such as the list ABACBD. The model of working memory proposed below uses strip maps to realize this property, as well as ART to categorize sequences of stored items.

A series of articles, starting in 1978, have characterized how biological working memories are designed, and have explained and predicted many psychological and neurobiological data about them (e.g., Grossberg, 1978a; Grossberg, 2018; Grossberg et al., 1997; Boardman et al., 1999; Grossberg and Myers, 2000; Grossberg and Pearson, 2008; Silver et al., 2012; Kazerounian and Grossberg, 2014; Grossberg and Kazerounian, 2016). These articles also explained why and how all working memories, whether linguistic, spatial, or motor, all share the same underlying kind of neural circuit; namely, a specialized recurrent on-center off-surround network whose cells obey membrane, or shunting, equations.

These working memories have been derived from postulates which ensure that list chunks can be learned and stably remembered. Working memories that obey the *LTM Invariance Principle* have this property. The LTM Invariance Principle guarantees, for example, that the first time a novel word, such as MYSELF, is stored in working memory, it does not force catastrophic forgetting of previously learned list chunks that code for its familiar subwords MY, ELF, and SELF. Without such a property, language, spatial, and motor sequential skills could not be learned.

It was shown, starting in Grossberg (1978a), how the LTM Invariance Principle could be satisfied by a working memory for which temporal sequences of items or events are converted into an evolving spatial pattern of activity over item chunks that store these events in working memory. Then, during rehearsal, the item stored with the largest activity is rehearsed first, the item with the next largest activity is rehearsed second, and so on. In other words, a *spatial gradient* of activity across item chunks encodes both the items that are stored in working memory and their temporal order. Such working memories are thus called Item-and-Order working memories. The LTM Invariance Principle is satisfied if the relative sizes, or ratios, of activities in this spatial gradient remain the same as new items are stored in working memory, even if their total sizes may change through time to approximately normalize the total activity that is stored by the recurrent shunting network.

If a *primacy gradient* is stored, then the first item is stored with the largest activity, the second item is stored with the next largest activity, and so on. Rehearsal from a primacy gradient can recall the items in the correct order in which they were stored. If a *recency gradient* is stored, with the last item having the largest activity, then items are rehearsed in the reverse order that they were stored, with the last item recalled first. If a *bowed gradient* is stored, with items at the beginning and end of the list stored with larger activities then items in the middle, then items at the beginning and end of the list are rehearsed before items in the list middle. Remarkably, as more items get stored, a primacy gradient is always converted into a bowed gradient. As a result, sufficiently long lists cannot be recalled in their correct temporal order from working memory.

A series of articles has illustrated the explanatory power of the hypothesis that all linguistic, spatial, and motor working memories use variations of a recurrent shunting on-center off-surround network. Data about bowed serial position effects are ubiquitous in the working memory literature, notably psychological data about the *linguistic* working memories whereby humans do immediate serial recall, and immediate, delayed, and continuous distractor free recall; and neurophysiological data recorded from monkeys about the *motor* working memories whereby planned arm movement sequences are stored and performed. Grossberg and Pearson (2008) and Grossberg (2017b) explain and quantitatively simulate these and other psychological and neurobiological data about working memory using homologous Item-Order-Rank working memories. Silver et al. (2012) use homologous Item-Order-Rank working memories to explain and simulate the *spatial* working memories whereby movement storage, planning, and control of sequential saccadic eye movements is achieved.

Working memories also need to be able to store sequences of events that may repeat themselves; e.g., ABACBD. This generalization of Item-and-Order working memories is called an Item-Order-Rank working memory. Item-Order-Rank working memories provide a foundation for learning both speech and language. It has, for example, been shown that a suitably designed

three-level network of Item-Order-Rank working memories can store and learn sequences of repeated words, such as "DOG EATS DOG."

Strip maps enter the story by enabling Item-Order-Rank working memories to store item sequences that contain repeats. Each of these strips is a kind of *item-rank hypercolumn*. For example, to store a list like ABACBD, the item representation of A would activate its item-rank hypercolumn in rank positions 1 and 3, B would activate its item-rank hypercolumn in rank positions 2 and 5, C in rank position 4, and D in rank position 6. The rank information is proposed to be projected to the prefrontal cortical working memory from numerical representations in the parietal cortex. This prediction uses properties of the Spatial Number Network, or SpaN, model of Grossberg and Repin (2003), that was described above, of how numerical maps in the inferior parietal cortex enable numerical quantities to be represented and compared. Properties of SpaN model neurons were supported by neurophysiological data of Nieder and Miller (2003, 2004), who also reported prefrontal projections of parietal numerical representations. In such an Item-Order-Rank working memory, relative activity still represents the temporal order of a sequence that is stored, and the off-surround of the network can still equally inhibit all other cells, including the cells in each item-rank hypercolumn.

Item-Order-Rank working memories have been used as part of larger neural architectures for learning and performing sequential tasks. One such architecture is the lisTELOS architecture of Silver et al. (2012) which explains and simulates how an Item-Order-Rank working memory in the prefrontal cortex stores and learns multiple spatial positions with which to control sequences of eye movements. Model simulations reproduced behavioral, anatomical, and electrophysiological data from multiple experimental paradigms, including visually-guided and memory-guided single and sequential saccadic eye movement tasks, and behavioral data from two microstimulation paradigms in which the supplementary eye fields were stimulated, thereby explaining how their seemingly inconsistent findings about saccade latency could be reconciled. It is explained below why similar working memory circuits and architectures can store and learn multiple types of sequential behaviors.

TOPOGRAPHIC MAPS OF FEATURE DETECTORS AND THEIR GAUSSIAN PEAK SHIFTS

Not all feature-selective maps need strip maps in order to function well. Several examples of this will now be summarized in order to illustrate the diversity of possibilities.

Steering During Optic Flow Navigation

Visually guided navigation enables humans and many other animals to move through cluttered natural scenes without colliding with obstacles. At least two parallel processes, with computationally complementary properties (Grossberg, 2000), contribute to this competence.

The first process uses the *optic flow* that is generated as an animal moves with respect to its environment in order to steer towards a goal. Optic flow is the information carried by the light that streams in time over the retina due to such movements (Gibson, 1950). For example, if the movement is straight ahead through a rigid environment, then the optic flow generates a radial motion pattern whose individual motion vectors emanate from a single position, which is called the focus of expansion. *Heading* is the direction that the observer is traveling at any time, and can be computed from a combination of optic flow information and outflow movement commands, called corollary discharges or efference copies, that code eye and head movements relative to the body. Browning et al. (2009a) provide a comparative review of the three main classes of heading models: differential motion, decomposition, and template models.

The second process separates objects—including goal objects and obstacles—from each other and the background using their relative motion to enable tracking of a goal without bumping into obstacles. Browning et al. (2009b) and Elder et al. (2009) review alternative models and data about tracking.

These two processes are computationally complementary because optic flow computations use *additive* processing of motion signals across an entire scene to compute an observer's heading, whereas *subtractive* processing separates an object's boundaries as they move relative to a background. These processes occur due to interactions between cortical areas MT^{-} and MSTv to compute heading, and between cortical areas MT^{+} and MSTd to control tracking. Supportive neurophysiological data for these hypotheses is provided in Born and Tootell (1992).

The ViSTARS (Visually-guided Steering, Tracking, Avoidance, and Route Selection) neural model (Browning et al., 2009a,b; Elder et al., 2009) proposes how primates use these two kinds of complementary motion information to segment objects and determine heading for purposes of goal approach and obstacle avoidance. The model simulated this competence in response to video inputs from real and virtual environments and thereby produced trajectories that match those of human navigators.

A topographic map enters the story because it is known that, during human visually-based navigation, goals behave like *attractors* and obstacles behave like *repellers* (Fajen and Warren, 2003). The ViSTARS model shows how a topographic map of movement directions can realize this kind of attractor-repeller control, leading to navigational trajectories that closely match human performance. In this map, the instantaneous directions of heading, goal object, and obstacle are represented by Gaussian activity profiles (**Figure 13**). The heading and goal object Gaussians add whereas the obstacle Gaussian activity profile is subtracted from them, thereby causing a *peak shift* of the direction of heading away from the obstacle.

Gaussian receptive fields occur in many topographic cortical maps. Whenever one of them is subtracted from another one whose activation represents a sufficiently nearby position in the feature map, a peak shift occurs in the direction opposite to the peak in the inhibitory Gaussian.

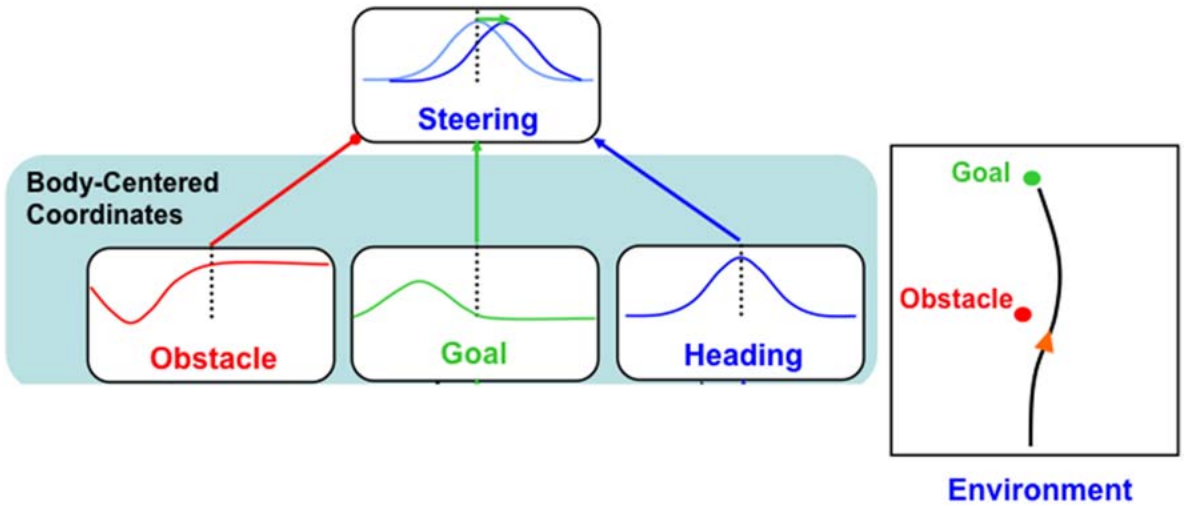

FIGURE 13 | A peak shift due to the negative Gaussian of an obstacle prevents a collision with the obstacle without losing the information that is coded in the sum of the goal and heading Gaussians of how to reach the goal [adapted with permission from Browning et al. (2009b)].

Peak Shift During Reinforcement Learning: Do We Know What We Like?

A peak shift can, for example, occur in situations where pigeons are trained using operant conditioning to respond to one colored light when it flashes on, and to *not* respond to other colored lights when they flash on. During learning by operant conditioning, animals or humans are rewarded or punished only after they emit a certain behavior, or set of behaviors (Skinner, 1938).

Suppose that a pigeon is trained to respond to a given colored light cue. After learning occurs, the pigeon also responds to other colors *via* a *generalization gradient*; that is, the pigeon responds progressively less as a function of how different the wavelength of the test light is compared to the training light. This result implies that color representations are organized in a topographic map. Further corroboration of this hypothesis can be found by additional training of the pigeon: After training with reward to respond to one colored light, train it with punishment to *not* respond to a different colored light, and do so using *errorless training* (Terrace, 1963). The rewarded wavelength activates an excitatory Gaussian, whereas the punished wavelength activates a negative Gaussian, due to interactions of their cortical sensory representations with affective centers like the amygdala. When pigeon responses are now tested to other colored lights, a remarkable effect called *peak shift and behavioral contrast* is observed.

Peak shift means that, just as in the case of optic flow navigation, the pigeon now pecks in response to a color that it has never experienced. This color is "repelled" from the wavelength on which the pigeon was earlier punished. *Behavioral contrast* means that the pigeon responds more to this novel color than it did to the rewarded color!

Grossberg (1975a) proposed that this happens because the net gradient that causes the peak shift is narrower than a single Gaussian gradient. Gaussian gradients are caused in this feature map by on-center off-surround intercellular interactions whose on-center and off-surround have Gaussian receptive fields. These interactions obey shunting laws, so their total activity tends to be approximately normalized. Because fewer active cells cause the net gradient, its peak activity is higher than that of a stand-alone gradient.

When one considers the great variety of ordered feature maps in our brains, it becomes clear that, after a lifetime of rewards and punishments, we may intensely like options that we never before experienced. In this sense, "we may not know what we like."

Peak Shifts During Motion Perception of an Object and Its Parts

Optic flow navigation and operant conditioning are not the only situations in which topographic feature maps exist and lead to peak shifts. One particularly interesting one, which will not be further explained here, concerns how we see an object's parts move relative to the object as the object itself moves in its environment. For example, how do we see a person's arms swing back and forth with respect to her body as she walks down the street? Such a percept is said to obey a rule of *vector decomposition* (Johansson, 1974).

Grossberg et al. (2011) have explained this percept by simulating how the motion direction of the object, again represented by a Gaussian receptive field, is subtracted from the direction of the object part's motion direction, which is also represented by a Gaussian, thereby causing a peak shift in the perceived direction of the part's motion relative to the

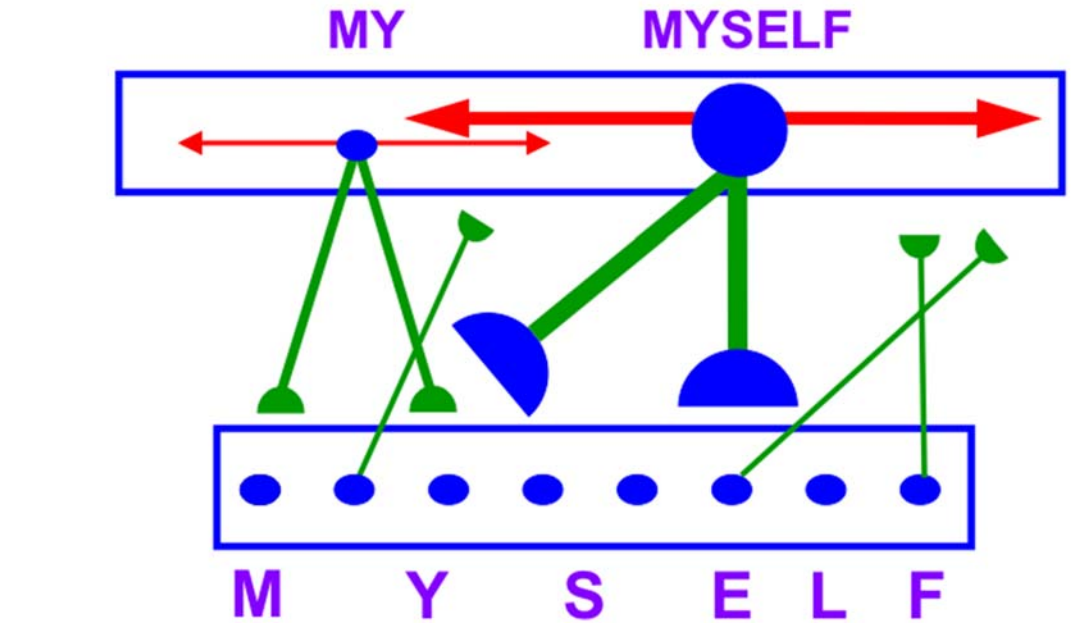

FIGURE 14 | A Masking Field is a recurrent shunting on-center off-surround network with multiple self-similar receptive field sizes. Self-similar growth during development leads to Masking Field list chunks such that longer words activate list chunks with stronger recurrent inhibitory connections and top-down adaptive excitatory connections. As a result, longer lists can preferentially activate larger list chunks (e.g., of MYSELF), which can thereby inhibit chunks of smaller subwords (e.g., MY) more than conversely.

object. Then objects and their parts are seen moving relative to a common reference frame.

List Chunks of Variable Length Lists: Masking Fields and Self-similar Map Development

The final example concerns how lists of variable length that are stored in working memory can learn to be categorized during behaviors in real-time (Kazerounian and Grossberg, 2014). The LTM Invariance Principle was described above to show how brains prevent storage in working memory of a novel word, such as MYSELF, from causing catastrophic forgetting of previously learned list chunks that code for its familiar subwords MY, ELF, and SELF. A related problem is: Why is not the brain forced to process the new word as a sequence of its smaller familiar words? How does a not-yet-established word representation overcome the salience of already well-established phoneme, syllable, or word representations to enable learning of the novel word to occur? This is called the Temporal Chunking Problem.

Cohen and Grossberg (1986, 1987) first showed how this problem can be overcome by a Masking Field network by using cells with multiple receptive field sizes, or spatial scales (**Figure 14**). A Masking Field is a recurrent on-center off-surround network whose cells obey the membrane equations of neurophysiology (shunting laws) that occur, as noted above, with multiple receptive field sizes, or spatial scales. These spatial scales are related to each other by a property of *self-similarity*; each scale's properties, including its cell body sizes and their excitatory and inhibitory connection lengths and interaction strengths, are (approximately) a multiple of the corresponding properties in another scale. This self-similarity property can develop as a result of simple activity-dependent growth laws in the following way.

During this developmental process, just like in many map development processes, two cortical levels interact. The cells in the cortical level that will eventually represent item chunks are endogenously active during a critical period of development. During this active phase, these cells send growing connections to the cortical level that will eventually represent the Masking Field. Suppose, for simplicity, that these growing connections are distributed randomly across the Masking Field. As a result of this growth, different Masking Field cells will receive different numbers of connections. Due to the endogenous activity, Masking Field cells that receive more connections will, on average, receive a larger total input activity through time.

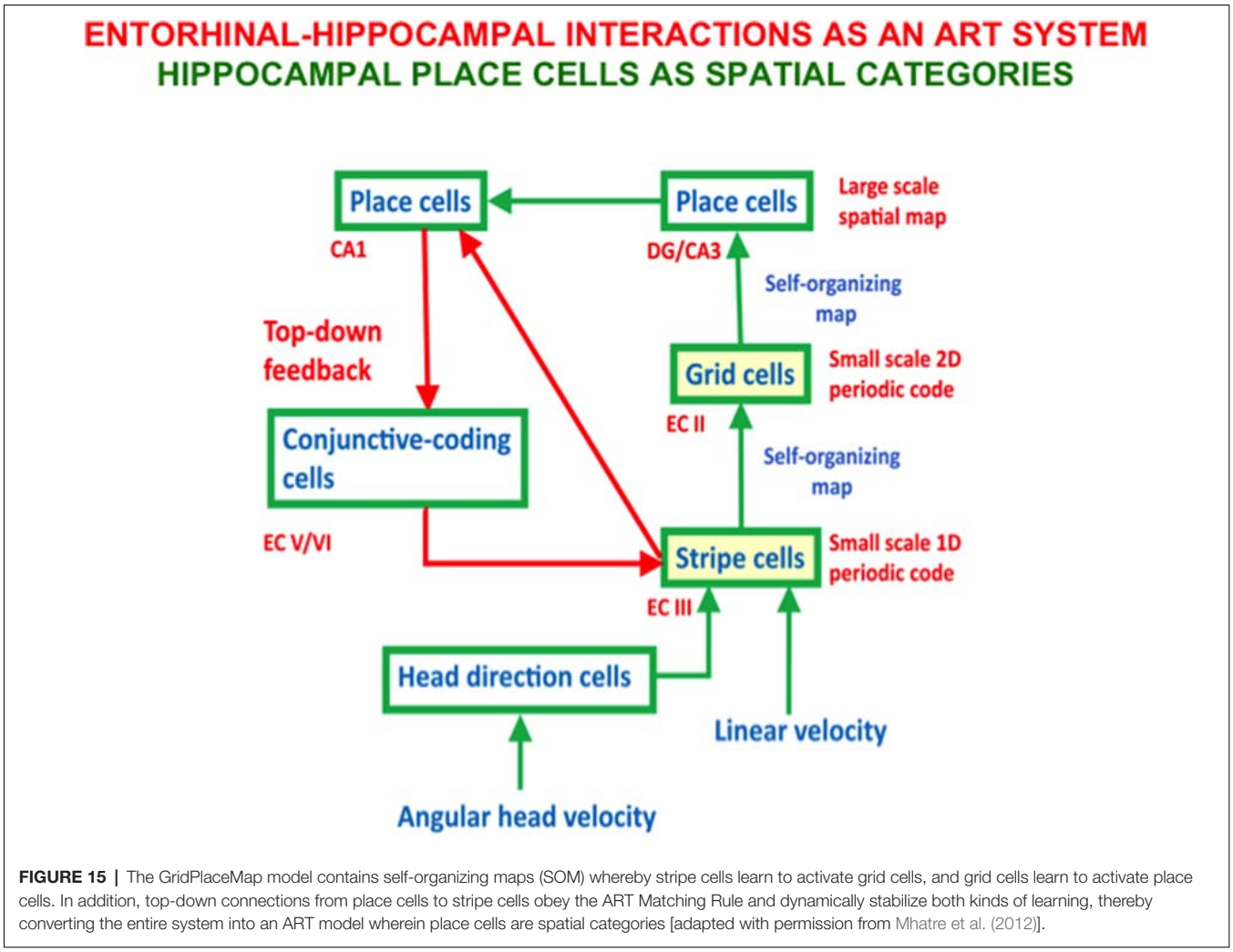

FIGURE 15 | The GridPlaceMap model contains self-organizing maps (SOM) whereby stripe cells learn to activate grid cells, and grid cells learn to activate place cells. In addition, top-down connections from place cells to stripe cells obey the ART Matching Rule and dynamically stabilize both kinds of learning, thereby converting the entire system into an ART model wherein place cells are spatial categories [adapted with permission from Mhatre et al. (2012)].

Activating Masking Field cells above a fixed threshold causes their cell bodies and connections to grow approximately proportionally. This is called *self-similar growth*. Cell growth terminates when the cell bodies become large enough to dilute their activities sufficiently in response to their inputs so that the total inputs no longer exceed the growth-triggering threshold. Because cells that receive more input connections also receive larger total inputs through time, they will grow larger than cells that receive fewer input connections. The effects of individual inputs are thus smaller on the firing of larger cells. Self-similar growth hereby *normalizes* the total effect of all the inputs that converge on a Masking Field cell. Consequently, a Masking Field cell will only fire vigorously if it receives active inputs from all of its item chunk cells. In other words, self-similar growth ensures that each Masking Field cell responds *selectively* to the input sequence that it codes.

Due to self-similar growth, larger Masking Field list chunks selectively represent longer lists because they need more inputs, and thus more evidence, to fire. Once they fire, their stronger inhibitory interaction strengths than those of smaller list chunks can inhibit the smaller list chunks more than conversely. This is another example of asymmetric competition. The stronger inhibition from list chunks of longer, but unfamiliar, lists (e.g., MYSELF) enables them to inhibit the chunks that represent shorter, but familiar, sublists (e.g., MY), more than conversely, thereby solving the Temporal Chunking Problem. Once developed, Masking Fields explains many data about recognition learning, including such phenomena as the Magical Number Seven Plus and Minus Two, the word length effect, and the word superiority effect.

RATE GRADIENTS INDUCE MAPS FOR LEARNING TIMING AND SPATIAL NAVIGATION

How Cell Populations Whose Cells Respond at Different Rates Represent Large Times and Spaces

How do our brains learn to bridge large time intervals of hundreds of milliseconds or even several seconds, and

thereby learn to associate events that are separated by time intervals that are behaviorally meaningful? How do our brains learn to represent large spatial regions, such as the large rooms and open fields within which humans and animals can successfully navigate? Answers to both of these questions must confront the fact that the typical biophysics and anatomy of individual neurons do not enable them to span such long times or large spaces. Remarkably, as will be summarized below, spatially ordered populations of neurons that respond at increasingly slow rates can achieve both capabilities. The emergent properties that these populations generate can, moreover, explain challenging parametric psychological and neurobiological data about temporal and spatial properties of behavior.

Spectral Timing and Spacing in Lateral and Medial Entorhinal-Hippocampal Systems

In particular, large spatial representations emerge within the entorhinal and hippocampal cortices using interactions between entorhinal grid cells and hippocampal place cells. There has been intense experimental and theoretical interest in how these properties emerge since the classical article of O'Keefe and Dostrovsky (1971) reported the existence of hippocampal place cells. John O'Keefe won the Nobel Prize in Physiology or Medicine in 2014 for this and subsequent work on how spatial navigation works. May-Britt and Edvard Moser shared the 2014 Nobel Prize in Physiology or Medicine with John O'Keefe for their discovery of entorhinal grid cells (Hafting et al., 2005).

Grossberg and Pilly (2012) provide a review and comparative analysis of the three main types of model mechanisms that have been proposed for how entorhinal grid cells form: oscillatory interference, 2D attractor, and SOM. Modeling hippocampal place cells has been no less active. Some approaches assume Gaussian receptive fields of place cells that are centered at different positions in a space defined by two-dimensional Cartesian (x, y) coordinates; e.g., Tsodyks and Sejnowski (1995). Such models can then be used to draw conclusions about spatial navigation that are based upon how these place cells may interact in this representation of space. Other approaches combine associative learning and reinforcement learning to generate place cells; e.g., Arleo and Gerstner (2000), but without an influence from grid cells.

My own work with Praveen Pilly attempts to provide a unified theory of the learning processes that support adaptively timed and spatial navigation behaviors (Grossberg and Pilly, 2012, 2014; Pilly and Grossberg, 2012, 2013a,b, 2014). The spatial navigation theory, whose properties are unified in our GridPlaceMap model, has many parsimonious and elegant properties. In particular, grid cells and place cells, despite their dramatically different receptive field properties, may arise during development through a learning process that uses the *same* SOM laws and circuits for learning both types of cells. Both grid cells and place cells are spatial categories in this hierarchy of SOMs. Moreover, each SOM amplifies and learns to categorize the most frequent and energetic co-occurrences of its inputs, while suppressing the representations of less frequent and energetic input patterns using its recurrent inhibitory interactions. The angular and linear velocity signals that drive these learning processes arise from head direction cells and stripe cells that are both modeled by homologous ring attractors. Additional homologs between spatial navigational learning and adaptively timed learning will be summarized below.

This section will sketch an explanation of why spatial and temporal representations that represent large spaces and times, unlike spatial attention and working memory, are both in a single part of the brain. The reason seems to be that, remarkably, these spatial and temporal representations seem to use variations of a single brain design that is characterized by similar equations. In particular, large time intervals can be bridged using a mechanism of *spectral timing* (Grossberg and Schmajuk, 1989; Grossberg and Merrill, 1992, 1996; Grossberg and Seidman, 2006; Franklin and Grossberg, 2017; Grossberg, 2017b) whereby a "spectrum" of *time cells* (MacDonald et al., 2011) along a dorsoventral gradient in the *lateral* entorhinal cortex, each with different reaction rates, can learn to match the statistical distribution of expected delays in reinforcement over hundreds of milliseconds, or even seconds.

The cells in this dorsoventral gradient respond at progressively slower rates from its dorsal to ventral end, and obey a Weber Law whereby cells that respond later do so with a proportionally larger variance of response times. Although each of the cells in such a spectrum reacts at different times, their population response as a whole can learn to bridge, and adaptively time, much longer time intervals at which events can be associated that are separated in time, as occurs during trace conditioning, delayed non-match to sample, and other conditioning paradigms with delays between offset of a conditioned stimulus and onset of an unconditioned stimulus.

In a similar way, large spaces can be navigated using a mechanism of *spectral spacing* (Grossberg and Pilly, 2012, 2014; Mhatre et al., 2012; Pilly and Grossberg, 2014) whereby a "spectrum" of *grid cells* (Hafting et al., 2005; McNaughton et al., 2006; Sargolini et al., 2006) can be learned along a dorsoventral gradient in the *medial* entorhinal cortex. As in the case of spectral timing, the cells in this spectrum, or gradient, respond at progressively slower rates from its dorsal to ventral end and exhibit spatial Weber Law properties. In this case, the Weber Law properties include larger spatial scales and spacing of grid cells as the dorsoventral gradient is traversed that match anatomical and neurophysiological data (Sargolini et al., 2006; Brun et al., 2008; Stensola et al., 2012). A wide range of additional neurophysiological data about cells in the dorsoventral gradient of medial entorhinal cortex can also be explained by this model, including simple ones like phase precession (Pilly and Grossberg, 2013b) and more subtle ones like the way in which reduction of theta rhythm by medial septum inactivation may covary with impaired entorhinal grid cell responses due to reduced cholinergic transmission (Pilly and Grossberg, 2013a).

Contiguous grid cells of different spatial scales can together, using properties of a SOM, drive the learning of *place cells* in the hippocampal cortex (O'Keefe and Dostrovsky, 1971) that can represent large spaces. As noted above, place cells are

spatial categories in this SOM. Critically, the spaces that such a place cell can represent are the *least common multiple* of the spatial scales of the grid cells that input to it (Gorchetchnikov and Grossberg, 2007; Pilly and Grossberg, 2012, 2013b). If the grid cells exhibit centimeter spatial scales, the corresponding place cells can represent spaces that are many meters in size. Place cells that are learned from grid cells can thus support navigational behaviors within the large spaces that are characteristic of terrestrial animals. At an early developmental stage, place cells can be directly learned without grid cells, and can perhaps represent the small spaces that rat pups traverse before they leave their nests (Langston et al., 2010; Wills et al., 2010, 2012; Pilly and Grossberg, 2014; Muessig et al., 2015).

ART Matching Rule Dynamically Stabilizes Learning in the Entorhinal-Hippocampal System

Place cell selectivity can develop within seconds to minutes and can remain stable for months (Wilson and McNaughton, 1993; Muller, 1996; Frank et al., 2004). This combination of fast learning and stable memory is yet another example of how the brain solves the *stability-plasticity dilemma*. To realize stable memory, the bottom-up SOM interactions that learn grid cells and place cells activate top-down interactions that obey the ART Matching Rule, which dynamically stabilizes the learning of these cells (**Figure 15**).

Neurophysiological data about the hippocampus from several labs are compatible with ART predictions about the role of top-down expectations and attentional matching in stabilizing learned grid cells and place cells. For example, Kentros et al. (2004) reported that "conditions that maximize place field stability greatly increase orientation to novel cues. This suggests that storage and retrieval of place cells are modulated by a top-down cognitive process resembling attention and that place cells are neural correlates of spatial memory." In addition, NMDA receptors, which support many learning processes in the brain, also mediate long-lasting hippocampal place field memory in novel environments (Kentros et al., 1998). Compatible data have shown that hippocampal plasticity reflects an "automatic recording of attendee experience" (Morris and Frey, 1997) and that hippocampal inactivation causes grid cells to lose their spatial firing patterns (Bonnevie et al., 2013).

In addition to the fact that both spectral timing and spectral spacing in the entorhinal-hippocampal system seem to exploit a similar temporal rate gradient to develop time cells and grid cells, respectively, spectral timing seems to be a variant of a brain design for adaptively timed learning that is also found in the cerebellum and basal ganglia, where it carries out different behavioral functions (Fiala et al., 1996; Brown et al., 1999; Grossberg, 2016b). In all cases, it seems that the timed spectrum is set up by a calcium gradient that modulates the dynamics of metabotropic glutamate (mGluR) receptors (e.g., Finch and Augustine, 1998; Takechi et al., 1998; Ichise et al., 2000; Miyata et al., 2000). Indeed, all of these neural circuits seem to exploit an ancient design that is found even in non-neural cells, such as HeLa cancer cells, where again a calcium gradient is implicated (Bootman and Berridge, 1996, p. 855). It remains to be seen if the spectral spacing gradient is also induced by a calcium-mediated gradient of mGluR dynamics.

CONCLUDING REMARKS

This article provides a unified overview of several of the design principles and mechanisms that cortical maps use to represent many different types of information across multiple modalities. One design explains how brains use a strip map that simultaneously enables one feature to be represented throughout its extent, as well as an ordered array of another feature at different positions of the strip. Strip maps include circuits to represent ocular dominance and orientation columns, place-value numbers, auditory streams, speaker-normalized speech, and cognitive working memories that can code repeated items. A second design explains how feature detectors for multiple functions develop in topographic maps. Such maps support optic flow navigation, reinforcement learning, motion perception, and category learning at multiple levels of brain organization. A third design explains how a spatial gradient of cells that respond at an ordered sequence of different rates enable time cells and grid cells to develop along a dorsoventral axis in the lateral and medial entorhinal-hippocampal systems, respectively. Populations of time cells can learn how to adaptively time behaviors over time intervals of hundreds of milliseconds, or several seconds. Populations of grid cells can induce learning of hippocampal place cells that can represent the large spaces in which animals navigate. A fourth design explains how and why all neocortical circuits are organized into layers, and how functionally distinct columns develop in these circuits to enable map development. A fifth, and final, design explains the role of Adaptive Resonance Theory top-down matching and attentional circuits in the dynamic stabilization of early development and adult learning.

AUTHOR CONTRIBUTIONS

The author confirms being the sole contributor of this work and has approved it for publication.

REFERENCES

Abbott, L. F., Varela, J. A., Sen, K., and Nelson, S. B. (1997). Synaptic depression and cortical gain control. *Science* 275, 220–224. doi: 10.1126/science.275.5297.221

Akerman, C. J., Smyth, D., and Thompson, I. D. (2002). Visual experience before eye-opening and the development of the retinogeniculate pathway. *Neuron* 36, 869–879. doi: 10.1016/s0896-6273(02)01010-3

Albus, K., and Wolf, W. (1984). Early post-natal development of neuronal function in the kitten's visual cortex: a laminar analysis. *J. Physiol.* 348, 153–185. doi: 10.1113/jphysiol.1984.sp015104

Allendoerfer, K. L., and Shatz, C. J. (1994). The subplate, a transient neocortical structure: its role in the development of connections between thalamus and

cortex. *Annu. Rev. Neurosci.* 17, 185–218. doi: 10.1146/annurev.ne.17.030194.001153

Alonso, J.-M., and Martinez, L. M. (1998). Functional connectivity between simple cells and complex cells in cat striate cortex. *Nat. Neurosci.* 1, 395–403. doi: 10.1038/1609

Ames, H., and Grossberg, S. (2008). Speaker normalization using cortical strip maps: a neural model for steady state vowel categorization. *J. Acoust. Soc. Am.* 124, 3918–3936. doi: 10.1121/1.2997478

Antonini, A., and Stryker, M. P. (1993). Functional mapping of horizontal connections in developing ferret visual cortex: experiments and modeling. *J. Neurosci.* 14, 7291–7305.

Arleo, A., and Gerstner, W. (2000). Spatial cognition and neuro-mimetic navigation: a model of hippocampal place cell activity. *Biol. Cybern.* 83, 287–299. doi: 10.1007/s004220000171

Atkinson, R. C., and Shiffrin, R. M. (1968). "Human memory: a proposed system and its control processes," in *The Psychology of Learning and Motivation: Advances in Research and Theory* (Vol. 2), eds K. W. Spence and J. T. Spence (New York: Academic Press), 89–195.

Baddeley, A. (2010). Working memory. *Curr. Biol.* 20, R136–R140. doi: 10.1016/j.cub.2009.12.014

Baddeley, A. D., and Hitch, G. J. (1974). "Working memory," in *The Psychology of Learning and Motivation: Advances in Research and Theory* (Vol. 8), ed. G. A. Bower (New York: Academic Press), 47–90.

Berardi, N., and Maffei, L. (1999). From visual experience to visual function: roles of neurotrophins. *J. Neurobiol.* 41, 119–126. doi: 10.1002/(SICI)1097-4695(199910)41:1%3C119::AID-NEU15%3E3.0.CO;2-N

Berzhanskaya, J., Grossberg, S., and Mingolla, E. (2007). Laminar cortical dynamics of visual form and motion interactions during coherent object motion perception. *Spat. Vis.* 20, 337–395. doi: 10.1163/156856807780919000

Bhatt, R., Carpenter, G., and Grossberg, S. (2007). Texture segregation by visual cortex: perceptual grouping, attention and learning. *Vision Res.* 47, 3173–3211. doi: 10.1016/j.visres.2007.07.013

Blasdel, G. G. (1992a). Orientation selectivity, preference and continuity in monkey striate cortex. *J. Neurosci.* 12, 3139–3161. doi: 10.1523/jneurosci.12-08-03139.1992

Blasdel, G. G. (1992b). Differential imaging of ocular dominance and orientation selectivity in monkey striate cortex. *J. Neurosci.* 12, 3115–3138. doi: 10.1523/jneurosci.12-08-03115.1992

Boardman, I., Grossberg, S., Myers, C., and Cohen, M. (1999). Neural dynamics of perceptual order and context effects for variable-rate speech syllables. *Percept. Psychophys.* 6, 1477–1500. doi: 10.3758/bf03213112

Bonnevie, T., Dunn, B., Fyhn, M., Hafting, T., Derdikman, D., Kubie, J. L., et al. (2013). Grid cells require excitatory drive from the hippocampus. *Nat. Neurosci.* 16, 309–319. doi: 10.1038/nn.3311

Bootman, M. D., and Berridge, M. J. (1996). Subcellular Ca2+ signals underlying waves and graded responses in HeLa cells. *Curr. Biol.* 6, 855–865. doi: 10.1016/s0960-9822(02)00609-7

Born, R. T., and Tootell, R. B. H. (1992). Segregation of global and local motion processing in primate middle temporal visual area. *Nature* 357, 497–499. doi: 10.1038/357497a0

Brannon, E. M., and Terrace, H. S. (1998). Ordering of the numerosities 1 to 9 by monkeys. *Science* 282, 746–749. doi: 10.1126/science.282.5389.746

Brannon, E. M., and Terrace, H. S. (2000). Representation of the numerosities 1 to 9 by rehesus macaques (Macaca mulatta). *J. Exp. Psychol. Anim. Behav. Process.* 26, 31–49. doi: 10.1037//0097-7403.26.1.31

Bregman, A. S. (1990). *Auditory Scene Analysis: The Perceptual Organization of Sound.* Cambridge, MA: MIT Press.

Brodmann, K. (1909). *Vergleichende Lokalisationslehre der Grosshirnrinde in Ihren Prinzipien Dargestellt auf Grund des Zellenbaues.* Leipzig: Barth.

Brown, J., Bullock, D., and Grossberg, S. (1999). How the basal ganglia use parallel excitatory and inhibitory learning pathways to selectively respond to unexpected rewarding cues. *J. Neurosci.* 19, 10502–10511. doi: 10.1523/JNEUROSCI.19-23-10502.1999

Brown, G. D., Yamada, S., and Sejnowski, T. J. (2001). Independent component analysis at the neural cocktail party. *Trends Neurosci.* 24, 54–63. doi: 10.1016/s0166-2236(00)01683-0

Browning, A., Grossberg, S., and Mingolla, M. (2009a). A neural model of how the brain computes heading from optic flow in realistic scenes. *Cogn. Psychol.* 59, 320–356. doi: 10.1016/j.cogpsych.2009.07.002

Browning, N., Grossberg, S., and Mingolla, M. (2009b). Cortical dynamics of navigation and steering in natural scenes: motion-based object segmentation, heading and obstacle avoidance. *Neural Netw.* 22, 1383–1398. doi: 10.1016/j.neunet.2009.05.007

Brun, V. H., Solstad, T., Kjelstrup, K. B., Fyhn, M., Witter, M. P., Moser, E. I., et al. (2008). Progressive increase in grid scale from dorsal to ventral medial entorhinal cortex. *Hippocampus* 18, 1200–1212. doi: 10.1002/hipo.20504

Cabelli, R. J., Hohn, A., and Shatz, C. J. (1995). Inhibition of ocular dominance column formation by infusion of NT-4/5 or BDNF. *Science* 267, 1662–1666. doi: 10.1126/science.7886458

Cabelli, R. J., Shelton, D. L., Segal, R. A., and Shatz, C. J. (1997). Blockade of endogenous ligands of trkB inhibits formation of ocular dominance columns. *Neuron* 19, 63–76. doi: 10.1016/s0896-6273(00)80348-7

Callaway, E. M. (1998). Local circuits in primary visual cortex of the macaque monkey. *Annu. Rev. Neurosci.* 21, 47–74. doi: 10.1146/annurev.neuro.21.1.47

Callaway, E. M., and Katz, L. C. (1990). Emergence and refinement of clustered horizontal connections in cat striate cortex. *J. Neurosci.* 10, 1134–1153. doi: 10.1523/jneurosci.10-04-01134.1990

Callaway, E. M., and Katz, L. C. (1991). Effects of binocular deprivation on the development of clustered horizontal connections in cat striate cortex. *Proc. Natl. Acad. Sci. U S A* 88, 745–749. doi: 10.1073/pnas.88.3.745

Callaway, E. M., and Katz, L. C. (1992). Development of axonal arbors of layer 4 spiny neurons in cat striate cortex. *J. Neurosci.* 12, 570–582. doi: 10.1523/jneurosci.12-02-00570.1992

Cameron, S., Grossberg, S., and Guenther, F. H. (1998). A self-organizing neural network architecture for navigation using optic flow. *Neural Comput.* 10, 313–352. doi: 10.1162/089976698300017782

Cao, Y., and Grossberg, S. (2005). A laminar cortical model of stereopsis and 3D surface perception: closure and da Vinci stereopsis. *Spat. Vis.* 18, 515–578. doi: 10.1163/156856805774406756

Cao, Y., and Grossberg, S. (2012). Stereopsis and 3D surface perception by spiking neurons in laminar cortical circuits: a method of converting neural rate models into spiking models. *Neural Netw.* 26, 75–98. doi: 10.1016/j.neunet.2011.10.010

Cao, Y., and Grossberg, S. (2014). How the Venetian blind percept emerges from the laminar cortical dynamics of 3D vision. *Front. Psychol.* 5:694. doi: 10.3389/fpsyg.2014.00694

Cao, Y., and Grossberg, S. (2018). "A laminar cortical model for 3D boundary and surface representations of complex natural scenes," in *From Parallel to Emergent Computing*, ed. A. Adamatzky, S. Akl and G. Sirakoulis (Milton Park, Oxfordshire: Taylor and Francis/CRC).

Carpenter, G. A., and Grossberg, S. (1987a). A massively parallel architecture for a self-organizing neural pattern recognition machine. *Comput. Vis. Graph. Image Process.* 37, 54–115. doi: 10.1016/s0734-189x(87)80014-2

Carpenter, G. A., and Grossberg, S. (1987b). ART 2: stable self-organization of pattern recognition codes for analog input patterns. *Appl. Opt.* 26, 4919–4930. doi: 10.1364/AO.26.004919

Carpenter, G. A., Grossberg, S., Markuzon, N., Reynolds, J. H., and Rosen, D. B. (1992). Fuzzy ARTMAP: a neural network architecture for incremental supervised learning of analog multidimensional maps. *IEEE Trans. Neural Netw.* 3, 698–713. doi: 10.1109/72.159059

Chakrabarty, S., and Martin, J. H. (2000). Postnatal development of the motor representation in primary motor cortex. *J. Neurophysiol.* 84, 2582–2594. doi: 10.1152/jn.2000.84.5.2582

Chance, F., Nelson, S., and Abbott, L. (1999). Complex cells as cortically amplified simple cells. *Nat. Neurosci.* 2, 277–282. doi: 10.1038/6381

Cohen, M. A., and Grossberg, S. (1986). Neural dynamics of speech and language coding: developmental programs, perceptual grouping and competition for short-term memory. *Hum. Neurobiol.* 5, 1–22.

Cohen, M. A., and Grossberg, S. (1987). Masking fields: a massively parallel neural architecture for learning, recognizing and predicting multiple groupings of patterned data. *Appl. Opt.* 26, 1866–1891. doi: 10.1364/AO.26.001866

Cohen, M. A., and Grossberg, S. (1997). Parallel auditory filtering by sustained and transient channels separates coarticulated vowels and consonants. *IEEE Trans. Speech Audio Process.* 5, 301–318. doi: 10.1109/89.593304

Cohen, M. A., Grossberg, S., and Stork, D. G. (1988). "Speech perception and production by a self-organizing neural network," in *Evolution, Learning, Cognition and Advanced Architectures*, eds Y. C. Lee (Hong Kong: World Scientific Publishers), 217–231.

Cohen, M. A., Grossberg, S., and Wyse, L. L. (1995). A spectral network model of pitch perception. *J. Acoust. Soc. Am.* 98, 862–879. doi: 10.1121/1.413512

Constantinidis, C., and Klingberg, T. (2016). The neuroscience of working memory capacity and training. *Nat. Rev. Neurosci.* 17, 438–449. doi: 10.1038/nrn.2016.43

Crair, M. C., Ruthazer, E. S., Gillespie, D. C., and Stryker, M. P. (1997a). Ocular dominance peaks at pinwheel center singularities of the orientation map in cat visual cortex. *J. Neurophysiol.* 77, 3381–3385. doi: 10.1152/jn.1997.77.6.3381

Crair, M. C., Ruthazer, E. S., Gillespie, D. C., and Stryker, M. P. (1997b). Relationship between the ocular dominance and orientation maps in visual cortex of monocularly deprived cats. *Neuron* 34, 307–318. doi: 10.1016/s0896-6273(00)80941-1

Das, A., and Gilbert, C. D. (1995). Long-range horizontal connections and their role in cortical reorganization revealed by optical recording of cat primary visual cortex. *Nature* 375, 780–784. doi: 10.1038/375780a0

Dehaene, S. (1997). *The Number Sense: How the Mind Creates Mathematics*. New York, NY: Oxford University Press.

Dehaene, S., Tzourio, N., Frak, V., Raynaud, L., Cohen, L., Mehler, J., et al. (1996). Cerebral activations during number multiplication and comparison: a PET study. *Neuropsychologia* 34, 1097–1106. doi: 10.1016/0028-3932(96)00027-9

Deutsch, D. (1975). Two-channel listening to musical scales. *J. Acoust. Soc. Am.* 57, 1156–1160. doi: 10.1121/1.380573

Duffy, K. R., Murphy, K. M., and Jones, D. G. (1998). Analysis of the postnatal growth of visual cortex. *Vis. Neurosci.* 15, 831–839. doi: 10.1017/s0952523898155049

Duifhuis, H., Willems, L. F., and Sluyter, R. (1982). Measurement of pitch in speech: an implementation of goldstein's theory of pitch perception. *J. Acoust. Soc. Am.* 71, 1568–1580. doi: 10.1121/1.387811

Dykes, R. W., Rasmusson, D. D., and Hoeltzell, P. B. (1980). Organization of primary somatosensory cortex in the cat. *J. Neurophysiol.* 43, 1527–1546. doi: 10.1152/jn.1980.43.6.1527

Elder, D., Grossberg, S., and Mingolla, M. (2009). A neural model of visually guided steering, obstacle avoidance and route selection. *J. Exp. Psychol. Hum. Percept. Perform.* 35, 1501–1531. doi: 10.1037/a0016459

Fajen, B. R., and Warren, W. H. (2003). Behavioral dynamics of steering, obstacle avoidance and route selection. *J. Exp. Psychol. Hum. Percept. Perform.* 29, 343–362. doi: 10.1037/0096-1523.29.2.343

Fang, L., and Grossberg, S. (2009). From stereogram to surface: how the brain sees the world in depth. *Spat. Vis.* 22, 45–82. doi: 10.1163/156856809786618484

Fiala, J. C., Grossberg, S., and Bullock, D. (1996). Metabotropic glutamate receptor activation in cerebellar Purkinje cells as substrate for adaptive timing of the classically conditioned eye blink response. *J. Neurosci.* 16, 3760–3774. doi: 10.1523/jneurosci.16-11-03760.1996

Finch, E. A., and Augustine, G. J. (1998). Local calcium signalling by inositol-1,4,5-triphosphate in Purkinje cell dendrites. *Nature* 396, 753–756. doi: 10.1038/25541

Formisano, E., Kim, D.-S., Di Salle, F., van de Moortele, P.-F., Ugurbil, K., and Goebel, R. (2003). Mirror-symmetric tonotopic maps in human primary auditory cortex. *Neuron* 40, 859–869. doi: 10.1016/s0896-6273(03)00669-x

Frank, L. M., Stanley, G. B., and Brown, E. N. (2004). Hippocampal plasticity across multiple days of exposure to novel environments. *J. Neurosci.* 24, 7681–7689. doi: 10.1523/JNEUROSCI.1958-04.2004

Franklin, D. J., and Grossberg, S. (2017). A neural model of normal and abnormal learning and memory consolidation: adaptively timed conditioning, hippocampus, amnesia, neurotrophins and consciousness. *Cogn. Affect. Behav. Neurosci.* 17, 24–76. doi: 10.3758/s13415-016-0463-y

Galuske, R. A., and Singer, W. (1996). The origin and topography of long-range intrinsic projections in cat visual cortex: a developmental study. *Cereb. Cortex* 6, 417–430. doi: 10.1093/cercor/6.3.417

Ghosh, A. (1995). "Subplate neurons and the patterning of thalamocortical connections," in *Ciba Found. Symp.*, eds G. Bock and G. Cardew (Chichester, New York: John Wiley), 150–165.

Ghosh, A., and Shatz, C. J. (1992). Involvement of subplate neurons in the formation of ocular dominance columns. *Science* 255, 1441–1443. doi: 10.1126/science.1542795

Ghosh, A., and Shatz, C. J. (1993). A role for subplate neurons in the patterning of connections from thalamus to neocortex. *Development* 117, 1031–1047.

Ghosh, A., and Shatz, C. J. (1994). Segregation of geniculocortical afferents during the critical period: a role for subplate neurons. *J. Neurosci.* 14, 3862–3880. doi: 10.1523/JNEUROSCI.14-06-03862.1994

Gibson, J. J. (1950). *The Perception of the Visual World*. Oxford, England: Houghton Mifflin.

Gilbert, C. D., and Wiesel, T. N. (1992). Receptive field dynamics in adult primary visual cortex. *Nature* 356, 150–152. doi: 10.1038/356150a0

Gorchetchnikov, A., and Grossberg, S. (2007). Space, time and learning in the hippocampus: how fine spatial and temporal scales are expanded into population codes for behavioral control. *Neural Netw.* 20, 182–193. doi: 10.1016/j.neunet.2006.11.007

Grinvald, A., Lieke, E., Frostig, R. D., Gilbert, C. D., and Wiesel, T. N. (1986). Functional architecture of cortex revealed by optical imaging of intrinsic signals. *Nature* 324, 361–364. doi: 10.1038/324361a0

Grossberg, S. (1968). Some nonlinear networks capable of learning a spatial pattern of arbitrary complexity. *Proc. Natl. Acad. Sci. U S A* 59, 368–372. doi: 10.1073/pnas.59.2.368

Grossberg, S. (1971). Pavlovian pattern learning by nonlinear neural networks. *Proc. Natl. Acad. Sci. U S A* 68, 828–831. doi: 10.1073/pnas.68.4.828

Grossberg, S. (1972a). A neural theory of punishment and avoidance, I: qualitative theory. *Math. Biosci.* 15, 39–67. doi: 10.1016/0025-5564(72)90062-4

Grossberg, S. (1972b). A neural theory of punishment and avoidance, II: quantitative theory. *Math. Biosci.* 15, 253–285. doi: 10.1016/0025-5564(72)90038-7

Grossberg, S. (1973). Contour enhancement, short-term memory and constancies in reverberating neural networks. *Stud. Appl. Math.* 52, 213–257. doi: 10.1002/sapm1973523213

Grossberg, S. (1975a). A neural model of attention, reinforcement and discrimination learning. *Int. Rev. Neurobiol.* 18, 263–327. doi: 10.1016/s0074-7742(08)60037-9

Grossberg, S. (1975b). On the development of feature detectors in the visual cortex with applications to learning and reaction-diffusion systems. *Biol. Cybern.* 21, 145–159. doi: 10.1007/bf00337422

Grossberg, S. (1976a). Adaptive pattern classification and universal recoding, I: parallel development and coding of neural feature detectors. *Biol. Cybern.* 23, 121–134. doi: 10.1007/bf00344744

Grossberg, S. (1976b). Adaptive pattern classification and universal recoding, II: feedback, expectation, olfaction and illusions. *Biol. Cybern.* 23, 187–202. doi: 10.1007/bf00340335

Grossberg, S. (1978a). "A theory of human memory: self-organization and performance of sensory-motor codes, maps and plans," in *Progress in Theoretical Biology* (Vol. 5), eds R. Rosen and F. Snell (New York, NY: Academic Press), 233–374.

Grossberg, S. (1978b). "Communication, memory and development," in *Progress in Theoretical Biology* (Vol. 5), eds R. Rosen and F. Snell (New York, NY: Academic Press), 183–232.

Grossberg, S. (1980). How does a brain build a cognitive code? *Psychol. Rev.* 87, 1–51. doi: 10.1007/978-94-009-7758-7_1

Grossberg, S. (1984). "Outline of a theory of brightness, color and form perception," in *Trends in Mathematical Psychology*, eds E. Degreef and J. van Buggenhaut (Amsterdam: North-Holland), 59–85.

Grossberg, S. (1988). Nonlinear neural networks: principles, mechanisms and architectures. *Neural Netw.* 1, 17–61. doi: 10.1016/0893-6080(88)90021-4

Grossberg, S. (1999a). How does the cerebral cortex work? Learning, attention and grouping by the laminar circuits of visual cortex. *Spat. Vis.* 12, 163–185. doi: 10.1163/156856899x00102

Grossberg, S. (1999b). The link between brain learning, attention and consciousness. *Conscious. Cogn.* 8, 1–44. doi: 10.1006/ccog.1998.0372

Grossberg, S. (2000). The complementary brain: unifying brain dynamics and modularity. *Trends Cogn. Sci.* 4, 233–246. doi: 10.1016/s1364-6613(00)01464-9

Grossberg, S. (2003). How does the cerebral cortex work? Development, learning, attention and 3D vision by laminar circuits of visual cortex. *Behav. Cogn. Neurosci. Rev.* 2, 47–76. doi: 10.1177/1534582303002001003

Grossberg, S. (2013). "Recurrent neural networks," in *Scholarpedia*. 8, 1888. Available online at: http://www.scholarpedia.org/article/Recurrent_neural_networks.

Grossberg, S. (2016a). Cortical dynamics of figure-ground separation in response to 2D pictures and 3D scenes: how V2 combines border ownership, stereoscopic cues and gestalt grouping rules. *Front. Psychol.* 6:2054. doi: 10.3389/fpsyg.2015.02054

Grossberg, S. (2016b). "Neural dynamics of the basal ganglia during perceptual, cognitive and motor learning and gating," in *The Basal Ganglia: Novel Perspectives on Motor and Cognitive Functions*, ed. J.-J. Soghomonian (Berlin: Springer), 457–512.

Grossberg, S. (2017a). Acetylcholine neuromodulation in normal and abnormal learning and memory: vigilance control in waking, sleep, autism, amnesia and Alzheimer's disease. *Front. Neural Circuits* 11:82. doi: 10.3389/fncir.2017.00082

Grossberg, S. (2017b). Towards solving the Hard Problem of Consciousness: the varieties of brain resonances and the conscious experiences that they support. *Neural Netw.* 87, 38–95. doi: 10.1016/j.neunet.2016.11.003

Grossberg, S. (2018). Desirability, availability, credit assignment, category learning and attention: cognitive-emotional and working memory dynamics of orbitofrontal, ventrolateral and dorsolateral prefrontal cortices. *Brain Neurosci. Adv.* 2:239821281877217. doi: 10.1177/2398212818772179

Grossberg, S. (2019). The embodied brain of SOVEREIGN2: from space-variant conscious percepts during visual search and navigation to learning invariant object categories and cognitive-emotional plans for acquiring valued goals. *Front. Comput. Neurosci.* 13:36. doi: 10.3389/fncom.2019.00036

Grossberg, S. (2020). *Conscious Mind/Resonant Brain: How Each Brain Makes a Mind*. New York: Oxford University Press.

Grossberg, S., Boardman, I., and Cohen, M. (1997). Neural dynamics of variable-rate speech categorization. *J. Exp. Psychol. Hum. Percept. Perform.* 23, 481–503. doi: 10.1037/0096-1523.23.2.481

Grossberg, S., Govindarajan, K. K., Wyse, L. L., and Cohen, M. A. (2004). ARTSTREAM: a neural network model of auditory scene analysis and source segregation. *Neural Netw.* 17, 511–536. doi: 10.1016/j.neunet.2003.10.002

Grossberg, S., and Grunewald, A. (2002). Temporal dynamics of binocular disparity processing with corticogeniculate interactions. *Neural Netw.* 15, 181–200. doi: 10.1016/s0893-6080(01)00149-6

Grossberg, S., and Howe, P. D. L. (2003). A laminar cortical model of stereopsis and three-dimensional surface perception. *Vision Res.* 43, 801–829. doi: 10.1016/s0042-6989(03)00011-7

Grossberg, S., and Kazerounian, S. (2011). Laminar cortical dynamics of conscious speech perception: a neural model of phonemic restoration using subsequent context in noise. *J. Acoust. Soc. Am.* 130, 440–460. doi: 10.1121/1.3589258

Grossberg, S., and Kazerounian, S. (2016). Phoneme restoration and empirical coverage of interactive activation and adaptive resonance models of human speech processing. *J. Acoust. Soc. Am.* 140:1130. doi: 10.1121/1.4946760

Grossberg, S., and Kelly, F. J. (1999). Neural dynamics of binocular brightness perception. *Vision Res.* 39, 3796–3816. doi: 10.1016/s0042-6989(99)00095-4

Grossberg, S., Léveillé, J., and Versace, M. (2011). How do object reference frames and motion vector decomposition emerge in laminar cortical circuits? *Atten. Percept. Psychophys.* 73, 1147–1170. doi: 10.3758/s13414-011-0095-9

Grossberg, S., and Levine, D. (1975). Some developmental and attentional biases in the contrast enhancement and short-term memory of recurrent neural networks. *J. Theor. Biol.* 53, 341–380. doi: 10.1016/s0022-5193(75)80009-9

Grossberg, S., and Merrill, J. W. L. (1992). A neural network model of adaptively timed reinforcement learning and hippocampal dynamics. *Cogn. Brain Res.* 1, 3–38. doi: 10.1016/0926-6410(92)90003-a

Grossberg, S., and Merrill, J. W. L. (1996). The hippocampus and cerebellum in adaptively timed learning, recognition and movement. *J. Cogn. Neurosci.* 8, 257–277. doi: 10.1162/jocn.1996.8.3.257

Grossberg, S., and Mingolla, E. (1985). Neural dynamics of perceptual grouping: textures, boundaries, and emergent segmentations. *Percept. Psychophys.* 38, 141–171. doi: 10.3758/bf03198851

Grossberg, S., and Myers, C. W. (2000). The resonant dynamics of speech perception: interword integration and duration-dependent backward effects. *Psychol. Rev.* 107, 735–767. doi: 10.1037/0033-295x.107.4.735

Grossberg, S., and Pearson, L. (2008). Laminar cortical dynamics of cognitive and motor working memory, sequence learning and performance: toward a unified theory of how the cerebral cortex works. *Psychol. Rev.* 115, 677–732. doi: 10.1037/a0012618

Grossberg, S., and Pessoa, L. (1998). Texture segregation, surface representation and figure-ground separation. *Vision Res.* 38, 2657–2684. doi: 10.1016/s0042-6989(97)00180-6

Grossberg, S., and Pilly, P. K. (2012). How entorhinal grid cells may learn multiple spatial scales from a dorsoventral gradient of cell response rates in a self-organizing map. *PLoS Comput. Biol.* 8:31002648. doi: 10.1371/journal.pcbi.1002648

Grossberg, S., and Pilly, P. K. (2014). Coordinated learning of grid cell and place cell spatial and temporal properties: multiple scales, attention and oscillations. *Philos. Trans. R. Soc. Lond. B Biol. Sci.* 369:20120524. doi: 10.1098/rstb.2012.0524

Grossberg, S., and Raizada, R. (2000). Contrast-sensitive perceptual grouping and object-based attention in the laminar circuits of primary visual cortex. *Vision Res.* 40, 1413–1432. doi: 10.1016/s0042-6989(99)00229-1

Grossberg, S., and Repin, D. (2003). A neural model of how the brain represents and compares multi-digit numbers: spatial and categorical processes. *Neural Netw.* 16, 1107–1140. doi: 10.1016/s0893-6080(03)00193-x

Grossberg, S., and Schmajuk, N. A. (1989). Neural dynamics of adaptive timing and temporal discrimination during associative learning. *Neural Netw.* 2, 79–102. doi: 10.1016/0893-6080(89)90026-9

Grossberg, S., and Seidman, D. (2006). Neural dynamics of autistic behaviors: cognitive, emotional, and timing substrates. *Psychol. Rev.* 113, 483–525. doi: 10.1037/0033-295x.113.3.483

Grossberg, S., and Seitz, A. (2003). Laminar development of receptive fields, maps and columns in visual cortex: the coordinating role of the subplate. *Cereb. Cortex* 13, 852–863. doi: 10.1093/cercor/13.8.852

Grossberg, S., and Swaminathan, G. (2004). A laminar cortical model for 3D perception of slanted and curved surfaces and of 2D images: development, attention and bistability. *Vision Res.* 44, 1147–1187. doi: 10.1016/j.visres.2003.12.009

Grossberg, S., and Versace, M. (2008). Spikes, synchrony and attentive learning by laminar thalamocortical circuits. *Brain Res.* 1218, 278–312. doi: 10.1016/j.brainres.2008.04.024

Grossberg, S., and Williamson, J. R. (2001). A neural model of how horizontal and interlaminar connections of visual cortex develop into adult circuits that carry out perceptual grouping and learning. *Cereb. Cortex* 11, 37–58. doi: 10.1093/cercor/11.1.37

Grossberg, S., and Yazdanbakhsh, A. (2005). Laminar cortical dynamics of 3D surface perception: stratification, transparency, and neon color spreading. *Vision Res.* 45, 1725–1743. doi: 10.1016/j.visres.2005.01.006

Grossberg, S., Yazdanbakhsh, A., Cao, Y., and Swaminathan, G. (2008). How does binocular rivalry emerge from cortical mechanisms of 3-D vision? *Vision Res.* 48, 2232–2250. doi: 10.1016/j.visres.2008.06.024

Grunewald, A., and Grossberg, S. (1998). Self-organization of binocular disparity tuning by reciprocal corticogeniculate interactions. *J. Cogn. Neurosci.* 10, 199–215. doi: 10.1162/089892998562654

Hackett, T. A., Stepniewska, I., and Kaas, J. H. (1998). Subdivisions of auditory cortex and ipsilateral cortical connections of the parabelt auditory cortex in macaque monkeys. *J. Comp. Neurol.* 394, 475–495. doi: 10.1002/(sici)1096-9861(19980518)394:4<475::aid-cne6>3.0.co;2-z

Hafting, T., Fyhn, M., Molden, S., Moser, M. B., and Moser, E. I. (2005). Microstructure of a spatial map in the entorhinal cortex. *Nature* 436, 801–806. doi: 10.1038/nature03721

Hubel, D. H., and Wiesel, T. N. (1962). Receptive fields, binocular interaction and functional architecture in the cat's visual cortex. *J. Physiol.* 160, 106–154. doi: 10.1113/jphysiol.1962.sp006837

Hubel, D. H., and Wiesel, T. N. (1968). Receptive fields and functional architecture of monkey striate cortex. *J. Physiol.* 195, 215–243. doi: 10.1113/jphysiol.1968.sp008455

Hubel, D. H., and Wiesel, T. N. (1974). Sequence regularity and geometry of orientation columns in the monkey striate cortex. *J. Comp. Neurol.* 158, 267–293. doi: 10.1002/cne.901580304

Hübener, M., Shoham, D., Grinvald, A., and Bonhoeffer, T. (1997). Spatial relationships among three columnar systems in cat area 17. *J. Neurosci.* 17, 9270–9284. doi: 10.1523/jneurosci.17-23-09270.1997

Ichise, T., Kano, M., Hashimoto, K., Yangihara, D., Nakao, K., Shigemoto, R., et al. (2000). mGluR1 in cerebellar Purkinje cells essential for long-term depression, synapse elimination, and motor coordination. *Science* 288, 1832–1835. doi: 10.1126/science.288.5472.1832

Imig, T. J., Ruggero, M. A., Kitzes, L. M., Javel, E., and Brugge, J. F. (1977). Organization of auditory cortex in the owl monkey. *J. Comp. Neurol.* 171, 111–128. doi: 10.1002/cne.901710108

Johansson, G. (1974). Vector analysis in visual perception of rolling motion. *Psychol. Forsch.* 36, 311–319. doi: 10.1007/bf00424568

Joy, N. M., Kothinti, S. R., and Umesh, S. (2018). FMLLR speaker normalization with i-vector: in pseudo-FMLLR and distillation framework. *IEEE/ACM Trans. Audio Speech Lang. Process.* 26, 797–805. doi: 10.1109/taslp.2018.2795754

Julesz, B. (1971). *Foundations of Cyclopean Perception*. Chicago, IL: The University of Chicago Press.

Kaas, J. H., and Hackett, T. A. (1998). Subdivisions of auditory cortex and levels of processing in primates. *Audiol. Neurootol.* 3, 73–85. doi: 10.1159/000013783

Kaas, J. H., and Hackett, T. A. (2000). Subdivisions of auditory cortex and processing streams in primates. *Proc. Natl. Acad. Sci. U S A* 97, 11793–11799. doi: 10.1073/pnas.97.22.11793

Kandel, E. R., and O'Dell, T. J. (1992). Are adult learning mechanisms also used for development? *Science* 258, 243–245. doi: 10.1126/science.1411522

Kanizsa, G. (1955). Margini quasi-percettivi in campi con stimulazione omogenea. *Rev. Psicol.* 49, 7–30.

Kanizsa, G. (1974). Contours without gradients or cognitive contours. *Ital. J. Psychol.* 9, 93–113.

Kanizsa, G. (1976). Subjective contours. *Sci. Am.* 234, 48–53. doi: 10.1038/scientificamerican0476-48

Kanold, P. O., Kara, P., Reid, R. C., and Shatz, C. J. (2003). Role of subplate neurons in functional maturation of visual cortical columns. *Science* 301, 521–525. doi: 10.1126/science.1084152

Kara, P., and Boyd, J. D. (2009). A micro-architecture for binocular disparity and ocular dominance in visual cortex. *Nature* 458, 627–631. doi: 10.1038/nature07721

Katz, L. C., Gilbert, C. D., and Wiesel, T. N. (1989). Local circuits and ocular dominance columns in monkey striate cortex. *J. Neurosci.* 9, 1389–1399. doi: 10.1523/jneurosci.09-04-01389.1989

Kazerounian, S., and Grossberg, S. (2014). Real-time learning of predictive recognition categories that chunk sequences of items stored in working memory. *Front. Psychol.* 5:1053. doi: 10.3389/fpsyg.2014.01053

Kelly, F. J., and Grossberg, S. (2000). Neural dynamics of 3-D surface perception: figure-ground separation and lightness perception. *Percept. Psychophys.* 62, 1596–1618. doi: 10.3758/bf03212158

Kentros, C. G., Agniotri, N. T., Streater, S., Hawkins, R. D., and Kandel, E. R. (2004). Increased attention to spatial context increases both place field stability and spatial memory. *Neuron* 42, 283–295. doi: 10.1016/s0896-6273(04)00192-8

Kentros, C. G., Hargreaves, E., Hawkins, R. D., Kandel, E. R., Shapiro, M., and Muller, R. V. (1998). Abolition of long-term stability of new hippocampal place cell maps by NMDA receptor blockade. *Science* 280, 2121–2126. doi: 10.1126/science.280.5372.2121

Kohonen, T. (1982). Self-organized formation of topologically correct feature maps. *Biol. Cybern.* 43, 59–69. doi: 10.1007/bf00337288

Komiya, H., and Eggermont, J. J. (2000). Spontaneous firing activity of cortical neurons in adult cats with reorganized tonotopic map following pure-tone trauma. *Acta Otolaryngol.* 120, 750–756. doi: 10.1080/00016480075000298

Langston, R. F., Ainge, J. A., Couey, J. J., Canto, C. B., Bjerknes, T. L., Witter, M. P., et al. (2010). Development of the spatial representation system in the rat. *Science* 328, 1576–1580. doi: 10.1126/science.1188210

LeVay, S., Stryker, M. P., and Shatz, C. J. (1978). Ocular dominance columns and their development in layer IV of the cat's visual cortex: a quantitative study. *J. Comp. Neurol.* 179, 223–244. doi: 10.1002/cne.901790113

Léveillé, J., Versace, M., and Grossberg, S. (2010). Running as fast as it can: how spiking dynamics form object groupings in the laminar circuits of visual cortex. *J. Comput. Neurosci.* 28, 323–346. doi: 10.1007/s10827-009-0211-1

Linsker, R. (1986a). From basic network principles to neural architecture: emergence of orientation columns. *Proc. Natl. Acad. Sci. U S A* 83, 8779–8783. doi: 10.1073/pnas.83.22.8779

Linsker, R. (1986b). From basic network principles to neural architecture: emergence of orientation-selective cells. *Proc. Natl. Acad. Sci. U S A* 83, 8390–8394. doi: 10.1073/pnas.83.21.8390

Linsker, R. (1986c). From basic network principles to neural architecture: emergence of spatial-opponent cells. *Proc. Natl. Acad. Sci. U S A* 83, 7508–7512. doi: 10.1073/pnas.83.19.7508

Löwel, S., and Singer, W. (1992). Selection of intrinsic horizontal connections in the visual cortex by correlated neuronal activity. *Science* 255, 209–212. doi: 10.1126/science.1372754

Luskin, M. B., and Shatz, C. J. (1985). Studies of the earliest generated cells of the cat's visual cortex: cogeneration of subplate and marginal zones. *J. Neurosci.* 5, 1062–1075. doi: 10.1523/jneurosci.05-04-01062.1985

MacDonald, C. J., Lepage, K. Q., Eden, U. T., and Eichenbaum, H. (2011). Hippocampal "time cells" bridge the gap in memory for discontiguous events. *Neuron* 71, 737–749. doi: 10.1016/j.neuron.2011.07.012

Mariño, J., Schummers, J., Lyon, D. C., Schwabe, L., Beck, O., Wiesing, P., et al. (2005). Invariant computations in local cortical networks with balanced excitation and inhibition. *Nat. Neurosci.* 8, 194–201. doi: 10.1038/nn1391

Markowitz, J., Cao, Y., and Grossberg, S. (2012). From retinal waves to activity-dependent retinogeniculate map development. *PLoS One* 7:e31553. doi: 10.1371/journal.pone.0031553

Martin, J. H. (1989). *Neuroanatomy: Text and Atlas*. Norwalk, CT: Appleton and Lange.

McAllister, A. K. (1999). Subplate neurons: a missing link among neurotrophins, activity and ocular dominance plasticity? *Proc. Natl. Acad. Sci. U S A* 96, 13600–13602. doi: 10.1073/pnas.96.24.13600

McConnell, S. K., Ghosh, A., and Shatz, C. J. (1994). Subplate pioneers and the formation of descending connections from cerebral cortex. *J. Neurosci.* 14, 1892–1907. doi: 10.1523/jneurosci.14-04-01892.1994

McNaughton, B. L., Battaglia, F. P., Jensen, O., Moser, E. I., and Moser, M. B. (2006). Path integration and the neural basis of the 'cognitive map'. *Nat. Rev. Neurosci.* 7, 663–678. doi: 10.1038/nrn1932

Mechler, F., and Ringach, D. L. (2002). On the classification of simple and complex cells. *Vision Res.* 42, 1017–1033. doi: 10.1016/s0042-6989(02)00025-1

Merzenich, M. M., and Brugge, J. F. (1973). Representation of the cochlear partition of the superior temporal plane of the macaque monkey. *Brain Res.* 50, 275–296. doi: 10.1016/0006-8993(73)90731-2

Mhatre, H., Gorchetchnikov, A., and Grossberg, S. (2012). Grid cell hexagonal patterns formed by fast self-organized learning within entorhinal cortex. *Hippocampus* 22, 320–334. doi: 10.1002/hipo.20901

Miller, G. A., Galanter, E., and Pribram, K. H. (1960). *Plans and the Structure of Behavior*. New York, NY: Henry Holt and Co.

Miller, K. D., Keller, J. B., and Stryker, M. P. (1989). Ocular dominance column development: analysis and simulation. *Science* 245, 605–615. doi: 10.1126/science.2762813

Miyata, M., Finch, E. A., Khiroug, L., Hashimoto, K., Hayasaka, S., Oda, S.-I., et al. (2000). Local calcium release in dendritic spines required for long-term synaptic depression. *Neuron* 28, 233–244. doi: 10.1016/s0896-6273(00)00099-4

Morel, A., Garraghty, P. E., and Kaas, J. H. (1993). Tonotopic organization, architectonic fields, and connections of auditory cortex in macaque monkeys. *J. Comp. Neurol.* 335, 437–459. doi: 10.1002/cne.903350312

Morel, A., and Kaas, J. H. (1992). Subdivisions and connections of auditory cortex in owl monkeys. *J. Comp. Neurol.* 318, 27–63. doi: 10.1002/cne.903180104

Morris, R. G. M., and Frey, U. (1997). Hippocampal synaptic plasticity: role in spatial learning or the automatic recording of attended experience? *P. R. Soc. B.* 1360, 1469–1503. doi: 10.1098/rstb.1997.0136

Movshon, J. A., Thompson, I. D., and Tolhurst, D. J. (1978). Receptive field organization of complex cells in the cat's striate cortex. *J. Physiol.* 283, 79–99. doi: 10.1113/jphysiol.1978.sp012489

Muessig, L., Hauser, J., Wills, T. J., and Cacucci, F. (2015). A developmental switch in place cell accuracy coincides with grid cell maturation. *Neuron* 86, 1167–1173. doi: 10.1016/j.neuron.2015.05.011

Muller, R. A. (1996). A quarter of a century of place cells. *Neuron* 17, 813–822. doi: 10.1016/s0896-6273(00)80214-7

Munoz, D. P., Pelisson, D., and Guitton, D. (1991). Movement of neural activity on the superior colliculus motor map during gaze shifts. *Science* 251, 1358–1360. doi: 10.1126/science.2003221

Murphy, P. C., Duckett, S. G., and Sillito, A. M. (1999). Feedback connections to the lateral geniculate nucleus and cortical response properties. *Science* 286, 1552–1554. doi: 10.1126/science.286.5444.1552

Nieder, A., and Miller, E. K. (2003). Coding of cognitive magnitude: compressed scaling of numerical information in the primate prefrontal cortex. *Neuron* 37, 149–157. doi: 10.1016/s0896-6273(02)01144-3

Nieder, A., and Miller, E. K. (2004). A parieto-frontal network for visual numerical information in the monkey. *Proc. Natl. Acad. Sci. U S A* 101, 7457–7462. doi: 10.1073/pnas.0402239101

Nieoullon, A., and Rispal-Padel, L. (1976). Somatotopic localization in cat motor cortex. *Brain Res.* 105, 405–422. doi: 10.1016/0006-8993(76)90590-4

O'Keefe, J., and Dostrovsky, J. (1971). The hippocampus as a spatial map. Preliminary evidence from unit activity in the freely-moving rat. *Brain Res.* 34, 171–175. doi: 10.1016/0006-8993(71)90358-1

Ohzawa, I., DeAngelis, G. C., and Freeman, R. D. (1990). Stereoscopic depth discrimination by the visual cortex: neurons ideally suited as disparity detectors. *Science* 249, 1037–1041. doi: 10.1126/science.2396096

Olson, S. J., and Grossberg, S. (1998). A neural network model for the development of simple and complex cell receptive fields within cortical maps of orientation and ocular dominance. *Neural Netw.* 11, 189–208. doi: 10.1016/s0893-6080(98)00003-3

Peterson, G. E., and Barney, H. L. (1952). Control methods used in a study of the vowels. *J. Acoust. Soc. Am.* 24, 175–184. doi: 10.1121/1.1906875

Petkov, C. I., Kayser, C., Augath, M., and Logothetis, N. K. (2006). Functional imaging reveals numerous fields in the monkey auditory cortex. *PLoS Biol.* 4:e215. doi: 10.1371/journal.pbio.0040215

Piaget, J. (1963). *The Origins of Intelligence in Children.* New York, NY: Norton.

Piazza, M., Izard, V., Pinel, P., Le Bihan, D., and Dehaene, S. (2004). Tuning curves for approximate numerosity in the human intraparietal sulcus. *Neuron* 44, 547–555. doi: 10.1016/j.neuron.2004.10.014

Piazza, M., Pinel, P., Le Bihan, D., and Dehaene, S. (2007). A magnitude code common to numerosities and number symbols in human intraparietal cortex. *Neuron* 53, 293–305. doi: 10.1016/j.neuron.2006.11.022

Pilly, P. K., and Grossberg, S. (2012). How do spatial learning and memory occur in the brain? Coordinated learning of entorhinal grid cells and hippocampal place cells. *J. Cogn. Neurosci.* 24, 1031–1054. doi: 10.1162/jocn_a_00200

Pilly, P. K., and Grossberg, S. (2013a). How reduction of theta rhythm by medial septum inactivation may covary with disruption of entorhinal grid cell responses due to reduced cholinergic transmission. *Front. Neural Circuits* 7:173. doi: 10.3389/fncir.2013.00173

Pilly, P. K., and Grossberg, S. (2013b). Spiking neurons in a hierarchical self-organizing map model can learn to develop spatial and temporal properties of entorhinal grid cells and hippocampal place cells. *PLoS One* 8:e0060599. doi: 10.1371/journal.pone.0060599

Pilly, P. K., and Grossberg, S. (2014). How does the modular organization of entorhinal grid cells develop? *Front. Hum. Neurosci.* 8:337. doi: 10.3389/fnhum.2014.00337

Pinel, P., Le Clec'H, G., van de Moortele, P.-F., Naccache, L., Le Bihan, D., and Dehaene, S. (1999). Event-related fMRI analysis of the cerebral circuit for number comparison. *Neuroreport* 10, 1473–1479. doi: 10.1097/00001756-199905140-00015

Poggio, G. F. (1972). Spatial properties of neurons in striate cortex of unanesthetized macaque monkey. *Invest. Ophthalmol.* 11, 369–377.

Poggio, G. F., and Poggio, T. (1984). The analysis of stereopsis. *Annu. Rev. Neurosci.* 7, 379–412. doi: 10.1146/annurev.ne.07.030184.002115

Raizada, R. D. S., and Grossberg, S. (2001). Context-sensitive bindings by the laminar circuits of V1 and V2: a unified model of perceptual grouping, attention and orientation contrast. *Vis. Cogn.* 8, 431–466. doi: 10.1080/13506280143000070

Raizada, R., and Grossberg, S. (2003). Towards a theory of the laminar architecture of cerebral cortex: computational clues from the visual system. *Cereb. Cortex* 13, 100–113. doi: 10.1093/cercor/13.1.100

Rakic, P. (1976). Prenatal genesis of connections subserving ocular dominance in the rhesus monkey. *Nature* 261, 467–471. doi: 10.1038/261467a0

Rauschecker, J. P., and Tian, B. (2004). Processing of band-passed noise in the lateral auditory belt cortex of the rhesus monkey. *J. Neurophysiol.* 91, 2578–2589. doi: 10.1152/jn.00834.2003

Read, J. C. A., Parker, A. J., and Cumming, B. G. (2002). A simple model accounts for the response of disparity-tuned V1 neurons to anticorrelated images. *Vis. Neurosci.* 19, 735–753. doi: 10.1017/s0952523802196052

Rojer, A. S., and Schwartz, E. L. (1990). Cat and monkey cortical columnar patterns modeled by bandpass-filtered 2D white noise. *Biol. Cybern.* 62, 381–391. doi: 10.1007/bf00197644

Sargolini, F., Fyhn, M., Hafting, T., McNaughton, B. L., Witter, M. P., Moser, M.-B., et al. (2006). Conjunctive representation of position, direction and velocity in entorhinal cortex. *Science* 312, 758–762. doi: 10.1126/science.1125572

Scheffers, M. T. (1983). Simulation of auditory analysis of pitch: an elaboration on the DWS pitch meter. *J. Acoust. Soc. Am.* 74, 1716–1725. doi: 10.1121/1.390280

Schiller, P. H. (1992). The ON and OFF channels of the visual system. *Trends Neurosci.* 15, 86–92. doi: 10.1016/0166-2236(92)90017-3

Schiller, P. H., Finlay, B. L., and Volman, S. F. (1976). Quantitative studies of single-cell properties in monkey streiate cortex. II. Orientation specificity ad ocular dominance. *J. Neurophysiol.* 39, 1320–1333. doi: 10.1152/jn.1976.39.6.1320

Shadlen, M. N., and Newsome, W. T. (1998). The variable discharge of cortical neurons: implications for connectivity, computation and information coding. *J. Neurosci.* 18, 3870–3896. doi: 10.1523/jneurosci.18-10-03870.1998

Sillito, A. M., Jones, H. E., Gerstein, G. L., and West, D. C. (1994). Feature-linked synchronization of thalamic relay cell firing induced by feedback from the visual cortex. *Nature* 369, 479–482. doi: 10.1038/369479a0

Silver, M. R., Grossberg, S., Bullock, D., Histed, M. H., and Miller, E. K. (2012). A neural model of sequential movement planning and control of eye movements: item-order-rank working memory and saccade selection by the supplementary eye fields. *Neural Netw.* 26, 29–58. doi: 10.1016/j.neunet.2011.10.004

Skinner, B. F. (1938). *The Behavior of Organisms: An Experimental Analysis.* New York, NY: Appleton-Century-Crofts.

Stanton, S. G., and Harrison, R. V. (2000). Projections from the medial geniculate body to primary auditory cortex in neonatally deafened cats. *J. Comp. Neurol.* 426, 117–129. doi: 10.1002/1096-9861(20001009)426:1<117::aid-cne8>3.0.co;2-s

Stensola, H., Stensola, T., Solstad, T., Frøland, K., Moser, M.-B., and Moser, E. I. (2012). The entorhinal grid map is discretized. *Nature* 492, 72–78. doi: 10.1038/nature11649

Sun, Y. J., Wu, G. K., Liu, B.-H., Li, P., Zhou, M., Xiao, Z., et al. (2010). Fine-tuning of pre-balanced excitation and inhibition during auditory cortical development. *Nature* 465, 927–931. doi: 10.1038/nature09079

Swindale, N. V. (1980). A model for the formation of ocular dominance stripes. *Proc. R. Soc. Lond. B Biol. Sci.* 208, 243–264. doi: 10.1098/rspb.1980.0051

Swindale, N. V. (1992). A model for the coordinated development of columnar systems in primate striate cortex. *Biol. Cybern.* 66, 217–230. doi: 10.1007/bf00198475

Szabó, B. T., Denham, S. L., and Winkler, I. (2016). Computational models of auditory scene analysis: a review. *Front. Neurosci.* 10:524. doi: 10.3389/fnins.2016.00524

Takechi, H., Eilers, J., and Konnerth, A. (1998). A new class of synaptic response involving calcium release in dendritic spines. *Nature* 396, 757–760. doi: 10.1038/25547

Tao, L., Shelley, M., McLaughlin, D., and Shapley, R. (2004). An egalitarian network model for the emergence of simple and complex cells in visual cortex. *Proc. Natl. Acad. Sci. U S A* 101, 366–371. doi: 10.1073/pnas.20364 60100

Terrace, H. S. (1963). Discrimination learning with and without "errors". *J. Exp. Anal. Behav.* 6, 1–27. doi: 10.1901/jeab.1963.6-1

Thorpe, S. J., Fize, D., and Marlot, C. (1996). Speed of processing in the human visual system. *Nature* 381, 520–522. doi: 10.1038/381520a0

Tootell, R. B., Hadjikhani, N. K., Vanduffel, W., Liu, A. K., Mendola, J. D., Sereno, M. I., et al. (1998). Functional analysis of primary visual cortex (V1) in humans. *Proc. Natl. Acad. Sci. U S A* 95, 811–817. doi: 10.1073/pnas. 95.3.811

Tootell, R. B., Silverman, M. S., Switkes, E., and DeValois, R. L. (1982). Deoxyglucose analysis of retinotopic organization in primate striate cortex. *Science* 218, 902–904. doi: 10.1126/science.7134981

Tsodyks, M., Pawelzik, K., and Markram, H. (1998). Neural networks with dynamic synapses. *Neural Comput.* 10, 821–835. doi: 10.1162/089976698300017502

Tsodyks, M., and Sejnowski, T. (1995). Associative memory and hippocampal place cells. *Int. J. Neural Syst.* 6, 81–86.

Turrigiano, G. G. (1999). Homeostatic plasticity in neuronal networks: the more things change, the more they stay the same. *Trends Neurosci.* 5, 221–227. doi: 10.1016/s0166-2236(98)01341-1

van Vreeswijk, C., and Sompolinsky, H. (1998). Chaotic balanced state in a model of cortical circuits. *Neural Comput.* 10, 1321–1371. doi: 10. 1162/089976698300017214

Varela, F. J., and Singer, W. (1987). Neuronal dynamics in the visual corticothalamic pathway revealed through binocular rivalry. *Exp. Brain Res.* 66, 10–20. doi: 10.1007/bf00236196

von der Heydt, R., Peterhans, E., and Baumgartner, G. (1984). Illusory contours and cortical neuron responses. *Science* 224, 1260–1262. doi: 10.1126/science. 6539501

von der Malsburg, C. (1973). Self-organization of orientation sensitive cells in the striate cortex. *Kybernetik* 14, 85–100. doi: 10.1007/bf00288907

von Helmholtz, H. (1866). *Handbuch der Physiologischen Optik.* Leipzig: Leopold Voss.

von Helmholtz, H. (1962). *Treatise on Physiological Optics.* J. P. C. Southall (Trans.). New York, NY: Dover.

Wallace, M. T., and Stein, B. E. (1996). Sensory organization of the superior colliculus in cat and monkey. *Prog. Brain Res.* 112, 301–311. doi: 10.1016/s0079-6123(08)63337-3

Weliky, M., and Katz, L. C. (1997). Disruption of orientation tuning in visual cortex by artificially correlated neuronal activity. *Nature* 386, 680–685. doi: 10.1038/386680a0

Williamson, J. R. (1996). Gaussian ARTMAP: a neural network for fast incremental learning of noisy multidimensional maps. *Neural Netw.* 9, 881–897. doi: 10.1016/0893-6080(95)00115-8

Williamson, J. R. (1997). A constructive, incremental-learning network for mixture modeling and classification. *Neural Comput.* 9, 1517–1543. doi: 10.1162/neco.1997.9.7.1517

Wills, T. J., Barry, C., and Cacucci, F. (2012). The abrupt development of adult-like grid cell firing in the medial entorhinal cortex. *Front. Neural Circuits* 6:21. doi: 10.3389/fncir.2012.00021

Wills, T. J., Cacucci, F., Burgess, N., and O'Keefe, J. (2010). Development of the hippocampal cognitive map in preweanling rats. *Science* 328, 1573–1576. doi: 10.1126/science.1188224

Willshaw, D. J., and von der Malsburg, C. (1976). How patterned neural connections can be set up by self-organization. *Proc. R. Soc. Lond. B Biol. Sci.* 194, 431–445. doi: 10.1098/rspb.1976.0087

Wilson, M. A., and McNaughton, B. L. (1993). Dynamics of the hippocampal ensemble code for space. *Science* 261, 1055–1058. doi: 10.1126/science.8351520

Wong, R. O., and Oakley, D. M. (1996). Changing patterns of spontaneous bursting activity of on and off retinal ganglion cells during development. *Neuron* 16, 1087–1095. doi: 10.1016/s0896-6273(00) 80135-x

Yazdanbakhsh, A., and Grossberg, S. (2004). Fast synchronization of perceptual grouping in laminar visual cortical circuits. *Neural Netw.* 17, 707–718. doi: 10.1016/j.neunet.2004.06.005

Conflict of Interest: The author declares that the research was conducted in the absence of any commercial or financial relationships that could be construed as a potential conflict of interest.

frontiers in Neuroanatomy

ORIGINAL RESEARCH
published: 11 February 2020
doi: 10.3389/fnana.2020.00001

Stereotaxic Diffusion Tensor Imaging White Matter Atlas for the *in vivo* Domestic Feline Brain

Philippa J. Johnson[1], Raluca Pascalau[2], Wen-Ming Luh[3], Ashish Raj[4], Sofia Cerda-Gonzalez[5] and Erica F. Barry[1]*

[1]Department of Clinical Sciences, College of Veterinary Medicine, Cornell University, Ithaca, NY, United States, [2]Faculty of Medicine, "Iuliu Hatieganu" University of Medicine and Pharmacy, Cluj-Napoca, Romania, [3]National Institute on Aging, National Institutes of Health, Baltimore, MD, United States, [4]Department of Radiology and Biomedical Imaging, University of California, San Francisco, San Francisco, CA, United States, [5]Medvet Chicago, Northbrook, IL, United States

The cat brain is a useful model for neuroscientific research and with the increasing use of advanced neuroimaging techniques there is a need for an open-source stereotaxic white matter brain atlas to accompany the cortical gray matter atlas, currently available. A stereotaxic white matter atlas would facilitate anatomic registration and segmentation of the white matter to aid in lesion localization or standardized regional analysis of specific regions of the white matter. In this article, we document the creation of a stereotaxic feline white matter atlas from diffusion tensor imaging (DTI) data obtained from a population of eight mesaticephalic felines. Deterministic tractography reconstructions were performed to create tract priors for the major white matter projections of Corpus callosum (CC), fornix, cingulum, uncinate, Corona Radiata (CR), Corticospinal tract (CST), inferior longitudinal fasciculus (ILF), Superior Longitudinal Fasciculus (SLF), and the cerebellar tracts. T1-weighted, fractional anisotropy (FA), mean diffusivity (MD), radial diffusivity (RD) and axial diffusivity (AD) population maps were generated. The volume, mean tract length and mean FA, MD, AD and RD values for each tract prior were documented. A structural connectome was then created using previously published cortical priors and the connectivity metrics for all cortical regions documented. The provided white matter atlas, diffusivity maps, tract priors and connectome will be a valuable resource for anatomical, pathological and translational neuroimaging research in the feline model. Multi-atlas population maps and segmentation priors are available at Cornell's digital repository: https://ecommons.cornell.edu/handle/1813/58775.2.

Keywords: cat, FA, MD, RD, AD, tractography, deterministic, connectome

OPEN ACCESS

Edited by:
Nick Swindale, University of British Columbia, Canada

Reviewed by:
Dong-Hoon Lee, University of Sydney, Australia
Giorgio Innocenti, Karolinska Institutet (KI), Sweden

****Correspondence:***
Philippa J. Johnson
pjj43@cornell.edu

Received: *25 September 2019*
Accepted: *16 January 2020*
Published: *11 February 2020*

Citation:
Johnson PJ, Pascalau R, Luh W-M, Raj A, Cerda-Gonzalez S and Barry EF (2020) Stereotaxic Diffusion Tensor Imaging White Matter Atlas for the in vivo Domestic Feline Brain. Front. Neuroanat. 14:1. doi: 10.3389/fnana.2020.00001

INTRODUCTION

The domestic cat (*Felis catus*) is a useful animal model for neuroanatomical, electrophysiological and neuropathological research (Preuss, 2000; Haller, 2013; Chambers et al., 2015; Kumar et al., 2016). Rapid advancements in functional and structural magnetic resonance imaging (MRI) techniques have enhanced our ability to evaluate the brain and there are many potential applications for these techniques in neuroscientific research where the domestic cat is a commonly used model.

Stereotaxic brain atlases play an important role in advanced neuroimaging research, being widely used for registration, identification and reporting cortical locations in a common coordinate system (Mori et al., 2008). For the cat, a three-dimensional (3D) cortical atlas and tissue probability maps of the brain have recently become available (Stolzberg et al., 2017). This atlas was created by the linear registration of T1-weighted structural MRI data and is a useful tool for normalization and segmentation of feline brain data. However, due to the limited ability for T1-weighted structural imaging data to evaluate the white matter, this atlas provides little information on white matter pathways and sub-regions and in the feline brain (Toga et al., 2006).

Diffusion tensor imaging (DTI) is a technique that is able to detect the characteristics of water diffusion within brain tissue (Alexander et al., 2007). White matter is composed of linear fascicle bundles, within which, water diffuses in a highly anisotropic fashion. DTI has been developed specifically to measure the random Brownian motion of water molecules in the body (Basser and Özarslan, 2014). This method is able to document the diffusivity characteristics of white matter tissue as well as inform on other neurological phenomena such as edema, infarction, and stroke by measuring the displacement of water molecules over time (Moseley et al., 1990; Jones, 2014). By using DTI, it is possible to infer anatomical characteristics of the underlying tissues per voxel (Smith et al., 2004). DTI is able to detect the orientation of this diffusion and by doing so, map the structure of white matter fibers within the brain in a method called tractography (Basser et al., 1994). There are two major forms of tractography; deterministic and probabilistic (Jones, 2008). Deterministic tractography assumes that there is a single dominant diffusion direction and links these dominant directions to create a tract. This technique is commonly used in neuro-navigation systems due to its simplicity and rapid results however it does have limitations in resolving curving, crossing or kissing tracts. Probabilistic tractography uses a complex algorithm to trace several thousand possible pathways from a starting seed region. This produces a highly sensitive probability distribution of connections that can be thresholded to include only the most likely connections (Jones, 2008). Both these forms of tractography have been used to create functional white matter brain maps that are routinely used, in the human, rhesus macaque, rat, mouse, dog and ferret research (Mori et al., 2008; Jiang and Johnson, 2011; Rumple et al., 2013; Zakszewski et al., 2014; Calabrese et al., 2015; Robinson et al., 2016; Hutchinson et al., 2017). Tractography techniques have been used to document the anatomy of feline white matter tracts (Jacqmot et al., 2017) and evaluate the development and regional variation of white matter in the juvenile feline brain (Takahashi et al., 2009; Dai et al., 2016). These articles have provided information on the location and diffusivity characteristics of several pathways; however, these previous articles do not compare *in vivo* tract reconstructions with *ex vivo* gross anatomic dissection. In addition, while previous articles provide a description of several tracks they do not provide open source diffusivity maps or tract-based priors of their atlases.

To enable automated segmentation of the white matter in the cat a white matter atlas and anatomic priors are required. In this study, we develop and make available a white matter brain atlas and structural connectome using DTI MRI data obtained *in vivo* at 3-tesla field strength from eight neurologically normal felines. We performed the tract reconstructions using deterministic tractography and the resulting tractography reconstructions are then compared directly to previously reported white matter gross anatomic dissections based on the Klingler method (Pascalau et al., 2016, 2018). We provide diffusivity maps and create a structural connectome to assess whole-brain connectivity. This comprehensive atlas will provide a valuable resource for scientists doing anatomical, pathological and translational neuroimaging research in the feline model.

MATERIALS AND METHODS

Animals and Anesthesia

This study was approved by Cornell University's Institutional Animal Care and Use Committee. Eight neurologically normal, mature (age at scanning mean = 1.52 years, standard deviation = 1.02 years), mixed-sex (four male and four female), domestic short-haired felines were recruited from research populations. After pre-anesthetic evaluations, each subject underwent intra-venous catheterization, pre-medication with dexmedetomidine (10 mg/kg) and was induced to general anesthesia with Propofol (10–20 mg/kg dosed to effect). All subjects were intubated and maintained under anesthetic with inhalant isoflurane/oxygen and supportive intravenous lactated ringer's solution fluids. All protocols were approved by a board-certified veterinary anesthesiologist (American College of Veterinary Anesthesia).

Image Acquisition

Imaging was performed in a General Electric Discovery MR750 3-Tesla unit (60 cm bore diameter), operating at 50 mT/m amplitude and 200 T/m/s slew-rate. Subjects were placed in dorsal recumbency with their head centered in a 16-channel small flex radio-frequency coil (NeoCoil, Pewaukee, WI, USA). The diffusion-tensor images were acquired using a single-shot echoplanar imaging DTI sequence that was acquired in the axial plane (TR = 7,000 ms, TE = 91.7 ms, flip angle = 90°, resolution = 1.5 mm^3, slice thickness 1.5 mm, matrix size = 96 × 96 × 48, slice number 48, acquisition time 7 min and 42 s) with 60 gradient directions and a single unweighted diffusion image. The *b*-value was set to 800 s/mm^2 within normal ranges for feline diffusion imaging. A high-resolution T1-weighted 3D inversion-recovery fast spoiled gradient echo sequence (Bravo) was performed in each subject with the following parameters; Isotropic voxels 0.5 mm^3, TE = 3.6 ms, TR = 8.4 ms, TI = 450 ms and a flip angle of 12°.

T1-Weighted Image Preprocessing and Population Template Creation

A study-specific T1-weighted template was created to allow for neuroanatomically informed tractography seed mask placement and anatomic referencing. T1-weighted images were corrected

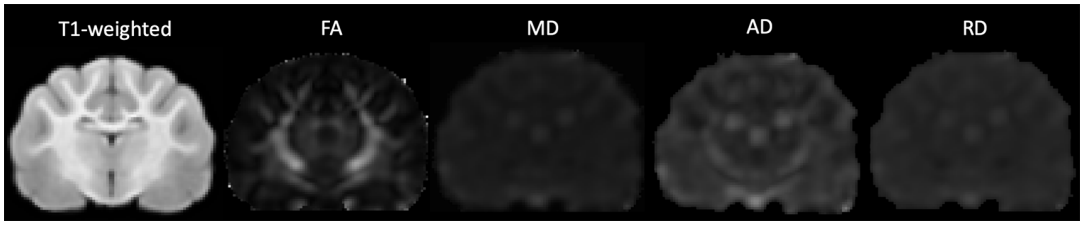

FIGURE 1 | The transverse image at the mid-brain level of the T1-weighted population template and fractional anisotropy (FA), mean diffusivity (MD), axial diffusivity (AD) and radial diffusivity (RD) diffusivity maps.

for low-frequency intensity inhomogeneity (Zhang et al., 2001). Initially, the Brain Extraction Toolbox (Smith, 2002) from the FSL toolbox (Smith et al., 2004; Woolrich et al., 2008; Jenkinson et al., 2012) was used to extract brain tissue from the skull, however since this algorithm is not optimized for canine brain extraction the brain mask was incomplete therefore manual removal of non-brain tissues and inclusion of brain issue was applied prior to the images being affine (linearly) registered using FMRIB's Linear Image Registration Tool (FLIRT; Jenkinson and Smith, 2001; Jenkinson et al., 2002) and spatially normalized which involved registering each individual subject to a population template details of the methodology is described in the following article (Friston et al., 1995). The origin of the images was set to the rostral commissure, then the data were reoriented to a standard FMRI Software Library (FSL) orientation for consistency (Jenkinson et al., 2012). After the creation of the T1 template, it was linearly registered to the diffusion population template using ITK-SNAP (Yushkevich et al., 2006) to provide a high-resolution anatomical reference.

DWI Image Preprocessing

DWI images were corrected for noise using principal component analysis (PCA) to estimate a noise map as described in detail in the following article (Veraart et al., 2016a,b). Corrections for phase distortion (Andersson et al., 2003; Smith et al., 2004), eddy current distortion and motion (Andersson and Sotiropoulos, 2016) were also implemented using the FSL[1] and MRTrix[2] software packages. Initially, a brain mask was estimated from the subject's diffusion data using dwi2mask command as part of the MRTrix toolbox (Tournier et al., 2012) however this masking was sub-optimal for feline subjects. Therefore, manual brain tissue segmentation was additionally applied by an experienced analyst (EFB) to remove non-brain tissue. Brain masks were then viewed and validated by an independent rater (PJJ). Diffusion tensor measures including fractional anisotropy (FA), mean diffusivity (MD), axial diffusivity (AD) and radial diffusivity (RD) were calculated using the FSL FMRIB's Diffusion Toolbox (Behrens et al., 2007). Diffusion tensor maps for each diffusivity parameter were obtained for each participant and visually inspected for quality assurance (**Figure 1**).

[1]https://fsl.fmrib.ox.ac.uk/
[2]https://www.mrtrix.org

DWI Population Template Creation

To create the population DWI template three types of registration were tested to identify the method created the optimal template. Both FLIRT (FMRIB's Linear Image Registration Tool) and non-linear methods (ANTs) were applied to the data. After preprocessing, each subject's data were registered to a common space and anatomically aligned using restricted linear registration FLIRT with 6° of freedom. With the exact alignment of each subject's brain, using the T1 weighted high-resolution data, non-linear registration and template creation using Advanced Normalization Tools (ANTs), was found to be the best method of population template creation (Avants et al., 2011). The resulting DWI template was then used for the deterministic tractography. A population template for fiber orientation distribution (FOD) images was processed and created with MRtrix for the creation of a structural connectome (Tournier et al., 2007).

White Matter Tractography

White matter tract reconstructions were performed using the FACT algorithm (Mori et al., 1999) with a step length of 0.5 mm and angle threshold of 35° in TrackVis (Wang et al., 2007) within a binary brain mask. The ROI seed placement adapted from that described by Catani and Thiebaut de Schotten (2008) and feline tractography descriptions (Dai et al., 2016; Jacqmot et al., 2017). Seed regions were delineated on the FA maps and once tracts were generated obvious spurious tracts were removed. All tracts were reviewed by a white matter anatomy expert (PR) and compared to previously published gross anatomic dissections (Pascalau et al., 2016). A description of each tract reconstruction follows:

Associative Tracts

Superior Longitudinal Fasciculus (SLF)

The superior longitudinal fasciculus (SLF) is an associative tract composed of both short and long fibers that form connections within the perisylvian cortex. It occupies a dorsal and lateral position in the brain. It was reconstructed using a single arcuate ROI placed over the mid and dorsal arcuate gyri, lateral to the Corona Radiata (CR) on the coronal plane image.

Inferior Longitudinal Fasciculus (ILF)

The inferior longitudinal fasciculus (ILF) is a caudoventrally located associative tract that connects the occipital (extrastriate cortex) and temporal (temporal pole, middle and inferior gyri)

lobes. This tract was reconstructed using two ROIs; an occipital ROI was placed over the occipital lobe on the coronal plane and a temporal ROI that spanned the mid-temporal lobe ventral and lateral to the external capsule on the coronal plane.

Uncinate Fasciculus (UF)

This is a small rostroventrally located associative tract that connects the rostral temporal lobe with the orbitofrontal cortex. This tract was reconstructed using a two ROI approach with one ROI placed over the rostral temporal lobe on the coronal plane and the other placed over the frontal white matter on the transverse plane.

Cingulum

A medially located associative tract with variably sized fibers connecting the frontal, parietal, occipital and temporal lobes within the cingulate gyrus. It was reconstructed using a single ROI placed along the length of the linear cingulum, immediately dorsal to the body of Corpus callosum (CC), to ensure both long and short fibers are incorporated.

Commissural Tract

Corpus Callosum (CC)

The CC is an extensive tract that connects homologous cortical areas on the right and left cerebral hemispheres. It was reconstructed using a single ROI method; a CC ROI was placed on the sagittal plane covering the body of CC at the mid-sagittal section.

Projection Tracts

Fornix

This central projection tract connects the mammillary bodies and hippocampus. It was reconstructed using a ROIs placed over the body and crura of the fornix, on the coronal plane, ventral to the CC.

Corona Radiata (CR)

This large projection system has fibers that ascend from the thalamus to the cerebral cortex, occupying the most medial position in the internal capsule. It was reconstructed by placing an ROI on the coronal plane over the internal capsule and applying an exclusion mask to remove fibers that extended the caudal to the thalamus.

Corticospinal Tract (CST)

This white matter pathway extends between the frontoparietal cortex and the spinal cord. It was reconstructed using a two ROI approach, with one placed over the internal capsule and the other further caudally within the ventral brainstem.

Cerebellar Tracts

Cerebellar Thalamocortical Tract (CTCT)

This is the efferent cerebellar tract and extends from the cerebellum, through the superior cerebellar peduncle, red nucleus and thalamus to terminate within the cerebral cortex (Habas and Manto, 2018). This tract was reconstructed by placing a rounded ROI over the superior cerebellar peduncle, at the level of the midbrain, on the coronal plane and a second ROI at the level of the internal capsule (Catani and Thiebaut de Schotten, 2008).

Dorsal Spinal-Cerebellar Tract (DSCT)

This is one of the afferent cerebellar tracts. It extends from the spinal cord through the inferior cerebellar peduncle. It was reconstructed using rounded ROIs placed on the coronal plane over the inferior cerebellar peduncles, lateral to the medulla oblongata and a second ROI placed over the caudal brain stem (Catani and Thiebaut de Schotten, 2008).

Ventral Spinal-Cerebellar Tract (VSCT)

This cerebellar tract extends from the ventral spinal cord into the superior cerebellar peduncle and into the ipsilateral cerebellum. It was reconstructed using a two ROI technique, one placed on the coronal plane over the superior cerebellar peduncle and the other placed on the axial plane over the spinal cord.

Pontocerebellar Tract (PCT)

This cerebellar tract contains efferent and afferent fibers and extends to the pons and further rostrally along the ventrolateral aspect of the mesencephalon (Habas and Manto, 2018). It was reconstructed using rounded ROIs placed on the coronal plane over the middle cerebellar peduncles (Catani and Thiebaut de Schotten, 2008).

Anatomic Prior Diffusivity and Volume

For each white matter tract fiber length (mean and standard deviation obtained from TrackVis software) and tract volumes were documented. In order to document diffusivity values, a white matter skeleton was created from the FA maps by thresholding to remove voxels that extended into gray matter (FA <0.15). This skeleton was applied to the tract masks to constrain these masks to the white matter only. The final tract masks were then applied to the diffusion tensor maps of FA, MD, RD, and AD to calculate the mean and standard deviation of these tensor measures within the tracts using FSL tools (Smith et al., 2004).

Connectome

Diffusion MRI can allow for the construction of a brain connectome on a macroscopic scale to explore the connectivity between regions and inter-regional pathways. A structural brain connectome is a collection of white matter pathways (edges) that connect a set number of regions of interests (nodes; Rubinov and Sporns, 2010). These white matter pathways are based on selecting a number of streamlines connecting two regions (Hagmann et al., 2010). The number of streamlines selected and their trajectory is determined by the choice of tractography algorithm (Tournier et al., 2011). In order to generate a structural connectome the following procedures were implemented. The individual subjects' diffusion and structural data were processed in accordance with methods for the template reconstruction (see above). After preprocessing, global intensity normalization was applied to the diffusion data in order to reduce intensity bias across subjects. The subjects' data were then up-sampled to a resolution of 0.5 mm^3. The global intensity normalization process produced an FA and white matter mask template (thresholded at 0.2). From the

TABLE 1 | Volume (mm^3), fiber length (mean and standard deviation (st dev), fractional anisotropy (FA; mean and st dev), mean diffusivity (MD; mean and st dev), axial diffusivity (AD; mean and st dev) and radial diffusivity (RD; mean and st dev) of each reconstructed tract.

	Volume (mm^3)	Fiber Length (mm)		FA		MD		AD		RD	
		Mean	St Dev	Mean	St Dev	Mean	St Dev	Mean	St Dev	Mean	St Dev
Left SLF	1,165.6	11.8	7.2	0.208	0.053	0.000061	0.00001	0.000074	0.000012	0.000055	0.000009
Right SLF	905.4	11.6	7.2	0.203	0.047	0.000061	0.000008	0.000074	0.000011	0.000055	0.000007
Left ILF	172.0	42.4	21.1	0.315	0.090	0.000062	0.000006	0.000084	0.000009	0.000051	0.000007
Right ILF	175.0	25.4	4.1	0.220	0.060	0.000062	0.000008	0.000077	0.000011	0.000055	0.000008
Left Uncinate	271.5	21.1	5.3	0.203	0.050	0.000072	0.000049	0.000088	0.00006	0.000064	0.000043
Right Uncinate	259.1	17.7	3.1	0.207	0.049	0.00005	0.000008	0.000061	0.00001	0.000044	0.000008
Left Cingulum	469.7	15.7	9.2	0.187	0.034	0.000058	0.000004	0.00007	0.000005	0.000052	0.000004
Right Cingulum	559.7	16.5	11.6	0.201	0.045	0.00006	0.000008	0.000074	0.00001	0.000054	0.000007
CC	2,568.1	30.0	15.1	0.222	0.060	0.000061	0.000007	0.000075	0.000009	0.000053	0.000007
Fornix	574.4	40.4	3.0	0.201	0.043	0.000064	0.000008	0.000079	0.00001	0.000057	0.000008
Left CR	1,110.0	23.8	7.7	0.286	0.091	0.00006	0.000011	0.000079	0.000015	0.000051	0.00001
Right CR	810.2	25.3	7.9	0.278	0.095	0.000059	0.000009	0.000077	0.000012	0.00005	0.000009
Left CST	844.8	47.7	7.7	0.315	0.114	0.000059	0.000019	0.000081	0.000026	0.000048	0.000017
Right CST	1,052.5	49.6	6.2	0.310	0.118	0.000059	0.000013	0.00008	0.000019	0.000048	0.000012
Left DSCT	187.5	13.4	5.1	0.221	0.058	0.000048	0.000014	0.000059	0.000017	0.000042	0.000012
Right DSCT	81.5	11.8	2.7	0.249	0.069	0.000052	0.000013	0.000066	0.000017	0.000045	0.000012
Left CTCT	386.7	47.8	5.5	0.299	0.117	0.000061	0.000011	0.000081	0.000016	0.00005	0.000011
Right CTCT	389.1	47.3	2.8	0.309	0.133	0.000059	0.00001	0.000079	0.000014	0.000048	0.000011
Left PCT	556.1	29.6	4.2	0.253	0.084	0.000068	0.000021	0.000087	0.000025	0.000059	0.000019
Right PCT	429.0	32.8	7.9	0.225	0.058	0.000065	0.00002	0.000082	0.000027	0.000057	0.000019

SLF, superficial longitudinal fasciculus; ILF, inferior longitudinal fasciculus; CC, corpus callosum; CR, corona radiata; CST, corticospinal tract; DSCT, dorsal spinal-cerebellar tract; CTCT, cerebellar thalamocortical tract; PCT, pontocerebellar tract.

normalized diffusion data across subjects a FOD template was created by estimating and averaging the response function of each subject than using constrained spherical deconvolution to create a group FOD template (Tournier et al., 2004). The FOD brain mask was created by registering each subjects' processed diffusion data to the FOD template, saving the registration matrices, then applying these matrices to the subjects' diffusion brain mask to create an averaged brain mask (Raffelt et al., 2011, 2012). This brain mask was visually inspected for any anatomical inaccuracies and was manually corrected to include all brain regions. A twenty million tract whole-brain tractogram was then created from the FOD template using the iFOD2 (Second-order Integration over Fiber Orientation Distributions; Tournier et al., 2010, 2012) which included a maximum angle of 35°, maximum tract length of 250, a minimum tract length of 10, and power of 1. The is weights were created using MRTrix3 spherical-deconvolution informed filtering of tractograms version 2 (SIFT2) by determining appropriate cross-sectional area multiplier for each streamline (Smith et al., 2015). This step allows for a more biologically accurate fiber connectivity measure and is further detailed in Smith et al. (2015). The CATLAS (Stolzberg et al., 2017) was then registered to the FOD template space using ITK-SNAP manual linear registration (Yushkevich et al., 2006). The transformed CATLAS regions were then used as nodes and labels for connectome generation. The structural connectivity matrix was generated using the 2 million track tractogram with SIFT2 track weights and CATLAS regions as nodes. This connectome included 151 regions as per the original CATLAS using the default streamline-parcel assignment mechanisms (Smith et al., 2015). The resulting connection strengths were divided by the sum of the voxels for both the seed and target regions to account for differences in volume between regions (Owen et al., 2013). The whole-brain weighted connectivity matrix was used to calculate connectivity metrics such as degree (the number of in and out links of a node), betweenness centralit (a measure of hub centrality based on the number of shortest paths through a node), strength (the sum of the weights of links connected to the node), and clustering coefficient (the fraction of triangles around each node relating the fraction of nodes neighbors who are also neighbors) generated and visualized using the Brain Connectivity Toolbox (BCT^3) in MATLAB (Rubinov and Sporns, 2010) and MRtrix (Tournier et al., 2012).

RESULTS

White Matter Atlas

Population maps for T1-weighted, FA, MD, AD and RD data are provided (**Figure 1**). Individual tract priors for the association, projection, commissural and cerebellar tracts were generated. The volumes, mean fiber lengths and MD parameters for each tract are provided in **Table 1**. The atlas is made available as an online resource at the following web address: https://ecommons.cornell.edu/handle/1813/58775.2.

Associative Tracts

Superior Longitudinal Fasciculus (SLF)

The SLF had an appropriate lateral position and exhibited fronto-parietotemporal connections (**Figure 2**). It ran in a frontoparietal direction, encircling the external capsule, consistent with that described on gross anatomic dissection (Pascalau et al., 2016). When compared to gross anatomic

[3]http://www.brain-connectivity-toolbox.net

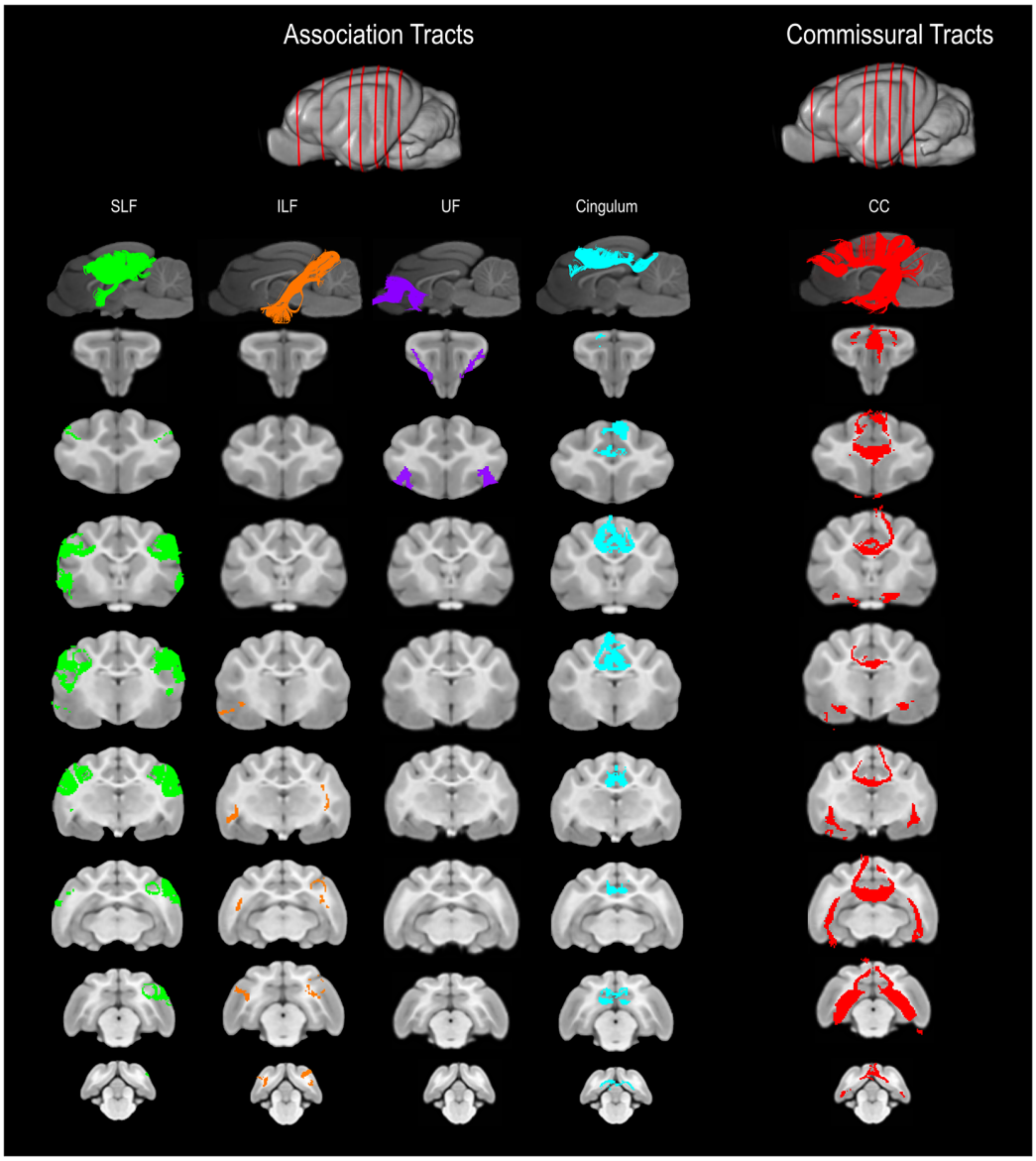

FIGURE 2 | Three-dimensional (3D) and 2-dimensional (2D) visual documentation of the association and commissural tract reconstructions overlaid on T1-weighted structural images in sagittal and transverse planes with slice reference images. SLF, superficial longitudinal fasciculus; ILF, inferior longitudinal fasciculus; UF, uncinate fasciculus; Cingulum and CC, corpus callosum.

dissections the size, location, course and connectivity of the SLF were very similar (**Figures 4A–C**). The right SLF was slightly larger than the left side (1,510.1 mm^3 and 1,165.6 mm^3 respectively), however, the mean tract length was longer on the left side than the right (11.8 mm and 11.4 mm respectively; **Table 1**).

Inferior Longitudinal Fasciculus (ILF)

The ILF extended between the occipital and temporal regions and was located caudal to the SLF (**Figure 2**). It contained long occipito-temporal fibers as well as shorter, more superficial fibers connecting adjacent areas. Its location was similar to that observed in gross anatomic dissections (**Figures 4A–C**). The reconstructed ILF tracts had the smallest volume of all included forebrain tracts and had similar volumes on both right and left sides (175.0 mm^3 and 172.0 mm^3 respectively; **Table 1**).

Uncinate Fasciculus (UF)

The uncinate fasciculus (UF) was observed to extend from the rostrolateral aspect of the temporal lobe to the frontal region (**Figure 2**). It had a similar location (lateral and ventral to the lenticular nucleus) and curvilinear shape to that observed in gross anatomic dissections (**Figures 4A–F**). These paired structures had similar volumes on the right and left sides (259.1 mm^3 and 271.5 mm^3 respectively; **Table 1**).

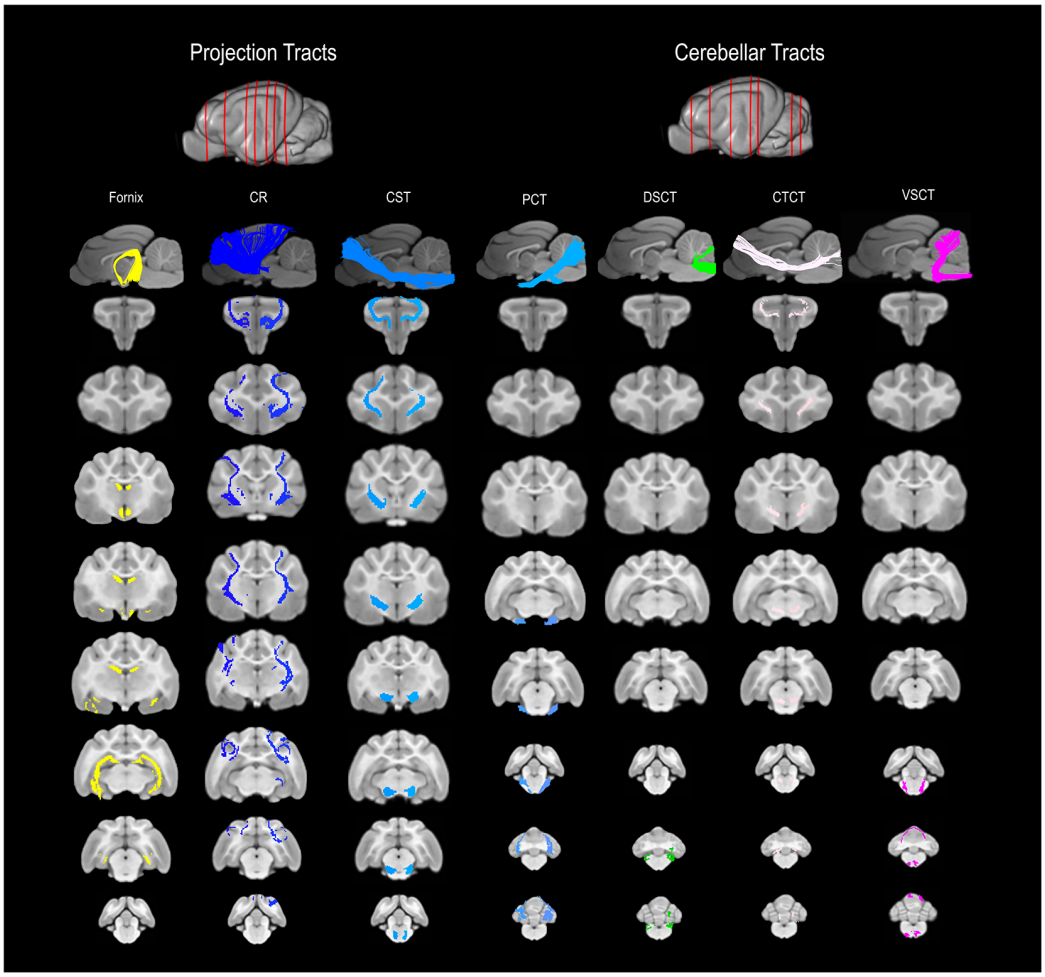

FIGURE 3 | 3D and 2D visual documentation of the projection and cerebellar tract reconstructions overlaid on T1-weighted structural images in sagittal and transverse planes with slice reference images. Project Tracts included Fornix; CR, corona radiate; CST, corticospinal tract. Cerebellar Tracts included PCT, pontocerebellar tract; DSCT, dorsal spinal-cerebellar tract; VSCT, ventral spinal-cerebellar tract and CTCT; cerebellar thalamocortical tract.

Cingulum

The cingulum tracked appropriately along the cingulate gyri and exhibited frontal connectivity consistent with that described in gross anatomic dissections and tractography (Dai et al., 2016; Pascalau et al., 2016; **Figures 2**, **4G–I**). Mean tract length was relatively low [left 15.66 ± 9.2 and right (16.5 ± 11.6)], likely due to the short radiating fibers that extend dorsally from the cingulum (**Table 1**).

Commissural Tract

Corpus Callosum (CC)

The reconstructed CC was the largest tract of the group (2,568.1 mm^3) and demonstrated strong inter-hemispheric connection between occipital, frontal, parietal and temporal lobes (**Figure 2**, **Table 1**). It was well delineated from the adjacent cingulum and fornix (**Figures 4J–L**). Although the majority of the callosal fibers projected dorsally, in a concave fashion, there was a well-represented group of ventrally oriented fibers connecting the temporal lobes which correspond to the tapetum. This structure is similar to that observed in previous tractography descriptions (Dai et al., 2016).

Projection Tracts

Fornix

The fornix formed distinct tracts extending around the thalamus, from the fimbria hippocampi to the subthalamic region (**Figures 3**, **4G–L**). The reconstruction had a volume of 574.4 mm^3 and was composed predominantly of longer fibers (mean fiber length 40.4 ± 3.0 mm; **Table 1**). The fibers are in close relation to the cerebral ventricles in multiple section planes. The structure of the fornix identified is consistent with that dissected anatomically and described with tractography (Dai et al., 2016; Jacqmot et al., 2017; Pascalau et al., 2018).

Corona Radiata (CR)

The CR formed a fan-shaped structure that extended within the internal capsule (**Figure 3**). It exhibited thalamocortical

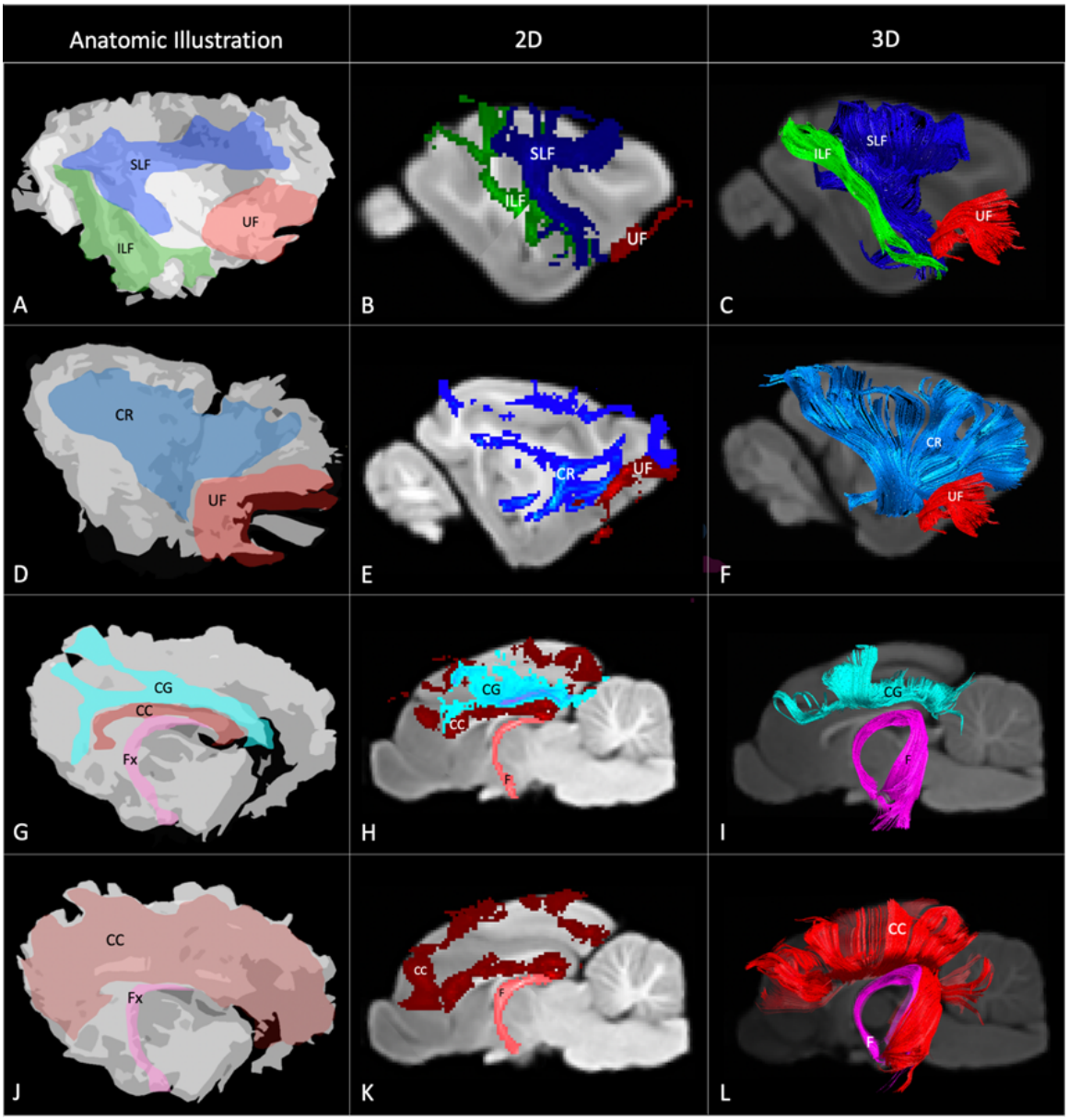

FIGURE 4 | Demonstrates anatomic illustrations (left column) and the 2D and 3D images of the associated white matter tract reconstructions overlaid on sagittal plane T1-weighted images. **(A)** Gross anatomic dissection illustration of the SLF, superficial longitudinal fasciculus; ILF, inferior longitudinal fasciculus; and UF, uncinate fasciculus. **(B)** 2D images of the SLF, ILF and UF overlain on a T1-weighted parasagittal slice. **(C)** 3D images of the SLF, ILF and UF overlain on a T1-weighted para-sagittal slice. **(D)** Gross anatomic dissection illustration of the CR, corona radiata and UF. **(E)** 2D images of the CR and UF overlain on a T1-weighted parasagittal slice. **(F)** 3D images of the CR and UF overlain on a T1-weighted para-sagittal slice. **(G)** Gross anatomic dissection illustration of the CG, cingulum; CC, corpus callosum and f, fornix. **(H)** 2D images of the CG, CC and F overlain on a T1-weighted mid-sagittal slice. **(I)** 3D images of the CG and F overlain on a T1-weighted mid-sagittal slice. **(J)** Gross anatomic dissection illustration of the CC and F. **(K)** 2D images of the CC and F overlain on a T1-weighted mid-sagittal slice. **(L)** 3D images of the CC and F overlain on a T1-weighted mid-sagittal slice. Illustrations created from previously published gross anatomic white matter dissections with author consent (Pascalau et al., 2016).

connectivity and extended to connect with the frontal, parietal and occipital regions (the later connections have a characteristic rostrocaudal direction and are known as the optic radiations (Pascalau et al., 2018; **Figures 4D–F**). The left CR was larger than the right side (1110.0 mm^3 vs. 810.2 mm^3 respectively; **Table 1**).

Corticospinal Tract (CST)

The corticospinal tract (CST) extended from the frontoparietal region and had an oblique path, passing through the cerebral peduncle (the ventral part of the midbrain) forming connectivity with the anterior horn of the spinal gray matter (**Figure 3**). These reconstructions had the longest fiber lengths of all

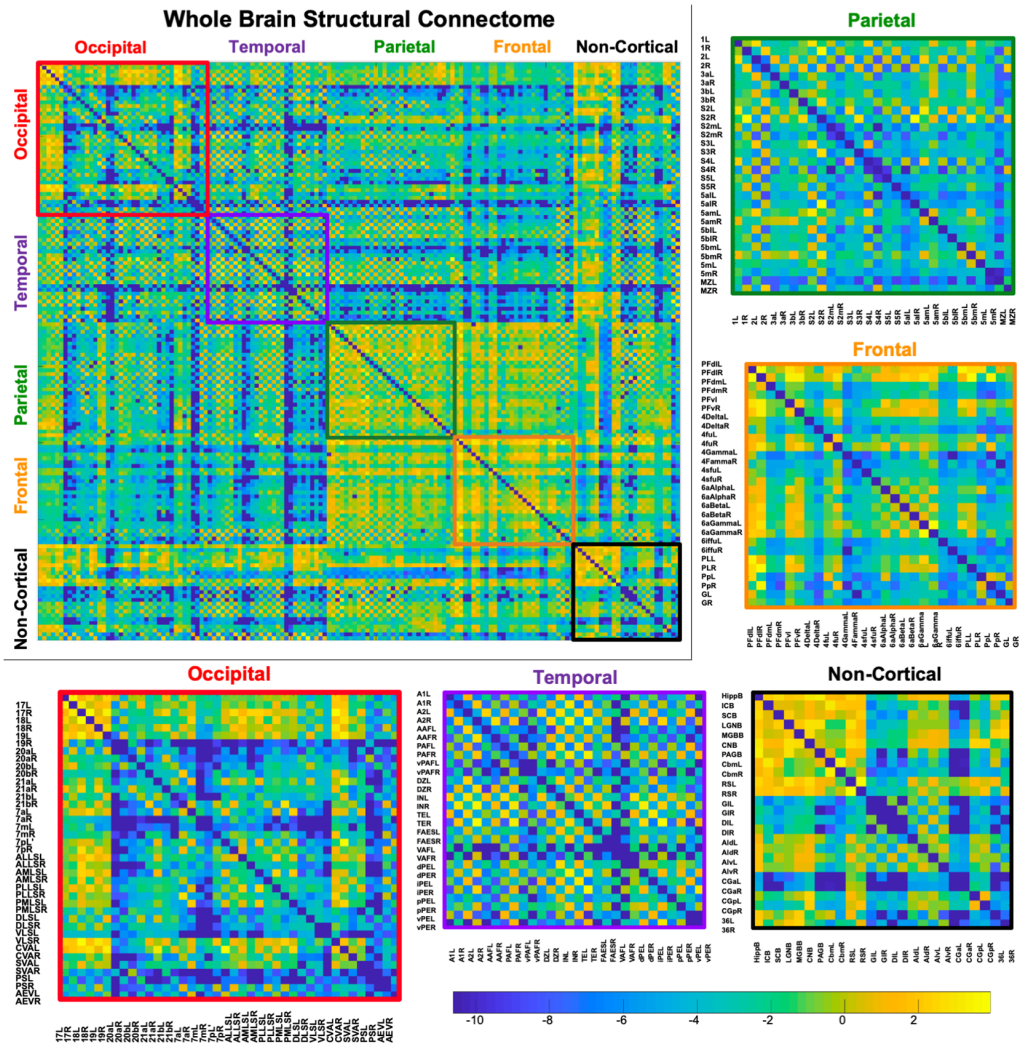

FIGURE 5 | Demonstrates a weighted undirected structural connectome adjusted for voxel size on a log scale. The connectome has been color-coded according to lobe origin (red = occipital, purple = temporal, green = parietal, orange = frontal, and black = non-cortical). The individual lobar matrices have been enlarged and node names are listed on the x and y axes.

dissected pathways (right; mean 49.6 ± 6.2 mm and left; mean 47.7 ± 7.7 mm; **Table 1**). The structure of the CST is similar to that observed in other tractography descriptions (Dai et al., 2016; Jacqmot et al., 2017).

Cerebellar Tracts

Cerebellar Thalamocortical Tract (CTCT)

The CTCT exhibited frontoparietal connectivity and ran medially to the CST until the midbrain where it took a separate route to the cerebellum, passing through the superior cerebellar peduncle (**Figure 3**). Similar to the CSTs the CTCT reconstructions had high mean fiber lengths (left; 47.8 ± 5.5 mm and right; 47.3 ± 2.8 mm; **Table 1**).

Dorsal Spinal-Cerebellar Tract (DSCT)

The DSCT was the smallest of all cerebellar tract reconstructions (right 187.5 mm^3 and left 81.5 mm^3) due to truncation as the field of view ends (**Figure 3**, **Table 1**). It runs through the inferior cerebellar peduncles and occupies a dorsal position in the medulla oblongata and the spinal cord.

Ventral Spinal-Cerebellar Tract (VSCT)

The VSCT was identified extending out of the superior cerebellar peduncle before extending down the ventral aspect of the medulla oblongata and spinal cord (**Figure 3**).

Pontocerebellar Tract (PCT)

This was the largest cerebellar reconstruction and the left side was mildly larger than the right (left; 556.1 mm^3, and right; 429.0 mm^3; **Figure 3**, **Table 1**). It was the most laterally located cerebellar tract, emerging from the pons and spreading in the entire white matter domain of the cerebellar hemispheres.

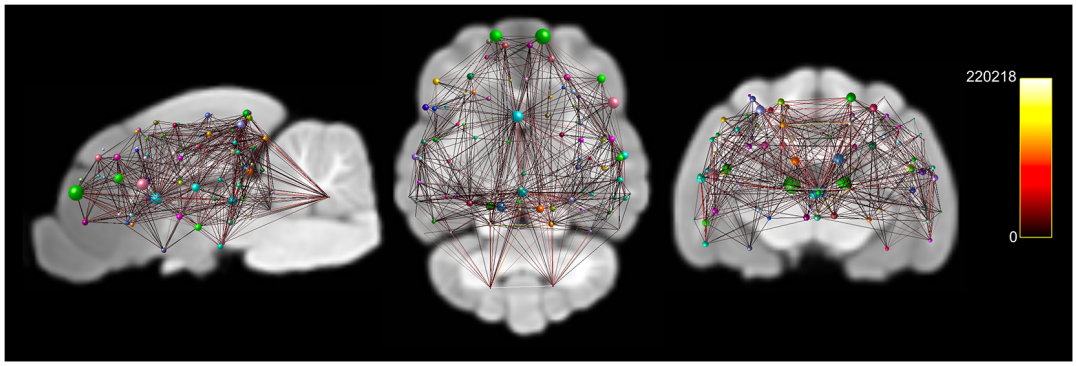

FIGURE 6 | Documents node based weighted connectivity maps overlain on the population average T1-weighted structural image in sagittal, coronal and transverse planes. Node size corresponds to the connectivity strength (sum of weights of links connected to the node) of a particular node. Edge visualization was thresholded at 3,500 for visualization purposes. The connectome weight of each edge is colored by a heatmap with a minimum of 0 and maximum of 220,218 from the weighted connectome.

Connectome

A whole-brain weighted undirected connectivity matrix that was adjusted for volume and node-based connectome maps are provided in **Figures 5**, **6**. A reference table containing connectivity metrics for each cortical region is also provided in the **Supplementary Table S1**. This includes the region number, label and lobar parcellation and their corresponding betweenness centrality, degree of connectivity, clustering coefficient and strength.

DISCUSSION

In this article, we document the creation of a stereotaxic white matter atlas using DTI data from a group of healthy mesaticephalic cats. We provide downloadable FA, RD, AD, MD and T1-weighted brain maps and priors for projection, association, commissural and cerebellar associated white matter tracts and create a structural connectome with connectivity metrics.

Despite the cat being a widespread preclinical animal model in neuroscientific research, this species lacks the open-source stereotaxic MRI-based brain atlases available in other species (Mori et al., 2008; Jiang and Johnson, 2011; Rumple et al., 2013; Zakszewski et al., 2014; Robinson et al., 2016). The only open-source stereotaxic feline MRI atlas currently available is created with structural T1-weighted MRI data and focuses on cortical and deep gray-matter structures (Stolzberg et al., 2017). Our atlas provides a stereotaxic DWI-based atlas of the white matter in the feline brain. It complements the aforementioned feline T1 atlas and can be applied for anatomic registration and segmentation of the white matter to aid in lesion localization or standardized regional analysis of specific parts of the brain.

Up until now, a manual region of interest analysis has been exclusively used for the segmentation and evaluation of DWI data in feline studies (Zhao et al., 2006; Mizoguchi et al., 2017). This technique, however, has several drawbacks as it is time-consuming, prone to hypothesis-driven bias, and is poorly reproducible (Lilja et al., 2016; Peterson et al., 2016). Our atlas provides the tools required for registration and parcellation of the white matter into tract-based regions, for a more standardized, rapid and reproducible evaluation of the data.

Previous diffusion-based stereotaxic white-matter atlases have utilized multiple methods for segmentation. Within the white-matter, both location-based manual segmentations and connection-based tractography methods have been used to define anatomic regions and white-matter tracts (Mori et al., 2009; Hutchinson et al., 2017). Location-based atlases are created using manual segmentation of color FA maps with the guidance of histology-based atlases for anatomic reference to help delineate regions representing deep white matter locations (Mori et al., 2008, 2009). For our atlas we wanted to create segmentations that represented structural connections within the brain, applying insight from histology work and diffusion atlases from other species (Catani and Thiebaut de Schotten, 2008; Pascalau et al., 2016). Therefore we elected to use deterministic tractography to create a white matter atlas based on feline neuroanatomy and connectivity. Tractography provides a method that utilizes tissue diffusion characteristics to identify tract location and boundaries. This connection-based method of segmentation delineates tract margins, without the limitations of manual segmentation, and has been shown to accurately reflect the macroscopic anatomy of the major white matter pathways (Mori et al., 2009). To ensure anatomic accuracy of our reconstructions, where possible, we compared directly to gross anatomic dissection of the feline brain performed by the Klingler method, a tridimensional dissection technique which is complementary to tractography and has been used for validation of tractographic reconstructions mostly in human brain studies (Pascalau et al., 2016, 2018). This direct anatomic comparison was not found in other feline tractography papers (Dai et al., 2016; Jacqmot et al., 2017).

Our stereotaxic white matter atlas contains the major white matter pathways of the feline brain. Tract reconstructions were made using previously published tractography descriptions

(Catani and Thiebaut de Schotten, 2008; Dai et al., 2016; Jacqmot et al., 2017). The resulting tractography reconstructions were reviewed for anatomic accuracy by a white matter anatomist (RP) and compared to gross anatomic white matter dissections. The inferior fronto-occipital fasciculus is not included in the atlas, as it was not identified even with liberal seed regions placed over the entire frontal and occipital regions. This fasciculus has been previously reconstructed in the feline using tractography (Jacqmot et al., 2017; Das and Takahashi, 2018). Although neuroanatomical connectivity analysis of the cat has shown both efferent and afferent connection between frontal and occipital regions (Scannell et al., 1995), the presence of a fronto-occipital fasciculus has not been identified on gross anatomic dissection (Pascalau et al., 2016). Histopathologic evaluation of the feline brain is required to confirm the presence or absence of this fasciculus in this species.

The diffusivity parameters we documented for each reconstructed tract prior are included in **Table 1**. Mean FA values have been documented for the developing feline brain and trended higher than our values (Dai et al., 2016). This may be due to the effect of subject age, differing acquisition technique, or be the consequence of taking averages from a population map rather than from individual subjects.

The structural connectome that was documented in this study provides an overview of the structural connectivity between cortical regions in the feline. Extensive neuroanatomic cortical-cortical connectivity analysis has been previously performed in the feline using electrophysiological methods (Scannell et al., 1995). These analyses identified that the sensory regions of the brain were connectionally isolated with stronger intra-lobar connectivity when compared to the connection between regions. This was thought to be either due to deletion of connections between lobes in the developing feline or be a consequence of experimental bias, where more work had been performed within sensory regions than between regions (Scannell et al., 1995). Our structural connectome did not identify stronger connectivity within sensory regions. These inconsistencies could potentially suggest that the previously identified sensory isolation may have been a consequence experimental bias however differences in experimental method, node parcellation, connectivity model or the difference in population sample size may account for the lack of coherence between studies. Further research into the structural and functional feline connectome using various methods such as DWI MRI and resting-state functional MRI with larger sample sizes is necessary.

A limitation of our atlas was that our DTI data only had a spatial resolution of 1.5 mm^3. The feline brain is significantly smaller than the human brain and therefore requires a higher spatial resolution data set to resolve the small structures in the brain. To account for this the DTI parameters were optimized to create the highest spatial resolution possible with our 3-Tesla system within an acceptable time frame and level of noise. Isotropic voxels of 1.5 mm^3 were an archivable compromise at 3-Tesla with 60 diffusion directions. While the DWI population template was upsampled to 0.5 mm^3 using advanced processing methods for structural connectome creation, these techniques use a significant amount of interpolation potentially biasing the data with artificial inflation. Higher-resolution DTI imaging has been achieved at higher field strengths or at the compromise of the number of diffusion directions (Zakszewski et al., 2014; Robinson et al., 2016; Hutchinson et al., 2017). In order to ensure that the lower resolution did not compromise the resulting tractography reconstructions, we validated our results by comparing our tract reconstructions to gross anatomic white matter dissections.

We provide a stereotaxic white matter atlas created from DTI and T1-weighted structural data. We created population maps for T1, FA, MD, RD and AD and white tract priors for the major white matter projections within the feline brain We documented the mean volume, fiber length and diffusivity parameters for each white matter prior and created a structural connectome. This atlas is available from the following online resource center: https://ecommons.cornell.edu/handle/1813/58775.2. It has potential applications of researchers using cats in neuroscientific research and for veterinarians undertaking research in clinical feline populations with spontaneous neurological disease.

DATA AVAILABILITY STATEMENT

The white matter atlas including white matter anatomic priors (Nifti and trk format), T1-weighted population template, and diffusivity maps for FA, MD, RD, and AD are available at the following online resource center: https://ecommons.cornell.edu/handle/1813/58775.2.

ETHICS STATEMENT

The animal study was reviewed and approved by Cornell University Institutional Animal Care and Use Committee.

AUTHOR CONTRIBUTIONS

The following parts of the study were performed by: PJ, SC-G and AR: study design. PJ, SC-G and W-ML: data acquisition. EB: data processing. PJ and EB: tractography dissections. RP: dissection anatomic validation. PJ: manuscript preparation. PJ, RP, W-ML, AR, SC-G and EB: manuscript review.

FUNDING

This work was supported by the Cornell Feline Health Center, Ithaca, NY, USA.

ACKNOWLEDGMENTS

We would like to acknowledge the financial support provided by the Cornell Feline Health Center.

SUPPLEMENTARY MATERIAL

The Supplementary Material for this article can be found online at: https://www.frontiersin.org/articles/10.3389/fnana.2020.00001/full#supplementary-material.

REFERENCES

Alexander, A. L., Lee, J. E., Lazar, M., and Field, A. S. (2007). Diffusion tensor imaging of the brain. *Neurotherapeutics* 4, 316–329. doi: 10.1016/j.nurt.2007.05.011

Andersson, J. L. R., Skare, S., and Ashburner, J. (2003). How to correct susceptibility distortions in spin-echo echo-planar images: application to diffusion tensor imaging. *NeuroImage* 20, 870–888. doi: 10.1016/s1053-8119(03)00336-7

Andersson, J. L. R., and Sotiropoulos, S. N. (2016). An integrated approach to correction for off-resonance effects and subject movement in diffusion MR imaging. *NeuroImage* 125, 1063–1078. doi: 10.1016/j.neuroimage.2015.10.019

Avants, B. B., Tustison, N. J., Song, G., Cook, P. A., Klein, A., and Gee, J. C. (2011). A reproducible evaluation of ANTs similarity metric performance in brain image registration. *NeuroImage* 54, 2033–2044. doi: 10.1016/j.neuroimage.2010.09.025

Basser, P. J., Mattiello, J., and LeBihan, D. (1994). Estimation of the effective self-diffusion tensor from the NMR spin echo. *J. Magn. Reson. B* 103, 247–254. doi: 10.1006/jmrb.1994.1037

Basser, P. J., and Özarslan, E. (2014). "Introduction to diffusion MR," in *Diffusion MRI*, eds Heidi Johansen-Berg and Timothy E.J. Behrens, 2nd Edn. (Cambridge, MA: Elsevier), 3–9.

Behrens, T. E. J., Berg, H. J., Jbabdi, S., Rushworth, M. F. S., and Woolrich, M. W. (2007). Probabilistic diffusion tractography with multiple fibre orientations: what can we gain? *NeuroImage* 34, 144–155. doi: 10.1016/j.neuroimage.2006.09.018

Calabrese, E., Badea, A., Coe, C. L., Lubach, G. R., Shi, Y., Styner, M. A., et al. (2015). A diffusion tensor MRI atlas of the postmortem rhesus macaque brain. *NeuroImage* 117, 408–416. doi: 10.1016/j.neuroimage.2015.05.072

Catani, M., and Thiebaut de Schotten, M. (2008). A diffusion tensor imaging tractography atlas for virtual *in vivo* dissections. *Cortex* 44, 1105–1132. doi: 10.1016/j.cortex.2008.05.004

Chambers, J. K., Tokuda, T., Uchida, K., Ishii, R., Tatebe, H., Takahashi, E., et al. (2015). The domestic cat as a natural animal model of Alzheimer's disease. *Acta Neuropathol. Commun.* 3:78. doi: 10.1186/s40478-015-0258-3

Dai, G., Das, A., Hayashi, E., Chen, Q., and Takahashi, E. (2016). Regional variation of white matter development in the cat brain revealed by *ex vivo* diffusion MR tractography. *Int. J. Dev. Neurosci.* 54, 32–38. doi: 10.1016/j.ijdevneu.2016.08.004

Das, A., and Takahashi, E. (2018). Characterization of white matter tracts by diffusion MR tractography in cat and ferret that have similar gyral patterns. *Cereb. Cortex* 28, 1338–1347. doi: 10.1093/cercor/bhx048

Friston, K. J., Ashburner, J., Frith, C. D., Poline, J.-B., Heather, J. D., and Frackowiak, R. S. J. (1995). Spatial registration and normalization of images. *Hum. Brain Mapp.* 3, 165–189. doi: 10.1002/hbm.460030303

Habas, C., and Manto, M. (2018). Probing the neuroanatomy of the cerebellum using tractography. *Handb. Clin. Neurol.* 154, 235–249. doi: 10.1016/B978-0-444-63956-1.00014-X

Hagmann, P., Cammoun, L., Gigandet, X., Gerhard, S., Grant, P. E., Wedeen, V., et al. (2010). MR connectomics: principles and challenges. *J. Neurosci. Methods* 194, 34–45. doi: 10.1016/j.jneumeth.2010.01.014

Haller, J. (2013). The neurobiology of abnormal manifestations of aggression—a review of hypothalamic mechanisms in cats, rodents, and humans. *Brain Res. Bull.* 93, 97–109. doi: 10.1016/j.brainresbull.2012.10.003

Hutchinson, E. B., Schwerin, S. C., Radomski, K. L., Sadeghi, N., Jenkins, J., Komlosh, M. E., et al. (2017). Population based MRI and DTI templates of the adult ferret brain and tools for voxelwise analysis. *NeuroImage* 152, 575–589. doi: 10.1016/j.neuroimage.2017.03.009

Jacqmot, O., Van Thielen, B., Michotte, A., Willekens, I., Verhelle, F., Goossens, P., et al. (2017). Comparison of several white matter tracts in feline and canine brain by using magnetic resonance diffusion tensor imaging. *Anat. Rec.* 300, 1270–1289. doi: 10.1002/ar.23579

Jenkinson, M., Bannister, P., Brady, M., and Smith, S. (2002). Improved optimization for the robust and accurate linear registration and motion correction of brain images. *NeuroImage* 17, 825–841. doi: 10.1006/nimg.2002.1132

Jenkinson, M., Beckmann, C. F., Behrens, T. E. J., Woolrich, M. W., and Smith, S. M. (2012). FSL. *NeuroImage* 62, 782–790. doi: 10.1016/j.neuroimage.2011.09.015

Jenkinson, M., and Smith, S. (2001). A global optimisation method for robust affine registration of brain images. *Med. Image Anal.* 5, 143–156. doi: 10.1016/s1361-8415(01)00036-6

Jiang, Y., and Johnson, G. A. (2011). Microscopic diffusion tensor atlas of the mouse brain. *NeuroImage* 56, 1235–1243. doi: 10.1016/j.neuroimage.2011.03.031

Jones, D. K. (2008). Studying connections in the living human brain with diffusion MRI. *Cortex* 44, 936–952. doi: 10.1016/j.cortex.2008.05.002

Jones, D. K. (2014). "Gaussian modeling of the diffusion signal," in *Diffusion MRI*, eds Heidi Johansen-Berg and Timothy E.J. Behrens (Cambridge, MA: Elsevier), 87–104.

Kumar, M., Duda, J. T., Yoon, S. Y., Bagel, J., O'Donnell, P., Vite, C., et al. (2016). Diffusion tensor imaging for assessing brain gray and white matter abnormalities in a feline model of α-mannosidosis. *J. Neuropathol. Exp. Neurol.* 75, 35–43. doi: 10.1093/jnen/nlv007

Lilja, Y., Gustafsson, O., Ljungberg, M., Nilsson, D., and Starck, G. (2016). Impact of region-of-interest method on quantitative analysis of DTI data in the optic tracts. *BMC Med. Imaging* 16:42. doi: 10.1186/s12880-016-0145-9

Mizoguchi, S., Hasegawa, D., Hamamoto, Y., Yu, Y., Kuwabara, T., Fujiwara-igarashi, A., et al. (2017). Interictal diffusion and perfusion magnetic resonance imaging features of cats with familial spontaneous epilepsy. *Am. J. Vet. Res.* 78, 305–310. doi: 10.2460/ajvr.78.3.305

Mori, S., Crain, B. J., Chacko, V. P., and van Zijl, P. C. (1999). Three-dimensional tracking of axonal projections in the brain by magnetic resonance imaging. *Ann. Neurol.* 45, 265–269. doi: 10.1002/1531-8249(199902)45:2<265::aid-ana21>3.0.co;2-3

Mori, S., Oishi, K., and Faria, A. V. (2009). White matter atlases based on diffusion tensor imaging. *Curr. Opin. Neurol.* 22, 362–369. doi: 10.1097/WCO.0b013e32832d954b

Mori, S., Oishi, K., Jiang, H., Jiang, L., Li, X., Akhter, K., et al. (2008). Stereotaxic white matter atlas based on diffusion tensor imaging in an ICBM template. *NeuroImage* 40, 570–582. doi: 10.1016/j.neuroimage.2007.12.035

Moseley, M. E., Cohen, Y., Kucharczyk, J., Mintorovitch, J., Asgari, H. S., Wendland, M. F., et al. (1990). Diffusion-weighted MR imaging of anisotropic water diffusion in cat central nervous system. *Radiology* 176, 439–445. doi: 10.1148/radiology.176.2.2367658

Owen, J. P., Ziv, E., Bukshpun, P., Pojman, N., Wakahiro, M., Berman, J. I., et al. (2013). Test-retest reliability of computational network measurements derived from the structural connectome of the human brain. *Brain Connect.* 3, 160–176. doi: 10.1089/brain.2012.0121

Pascalau, R., Aldea, C. C., Padurean, V. A., and Szabo, B. (2016). Comparative study of the major white matter tracts anatomy in equine, feline and canine brains by use of the fibre dissection technique. *Anat. Histol. Embryol.* 45, 373–385. doi: 10.1111/ahe.12208

Pascalau, R., Popa Stanila, R., Sfrângeu, S., and Szabo, B. (2018). Anatomy of the limbic white matter tracts as revealed by fiber dissection and tractography. *World Neurosurg.* 113, e672–e689. doi: 10.1016/j.wneu.2018.02.121

Peterson, D. E., Chen, S. D., Calabrese, E., White, L. E., and Provenzale, J. M. (2016). Automated segmentation of the canine corpus callosum for the measurement of diffusion tensor imaging. *Neuroradiol. J.* 29, 4–12. doi: 10.1177/1971400915610924

Preuss, T. M. (2000). Taking the measure of diversity: comparative alternatives to the model-animal paradigm in cortical neuroscience. *Brain Behav. Evol.* 55, 287–299. doi: 10.1159/000006664

Raffelt, D., Tournier, J.-D., Crozier, S., Connelly, A., and Salvado, O. (2012). Reorientation of fiber orientation distributions using apodized point spread functions. *Magn. Reson. Med.* 67, 844–855. doi: 10.1002/mrm.23058

Raffelt, D., Tournier, J.-D., Fripp, J., Crozier, S., Connelly, A., and Salvado, O. (2011). Symmetric diffeomorphic registration of fibre orientation distributions. *NeuroImage* 56, 1171–1180. doi: 10.1016/j.neuroimage.2011.02.014

Robinson, J. L., Baxi, M., Katz, J. S., Waggoner, P., Beyers, R., Morrison, E., et al. (2016). Characterization of structural connectivity of the default mode network in dogs using diffusion tensor imaging. *Sci. Rep.* 6:36851. doi: 10.1038/srep36851

Rubinov, M., and Sporns, O. (2010). Complex network measures of brain connectivity: uses and interpretations. *NeuroImage* 52, 1059–1069. doi: 10.1016/j.neuroimage.2009.10.003

Rumple, A., McMurray, M., Johns, J., Lauder, J., Makam, P., Radcliffe, M., et al. (2013). 3-dimensional diffusion tensor imaging (DTI) atlas of the rat brain. *PLoS One* 8:e67334. doi: 10.1371/journal.pone.0067334

Scannell, J. W., Blakemore, C., and Young, M. P. (1995). Analysis of connectivity in the cat cerebral cortex. *J. Neurosci.* 15, 1463–1483. doi: 10.1523/JNEUROSCI.15-02-01463.1995

Smith, S. M. (2002). Fast robust automated brain extraction. *Hum. Brain Mapp.* 17, 143–155. doi: 10.1002/hbm.10062

Smith, S. M., Jenkinson, M., Woolrich, M. W., Beckmann, C. F., Behrens, T. E. J., Johansen-Berg, H., et al. (2004). Advances in functional and structural MR image analysis and implementation as FSL. *NeuroImage* 23, S208–S219. doi: 10.1016/j.neuroimage.2004.07.051

Smith, R. E., Tournier, J.-D., Calamante, F., and Connelly, A. (2015). The effects of SIFT on the reproducibility and biological accuracy of the structural connectome. *NeuroImage* 104, 253–265. doi: 10.1016/j.neuroimage.2014.10.004

Stolzberg, D., Wong, C., Butler, B. E., and Lomber, S. G. (2017). Catlas: an magnetic resonance imaging-based three-dimensional cortical atlas and tissue probability maps for the domestic cat (*Felis catus*). *J. Comp. Neurol.* 525, 3190–3206. doi: 10.1002/cne.24271

Takahashi, E., Dai, G., Wang, R., Ohki, K., Rosen, G. D., Galaburda, A. M., et al. (2009). Development of cerebral fiber pathways in cats revealed by diffusion spectrum imaging. *NeuroImage* 49, 1231–1240. doi: 10.1016/j.neuroimage.2009.09.002

Toga, A. W., Thompson, P. M., Mori, S., Amunts, K., and Zilles, K. (2006). Towards multimodal atlases of the human brain. *Nat. Rev. Neurosci.* 7, 952–966. doi: 10.1038/nrn2012

Tournier, J.-D., Calamante, F., and Connelly, A. (2007). Robust determination of the fibre orientation distribution in diffusion MRI: non-negativity constrained super-resolved spherical deconvolution. *NeuroImage* 35, 1459–1472. doi: 10.1016/j.neuroimage.2007.02.016

Tournier, J.-D., Calamante, F., and Connelly, A. (2010). Improved probabilistic streamlines tractography by 2nd order integration over fibre orientation distributions. *Proc. Intl. Soc. Magn. Reson. Med.* 18:1670.

Tournier, J.-D., Calamante, F., and Connelly, A. (2012). MRtrix: diffusion tractography in crossing fiber regions. *Int. J. Imaging Syst. Technol.* 22, 53–66. doi: 10.1002/ima.22005

Tournier, J.-D., Calamante, F., Gadian, D. G., and Connelly, A. (2004). Direct estimation of the fiber orientation density function from diffusion-weighted MRI data using spherical deconvolution. *NeuroImage* 23, 1176–1185. doi: 10.1016/j.neuroimage.2004.07.037

Tournier, J.-D., Mori, S., and Leemans, A. (2011). Diffusion tensor imaging and beyond. *Magn. Reson. Med.* 65, 1532–1556. doi: 10.1002/mrm.22924

Veraart, J., Fieremans, E., and Novikov, D. S. (2016a). Diffusion MRI noise mapping using random matrix theory. *Magn. Reson. Med.* 76, 1582–1593. doi: 10.1002/mrm.26059

Veraart, J., Novikov, D. S., Christiaens, D., Ades-Aron, B., Sijbers, J., and Fieremans, E. (2016b). Denoising of diffusion MRI using random matrix theory. *NeuroImage* 142, 394–406. doi: 10.1016/j.neuroimage.2016.08.016

Wang, R., Benner, T., Sorensen, A. G., and Wedeen, V. J. (2007). Diffusion toolkit: a software package for diffusion imaging data processing and tractography. *Proc. Intl. Soc. Magn. Reson. Med.* 15:3720.

Woolrich, M. W., Jbabdi, S., Patenaude, B., Chappell, M., Makni, S., Behrens, T., et al. (2008). Bayesian analysis of neuroimaging data in FSL. *NeuroImage* 45, S173–S186. doi: 10.1016/j.neuroimage.2008.10.055

Yushkevich, P. A., Piven, J., Hazlett, H. C., Smith, R. G., Ho, S., Gee, J. C., et al. (2006). User-guided 3D active contour segmentation of anatomical structures: significantly improved efficiency and reliability. *NeuroImage* 31, 1116–1128. doi: 10.1016/j.neuroimage.2006.01.015

Zakszewski, E., Adluru, N., Tromp do, P. M., Kalin, N., and Alexander, A. L. (2014). A diffusion-tensor-based white matter atlas for rhesus macaques. *PLoS One* 9:e107398. doi: 10.1371/journal.pone.0107398

Zhang, Y., Brady, M., and Smith, S. (2001). Segmentation of brain MR images through a hidden Markov random field model and the expectation-maximization algorithm. *IEEE Trans. Med. Imaging* 20, 45–57. doi: 10.1109/42.906424

Zhao, F. Y., Kuroiwa, T., Miyasakai, N., Tanabe, F., Nagaoka, T., Akimoto, H., et al. (2006). Diffusion tensor feature in vasogenic brain edema in cats. *Acta Neurochir. Suppl.* 96, 168–170. doi: 10.1007/3-211-30714-1_37

Conflict of Interest: The authors declare that the research was conducted in the absence of any commercial or financial relationships that could be construed as a potential conflict of interest.

frontiers in Systems Neuroscience

REVIEW
published: 03 March 2020
doi: 10.3389/fnsys.2020.00010

Origins of Functional Organization in the Visual Cortex

Michael Ibbotson[1,2]* *and Young Jun Jung*[1,2]*

[1] Australian College of Optometry, National Vision Research Institute, Carlton, VIC, Australia, [2] Department of Optometry and Vision Science, The University of Melbourne, Parkville, VIC, Australia

How are the complex maps for orientation selectivity (OS) created in the primary visual cortex (V1)? Rodents and rabbits have a random distribution of OS preferences across V1 while in cats, ferrets, and all primates cells with similar OS preferences cluster together into relatively wide cortical columns. Given other clear similarities in the organization of the visual pathways, why is it that maps coding OS preferences are so radically different? Prominent models have been created of cortical OS mapping that incorporate Hebbian plasticity, intracortical interactions, and the properties of growing axons. However, these models suggest that the maps arise primarily through intracortical interactions. Here we focus on several other features of the visual system and brain that may influence V1 structure. These are: eye divergence, the total number of cells in V1, the thalamocortical networks, the topography of the retina and phylogeny. We outline the evidence for and against these factors contributing to map formation. One promising theory is that the central-to-peripheral ratio (CP ratio) of retinal cell density can be used to predict whether or not a species has pinwheel maps. Animals with high CP ratios (>7) have orientation columns while those with low CP ratios (<4) have random OS maps. The CP ratio is related to the total number of cells in cortex, which also appears to be a reasonable contributing factor. However, while these factors correlate with map structure to some extent, there is a gray area where certain species do not fit elegantly into the theory. A problem with the existing literature is that OS maps have been investigated in only a small number of mammals, from a small fraction of the mammalian phylogenetic tree. We suggest four species (agouti, fruit bat, sheep, and wallaby) that have a range of interesting characteristics, which sit at intermediate locations between primates and rodents, that make them good targets for filling in the missing gaps in the literature. We make predictions about the map structures of these species based on the organization of their brains and visual systems and, in doing so, set possible paths for future research.

Keywords: primary visual cortex (V1), orientation selectivity, cortical maps, retinotopy, phylogeny, visual system

OPEN ACCESS

Edited by:
Geoffrey Goodhill,
The University of Queensland,
Australia

Reviewed by:
Gregor Rainer,
Université de Fribourg, Switzerland
Robert Shapley,
New York University, United States
Nick Swindale,
The University of British Columbia,
Canada

***Correspondence:**
Michael Ibbotson
mibbotson@nvri.org.au
Young Jun Jung
jungy@student.unimelb.edu.au

Received: *10 October 2019*
Accepted: *04 February 2020*
Published: *03 March 2020*

Citation:
Ibbotson M and Jung YJ (2020) Origins of Functional Organization in the Visual Cortex. Front. Syst. Neurosci. 14:10. doi: 10.3389/fnsys.2020.00010

INTRODUCTION

The cerebral cortex is common to all mammals. While different regions of the cerebral cortex specialize in processing disparate signals, e.g. sensory coding, motor output, decision making, it is striking that the fundamental structure of the cortex is conserved across these regions. Anatomically, almost all regions of the mammalian cortex are composed of six distinct neuronal layers with a common set of neuronal circuit elements (Briggs, 2010; Seelke et al., 2012;

Markram et al., 2015). Functionally, cortical architecture is structured similarly between brain regions, each possessing systematic maps of the features they code: e.g. retinotopy in visual areas (**Figure 1A**; Brewer et al., 2002), tonotopy in auditory areas (Pantev et al., 1995), and homunculi (maps of the body) in somatosensory and motor areas (Feldman and Brecht, 2005; Harrison et al., 2012). *It is generally believed that these patterned maps are an integral part of the computations performed by the cortical circuits.*

Comparative approaches have proved very useful for identifying genetically driven distinctions in the functional organization of mammalian nervous systems. For example, the corpus callosum is not present in monotremes and marsupials (metatherians) but is found in placental (eutherian) mammals, providing a timeline for the emergence of this feature (reviewed in Kaas, 2017). While this article reviews what is currently known, the relative lack of data in some areas has led us, here, to take an expanded approach – we propose several theories and experiments that would greatly assist in creating a better understanding of map structures in cortex. The rationale for such experiments is placed into the context of the reviewed literature.

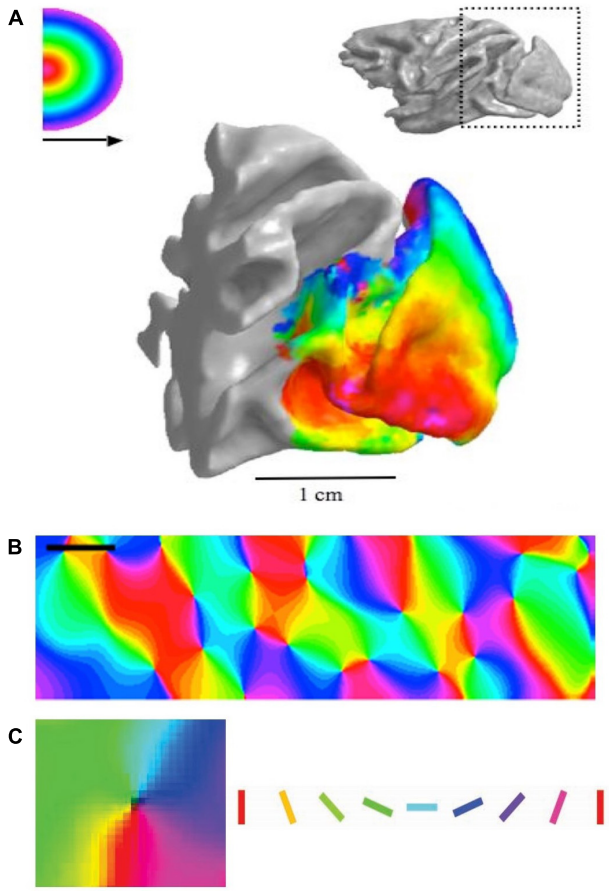

FIGURE 1 | (A) Retinotopic map in monkey visual cortex (fMRI data). **(B)** Orientation map in cat cortex measured using optical imaging, with orientation selectivity coded by specific colors. Scale = 1 mm. **(C)** Zoom onto a single pinwheel in cat cortex. Square width = 1 mm. Oriented bars show color code in panels **B** and **C**. Panel **A** reproduced from Brewer et al. (2002) with permission from the copyright holder. Panels **B** and **C** adapted from Cloherty et al. (2016) with permission from the copyright holder.

Cortical Maps

In every mammalian species studied, V1 has a retinotopic map in which information from the visual field is coded onto a two-dimensional surface that retains the image's spatial organization. Embedded in the retinotopic map, V1 also codes other stimulus features, e.g. the orientation of edges, the eye of origin (ocular dominance), spatial frequency, and the direction of motion (Goodhill, 2007). There is an extensive literature describing how various stimulus features can be mapped onto the cortex, which shows that self-organizing mechanisms are good at reproducing V1 maps in species such as cats, ferrets, and primates, but they may not provide all the answers (Hubel et al., 1977; Blasdel and Salama, 1986; Bonhoeffer and Grinvald, 1991; Bartfeld and Grinvald, 1992; Obermayer and Blasdel, 1993; Hübener et al., 1997; Nauhaus et al., 2012).

Here, we will focus on the maps of orientation selectivity (OS), which need to code oriented structures in every patch of visual space through the full 180°. It has been suggested that detecting the orientation of edges in visual scenes is as fundamental to visual processing as detecting brightness (Bell and Sejnowski, 1997). Some species (e.g. primates and cats) organize their OS cells into highly structured orientation columns, where cells with the same preference cluster together into columns that are 0.2–0.7 mm in diameter (**Figure 1B**; e.g. Cloherty et al., 2016). In these species, all cells through all six cortical layers have the same OS, suggesting an emphasis on vertical integration of feature selectivity through the cortical layers. To ensure that all orientations are represented in every patch of the retinotopic map, the orientation columns representing different orientations are arranged radially around a central location in the horizontal plane, centered on a particular point in the retinotopic map (**Figure 1C**). This cortical architecture is known as a "pinwheel" OS map. Other species have a random distribution of orientation selective cells, i.e. most cells are OS but those with different orientation preferences are juxtaposed in a random fashion (rodents/rabbits: Ohki et al., 2005; Van Hooser et al., 2005; Bonin et al., 2011; Espinosa and Stryker, 2012; Reid, 2012). The cells are intermingled both horizontally across the retinotopic map and vertically through the six cortical layers. This is known as a "random" or "salt-and-pepper" OS map.

Essential Techniques

Five essential experimental techniques need to be briefly discussed before reviewing current and future directions in this field. (1) Intrinsic optical imaging (OI) is a technique that allows cortical maps to be measured with a high degree of accuracy over relatively wide regions of the cortex down to depths of 600–1000 μm, with a horizontal resolution of ∼50 μm. This technique is simple in principle but complex in operation. A bright red or green light is shone onto the cortex and this partially penetrates into the neural tissue (Grinvald et al., 1986; for recent red–green comparison, see Cloherty et al., 2016). Areas that have large volumes of blood or increase in deoxy-hemoglobin concentration

due to high levels of neural activity do not reflect much light, so they appear dark. In contrast, areas with less blood flow reflect more light, so they appear brighter. In this way, it is possible to determine which areas of cortex are active and which are not, thus allowing the measurement of cortical maps (**Figures 1B,C**). (2) Two photon calcium imaging allows much higher spatial resolution in three-dimensions but is restricted to far smaller areas of the cortex. This technique, for example, allows the visualization of single neurons in an entire column of cortex (Tischbirek et al., 2019). The two-photon technique requires the cells to be loaded with a calcium sensitive dye or made to express a genetically encoded calcium indicator. Both techniques allow the activity-dependent fluorescent signals to be measured, thus allowing fine detailed mapping of cortical areas. (3) Whenever investigating cortex, it is useful to record electrical responses from cortical cells at the spiking level. This not only provides essential information about neural processing but also validates the data from the OI (Zepeda et al., 2004). In recent years multi-electrode recordings have become possible and this has greatly improved the capacity to correlate OI with massed recording techniques (Nauhaus and Ringach, 2007). (4) Dye injection into various regions of brains allows the local and long-distance connectivity to be established (Bosking et al., 1997). This is fundamental to understanding cortical map structures. For example, dye injections into the lateral geniculate nucleus (LGN), which is the relay center between the retina and V1 can establish the topography of the retinal cells that provide the input to V1 (e.g. Wimborne et al., 1999). (5) Finally, computer modeling is a critical technique in understanding cortical maps in several important ways (Durbin and Mitchison, 1990; Swindale, 1996; Koulakov and Chklovskii, 2001; Goodhill, 2007). These models offer potential mechanisms that can be tested experimentally and provide quantitative methods for developing new theories.

Understanding Cortical Maps Through Comparative Physiology

Why do some mammals have salt-and-pepper OS maps and others pinwheel OS maps? This question is a hotly debated topic in the fields of visual neuroscience and developmental neurobiology (Horton and Adams, 2005; Van Hooser et al., 2005; Kaschube et al., 2010; Scholl et al., 2013; Vidyasagar and Eysel, 2015; Kremkow et al., 2016). There are many factors that might influence evolution's choice of OS map. These include (a) predator versus prey, (b) the degree to which animals are nocturnal, (c) the need for binocular processing based on the divergence of the eyes, (d) the size of the brain (or visual cortex), (e) the sophistication of the cortical architecture, (f) the resolution of the visual system, (g) the thalamocortical networks that provide their visual inputs, (h) the distribution of retinal ganglion cells (RGCs) in the retina, which is thought to be related to each species' visual environment (Hughes, 1977), or (i) a genetic factor related to phylogeny.

We will begin by discounting the first two things on this list. Might predators have pinwheel structures and herbivores a salt-and-pepper structure? Primates contradict this notion as all have pinwheel maps but most are fructivores. Moreover, a carnivorous rodent has been shown to have a salt-and-pepper OS map (Scholl et al., 2017). Could OS map structure be related to nocturnal versus diurnal lifestyles? This is unlikely as cats and some primates are primarily nocturnal but have pinwheel OS maps. Also, some rodents (squirrels) are diurnal but have salt-and-pepper OS maps. We will compare several possibilities: eye divergence, the total number of cells in V1, the thalamocortical networks that provide their visual inputs, the topography of the retina and the phylogenetic relationships between mammalian species, and discuss how each factor may influence cortical map structure. We propose that the central-to-peripheral ratio (CP ratio) of retinal cell density is good at predicting the presence or absence of OS maps.

Understanding Cortical Maps Through Eye Divergence

Could animals with frontal eyes have pinwheel OS maps while lateral eyed animals have salt-and-pepper maps? **Figure 2** plots binocular overlap in the visual field against eye divergence for mammals that have had their cortical OS maps assessed. Pupillary (eye) divergence can be quantified by photographing the eyes while the animal is facing a distant light source. The images of this light, formed by reflection at the corneas, coincide approximately with the optical centers of the eyes, and the distance by which the separation of the pupils exceeds the separation of these images is defined as pupillary divergence (Olson and Freeman, 1978). **Figure 2** shows which species have pinwheel (blue) or salt-and-pepper (red) maps. The species in blue at the top left are from humans, macaques, squirrel monkeys, owl monkeys, bushbabies, and the domestic cat. The species in red at the bottom right are squirrels, rats, mice, and rabbits. If our analysis stopped there, we could draw quite a robust conclusion that a lack of orientation columns in the cortex is associated with animals that have highly diverged eyes and small binocular fields, while those with pinwheel structures in cortex have small eye divergence and large binocular fields. However, tree shrews and ferrets (green diamonds) contradict this simple theory because both have quite laterally positioned eyes and small binocular overlaps, yet they have exquisite pinwheel OS maps (Bosking et al., 1996; Rao et al., 1997). The species in gray in **Figure 2** show four species of mammals that have not had their cortices imaged (i.e. sheep, wallaby, fruit bat, and agouti). Measuring the cortical map structures in these species would clearly help to fill in essential missing data.

The agouti clearly has quite lateral eyes but no specific optical measure has been conducted, so we show it as a span of eye divergence angles (horizontal gray line). However, its binocular overlap has been measured as 20° (Picanço-Diniz et al., 2011). The wallaby is a particularly interesting species to study as its eye divergence is almost exactly 45°, placing it between the two extremes. The bat and the sheep are also interesting species to examine as they naturally cluster on this plot, respectively, with the frontal or lateral eyed species but electrophysiological evidence suggests that the sheep might have pinwheel cortical maps (see below), while we can only hypothesize about the bat at present.

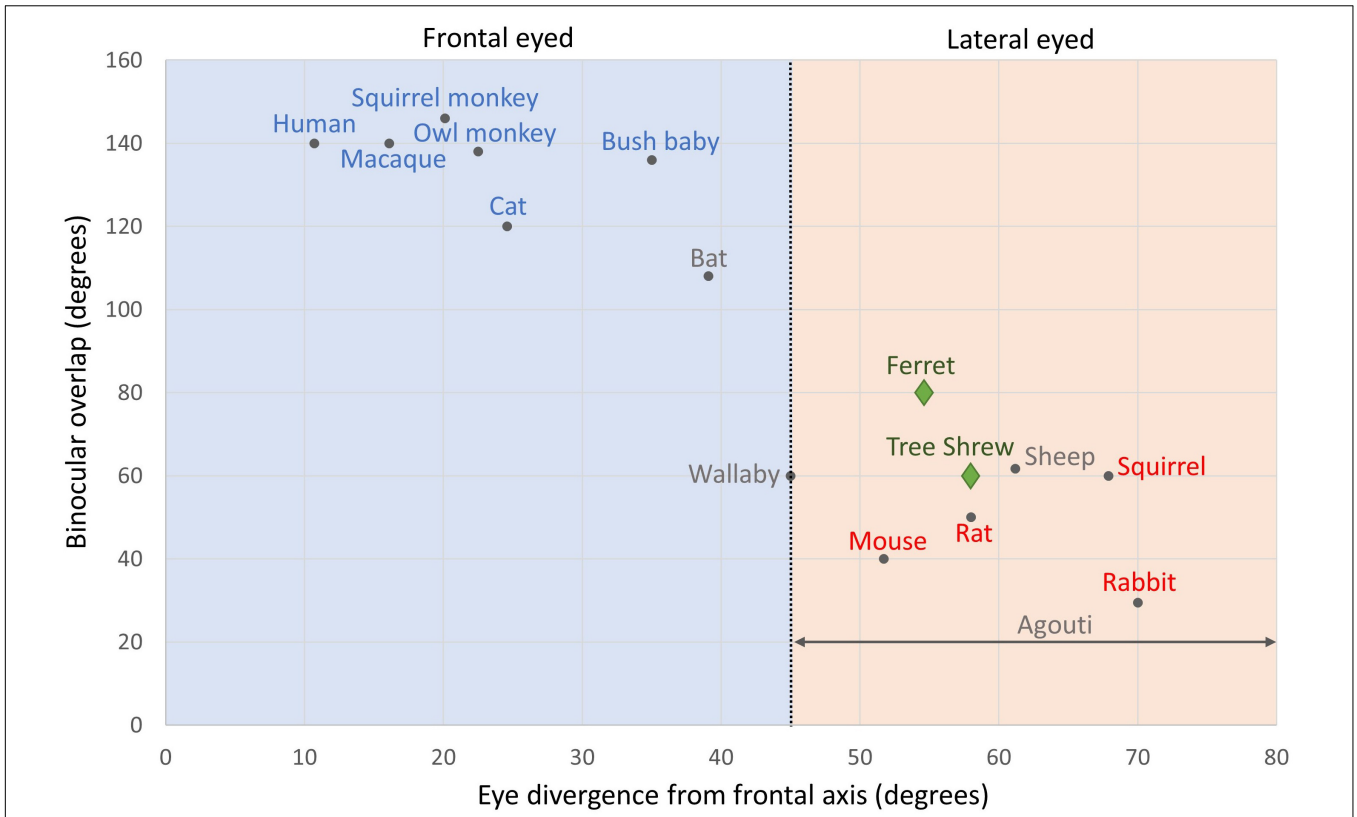

FIGURE 2 | Binocular overlap plotted against eye divergence in mammals. The black vertical line shows an eye divergence of 45 degrees, which divides frontal from lateral eyed animals: Eye divergence = 90 degrees – Orbit convergence. Species names in blue have pinwheel maps. Species names in red have salt-and-pepper maps. Ferrets and tree shrews have names and symbols in green: both have pinwheel maps. Species names in gray are those that we suggest should be investigated in future studies: agouti, fruit bat, sheep, and wallaby. Adapted from Heesy (2004) with permission from the copyright holder. Binocular overlap data for agouti is from Picanço-Diniz et al. (2011).

Understanding Cortical Maps Through V1 Cell Numbers, Cortical Complexity, and Spatial Resolution

Could it be that mammals with smaller primary visual cortices, relatively undifferentiated cortices or poor-resolution vision are restricted to having salt-and-pepper OS maps? These concepts were thoroughly investigated by selecting a rodent that has good spatial resolution, and a V1 that is highly differentiated and has a surface area similar to that of animals with pinwheel OS maps; the species selected was the gray squirrel (Van Hooser et al., 2005). It was found that despite a well-developed cortex the squirrel has a salt-and-pepper map. Despite the findings from the squirrel, Harris and Mrsic-Flogel (2013) later proposed that an ordered orientation map in a physically small cortex would lead to poorer coverage of orientations in their visual field than a random structure. However, this suggestion breaks down somewhat when comparing tree shrews and rabbits. The area of V1 is in fact smaller in tree shrews (60 mm^2) (Muly and Fitzpatrick, 1992) than rabbits (80 mm^2) (Hughes, 1971) but tree shrews have orientation columns while they are absent in rabbits.

More recently, Weigand et al. (2017) reactivated the discussion about the relationship between the size of V1 and the type of OS map structure. They presented a model in which the number of cells in V1 influences the interactions between neurons – according to their model, the more cells the more likely the brain organizes itself into columns. To support this notion, they presented a graph that plotted cell number in cortex against the existence, or not, of OS maps. We present a modified and updated version of that plot in **Figure 3**. It shows that all primates and the cat have large cortical cell populations (>30 M) and pinwheel maps, while all rodents that have had their OS maps studied have low numbers of cortical cells (<3 M) and salt-and-pepper maps. However, it is species that fall between these extremes that create a problem for their "more cells more complexity" theory. The rabbit has nearly 6 M cells in its V1 and a clear salt-and-pepper design. The ferret and tree shrew have, respectively, 7.6 and 8 M cells, which is not dissimilar to rabbits. If only the number of cells dictates the map structure in visual cortex, the threshold must be finely balanced between 6 (rabbit) and 7.6 M cells (ferret).

Unfortunately, other species that Weigand et al. (2017) highlight have not had their orientation map structures examined using OI (stars, **Figure 3**). For example, the agouti is a large rodent that has 12 M cells in visual cortex. While no OI has been done, a correlation of orientation preferences based on

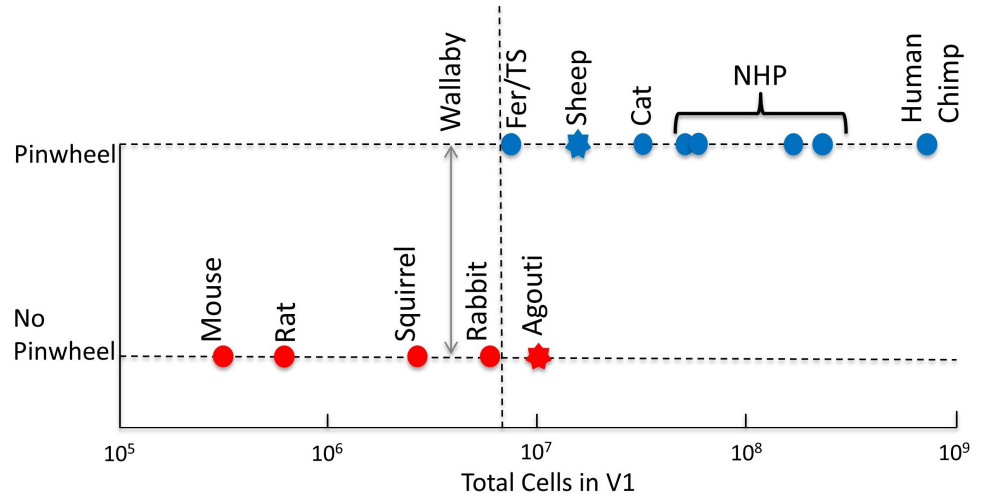

FIGURE 3 | Existence of pinwheels plotted against the number of cells in V1. Red, no pinwheels; blue, pinwheels. Circles show results from intrinsic optical imaging. Stars show results obtained only from single-cell recording. The dotted vertical line shows the possible threshold between species with pinwheels and those without. Note that the Agouti has more cells in V1 than both ferrets and tree shrews but the indication is that they have a salt-and-pepper map. The double-headed vertical arrow shows the cell count in wallaby V1 – it is not yet known if they have pinwheels. Fer, ferret; TS, tree shrew; NHP, non-human primates (including marmoset, bush baby, owl monkey, squirrel monkey, macaque); Chimp, chimpanzee. Reproduced from Weigand et al. (2017) with permission from the copyright holder.

distance across the cortex has been conducted for the agouti (Ferreiro, 2018). It showed that the local correlations in OS were similar to those of the mouse and very different to the cat. In the cat the similarity of orientation preferences changes slowly and smoothly, which corresponds with a pinwheel map structure. These smooth changes did not occur in the agouti. Instead there were abrupt changes in the OS of neighboring cells with a clustering of cells with similar orientation preferences occurring only over very short ranges. Therefore, the agouti may at most have minicolumns, which would appear with two-photon calcium imaging, as is the case in mice (Kondo et al., 2016). This mapping does not support Weigand et al.'s (2017) theory (because ferret and tree shrew have far smaller cell numbers in cortex) but does support the theory that all rodents have a consistent lack of the classic pinwheel OS maps, as found in other mammals (see the section "Understanding Cortical Maps Through Phylogeny"). Given Ferreiro's results, we have tentatively placed the agouti on the "no pinwheel" line in **Figure 3**.

The sheep has 18 M cells in cortex, but its OS map structure remains unknown. Based on the observation that orientation preferences changed slowly during single electrode recordings it is likely that the sheep has a structured, pinwheel-like orientation map (Clarke et al., 1976; Ramachandran et al., 1977; Kennedy et al., 1983). Therefore, we have tentatively placed the sheep on the "has pinwheel" line in **Figure 3**. Clearly, an imaging investigation of agouti and sheep cortices would be a very useful way of filling in the missing data to confirm or reject the theory of Weigand et al. (2017). Rather than thinking of the data confirming or rejecting the theory, it is also worth considering that the theory has merit but in the transition zone between large and small numbers of cortical cells, other factors also play important roles, as outlined below. Unfortunately, we could not add the fruit bat into **Figure 3** because we do not yet have a reliable measure of the number of cells in fruit bat V1.

Understanding Cortical Maps Through Understanding the Visual Pathways

Recent work suggests that cortical maps are seeded by the thalamocortical networks that provide their input (Paik and Ringach, 2011; Nauhaus and Nielsen, 2014; Wang et al., 2015; Kremkow et al., 2016; Lee et al., 2016). The visual pathway to the cortex is from RGCs to LGN to V1. Each V1 neuron receives input from a bundle of thalamic afferents that control the shape of the cortical receptive field. The ON and OFF thalamic afferents rotate around each other to minimize the cortical wiring needed to represent visual points (Schummers et al., 2002). It has been revealed through experimental studies that the receptive field structure of ON and OFF thalamic afferents can predict orientation preference and the clustering of cells in cortical domains (Koch et al., 2016; Kremkow et al., 2016). However, it remains unknown whether ON–OFF rotation in receptive field position is developed by the mosaic arrangement of ON and OFF ganglion cells in retina (Wässle et al., 1981; Soodak et al., 1987; Ringach, 2004; Paik and Ringach, 2011) or by the strongly correlated firing between ON and OFF thalamic afferents (Miller, 1994; Goodhill and Löwel, 1995; Nakagama et al., 2000).

A theory proposed by Paik and Ringach (2011) suggests that Moire interference patterns formed by the ON and OFF ganglion cell arrays create different patterns of OS in the cortex, which resemble pinwheel maps. If true, this model could have a role in determining whether a species has pinwheel maps. However, the model requires that the ON and OFF arrays are geometrically precise while the system is imprecise in lining up the two arrays.

Hore et al. (2012) showed that the RGCs do not have the spatial distributions required to create perfect ON and OFF retinal mosaics. Additionally, a more recent computational model by Schottdorf et al. (2014) suggests that the spatial structure of cat and macaque retinal mosaics are not plausible for seeding the orientation preference maps of the primary visual cortex. It is also not clear how the geometrical realities imposed by different retinal designs might affect the arrangement of ON and OFF RGCs (see below for retinal designs).

Mazade and Alonso (2017) propose that the spacing between thalamic axon patches with overlapping receptive fields needs to be greater than 2 axon patches to allow afferents to cluster within different cortical domains. As shown in **Figure 4A**, as the number of LGN neurons increases, the size of V1 increases in a non-linear fashion, as shown by the exponential plot ($y = 770x^{1.23}$, $R^2 = 0.98$) (Stevens, 2001), i.e. V1's size becomes much larger than that expected from a linear co-scaling of thalamus and cortex. In primates, carnivores, and scandentia (e.g. tree shrew), the overexpansion of area V1 makes the density of LGN axons per mm^2 of cortical area smaller. In **Figure 4B**, we can see that species with low densities of LGN axons in V1 have pinwheel maps, while in species with high LGN densities ($>$2000 axons/mm^2) the pinwheels are absent. It seems that there is a certain threshold between species with pinwheels and those without, which we have tentatively drawn as a dashed line at 2000 axons/mm^2. Unfortunately, we do not have information regarding the LGN densities of the four species that we have highlighted above as future candidates, making such studies worthwhile future pursuits.

The high total number of LGN neurons in primates and carnivores are associated with larger numbers of central RGCs (Kremkow and Alonso, 2018). As a result of evolutionary pressure, primates and carnivores have greater binocular overlap and in turn, there is a greater percentage of RGCs projecting to the LGN. In primates and cats, most RGCs project to the LGN and very few project to other subcortical regions (Illing and Wässle, 1981; Perry and Cowey, 1984). In comparison, most of the mouse and rabbit RGCs project to the superior colliculus and other subcortical regions responsible for visual navigation (Ellis et al., 2016).

Different mammalian species have different ways of organizing their retinal inputs to accommodate their visual needs. For example, the retinal inputs in rabbits are devoted to peripheral vision and offer a panoramic view of the environment. This gives them the best opportunity to lookout for predators (Oyster et al., 1981). On the other hand, primates have a strong retinal bias toward central vision to process high acuity vision. Therefore, the spatial distribution of retinal inputs is an important factor determining the number of thalamic afferents to V1 (see below for more on retinal topography).

Understanding Cortical Maps Through Retinal Topography

Here we use a centroperipheral ratio, CP, which is the ganglion cell density in the center of the retinal specialization divided by the peripheral cell density (Navarro-Sempere et al., 2018). We propose that the CP ratio is high among species with organized pinwheel maps and low in those without. Moreover, the CP ratios correlate strongly with pinwheel density (per mm^2) in species with pinwheel maps. To show this, we have conducted a comparative analysis of ganglion cell distribution maps across various species for which visual cortex has been studied. Each species has a unique arrangement of retinal specializations (areas of higher cell density), which appears to be influenced by ecological and developmental selective pressures in its ecological niche and habitat (Hughes, 1977; Collin, 1999, 2008). Mammalian retinas have been traditionally divided into two types: those with an *area centralis* (AC) and those with a visual streak (VS) (**Figure 5**; Moore et al., 2012). However, this terminology does not tell the whole story. A quantitative measure such as the CP factor may help us understand in more detail how RGC organization influences V1 organization.

Published retinal topography maps have iso-density contour lines showing variations in cell density across the retina. The iso-density lines are used to measure the changes in cell density from retinal periphery to the retinal specialization (Moore et al., 2012). The center of retinal specialization is the point with the highest RGC density, which is often marked as a black dot in the topographic maps. If this point was not reported in published maps, the center of retinal specialization density was determined as the density marked on the inner most iso-contour line of the map. The peripheral density was defined as the density at the extreme edge of the retina (in nasal and temporal regions). When the outer perimeter of the retina was not available, the cell density of the first iso-density line shown nearest the outer perimeter of the retina was halved. This method was utilized by Moore et al. (2012), based on the patterns observed in the topographic maps that included information on the outer perimeter of the retina. In most species, the cell densities of nasal and temporal periphery were the same, but for mouse, cat, sheep, and agouti, they were different. So, the nasal and temporal peripheral values were averaged for these species. We assumed that the retinal whole-mount methodology was similar across studies to produce the topographic maps. For instance, we assumed that the wholemount was correctly oriented and the degree of shrinkage was similar across studies. Also, we assumed that the cells counted were all RGCs, because in some studies the amacrine cells were difficult to distinguish from the ganglion cell layers (Hughes, 1975; Vitek et al., 1985), thus, potentially resulting in higher cell densities in the periphery. We understand that the assumptions mentioned above could introduce a certain degree of error in our measurements. Despite these limitations, we believe the CP ratios can be used to study how retinal topography influences cortical OS maps.

Arboreal species or those inhabiting dense forests generally have an AC, i.e. cell isodensity contours are circular and are centered roughly on the middle of the retina (e.g. **Figures 5A–C**). This type of design provides a range of acuities across the visual field in all directions. However, not all retinas with an AC are the same. Three general types of AC have been identified (Hughes, 1977). Some species with an AC have low ganglion cell densities with little centroperipheral gradient (CP ratio $<$ 3.0). This is common in small nocturnal animals living in

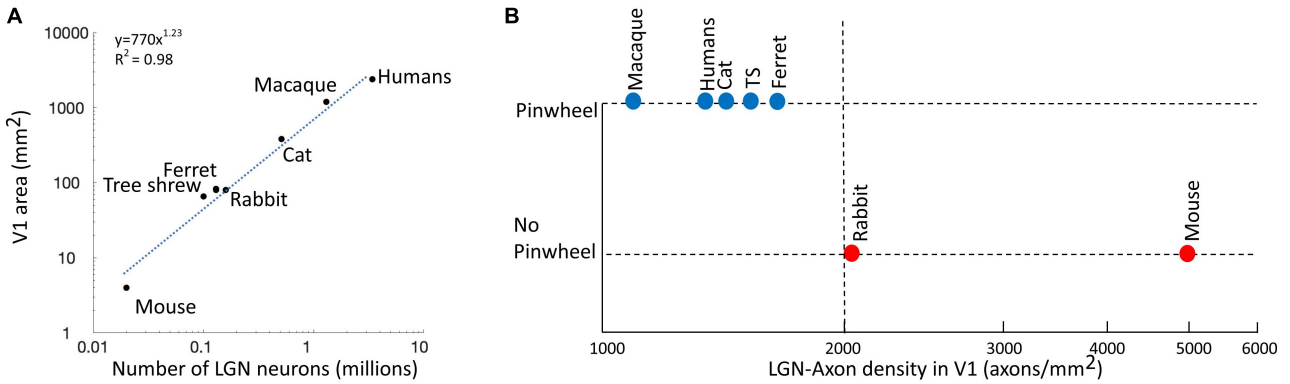

FIGURE 4 | The LGN-axon densities in V1. **(A)** The number of LGN cells is correlated to the size of area V1. Blue dotted line shows an exponential plot ($y = 770x^{1.23}$, $R^2 = 0.98$). **(B)** Existence of pinwheels plotted against the LGN-axon density in V1. Red, no pinwheels; blue, pinwheels. The dotted vertical line shows the possible threshold between species with pinwheels and those without. Reproduced from Mazade and Alonso (2017) with permission from the copyright holder.

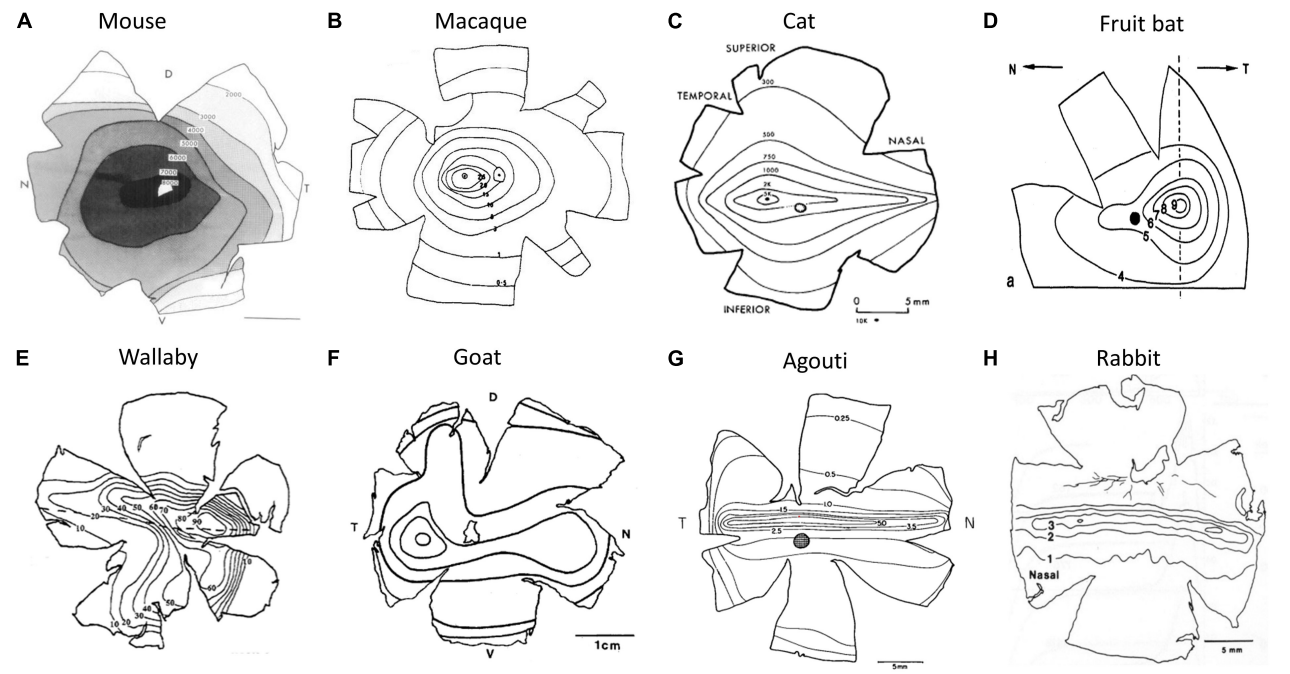

FIGURE 5 | Retinal cell isodensity contour maps. **(A)** Mouse retina, **(B)** rhesus macaque retina, **(C)** cat retina, **(D)** bat retina, **(E)** wallaby retina, **(F)** goat retina, **(G)** agouti, and **(H)** rabbit. Parts **A** reproduced from Dräger and Olsen (1981), **B** from Perry and Cowey (1985), **C** from Hughes (1975), **D** from Pettigrew (1986), **E** from Wimborne et al. (1999), **F** from Gonzalez-Soriano et al. (1997), **G** from Silveira et al. (1989), and **H** from Oyster et al. (1981) with permission from the copyright holder.

scrubland, such as mice, rats, and guinea pigs (**Figure 5A**). Others have moderate ganglion cell densities but the centroperipheral density gradient remains low (<4.0). This characteristic is predominant in small diurnal animals with relatively high visual acuity (e.g. squirrels). Finally, there are species with very large centroperipheral density gradients (>30). This final category, which is most often associated with primates, offers very high visual acuity in the central visual field (**Figure 5B** and **Table 1**).

Instead of circular isodensity contours in the retina, many species have an elongated, horizontal region of the retina that has relatively high cell density, referred to as a VS. However, there are two types of VS design. Some mammals have a VS in which cell density is consistent along the entire horizon, such as rabbits and agouti (**Figures 5G,H**). This design is usually associated with prey species that have lateral eyes. Such a design offers a panoramic view of the environment without having to make horizontal head movements (Hughes, 1977). The second type of VS occurs in a wide variety of mammals. In this case there is a horizontal streak but the region of the retina that points directly forward has a zone of particularly high cell density (**Figures 5D–F**). In cats the adult eye divergence from the frontal axis is around 8 degrees (Olson and Freeman, 1978). The region of higher density in

TABLE 1 | Relationship between retinal ganglion cell arrangement and orientation map design.

Species	Center of retinal specialization density (cells/sq. mm)	Temporal periphery (cells/sq. mm)	Nasal periphery (cells/sq. mm)	Retinal design	Centro-peripheral density	Pinwheel density (mm^2)	Total pinwheels in V1
Rat (*R. norvegicus*)	>6000	4250	4250	AC	1.4	–	–
Mouse (genus *Mus*)	>8000	1500	4500	AC	2.7	–	–
Rabbit (*Oryctolagus cuniculus*)	>4000	1500	1500	VS	2.7	–	–
Ground squirrel (*Spermophilus beecheyi*)	>24,000	7500	7500	VS	3.2	–	–
Tree shrews	>19,000	2500	2500	AC and VS	7.6	9.4	564
Ferret (*M. putorius*)	>5500	500	500	AC and VS	11.0	5.5	429
Cat (*Felis catus*)	>10,000	150	400	AC and VS	36.4	3.0	1140
Bush baby (*galgos*)	>11,000	250	250	AC and VS	44.0	6.4	890
Owl monkey (*Simia trivirgata*)	>7000	150	150	Fovea	46.7	7.4	2124
Rhesus macaque (*Macaca mulatta*)	>30,000	500	500	Fovea	60.0	8.0	10,152
Agouti (*Dasyprocta*)	>5000	125*	1750	VS	2.9	?	?
Fruit bat (*Pteropus* spp.)	>9000	2000	2000	AC	4.5	?	?
Sheep (*Ovis aries*)	>5000	375	750	AC and VS	8.9	?	?
Wallaby (*Macropus eugenii*)	>5000	250	250	AC and VS	20	?	?

*Shading shows data from animals suggested for future research. Retinal ganglion cell values for mouse: Dräger and Olsen (1981); rat: Jeffery (1985); rabbit: Oyster et al. (1981); Ground squirrel: Long and Fisher (1983); tree shrew: DeBruyn (1983); ferret: Vitek et al. (1985); cat: Hughes (1975); bush baby: DeBruyn et al. (1980); owl monkey: Webb and Kaas (1976); Rhesus Macaque: Perry and Cowey (1985); agouti: Silveira et al. (1989); fruit bat: Pettigrew (1986); sheep: Hebel (1976); and wallaby: Wimborne et al. (1999). Except for ferret, all pinwheel densities are from Xu et al. (2004), which are averages calculated from the following sources: bush baby: Bosking et al. (1996); owl monkey: Xu et al. (2004); squirrel monkey: Blasdel and Campbell (2001); macaque monkey: Obermayer and Blasdel (1997); tree shrew: Bosking et al. (1997); and cat: Müller et al. (2000). Ferret pinwheel density is from Rao et al. (1997). *For agouti, only the cell density from the nasal side is used in calculating the CP ratio because very few iso-density lines are on the temporal side of the retina.*

their VS is concomitantly displaced laterally by around 8 degrees in each eye to maximize visual acuity frontally. In the case of the cat, most authors state that they have an AC but in reality they have a combination of a VS and an AC. Similarly, in the sheep/goat retina, the lateral region of the VS has very high cell density at the point associated with frontal vision (Clarke and Whitteridge, 1976; Hebel, 1976). We do not have a contour map from the sheep but instead provide one from the goat retina (**Figure 5F**). Indeed, while sheep/goats are usually said to have a VS, the displaced region of high cell density has higher cell counts than the central region of the cat eye. Many herbivores have this combination of a VS and a lateral region of high cell density, e.g. goats, horses, and red kangaroos (Hughes, 1977). However, many carnivores also have this retinal arrangement, e.g. dogs and cats (McGreevy et al., 2004).

The CP ratio varies significantly across species. Based on the data in **Figure 6A** and **Table 1**, we can see that for species without a pinwheel map (e.g. rat, gray squirrel, mouse, and rabbit), their CP ratios are all <4 (**Figure 6A**). That is, the central density is never more than four times that of the periphery. The agouti also has a low CP ratio due to its rabbit-like VS (red star, **Figure 6A**). Evidence suggests that the agouti may have a salt-and-pepper OS map, so it should sit in the left side of **Figure 6A** with all the other rodents. In primates and cats we can see a positive, linear correlation between CP ratios and pinwheel density (**Figure 6B**). Macaque monkeys have a high CP ratio of 60 and the cortical pinwheel maps are dense (8 pinwheels per mm^2). In bushbabies and owl monkeys the CP ratios are 44 and 47 and the respective pinwheel densities 6.4 and 7.4 (**Table 1**). In the cat, where the displaced AC is prominent and has a high-density gradient close to primates (CP ratio of 36), the orientation columns are unexpectedly broad (3 pinwheels per mm^2) (**Figure 6**).

Tree shrews and ferrets have moderate CPs and they have orientation columns but they seem to be intermediate between species that have pinwheels and those without. In the ferret the CP ratio is 11, which is much lower than the cat, but its pinwheel density is closer to that of a primate (5.5 pinwheels per mm^2). Similarly, in the tree shrew the CP ratio is <8, which is even lower than the ferret, but its pinwheel density is higher than recorded in primates (9.4 pinwheels per mm^2). These inter-species variations probably highlight the influence of multiple factors controlling retinal design and, possibly, cortical map structures in tree shrews and ferrets.

Based on these observations we suggest that the density of cells providing input to the cortex may be related by an all-or-nothing rule that dictates the existence of pinwheel maps versus salt-and-pepper maps. That is, if the CP ratio is <4 the cortex is salt-and-pepper. If the CP ratio is >7 the cortex has a pinwheel structure. A strong bias toward central vision increases the number of retinal inputs to the thalamus, which overexpands V1 and provides the spacing between thalamic axon patches to allow clustering within different cortical domains. Moreover, if a pinwheel map is present, the CP ratio may dictate the density of pinwheels (per mm^2). Therefore, if we find pinwheel OS maps, we expect to see a gradation in orientation column widths that relates to the CP ratio of the retinal inputs (**Figure 6B**).

We can use the four species that we have highlighted as future candidates to fill-in the gaps in **Figures 2**, **3**, **6A**. (1) The wallaby is known to have a centralized retinal input to the cortex (**Figure 5F**), with a CP ratio of 20, but its OS map

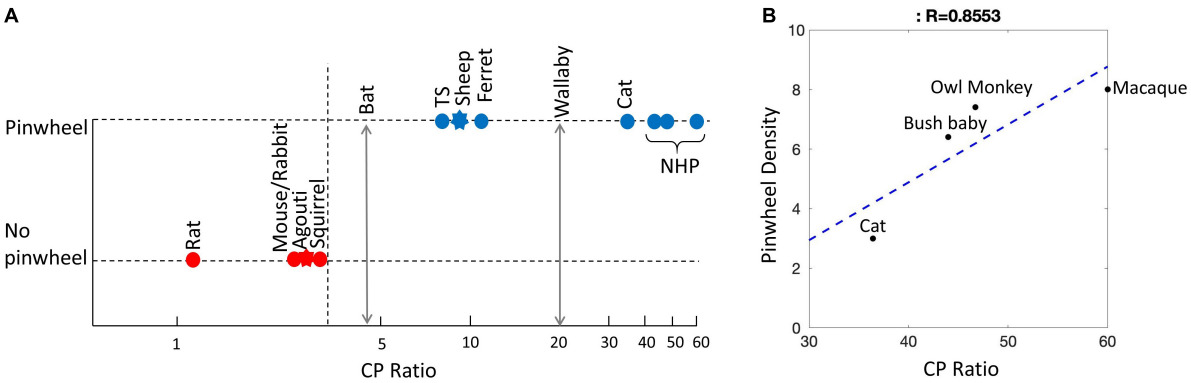

FIGURE 6 | Relationship between retinal ganglion cell arrangement and orientation map design. **(A)** Existence of pinwheels plotted against the CP ratios. Red, no pinwheels; blue, pinwheels. Circles show results from intrinsic optical imaging. Stars show results obtained only from single-cell recording. The dotted vertical arrow shows the possible threshold between species with pinwheels and those without. The double-headed vertical arrows show wallaby and bat CP ratios – it is not yet known if they have pinwheels. TS, tree shrew; NHP, non-human primates (including bush baby, owl monkey, macaque). **(B)** For cat and primates, the pinwheel density (per mm^2) is plotted as a function of CP ratio. The linear regression is shown as a blue dashed line (R = 0.8553).

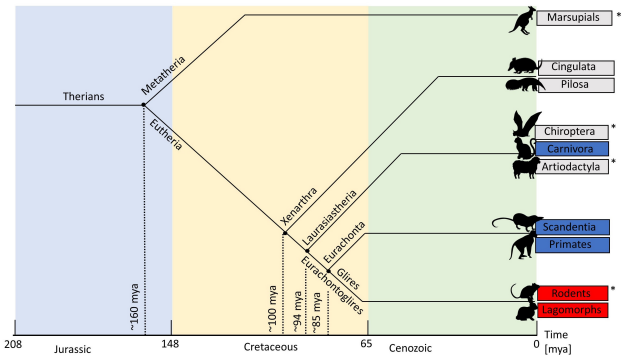

FIGURE 7 | Mammalian phylogenetic tree. Mammalian order names in blue have pinwheels. Order names in red have salt-and-pepper. Order names in gray are those without optical imaging data. Asterisks are those that we suggest should be investigated in future studies: wallaby (Marsupial), fruit bat (Chiroptera), sheep (Artiodactyla), and agouti (Rodents). The dotted lines show where the mammalian clades diverge. MYA, millions of years ago.

structure is not known. Based on our CP theory, we would expect it to have a pinwheel structure. However, the wallaby has an intermediate number of cells in cortex (3.5 M, **Figure 3**) that sits between the squirrel and rabbit, which would suggest a salt-and-pepper structure based on the "more cells more structure" theory (Weigand et al., 2017). (2) Evidence from electrophysiological, rather than optical, recording suggests that the agouti may have a salt-and-pepper OS map (Ferreiro, 2018), and it has a low CP ratio of 2.9. We are reasonably confident that the agouti will not have a pinwheel map. (3) The sheep/goat has a mixture of a VS and a small, temporally located "AC" (Shinozaki et al., 2010). They have high retinal cell density and a CP ratio close to 9. Sheep have surprisingly good visual acuity that exceeds that of domestic cats (Clarke and Whitteridge, 1976). We cannot predict with certainty at this point whether the sheep will have pinwheel maps, but we think the evidence favors this prediction, particularly as the electrophysiology data support this notion (Clarke et al., 1976). Also, recall that the sheep has a large cell count in visual cortex, which also supports the idea of a pinwheel map structure (**Figure 3**). (4) Fruit bats have a centralized retinal input to the cortex, but their CP ratio of 4.5 is low so it will be interesting to know if they have a pinwheel map structure. It is worth noting that while the CP ratio is low in bats, unlike most mammals the drop-off in the periphery is mild, so while the CP ratio is low it is because the peripheral cell density is usually high, compared to the central cell density.

Interestingly, a study was conducted in which nose length and retinal design were compared in dogs (McGreevy et al., 2004). All of the dogs were from the same species (*Canis lupus familiaris*) but were from different man-reared breeds. It was found that dogs with short noses and frontal eyes (e.g. pugs) had a retinal design best described as an AC, while dogs with long noses and lateral eyes (e.g. greyhound) had VSs not dissimilar to rabbits. This finding shows that there may well be a close link between the genetics controlling head configuration and retinal design. Alternatively, being born with eyes that point either frontally or laterally might promote a developmental predisposition toward a particular retinal design. Unfortunately, it was not possible in McGreevy et al.'s (2004) post-mortem study to investigate cortical design in the various dog breeds. While probably impossible to do based on the sensitivity of the community to research on dogs, an obvious experiment to establish the importance of retinal design on cortical organization would be to record cortical maps in dog breeds that have VSs compared to those with an AC. Such an experiment has the natural control that all animals are from the same species.

Understanding Cortical Maps Through Phylogeny

Figure 7 provides a visual guide to mammalian phylogeny (Springer et al., 2003; Luo et al., 2011). Virtually everything we

know about visual cortex in mammals comes from work on rodents, rabbits, members of the order Carnivora, and primates. These species comprise an extremely small subset (<0.1%) of extant mammals. Rodents and rabbits belong to the mammalian clade Glires and will be referred to collectively by this name (**Figure 7**). It is not clear whether the Glires have a genetic predisposition not shared by other mammals toward a salt-and-pepper OS map or it is another factor, independent of the phylogenetic relationship, which dictates the map type. From **Figure 7**, note the large phylogenetic distance between primates (clade, Euarchonta) and the Carnivora (clade, Laurasiatheria), both of which contain species with pinwheel OS maps. In contrast, members of the mammalian clade Glires, which are on the same branch as the primates (**Figure 7**), have salt-and-pepper maps. As it stands at present, the only clear phylogenetic pattern is that all of the Glires studied so far have a salt-and-pepper map structure, probably including the agouti (Ferreiro, 2018). Given that none of the other mammals studied so far have this pattern, the data suggest that salt-and-pepper maps may be a genetically determined feature of the Glires. However, without adding more species from diverse mammalian orders, this conclusion cannot be verified.

From a phylogenetic standpoint, one very obvious path to take is to study marsupial mammals. Marsupials split away from the placental mammals 130–180 million years ago (Samollow, 2008). Even if just one species has a pinwheel OS map, the genetic code has probably been with the mammals from the beginning (with the proviso that it may have been re-invented through convergent evolution). In the plots presented here we have used the wallaby because its cortex is quite well understood (e.g. Vidyasagar et al., 1992; Ibbotson et al., 1994; Hemmi and Mark, 1998; Ibbotson and Mark, 2003). For reasons already discussed, the rodent agouti and the sheep are also good targets for intrinsic OI. Fruit bats (flying foxes) belong to the mammalian order Chiroptera. These bats have excellent frontal vision similar to that in cats (**Figure 7**). There has been considerable interest in the primary visual cortex of fruit bats because the structure of the subcortical visual pathways is similar to the "unique" pathways found in primates (Pettigrew, 1986). While the retinotopy of fruit bat visual cortex has been studied and reveals a strong cortical magnification factor in the areas of retinal specialization (Rosa et al., 1993), no measurement of OS maps using OI has occurred.

CONCLUSION

Cortical V1 maps in rodents and rabbits do not cluster together cells with similar orientation selectivities. Conversely, all other mammals that have been studied have V1s where cells with similar OS are clustered into highly organized orientation columns. We have pointed out that there are many differences between the eye divergences, retinal designs, visual pathways, and cell counts in V1 between mammalian species. There appears to be a consistent correlation between the CP ratio, which compares retinal cell densities in the central and peripheral retinas, and the presence or absence of OS maps. Other characteristics such as the number of cells in V1 also show reasonable correlations with map design but several species break the clear trend. What is clearly missing in the literature is measurement of OS maps in species that have visual pathway and brain structures that are intermediate between rodents and primates. Therefore, we believe that more comparative observations are essential to constrain future suggestions of OS map formation.

AUTHOR CONTRIBUTIONS

MI and YJ wrote the manuscript, produced the figures, developed the concepts discussed, contributed to the manuscript revision, and read and approved the submitted version of the manuscript.

FUNDING

This work was supported by the ARC Centre Of Excellence For Integrative Brain Function grant number: CE140100007.

REFERENCES

Bartfeld, E., and Grinvald, A. (1992). Relationships between orientation-preference pinwheels, cytochrome oxidase blobs, and ocular-dominance columns in primate striate cortex. *Proc. Natl. Acad. Sci. U.S.A.* 89, 11905–11909. doi: 10.1073/pnas.89.24.11905

Bell, A. J., and Sejnowski, T. J. (1997). The "independent components" of natural scenes are edge filters. *Vision Res.* 37, 3327–3338. doi: 10.1016/s0042-6989(97)00121-1

Blasdel, G., and Campbell, D. (2001). Functional retinotopy of monkey visual cortex. *J. Neurosci.* 21, 8286–8301. doi: 10.1523/jneurosci.21-20-08286.2001

Blasdel, G. G., and Salama, G. (1986). Voltage-sensitive dyes reveal a modular organization in monkey striate cortex. *Nature* 321, 579–585. doi: 10.1038/321579a0

Bonhoeffer, T., and Grinvald, A. (1991). Iso-orientation domains in cat visual cortex are arranged in pinwheel-like patterns. *Nature* 353, 429–431. doi: 10.1038/353429a0

Bonin, V., Histed, M. H., Yurgenson, S., and Reid, R. C. (2011). Local diversity and fine-scale organization of receptive fields in mouse visual cortex. *J. Neurosci.* 31, 18506–18521. doi: 10.1523/jneurosci.2974-11.2011

Bosking, L. E., White, L. E., Casagrande, V. A., and Fitzpatrick, D. (1996). Functional organization of areas V1 and V2 in the prosimian galago revealed by optical imaging. *In Soc. Neurosci. Abstr.* 22:1610.

Bosking, W. H., Zhang, Y., Schofield, B., and Fitzpatrick, D. (1997). Orientation selectivity and the arrangement of horizontal connections in tree shrew striate cortex. *J. Neurosci.* 17, 2112–2127. doi: 10.1523/jneurosci.17-06-02112.1997

Brewer, A. A., Press, W. A., Logothetis, N. K., and Wandell, B. A. (2002). Visual areas in macaque cortex measured using functional magnetic resonance imaging. *J. Neurosci.* 22, 10416–10426. doi: 10.1523/jneurosci.22-23-10416.2002

Briggs, F. (2010). Organizing principles of cortical layer 6. *Front. Neural Circuits* 4:3. doi: 10.3389/neuro.04.003.2010

Clarke, P. G., Donaldson, I. M., and Whitteridge, D. (1976). Binocular visual mechanisms in cortical areas I and II of the sheep. *J. Physiol.* 256, 509–526. doi: 10.1113/jphysiol.1976.sp011336

Clarke, P. G., and Whitteridge, D. (1976). The cortical visual areas of the sheep. *J. Physiol.* 256, 497–508. doi: 10.1113/jphysiol.1976.sp011335

Cloherty, S. L., Hughes, N. J., Hietanen, M. A., Bhagavatula, P. S., Goodhill, G. J., and Ibbotson, M. R. (2016). Sensory experience modifies feature map relationships in visual cortex. *eLife* 5:e13911. doi: 10.7554/elife.13911

Collin, S. P. (1999). "Behavioural ecology and retinal cell topography," in *Adaptive Mechanisms in the Ecology of Vision*, eds S. N. Archer, M. B. A. Djamgoz, E. R. Loew, J. C. Partridge, S. Vallerga (Dordrecht: Springer), 509–535. doi: 10.1007/978-94-017-0619-3_17

Collin, S. P. (2008). A web-based archive for topographic maps of retinal cell distribution in vertebrates. *Clin. Exp. Optom.* 91, 85–95. doi: 10.1111/j.1444-0938.2007.00228.x

DeBruyn, E., Wise, V., and Casagrande, V. (1980). The size and topographic arrangement of retinal ganglion cells in the galago. *Vision Res.* 20, 315–327. doi: 10.1016/0042-6989(80)90018-8

DeBruyn, E. J. (1983). *The Organization and Central Terminations of Retinal Ganglion Cells in the Tree Shrew (Tupaia glis)*. Ph.D. Dissertation, Vanderbilt University, Nashville, TN.

Dräger, U. C., and Olsen, J. F. (1981). Ganglion cell distribution in the retina of the mouse. *Invest. Ophthalmol. Vis. Sci.* 20, 285–293.

Durbin, R., and Mitchison, G. (1990). A dimension reduction framework for understanding cortical maps. *Nature* 343, 644–647. doi: 10.1038/343644a0

Ellis, E. M., Gauvain, G., Sivyer, B., and Murphy, G. J. (2016). Shared and distinct retinal input to the mouse superior colliculus and dorsal lateral geniculate nucleus. *J. Neurophysiol.* 116, 602–610. doi: 10.1152/jn.00227.2016

Espinosa, J. S., and Stryker, M. P. (2012). Development and plasticity of the primary visual cortex. *Neuron* 75, 230–249. doi: 10.1016/j.neuron.2012.06.009

Feldman, D. E., and Brecht, M. (2005). Map plasticity in somatosensory cortex. *Science* 310, 810–815. doi: 10.1126/science.1115807

Ferreiro, D. N. (2018). *Orientation Selectivity of Neurons and their Spatial Layout in Cat and Agouti Primary Visual Cortex*. Natal: Universidade Federal do Rio Grande do Norte.

Gonzalez-Soriano, J., Mayayo-Vicente, S., Martinez-Sainz, P., Contreras-Rodriguez, J., and Rodriguez-Veiga, E. (1997). A quantitative study of ganglion cells in the goat retina. *Anat. Histol. Embryol.* 26, 39–44. doi: 10.1111/j.1439-0264.1997.tb00101.x

Goodhill, G. J. (2007). Contributions of theoretical modeling to the understanding of neural map development. *Neuron* 56, 301–311. doi: 10.1016/j.neuron.2007.09.027

Goodhill, G. J., and Löwel, S. (1995). Theory meets experiment: correlated neural activity helps determine ocular dominance column periodicity. *Trends Neurosci.* 18, 437–439. doi: 10.1016/0166-2236(95)94490-v

Grinvald, A., Lieke, E., Frostig, R. D., Gilbert, C. D., and Wiesel, T. N. (1986). Functional architecture of cortex revealed by optical imaging of intrinsic signals. *Nature* 324, 361–364. doi: 10.1038/324361a0

Harris, K. D., and Mrsic-Flogel, T. D. (2013). Cortical connectivity and sensory coding. *Nature* 503, 51–58. doi: 10.1038/nature12654

Harrison, T. C., Ayling, O. G., and Murphy, T. H. (2012). Distinct cortical circuit mechanisms for complex forelimb movement and motor map topography. *Neuron* 74, 397–409. doi: 10.1016/j.neuron.2012.02.028

Hebel, R. (1976). Distribution of retinal ganglion cells in five mammalian species (pig, sheep, ox, horse, dog). *Anat. Embryol.* 150, 45–51.

Heesy, C. P. (2004). On the relationship between orbit orientation and binocular visual field overlap in mammals. *Anat. Rec.* 281A, 1104–1110. doi: 10.1002/ar.a.20116

Hemmi, J. M., and Mark, R. F. (1998). Visual acuity, contrast sensitivity and retinal magnification in a marsupial, the tammar wallaby (*Macropus eugenii*). *J. Comp. Physiol. A Sens. Neural Behav. Physiol.* 183, 379–387. doi: 10.1007/s003590050264

Hore, V. R., Troy, J. B., and Eglen, S. J. (2012). Parasol cell mosaics are unlikely to drive the formation of structured orientation maps in primary visual cortex. *Vis. Neurosci.* 29, 283–299. doi: 10.1017/s0952523812000338

Horton, J. C., and Adams, D. L. (2005). The cortical column: a structure without a function. *Philos. Trans. R. Soc. B Biol. Sci.* 360, 837–862. doi: 10.1098/rstb.2005.1623

Hubel, D. H., Wiesel, T. N., and LeVay, S. (1977). Plasticity of ocular dominance columns in monkey striate cortex. *Philos. Trans. R. Soc. Lond. B Biol. Sci.* 278, 377–409. doi: 10.1098/rstb.1977.0050

Hübener, M., Shoham, D., Grinvald, A., and Bonhoeffer, T. (1997). Spatial relationships among three columnar systems in cat area 17. *J. Neurosci.* 17, 9270–9284. doi: 10.1523/jneurosci.17-23-09270.1997

Hughes, A. (1971). Topographical relationships between the anatomy and physiology of the rabbit visual system. *Doc. Ophthalmol.* 30, 33–159. doi: 10.1007/bf00142518

Hughes, A. (1975). A quantitative analysis of the cat retinal ganglion cell topography. *J. Comp. Neurol.* 163, 107–128. doi: 10.1002/cne.901630107

Hughes, A. (1977). "The topography of vision in mammals of contrasting life style: comparative optics and retinal organisation," in *The Visual System in Vertebrates Handbook of Sensory Physiology*, ed. F. Crescitelli, (Berlin: Springer), 613–756. doi: 10.1007/978-3-642-66468-7_11

Ibbotson, M. R., and Mark, R. F. (2003). Orientation and spatiotemporal tuning of cells in the primary visual cortex of an Australian marsupial, the wallaby *Macropus eugenii*. *J. Comp. Physiol. A* 189, 115–123. doi: 10.1007/s00359-002-0379-6

Ibbotson, M. R., Mark, R. F., and Maddess, T. L. (1994). Spatiotemporal response properties of direction-selective neurons in the nucleus of the optic tract and dorsal terminal nucleus of the wallaby, *Macropus eugenii*. *J. Neurophysiol.* 72, 2927–2943. doi: 10.1152/jn.1994.72.6.2927

Illing, R.-B., and Wässle, H. (1981). The retinal projection to the thalamus in the cat: a quantitative investigation and a comparison with the retinotectal pathway. *J. Comp. Neurol.* 202, 265–285. doi: 10.1002/cne.902020211

Jeffery, G. (1985). The relationship between cell density and the nasotemporal division in the rat retina. *Brain Res.* 347, 354–357. doi: 10.1016/0006-8993(85)90198-2

Kaas, J. H. (2017). "Changing concepts of visual cortex organization in primates," in *Neuropsychology of Visual Perception*, ed. J. W. Brown (Didcot: Taylor & Francis group), 3–32.

Kaschube, M., Schnabel, M., Lowel, S., Coppola, D. M., White, L. E., and Wolf, F. (2010). Universality in the evolution of orientation columns in the visual cortex. *Science* 330, 1113–1116. doi: 10.1126/science.1194869

Kennedy, H., Martin, K., and Whitteridge, D. (1983). Receptive field characteristics of neurones in striate cortex of newborn lambs and adult sheep. *Neuroscience* 10, 295–300. doi: 10.1016/0306-4522(83)90134-3

Koch, E., Jin, J., Alonso, J. M., and Zaidi, Q. (2016). Functional implications of orientation maps in primary visual cortex. *Nat. Commun.* 7:13529. doi: 10.1038/ncomms13529

Kondo, S., Yoshida, T., and Ohki, K. (2016). Mixed functional microarchitectures for orientation selectivity in the mouse primary visual cortex. *Nat. Commun.* 7:13210. doi: 10.1038/ncomms13210

Koulakov, A. A., and Chklovskii, D. B. (2001). Orientation preference patterns in mammalian visual cortex. *Neuron* 29, 519–527. doi: 10.1016/s0896-6273(01)00223-9

Kremkow, J., and Alonso, J.-M. (2018). Thalamocortical circuits and functional architecture. *Annu. Rev. Vis. Sci.* 4, 263–285. doi: 10.1146/annurev-vision-091517-034122

Kremkow, J., Jin, J., Wang, Y., and Alonso, J. M. (2016). Principles underlying sensory map topography in primary visual cortex. *Nature* 533, 52–57. doi: 10.1038/nature17936

Lee, K.-S., Huang, X., and Fitzpatrick, D. (2016). Topology of ON and OFF inputs in visual cortex enables an invariant columnar architecture. *Nature* 533, 90–94. doi: 10.1038/nature17941

Long, K. O., and Fisher, S. K. (1983). The distributions of photoreceptors and ganglion cells in the California ground squirrel, *Spermophilus beecheyi*. *J. Comp. Neurol.* 221, 329–340. doi: 10.1002/cne.902210308

Luo, Z.-X., Yuan, C.-X., Meng, Q.-J., and Ji, Q. (2011). A Jurassic eutherian mammal and divergence of marsupials and placentals. *Nature* 476, 442–445. doi: 10.1038/nature10291

Markram, H., Muller, E., Ramaswamy, S., Reimann, M. W., Abdellah, M., Sanchez, C. A., et al. (2015). Reconstruction and simulation of neocortical microcircuitry. *Cell* 163, 456–492.

Mazade, R., and Alonso, J. M. (2017). Thalamocortical processing in vision. *Vis. Neurosci.* 34:E007. doi: 10.1017/s0952523817000049

McGreevy, P., Grassi, T. D., and Harman, A. M. (2004). A strong correlation exists between the distribution of retinal ganglion cells and nose length in the dog. *Brain Behav. Evol.* 63, 13–22. doi: 10.1159/000073756

Miller, K. (1994). A model for the development of simple cell receptive fields and the ordered arrangement of orientation columns through activity-dependent

competition between ON- and OFF-center inputs. *J. Neurosci.* 14, 409–441. doi: 10.1523/jneurosci.14-01-00409.1994

Moore, B. A., Kamilar, J. M., Collin, S. P., Bininda-Emonds, O. R. P., Dominy, N. J., Hall, M. I., et al. (2012). A novel method for comparative analysis of retinal specialization traits from topographic maps. *J. Vis.* 12:13. doi: 10.1167/12.12.13

Müller, T. M., Stetter, M., Hübener, M., Sengpiel, F., Bonhoeffer, T., Gödecke, I., et al. (2000). An analysis of orientation and ocular dominance patterns in the visual cortex of cats and ferrets. *Neural Comput.* 12, 2573–2595. doi: 10.1162/089976600300014854

Muly, E., and Fitzpatrick, D. (1992). The morphological basis for binocular and ON/OFF convergence in tree shrew striate cortex. *J. Neurosci.* 12, 1319–1334. doi: 10.1523/jneurosci.12-04-01319.1992

Nakagama, H., Saito, T., and Tanaka, S. (2000). Effect of imbalance in activities between ON- and OFF-center LGN cells on orientation map formation. *Biol. Cybern.* 83, 85–92. doi: 10.1007/s004220000148

Nauhaus, I., and Nielsen, K. J. (2014). Building maps from maps in primary visual cortex. *Curr. Opin. Neurobiol.* 24, 1–6. doi: 10.1016/j.conb.2013.08.007

Nauhaus, I., Nielsen, K. J., Disney, A. A., and Callaway, E. M. (2012). Orthogonal micro-organization of orientation and spatial frequency in primate primary visual cortex. *Nat. Neurosci.* 15, 1683–1690. doi: 10.1038/nn.3255

Nauhaus, I., and Ringach, D. L. (2007). Precise alignment of micromachined electrode arrays with V1 functional maps. *J. Neurophysiol.* 97, 3781–3789. doi: 10.1152/jn.00120.2007

Navarro-Sempere, A., Segovia, Y., and García, M. (2018). Comparative analysis of retinal ganglion cell topography and behavioral ecology in Australian marsupials. *Int. J. Morphol.* 36, 248–257. doi: 10.4067/s0717-95022018000100248

Obermayer, K., and Blasdel, G. (1993). Geometry of orientation and ocular dominance columns in monkey striate cortex. *J. Neurosci.* 13, 4114–4129. doi: 10.1523/jneurosci.13-10-04114.1993

Obermayer, K., and Blasdel, G. G. (1997). Singularities in primate orientation maps. *Neural Comput.* 9, 555–575. doi: 10.1162/neco.1997.9.3.555

Ohki, K., Chung, S., Chng, Y. H., Kara, P., and Reid, R. C. (2005). Functional imaging with cellular resolution reveals precise micro-architecture in visual cortex. *Nature* 433, 597–603. doi: 10.1038/nature03274

Olson, C. R., and Freeman, R. D. (1978). Development of eye alignment in cats. *Nature* 271, 446–447. doi: 10.1038/271446a0

Oyster, C., Takahashi, E., and Hurst, D. (1981). Density, soma size, and regional distribution of rabbit retinal ganglion cells. *J. Neurosci.* 1, 1331–1346. doi: 10.1523/jneurosci.01-12-01331.1981

Paik, S.-B., and Ringach, D. L. (2011). Retinal origin of orientation maps in visual cortex. *Nat. Neurosci.* 14, 919–925. doi: 10.1038/nn.2824

Pantev, C., Bertrand, O., Eulitz, C., Verkindt, C., Hampson, S., Schuierer, G., et al. (1995). Specific tonotopic organizations of different areas of the human auditory cortex revealed by simultaneous magnetic and electric recordings. *Electroencephalogr. Clin. Neurophysiol.* 94, 26–40. doi: 10.1016/0013-4694(94)00209-4

Perry, V., and Cowey, A. (1984). Retinal ganglion cells that project to the superior colliculus and pretectum in the macaque monkey. *Neuroscience* 12, 1125–1137. doi: 10.1016/0306-4522(84)90007-1

Perry, V. H., and Cowey, A. (1985). The ganglion cell and cone distributions in the monkeys retina: implications for central magnification factors. *Vision Res.* 25, 1795–1810. doi: 10.1016/0042-6989(85)90004-5

Pettigrew, J. (1986). Flying primates? Megabats have the advanced pathway from eye to midbrain. *Science* 231, 1304–1306. doi: 10.1126/science.3945827

Picanço-Diniz, C. W., Rocha, E. G., Silveira, L. C. L., Elston, G., and Oswaldo-Cruz, E. (2011). Cortical representation of the horizon in V1 and peripheral scaling in mammals with lateral eyes. *Psychol. Neurosci.* 4, 19–27. doi: 10.3922/j.psns.2011.1.004

Ramachandran, V. S., Clarke, P. G. H., and Whitteridge, D. (1977). Cells selective to binocular disparity in the cortex of newborn lambs. *Nature* 268, 333–335. doi: 10.1038/268333a0

Rao, S. C., Toth, L. J., and Sur, M. (1997). Optically imaged maps of orientation preference in primary visual cortex of cats and ferrets. *J. Comp. Neurol.* 387, 358–370. doi: 10.1002/(sici)1096-9861(19971027)387:3<358::aid-cne3>3.0.co;2-#

Reid, R. C. (2012). From functional architecture to functional connectomics. *Neuron* 75, 209–217. doi: 10.1016/j.neuron.2012.06.031

Ringach, D. L. (2004). Haphazard wiring of simple receptive fields and orientation columns in visual cortex. *J. Neurophysiol.* 92, 468–476. doi: 10.1152/jn.01202.2003

Rosa, M. G. P., Schmid, L. M., Krubitzer, L. A., and Pettigrew, J. D. (1993). Retinotopic organization of the primary visual cortex of flying foxes (*Pteropus poliocephalus* and *Pteropus scapulatus*). *J. Comp. Neurol.* 335, 55–72. doi: 10.1002/cne.903350105

Samollow, P. B. (2008). The opossum genome: insights and opportunities from an alternative mammal. *Genome Res.* 18, 1199–1215. doi: 10.1101/gr.065326.107

Scholl, B., Pattadkal, J. J., Rowe, A., and Priebe, N. J. (2017). Functional characterization and spatial clustering of visual cortical neurons in the predatory grasshopper mouse *Onychomys arenicola*. *J. Neurophysiol.* 117, 910–918. doi: 10.1152/jn.00779.2016

Scholl, B., Tan, A. Y. Y., Corey, J., and Priebe, N. J. (2013). Emergence of orientation selectivity in the mammalian visual pathway. *J. Neurosci.* 33, 10616–10624. doi: 10.1523/jneurosci.0404-13.2013

Schottdorf, M., Eglen, S. J., Wolf, F., and Keil, W. (2014). Can retinal ganglion cell dipoles seed Iso-orientation domains in the visual cortex? *PLoS One* 9:e86139. doi: 10.1371/journal.pone.0086139

Schummers, J., Mariño, J., and Sur, M. (2002). Synaptic integration by V1 neurons depends on location within the orientation map. *Neuron* 36, 969–978. doi: 10.1016/s0896-6273(02)01012-7

Seelke, A. M. H., Dooley, J. C., and Krubitzer, L. A. (2012). The emergence of somatotopic maps of the body in S1 in rats: the correspondence between functional and anatomical organization. *PLoS One* 7:e32322. doi: 10.1371/journal.pone.0032322

Shinozaki, A., Hosaka, Y., Imagawa, T., and Uehara, M. (2010). Topography of ganglion cells and photoreceptors in the sheep retina. *J. Comp. Neurol.* 518, 2305–2315. doi: 10.1002/cne.22333

Silveira, L. C. L., Picanço-Diniz, C. W., and Oswaldo-Cruz, E. (1989). Distribution and size of ganglion cells in the retinae of large Amazon rodents. *Vis. Neurosci.* 2, 221–235. doi: 10.1017/s0952523800001140

Soodak, R. E., Shapley, R. M., and Kaplan, E. (1987). Linear mechanism of orientation tuning in the retina and lateral geniculate nucleus of the cat. *J. Neurophysiol.* 58, 267–275. doi: 10.1152/jn.1987.58.2.267

Springer, M. S., Murphy, W. J., Eizirik, E., and Obrien, S. J. (2003). Placental mammal diversification and the cretaceous-tertiary boundary. *Proc. Natl. Acad. Sci.* 100, 1056–1061. doi: 10.1073/pnas.0334222100

Stevens, C. F. (2001). An evolutionary scaling law for the primate visual system and its basis in cortical function. *Nature* 411, 193–195. doi: 10.1038/35075572

Swindale, N. V. (1996). The development of topography in the visual cortex: a review of models. *Network* 7, 161–247. doi: 10.1088/0954-898x_7_2_002

Tischbirek, C. H., Noda, T., Tohmi, M., Birkner, A., Nelken, I., and Konnerth, A. (2019). In vivo functional mapping of a cortical column at single-neuron resolution. *Cell Rep.* 27, 1319–1326.e5. doi: 10.1016/j.celrep.2019.04.007

Van Hooser, S. D., Alexander, J. F. H., Sooyoung, C., Sacha, B. N., and Louis, J. T. (2005). Orientation selectivity without orientation maps in visual cortex of a highly visual mammal. *J. Neurosci.* 25, 19–28. doi: 10.1523/jneurosci.4042-04.2005

Vidyasagar, T. R., and Eysel, U. T. (2015). Origins of feature selectivities and maps in the mammalian primary visual cortex. *Trends Neurosci.* 38, 475–485. doi: 10.1016/j.tins.2015.06.003

Vidyasagar, T. R., Wye-Dvorak, J., Henry, G. H., and Mark, R. F. (1992). Cytoarchitecture and visual field representation in area 17 of the tammar wallaby (*macropus eugenii*). *J. Comp. Neurol* 325, 291–300. doi: 10.1002/cne.903250211

Vitek, D. J., Schall, J. D., and Leventhal, A. G. (1985). Morphology, central projections, and dendritic field orientation of retinal ganglion cells in the ferret. *J. Comp. Neurol.* 241, 1–11. doi: 10.1002/cne.902410102

Wang, W., Arora, R., Livescu, K., and Bilmes, J. (2015). "On deep multi-view representation learning," in *Proceedings of the International Conference on Machine Learning*, Lille, 1083–1092.

Wässle, H., Boycott, B. B., and Illing, R. B. (1981). Morphology and mosaic of on- and off-beta cells in the cat retina and some functional considerations. *Proc. R. Soc. Lond. Ser. B Biol. Sci.* 212, 177–195. doi: 10.1098/rspb.1981.0033

Webb, S., and Kaas, J. (1976). The sizes and distribution of ganglion cells in the retina of the owl monkey, *Aotus trivirgatus*. *Vision Res.* 16, 1247–1254. doi: 10.1016/0042-6989(76)90049-3

Weigand, M., Sartori, F., and Cuntz, H. (2017). Universal transition from unstructured to structured neural maps. *Proc. Natl. Acad. Sci.* 114, E4057–E4064. doi: 10.1073/pnas.1616163114

Wimborne, B., Mark, R., and Ibbotson, M. (1999). Distribution of retinogeniculate cells in the Tammar wallaby in relation to decussation at the optic chiasm. *J. Comp. Neurol.* 405, 128–140. doi: 10.1002/(sici)1096-9861(19990301)405:1<128::aid-cne9>3.0.co;2-h

Xu, X., Bosking, W., Sáry, G., Stefansic, J., Shima, D., and Casagrande, V. (2004). Functional organization of visual cortex in the owl monkey. *J. Neurosci.* 24, 6237–6247. doi: 10.1523/jneurosci.1144-04.2004

Zepeda, A., Arias, C., and Sengpiel, F. (2004). Optical imaging of intrinsic signals: recent developments in the methodology and its applications. *J. Neurosci. Methods* 136, 1–21. doi: 10.1016/j.jneumeth.2004.02.025

Conflict of Interest: The authors declare that the research was conducted in the absence of any commercial or financial relationships that could be construed as a potential conflict of interest.

frontiers in Neuroinformatics

ORIGINAL RESEARCH
published: 20 August 2020
doi: 10.3389/fninf.2020.00041

Development and Reorganization of Orientation Representation in the Cat Visual Cortex: Experience-Dependent Synaptic Rewiring in Early Life

Shigeru Tanaka[1], Masanobu Miyashita[2], Nodoka Wakabayashi[3], Kazunori O'Hashi[4], Toshiki Tani[5] and Jérôme Ribot[6]*

[1] Center for Neuroscience and Biomedical Engineering, The University of Electro-Communications, Chofu, Japan, [2] Department of Control and Computer Engineering, National Institute of Technology, Numazu College, Numazu, Japan, [3] Power Plant Engineering, Engineering & Maintenance Center, All Nippon Airways Co., Ltd., Tokyo, Japan, [4] Department of Mental Disorder Research, National Institute of Neuroscience, National Center of Neurology and Psychiatry, Kodaira, Japan, [5] Laboratory for Molecular Analysis of Higher Brain Functions, RIKEN Center for Brain Science, Wako, Japan, [6] Centre for Interdisciplinary Research in Biology, Collège de France, Paris, France

To date, numerous mathematical models have been proposed on the basis of some types of Hebbian synaptic learning to account for the activity-dependent development of orientation maps as well as neuronal orientation selectivity. These models successfully reproduced orientation map-like spatial patterns. Nevertheless, we still have questions: (1) How does synaptic rewiring occur in the visual cortex during the formation of orderly orientation maps in early life? (2) How does visual experience contribute to the maturation of orientation selectivity of visual cortical neurons and reorganize orientation maps? (3) How does the sensitive period for orientation plasticity end? In this study, we performed animal experiments and mathematical modeling to understand the mechanisms underlying synaptic rewiring for experience-dependent formation and reorganization of orientation maps. At first, we visualized orientation maps from the intrinsic signal optical imaging in area 17 of kittens reared under single-orientation exposure through cylindrical-lens-fitted goggles. The experiments revealed that the degree of expansion of cortical domains representing the experienced orientation depends on the age at which the single-orientation exposure starts. As a result, we obtained the sensitive period profile for orientation plasticity. Next, we refined our previously proposed mathematical model for the activity-dependent self-organization of thalamo-cortical inputs on the assumption that rewiring is caused by the competitive interactions among transient synaptic contacts on the same dendritic spine. Although various kinds of molecules have been reported to be involved in such interactions, we attempt to build a mathematical model to describe synaptic rewiring focusing on brain-derived neurotrophic factor (BDNF) and its related molecules. Performing computer simulations based on the refined model, we successfully reproduced orientation maps reorganized in kittens reared under single-orientation exposure as well as normal visual experience. We also reproduced the experimentally obtained sensitive period profile

OPEN ACCESS

Edited by:
Ludovico Minati,
Tokyo Institute of Technology, Japan

Reviewed by:
Geoffrey Goodhill,
The University of Queensland, Australia
Nick Swindale,
The University of British Columbia, Canada

***Correspondence:**
Shigeru Tanaka
shigeru@uec.ac.jp

Received: *06 December 2019*
Accepted: *28 July 2020*
Published: *20 August 2020*

Citation:
Tanaka S, Miyashita M, Wakabayashi N, O'Hashi K, Tani T and Ribot J (2020) Development and Reorganization of Orientation Representation in the Cat Visual Cortex: Experience-Dependent Synaptic Rewiring in Early Life. Front. Neuroinform. 14:41. doi: 10.3389/fninf.2020.00041

for orientation plasticity. The excellent agreement between experimental observations and theoretical reproductions suggests that the BDNF-induced competitive interaction among synaptic contacts from different axons on the same spine is an important factor for the experience-dependent formation and reorganization of orientation selectivity and orientation maps.

Keywords: orientation maps, self-organization, visual experience, development, sensitive period

INTRODUCTION

In the visual cortices of cats and macaques, there are representations of specific visual features, such as orientation preference, direction of motion preference, ocular dominance, and retinotopy (Hubel and Wiesel, 1962, 1968, 1974, 1977; Hubel et al., 1977; Tusa et al., 1978, 1979; Swindale et al., 1987; Swindale, 1988). These feature representations emerge as columns in the 3D visual cortex, because neuronal response properties are similar in the depth direction from the pia mater to white matter. In particular, the tangential patterns of the columns along the cortical surface are called functional maps, such as orientation maps and ocular dominance maps (Bonhoeffer and Grinvald, 1991; Kim et al., 1999). The development of ocular dominance has been studied in depth because of the relative ease of visual experience manipulations in experiments. In macaques and cats, numerous experiments have shown that monocular deprivation in young animals induced the expansion of cortical domains receiving non-deprived eye inputs and the shrinkage of domains receiving deprived eye inputs (Hubel and Wiesel, 1965; Hubel et al., 1977; Shatz and Stryker, 1978; LeVay et al., 1980; Olson and Freeman, 1980). Even for the rodent visual cortex, it has been revealed that neurons in the binocular zone in the primary visual cortex decreased responses to visual stimuli presented to the deprived eye (Fagiolini et al., 1994; Bear and Rittenhouse, 1999; Fagiolini and Hensch, 2000). In contrast, the experimental manipulation of orientation experience is more difficult than the manipulation needed for the induction of ocular dominance shift. For example, Blakemore and Cooper (1970) exposed kittens to a vertical or horizontal orientation for several hours a day, keeping the kittens inside a drum where vertical or horizontal lines were painted on the inner wall. At other times, they reared the animals in a dark room with their mother cats to prevent visual experience other than vertical or horizontal lines. They demonstrated that neurons selectively responding to experienced orientations were more frequently encountered in their electrophysiological recordings conducted after the visual experience manipulation for several months (Blakemore and Cooper, 1970; Hirsch and Spinelli, 1970). Later, Stryker and Sherk (1975) repeated similar experiments but they were not able to reproduce Blakemore and Cooper's results with statistical significance.

So far, a few groups have conducted intrinsic signal optical imaging in the cat visual cortex to elucidate the effect of single-orientation exposure on orientation maps, and showed the expansion of cortical territory representing the exposed orientation (Sengpiel et al., 1999; Cloherty et al., 2016). However, in the previous studies, daily dark rearing periods were intervened between single-orientation exposure for several hours a day using either a drum or goggles, so that kittens were cared by their mother cats in dark rooms without exposure to orientations other than the intended orientation (Blakemore and Cooper, 1970; Hirsch and Spinelli, 1970; Rauschecker and Singer, 1981; Sengpiel et al., 1999; Cloherty et al., 2016). To get rid of the dark rearing periods and expose animals to a single orientation stably in the standard animal cages with their mother cats, we have fabricated cylindrical-lens-fitted goggles and developed a method to mount them on the foreheads of kittens (Tanaka et al., 2007). Using these goggles, we have successfully realized continuous single-orientation exposure for a few months without daily dark rearing intervention. Owing to this visual experience manipulation method and using intrinsic signal optical imaging, we have observed the conspicuous expansion of cortical domains representing the exposed orientation (Tanaka et al., 2006), and obtained the sensitive period profile for orientation plasticity in area 17 of kittens, in which 2-week goggle rearing (GR) started from postnatal day 10 (P10) to P73 (Tanaka et al., 2009).

To elucidate biologically plausible mechanisms of synaptic rewiring underlying the map reorganization, we focused on the effects of brain-derived neurotrophic factor (BDNF) and its functionally related molecules on structural plasticity of synaptic connections. We refined our previously proposed model of the self-organization of afferent inputs (Tanaka et al., 2004; Tanaka and Miyashita, 2009), postulating that postsynaptic dendritic spines, presynaptic axonal terminals, and astrocytic processes interact with each other for the formation and elimination of synaptic contacts during development. We applied this model to the development of afferent inputs from the lateral geniculate nucleus (LGN) to the primary visual cortex to examine whether the activity-dependent synaptic rewiring accounts for our experimental observations. At first, we generated random afferent inputs with rough retinotopy. Then, we performed simulations presenting 24 directional drifting gratings to the model retina (12-orientation exposure) for different simulation steps. Next, we resumed simulations presenting only a vertically oriented grating (single-orientation exposure) for a fixed number of simulation steps, using afferent input patterns self-organized under 12-orientation exposure for certain simulation steps. As a result, cortical neurons selectively responding to the exposed vertical orientation increased in number. However, the longer the model experienced gratings from all 12 orientations before only a single orientation was presented, the fewer neurons became selective for this orientation. On the basis of the simulation results, we obtained a theoretical profile of the sensitive period for orientation plasticity, which resembled the experimentally observed one. The excellent agreement between experimental findings and simulation results may shed light on

the molecular mechanisms underlying synaptic rewiring in the developing visual cortex.

MATERIALS AND METHODS

Experiments on Cats

The surgical operation and optical imaging were approved by the Institutional Animal Research Committee in RIKEN (No. H13-B040 and H17-2B043) and were performed in accordance with the "*Guiding Principles for the Care and Use of Animals in the Field of Physiological Science*" of the Japanese Physiological Society.

Goggles for Single-Orientation Exposure

To realize continuous single-orientation exposure without the intervention of daily dark rearing periods and stabilize the experienced orientation in the retinal coordinate, we fabricated goggles fitted with planoconvex acrylic cylindrical lenses (**Figure 1A**; lens thickness, 10.0 mm; lens aperture diameter, 15.0 mm; lens power, +67 D), through which the animals experienced elongated visual images of their environments (**Figures 1B,C**; Tanaka et al., 2007). The goggles were easily attached to and detached from the head holder fixed on the foreheads of kittens (**Figure 1A**), which enabled us to clean the lenses within a few minutes every day. Using this method, we were able to continuously expose kittens to a single orientation for 4 months in the standard animal cages. The behavior of goggle-mounted kittens was generally not distinct from that of normally reared kittens. We carried out intrinsic signal optical imaging of neural activities in areas 17 and 18 of kittens reared with/without cylindrical-lens-fitted goggles under a normal visual environment to observe how orientation maps are reorganized by single-orientation exposure. The use of cylindrical-lens-fitted goggles is an excellent rearing regimen for single-orientation exposure, which is comparable to monocular deprivation to study the mechanisms of ocular dominance shift. Our intrinsic signal optical imaging showed a marked over-representation of the experienced orientation for any exposed orientation (Tanaka et al., 2006). Surgical operations and optical imaging methods are described elsewhere in detail (Tanaka et al., 2006, 2009), but the basic experimental procedures are shown below.

Surgical Procedure

Initial anesthesia was induced using ketamine hydrochloride (5.0 mg/kg, i.m.) following sedation with medetomidine hydrochloride (0.1 mg/kg, i.m.). The animals were fixed on a stereotaxic apparatus and were artificially ventilated with a 60:40% mixture of N_2O and O_2 containing 0.5–1.0% isoflurane. Heart rate, end-tidal CO_2 concentration, and rectal temperature were continuously monitored during surgery. A metal head holder for fixing the goggles and a metal chamber for optical imaging were cemented on the animal's skull using dental resin, and the skull and dura mater covering the recording area of the lateral gyrus were removed. The cranial window (17 mm × 12 mm) was positioned approximately from P5 to A12 on the AP axis, spanning the midline (**Figure 2**). Next, the chamber was filled with 2% agar and sealed with a polyvinylidene chloride thin film and a plastic plate. Finally, the frame of the goggles was fixed to a head holder, and the position of the goggles was

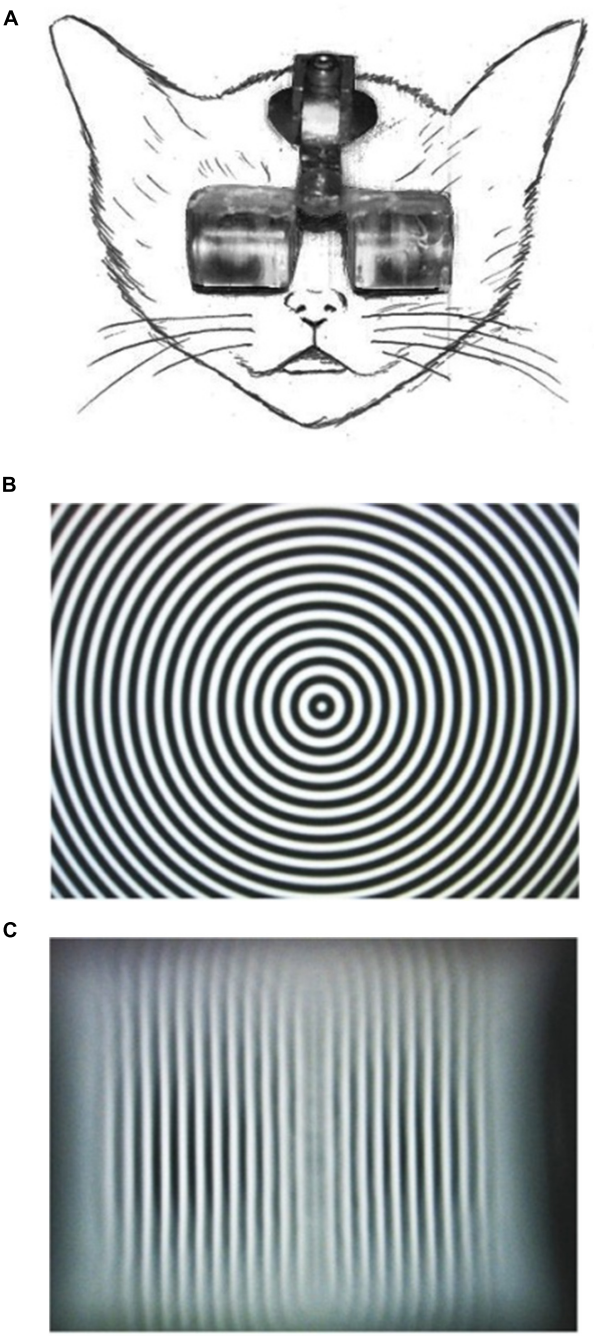

FIGURE 1 | Picture of a goggle-mounted kitten **(A)**, and transformation of a circular stripe **(B)** to a vertical stripe **(C)** by viewing through the goggles.

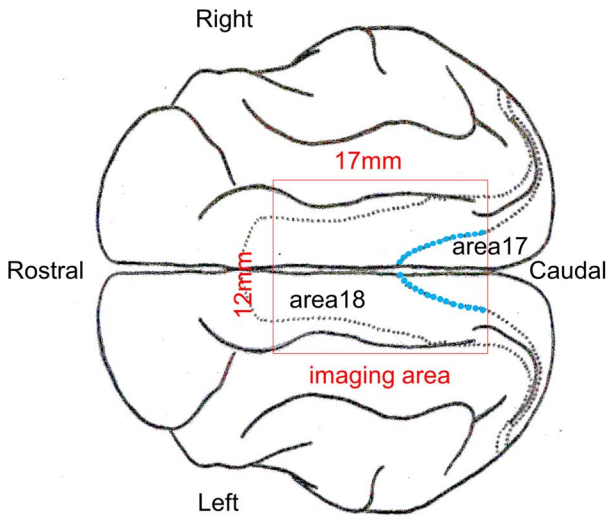

FIGURE 2 | Schematic picture of a cat cerebral cortex in the top view. The optical imaging was performed inside the red rectangle. The anatomically identified border between areas 17 and 18 in each hemisphere inside the imaging area is indicated by the blue dotted curve.

calibrated so that the cylindrical lenses covered the visual field as widely as possible.

Optical Imaging

Animals were anesthetized as in surgery and paralyzed with pancuronium bromide (0.1 mg/kg/h). Then, goggles were taken off for optical imaging in goggle-reared kittens. The animals were artificially ventilated. Contact lenses with appropriate curvatures were used to prevent the drying of the eyes. The cortex was illuminated with a 700-nm wavelength light. The focal plane was adjusted to 500 μm below the cortical surface using a tandem-lens macroscope arrangement (Bonhoeffer and Grinvald, 1996). Intrinsic optical signals were measured while the animals were exposed to visual stimuli displayed on a 20-inch CRT monitor placed 30 cm in front of the animal. Images were obtained with a CCD video camera, and digitized and stored using CAPOS (320 × 240 pixels) (Tsunoda et al., 2001) or Imager 3001 (744 × 480 pixels) (Optical imaging Inc. New York). For each stimulus presentation, the intrinsic signal was recorded for 1.0 s before and 5.0 s after the stimulus onset. A blank stimulus (a uniform gray stimulus) was presented for 15 s between successive captures of intrinsic signals. Each visual stimulus was presented once in a pseudorandom sequence in a single trial of recordings. Twenty-six to 30 trials were collected in each recording session. As visual stimuli, we used full-screen square-wave gratings, which drifted in two directions at six equally spaced orientations (30° interval). In the cat visual cortex, orientation maps appeared in area 18 as well as in area 17. It has been reported that spatial frequencies of 0.5 and 0.15 cpd are optimal for neuronal activation in areas 17 and 18, respectively (Movshon et al., 1978; Bonhoeffer and Grinvald, 1991; Ohki et al., 2000). Thus, we used these two spatial frequencies of grating stimuli to identify areas 17 and 18 differentially. The temporal frequency of the gratings was fixed at 2.0 Hz. The optical imaging in one session was completed within 5 h.

Analysis Methods of Intrinsic Signals

One trial of imaging was composed of six frames (duration of each frame, 1 s). To extract stimulus-related intrinsic signals, we subtracted signals recorded in the first frame (without stimulus presentation) from those signals recorded in succeeding frames with stimulus presentations. Then, we averaged the subtracted signals over the 4th to 6th frames for each trial. Next, we applied the generalized indicator function method (GIFM) to these averaged signals (Yokoo et al., 2001), which efficiently excluded noisy signals originating from volume and oxygenation changes in thick blood vessels and spatially slowly varying fluctuations of signals inherent in the recorded intrinsic signals. The GIFM eliminates spatially slowly varying point-spread components of intrinsic signal (Gilbert et al., 1996), which may partially contain responses to the exposed orientation. Therefore, the image data processing based on the GIFM underestimates the degree of over-representation of exposed orientation induced by GR.

Then, we summed the stimulus-related signals over all trials for each stimulus orientation and applied Gaussian low-pass filtering with a 150-mm standard deviation to eliminate high-frequency noise. In this way, we constructed a single-orientation map for each stimulus orientation. We also defined an integrated response-strength map by summing single-orientation maps over all stimulus orientations.

The preferred orientation and orientation magnitude at each pixel were determined by the vector sum method (Bonhoeffer and Grinvald, 1991). The orientation magnitude, which is the modulation amplitude of the second harmonic components in the Fourier expansion of signals with respect to the stimulus orientation, was used as one of indices for orientation selectivity. The orientation polar map was constructed with the preferred orientation and orientation magnitude as color and brightness, respectively.

Area 17 was identified to be the cortical domains, in which the integrated response strength for the stimulus spatial frequency of 0.5 cpd is larger than a half of those averaged inside the recorded area. In orientation polar maps, we delimited such functionally identified area 17 by the white lines. Although the orientation selectivity of neurons in the two areas seems to develop almost in parallel, we focused on the development and reorganization of orientation maps in area 17 in this paper (**Supplementary Figure 1**).

Mathematical Modeling

Hypothetical Mechanisms of Synaptic Rewiring

For building a mathematical model of synaptic rewiring during development, our basic idea is that individual synapses compete for survival, and only functionally adequate synapses can survive. Such synapse competition may be mediated and/or modulated by interactions among various types of molecules, such as cell adhesion molecules, chondroitin sulfate proteoglycans, neurotrophins, and proteases. These molecules

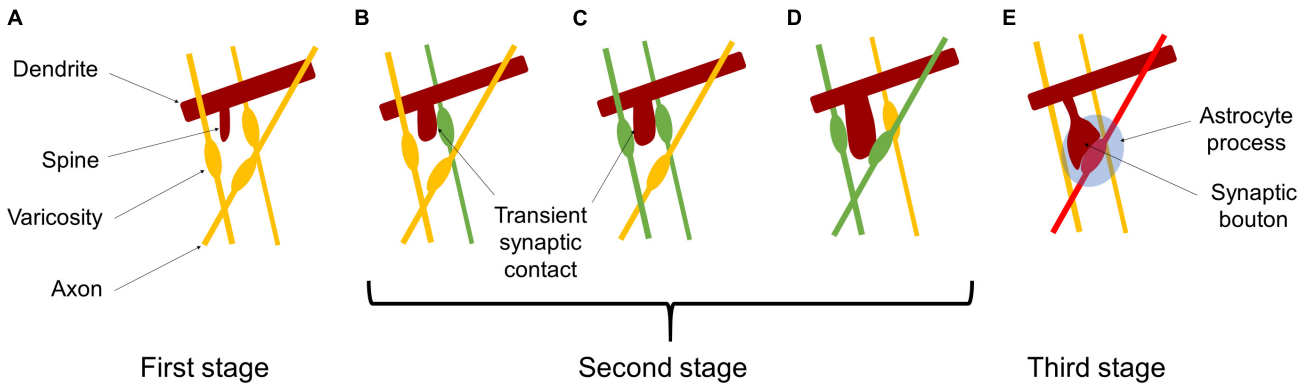

FIGURE 3 | Schematic pictures of synaptic rewiring. **(A)** A spine (brown) is generated and elongated toward adjacent axonal varicosities (orange). **(B)** The spine catches one of axonal varicosities to make a transient synaptic contact (green). **(C)** The spine changes its shape and moves to make another transient synaptic contact (green), and the two synaptic contacts start to compete each other. **(D)** One of the transient synapses survives on the spine (green) and the other retracts (orange). On the other hand, the spine makes a transient synaptic contact with another axon to start competition again. **(E)** In the late stage of the sensitive period, one transient synaptic contact wins the competition as a stabilized synapse (red). Pre- and postsynaptic structures are wrapped by the astrocyte process, forming a tripartite synapse.

and functional proteins, which are expressed on the cell surface or released to the extracellular space, may work to stabilize labile synaptic contacts in some cases and destabilize synapses in some other cases. Three stages of synapse maturation are schematically shown in **Figure 3**. At the first stage (**Figure 3A**), a neurite (brown) generated on a dendrite and elongated toward neighboring varicosities on presynaptic axons (yellow). At the second stage, one of the varicosities wins the competition to make a transient synaptic contact (green), as shown in **Figure 3B**. Then, another axonal varicosity makes a transient synaptic contact (green), and the two synaptic contacts start competing to occupy the spine, as shown in **Figure 3C**. One of the transient synaptic contacts survives (green) on the spine and the other retracts (yellow), as depicted in **Figure 3D**. Such a rewiring process of transient synaptic contacts is repeated during the sensitive period (**Figures 3B–D**). At the third stage, transient and labile synaptic contacts disappear leaving one stabilized synapse (red). Finally pre- and postsynaptic structures are wrapped by the astrocyte process, forming a tripartite synapse (Araque et al., 1999), as shown in **Figure 3E**.

To mathematically describe synapse competition that may occur on small regions of dendrites, resulting in the stabilization and elimination of transient synapses, here we postulate the following Lotka-Volterra equations (Hofbauer and Sigmund, 1988; Fukai and Tanaka, 1997) in an analogy to ecological systems in which species compete with each other for the same resources and/or niches. When ρ_k represents the population of kth species, the dynamics of $\{\rho_k\}$ is given by:

$$\frac{d}{dt}\rho_k = a_k\rho_k - \sum_{k'}\rho_{k'}\rho_k \tag{1}$$

where a_k describes the effect of common resources on the growth rate of the kth species population. The second term represents competition among species. According to the basic property of the competitive Lotka–Volterra equation, a winner of the competition is determined to be a non-zero element of a stable fixed point solution to Equation (1). When a_{k_0} is the maximum of all $a_k{}'$ s, that is,

$$k_0 = \arg\max_k \{a_k\} \tag{2}$$

the steady-state solution is given by

$$\rho_{k_0} = a_{k_0} \quad \text{and} \quad \rho_k = 0 \ \left(\text{for } k \neq k_0\right) \tag{3}$$

For synapse formation, a_k corresponds to the growth rate of synaptic contacts at a small region of a target dendrite, mediated by various types of cell adhesion molecules and neurotrophins; some molecules are secreted in an activity-dependent manner. Among them, we pay a special attention to the effects of the BDNF (Binder and Scharfman, 2004) and tissue-plasminogen activator (tPA) (Mataga et al., 2002, 2004).

BDNF regulates the late-phase long-term potentiation (L-LTP) of synaptic transmission efficacy (Frey et al., 1996) and facilitates survival of synapses in the developing brain (Cunha et al., 2010; Numakawa et al., 2010). BDNF is synthesized as pre-proBDNF, and its presequence is cleaved off in the endoplasmic reticulum. Then, proBDNF is sorted in the Golgi apparatus into the regulated pathway and constitutive pathway (Kuczewski et al., 2009). In these pathways, proBDNF is considered to be partially converted to mature BDNF (mBDNF), and proBDNF and mBDNF are contained inside vesicles. In the regulated pathway, they are released to the extracellular space by Ca^{2+}-induced exocytosis. Released proBDNF and mBDNF bind to pan-neurotrophin receptor p75 and TrkB receptors, respectively (Yang et al., 2016), which are expressed on the cell surface of neurons and glial cells. During development, proBDNF signaling through $p75^{NTR}$ leads to the elimination of transient

synaptic contacts (Teng et al., 2005; Singh et al., 2008), and the binding of mBDNF to TrkB leads to L-LTP (Pang et al., 2004) and stabilizes transient synaptic contacts. Particularly, in neuromuscular junctions, synaptic retraction has been reported to be mediated by presynaptic $p75^{NTR}$ signaling during synaptic competition (Je et al., 2012). In the rat visual cortex, $p75^{NTR}$ expression in parvalbumin-positive (PV) cells and putative pyramidal neurons is likely to be temporally regulated during development (Bracken and Turrigiano, 2009), and decreases between P14 and P26, at a time when PV cell synapse numbers increase dramatically (Baho et al., 2019).

On the other hand, tPA is known to be a protease that cleaves plasminogen to generate plasmin (Tsai, 2017). In turn, plasmin cleaves perineuronal nets composed of a condensed matrix of chondroitin sulfate proteoglycans (Berardi and Pizzorusso, 2004; McRae and Porter, 2012), and converts proBDNF to mBDNF in the extracellular space. In addition, it has been reported that the secretion of tPA from neurons is also triggered by intracellular calcium concentration elevated by neuronal activity. Importantly, for a higher elevation of Ca^{2+} concentration, which occurs as in tetanic stimulation, tPA is released to activate the tPA/plasmin system, and the resultant plasmin converts proBDNF to further increase the amount of mBDNF in the extracellular space (Greenberg et al., 2009; Nagappan et al., 2009). This results in the induction of L-LTP and the stabilization of transient synaptic contacts. In contrast, a moderate elevation of Ca^{2+} concentration releases less tPA, which is unlikely to activate the tPA/plasmin system. A higher ratio of the amount of proBDNF to that of mBDNF in the synaptic cleft induces LTD and consequently elimination of transient synapses. On the basis of these facts, we hypothesize that a high concentration of intracellular Ca^{2+} taken up through NMDA channels and/or voltage-dependent calcium channels tends to assist the survival and stabilization of synapses. A moderate Ca^{2+} concentration tends to facilitate synapse pruning.

Brain-derived neurotrophic factor is also secreted from the constitutive pathway in an activity-independent manner (Lesmann and Brigadski, 2009; Cunha et al., 2010). The release of BDNF from the constitutive pathway and/or from presynaptic axons may contribute to the attractive interaction between dendritic spines and varicosities along the axons at the first and second stages of synaptogenesis (**Figures 3A–D**). BDNF released from postsynaptic dendrites may also induces competition of a presynaptic contact with other contacts (**Figures 3B–D**). At the late stage (**Figure 3E**), the expression of $p75^{NTR}$ on the surfaces of pre- and postsynaptic neurons increases to bind proBDNF, resulting in the weakening of synaptic contacts. Instead, processes of a neighboring astrocyte expand contact area with the dendrite. The competition between the synaptic contacts and the processes of the astrocyte leads to the morphological changes of the dendritic spine, and finally the formation of stable tripartite synapses.

Thus, we propose the following dynamics of the synaptic contact area ρ_k at the second stage:

$$\tau_{syn}\frac{d}{dt}\rho_k = \left(a_k + b_k\right)\rho_k - \sum_{k'}\rho_{k'}\rho_k \tag{4}$$

$$a_k = \bar{a} + \Delta a_k \tag{5}$$

$$b_k = b_k^{mature} - b_k^{pro} \tag{6}$$

a_k represents the activity-independent synapse growth rate, which is assumed to be proportional to the amount of cell adhesion molecules and BDNF secreted from the constitutive pathway. Owing to its activity independence, $a_k$is regarded to be constant over time. However, it may vary for different locations, because different amounts of cell adhesion molecules may be expressed at different synaptic contacts. The mean and fluctuation of a_k are denoted as $\bar{a}$ andΔa_k, respectively. $b_k$represents the Ca^{2+}-dependent synapse growth rate, which is given by the difference in the amounts of mBDNF and proBDNF, $b_k^{mature} - b_k^{pro}$. $\tau_{syn}$is a constant related to the time scale of synaptic modification. In early life, in which the perineuronal net is labile, $\tau_{syn}$is small and synaptic contacts are easy to change, whereas after the perineuronal net is robustly established, $\tau_{syn}$is sufficiently large and synaptic connections no longer change. Without loss of generality, we set $\bar{a} = 1$.

A higher elevation of Ca^{2+} concentration is likely to occur when NMDA receptor activation coincides with backpropagating action potential (bAP) (Markram et al., 1997; Koester and Sakmann, 1998, 2000; Nevian and Sakmann, 2004) and triggers a Ca^{2+}-dependent dendritic release of tPA as well as BDNF. The released BDNF is cleaved by tPA in the extracellular space to produce mBDNF. In contrast, a moderate elevation of Ca^{2+} concentration may take place when only NMDA receptors are activated in the absence of bAPs. In this case, the proBDNF may be richer in the released BDNF, because the tPA/plasmin system is less activated. Consequently, b_k at the kth synaptic contact is obtained as

$$b_k = \Theta(\varsigma^{post} - \vartheta)\varsigma^{post}\eta_k^{pre} - c^{D/P}\left(1 - \Theta(\varsigma^{post} - \vartheta)\right)\varsigma^{post}\eta_k^{pre} \tag{7}$$

Here, ς^{post} andϑ are postsynaptic membrane depolarization and the threshold for the generation of action potential, respectively. η_k^{pre} represents firing frequency transmitted through the kth synaptic contact. $\Theta(x)$ is the Heaviside function of x. $\Theta(\varsigma^{post} - \vartheta)$ takes unity for the arrival of a bAP generated at the cell body ($\varsigma^{post} > \vartheta$), and 0 otherwise. Therefore, the first term on the right-hand side of Equation (7) represents the amount of mBDNF that facilitates L-LTP induction. In contrast, the second term represents the amount of proBDNF that facilitates LTD. Here, $1 - \Theta(\varsigma^{post} - \vartheta)$ indicates the absence of bAPs. The coefficient $c^{D/P}$ is the efficiency ratio of depression to potentiation. The basic logic mentioned above is common to that of the BCM model (Bienenstock et al., 1982). However, the present model is devoted to the rewiring of synaptic contacts rather than synaptic efficacy changes at individual synapses. The synaptic efficacy at the kth axonal bouton changes depending on b_k alone: LTP occurs for

$b_k > 0$, whereas LTD occurs for $b_k < 0$. The rewiring of synaptic contacts from the kth axonal bouton to the k'th axonal bouton is determined by the difference of the growth rates $b_{k'} - b_k$, as described in the following section.

Neuronal activity changes in the order of milliseconds, but synaptic contacts change in longer time scales τ_{syn}. Therefore, the dynamics of synaptic contacts can be approximately described by an equation in which b_k is replaced with its temporal average $\langle b_k \rangle$.

Activity-Dependent Synaptic Rewiring

The present model focuses on synaptic competitive rewiring repeatedly occurs during the second stage (**Figures 3B–D**). It is considered that a transient synaptic contact receiving a larger amount of mBDNF and a less amount of proBDNF is likely to win the competition against the other transient synaptic contacts. More specifically, when there are two transient synaptic contacts from the kth and k'th axons to the spine in question, for $\langle b_{k'} \rangle > \langle b_k \rangle$ k'th synaptic contact is stabilized to survive, and the kth contact is disconnected. Then, the spine changes its morphology to make a transient contact with another adjacent axon as a next competitor. After repeated rewiring of transient synaptic contacts, adequate synapses are formed at suitable locations of a target neuron.

Here, we rewrite a steady-state solution to Equation (3) with respect to $\{\rho_k\}$as$\left\{\sigma_k \middle| \sigma_k = 1, 0; \sum_k \sigma_k = 1\right\}$, omitting the absolute value that may represent synaptic transmission efficacy. The mathematical expression $\sigma_k = 1$ or 0 indicates the presence or absence of a synaptic connection. This approximation is based on the idea that activity propagation during development depends more on the variation in the number of synaptic connections than the variation in the transmission efficacy at each synapse. The probability of synaptic rewiring from $\{\sigma_k = 1, \sigma_{k'} = 0\}$ to $\{\sigma_k = 0, \sigma_{k'} = 1\}$ is given by the ensemble-averaged Heaviside function of the difference in the synapse growth rates as follows:

$$P(\sigma_k = 1 \to \sigma_{k'} = 1) = \left[\Theta\left(\langle b_{k'} \rangle + \Delta a_{k'} - \langle b_k \rangle - \Delta a_k\right)\right]_{av} \tag{8}$$

where $[X]_{av}$ indicates ensemble averaging of X with respect to fluctuation $\{\Delta a_k\}$. When we assume that $\{\Delta a_k\}$ obeys the Gaussian distribution with mean 0 and variance s^2 for mathematical simplicity, the ensemble-averaged rewiring probability is given by the error function. The error function is approximated by the logistic function with an excellent fitness (Tanaka, 1990). Finally, the rewiring probability of transient synaptic contacts is obtained as

$$P(\sigma_k = 1 \to \sigma_{k'} = 1) = \frac{1}{1 + e^{-\beta(\langle b_{k'} \rangle - \langle b_k \rangle)}} \tag{9}$$

Using s, the inverse fictitious temperature β in Equation (9) is given as

$$\beta = \frac{2}{\sqrt{\pi} s} \tag{10}$$

The spine motility, which is also regulated by the balance in the activation of TrkB and $p75^{NTR}$, affects the accessibility to an adjacent axonal varicosity as a next competitor. BDNF released from the constitutive pathway of a target dendrite and/or released from varicosities along the presynaptic axons may be responsible for the TrkB and $p75^{NTR}$ activation. It is considered that the probability of transition from an axonal varicosity to a transient synaptic contact is given by a similar form of Equation (9) as

$$P(\sigma_k = 0 \to \sigma_k = 1) = \frac{1}{1 + e^{-\beta g_k(t)}} \tag{11}$$

where $g_k(t)$ represents the growth rate of a dendritic spine toward a varicosity on the kth axon to make a transient synaptic contact. It is mainly determined by the difference in the activation of TrkB and $p75^{NTR}$ expressed on the spine in question. For simplicity, we consider that BDNF released from the activity-independent constitutive pathway signals to the spine in an autocrine fashion, and that the expression of $p75^{NTR}$ strongly depend on the age: In the middle of the sensitive period, the expression level of $p75^{NTR}$ is sufficiently low, and at the late stage, however, the level of $p75^{NTR}$ increases. To model the effect of the age-dependent expression of $p75^{NTR}$, we adopt the following form of $g_k(t)$:

$$g_k(t) = -\xi_{\max}\left(\frac{t}{T_p + t}\right)^4 \tag{12}$$

Here, $\xi_{\max}$ is proportional to the maximum amount of $p75^{NTR}$ expression on the kth axonal bouton around the end of the sensitive period, and T_p is a time constant that determines the width of the time window of synaptic plasticity. For simplicity, $\xi_{\max}$ and T_p are assumed to be constant over the primary visual cortex. $g_k(t)$ should be rapidly increasing and then saturated within the sensitive period. Simulation results suggest that the exponent 4 in Equation (12) well reproduces the sensitive period profile for orientation plasticity.

Now, we apply the mathematical framework derived above to the activity-dependent rewiring of geniculo-cortical afferent inputs for the formation of oriented RFs of individual cortical neurons and the formation of orientation representations. We assumed retinotopic projection from the retina to LGN and the presence of four types of LGN neuron: lagged and non-lagged types (Saul and Humphrey, 1990) for each of the ON- and OFF-center cells. When k represents a position of an LGN neuron, and $\mu_1 = 1(-1)$ and $\mu_2 = 1(-1)$ represent ON (OFF)-center and non-lagged (lagged) types, respectively, Equation (7) in this specific application is rewritten as

$$\begin{aligned}\langle b_{i,k,\mu_1,\mu_2} \rangle = &\left(1 + c^{D/P}\right)\left\langle \Theta(\varsigma_i^{CX} - \vartheta_i)\varsigma_i^{CX}\eta_{k,\mu_1,\mu_2}^{LGN}\right\rangle \\ &- c^{D/P}\left\langle \varsigma_i^{CX}\eta_{k,\mu_1,\mu_2}^{LGN}\right\rangle\end{aligned} \tag{13}$$

ς_i^{CX} and η_i^{CX} represent the membrane potential and firing rate of the i th cortical neuron, respectively. $\eta_{k,\mu_1,\mu_2}^{LGN}$ is the firing rate of the LGN neuron specified by cell type μ_1 and μ_2 and retinotopic position k. Here, we assume that electrotonic distance is sufficiently long beyond the dendritic extent of a postsynaptic neuron, and the evoked membrane potential is independent of the location of a synaptic input on the dendrite. The membrane potential of a cortical neuron ς_i^{CX} measured from the resting level

is given by the sum of the afferent input of LGN neurons' activities ς_i^{AFF} and the lateral interaction:

$$\begin{aligned}\varsigma_i^{CX} &= \varsigma_i^{AFF} + \sum_{i' \neq i} U_{i,i'} \eta_{i'}^{CX} \\ &= \nu \sum_{k,\mu_1,\mu_2} n_{i,k,\mu_1,\mu_2} \eta_{k,\mu_1,\mu_2}^{LGN} + \sum_{i' \neq i} U_{i,i'} \eta_{i'}^{CX} \end{aligned} \quad (14)$$

where n_{i,k,μ_1,μ_2} is the total number of synaptic connections from a presynaptic neuron (k, μ_1, μ_2) to different locations on the dendrites of postsynaptic neuron i:

$$n_{i,k,\mu_1,\mu_2} = \sum_j \sigma_{i,j,k,\mu_1,\mu_2} \quad (15)$$

Using the function $F(x) = x\Theta(x)$, the firing rate of the postsynaptic neuron is half-rectified as

$$\eta_i^{CX} = F\left(\varsigma_i^{CX} - \vartheta_i\right) \quad (16)$$

The threshold ϑ_i at the ith neuron is assumed to be the long-time average of the membrane potential ς_i^{CX}.

The function $U_{i,i'}$ represents short-range excitatory and long-range inhibitory lateral connections between model cortical neurons i and i' given as

$$U_{i,i'} = q\left(\frac{1}{2\pi\lambda_{ex}^2} e^{-\frac{\left(\vec{x}_i - \vec{x}_{i'}\right)^2}{2\lambda_{ex}^2}} - \frac{\kappa_{inh/ex}}{2\pi\lambda_{inh}^2} e^{-\frac{\left(\vec{x}_i - \vec{x}_{i'}\right)^2}{2\lambda_{inh}^2}}\right) \quad (17)$$

$\vec{x}_i$ indicates the position of neuron i in the model visual cortex. The parameters λ_{ex} and λ_{inh} represent the extent of excitatory and inhibitory lateral connections, respectively. q and $\kappa_{inh/ex}$ are the strength of lateral interaction and the ratio of the strengths of inhibition to excitation, respectively.

A schematic diagram of visual pathways in our model is shown in **Figure 4**. In simulations for the development of visual cortical neurons under normal visual conditions, model LGN neurons are activated by the balanced presentation of grating stimuli drifting in 24 directions. In simulations for the development under the exposure to a single orientation through cylindrical-lens-fitted goggles, model LGN neurons are activated by the presentation of only a vertically oriented grating drifting leftward or rightward.

Activities of Model LGN Neurons

The reverse correlation method of electrophysiology has revealed that LGN neurons have spatiotemporally separable ON- or OFF-center RFs (DeAngelis et al., 1995). We use the following mathematical expressions of the LGN RFs, assuming the difference of Gaussian functions as spatial components, and the products of exponential and trigonometric functions as temporal components:

$$R_{k,\mu_1,\mu_2;l}^{LGN}(t) = S_{k,\mu_1;l} T_{\mu_2}(t) \quad (18)$$

Here, the spatial component $S_{k,\mu_1;l}$ and temporal one $T_{\mu_2}(t)$ are given, respectively, as

$$S_{k,\mu_1;l} = \mu_1 \left[\frac{1}{2\pi\lambda_c^2} \exp\left(-\frac{d_{k,l}^2}{2\lambda_c^2}\right) - \frac{\kappa_{s/c}}{2\pi\lambda_s^2} \exp\left(-\frac{d_{k,l}^2}{2\lambda_s^2}\right)\right] \quad (19)$$

$$\mathrm{T}_{+1}(t) = A \exp\left(-\frac{t}{\tau_{decay}}\right) \sin\left(2\pi f_{RFfreq} t\right) \Theta(t) \Theta\left(T_{window} - t\right) \quad (20a)$$

$$\begin{aligned}\mathrm{T}_{-1}(t) = -A \exp&\left(-\frac{T_{window} + \tau_{latency} - t}{\tau_{decay}}\right) \\ &\times \sin\left[2\pi f_{RFfreq}\left(t - \tau_{latency}\right)\right] \\ &\times \Theta\left(t - \tau_{latency}\right) \Theta\left(T_{window} + \tau_{latency} - t\right)\end{aligned} \quad (20b)$$

Parameters λ_c and λ_S indicate the extents of the center and surround subfields of LGN neurons, respectively. $\kappa_{s/c}$is the ratio of the strength of the response to a surround subfield stimulation to that to a center subfield stimulation. $\mathrm{d}_{k,l}$ is the distance in the visual field between positions of the RF center of an LGN neuron k and a light spot presented at l. T_{window}, $\tau_{latency}$, τ_{decay}, and f_{RFfreq} represent the time window of temporal RF, the latency of the lagged response to the non-lagged response, the decay constant of temporal RF, and the temporal frequency of RF, respectively. The values of all parameters in Equations (19), (20a), and (20b) were estimated by the least squares method to fit the experimental data (DeAngelis et al., 1995), and listed in **Table 1**.

In simulations, we used a set of sinusoidal moving grating stimuli $\left\{z_l\left(t \middle| \theta_{DR}, f_{spat}, f_{temp}\right)\right\}$:

$$\begin{aligned}&z_l\left(t \middle| \theta_{DR}, f_{spat}, f_{temp}\right) \\ &\quad = \cos\left[2\pi f_{spat}\left(x_l \cos\theta_{DR} + y_l \sin\theta_{DR}\right) - 2\pi f_{temp} t\right]\end{aligned} \quad (21)$$

where θ_{DR}, f_{spat}, and f_{temp} indicate the direction of movement, spatial frequency, and temporal frequency of a stimulus grating, respectively. x_l and $y_l$are the two components of a given position vector of the lth pixel in the 2D visual field. Responses of model LGN neurons are given by

$$\begin{aligned}&\eta_{k,\mu_1,\mu_2}^{\mathrm{LGN}}(t) \\ &= F\left[\sum_l \int_{-\infty}^{t} dt' R_{k,\mu_1,\mu_2}^{\mathrm{LGN}}(t - t') z_l(t' | \theta_{DR}, f_{spat}, f_{temp})\right]\end{aligned} \quad (22)$$

It is considered that LGN neurons transmit only signals localized around spatial and temporal frequencies characteristic of their receptive fields. Spatial frequencies are band-pass-filtered by the Difference of Gaussian function in Equation (19), and temporal frequencies are also band-pass-filtered by the trigonometric functions in Equations (20a) and (20b). To save time for simulations, we presented only a grating of spatial and temporal frequencies, whose values were close to that of LGN characteristic frequencies. Even if we carry

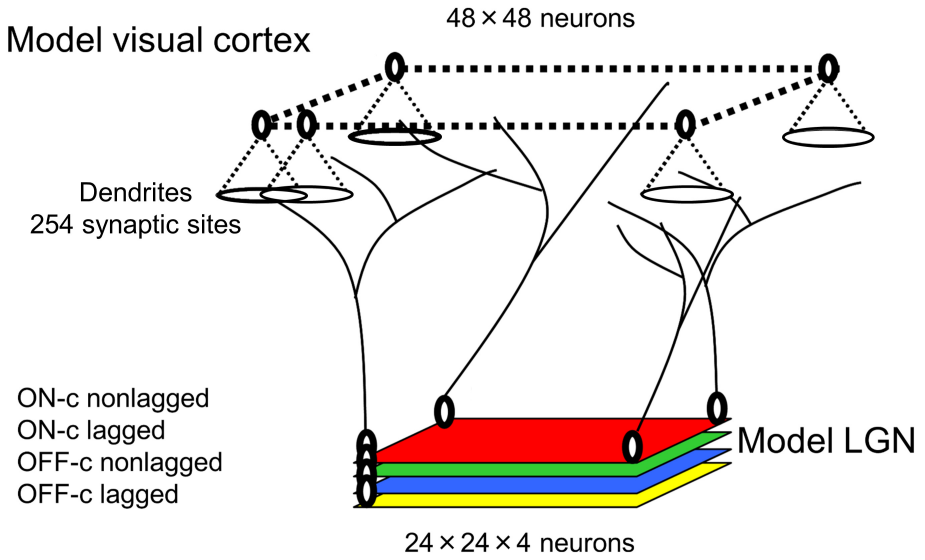

FIGURE 4 | Model visual pathways and layer configurations.

out simulation presenting some range of spatial and temporal frequencies around LGN characteristic frequencies at the expense of time for simulation, we may see cortical neurons strongly responding to narrow ranges of spatial and temporal frequencies. Such simulations remain to be performed in the future study.

More essentially, there is a question about whether patterned visual experience such as grating stimuli in the present model is needed to form orientation selectivity of individual cortical neurons and orderly orientation maps. The formation of orientation-selective receptive fields requires the parallel alignments of receptive field centers of ON- and OFF-center LGN neurons. This requires a specific structure of the activity correlations in three types of LGN neuron pairs: ON-c/ON-c, ON-c/OFF-c, OFF-c/OFF-c. If orientation maps emerge without pattern vision, correlated activities may stem from the LGN or retinal intrinsic circuits. In the present study, we do not address this question, focusing on the issue of experience of drifting oriented gratings on cortical orientation representation.

TABLE 1 | List of parameters and their values.

Parameter	Comments	Value
Afferent input-induced membrane potential		
v	Contribution of afferent inputs to membrane potential	0.045
Cortical interaction function		
λ_{ex}	Extent of excitatory interaction function	82 mm
λ_{inh}	Extent of inhibitory interaction function	328 mm
q	Strength of cortical interaction	4.0
$\kappa_{inh/ex}$	Inhibition/excitation ratio	1.0
Model visual cortex		
$a^{cell-cell}$	Distance between nearest neighbor neurons	50 mm
$a^{spine-spine}$	Distance between nearest neighbor spines	15 mm
LGN receptive field		
λ_c	Extent of center subfield	0.225 deg
λ_s	Extent of surround subfield	0.9 deg
$\kappa_{s/c}$	Surround/center ratio	1.0
A	Coefficient of RF	1.0
τ_{decay}	Decay constant of temporal RF	100 ms
f_{RFfreq}	Temporal frequency of RF	5 Hz
T_{window}	Time window of temporal RF	200 ms
$\tau_{latency}$	Latency of lagged response	57 ms
Sinusoidal moving grating stimulus		
f_{spat}	Spatial frequency of gratings	0.4 cpd
f_{temp}	Temporal frequency of gratings	4 Hz
Transition probability function		
β	Fictitious inverse temperature	250
$c^{D/P}$	Efficiency ratio of depression to potentiation	2.0
ξ_{max}	Maximum amount of p75NTR expression	0.8
T_p	Time window that enables synapses to be rewired	15.75 MCs

Computer Simulation Methods

All programs coding the algorithms for experience-dependent synaptic rewiring of geniculo-cortical afferent inputs and the analysis of response properties of individual neurons and orientation representation in the model visual cortex are available at https://github.com/slforg/synaptic_rewiring_ programs. As shown in **Figure 4**, our model visual cortex consists of neurons in 48 × 48 square arrangements, each of which has a disk-shaped dendritic field of 254 synaptic sites. The model LGN is composed of four layers of 24 × 24 square arrangements of neurons, where the layers represent ON-center non-lagged, OFF-center non-lagged, ON-center lagged, and OFF-center lagged types (Saul and Humphrey, 1990, 1992). The four types of neuron in the model LGN send axons to the model visual cortex. Before conducting simulations, each cortical neuron receives randomized afferent inputs from 324 (9 × 9 × 4) LGN neurons around a position that retinotopically

corresponds to the position of the synaptic site in the model cortex. This randomization process prepares a rough retinotopic projection from the LGN to the visual cortex as an initial pattern of afferent inputs. To avoid the edge effect of the finite model cortex and LGN, we impose periodic boundary conditions on the cortex and LGN. The computer simulation of synaptic rewiring was performed by the Monte Carlo (MC) simulation method (Metropolis et al., 1953).

Let us suppose the synaptic input to originate from the LGN neuron specified by (k, μ_1, μ_2) and let the selected cortical neuron be the i th neuron. At each trial of synaptic update, at first a synaptic site of a cortical neuron is randomly selected. Then, an LGN neuron is randomly picked up from $9 \times 9 \times 4$ LGN neurons, which are retinotopically close to the i th cortical neuron, according to the probability given by Equation (11). The values of $\langle b_{i,k,\mu_1,\mu_2} \rangle$ and $\left\langle b_{i,k',\mu_1',\mu_2'} \right\rangle$ are calculated using a synaptic input pattern $\{n_{i,k,\mu_1,\mu_2}\}$ before and after synaptic update. A current synaptic input (k, μ_1, μ_2) is replaced with a candidate synaptic input (k', μ_1', μ_2') according to the rewiring probability given by Equation (9). Since the MC simulation does not solve the dynamical equations of synaptic inputs, the simulation step does not represent the real time of evolution. Nevertheless, it is regarded to be real time t in this study. One MC step is set to be 585216 ($48 \times 48 \times 254$) trials of the update of afferent synaptic inputs, which correspond to the total number of synaptic sites. That is, the update of all synaptic sites is attempted on average once for one MC step. In the computer simulation of orientation map formation, there is a critical inverse temperature β_c. For $\beta > \beta_c$, orientation maps emerge, whereas for $\beta < \beta_c$, no orientation maps are formed. In our parameter setting of simulations, $\beta_c \approx 28$ (see **Supplementary Figure 2**). In the simulations to reproduce the sensitive period profile for orientation plasticity, we assume that orientation map formation starts at $t = 0$. In other words, $0 < \beta < \beta_c$ at $t < 0$ and $\beta > \beta_c$ at $t > 0$. $t = 0$ may correspond to some postnatal day between P20 and P24.

To calculate the firing rate η_i^{CX} of the i th cortical neuron using Equations (14) and (16), we need firing rates $\{\eta_{i'}^{CX}\}_{i' \neq i}$ of other cortical neurons to calculate the contribution of the lateral interaction term. This makes it difficult to calculate the growth rate $\langle b_{i,k,\mu_1,\mu_2} \rangle$ in Equation (13). To obtain its approximate expression of the growth rate at the ith cortical neuron, the contribution of the other neurons' activities through the lateral connections to the membrane depolarization ς_i^{CX} is assumed to be sufficiently smaller than the contribution of LGN neurons' activities through the afferent inputs ς_i^{AFF}. We expand η_i^{CX} and $\langle b_{i,k,\mu_1,\mu_2} \rangle$ with respect to the lateral interaction, and neglect terms higher than the first order. We also omit the delta function appearing as the derivative of the Heaviside function, because in the discrete numerical calculation, the argument of the delta function rarely become exact zero. Thus, we obtain the following expressions:

$$\eta_i^{CX} \approx \eta_i^{AFF} + \Theta\left(\varsigma_i^{AFF} - \vartheta_i\right) \sum_{i' \neq i} U_{i,i'} \eta_{i'}^{AFF} \tag{16'}$$

$$\begin{aligned} \langle b_{i,k,\mu_1,\mu_2} \rangle \approx & \left(1 + c^{D/P}\right) \left[\left\langle \eta_i^{AFF} \eta_{k,\mu_1,\mu_2}^{LGN} \right\rangle + \vartheta \left\langle \Theta(\varsigma_i^{AFF} - \vartheta_i) \eta_{k,\mu_1,\mu_2}^{LGN} \right\rangle \right] \\ & - c^{D/P} \left\langle \varsigma_i^{AFF} \eta_{k,\mu_1,\mu_2}^{LGN} \right\rangle + \left(1 + c^{D/P}\right) \\ & \times \left\langle \Theta(\varsigma_i^{AFF} - \vartheta_i) \sum_{i' \neq i} U_{i,i'} \eta_{i'}^{AFF} \eta_{k,\mu_1,\mu_2}^{LGN} \right\rangle \\ & - c^{D/P} \left\langle \sum_{i' \neq i} U_{i,i'} \eta_{i'}^{AFF} \eta_{k,\mu_1,\mu_2}^{LGN} \right\rangle \end{aligned} \tag{13'}$$

Here we define η_i^{AFF} as $\eta_i^{AFF} = \left(\varsigma_i^{AFF} - \vartheta_i\right) \cdot \Theta\left(\varsigma_i^{AFF} - \vartheta_i\right)$. The right-hand sides of the above expressions do not contain η_i^{CX}, and we can avoid iterative calculations. The algorithm for the simulations was implemented with these expressions.

RESULTS

Experimental Results

Orientation Maps in Kittens Reared Under Single-Orientation Exposure

We examined a kitten reared with goggles fitted with zero-power lenses to confirm the effect of lens power on orientation map alteration (**Supplementary Figure 3**). The transparent zero-power lens did not interfere with the formation of a regular orientation map. This suggests that the marked over-representation of the exposed orientation could not be induced accidentally or spontaneously without non-zero-power lenses. It is natural to believe that the over-representation of the exposed orientation is caused by single-orientation exposure through high-power cylindrical lenses.

Figure 5 shows typical results obtained from the optical imaging of area 17 of eight kittens that experienced only vertical orientation for 2 weeks after they were reared in the normal visual environment without goggles. Ages of GR onset and execution of optical imaging are shown to the left in **Figure 5**. Orientation polar maps at the ages of P31, P36, P41, P46, P51, and P54 show that cortical domains specifically representing vertical orientation occupied a larger cortical territory (left column in **Figure 5**). Such over-representation of vertical orientation was clear in orientation histograms (right column in **Figure 5**). The degree of over-representation differed at different ages of GR onset. The maximal over-representation was seen in the kitten in which 2-week GR started at P27. The over-representation of exposed orientation was not found in the kitten in which 2-week GR started at P54, or rather, horizontal bias and slight under-representation of vertical orientation were observed, as in normally reared young kittens (**Supplementary Figure 1**). The orientation magnitude (brightness) at the age of P24 is very low, and the shape of the orientation histogram is between a U and a W. If the single-orientation exposure affected orientation selectivity formation from P10 to P24, the histogram should have a single peak at 90°. These observations suggest that the experience-dependent formation of orientation selectivity starts around P24.

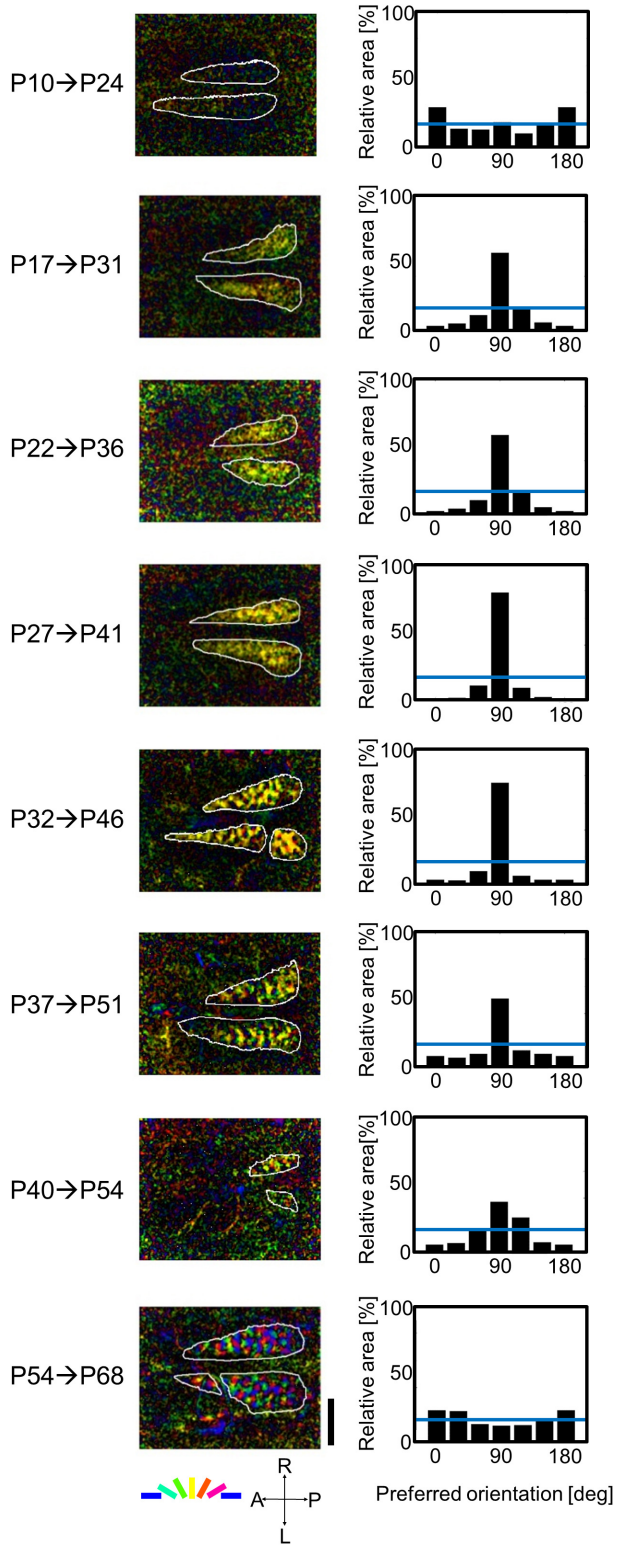

FIGURE 5 | Orientation polar maps and orientation histograms of eight kittens, in which 2-week GR started at P10, P17, P22, P27, P32, P37, P40, and P54, and optical imaging was conducted immediately after GR. The **(left column)** shows orientation polar maps obtained from intrinsic signals evoked by

(Continued)

FIGURE 5 | Continued

moving grating stimuli of the spatial frequency of 0.5 cpd. Preferred orientation is color coded. The orientation magnitude is indicated by the brightness. The scale bar indicates 4 mm. The **(right columns)** show orientation histograms. The vertical axes of the orientation histograms represent the relative area inside the functionally identified area 17. The horizontal blue lines in the orientation histograms indicate the mean relative area (16.7%). A, anterior; P, posterior; R, right; and L, left in the coordinate system.

Sensitive Period Profile for Orientation Plasticity

Here, we quantified orientation plasticity as the normalized relative area of cortical domains devoted to the exposed orientation in area 17 (over-representation index, ORI) at different ages. The definition of the ORI is given as

$$ORI = \frac{\text{Relative area representing } 90^\circ \text{ [\%]} - 16.667}{100 - 16.667} \tag{23}$$

This definition of the ORI is based on 6-bin orientation histograms, as shown in **Figure 5**. The ORI takes 1 for the complete over-representation of the exposed orientation, and 0 for the unbiased orientation representation. All data points in **Figure 6A** were taken from kittens reared with vertical goggles for 2 weeks (**Supplementary Table 1**). This provides the sensitive period profile for orientation plasticity. Although it is difficult to mention exactly when the sensitive period starts and ends owing to the ambiguity of 2 weeks for GR, the profile suggests the existence of such a limited period in early life, in which visual cortical neurons alter their preferred orientations so as to respond strongly to more frequently exposed orientations. According to the profile shown in **Figure 6A**, it is likely that the sensitive period for orientation plasticity in cat area 17 starts immediately before P24 and ends between P54 and P68. Combined with our experimental observation that orientation maps were not visible in area 17 earlier than P21, the sensitive period for the spatial clustering of neurons with similar orientation preferences may start between P21 and P24, although some neurons are orientation-selective before P20 (Albus and Wolf, 1984).

To examine how the orientation selectivity changes under single-orientation exposure, we define the orientation selectivity index (OSI) of the i th pixel inside the region of interest as

$$OSI(i) = \left(1 - \frac{r_{\min}(i)}{r_{\max}(i)}\right)\left(1 - \frac{w(i)}{180}\right) \tag{24}$$

$r_{\max}(i)$ and $r_{\min}(i)$ denote the maximum and minimum stimulus-related intrinsic signals at the ith pixel, respectively. $w(i)$ indicates the full width at half height (FWHH) of the orientation tuning curve of intrinsic signals at the i th pixel. In addition, the value of the OSI is determined to be zero when the tuning curve intersects more than three times with the horizontal line at half height, because we cannot determine a preferred orientation uniquely in such a situation. According to Equation (24), OSI increases toward 1 as the orientation tuning curve becomes sharper. The OSI was used as one of indices to characterize orientation selectivity along with orientation magnitude obtained from the vector sum method.

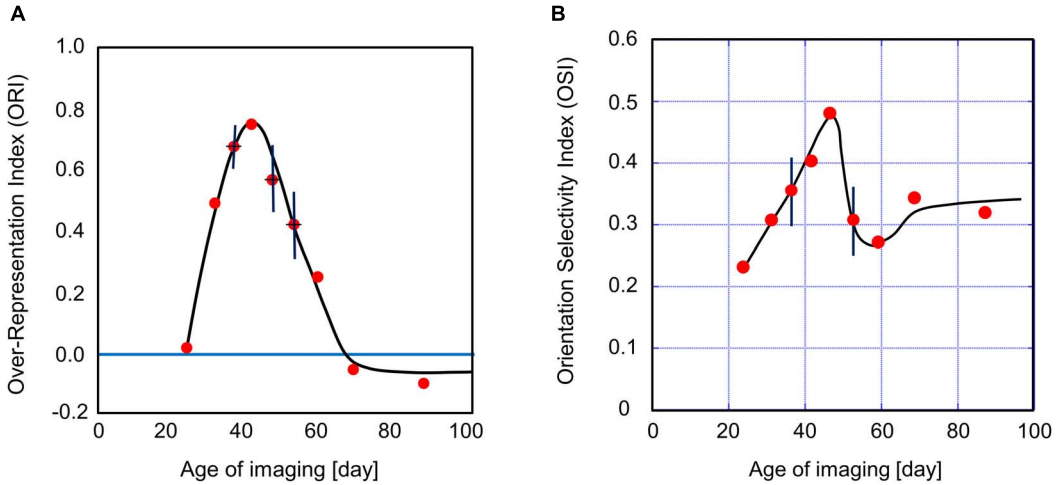

FIGURE 6 | Sensitive period profile for orientation plasticity and changes in the average OSI in area 17 of kittens exposed to single orientation through the goggles for 2 weeks. **(A)** The vertical axis indicates the over-representation index, i.e., the normalized relative area of cortical domains selectively responding to the exposed vertical orientation. The red dots represent the over-representation indices plotted at the age when optical imaging was performed. The most sensitive period is several days around P34. The sensitive period is followed by a period in which single-orientation exposure induces the under-representation of the exposed vertical orientation after about P60 of 2-week GR onset. **(B)** The vertical axis indicates the average OSI over all pixels inside of the functionally identified area 17. The red dots represent the average OSI plotted at the ages when optical imaging was performed. The value of the average OSI was the maximum at P46 and the minimum at P59, which were located in the declining phase of the orientation sensitive period in **(A)**. The error bars shown in **(A,B)** indicate SEs estimated using data in which optical imaging was conducted using more than three cats a few days around the mean age. The cat IDs and numerical data used in **(A,B)** are shown in **Supplementary Table 1**.

We show the age-dependent changes in the OSI averaged over the imaged area 17 in **Figure 6B**. The average OSI increased from P24 to P46 of the ages of optical imaging following 2-week GR. Then it decreased until P54, and increased again toward a plateau value. The average OSI under single-orientation exposure is characterized by the dip appearing in the ORI decreasing phase between P46 and P68. This dip may be attributed to the broadening of tuning widths caused by the interference of orientation preferences between the original preferred orientations and the exposed vertical orientation.

Orientation Selectivity Modification Under GR Within or Beyond the Sensitive Period

Now, a question is raised about whether the orientation map once markedly over-representing exposed orientation returns to regular orientation maps equally representing all orientations by removing the goggles during the sensitive period. To address this question, we conducted optical imaging three times for the same kitten at P28, P38, and P45 using drifting grating stimuli with the spatial frequency of 0.5 cpd. The first optical imaging was conducted at P28 to observe the intact orientation representation. From P31, the animal was reared with goggles for 1 week, and optical imaging was conducted at P38. After the imaging experiment, the animal was reared without goggles in the normal visual environment for 1 week, and the third optical imaging was performed at P45.

Figure 7 shows orientation polar maps reconstructed from optical imaging experiments conducted three times on the same kitten (cat ID: GYe). The orientation histograms were obtained from 4 to 6 kittens that underwent the same visual experience and imaging experiments at almost the same age (**Supplementary Table 2**). We obtained a regular orientation map in functionally identified area 17 (**Figure 7A**), and the relative areas for preferred orientations were almost uniform (**Figure 7B**) at P28. One-week GR showed remarkable expansion of cortical domains selectively responding to vertical orientation (**Figure 7C**). Consequently, the orientation histogram exhibited a skewed distribution biased to the exposed orientation (**Figure 7D**). One-week normal viewing following 1-week GR, however, altered the orientation map to a normal-like map (**Figure 7E**), so that the relative areas for preferred orientations changed to a uniform distribution (**Figure 7F**). The tendency of these changes in the relative areas of iso-orientation domains was reproducibly observed in other kittens goggle-reared in a similar manner (**Supplementary Table 2**). These findings suggest that even if conspicuous over-representation of a single orientation is induced, a regular orientation map with uniform orientation representation can be restored by keeping kittens in the normal visual environment for 1 week at the latest before P45. In other words, the cat visual cortex has high flexibility to represent any experienced orientation within the sensitive period for orientation plasticity.

Another question is raised about whether orientation maps exhibiting the marked over-representation of the exposed orientation by prolonged GR beyond the end of the sensitive period can be recovered to regular orientation maps by returning animals to the normal rearing condition. To answer this question, we conducted optical imaging experiments on three kittens that experienced prolonged GR. **Figure 8** shows orientation polar maps and histograms of three kittens: two kittens exposed to vertical orientation and one kitten exposed to vertical orientation

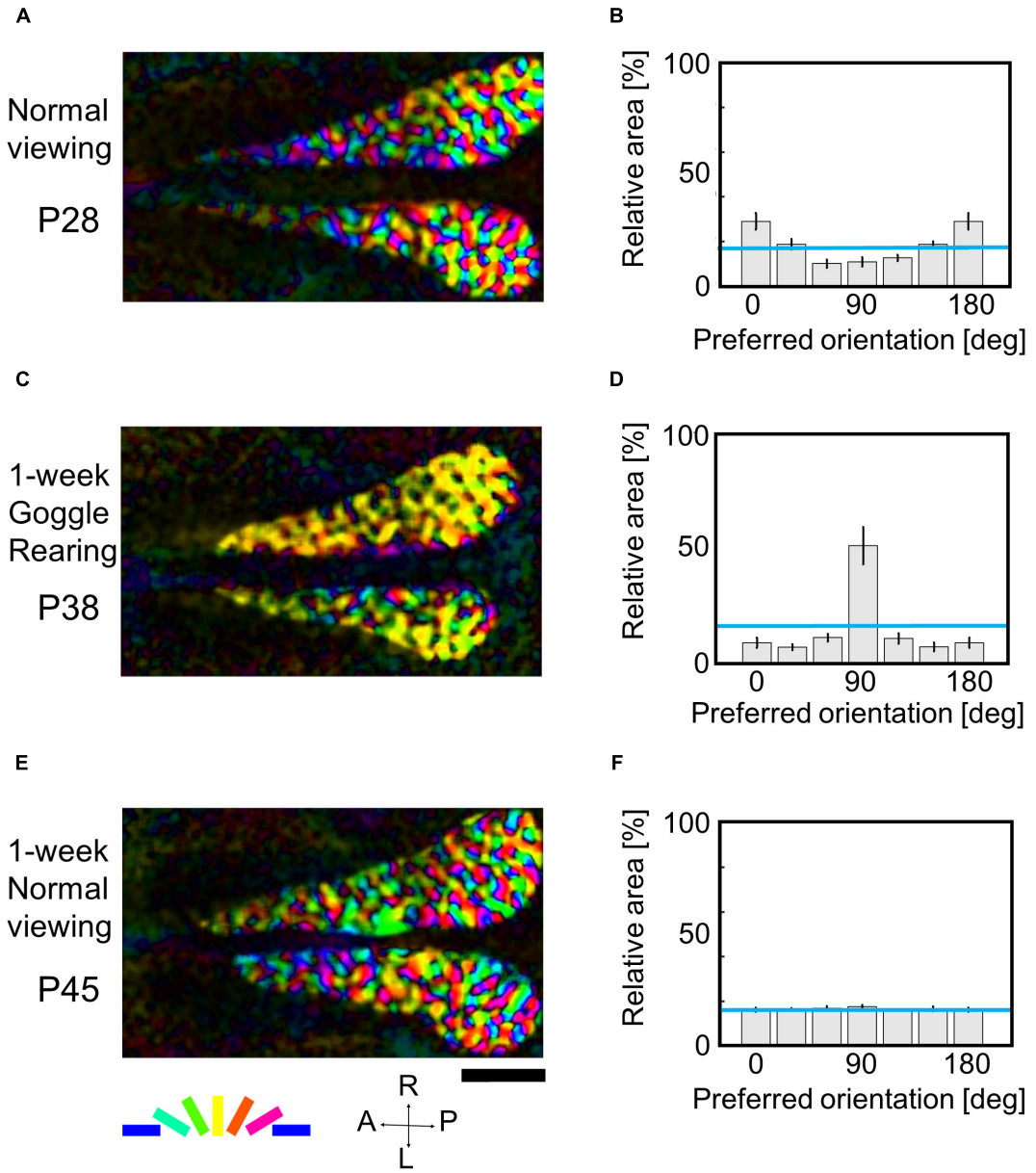

FIGURE 7 | Flexible changes in orientation representation of the same kitten within the sensitive period. **(A,C,E)** Orientation polar maps at P28, P38, and P45, respectively. **(B,D,F)** Orientation histograms at P28, P38, and P45, respectively. The error bars shown in the orientation histograms indicate SEs. All conventions are as in **Figure 5**. The cat IDs and numerical data used in this figure are shown in **Supplementary Table 2**.

in the right eye and horizontal orientation in the left eye. The comparison between **Figures 8A,C**, **Figures 8E,G**, and **Figures 8I,K** reveals that orientation polar maps shared common basic structure. Reflecting the preserved over-representation of exposed orientation, pairs of orientation histograms in **Figures 8B,D**, in **Figures 8F,H**, and in **Figures 8J,L** showed remarkable bias toward the exposed orientations, although the relative areas at each preferred orientation were slightly different between the two.

The preservation of orientation representations once-reorganized by prolonged GR should be compared with the finding that only 1-week normal viewing returned the marked over-representation of exposed orientation to the uniform representation between P38 and P45 (**Figures 7E,F**). These findings suggest that orientation representation was consolidated after P73, until which the time window of orientation plasticity was closed, as shown in **Figure 6A**.

Simulation Results

Orientation Map Development

First of all, we attempted to reproduce the development of a regular orientation map in the visual cortex of cats reared

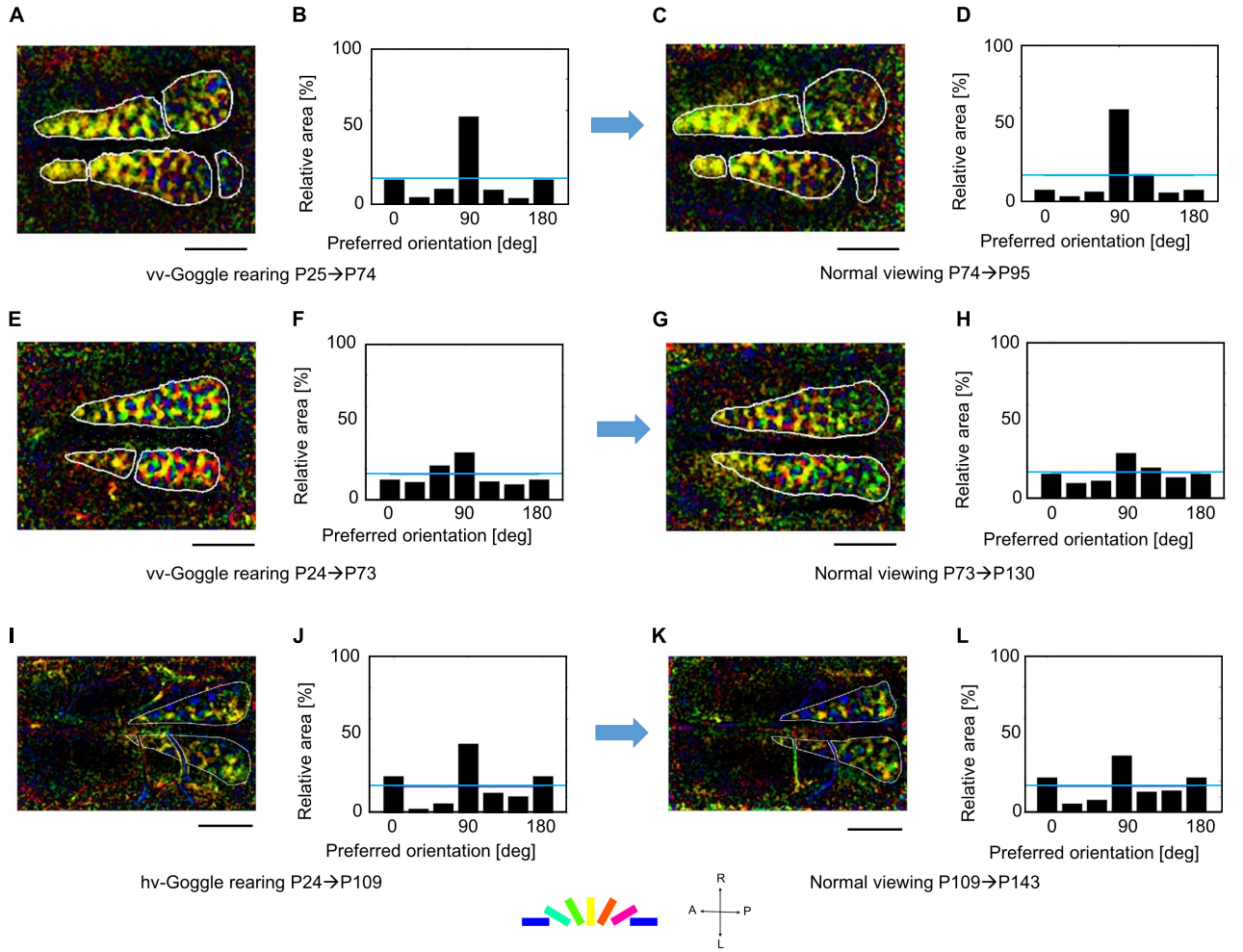

FIGURE 8 | Robustness of orientation representation against visual experience after the end of the sensitive period. **(A,B)** Orientation polar map and histogram at P74 after vertical orientation exposure in the two eyes for 49 days. **(C,D)** Orientation polar map and histogram at P95 after normal viewing for 21 days. **(E,F)** Orientation polar map and histogram at P73 after vertical orientation exposure in the two eyes for 49 days. **(G,H)** Orientation polar map and histogram at P130 after normal viewing for 57 days. **(I,J)** Orientation polar map and histogram at P109 after horizontal and vertical orientation exposure in the left and right eyes, respectively, for 85 days. **(K,L)** Orientation polar map and histogram at P143 after normal viewing for 34 days. All conventions are as in **Figure 5**. The cat IDs and numerical data in this figure are shown in **Supplementary Table 3**.

under normal visual conditions. In computer simulations, model LGN cells were activated by the balanced presentation of grating stimuli drifting in 24 directions (12 orientations). This visual condition is supposed to be a model of the normal visual conditions that animals experience. The left half of **Figure 9** illustrates the development of an orientation map as the simulation step increases (from top to bottom in **Figure 9**). Even a relatively short run of the simulation for 1.57 MC steps formed a regular orientation map, although the segregation into iso-orientation domains was somewhat vague. Once a map structure emerged in an early stage, it was likely that preferred orientations no longer change and only orientation magnitude monotonically increases up to a certain level. The orientation histograms exhibited almost uniform distributions.

The simulation method of synaptic rewiring under single-orientation exposure is the same as the simulation under balanced exposure to 12 orientations except for stimulus patterns presented in the model retina. Model LGN cells were activated by the presentation of only a vertically oriented grating drifting leftward or rightward. This visual condition may correspond to the visual experience of kittens with cylindrical-lens-fitted goggles. We changed the duration of the simulation under 12-orientation exposure before the simulation was performed under single-orientation exposure.

The right half of **Figure 9** shows how orientation representations produced under 12-orientation exposure were altered by simulations conducted under single-orientation exposure. Different durations of simulations performed under 12-orientation exposure induce different degrees of over-representation of exposed orientation. We can see the effect of the duration of 12-orientation exposure in orientation histograms as well as in orientation polar maps. After long

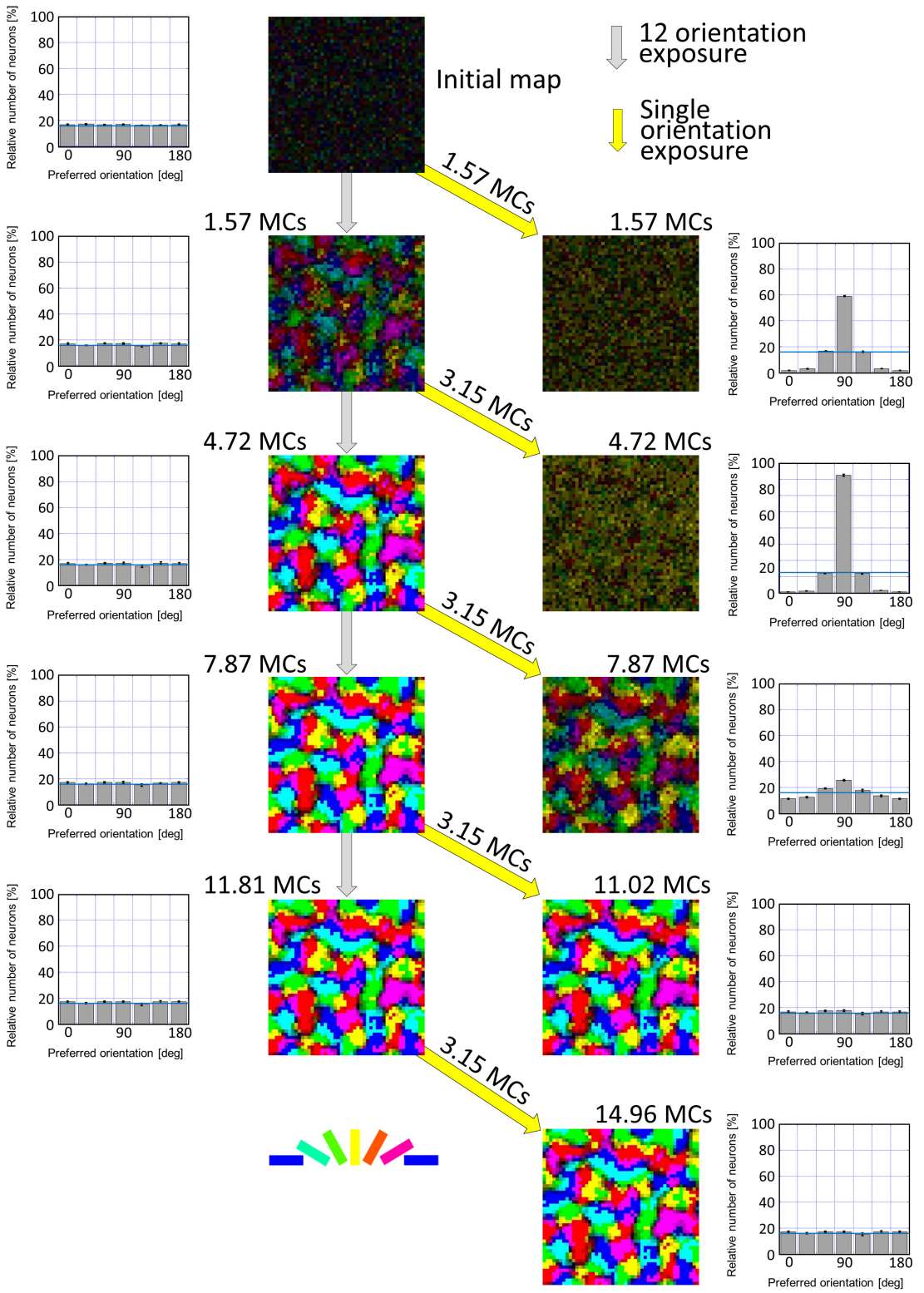

FIGURE 9 | Simulated results of experience-dependent orientation map development. The left half of **Figure 9** illustrates the development of an orientation map from an initial map as the simulation step increases. The initial map was produced by random afferent inputs from model LGN neurons to model visual cortical neurons. The simulation for 1.57 MCs formed a regular orientation map, although the segregation into iso-orientation domains was somewhat vague. Once a map structure emerged in an early stage, it was likely that preferred orientations no longer change and only orientation magnitude monotonically increases up to a certain

(Continued)

FIGURE 9 | Continued
level. The orientation histograms exhibited almost uniform distributions. The simulations under single-orientation exposure were resumed from orientation maps formed under 12-orientation exposure. The right half of **Figure 9** shows orientation polar maps and orientation histograms for different durations of the simulations under 12-orientation exposure before the simulation under single-orientation exposure. Different durations of simulations performed under the balanced exposure to 12 orientations induce different degrees of over-representation of exposed orientation. We can see the effect of balanced exposure to 12 orientations in orientation histograms as well as in orientation polar maps. After long simulation under 12-orientation exposure (e.g., 7.87 or 11.81 MC steps), single-orientation exposure for 3.15 MC steps did not alter the orientation map and hence orientation histograms were uniform. This indicates that the sensitive period was closed. The preferred orientation is color-coded shown below. The values of the SE calculated from five trials of simulation with different patterns of initial random afferent inputs are added as vertical bars in the orientation histograms. Numerical data of this figure are shown in **Supplementary Table 4** (12-orientation exposure) and **Supplementary Table 5** (single-orientation exposure).

simulation under 12-orientation exposure (e.g., 7.87 or 11.81 MC steps), single-orientation exposure for 3.15 MC steps did not alter the orientation map and hence orientation histograms were uniform. This indicates that the sensitive period was closed.

Sensitive Period Profile for Orientation Plasticity

The values of the ORI obtained from simulations are plotted in **Figure 10A**. As determined by intrinsic signal optical imaging, clusters of neurons with similar preferred orientations are likely to emerge around P21 to P24, as long as we use the intrinsic signal optical imaging technique. It may therefore be reasonable to set the origin of the simulation time $t = 0$ to be P24. We may assume that an orientation map is not formed at $t < 0$ because the inverse temperature β is smaller than β_c (**Supplementary Figure 2**) at $t < 0$, whereas an orientation map is formed at $t > 0$ in an experience-dependent manner, because β is sufficiently larger than β_c at $t > 0$. Note that the effective duration of single-orientation exposure should be shorter than 3.15 MCs when it starts before t = 3.15 MCs. Consequently, the short-term single-orientation exposure was not sufficient to induce conspicuous over-representation. This may account for the observation that the over-representation of the exposed orientation did not appear clearly in the kitten goggle-reared from P10 to P24 (top row in **Figure 5**). When we assume that 3.15 MCs corresponds to 2 weeks and the simulation step is linearly dependent on real time, we can reproduce qualitative features of the sensitive period for orientation plasticity. The putative ages are shown at the top of **Figure 10**. The sensitive period profile for orientation plasticity obtained from simulations agrees well as a whole with the experimentally observed profile. The single-orientation exposure induced under-representation observed later than P68 in **Figure 6A** was not reproduced in **Figure 10A**. The dashed curve in **Figure 10B** indicates the average OSI reproduced by simulations under 12-orientation exposure alone, which predicts the age-dependent OSI changes in normally reared kittens. The solid curve in **Figure 10B** shows the average OSI reproduced by simulations under single-orientation exposure following 12-orientation exposure, which is a theoretical counterpart to the experimentally observed OSI behavior in the 2-week goggle-reared kittens (**Figure 6B**). In the early stage (0 – 5 MCs), the OSI for single-orientation exposure more rapidly increases than that for 12-orientation exposure. In the late stage (5 – 10 MCs), the OSI once decreases drastically and then increases again to approach the OSI for 12-orientation exposure around the end of the sensitive period ($\sim$10 MCs). The dip in the solid curve appeared in the decreasing phase (5–10 MCs) of the sensitive period profile shown in **Figure 10A**.

Spatiotemporal Receptive Fields and Orientation Tuning Curves

To obtain a better understanding of the emergence of the dip, we analyzed spatiotemporal receptive fields (DeAngelis et al., 1995) and orientation tuning curves of a typical unidirectional cell in **Figure 11**. The spatiotemporal receptive field of the i th cortical neuron is calculated using the first term of the right-hand side of Equation (14), which represents the afferent component of the membrane potential of the neuron. The receptive field is given by the sum of the products of the number of synaptic inputs and LGN neurons' activities in response to light and dark spots, as in the reverse correlation method in electrophysiology (DeAngelis et al., 1995). However, we use a simpler estimation method: the LGN spatiotemporal receptive fields $R^{LGN}_{k,\mu_1,\mu_2;l}(t)$ given by Equation (18) are summed up with the weight of the number of synaptic inputs $\{n_{i,k,\mu_1,\mu_2}\}$. That is, $R^{CX}_{i;l}(t) = \sum_{k,\mu_1,\mu_2} R^{LGN}_{k,\mu_1,\mu_2,l}(t)\, n_{i,k,\mu_1,\mu_2}$. **Figure 11** shows spatiotemporal receptive fields of the same cortical neuron obtained in this way. The red and green regions represent ON and OFF subfields. Since LGN neurons have spatially concentric receptive field, elongated subfields aligned along the axis of the preferred orientation are made of the alignment of four types of LGN neurons that send afferent synaptic inputs to the cortical neurons (**Supplementary Figure 4**). **Figure 11A** illustrates the immature spatiotemporal receptive field formed by simulation under the balanced presentation of 12 orientations for1.57 MCs. On the other hand, **Figure 11B** is the spatiotemporal receptive field formed by simulation under single-orientation exposure for 3.15 MCs, which resumed from simulation under the balanced presentation of 12 orientations for 1.57 MCs. **Figure 11C** shows the orientation tuning curves for A (red) and B (blue). The maximum response of this neuron to the stimulus orientation of 30° changed to the maximum response to the orientation of 90° by the vertical orientation exposure. The blue tuning curve for H in the left panel shows that a FWHH is about 90° at 7.88 MCs, whereas the red tuning curve for G at 4.73 MCs exhibits a FWHH about 60°. The tuning width for H becomes the broadest among all tuning curves shown in **Figure 11**. This causes the OSI of this neuron to be small. This implies that orientation tuning of large proportion of neurons at 7.88 MCs tend to be broad and that the average OSI decreases, as observed between 5 and 10 MCs in **Figure 10B**. The spatiotemporal receptive

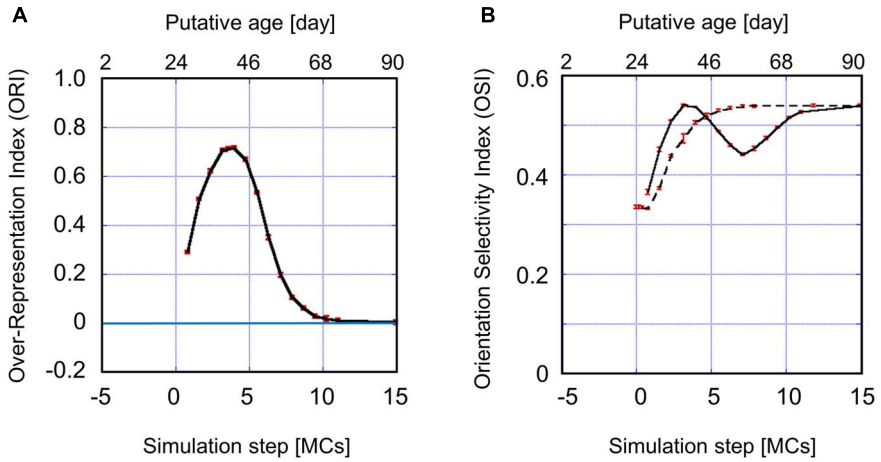

FIGURE 10 | (A) Sensitive period profile for orientation plasticity reproduced by computer simulations. The vertical axis indicates the over-representation index (ORI). The horizontal axis indicates the total simulation step t, which is given as the sum of durations of 12-orientation exposure and single-orientation exposure. When we assume that 10 days for kittens correspond to 2.25 MCs and map formation starts on P24, we can interpret the simulation step as the age of kittens. Putative ages are shown above the figure. The simulated sensitive period profile behaves similarly to the experimentally observed profile (**Figure 6A**). The simulated sensitive period is closed around $t \simeq 10$ MCs, corresponding to P68 of the age of cats. **(B)** The average OSI reproduced by computer simulations under 12-orientation exposure alone (dashed curve) and single-orientation exposure following 12-orientation exposure (solid curve). The solid curve is a theoretical counterpart to the experimentally observed OSI behavior in the 2-week goggle-reared kittens (**Figure 6B**). In the early stage (0 – 5 MCs), the OSI for single-orientation exposure is rapidly increasing and larger than that for 12-orientation exposure. In **(A,B)**, the red vertical bars indicate SEs for five trials of simulation with different patterns of initial random inputs from the LGN to the visual cortex. Numerical data of ORI and OSI are shown in **Supplementary Tables 5, 6**, respectively.

fields becomes robust after long simulation under the balanced presentation of 12 orientations, and the receptive fields does not change and the tuning curves are almost the same. This indicates that the sensitive period for orientation plasticity of individual neurons ends.

Effects of Short-Term GR and Prolonged GR

To examine the existence of the sensitive period for orientation plasticity, we carried out two simulations: One was simulation under short-term single-orientation exposure and successive recovery, and the other was simulation under prolonged single-orientation exposure and successive long recovery. **Figure 12** shows the results of the two simulations. At first, we performed simulation under balanced presentation of 12 orientations for 1.57 MCs (1-week NR in the experiment). The resultant orientation map and orientation histogram are shown in **Figure 12A**. The two simulations were resumed from the synaptic arrangements after 12-orientation exposure. Short-term single-orientation exposure for 1.57 MCs (1-week GR in the experiment) induced marked over-representation of the exposed orientation (**Figure 12B**). The successive simulation under 12-orientation exposure for 1.57 MCs restored regular orientation map with clear iso-orientation domains and reduced the over-representation of the vertical orientation (**Figure 12C**), although the orientation histogram did not return to uniform distribution as shown in **Figure 12A**. In contrast, prolonged single-orientation exposure for 7.85 MCs (about 5 weeks in the experiment) induced an extreme over-representation (**Figure 12D**). This over-representation was preserved even after the long-term 12-orientation exposure for 7.09 MCs (4.5 weeks in the experiment) (**Figure 12E**). The simulation under short-term single-orientation exposure and successive 12-orientation exposure attempted to reproduce the experiment shown in **Figure 7**. The simulation under prolonged single-orientation exposure and long-term 12-orientation exposure aimed to reproduce the effect of prolonged GR beyond the end of the sensitive period, as shown in **Figure 8**. Rough features of experimental results were reproduced by the simulations, although the degrees of the over-representation of exposed orientations and to what extent orientation maps return to original maps are different. Based on these simulation results, we may say that in the cat visual cortex, orientation maps are modifiable flexibly by visual experience within the sensitive period, but orientation maps are reorganized by prolonged GR beyond the end of the sensitive period never return to original regular maps. Through the comparisons between the theoretical and experimental studies, it is suggested that the sensitive period for orientation plasticity is closed around P68 (10MCs in the model).

DISCUSSION

Onset Age of Visual Experience

According to Albus and Wolf's electrophysiological experiments (Albus and Wolf, 1984) on kittens, in layer 4, a large proportion of neurons are orientation-selective as early as P14. In contrast, in layers 2/3, orientation-selective neurons were observed first between P14 and P18, and a similar percentage of layer 2/3 neurons remained orientation-selective up to the age of P24. Similar results have been reported by other groups (Wiesel and Hubel, 1974; Blakemore and Van Sluyters, 1975). It is likely that

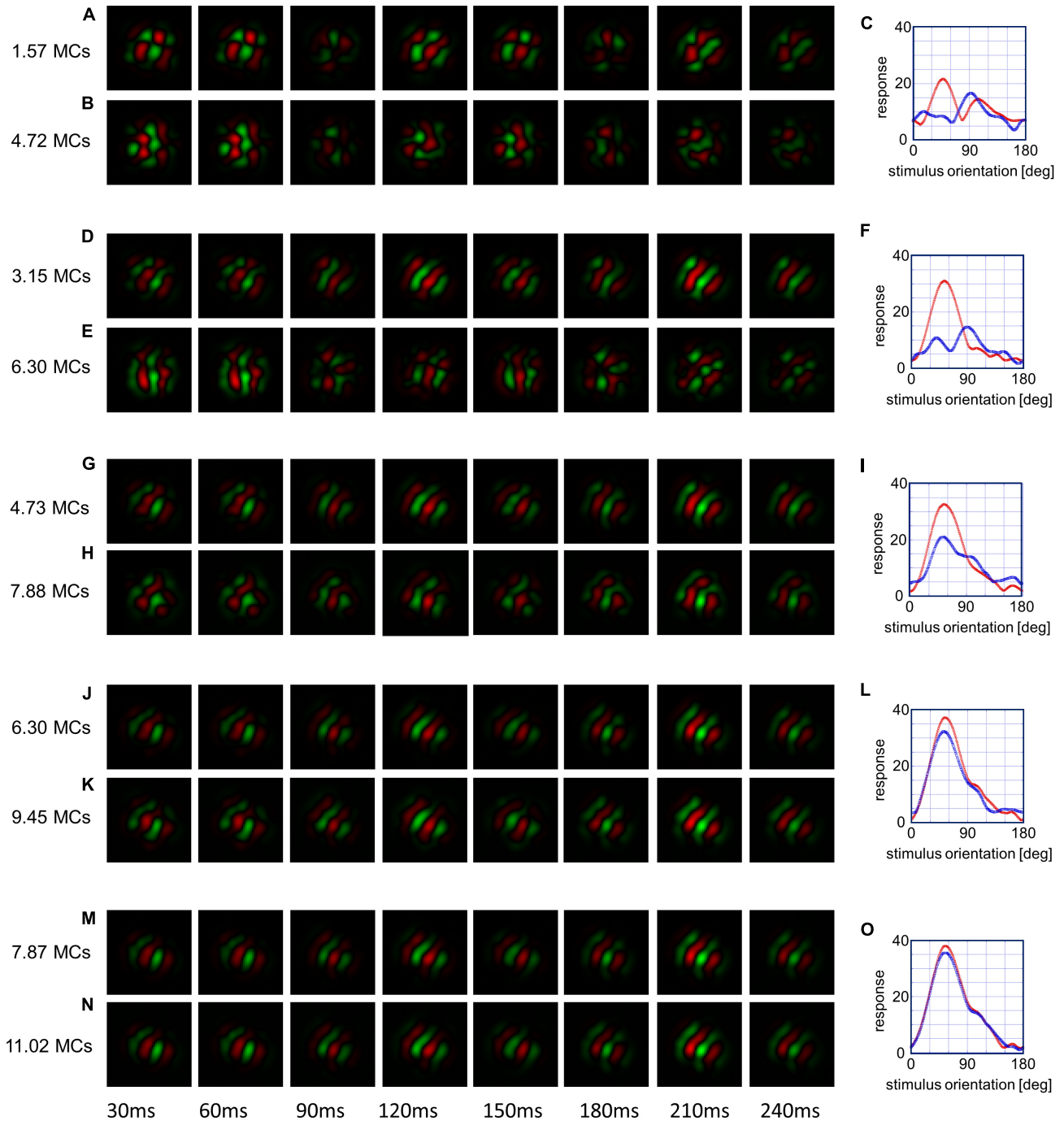

FIGURE 11 | Snapshots of the representative spatiotemporal receptive field of the same neuron. The spatiotemporal receptive field is shown as a spatial receptive field sampled every 10 ms. Changes in snapshots from simulations under 12-orientation exposure for certain MCs to simulation resumed under single-orientation exposure for 3.15 MCs are shown in the pairs of **(A,B)**, **(D,E)**, **(G,H)**, **(J,K)**, and **(M,N)**. Changes in orientation tuning curves are shown in **(C,F,I,L,O)**, where the red and blue curves represent orientation tuning curves immediately before and after single-orientation exposure for 3.15 MCs, respectively.

orientation maps in layer 2/3 emerge at certain days between P14 and P24. Although in our group, orientation maps have never been detected in area 17 of kittens younger than P22, Crair et al. (1998) reported that orientation maps existed in area 17 at P14. It is implied that this discrepancy was caused by the possibilities that different camera systems were used for optical imaging and the different spatial frequencies of stimulus gratings might be used. However, they demonstrated that at about P21, orientation maps for the left- and right-eye stimulation become and remain nearly identical to one another in normally reared

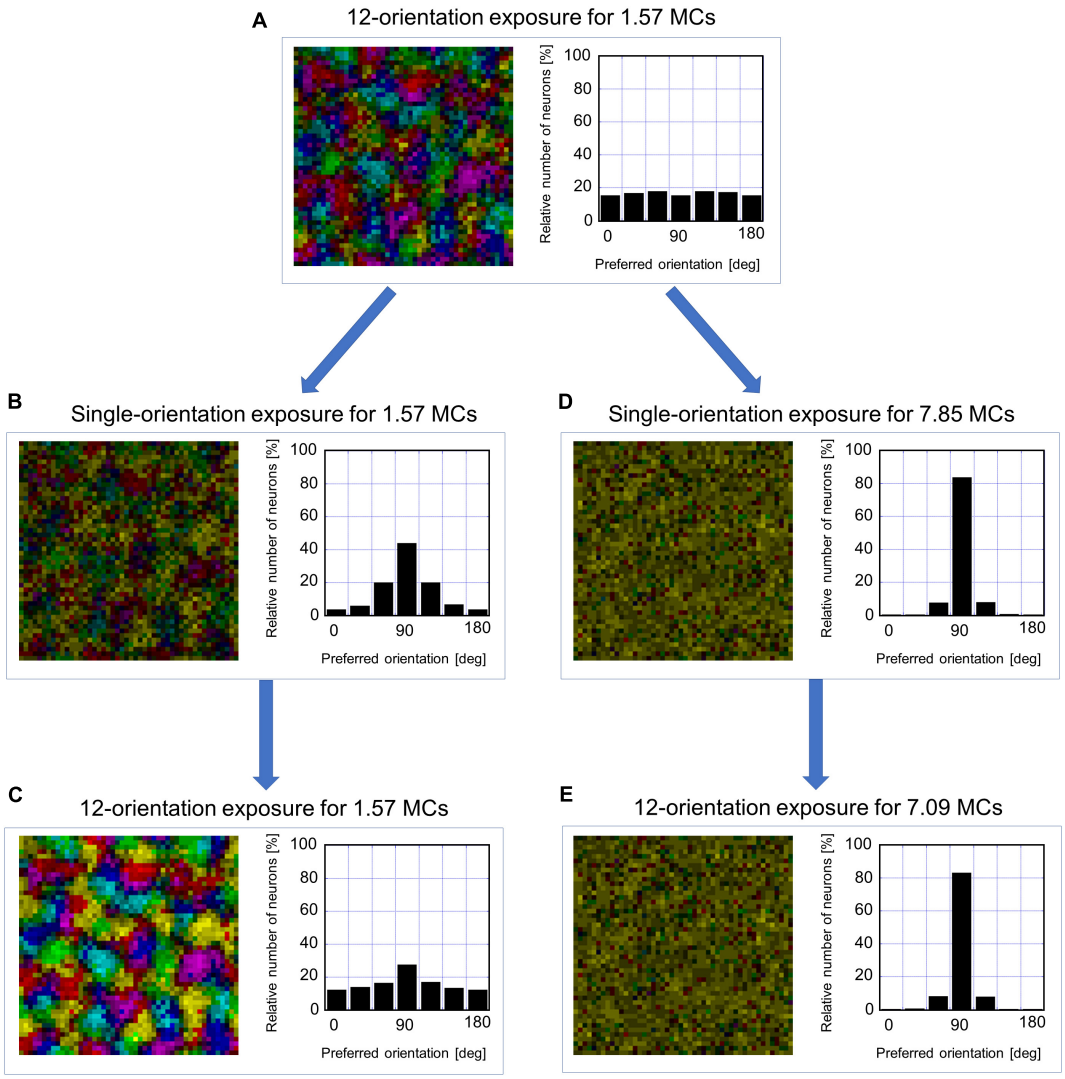

FIGURE 12 | Flexibility or rigidity in orientation representation against the change of visual experience within or after the sensitive period. **(A)** orientation polar map and histogram after simulation under 12-orientation exposure for 1.57 MCs. **(B)** Orientation polar map and histogram after simulation resumed from the state of A under single-orientation exposure for 1.57 MCs. **(C)** Orientation polar map and histogram after simulation resumed from the state of B under 12-orientation exposure for 1.57 MCs. **(D)** Orientation polar map and histogram after simulation resumed from the state of A under single-orientation exposure for 7.85 MCs. **(E)** Orientation polar map and histogram after simulation resumed from the state of D under 12-orientation exposure for 7.09 MCs. The preferred orientation is color-coded as in **Figure 9**.

kittens, whereas maps begin to deteriorate and the two eyes' maps become less similar in binocularly deprived kittens. These experimental results indicate that visual experience begins to affect orientation maps at P21. On the other hand, based on **Figure 6A**, single-orientation exposure starts around P24, as mentioned in section "Orientation Map Development." Taken together, experience-dependent alteration of orientation maps in area 17 of cats may occurs at the age from P21 to P24.

Lens Power Effects on Orientation Map Alteration

In our experiment, 2-week GR of kittens exposed to vertical orientation with plano-convex lenses of +67 diopter from P27 exhibited the maximum over-representation of the exposed orientation. When GR started at P27 or earlier, pinwheel centers around which all orientations are arranged continuously were hard to identify (**Figure 5**) because all orientations were not represented. Sengpiel et al. (1999) also observed the over-representation of the exposed orientation. However, the cortical territory representing the exposed orientation was moderately expanded, but they emphasized that basic structure of orientation maps was robust and all orientations were represented. Such a difference may be attributed partly to the lens power (−25 diopter vs. +67 diopter) and partly to the time for single-orientation exposure a day (6 h vs. 24 h). The images transformed through lenses of these powers can be seen in Figure 1 of

Tanaka et al. (2006). In a recent experiment on kittens reared with discordant goggles in the two eyes, plano-concave lenses of −10 diopter were adopted, which were fitted to a rubber mask (Cloherty et al., 2016). Such lenses of weak power showed that orientation maps, in which all preferred orientation were represented, enabled to analyze geometric properties of pinwheel centers. In this sense, visual restriction with week-power lenses would be advantageous to elucidate the effects of visual experience on the geometric relationships among orientation gradients, pinwheel centers and ocular dominance maps, by comparing with simulation results (Carreira-Perpinăń et al., 2005; Giacomantonio et al., 2010; Cloherty et al., 2016).

Comparisons Among Models

Some abstract models such as the self-organizing map (SOM) (Obermayer et al., 1990; Kohonen, 1997) and the elastic net model (Durbin and Mitchison, 1990; Carreira-Perpinăń et al., 2005; Goodhill, 2007) may provide a computational principle of map formation optimizing the quantities such as "coverage" and "continuity". In these models, based on the *a priori* assumption that each neuron has receptive field parameters such as preferred orientation, preferred direction of motion, and ocular dominance, these parameters are represented over the visual cortical surface as continuously as possible. Actually, regular and bandpass-filter-like orientation maps with pinwheel centers have been well reproduced, as observed in cats, ferrets, and macaques. However, experimental results were not always consistent with the continuity assumption of visual features. In electrophysiological recording in the visual cortex of cats reared with stripe environment, the preferred orientation did not change continuously along the electrode track due to the singular intervention of orientation non-selective or unresponsive neurons (Figure 5 in Stryker et al., 1978). Later we will demonstrate that our model reproduces the phenomenon of discontinuous orientation representations in the cats reared in the stripe environment.

On the other hand, another type of models has been proposed to reproduce orientation maps on the basis of the Hebbian learning (Hebb, 1949) of afferent synaptic inputs from the LGN (Miller, 1992, 1994; Miyashita and Tanaka, 1992; Miyashita et al., 1997). These models describe the activity-dependent self-organization of synaptic inputs explicitly, called correlation-based learning model. Unfortunately, these models generated low-pass filter-like orientation maps with large fluctuation in the size of iso-orientation domains (Erwin et al., 1995). This may be related to the absence of the *a priori* coverage assumption. In addition, this type of models requires some normalization constraints on the synaptic strength (Goodhill and Barrow, 1994; Miller, 1994; Miller and Mackay, 1994) or the number of synaptic inputs (Tanaka and Miyashita, 2009) to prevent visual cortical neurons from receiving exuberant synaptic inputs from a particular LGN neuron. If the correlation-based learning models are improved getting rid of these defects, they may be able to give us a logical linkage between molecular mechanisms for synaptic rewiring to the experience-dependent development of orientation maps. Thus, we attempted to build a synaptic rewiring model, refining the correlation-based learning so that it can reproduce band-pass filter-like orientation maps.

For microscopic mechanisms of synaptic rewiring, we focused on BDNF and its related receptors, reducing numerous molecules that may be related to synaptic rewiring, and suggest that activity-dependent and independent release of BDNF is an essential for experience-dependent orientation map formation/reorganization. For intracellular Ca^{2+} concentration, which controls the release of BDNF and tPA from the postsynaptic site, we simply assumed the enhancement of Ca^{2+} concentration by the coincidental bAP (Nevian and Sakmann, 2004). The model obtained on this basis resolved the defects of the correlation-based learning, and would be a minimal model to show the sensitive period for orientation plasticity as well as biologically plausible orientation maps. In addition, the model accounted for the formation of spatiotemporal receptive fields of simple cells based on self-organized afferent inputs from four types of LGN neurons. This reproducibility is another successful demonstration of the model at the electrophysiological level.

The Hebbian coincidence of presynaptic activity with the postsynaptic activity (Hebb, 1949) has been assumed, in most mathematical models for activity-dependent synaptic plasticity, and the coincidence level is reflected by Ca^{2+} influx through the NMDA channel (e.g., Graupner and Brunel, 2010). In our model, we assumed the enhancement of intracellular Ca^{2+} concentration associated with the arrival of bAPs, in addition to Ca^{2+} influx through NMDA channels triggered by the coincidence of presynaptic activity with postsynaptic membrane depolarization (Nevian and Sakmann, 2004). This triple coincidence causes a large increase in Ca^{2+} concentration in the vicinity of the synaptic contact on the postsynaptic dendritic spine, and release the sufficient amount of mBDNF locally at the synaptic contact, which works to be advantageous for the synaptic contact in the competition with other synaptic contacts. If this triple coincidence happens at a newly formed synapse, the synapse may be stabilized to survive longer. On the other hand, the simple coincidence of the presynaptic activity with the postsynaptic depolarization induces a moderate increase in Ca^{2+} concentration, which facilitates to release locally the larger amount of proBDNF relatively to that of mBDNF. This tends to act to be advantageous for the other synaptic contacts on the same spine, and likely to eliminate the synaptic contact in question. This coincidence may serve to normalize the number of synaptic connections to avoid a situation in which exuberant afferent inputs from a presynaptic neuron occupy a large portion of dendritic sites of a postsynaptic neuron. Such a constraint is indispensable to generate simple cell-like receptive fields (Miyashita and Tanaka, 1992; Miyashita et al., 1997). Otherwise, receptive fields of visual cortical neurons become a center-surround antagonistic receptive fields, as seen in the LGN relay neurons.

Although the correlation-based learning models reproduced simple-cell receptive fields characterized by orientation and phase parameters, and generated orientation map-like patterns. However, the orientation maps were low-pass filter-like, as indicates that the size of iso-orientation domains was highly

fluctuating, as Erwin et al. (1995) pointed out. The emergence of low-pass filter-like maps is speculated to be caused by the mutual interference between the preferred orientation map and the receptive field phase map, because this type of models tends to regularly arrange any receptive field parameter over the model cortex. It should be noted that the receptive field phase seems to be randomly distributed tangentially along the cat visual cortex (DeAngelis et al., 1999). Simulations of the present model with the triple coincidence demonstrated that receptive field phases are randomly arranged over the model cortex (data not shown). Driving out the phase maps results in the formation of regular orientation maps characterized by a band-pass filter-like structure. This property of orientation maps reproduced by the present model can be confirmed by the power spectra shown in **Supplementary Figure 2**.

If the postsynaptic neuron's firing is blocked in some way, what happens? According to the present model, the activity-dependent release of proBDNF is dominant over that of mBDNF, when the absence of bAP does not enhance Ca^{2+} concentration sufficiently. In Equation (13), the first term on the right-hand side vanishes due to the suppression of bAP, and only the second term remains. In this situation, the activity-dependent component of the synapse growth rate becomes negative. This indicates that the synaptic rewiring probability that a weaker synaptic contact survives and a stronger contact is retracted becomes larger than the probability of the opposite process. Reiter and Stryker (1988) have reported the reversal shift of ocular dominance to the deprived eye but not to the non-deprived eye in monocularly deprived kittens whose visual cortices were infused with the GABA receptor agonist muscimol. This odd phenomenon should be reproduced because the synapse growth rate always takes more negative values for non-deprived-eye inputs than for deprived-eye inputs, although the present model was not extended to the model with binocular inputs. This experimental finding is expected to support any models based on the assumption that LTP is induced for high intracellular Ca^{2+} concentration and LTD is induced for moderate Ca^{2+} concentration by manipulating the threshold for the switching between LTP induction and LTD induction.

As mentioned in section "Hypothetical Mechanisms of Synaptic Rewiring," our hypothetical mechanism is basically the same as the BCM theory, although the explicit variable representing the Ca^{2+} concentration does not appear in our model. However, one of the differences between the BCM model and ours rather consists in how to use the rule for synaptic update. The synapse growth rate corresponds to the synaptic efficacy change in the BCM model. In our model, only a synaptic contact having the maximum synapse growth rate can be stabilized to survive, and the other contacts are eliminated. Even if the synapse growth rate of a synaptic contact is positive, it will be defeated by another contact with larger synapse growth rate. This process is realized by the algorithm in which a synaptic contact is replaced with a stronger contact, keeping the total number of synaptic contacts on a cortical neuron constant. However, after synaptic rewiring is completed (**Figure 3E**) and only a single axonal bouton contacts with the spine in question, the sign of the synapse growth rate determines the direction of the synaptic efficacy toward LTP (positive) or LTD (negative).

Tuning Curves Changed by Single-Orientation Exposure

In **Figure 6B**, the average OSI seen experimentally changed depending on age in a non-monotonic manner. **Figure 10B** obtained from simulations also showed a similar behavior of the average OSI. At the early stage of the sensitive period, the orientation tuning curves of most neurons are immature and broad. Restricted exposure to vertical orientation for 2 weeks (3.15 MCs in the model) alters their preferred orientations toward the exposed orientation. In **Figure 10B**, the OSI for single-orientation exposure was larger than that for 12-orientation exposure from 0 to 5 MCs. This suggests that orientation selectivity is sharper than that of kittens reared in the normal visual environment at this stage. At the late stage of the sensitive period, the orientation selectivity is almost matured, and the orientation tuning curves generated by normal visual experience (12-orientations in the model) tend to be restored despite single-orientation exposure. Both in **Figures 6B**, **10B**, the dip of the OSI for single-orientation exposure appeared at the ORI declining phase in the sensitive period. At this stage, the OSI of individual neurons are likely to decrease as the orientation tuning curves become broadened or bimodal. In the bimodal orientation tuning curves, one peak appears at the original preferred orientation and the other at the exposed orientation. Such modifications of tuning curves are caused by the disruption of ON or OFF responsive subfields elongated in parallel to the preferred orientation under the influence of the exposed orientation. This can be seen in the comparisons between the changes in responsive subfields (**Figure 11D,E,G,H**) and the changes in tuning curves (the red curves to blue curves in **Figures 11F,I**). Broad tuning curves after single-orientation exposure (e.g., blue curve in **Figure 11I**) are likely to appear in the transition from the bimodal distribution (e.g., blue curve in **Figure 11F**) to the unimodal distribution (e.g., blue curve in **Figure 11L**).

Related to this, in orientation maps obtained from simulations under single-orientation exposure (e.g., map at 4.73 MCs in **Figure 9**), almost continuous changes in preferred orientations of neurons (bright pixels) were interleaved with orientation-nonselective neurons (dark pixels), whose orientation tuning curves were not unimodal. The emergence of non-selective neurons between clusters of orientation-selective neurons can be more clearly observed in **Figure 13**. Starting from a common initial state which receives random afferent inputs from the model LGN, simulations were conducted under 12-orientation exposure for 1.57 MCs or 2.36 MCs at the beginning, and then resumed under the same condition or single-orientation exposure for 3.15 MCs. **Figure 13** shows typical one-dimensional changes in the preferred orientation sampled from neurons along the same line on the model cortex (red circles). It also shows the positions of orientation-nonselective neurons along the same line (black dots with vertical lines), where orientation-nonselective neurons were defined by neurons with OSI = 0 and orientation magnitudes (in the sense of the vector

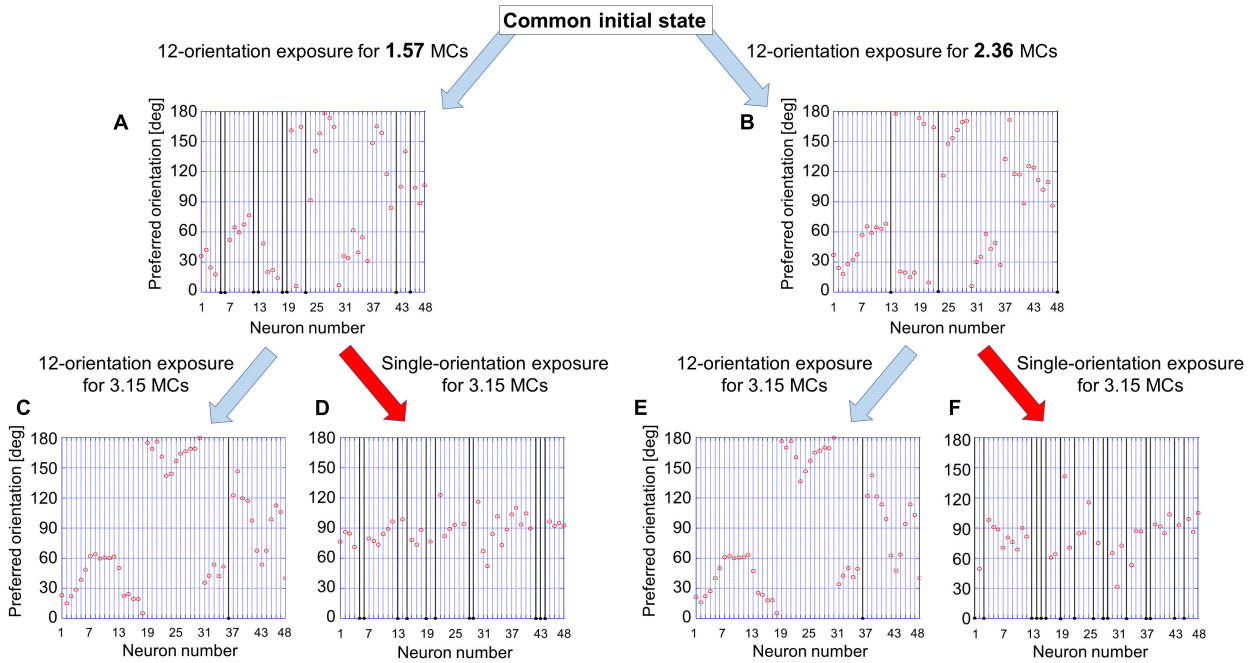

FIGURE 13 | Preferred orientation as a function of the neuron's position along the same line in the model visual cortex for different stimulation conditions and different simulation steps. **(A,B)** The preferred orientations changing with the one-dimensional position, and positions of orientation-nonselective neurons obtained from simulations under 12-orientation exposure for 1.57 MCs and 2.36 MCs, respectively. A pattern of initial random inputs from the model LGN to the model cortex was common for **(A,B)**. **(C,D)** The preferred orientations and orientation-nonselective neurons along the same line obtained from simulations resumed for 3.15 MCs from **(A)** under 12-orientation and single-orientation exposures, respectively. **(E,F)** The preferred orientations and orientation-nonselective neurons along the same line obtained from simulations resumed for 3.15 MCs from **(B)** under 12-orientation and single-orientation exposures, respectively. Preferred orientations are indicated by red circles, and positions of orientation-nonselective neurons are indicated by black dots with vertical bars. Numerical data are shown in **Supplementary Table 7**.

sum method) smaller than a half of the magnitude averaged over the model cortex. Orientation-nonselective neurons were shown to appear interleaving clusters of orientation-selective neurons even in the streams of simulations under 12-orientation exposure as in A–C, or B–E. There was a tendency that the number of orientation-nonselective neurons decreases as the simulation step of 12-orientation exposure. In contrast, after 3.15 MCs of simulations under single-orientation exposure following 12-orientation exposure, many nonselective neurons appeared disrupting the gradual changes in the preferred orientation, as shown in **Figures 13D,F**. These simulation results are consistent with the experimental findings reported by Stryker et al. (1978). They reported that the regions of orientation-selective cells were separated by gaps containing only non-selective or unresponsive cells along the electrode track in the visual cortex of cats reared viewing horizontal stripes with both eyes (see Figure 5C in Stryker et al., 1978).

What Determines the Closure of the Sensitive Period?

Figures 7, **8** indicate the existence of a period in which the orientation representation is modifiable by altered visual experience, and orientation maps are unable to change after the period. The factor determining the end of the sensitive period consists in the probability of postsynaptic dendritic spines change their morphology to reach varicosities along the geniculo-cortical axons to make transient synaptic contacts. We assumed that the expression of $p75^{NTR}$ changes with age in early life, and the binding of proBDNF secreted from the constitutive pathway to $p75^{NTR}$ facilitates the elimination of labile synaptic contacts. This elimination is considered being caused by the decrease of the probability that a postsynaptic spine moves and changes its shape to encounter axonal varicosities to make a transient synaptic contact, as expressed by Equation (11). We assumed the age-dependent increase in the expression of $p75^{NTR}$ as seen in Equation (12). As a result, the frequency of a postsynaptic spine making another transient synaptic contact for rewiring decreases, and the orientation map modifiability disappears. Consequently, the end of the sensitive period is determined by the time when the probability given by Equation (11) becomes sufficiently small. So far, the regulatory pathway of BDNF secretion has attracted much attention, because the pathway is considered being relevant to activity-dependent synaptic plasticity underlying the elaboration of neural networks during development, and in adult learning and memory. However, the activity-independent mechanism of BDNF secretion works in the constitutive pathway in addition to the activity-dependent mechanism in the regulatory pathway. In the present model, activity-independent mechanisms of BDNF secretion and $p75^{NTR}$ expression, which are related to the inverse temperature β and the closure of the sensitive period, respectively, are important factors to obtain a better understanding of how

synaptic rewiring occurs and how visual experience influences orientation map development.

It has been widely accepted that proBDNF and mBDNF have opposing functions in the early development of neuromuscular junctions, which induces competition among different inputs to eliminate inadequate inputs and stabilize the most adequate input as a winner (Je et al., 2012, 2013). Analogously, we hypothesized that mBDNF and proBDNF in the visual cortex during postnatal development serve to stabilize synaptic contacts that transmit neural signals most efficiently and eliminate other inefficient contacts. The survival or extinction of transient synaptic contacts is determined by the difference of the synapse growth rates in the vicinity of individual contacts [**Figures 3B–D**, Equation (7)]. Since the amounts of secretion of mBDNF and proBDNF depend on the intracellular Ca^{2+} concentration, one would be able to argue such synaptic rewiring in terms of the dynamics of Ca^{2+} concentration alone without referring to the roles of BDNF, neurotrophin receptors, and tPA. However, the present model built explicitly on those molecules is more likely to account for the sensitive period for synaptic plasticity than other models based only on Ca^{2+} dynamics. Particularly, the age-dependent expression of $p75^{NTR}$ considered in the present model is determinant. There are findings that the mRNA level of $p75^{NTR}$ decreases in the visual cortex of rats around the sensitive period (Bracken and Turrigiano, 2009) and proBDNF collapses neurite outgrowth through $p75^{NTR}$ activation (Sun et al., 2012). In our model, assuming that the $p75^{NTR}$ expression steeply decreased around eye opening increases around the end of the sensitive period, which reduces the chance of participation of candidate synaptic contacts to synaptic competition owing to the pruning of dendritic spines and/or terminaux boutons along the presynaptic axons, the model successfully reproduced the sensitive period profile (**Figure 10A** compared with **Figure 6A**). Although the present model remains to be extended to a model with the left and right eye inputs, it may be able to account for previous experimental results: The intracortical blockade of tPA or plasmin selectively prevents recovery from monocular-deprivation induced dysfunction during reverse occlusion (Müller and Griesinger, 1998); and the cortical infusion of exogenous BDNF inhibits ocular dominance column formation during postnatal development (Cabelli et al., 1995). Furthermore, the model may contribute to the designing of experiments to explore possible methods for the restoration of developmental plasticity even in the adulthood.

DATA AVAILABILITY STATEMENT

The raw data supporting the conclusions of this article will be made available by the authors, without undue reservation, to any qualified researcher.

ETHICS STATEMENT

The animal study was reviewed and approved by the Institutional Animal Research Committee at RIKEN and performed in accordance with the guideline of the Japanese Physiological Society.

AUTHOR CONTRIBUTIONS

ST built the mathematical model of synaptic rewiring and wrote the manuscript. MM coded the Fortran programs based on the synaptic rewiring algorithm and carried out the simulations. NW carried out the simulations and provided the simulation results. KO'H and TT provided the part of the experimental data. JR built a systematic analysis method of evoked intrinsic signals. All the authors contributed to the article and approved the submitted version.

FUNDING

This work was supported by JSPS KAKENHI Grant Number JP17K07050.

ACKNOWLEDGMENTS

The authors thank for JR at Centre for Interdisciplinary Research in Biology (CIRB), Collège de France for his arrangement of systematic methods for the visualization and numerical analysis of intrinsic signals evoked in the cat visual cortex.

SUPPLEMENTARY MATERIAL

The Supplementary Material for this article can be found online at: https://www.frontiersin.org/articles/10.3389/fninf.2020.00041/full#supplementary-material

REFERENCES

Albus, K., and Wolf, W. (1984). Early post-natal development of neuronal function in the kitten's visual cortex: a laminar analysis. *J. Physiol.* 348, 153–185. doi: 10.1113/jphysiol.1984.sp015104

Araque, A., Parpura, V., Sanzgiri, R. P., and Haydon, P. G. (1999). Tripartite synapses: glia, the unacknowledged partner. *Trends Neurosci.* 22, 208–215. doi: 10.1016/s0166-2236(98)01349-6

Baho, E., Chattopadhyaya, B., Lavertu-Jolin, M., Mazziotti, R., Awad, P. N., Chehrazi, P., et al. (2019). p75 neurotrophin receptor regulates the timing of the maturation of cortical parvalbumin cell connectivity and promotes ocular dominance plasticity in adult visual cortex. *J. Neurosci.* 39, 4489–4510. doi: 10.1523/jneurosci.2881-18.2019

Bear, M. F., and Rittenhouse, C. D. (1999). Molecular basis for induction of ocular dominance plasticity. *J. Neurobiol.* 41, 83–91. doi: 10.1002/(sici)1097-4695(199910)41:1<83::aid-neu11>3.0.co;2-z

Berardi, N., and Pizzorusso, T. (2004). Extracellular matrix and visual cortical plasticity: freeing the synapse. *Neuron* 44, 905–908. doi: 10.1016/s0896-6273(04)00796-2

Bienenstock, E. L., Cooper, L., and Munro, P. (1982). Theory for the development of neuron selectivity: orientation specificity and binocular interaction in visual cortex. *J. Neurosci.* 2, 32–48. doi: 10.1523/jneurosci.02-01-00032.1982

Binder, D. K., and Scharfman, H. E. (2004). Brain-derived neurotrophic factor. *Growth Fact.* 22, 123–131.

Blakemore, C., and Cooper, G. F. (1970). Development of the brain depends on visual environment. *Nature* 228, 477–478. doi: 10.1038/228477a0

Blakemore, C., and Van Sluyters, R. C. (1975). Innate and environmental factors in the development of the kitten's visual cortex. *J. Physiol.* 248, 663–716. doi: 10.1113/jphysiol.1975.sp010995

Bonhoeffer, T., and Grinvald, A. (1991). Iso-orientation domains in cat visual cortex are arranged in pinwheel-like patterns. *Nature* 353, 429–431. doi: 10.1038/353429a0

Bonhoeffer, T., and Grinvald, A. (1996). "Optical imaging based on intrinsic signals: the methodology," in *Brain Mapping: The Methods*, eds A. Toga, and J. C. Mazziotta, (San Diego: Academic Press), 55–97.

Bracken, B. K., and Turrigiano, G. G. (2009). Experience-dependent regulation of TrkB isoforms in rodent visual cortex. *Dev. Neurobiol.* 69, 267–278. doi: 10.1002/dneu.20701

Cabelli, R. J., Hohn, A., and Shatz, C. J. (1995). Inhibition of ocular dominance column formation by infusion of NT-4/5 or BDNF. *Science* 267, 1662–1666. doi: 10.1126/science.7886458

Carreira-Perpinăń, M. Á, Lister, R., and Goodhill, G. J. (2005). A computational model for the development of multiple maps in primary visual cortex. *Cereb. Cortex* 15, 1222–1233. doi: 10.1093/cercor/bhi004

Cloherty, S. L., Hughes, N. J., Hietanen, M. A., Bhagavatula, P. S., Goodhill, G. J., and Ibbotson, M. R. (2016). Sensory experience modifies feature map relationships in visual cortex. *eLife* 5:e13911. doi: 10.7554/eLife.13911

Crair, M. C., Gillespie, D. C., and Stryker, M. P. (1998). The role of visual experience in the development of columns in cat visual cortex. *Science* 279, 566–570. doi: 10.1126/science.279.5350.566

Cunha, C., Brambilla, R., and Thomas, K. L. (2010). A simple role for BDNF in learning and memory? *Front. Mol. Neurosci.* 3:1. doi: 10.3389/neuro.02.001.2010

DeAngelis, G. C., Ghose, G. M., Ohzawa, I., and Freeman, R. D. (1999). Functional micro-organization of primary visual cortex: receptive field analysis of nearby neurons. *J. Neurosci.* 19, 4046–4064. doi: 10.1523/JNEUROSCI.19-10-04046.1999

DeAngelis, G. C., Ohzawa, I., and Freeman, R. D. (1995). Receptive-field dynamics in the central visual pathways. *Trends Neurosci.* 18, 451–458. doi: 10.1016/0166-2236(95)94496-r

Durbin, R., and Mitchison, G. (1990). A dimension reduction framework for understanding cortical maps. *Nature* 343, 644–647. doi: 10.1038/343644a0

Erwin, E., Obermayer, K., and Schulten, K. (1995). Models of orientation and ocular dominance columns in the visual cortex: a critical comparison. *Neural Comput.* 7, 425–468. doi: 10.1162/neco.1995.7.3.425

Fagiolini, M., and Hensch, T. K. (2000). Inhibitory threshold for critical-period activation in primary visual cortex. *Nature* 404, 183–186. doi: 10.1038/35004582

Fagiolini, M., Pizzorusso, T., Berardi, N., Domenici, L., and Maffei, L. (1994). Functional postnatal development of the rat primary visual cortex and the role of visual experience: dark rearing and monocular deprivation. *Vis. Res.* 34, 709–720. doi: 10.1016/0042-6989(94)90210-0

Frey, U., Frey, S., Schollmeier, F., and Krug, M. (1996). Influence of actinomycin D, a RNA synthesis inhibitor, on long-term potentiation in rat hippocampal neurons in vivo and in vitro. *J. Physiol.* 490, 703–711. doi: 10.1113/jphysiol.1996.sp021179

Fukai, T., and Tanaka, S. (1997). A simple neural network exhibiting selective activation of neuronal ensembles: from winner-take-all to winner-share-all. *Neural Comput.* 9, 77–97. doi: 10.1162/neco.1997.9.1.77

Giacomantonio, C. E., Ibbotson, M. R., and Goodhill, G. J. (2010). The influence of restricted orientation rearing on map structure in primary visual cortex. *Neuroimage* 52, 875–883. doi: 10.1016/j.neuroimage.2009.12.066

Gilbert, C. D., Das, A., Ito, M., Kapadia, M., and Westheimer, G. (1996). Spatial integration and cortical dynamics. *Proc. Natl. Acad. Sci. U.S.A.* 93, 615–622. doi: 10.1073/pnas.93.2.615

Goodhill, G. J. (2007). Contributions of theoretical modeling to the understanding of neural map development. *Neuron* 56, 301–311. doi: 10.1016/j.neuron.2007.09.027

Goodhill, G. J., and Barrow, H. G. (1994). The role of weight normalization in competitive learning. *Neural Comput.* 6:1994.

Graupner, M., and Brunel, N. (2010). Mechanisms of induction and maintenance of spike-timing dependent plasticity in biophysical synapse models. *Front. Comput. Neurosci.* 4:136. doi: 10.3389/fncom.2010.00136

Greenberg, M. E., Xu, B., Lu, B., and Hempstead, B. (2009). New insights in the biology of BDNF synthesis and release: implications in CNS function. *J. Neurosci.* 29, 12764–12767. doi: 10.1523/jneurosci.3566-09.2009

Hebb, D. O. (1949). *The Organization of Behavior*. New York, NY: Wiley.

Hirsch, H. V. B., and Spinelli, D. N. (1970). Visual experience modifies distribution of horizontally and vertically oriented receptive fields in cats. *Science* 168, 869–871. doi: 10.1126/science.168.3933.869

Hofbauer, J., and Sigmund, K. (1988). *The Theory of Evolution and Dynamical System, London Mathematical Society Student Texts*. New York, NY: Cambridge University Press.

Hubel, D. H., and Wiesel, T. N. (1962). Receptive fields, binocular interaction and functional architecture in the cat's visual cortex. *J. Physiol.* 160, 106–154. doi: 10.1113/jphysiol.1962.sp006837

Hubel, D. H., and Wiesel, T. N. (1965). Comparison of the effects of unilateral and bilateral eye closure on cortical unit responses in kittens. *J. Neurophysiol.* 28, 1029–1040. doi: 10.1152/jn.1965.28.6.1029

Hubel, D. H., and Wiesel, T. N. (1968). Receptive fields and functional architecture of monkey striate cortex. *J. Physiol.* 195, 215–243. doi: 10.1113/jphysiol.1968.sp008455

Hubel, D. H., and Wiesel, T. N. (1974). Sequence regularity and geometry of orientation columns in the monkey striate cortex. *J. Comp. Neurol.* 158, 267–294.

Hubel, D. H., and Wiesel, T. N. (1977). Ferrier lecture. Functional architecture of macaque monkey visual cortex. *Proc. R. Soc. Lond Ser. B* 198, 1–59. doi: 10.1098/rspb.1977.0085

Hubel, D. H., Wiesel, T. N., and LeVay, S. (1977). Plasticity of ocular dominance columns in monkey striate cortex. *Philos. Trans. R. Soc. B* 278, 131–163.

Je, H. S., Yang, F., Ji, Y., Nagappan, G., Hempstead, B. L., and Lu, B. (2012). Role of pro-brain-derived neurotrophic factor (proBDNF) to mature BDNF conversion in activity-dependent competition at developing neuromuscular synapses. *Proc. Natl. Acad. Sci. U.S.A.* 109, 15924–15929. doi: 10.1073/pnas.1207767109

Je, H. S., Yang, F., Ji, Y., Potluri, S., Fu, X.-Q., Luo, Z.-G., et al. (2013). ProBDNF and mature BDNF as punishment and reward signals for synapse elimination at mouse neuromuscular junctions. *J. Neurosci.* 33, 9957–9962. doi: 10.1523/jneurosci.0163-13.2013

Kim, D.-S., Matsuda, Y., Ohki, K., Ajima, A., and Tanaka, S. (1999). Geometrical and topological relationships between multiple functional maps in cat primary visual cortex. *Neuroreport* 10, 2515–2522. doi: 10.1097/00001756-199908200-00015

Koester, H. J., and Sakmann, B. (1998). Calcium dynamics in single spines during coincident presynaptic and postsynaptic activity depend on relative timing of back-propagating action potentials and subthreshold excitatory postsynaptic potentials. *Proc. Natl. Acad. Sci. U.S.A.* 95, 9596–9601. doi: 10.1073/pnas.95.16.9596

Koester, H. J., and Sakmann, B. (2000). Calcium dynamics associated with action potentials in single nerve terminals of pyramidal cells in layer 2/3 of the young rat neocortex. *J. Physiol.* 529, 625–646. doi: 10.1111/j.1469-7793.2000.00625.x

Kohonen, T. (1997). *Self-Organizing Maps*. Berlin: Springer-Verlag.

Kuczewski, N., Porcher, C., Lessmann, V., Medina, I., and Gaiarsa, J. L. (2009). Activity-dependent dendritic release of BDNF and biological consequences. *Mol. Neurobiol.* 39, 37–49. doi: 10.1007/s12035-009-8050-7

Lesmann, V., and Brigadski, T. (2009). Mechanisms, locations, and kinetics of synaptic BDNF secretion: an update. *Neurosci. Res.* 65, 11–22. doi: 10.1016/j.neures.2009.06.004

LeVay, S., Wiesel, T. N., and Hubel, D. H. (1980). The development of ocular dominance columns in normal and visually deprived monkeys. *J. Comp. Neurol.* 191, 1–51. doi: 10.1002/cne.901910102

Markram, H., Lubke, J., Frotscher, M., and Sakmann, B. (1997). Regulation of synaptic efficacy by coincidence of postsynaptic APs and EPSPs. *Science* 275, 213–215. doi: 10.1126/science.275.5297.213

Mataga, N., Mizuguchi, Y., and Hensch, T. K. (2004). Experience-dependent pruning of dendritic spines in visual cortex by tissue plasminogen activator. *Neuron* 44, 1031–1041. doi: 10.1016/j.neuron.2004.11.028

Mataga, N., Nagai, N., and Hensch, T. K. (2002). Permissive proteolytic activity for visual cortical plasticity. *Proc. Natl. Acad. Sci. U.S.A.* 99, 7717–7721. doi: 10.1073/pnas.102088899

McRae, P. A., and Porter, B. E. (2012). The perineuronal net component of the extracellular matrix in plasticity and epilepsy. *Neurochem. Int.* 61, 963–972. doi: 10.1016/j.neuint.2012.08.007

Metropolis, N., Rosenbluth, A. W., Rosenbluth, M. N., Teller, A. H., and Teller, E. (1953). Equation of state calculations by fast computing machines. *J. Chem. Phys.* 21, 1087–1092. doi: 10.1063/1.1699114

Miller, K. D. (1992). Development of orientation columns via competition between ON- and OFF-center inputs. *Neuroreport* 3, 73–76. doi: 10.1097/00001756-199201000-00019

Miller, K. D. (1994). A model for the development of simple cell receptive fields and the ordered arrangement of orientation columns through the activity dependent competition between ON- and OFF-center inputs. *J. Neurosci.* 14, 409–441. doi: 10.1523/jneurosci.14-01-00409.1994

Miller, K. D., and Mackay, D. J. (1994). The roles of constraints in Hebbian learning. *Neural Comput.* 6, 100–126. doi: 10.1162/neco.1994.6.1.100

Miyashita, M., Kim, D. S., and Tanaka, S. (1997). Cortical directional selectivity without directional experience. *Neuroreport* 8, 1187–1191. doi: 10.1097/00001756-199703240-00026

Miyashita, M., and Tanaka, S. (1992). A mathematical model for the self-organization of orientation columns in visual cortex. *Neuroreport* 3, 69–72. doi: 10.1097/00001756-199201000-00018

Movshon, J. A., Thompson, I. D., and Tolhurst, D. J. (1978). Spatial and temporal contrast sensitivity of neurones in areas 17 and 18 of the cat's visual cortex. *J. Physiol.* 283, 101–120. doi: 10.1113/jphysiol.1978.sp012490

Müller, C., and Griesinger, C. (1998). Tissue plasminogen activator mediates reverse occlusion plasticity in visual cortex. *Nat. Neurosci.* 1, 47–53. doi: 10.1038/248

Nagappan, G., Zaitsev, E., Senatorov, V. V. Jr., Yang, J., Hempstead, B. L., and Lu, B. (2009). Control of extracellular cleavage of proBDNF by high frequency neuronal activity. *Proc. Natl. Acad. Sci. U.S.A.* 106, 1267–1272. doi: 10.1073/pnas.0807322106

Nevian, T., and Sakmann, B. (2004). Single spine Ca2+ signals evoked by coincident EPSPs and backpropagating action potentials in spiny stellate cells of layer 4 in the juvenile rat somatosensory barrel cortex. *J. Neurosci.* 24, 1689–1699. doi: 10.1523/jneurosci.3332-03.2004

Numakawa, T., Suzuki, S., Kumamaru, E., Adachi, N., Richards, M., and Kunugi, H. (2010). BDNF function and intracellular signaling in neurons. *Histol. Histopathol.* 25, 237–258.

Obermayer, K., Ritter, H., and Schulten, K. (1990). A principle for the formation of the spatial structure of cortical feature maps. *Proc. Nad. Acad. Sci. U.S.A.* 87, 8345–8349. doi: 10.1073/pnas.87.21.8345

Ohki, K., Matsuda, Y., Ajima, A., Kim, D.-S., and Tanaka, S. (2000). Arrangement of orientation pinwheel centers around area 17/18. *Cereb. Cortex* 10, 593–601. doi: 10.1093/cercor/10.6.593

Olson, C. R., and Freeman, R. D. (1980). Profile of the sensitive period for monocular deprivation in kittens. *Exp. Brain Res.* 39, 17–21.

Pang, T. P., Teng, H. K., Zaitsev, E., Woo, N. T., Sakata, K., Zhen, S., et al. (2004). Cleavage of proBDNF by tPA/plasmin is essential for long-term hippocampal plasticity. *Science* 306, 487–491. doi: 10.1126/science.1100135

Rauschecker, J. P., and Singer, W. (1981). The effects of early visual experience on the cat's visual cortex and their possible explanation by Hebb synapses. *J. Neurophysiol.* 310, 215–239. doi: 10.1113/jphysiol.1981.sp013545

Reiter, H. O., and Stryker, M. P. (1988). Neural plasticity without postsynaptic action potentials: Less-active inputs become dominant when kitten visual cortical cells are pharmacologically inhibited. *Proc. Natl. Acad. Sci. U.S.A.* 85, 3623–3627. doi: 10.1073/pnas.85.10.3623

Saul, A. B., and Humphrey, A. L. (1990). Spatial and temporal response properties of lagged and nonlagged cells in cat lateral geniculate nucleus. *J. Neurophysiol.* 64, 206–224. doi: 10.1152/jn.1990.64.1.206

Saul, A. B., and Humphrey, A. L. (1992). Evidence of input from lagged cells in the lateral geniculate nucleus to simple cells in cortical area 17 of the cat. *J. Neurophysiol.* 68, 1190–1208. doi: 10.1152/jn.1992.68.4.1190

Sengpiel, F., Stawinski, P., and Bonhoeffer, T. (1999). Influence of experience on orientation maps in cat visual cortex. *Nat. Neurosci.* 2, 727–732. doi: 10.1038/11192

Shatz, C. J., and Stryker, M. P. (1978). Ocular dominance columns in layer IV of the cat's visual cortex and the effects of monocular deprivation. *J. Physiol.* 281, 267–283. doi: 10.1113/jphysiol.1978.sp012421

Singh, K., Park, K., Hong, E., Kramer, B. M., Greenberg, M. E., Kaplan, D. R., et al. (2008). Developmental axon pruning mediated by BDNF-p75NTR-dependent axon degeneration. *Nat. Neurosci.* 11, 649–658. doi: 10.1038/nn.2114

Stryker, M. P., and Sherk, H. (1975). Modification of cortical selectivity in the cat by restricted visual experience: a reexamination. *Science* 190, 904–906. doi: 10.1126/science.1188372

Stryker, M. P., Sherk, H., Leventhal, A. G., and Hirsch, H. V. R. (1978). Physiological consequences for the cat's visual cortex of effectively restricting early visual experience with oriented contours. *J. Neurophyiol.* 41, 894–909.

Sun, Y., Lim, Y., Li, F., Liu, S., Lu, J.-J., Haberberger, R., et al. (2012). ProBDNF collapses neurite outgrowth of primary neurons by activating RhoA. *PLoS One* 7:e35883. doi: 10.1371/journal.pone.0035883

Swindale, N. V. (1988). Role of visual experience in promoting segregation of eye dominance patches in the visual cortex of the cat. *J. Comp. Neurol.* 267, 472–488. doi: 10.1002/cne.902670403

Swindale, N. V., Matsubara, J. A., and Cynader, M. S. (1987). Surface organization of orientation and direction selectivity in cat area 18. *J. Neurosci.* 7, 1414–1427. doi: 10.1523/jneurosci.07-05-01414.1987

Tanaka, S. (1990). Theory of self-organization of cortical maps: mathematical framework. *Neural Netw.* 3, 625–640. doi: 10.1016/0893-6080(90)90053-n

Tanaka, S., and Miyashita, M. (2009). Constraint on the number of synaptic inputs to a visual cortical neuron controls receptive field formation. *Neural. Comput.* 21, 2554–2580. doi: 10.1162/neco.2009.04-08-752

Tanaka, S., Miyashita, M., and Ribot, J. (2004). Roles of visual experience and intrinsic mechanism in the activity-dependent self-organization of orientation maps: theory and experiment. *Neural Netw.* 17, 1363–1375. doi: 10.1016/j.neunet.2004.06.014

Tanaka, S., Ribot, J., Imamura, K., and Tani, T. (2006). Orientation-restricted continuous visual exposure induces marked reorganization of orientation maps in early life. *Neuroimage* 30, 462–477. doi: 10.1016/j.neuroimage.2005.09.056

Tanaka, S., Tani, T., Ribot, J., O'Hashi, K., and Imamura, K. (2009). A postnatal critical period for orientation plasticity in the cat visual cortex. *PLoS One* 4:e5380. doi: 10.1371/journal.pone.005380

Tanaka, S., Tani, T., Ribot, J., and Yamazaki, T. (2007). Chronically mountable goggles for persistent exposure to single orientation. *J. Neurosci. Methods* 160, 206–214. doi: 10.1016/j.jneumeth.2006.09.004

Teng, H. K., Teng, K. K., Lee, R., Wright, S., Tevar, S., Almeida, R. D., et al. (2005). ProBDNF induces neuronal apoptosis via activation of a receptor complex of p75NTR and sortilin. *J. Neurosci.* 25, 5455–5463. doi: 10.1523/jneurosci.5123-04.2005

Tsai, S. J. (2017). Role of tissue-type plasminogen activator and plasminogen activator inhibitor-1 in psychological stress and depression. *Oncotarget* 8, 113258–113268. doi: 10.18632/oncotarget.19935

Tsunoda, K., Yamane, Y., Nishizaki, M., and Tanifuji, M. (2001). Complex objects are represented in macaque inferotemporal cortex by the combination of feature columns. *Nat. Neurosci.* 4, 832–838. doi: 10.1038/90547

Tusa, R. J., Palmer, L. A., and Rosenquist, A. C. (1978). The retinotopic organization of area 17 (striate cortex) in the cat. *J. Comp. Neurol.* 177, 213–236.

Tusa, R. J., Rosenquist, A. C., and Palmer, L. A. (1979). Retinotopic organization of areas 18 and 19 in the cat. *J. Comp. Neurol.* 185, 657–678. doi: 10.1002/cne.901850405

Wiesel, T. N., and Hubel, D. H. (1974). Ordered arrangement of orientation columns in monkeys lacking visual experience. *J. Comp. Neurol.* 158, 307–318. doi: 10.1002/cne.901580306

Yang, B., Yang, C., Ren, Q., Zhang, J. C., Chen, Q. X., Shirayama, Y., et al. (2016). Regional differences in the expression of brain-derived neurotrophic factor (BDNF) pro-peptide, proBDNF and pre-proBDNF in the brain confer stress resilience. *Eur. Arch. Psychiatry Clin. Neurosci.* 266, 765–769. doi: 10.1007/s00406-016-0693-6

Yokoo, T., Knight, B. W., and Sirovich, L. (2001). An optimization approach to signal extraction from noisy multivariate data. *Neuroimage* 14, 1309–1326. doi: 10.1006/nimg.2001.0950

Conflict of Interest: NW was employed by the company All Nippon Airways Co., Ltd.

The remaining authors declare that the research was conducted in the absence of any commercial or financial relationships that could be construed as a potential conflict of interest.

frontiers in Neuroinformatics

ERRATUM
published: 29 October 2020
doi: 10.3389/fninf.2020.607901

Erratum: Development and Reorganization of Orientation Representation in the Cat Visual Cortex: Experience-Dependent Synaptic Rewiring in Early Life

*Frontiers Production Office**

Frontiers Media SA, Lausanne, Switzerland

OPEN ACCESS

Approved by:
Frontiers Editorial Office, Frontiers Media SA, Switzerland

***Correspondence:**
Frontiers Production Office
production.office@frontiersin.org

Received: *18 September 2020*
Accepted: *23 September 2020*
Published: *29 October 2020*

Citation:
Frontiers Production Office (2020) Erratum: Development and Reorganization of Orientation Representation in the Cat Visual Cortex: Experience-Dependent Synaptic Rewiring in Early Life. Front. Neuroinform. 14:607901. doi: 10.3389/fninf.2020.607901

Keywords: orientation maps, self-organization, visual experience, development, sensitive period

An Erratum on

Development and Reorganization of Orientation Representation in the Cat Visual Cortex: Experience-Dependent Synaptic Rewiring in Early Life
by Tanaka, S., Miyashita, M., Wakabayashi, N., O'Hashi, K., Tani, T., and Ribot, J. (2020). Front. Neuroinform. 14:41. doi: 10.3389/fninf.2020.00041

Due to a production error when converting the original pdf version into other formats the equations included notation errors (zeta–>sigma). These are Equations (7), (8), (13), (14), (16), (16′), and (13′). In addition, there are several notation errors in the sentences around those equations.

The publisher apologizes for this mistake. The original article has been updated.

frontiers in Neuroanatomy

BRIEF RESEARCH REPORT
published: 23 July 2021
doi: 10.3389/fnana.2021.715571

Track-Density Ratio Mapping With Fiber Types in the Cerebral Cortex Using Diffusion-Weighted MRI

Sang-Han Choi[1], Gangwon Jeong[2], Young-Eun Hwang[1], Yong-Bo Kim[3], Haigun Lee[4] and Zang-Hee Cho[1,2]**

[1]Neuroscience Convergence Center, Korea University, Seoul, South Korea, [2]AICT, Seoul National University, Seoul, South Korea, [3]Neuroscience Research Institute, Gachon University, Incheon, South Korea, [4]Green Manufacturing Research Center, Korea University, Seoul, South Korea

The nerve fibers are divided into three categories: projection, commissural, and association fibers. This study demonstrated a novel cortical mapping method based on these three fiber categories using MR tractography data. The MR fiber-track data were extracted using the diffusion-weighted 3T-MRI data from 19 individuals' Human Connectome Project dataset. Anatomical MR images in each dataset were parcellated using FreeSurfer software and Brainnetome atlas. The 5 million extracted tracks per subject by MRtrix software were classified based on the basic cortical structure (cortical area in the left and right hemisphere, subcortical area), after the tracks validation procedure. The number of terminals for each categorized track per unit-sized cortical area (1 mm^3) was defined as the track-density in that cortical area. Track-density ratio mapping with fiber types was achieved by mapping the density-dependent color intensity for each categorized tracks with a different primary color. The mapping results showed a highly localized, unique density ratio map determined by fiber types. Furthermore, the quantitative group data analysis based on the parcellation information revealed that the majority of nerve fibers in the brain are association fibers, particularly in temporal, inferior parietal, and occipital lobes, while the projection and commissural fibers were mainly located in the superior part of the brain. Hemispheric asymmetries in the fiber density were also observed, such as long association fiber in the Broca's and Wernicke's areas. We believe this new dimensional brain mapping information allows us to further understand brain anatomy, function.

Keywords: nerve fibers, brain mapping, diffusion-weighted MRI, human connectome project, tractography

OPEN ACCESS

Edited by:
Nick Swindale, University of British Columbia, Canada

Reviewed by:
Guy Elston, Centre for Cognitive Neuroscience Ltd, Australia
Noritaka Ichinohe, National Center of Neurology and Psychiatry (Japan), Japan

****Correspondence:***
Haigun Lee
haigunlee@korea.ac.kr
Zang-Hee Cho
zhcho36@gmail.com

Received: *27 May 2021*
Accepted: *08 July 2021*
Published: *23 July 2021*

Citation:
Choi S-H, Jeong G, Hwang Y-E, Kim Y-B, Lee H and Cho Z-H (2021) Track-Density Ratio Mapping With Fiber Types in the Cerebral Cortex Using Diffusion-Weighted MRI. Front. Neuroanat. 15:715571. doi: 10.3389/fnana.2021.715571

INTRODUCTION

Neurons in the cerebral cortex are connected with three major brain regions, subcortical, inter-cortical, and intra-cortical regions. Depending on these connected brain regions, the nerve fibers are broadly divided into three categories, i.e., projection, commissural, and association fibers. Projection fibers, also called corticofugal fibers, are connected with numerous subcortical structures in the telencephalon, diencephalon, brain stem, and

spinal cord *via* the internal capsule. Association fibers are intra-cortical fibers that connect with cortical regions in the ipsilateral hemisphere, either nearby (short association) or at a distance (long association). Commissural fibers are inter-cortical connections fibers connected with cortical regions in the contralateral hemisphere *via* the corpus callosum and anterior commissure (Afifi and Bergman, 1998; Anthony et al., 2002; David and Anil, 2010).

Briefly, the trajectory for each categorized fiber is clearly distinguished; for example, projection fibers, association fibers, and commissural fibers in the left hemisphere (LH) are connected with the subcortical area, LH, and right hemisphere (RH), respectively. Therefore, it can be presumed that the density of each categorized fiber in each cortical region is also distinguishable. Furthermore, a novel brain mapping method can be considered based on the track-density distribution characteristic for each categorized fiber in the cerebral cortex using brain imaging data, such as the diffusion-weighted MR-based tractography data (Basser et al., 1994, 2000).

The tractography data from the diffusion-weighted imaging (DWI) has been applied for lots of research topics for the human brain, such as analyzing the pattern of the brain connectivity and connectome (Gong et al., 2009; van den Heuvel and Sporns, 2011; Irimia et al., 2012), composing the whole-brain of connectivity-based-parcellation (Fan et al., 2016; Glasser et al., 2016a), clinical studies (Yamada et al., 2009), brain atlas (Oishi et al., 2011; Cho et al., 2015a), and nerve fiber structure (Cho et al., 2015b; Choi et al., 2019, 2020). There are also several studies that applied the tractography data for brain mapping (Behrens et al., 2003; Tomassini et al., 2007; Park et al., 2008; Mars et al., 2011; Liu et al., 2016; Cerliani et al., 2017). Unlike the study for the connectivity-based-parcellation using the tractography data (Fan et al., 2016; Glasser et al., 2016a), the study for the tractography data-based brain mapping does not utilize the detailed brain parcellation information, or the results are not directly associated with the preceded brain parcellation information.

However, most of the previous tractography data-based cortical mapping methods only considered a limited group of nerve fibers in the brain, not whole-brain tractography data. The nerve fibers in the previous tractography-based mapping studies were only associated with a specific brain region, such as the premotor cortex (Tomassini et al., 2007), parietal cortex (Mars et al., 2011), and frontal cortex (Cerliani et al., 2017). Even if not, the nerve fibers in these mapping methods were only interested in particular fiber types, such as the projection fibers from the thalamus for the thalamus segmentation (Behrens et al., 2003). Or they were only considered in commissural fibers for the segmentation of the corpus callosum (Park et al., 2008) or association fibers for the characterization of the cerebral cortex (Liu et al., 2016). Even in the case of cortical mapping that considers the entire nerve fibers, only one-dimensional information was regarded, such as the fiber length (Bajada et al., 2019).

These kinds of brain mapping approaches have enabled a precise understanding of connectivity and function in specific brain regions or brain functions. However, it remains challenging to gain general information of whole-brain states or function through this limited particular fiber connectivity information or single-dimensional information. For understanding the overall aspect of the whole-brain states and functions, there is a need for a mapping approach in which various types of fibers are reflected in multiple dimensions. Therefore, in this report, we demonstrated a multiple- dimensional cortical mapping using a non-specific whole-brain MR fiber-tracking based on the three types of the nerve fiber. Furthermore, the quantitative analysis of the track-density information was also performed.

MATERIALS AND METHODS

DWI and anatomical T1-weighted MR imaging data from 3.0T MRI (University of Minnesota, Siemens Skyra 3T) were used in this study. The dataset was obtained from the Human Connectome Project (HCP; Glasser et al., 2016b); 19 individual MRI datasets were selected without any criteria or prior knowledge about subjects (we did not perform any experiment to obtain additional data). The HCP dataset is freely downloadable after a verification process from https://db.humanconnectome.org/app/template/SubjectDashboard.vm?project = HCP_1200&subjectGroupName = Subjects%20with%207T%20MR%20Session%20Data. The data contain preprocessed diffusion data with the HCP diffusion pipeline, including diffusion weighting, direction, time series, brain mask, a file that can be used to account for gradient nonlinearities during model fitting, and log files of EDDY processing. Furthermore, they provide 3.0T MRI data that structurally preprocessed for diffusion data with the HCP structural pipeline.

The DWI dataset were acquired using a 2D echo-planar imaging sequence with the following parameters: number of directions = 96, flip angle = 78°, repetition time/echo time = 5,200/89.5 ms, FOV = 1,584 mm × 1,848 mm, resolution = 1.25 mm isotropic, maximum *b*-value = 3,100 s/mm^2, pixel bandwidth = 1,490 Hz/px, total acquisition time = 11 min 27 s. The T1-weighted MRI dataset for the localization of the seed voxels was acquired using a 3D MPRAGE sequence with the following parameters: repetition time/echo time = 2,400/2.14 ms, inversion time = 1,000 ms, flip angle = 8°, field-of-view = 22.4 cm × 22.4 cm, resolution = 0.7 mm isotropic, pixel bandwidth = 210 Hz/px, total acquisition time = 7 min 40 s.

The identification numbers of each 19 individuals selected from the HCP 3T-DWI dataset in this study are as follows: HCP102816, HCP104416, HCP105923, HCP108323, HCP109123, HCP111312, HCP111514, HCP114823, HCP115017, HCP115825, HCP116726, HCP118225, HCP125525, HCP126426, HCP128935, HCP130114, HCP130518, HCP131217, HCP131722. From these datasets, fully automated four-step data processing was undertaken in this study as follows: (1) Brain parcellation and track extraction; (2) Track validation and classification; (3) Track-density ratio mapping; and (4) Group data analysis.

Brain Parcellation and Track Extraction

The anatomical T1 MR images in each dataset were parcellated individually using the Brainnetome atlas[1], Fan et al., 2016 and FreeSurfer software[2]. The Brainnetome atlas is a highly detailedly parcellated framework of the human cortex based on the fiber connectivity model and Brodmann's area (Brodmann, 1909; Fan et al., 2016). **Supplementary Figure 1** and **Supplementary Table 1** show the label number with the names and location of the parcellated Brainnetome brain areas.

After that, 5 million tracks were extracted per each individual MR-DWI data using the track extracting function in the MRtrix software (Brain Research Institute, Florey Neuroscience Institutes, Melbourne, Australia[3]). The fixed parameters for the entire dataset in this track extraction step were set as follows: tracking type = SD-PROB (probabilistic), direction of the fiber-tracking = uni-direction, step-size = 0.2 mm, curvature radius constraint = 0.8 mm, cutoff = 0.1. The inner scalp area of each MR brain image was used to set the seeding and masking regions in this track extraction procedure (Tournier et al., 2012; Cho et al., 2015b; Choi et al., 2019, 2020).

Track Validation and Classification

The analysis and representation of the extracted track data were performed by homemade code with Matlab (MathWorks, Massachusetts, USA[4]), and the codes for all analyses in this report are available. As the first step, appropriate tracks in the obtained track dataset were selected by removing the noise tracks and ineffective tracks using the basic brain segmentation information by FreeSurfer (white matter area, cortical area, subcortical area). In other words, all extracted tracks have two end-terminals in each direction. We assessed and removed any track with a terminal in the white matter area as a noise track and any track without a terminal in the cerebral cortex as an ineffective track.

After that, the validated tracks were classified into four categories (tracks for projection, commissural, short association, and long association fiber) using the basic brain segmentation information that divided into three areas: cortical area in the RH and LH and subcortical area by FreeSurfer. In more detail, validated tracks with terminals in the subcortical structure were classified as projection fibers (subcortical$\leftarrow\rightarrow$cortical), and tracks that had cortical terminals in the contralateral hemisphere were classified as commissural fiber (cortical in LH$\leftarrow\rightarrow$cortical in RH). The remaining validated tracks that had cortical terminals in the ipsilateral hemisphere were classified as association fibers (cortical in LH$\leftarrow\rightarrow$cortical in LH, cortical in RH$\leftarrow\rightarrow$cortical in RH). The tracks for association fibers were classified once more into two categories by fiber length. Bajada et al. (2019) has characterized the short fiber as the fiber under 52 mm fiber length. In this study, a shorter than 6 cm track was classified as a short association fiber and a longer than 6 cm track as a long association fiber. **Supplementary Figure 2** shows the actual tracks that are classified with this method. These distributed patterns of each classified fiber-tracking were well matched with the conventional anatomical knowledge about the fiber structure (Catani and Thiebaut de Schotten, 2008; Bajada et al., 2019).

Track-Density Ratio Mapping

The categorized track dataset was used to obtain the track-density information in the cerebral cortex. We counted the number of terminals for each four categorized fiber per unit-sized voxel (1 mm^3) area in all the cortical regions. The track-density value in each voxel is the number of terminals of each fiber type in the unit-sized voxel. The track-density ratio information was represented by density-dependent color intensity for each categorized fiber with three different primary colors (tracks for the commissural fiber = red, projection fiber = green, association fiber = blue) in each voxel.

To make the mapping result 3D-like-view from the 2D slices image dataset of the track-density information, we stacked each track-density slice image from the starting slice to the ending slice direction. For example, to get the 3D-like superior view of the brain mapping result, all the axial images of the mapping results were stacked from the inferior slice image to a superior slice image direction. In this slice stacking step, the noise data point and the black background data were removed in the 3D-like mapping result by excluding the voxel, which has a minimum track-density level. **Figure 1** shows a representative result image (subject ID: 105923) of the track-density ratio map (TDRM) in the surface of the brain from various views.

The histogram of the track-density for each voxel in the TDRM showed the form of an exponential decay graph. To enhance the contrast of the mapping images, non-linear methods based on exponential functions were applied in the intensity mapping according to track density. In more detail, the mapping intensity according to track-density was determined by the logarithmic function based normalization, such as $1 - e^{-30 \times density/max\_density}$ in the voxel-based ratio density mapping (**Figures 1–3**), $1 - e^{-8 \times density/max\_density}$ in the parcellation-based ratio density mapping (**Figures 2, 3**), $1 - e^{-2 \times density/max\_density}$ in the parcellation-based grayscaled total density mapping (**Figures 3F,L**). The column bars in **Figure 1A**, **Figure 2A**, and **Figure 3** indicate the corresponding non-linear scale.

Group Data Analysis

For the group data analysis, each validated track from 19 individual subjects were categorized by four kinds of fiber types. **Supplementary Table 2** summarized the counting number of the validated tracks of each fiber type. Many tracks were terminated in the white matter area (not cortical area), and over 90% of the extracted tracks were excluded in the track validation step; the mean number of the validated tracks was 416,672 from 5 million extracted tracks. The data from individual ID 115825, 118225, and 130114 were excluded in the further analysis because of their anomalous high number of total validated tracks and abnormal track-ratio for commissural fibers compared with other datasets. Two kinds of group mapping were performed

[1]http://atlas.brainnetome.org
[2]https://surfer.nmr.mgh.harvard.edu/
[3]https://mrtrix.readthedocs.io/en/latest/
[4]https://mathworks.com/

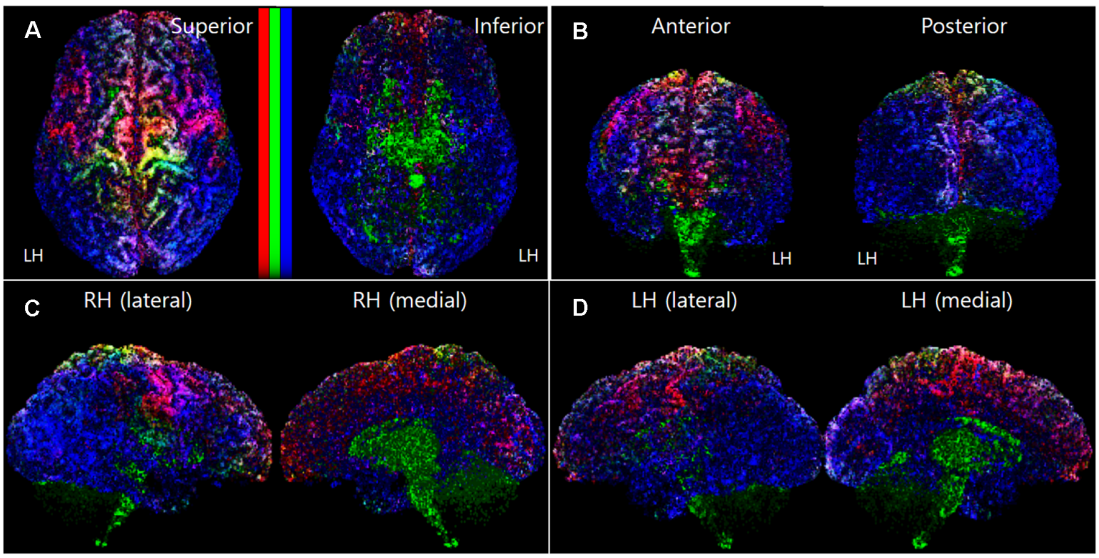

FIGURE 1 | A representative voxel-based TDRM (dataset ID: 105923) in the cerebral cortex with the three different primary colors (tracks for commissural fiber = red, projection fiber = green, association fiber = blue). **(A)** Superior and inferior view. **(B)** Anterior and posterior view. **(C)** Right hemisphere in lateral and medial view. **(D)** Left hemisphere in lateral and medial view. LH, left hemisphere; RH, right hemisphere; TDRM, track-density ratio map.

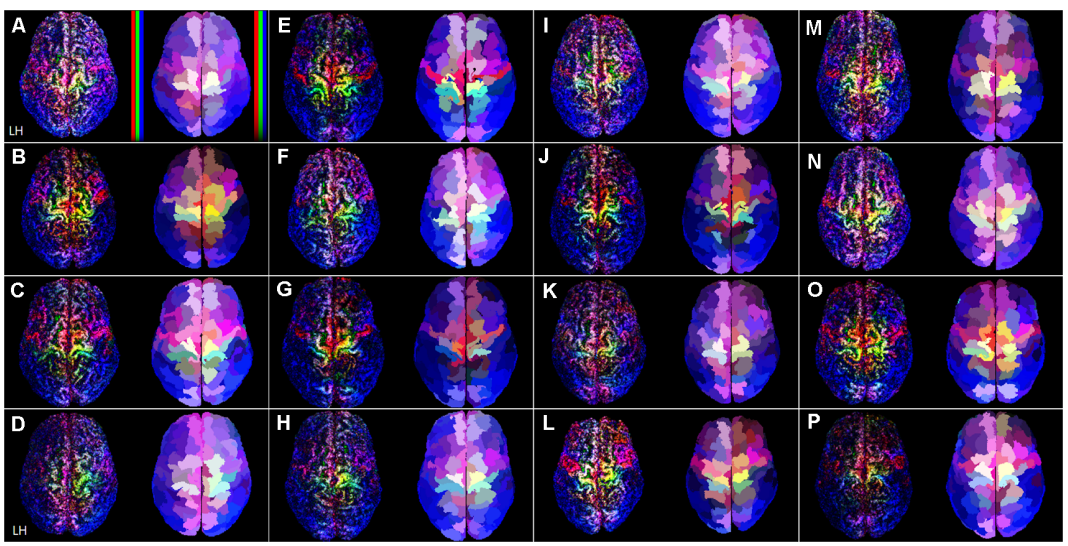

FIGURE 2 | The TDRM from all 16 datasets in the superior view. In each image box, the left figures are the unit-sized voxel (1 mm^3) based TDRMs, and the right figures are parcellation-piece-based TDRMs. In panel **(A)**, non-linear scaled color bars represent mapping density in each type of fiber track (tracks for commissural fiber = red, projection fiber = green, association fiber = blue). The capital letters in each image box **(A–P)** indicate the dataset ID (see **Supplementary Table 2**). TDRM, track-density ratio map.

from the remaining 16 case datasets, voxel-based mean-TDRM in the surface area and parcellation-piece-based mean-TDRM.

To get the mean-TDRM in the surface of the normalized space by matching the voxel place across the subject brain, the fiber tracking results per each subject were transformed to Montreal Neurological Institute (MNI) template space through the "tcktransform" function in MRtrix. The transformed track per subject was reconstructed to the normalized TDRM, and the mean-TDRM in the surface was obtained by averaging the normalized TDRMs per voxel. The averaged mapping results help us to figure out the general trend of the individual TDRMs.

For quantitative group analysis, the mean-TDRM in the volume of the parcellated brain was composed and we used the Brainnetome-based parcellation information. Because the unit areas in this mapping approach are the piece_volume in the cortex, not a unit-sized single voxel on the surface, this mapping

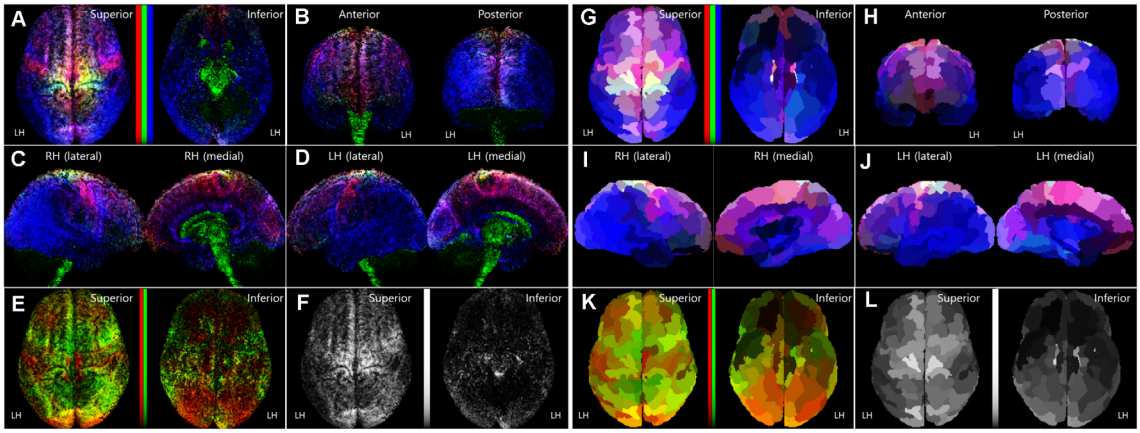

FIGURE 3 | Normalized TRRMs from the 16 subject datasets. **(A–F)** Averaging image of the voxel-based TDRMs. **(G–L)** Parcellation-piece-based mean TDRMs (tracks_amount/piece_volume). The display scheme of each image **(A–D, G–J)** in this figure is the same as **Figure 1**. In panels **(A,E,F,G,K)**, non-linear scaled color bars represent the mapping density of tracks for each fiber type. **(A–D, G–J)** TDRMs results with the three different primary colors (tracks for commissural fiber = red, projection fiber = green, association fiber = blue). **(E,K)** TDRMs for the association fiber-related tracks, with the two different primary colors (short association fiber = red, long association fiber = green). **(F,L)** Total track-density maps using the grayscaled intensity. LH, left hemisphere; RH, right hemisphere; TDRM, track-density ratio map.

result is more reliable and reproducible than the prior voxel-based mapping result. Per each parcellation-piece, we measured the volume size of the parcellation-piece (piece_volume) and counted the number of the terminals (tracks_amount) of each categorized validated track. After that, we regarded the ratio "tracks_amount/piece_volume" of each parcellation-piece as the relative track-density in the parcellated brain area.

RESULTS

Individual Data Observation

Figure 2 shows the superior view of the track-density ratio mapping results into the native space for all the 16 individuals' data. The left and right images in each image box are the results of the voxel-based TDRM in the surface area and parcellation-piece-based TDRM in each volume. The voxel-based TDRMs that are on the left side are independent of the preceded brain parcellation information. Nevertheless, each mapping result shows a highly localized distribution according to the fiber type in the cerebral cortex. The major gyri and sulci boundaries, such as the longitudinal fissure and central sulcus, were clearly identified in the results. Furthermore, the mapping results in the superior brain show splendid colors cluster according to the types of fiber tracks.

On the other hand, the parcellation-piece-based TDRMs represented the track-density ratio in each cerebral cortex area based on the preceded brain parcellation information, the Brainnetome Atlas. A large proportion of the cerebral cortex is consistently covered with bluish color, which is the color assigned to tracks for association fibers, in both the voxel-based and parcellation-piece-based TDRMs. The group data about the tracks counting show that over 60% of the total validated tracks are association fibers (**Supplementary Table 2**). On the other hand, the tracking ratio of the projection fibers and commissural fibers was similar: 18.3% and 20.2%. The left images of each image box in **Figure 2** reveal that the abundant commissural fibers (red) are located in the precentral gyrus and superior part of the frontal cortex. Meanwhile, the projection fibers (green) are dominant in the superior part of the postcentral gyrus. The yellowish color found in the superior part of the precentral gyrus in **Figure 2** indicates that this region is densely packed with a similar proportion of commissural and projection fibers.

Normalized Mapping of the Group Data

Figures 3A–F show the averaging image of the voxel-based TDRMs from the 16 subject datasets. Because of the track-normalization procedure with the MNI template brain, the mapping results are a little bit blurred. However, the averaging data's mapping appearance is similar to the trend of the individual TDRMs' aspect. For example, the difference of the track-density ratio between precentral gyrus for the motor control (red: commissural fiber) and postcentral gyrus for somatosensory (blue: association fiber) in the track-density ratio is clearly shown in the mean mapping result (**Figure 3A**) as well, like the individual mapping results (**Figure 2**).

Furthermore, the results in the medial view of the left and right hemispheres (**Figures 3C,D**) reveal that the major fiber in the subcortical area is the projection fiber (green), and the major fiber in the medial cortex except for the cingulate area (magenta) is the association fiber (blue) and commissural fiber (red). The result also shows that the high-density result for association fiber (green) in the temporal lobe and lateral part of the occipital lobe (**Figure 3B**).

Quantitative Analysis of the Group Data

The six graphs in **Figure 4** show the relative track-density level (tracks_amount/piece_volume) in each parcellated brain area per each fiber category from the 16 validated datasets. In the graph of the tracks for projection fibers (**Figure 4A**), part

of the superior frontal gyrus (1–5), precentral gyrus (28–30), superior parietal lobule (63, 66), and postcentral gyrus (81) are the regions with high track-density. The cortical distribution of the relative track-density of commissural fiber (**Figure 4B**) is similar to that of projection fiber in these figures. With the mentioned common regions, part of the middle frontal gyrus (12, 13), and paracentral lobule (33, 34) are additional high-density regions of the commissural fibers. The projection fibers have single terminals in the cerebral cortex, and the other is in the subcortical area. This is in contrast to commissural and association fibers, which have double terminals. Therefore, the level of the tracks for projection fibers density is about half of the tracks for commissural fiber, although their track-density was similar (**Supplementary Table 2**).

Meanwhile, the aspect of the distributions for the relative track-density of the association fiber (**Figures 4C–E**) was different. They were distributed widely throughout the cerebral cortex, except for some brain regions, such as the orbital gyrus (21–26). In the occipital cortex (95–105), tracks for short association fiber (**Figure 4C**) show relatively high-density (see **Supplementary Figure 2**), while tracks for long association fiber (**Figure 4D**) show relatively low-density (Bajada et al., 2019). In the result of the total track-density (**Figure 4F**), the most densely populated area of the nerve fiber in the brain was the precentral gyrus—trunk region (30). The superior frontal gyrus (1–7), paracentral lobule (33, 34), postcentral gyrus—trunk region (81) also had a high-density of the total nerve fiber in the graph.

The group data also show the asymmetricity of the track-density in the LH and RH. Although the total track-density had a similar level, there were significantly more tracks in the RH compared with the LH, in long association fibers (p-value = 0.0017). The mean of the relative track-density for each categorized track from 16 subject datasets in the LH and RH is as follows: projection fiber (LH: 0.1326, RH: 0.1399), commissural (LH: 0.2922, RH: 0.2672), short association (LH: 0.4804, RH: 0.4674), long association (LH: 0.3968, RH: 0.4255), total association (LH: 0.8772, RH: 0.8936), and total fiber (LH: 1.4345, RH: 1.4406). The density asymmetricity between hemispheres was particularly significant in association fibers. In the relative track-density for the total association fiber (**Figure 4E**), the entorhinal cortex (58, p-value = 0.02) and insular gyrus (82–87, p-value = 2.52e-08) showed significant LH dominance, and the temporal gyrus (41–54, p-value = 5.46e-06) and parietal lobule (63–73, p-value = 1.07e-06) showed significant RH dominance.

Quantitative Mapping of the Group Data

The parcellation-piece-based track-density data in **Figure 4** were reconstructed in the parcellated brain (ID: 105923) to make the data more understandable. The images in **Figures 3G–L** show the TDRMs based on the mean track-density level of the 16 datasets in each parcellated region. These figures more clearly reveal that the association fiber is dominant in the temporal, inferior parietal, and lateral occipital lobes (bluish color in the inferior and posterior part of the cerebral cortex). They also indicate that the abundant projection and commissural fibers are in the superior part of the frontal and parietal cortex (un-bluish color in the anterior and superior part of the cerebral cortex). Because this quantitative mapping analysis assessed the cerebral cortex alone, the track-density for projection fibers observed in the diencephalon, cerebellum, and diencephalon in **Figures 3C,D** with green color is not reflected in this map. This is also why the tracks for the greenish projection fibers are less prominent in this parcellation-piece-based TDRM.

Figures 3K,L include one or two-dimensional track-density information in the parcellated brain area from superior (left) and inferior (right) views. **Figure 3K** with **Figures 4C,D** shows that the track distribution for the short association fibers (red) is denser than the long association fibers (blue) in broad regions in the inferior frontal gyrus of the LH, and occipital lobe. Also, **Figure 3L** implies that the superior frontal cortex has the most density of nerve fibers among all the brain regions, and the inferior frontal, and inferior frontal, and inferior temporal areas have sparser nerve fibers than other brain regions.

DISCUSSION AND CONCLUSIONS

The TDRMs presented here were implemented using a fully automated protocol; therefore, the reproducibility is expected of the results according to the described method. However, there is a flaw in the approach due to the problem in the DWI-MR image. The inferior part of the brain, such as the orbitofrontal cortex and medial temporal gyrus, are likely to be distorted in DWI-MRI images due to susceptibility artifacts. Because of the artifacts, it is hard to avoid distortion of the TDRM data in the inferior part of the brain. The signal loss due to distortions in the DWI data should be considered in interpreting the track-density data in inferior brain regions. Other distortions in the extracted track are the bias to terminate preferentially on gyral crowns rather than the banks of sulci, and inaccessibility to the cortical surface in the current fiber tracking algorithms (Reveley et al., 2015; Schilling et al., 2018). Because of the inaccessibility, 90% of the extracted tracks have been excluded in the track validation step from this study. Furthermore, because of the gyral bias, the signal loss in the sulci area should be considered in interpreting the track-density maps as well.

Finally, the TDRM results are affected by the fiber extraction method. The whole-brain random fiber tracking approach that we adopt as a conventional default fiber extraction method is robust in human bias or mistake. However, it does not mean that the conventional method is optimal, therefore, it can introduce biases in detecting fiber pathways and limiting coverage. These problems can be solved by improving the scheme of fiber extraction. For example, underestimated commissural fiber mass in the parietal lobe in our results can be enhanced by adapting the multi-stage region-of-interest-based fiber tracking (Jarbo et al., 2012).

The TDRMs results can be discussed in relation to the cortical circuit as they can be affected by the regional specialization of the cortical connectivity. The cortical circuit information based on the cytoarchitecture scale analysis differentiates between input and output fiber information to the cortex and reflects the

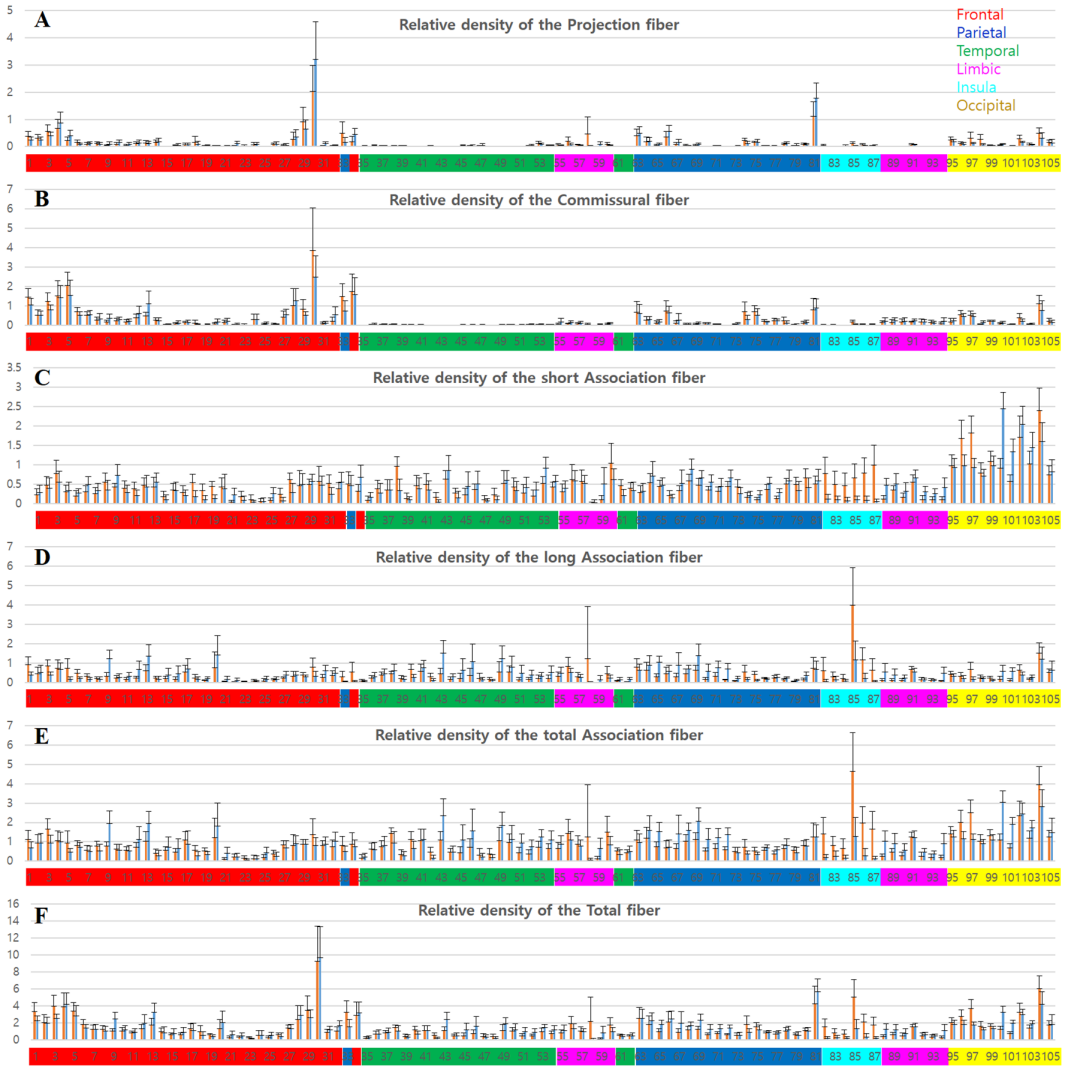

FIGURE 4 | Graphs of the tracks density in each parcellation-piece from all 16 datasets per parcellation-piece. The X-axes indicate the parcellation label of the Brainnetome Atlas (see **Supplementary Figure 1** and **Supplementary Table 1**). The label numbers were coded by color depending on the lobes of the brain as follows: frontal lobe (red), parietal lobe (blue), temporal lobe (green), limbic lobe (magenta), insular lobe (cyan), and occipital lobe (yellow). The Y-axes indicate the relative density of the tracks in the volume (tracks_amount/piece_volume). The bar in the left-side (red) and right-side (blue) in each label number is the results from the left and right hemispheres, respectively. **(A–E)** Mean and standard deviation of the relative track-density for the **(A)** projection, **(B)** commissural, **(C)** short association, **(D)** long association, **(E)** total association, and **(F)** total fibers.

connectivity within the cortical area (Elston, 2003; Rockland, 2019), which cannot be reflected in the TDRMs results that are based on the macro or mesoscale analysis. Several reports describe that the cortical circuit in the cerebral cortex is not generalized and has regional differences, through the observation of the size or dendritic property in the supragranular pyramidal cells (Jacobs et al., 2001; Luebke, 2017). Moreover, they suggested these structural differences with the cortical difference in the integrated ability or functional capacities because these differences are significant in the high integration area, especially in the prefrontal cortex that is considered the high-level cognitive functional area (Elston et al., 2001; Jacobs et al., 2001; Elston, 2003; Luebke, 2017). The cortical specialization results have a chance to be correlated and combined with our track-density results. Actually, there is a macro-scaled connectivity study based on the tract tracer injection in the cortex (Markov et al., 2014; Oligschläger et al., 2019), and the projection of each fiber type (projection, commissural, and association fibers) to the cortex is distinguished at the laminar level (Figure 2 in Rockland, 2019). For example, like cortical specialization results, the TDRM in the frontal area is distinguished from the TDRM in other posterior areas that showing association fiber dominance. Furthermore, like the connection at the laminar level (Figure 1 in Rockland, 2019), ascending sensory area is clearly distinguished from the descending motor area, in the TDRM.

In the proposed TDRM method, the density information of multiple categorized fibers in the cerebral cortex was represented in a single image using a combination of the three different primary colors. The representation approach using the combination of the primary colors for the track-density imaging is already implemented in diffusion tensor imaging (DTI) data (Pajevic and Pierpaoli, 1999) and track-density imaging (TDI) data (Calamante et al., 2010). The difference is that the three primary colors in the DTI and TDI reflect fiber direction, not fiber type. Like the DTI and TDI images do, even by a single resulted image, the TDRMs can represent the multiple types of track-density more effectively and aggregately. Furthermore, the mapping results are more comfortable to figure out the overall state of the multiple types of track-density.

Because of the strength, the mapping method used in this study can be applied to various fields. For example, this method is applicable to brain function studies. The functional role of each categorized nerve fiber is likely to differ based on differences in their trajectories. For example, the projection fiber is intimately involved in the arousal response and motor control, and damage to association fiber can result in altered language function and behavior (Afifi and Bergman, 1998; David and Anil, 2010). Therefore, analyses of track-density and fiber-type in each cortical region and their regional difference allow us to get insight for understanding each cortical region's functional specialization in brain computations. For example, TDRMs of the group data (**Figure 3**) indicate that roughly the posterior part of the brain has a high distribution density of association fibers, while the anterior part of the brain is shown a high distribution density of projection and commissural fibers. This difference in the fiber-type between anterior to posterior parts of the brain can be correlated with that the overall functional role between them is discriminated, such as motor-related and sensory-related function, respectively.

Furthermore, functional localization between the left and right hemispheres may be interpreted by analyzing the asymmetry in the TDRM. From **Figures 3G–L** and **Figure 4**, we found several brain areas that show the significant asymmetry in track-density, particularly in the track for association fibers. The asymmetry in the fiber structure between the left and right hemispheres suggests the functional laterality in the corresponding area. Finally, this technique has the potential for diagnosing brain diseases by characterizing the anatomical distinction of the fiber amount and fiber type between populations in the cerebral cortex (Nir et al., 2015; Henderson et al., 2020). The TDRM hopes to be used as an alternative biomarker to diagnose neurodegenerative diseases (Prasad et al., 2013; Nir et al., 2015) or tumor (Stadlbauer et al., 2010; Henderson et al., 2020) in the brain associated with abnormalities in the distribution characteristics of that.

In conclusion, we implemented TDRMs in this study, a novel cortical mapping method based on the nerve fiber's type using MR tractography data. Their quantitative results from the group data analysis provided more detailed and reliable information on the track-density ratio, including the hemispheric asymmetries in the association fibers' density. We expect that the information from the TDRMs provides new dimensional information for the understanding of brain anatomy and function, and neurodegenerative diseases.

DATA AVAILABILITY STATEMENT

The original contributions presented in the study are included in the article/**Supplementary Material**, further inquiries can be directed to the corresponding author/s.

AUTHOR CONTRIBUTIONS

S-HC suggested the model, processed the data, and drafted the manuscript. GJ and Y-EH processed the HCP data. Y-BK assisted with the neuroanatomical information. Z-HC and HL performed the super-resolution tractography and its application to the study of neural circuits. All authors contributed to the article and approved the submitted version.

FUNDING

This work was supported by the Brain Research Program of the National Research Foundation of Korea (NRF), which is funded by the Ministry of Science and ICT (2017M3C7A1049026). Data were provided by the Human Connectome Project, WU-Minn Consortium (Principal Investigators: David Van Essen and Kamil Ugurbil; 1U54MH091657) funded by the NIH Institutes and Centers that support the NIH Blueprint for Neuroscience Research; and by the McDonnell Center for Systems Neuroscience at Washington University.

SUPPLEMENTARY MATERIAL

The Supplementary Material for this article can be found online at: https://www.frontiersin.org/articles/10.3389/fnana.2021.715571/full#supplementary-material.

REFERENCES

Afifi, A. K., and Bergman, R. A. (1998). *Functional Neuroanatomy - Text and Atlas*. New York, NY: McGraw-Hill, pp. 232–238.

Anthony, J. C., Edward, J. N., Robert, D. W., and Michael, P. M. (2002). *Neuroscience: An Outline Approach*. Maryland Heights, MO: Mosby, pp. 235–238.

Bajada, C. J., Schreiber, J., and Caspers, S. (2019). Fiber length profiling: A novel approach to structural brain organization. *Neuroimage* 186, 164–173. doi: 10.1016/j.neuroimage.2018.10.070

Basser, P. J., Mattiello, J., and LeBihan, D. (1994). MR diffusion tensor spectroscopy and imaging. *Biophys. J.* 66, 259–267. doi: 10.1016/S0006-3495(94)80775-1

Basser, P. J., Pajevic, S., Pierpaoli, C., Duda, J., and Aldroubi, A. (2000). *In vivo* fiber tractography using DT-MRI data. *Magn. Reson. Med.* 44, 625–632. doi: 10.1002/1522-2594(200010)44:4<625::aid-mrm17>3.0.co;2-o

Behrens, T. E., Johansen-Berg, H., Woolrich, M. W., Smith, S. M., Wheeler-Kingshott, C. A., Boulby, P. A., et al. (2003). Non-invasive mapping of connections between human thalamus and cortex using diffusion imaging. *Nat. Neurosci.* 6, 750–757. doi: 10.1038/nn1075

Brodmann, K. (1909). *Vergleichende Lokalisationslehre Der Grosshirnrinde in Ihren Prinzipien Dargestellt Auf Grund Des Zellenbaues*. Leipzig: Barth.

Calamante, F., Tournier, J. D., Jackson, G. D., and Connelly, A. (2010). Track-density imaging (TDI): Super-resolution white matter imaging using whole-brain track-density mapping. *Neuroimage* 53, 1233–1243. doi: 10.1016/j.neuroimage.2010.07.024

Catani, M., and Thiebaut de Schotten, M. (2008). A diffusion tensor imaging tractography atlas for virtual *in vivo* dissections. *Cortex* 44, 1105–1132. doi: 10.1016/j.cortex.2008.05.004

Cerliani, L., D'Arceuil, H., and Thiebaut de Schotten, M. (2017). Connectivity-based parcellation of the macaque frontal cortex and its relation with the cytoarchitectonic distribution described in current atlases. *Brain Struct. Funct.* 222, 1331–1349. doi: 10.1007/s00429-016-1280-3

Cho, Z. H., Calamante, F., and Chi, J. G. (2015a). *7.0 Tesla MRI Brain White Matter Atlas*, 2nd Edn. Berlin, Germany: Springer-Verlag.

Cho, Z. H., Chi, J. G., Choi, S. H., Oh, S. H., Park, S. Y., Peak, S. H., et al. (2015b). A newly identified frontal path from fornix in septum pellucidum with 7.0T MRI track-density imaging (TDI)—The septum pellucidum tract (SPT). *Front. Neuroanat.* 9:151. doi: 10.3389/fnana.2015.00151

Choi, S. H., Jeong, K., Kim, Y. B., and Cho, Z. H. (2020). Proposal for human visual pathway in the extrastriate cortex by fiber tracking method using diffusion-weighted MRI. *Neuroimage* 220:117145. doi: 10.1016/j.neuroimage.2020.117145

Choi, S. H., Kim, Y. B., Paek, S. H., and Cho, Z. H. (2019). Papez circuit observed by *in vivo* human brain with 7.0T MRI super-resolution track-density imaging and track tracing. *Front. Neuroanat.* 13:17. doi: 10.3389/fnana.2019.00017

David, L. F., and Anil, N. S. (2010). *Netter's Atlas of Neuroscience*. Philadelphia, PA: Saunders Elsevier, pp. 306–312.

Elston, G. N. (2003). Cortex, cognition and the cell: new insights into the pyramidal neuron and prefrontal function. *Cereb. Cortex* 13, 1124–1138. doi: 10.1093/cercor/bhg093

Elston, G. N., Benavides-Piccione, R., and DeFelipe, J. (2001). The pyramidal cell in cognition: a comparative study in human and monkey. *J. Neurosci.* 21:RC163. doi: 10.1523/JNEUROSCI.21-17-j0002.2001

Fan, L., Li, H., Zhuo, J., Zhang, Y., Wang, J., Chen, L., et al. (2016). The human brainnetome atlas: a new brain atlas based on connectional architecture. *Cereb. Cortex* 26, 3508–3526. doi: 10.1093/cercor/bhw157

Glasser, M. F., Coalson, T. S., Robinson, E. C., Hacker, C. D., Harwell, J., Yacoub, E., et al. (2016a). A multi-modal parcellation of human cerebral cortex. *Nature* 536, 171–178. doi: 10.1038/nature18933

Glasser, M. F., Smith, S. M., Marcus, D. S., Andersson, J. L., Auerbach, E. J., Behrens, T. E., et al. (2016b). The human connectome project's neuroimaging approach. *Nat. Neurosci.* 19, 1175–1187. doi: 10.1038/cnn.4361

Gong, G., He, Y., Concha, L., Lebel, C., Gross, D. W., Evans, A. C., et al. (2009). Mapping anatomical connectivity patterns of human cerebral cortex using *in vivo* diffusion tensor imaging tractography. *Cereb. Cortex* 19, 524–536. doi: 10.1093/cercor/bhn102

Henderson, F., Abdullah, K. G., Verma, R., and Brem, S. (2020). Tractography and the connectome in neurosurgical treatment of gliomas: the premise, the progress and the potential. *Neurosurg. Focus* 48:E6. doi: 10.3171/2019.11.FOCUS19785

Irimia, A., Chambers, M. C., Torgerson, C. M., and Van Horn, J. D. (2012). Circular representation of human cortical networks for subject and population-level connectomic visualization. *Neuroimage* 60, 1340–1351. doi: 10.1016/j.neuroimage.2012.01.107

Jacobs, B., Schall, M., Prather, M., Kapler, E., Driscoll, L., Baca, S., et al. (2001). Regional dendritic and spine variation in human cerebral cortex: a quantitative golgi study. *Cereb. Cortex* 11, 558–571. doi: 10.1093/cercor/11.6.558

Jarbo, K., Verstynen, T., and Schneider, W. (2012). *In vivo* quantification of global connectivity in the human corpus callosum. *Neuroimage* 59, 1988–1996. doi: 10.1016/j.neuroimage.2011.09.056

Liu, K., Zhang, T., Zhang, Q., Sun, Y., Wu, J., Lei, Y., et al (2016). Characterization of the fiber connectivity profile of the cerebral cortex in schizotypal personality disorder: a pilot study. *Front. Psychol.* 7:809. doi: 10.3389/fpsyg.2016.00809

Luebke, J. I. (2017). Pyramidal neurons are not generalizable building blocks of cortical networks. *Front. Neuroanat.* 11:11. doi: 10.3389/fnana.2017.00011

Markov, N. T., Ercsey-Ravasz, M. M., Ribeiro Gomes, A. R., Lamy, C., Magrou, L., Vezoli, J., et al. (2014). A weighted and directed interareal connectivity matrix for macaque cerebral cortex. *Cereb. Cortex* 24, 17–36. doi: 10.1093/cercor/bhs270

Mars, R. B., Jbabdi, S., Sallet, J., O'Reilly, J. X., Croxson, P. L., Olivier, E., et al. (2011). Diffusion-weighted imaging tractography-based parcellation of the human parietal cortex and comparison with human and macaque resting-state functional connectivity. *J. Neurosci.* 31, 4087–4100. doi: 10.1523/JNEUROSCI.5102-10.2011

Nir, T. M., Villalon-Reina, J. E., Prasad, G., Jahanshad, N., Joshi, S. H., Toga, A. W., et al. (2015). Diffusion weighted imaging-based maximum density path analysis and classification of Alzheimer's disease. *Neurobiol. Aging* 36, S132–S140. doi: 10.1016/j.neurobiolaging.2014.05.037

Oishi, K., Faria, A., van Zijl, P. C. M., and Mori, S. (2011). *MRI Atlas of Human White Matter*, 2nd Edn. London: Academic Press.

Oligschläger, S., Xu, T., Baczkowski, B. M., Falkiewicz, M., Falchier, A., Linn, G., et al. (2019). Gradients of connectivity distance in the cerebral cortex of the macaque monkey. *Brain Struct. Funct.* 224, 925–935. doi: 10.1007/s00429-018-1811-1

Pajevic, S., and Pierpaoli, C. (1999). Color schemes to represent the orientation of anisotropic tissues from diffusion tensor data: application to white matter fiber tract mapping in the human brain. *Magn. Reson. Med.* 42, 526–540.

Park, H., Kim, J. J., Lee, S., Seok, J. H., Chun, J., Kim, D. I., et al. (2008). Corpus callosal connection mapping using cortical gray matter parcellation and DT-MRI. *Hum. Brain Mapp.* 29, 503–516. doi: 10.1002/hbm.20314

Prasad, G., Nir, T. M., Toga, A. W., and Thompson, P. M. (2013). Tractography density and network measures in Alzheimer's disease. *Proc. IEEE Int. Symp. Biomed. Imaging* 2013, 692–695. doi: 10.1109/ISBI.2013.6556569

Reveley, C., Seth, A. K., Pierpaoli, C., Silva, A. C., Yu, D., Saunders, R. C., et al. (2015). Superficial white matter fiber systems impede detection of long-range cortical connections in diffusion MR tractography. *Proc. Natl. Acad. Sci. U S A* 112, E2820–E2828. doi: 10.1073/pnas.1418198112

Rockland, K. S. (2019). What do we know about laminar connectivity. *Neuroimage* 197, 772–784. doi: 10.1016/j.neuroimage.2017.07.032

Schilling, K., Gao, Y., Janve, V., Stepniewska, I., Landman, B. A., and Anderson, A. W. (2018). Confirmation of a gyral bias in diffusion MRI fiber tractography. *Hum. Brain Mapp.* 39, 1449–1466. doi: 10.1002/hbm.23936

Stadlbauer, A., Buchfelder, M., Salomonowitz, E., and Ganslandt, O. (2010). Fiber density mapping of gliomas: histopathologic evaluation of a diffusion-tensor imaging data processing method. *Radiology* 257, 846–853. doi: 10.1148/radiol.10100343

Tomassini, V., Jbabdi, S., Klein, J. C., Behrens, T. E. J., Pozzilli, C., Matthews, P. M., et al. (2007). Diffusion-weighted imaging tractography-based parcellation of the human lateral premotor cortex identifies dorsal and ventral subregions with anatomical and functional specializations. *J. Neurosci.* 27, 10259–10269. doi: 10.1523/JNEUROSCI.2144-07.2007

Tournier, J. D., Calamante, F., and Connelly, A. (2012). MRtrix: diffusion tractography in crossing fiber regions. *Int. J. Imaging Sys. Technol.* 22, 53–66. doi: 10.1002/ima.22005

van den Heuvel, M. P., and Sporns, O. (2011). Rich-club organization of the human connectome. *J. Neurosci.* 31, 15775–15786. doi: 10.1523/JNEUROSCI.3539-11.2011

Yamada, K., Sakai, K., Akazawa, K., Yuen, S., and Nishimura, T. (2009). MR tractography: a review of its clinical applications. *Magn. Reson. Med. Sci.* 8, 165–174. doi: 10.2463/mrms.8.165

Conflict of Interest: The authors declare that the research was conducted in the absence of any commercial or financial relationships that could be construed as a potential conflict of interest.

frontiers | Frontiers in Systems Neuroscience

HYPOTHESIS AND THEORY
published: 27 May 2022
doi: 10.3389/fnsys.2022.787737

Topological Maps and Brain Computations From Low to High

Martin I. Sereno[1,2]*, *Mariam Reeny Sood*[2] *and Ruey-Song Huang*[3]

[1] Department of Psychology, San Diego State University, San Diego, CA, United States, [2] Department of Psychological Sciences, Birkbeck, University of London, London, United Kingdom, [3] Centre for Cognitive and Brain Sciences, University of Macau, Macau, Macao SAR, China

We first briefly summarize data from microelectrode studies on visual maps in non-human primates and other mammals, and characterize differences among the features of the approximately topological maps in the three main sensory modalities. We then explore the almost 50% of human neocortex that contains straightforward topological visual, auditory, and somatomotor maps by presenting a new parcellation as well as a movie atlas of cortical area maps on the FreeSurfer average surface, *fsaverage*. Third, we review data on moveable map phenomena as well as a recent study showing that cortical activity during sensorimotor actions may involve spatially locally coherent traveling wave and bump activity. Finally, by analogy with remapping phenomena and sensorimotor activity, we speculate briefly on the testable possibility that coherent localized spatial activity patterns might be able to 'escape' from topologically mapped cortex during 'serial assembly of content' operations such as scene and language comprehension, to form composite 'molecular' patterns that can move across some cortical areas and possibly return to topologically mapped cortex to generate motor output there.

Keywords: extrastriate cortex, retinotopy, tonotopy, somatotopy, cortical computation, serial assembly of content

OPEN ACCESS

Edited by:
Nick Swindale,
The University of British Columbia, Canada

Reviewed by:
Josef P. Rauschecker,
Georgetown University, United States
Matthew F. Glasser,
Washington University in St. Louis, United States

***Correspondence:**
Martin I. Sereno
msereno@ucsd.edu

Received: *01 October 2021*
Accepted: *29 March 2022*
Published: *27 May 2022*

Citation:
Sereno MI, Sood MR and Huang R-S (2022) Topological Maps and Brain Computations From Low to High.
Front. Syst. Neurosci. 16:787737.
doi: 10.3389/fnsys.2022.787737

INTRODUCTION

There is a long history of trying to compactly characterize the canonical computational principles of cerebral cortex (and other) areas in the brain. Given the incredibly diverse nature of sensory information arriving from different sensory modalities as well as the diverse geometry of motor output structures (e.g., eye muscles versus arm muscles), this might seem at first too quixotic a quest.

Two prominent features that are found throughout much of the cerebral cortex are: (1) a strong predominance of extremely local connections, and (2) longer-range interareal connections that form topological maps. Though visually attractive patchy local connections (e.g., innervating adjacent cytochrome oxidase blobs) are often highlighted in neuroanatomical and modeling studies, more local connections (within a 1 mm radius) are strongly numerically dominant throughout the cortex (see **Figure 1**, redrawn from multiple figures in Lund et al., 1993, with different cortical regions all set to the same scale). Zooming out to an intermediate scale, longer-range connections between areas are then most commonly arranged as approximately topological (neighbor-preserving) maps, initially maps of sensory surfaces, and then at the output, maps of

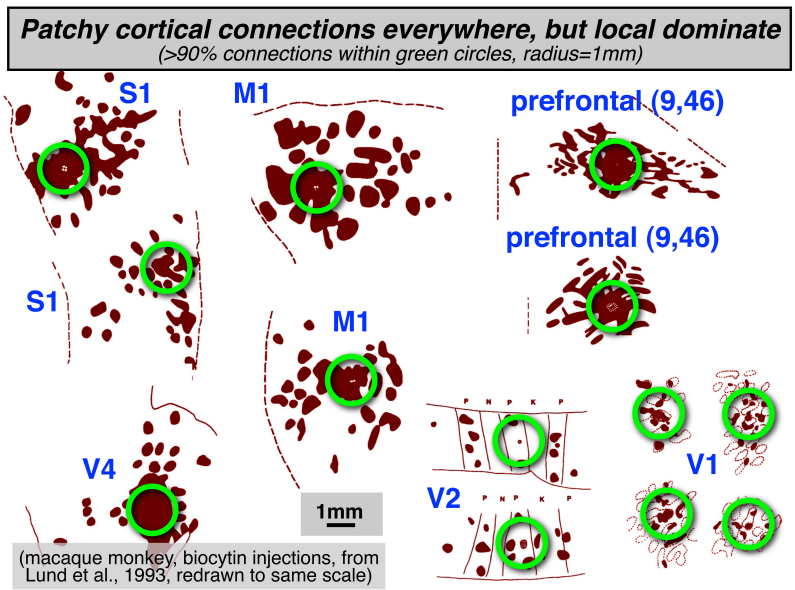

FIGURE 1 | Patchy local structures and connections are found everywhere in the cortex. However, the numerical majority of connections are made within a 1 mm radius (green circles).

muscle arrays or effector output space. As sensory and motor information is passed from station to station, topological maps remain an extremely common motif.

We don't want to downplay the beautifully and complexly intercalated maps of different local stimulus features such as orientation (interblobs), and brightness and color (blobs) that have been studied in the greatest detail in area V1 in cats and primates (e.g., Swindale et al., 2000; Carreira-Perpin and Goodhill, 2004; Sincich and Horton, 2005; Yu et al., 2005). This pattern of embedding multiple streams of information that emphasize different features within an overall topological map is ubiquitous throughout the visual (and auditory and somatosensory) systems. Higher level examples from the visual system include subdivisions within V2 stripes (Wang et al., 2007; Lim et al., 2009), MT direction columns and band/interbands that respect or ignore background motion (Albright, 1984; Born and Tootell, 1992; Diogo et al., 2020). For the present purposes, it is merely that we have zoomed out to concentrate on the retinotopic (and tonotopic and somatotopic) maps.

This topological, neighbor-preserving mode of intermediate scale neural interconnection is surprisingly ubiquitous throughout the brain. Approximately topological map connections extend not only to thalamic structures projecting to and receiving inputs from visual, auditory, and somatosensory cortical areas, but are seen in many other structures not as well known for containing topological maps.

Here are just a handful of hundreds of possible examples: (1) The projections from the caudate and putamen to both components of the substantia nigra (GABAergic pars reticulata and dopaminergic pars compacta) are about as topological as the projection from V1 to V2 (Parent and Hazrati, 1994). (2) There are approximately topological connections between many cortical areas and the subthalamic nucleus (the 'hyperdirect' pathway; Haynes and Haber, 2013). (3) Odor-specific olfactory receptors in the olfactory epithelium sort themselves into a spatial odor map in their projection to the olfactory bulb (Nakashima et al., 2021), and then topological intrabulbar (left-right and right-left) projections respect this odor map (Schoenfeld et al., 1985). (4) Topological sensory maps are found in a modified form in the large surface area of the cerebellar cortex (Sereno et al., 2020), within the small patches that make up the unique 'fractured somatotopy' mosaic found there (Shambes et al., 1978). (5) The cerebellar-connected inferior olive and the cerebellar dentate nucleus are each crumpled into miniature cortical surfaces embedded within the brainstem in order to preserve two-dimensional maps there (Ding et al., 2016, their pp. 215, 243).

Approximately topological maps are also common in output structures (e.g., the cerebellar dentate nucleus just mentioned). The spatial array of muscles controlled by motor cortex was in fact the first cortical topological brain maps uncovered experimentally (Fritsch and Hitzig, 1870). Another well-known topological map is found in the deeper layers of the superior colliculus – a map of saccade and neck movement vectors – which receives topological map connections from the retinotopic superficial superior colliculus (Sparks, 1986) and manipulates topological maps of auditory- and somatosensory-space targets by shifting them to keep them aligned with the retinotopic map after each saccade by using eye position information (e.g., Jay and Sparks, 1984). It could fairly be said that topological maps are the first principal component of mid-scale brain organization.

Despite their ubiquity, however, there has also been the intuition that areas containing maps must somehow *not* be appropriate for supporting higher level cognition (e.g.,

Pylyshyn, 1984; McClelland and Rumelhard, 1986). This is only the latest rehearsal of a several centuries-long debate between "field" and "localization" theories of cortical function. As a foil, there has been an equally long history of trying to mimic biological topological maps using artificial neural networks (e.g., Fukushima, 1980; Linsker, 1986; Sereno and Sereno, 1991). Although the implicit bias against using tiered topological maps in machine learning has been much relaxed in recent years with the popularity of 'convolutional neural networks' (LeCun et al., 2015), the intuition of many researchers that use human neuroimaging methods in cognitive neuroscience is still that most important 'higher level' areas in the cortex must *not* contain simple topological maps.

Several possibilities come to mind at this juncture. First, it may be true that 'higher areas' do in fact compute without maps of any kind (though certainly after being fed inputs from areas with maps), using distributed activity patterns that would appear on casual inspection to be spatially random. Second, higher areas might contain static spatial feature maps (e.g., Kohonen, 1982); but we might have only begun to divine their mostly unknown coordinates (this might be near to the consensus view). A third more speculative possibility explored here is that certain regions of the cortex might host coherent, spatially localized patterns of activity capable of moving across the cortex and bonding with each other while maintaining their internal spatial structure (Sereno, 1991, 2014); despite having coherent, spatially localized structure from moment to moment, these moveable activity patterns might be difficult to detect using standard, low temporal precision fMRI mapping methods.

We first briefly summarize data from microelectrode studies on visual maps in non-human primates and other animals, and describe how approximately topological maps differ among the three main sensory modalities. We then describe the almost 50% of human neocortex that does contain straightforward topological visual, auditory, and somatomotor maps and present a new downloadable cortical parcellation and atlas movie of those 117 areas in each hemisphere that is based on the FreeSurfer average surface, subject *fsaverage*. Third, we review recent data on moveable maps and then review a recent experiment suggesting that cortical activity during sensorimotor actions involves coherent traveling waves and bumps. Finally, we speculate briefly on the third possibility introduced above, that coherent localized spatial activity patterns might be able to 'escape' from mapped areas and move across cortical areas that do not contain straightforward sensory maps, by analogy with remapping phenomena, and that they may eventually re-enter topological maps on the way to motor output.

MATERIALS AND METHODS

Microelectrode Retinotopic Mapping and Parcellation

To characterize retinotopic maps at a 100 micron scale, dense retinotopy data sets were obtained by microelectrode visual receptive field mapping in dorsal and lateral visual cortex of anesthetized owl monkeys and then parcellated using the visual field sign method, which measures the local relation between the cortical gradient in polar angle and the cortical gradient in eccentricity to distinguish mirror-image from non-mirror-image visual field representations (Sereno et al., 1994). Afterward, the neocortex was physically flatmounted and penetration photograph recording locations were warped into alignment with the flattened myelin-stained cortex using marker lesions and a deformable template algorithm (see Sereno et al., 2015, for details).

fMRI Mapping Experiments

To comprehensively catalog topological maps in humans, phase-encoded retinotopic, tonotopic, and somatomotor-o-topic fMRI data (see Dick et al., 2012; Huang and Sereno, 2013, 2018; Sood and Sereno, 2016, 2018, for more details) were collected at 1.5T and 3T using the X11/OpenGL phase-encoded stimulus program, *mapper*.[1] For visual experiments, a wide-field, direct-view in-bore screen (projection from the front) was used, which stimulated eccentricities to 50 deg at all polar angles. Auditory stimuli (bandpass filtered sweeps of emotional vocalizations taken from Dick et al. (2012) were presented through piezoelectric drivers (Sensimetrics). Somatomotor mapping was done by using brief auditory cues to subjects who carefully and minimally moved individual body parts in a repeated sequence. Quantitative T1-mapping data to map myelination from an overlapping set of subjects (Sereno et al., 2012) was also consulted.

However, to reduce blurring, the data directly used for drawing areal borders here was restricted to the set of experiments reported in Sood and Sereno (2016). That data was collected in the same set of subjects across the three different modalities, in a 1.5T scanner (Siemens Avanto), all using a 32-channel head coil (modified to remove the two eye coils in order to unblock the visual field). 80% of the fMRI data used the Minnesota Center for Magnetic Resonance Research multiband pulse sequence, with 4 simultaneously excited slices, no GRAPPA acceleration, a voxel size of 3.2 mm × 3.2 mm × 3.2 mm, a repetition time (TR) of 1 s, echo time (TE) of 54.8 ms, and 512 data volumes per scan, so each individual mapping scan was 8 min, 32 s. The initial 20% of the data used slightly thicker 3.8 mm slices and the unaccelerated Siemens product EPI sequence with TR = 2 s. Four scans were done for each subject for each modality for a typical total of 6,144 data volumes per subject. A T1-weighted alignment scan with the same block center and orientation was used to initialize the registration, which was then refined using FreeSurfer *bbregister*. No field maps were acquired, but spatial distortions at 1.5T in visual, auditory, and somatosensory areas were minimal.

Individual cortical surfaces were first reconstructed from the average of two T1-weighted scans (MP-RAGE, 1 mm × 1 mm × 1 mm, flip = 7 deg, TI = 1,000 ms, TR = 8.4 ms, TE = 3.57 ms) using FreeSurfer 5.3[2] (Dale et al., 1999; Fischl et al., 1999a,b). Subsequent processing steps were performed using FreeSurfer-compatible *csurf*[3], another extension of the

[1]https://cogsci.ucsd.edu/~sereno/mapper/

[2]https://surfer.nmr.mgh.harvard.edu/

[3]https://cogsci.ucsd.edu/~sereno/csurf/

core surface reconstruction tools introduced in Dale and Sereno (1993). Phase-encoded fMRI data sets were analyzed using Fourier-based methods (Engel et al., 1994; Sereno et al., 1995) and then computed 3D statistics were sampled to individual subject's cortical surfaces along the surface normal to each vertex. Surface-based data were averaged across subjects using surface-based alignment driven by sulcal depth (FreeSurfer *mris_register*), masked by calculating a complex-valued F-ratio (Hagler et al., 2007, implemented in *csurf*), and then displayed on the FreeSurfer 40-subject average cortical surface (subject *fsaverage*) in unfolded and flattened views.

The improved *inflated_avg* surfaces (distorted triangles around north/south 'poles' repaired) and the new flattened surfaces (*cortex2.patch.flat*) made from them that were used here are included in the *csurf* distribution above. The *inflated_avg* surfaces are much less distorted than the more familiar *inflated* surface (and the flattenings made from it) in the standard FreeSurfer distribution. The standard *inflated* surface for subject *fsaverage* is made by surface-averaging the coordinates of the *orig* (folded) surfaces of individual subjects, and then inflating the result. By contrast, the fsaverage *inflated_avg* surface is made by first inflating the folded surface for each individual subject and then surface-averaging the coordinates of the already inflated surfaces. These subtly different processing streams (folded/average/inflate *versus* folded/inflate/average) result in markedly different outcomes as a result of the many idiosyncratic local crinkles in the major sulci of individual brains. When folded surface coordinates are surface-averaged, these crinkles are removed and average sulci are straightened. However, this process also selectively reduces the surface area of the sulci in the average surface; as a result, the total surface area of the average *inflated* surface is reduced by about 1/3 compared to a typical individual brain surface. By first removing the idiosyncratic sulcal crinkles by inflating individual subject surfaces, and then surface-averaging the individual *inflated* surfaces to produce the *inflated_avg* surface, the anisotropic surface shrinkage bias is removed. These less distorted inflated surfaces can then be flattened to give a more veridical flattened template.

Topological cortical maps were defined as contiguous groups of surface vertices with significant periodic response to phase-encoded mapping stimuli that included a range of response phases. For visual mapping, we averaged two counter-clockwise and two time-reversed clockwise rotating polar angle wedge scans, for auditory mapping, two ascending and two time-reversed descending bandpass-filtered non-verbal vocalization scans (cf. Rauschecker et al., 1995), and for somatomotor mapping, two face-to-foot and two time-reversed foot-to-face bilateral cued voluntary movement of individual body part scans (see Huang and Sereno, 2013, 2018; Sood and Sereno, 2016, 2018 for details). Time-reversed datasets were time-shifted 5 sec before being averaging with unreversed data to account for estimated average hemodynamic delays; the time-reversal cancels delay *differences* between different regions. After aligning individual subject spheres with the *fsaverage* sphere (FreeSurfer *mris_register*), data was sampled to the average space with one step of nearest neighbor surface smoothing (FreeSurfer *mri_surf2surf*). Average data was then smoothed with one additional nearest neighbor smoothing step for display. Together, that corresponds to a 2D FWHM kernel of only 1.4 mm (Hagler et al., 2007), substantially narrower than the 3.2 mm fMRI voxel width.

Manual Parcellation of Cross-Subject Average fMRI Data

Single cortical area labels for the surface-averaged data for each modality were then manually generated using csurf *tksurfer* tools by cutting and surface-filling individual connected cortical surface patches for the left and right hemispheres that each contained a topological map representing most of each corresponding sensory receptor (hemi-) surface, respecting as best as possible the sometimes conflicting definitions of cortical areas from our three papers as well as a large number of similar papers from the literature (including, but not limited to: visual: Tootell et al., 1997; Press et al., 2001; Sereno et al., 2001; Wandell et al., 2005; Larsson and Heeger, 2006; Swisher et al., 2007; Caspers et al., 2008; Amano et al., 2009; Kolster et al., 2010; Pitzalis et al., 2010; Wandell and Winawer, 2011; Huang and Sereno, 2013, 2018; Wang et al., 2015; Glasser et al., 2016; Sood and Sereno, 2016; auditory: Pandya and Sanides, 1973; Kaas and Hackett, 2000; Talavage et al., 2004; Kusmierek and Rauschecker, 2009; Rauschecker, 2011; Striem-Amit et al., 2011; Dick et al., 2012; Moerel et al., 2014; Leaver and Rauschecker, 2016; Frank and Greenlee, 2018; Zeharia et al., 2019; somatomotor: Krubitzer et al., 1995; Padberg et al., 2007; Meier et al., 2008; Filimon et al., 2009; Seelke et al., 2011; Huang et al., 2012; Serra et al., 2019; general: Campbell, 1905; Brodmann, 1909; von Economo and Koskinas, 1925; Triarhou, 2007). Though we are familiar with the large mapping literature in nonhuman primates, carnivores, and other mammals, we could only superficially discuss it here [e.g., multiple 'primary' auditory areas were initially recognized in cats (Knight, 1977), but the relation to primates was obscured by the greatly reduced rotation of the temporal lobe in carnivores].

It is an unfortunate fact that picking any single name for a cortical region outside of V1/V2, 3b/1, and A1 will unavoidably conflict with many papers from many different laboratories. We attempted to use (or adapt) existing areal names with a preference for initial use in the literature. We constrained same-named areas in the left and right hemisphere to be in similar positions, with similar neighbors, and with similar orientations of the topological map gradient (gradient of the phase angle of the periodic response with respect to local tangential 2D cortical position). Arrow fields representing the gradient of map phase were computed and displayed using csurf tksurfer *compute_surf_grad* on both the folded or inflated surfaces to aid our manual parcellation (cf. Leaver and Rauschecker, 2016).

Cortical Parcellation and Public Distribution

The collections of individual labels for each modality were then assembled into a parcellation of the entire neocortex of each hemisphere, and presented as FreeSurfer "annotation" files (rh-CsurfMaps1.annot, lh-CsurfMaps1.annot) for the right and left hemisphere FreeSurfer average surfaces (subject *fsaverage*).

These parcellations define an area name and an area color for each vertex on the FreeSurfer average surfaces. They were assembled using csurf tksurfer *write_mgh_annot*, as directed by the color lookup table text file, CsurfColorLUT.txt. The FreeSurfer "annotation" files for each *fsaverage* hemisphere were also converted to GIFTI xml files (*.label.gii suffix) for use in other programs. Both annotation file types, the ASCII color table, and high resolution figure images are included in the *csurf* distribution above, and are also available for individual download here: https://cogsci.ucsd.edu/~sereno/csurf/fsaverage-labels/.

In more detail, the FreeSurfer annotation files specify an RGB color for each vertex on the left and right hemispheres of the FreeSurfer, *fsaverage*, followed by a color lookup table where each line lists a unique region RGB color, region name, and region ID number. The functionally equivalent GIFTI xml files begin with a color lookup table in the same format followed (more standardly) by a list of the integer region id numbers for each vertex that refer to the color lookup table. The FreeSurfer (or GIFTI) parcellation files can be used to sample ROIs from any data set that has been mapped onto the FreeSurfer average surface; in addition, the average surface cortical areas can be mapped back to an individual subject's surface (e.g., using FreeSurfer *mri_surf2surf*) in order to pick out 2D regions of interest from an individual subject's data. From there, the individual subject surface patches can also be used to pick out surface-normal-intersecting 3D-voxel-based gray matter ROI's in subject-native fMRI space (e.g., using csurf tksurfer *annot2roi.tcl*). Finally, instructions for converting the GIFTI annotation files to the hemisphere independent (fs_LR) Human Connectome Project HCP sphere can be found here: https://wiki.humanconnectome.org/download/attachments/63078513/Resampling-FreeSurfer-HCP_5_8.pdf.

Average Map Color Scales

Visual, auditory, and somatomotor maps are displayed with similar, easy-to-remember color scales: *green* for lower field, low frequency, or leg/foot; *blue* for horizontal meridian, mid frequency, or arm/hand, and *red* for upper field, high frequency, or face. Though more hues can be used to visually distinguish more levels of each map coordinate, more hues are also harder to keep in mind; and with more hues, small overall offsets in map coordinates can result in more distracting changes in visual appearance.

Parcellation Philosophy

The goal of this exercise was to produce a tentative parcellation of contiguous areas based almost entirely on topological mapping data for the three main sensory modalities, while respecting approximate bilateral symmetry. By contrast, it has often been noted, by ourselves and others (Felleman and Van Essen, 1991; Sereno and Allman, 1991), that in the fullness of time, cortical areas are best defined by combining multiple features, which can include, for example, surface-based coordinates (e.g., after surface-based alignment driven by sulcus depth and/or other measures), topological sensorimotor map coordinates (what we are using here), functional connectivity measures, estimates of quantitative T1 values (Sereno et al., 2012; Glasser et al., 2016), diffusion surface (HARDI) features referenced to the local cortical surface normal (Nagy et al., 2013; Ganepola et al., 2018, 2021), responses from cognitive subtraction paradigms, effects of lesions, and so on. An obvious advantage of combining features for parcellation is that a border not detectable by one feature (e.g., T1 value) may be easily visualized when using a different feature (e.g., retinotopy).

However, one advantage of having parcellations primarily based on a single feature is that it is more straightforward for subsequent studies to assess which borders are robustly and independently localized by multiple features and which ones depend only on a single feature, and are therefore less robust. In addition, without maps of individual features (like the topological map boundaries here), it is more difficult to investigate cases where different map features disagree on the location of borders. One of our goals is to provide a resource that can be reused or revised in future multi-feature parcellations. Trying to keep parcellations editable, interchangeable, and combinable is a challenge given different software environments, but a worthy goal because cortical parcellations should best be viewed as works that are permanently in progress (Fischl and Sereno, 2018).

RESULTS

Visual Areas in Non-human Primates Defined by Microelectrode Retinotopic Mapping

An extensive history of using microelectrode retinotopic mapping experiments to define visual areas in non-human primates and other animals has shown that large, early visual areas such as V1 and V2 can be relatively easily located and mapped. However, the difficulty of defining visual areas increases substantially with higher areas, which are invariably smaller, somewhat more variable across individuals and species, and which often contain partial representations of the visual hemifield. Perhaps the 'next best' cortical visual area to V1 and V2 in primates is area MT, which reliably contains a simple hemifield map, with 2/3 of its border marked by a clear change in myelination (Sereno et al., 2015, their Figure 3).

Parcellation by Visual Field Sign

By using high microelectrode penetration densities, it has been possible to demarcate a large number of additional visual areas beyond V1, V2, and MT. For example, **Figure 2** (modified from Sereno et al., 2015) shows the retinotopic organization of dorsal and lateral visual areas in the owl monkey, using local visual field sign (mirror-image vs. non-mirror-image representation) to parcellate the data sets. Almost all of the visual areas in the owl monkey exhibit a substantial degree of retinotopic organization, which was apparently absent only in anterior inferotemporal cortex.

The large number of higher level areas combined with their small size (some containing full visual quadrant representations spanning barely more than 1 mm of cortex – see scale bar), has

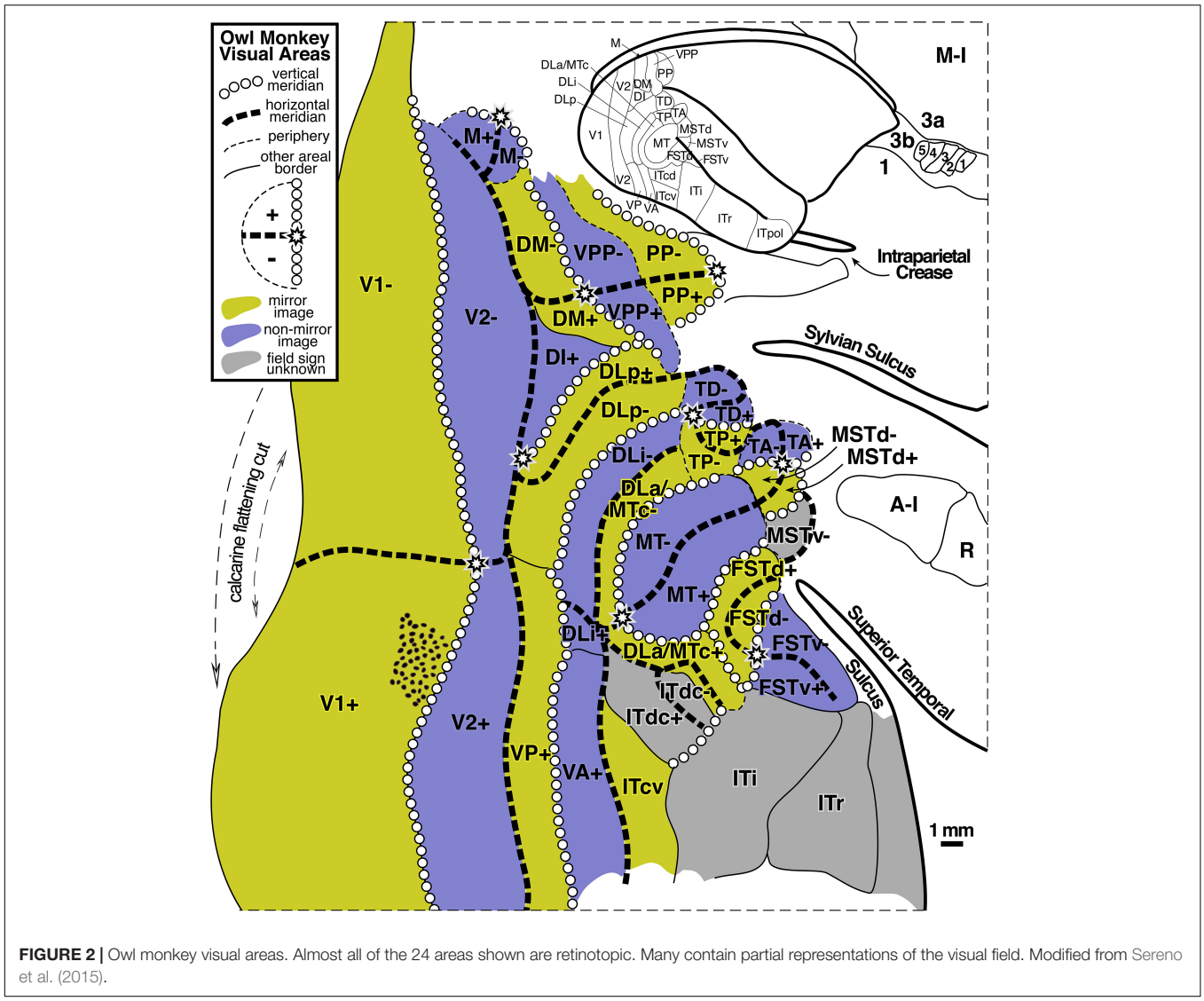

FIGURE 2 | Owl monkey visual areas. Almost all of the 24 areas shown are retinotopic. Many contain partial representations of the visual field. Modified from Sereno et al. (2015).

made it challenging to reliably locate and identify similar areas across individuals and across species, and some uncertainty about how to combine partial visual field representations remains. For a slightly different parcellation of visual areas in marmosets, another New World monkey, see Angelucci and Rosa (2015). For a visual field sign analysis of fMRI data from Old World macaque monkeys suggesting stronger than expected similarities between retinotopic map organization in New and Old World monkeys, see Janssens et al. (2014), Kolster et al. (2014), and Zhu and Vanduffel (2019).

Visual Receptive Field Position Is Continuous for Small Tangential Movements Across Cortex

These and many similar experiments have established that discontinuities in the cortical representation of visual space – defined as instances where a small movement tangential to the cortical surface in the recording location results in a discontinuous jump in the location of the corresponding visual receptive field – are extremely rare across the large expanse of extrastriate areas. In all but a very few instances, nearby recording sites (within 0.25 mm) have partially overlapping receptive fields (see Sereno et al., 2015, their Figure 9 for an extremely rare exception to this rule, and compare Yu et al., 2020, for an interesting proposal that a visual area in this region has a 'twisted' representation that contains adjoined mirror-image and non-mirror image parts, which would require a localized discontinuity at their border).

This finding also implies that the great majority of the borders between visual areas are 'congruent,' which means that adjoining areas virtually always have representations of similar (duplicated) visual field locations on either side of their shared border, the paradigm case being the vertical meridian border between V1 and V2 (Allman and Kaas, 1975).

Visual Maps Can Be Very Small

Experiments on mice (anatomical: Wang and Burkhalter, 2007; visual field sign analysis of intrinsic optical signals: Garrett et al., 2014), have revealed that their higher level visual areas can be

truly tiny, with an entire representation of the visual hemifield crammed into a narrow column extending through the layers of the cortex that covers only 0.1 square mm of the cortical surface. Though it is not thought that visual areas in humans ever get this small, in part because human cortex is several times thicker than mouse cortex, the fact that complete visual areas *can* be so small suggests that we keep an open mind about what the minimum size of a cortical area map in humans is until positive data with high enough resolution has definitively set a lower size bound. In any case, the owl monkey data show that a complete visual quadrant representation can in many cases be narrower than a single standard 2–3 mm wide fMRI voxel (see area DLa/MTc in the middle of **Figure 2**).

Differences Between Topological Maps in Different Modalities

As a preface to discussing topological maps in other modalities beyond vision, it is important to recognize several fundamental differences among the approximately topological maps in the visual system, the somatosensory system, and the auditory system.

Cortical Map Discontinuities (in Receptive Field Position as Function of Cortical Position)

The visual system moves a retina smoothly over objects in visual scenes. Because fixation points on scenes (and the content of scenes themselves) are so various, nearby points on the retina will tend to be activated across time in strongly correlated ways – that is, it is rare for object boundaries or other image discontinuities to repeatedly fall on the exact same retinal location so that one retinal region is repeatedly stimulated in a different way than a directly adjoining retinal region. This retinal stimulation pattern may explain – in the context of a correlation-based (Hebbian) topological map refinement rule (or other local substance-dependent learning rule) – the empirical observation noted above that short movements in recording location tangential to visual cortical areas very rarely result in discontinuous jumps in the location of the corresponding visual receptive field position.

By contrast, in the somatosensory system, it is trivial to generate stimuli that reliably respect a specific border between adjoining cortical regions. For example, one can easily stimulate the underside of the index finger while simultaneously completely avoiding stimulating the underside of the middle finger. Because the representations of the hairless (glabrous) undersurface of the five fingers are immediately adjacent to each other in area 3b, neurons on either side of the cortical border between adjacent fingers can reliably have uncorrelated responses; this is much less likely to reliably occur with any pair of nearby neurons in a visual cortical map.

A second difference between the visual and somatosensory system is that the retinal surface does not have anywhere near as much regionally-variable intrinsic (Gaussian) curvature as does the surface of the skin. This makes it less problematic to map the retinal surface to the cortical surface without introducing a large amount of local areal distortion. This is readily appreciated by imagining physically flattening a hemiretina, roughly a quarter of a sphere, which would hardly even require cuts. By contrast, trying to flatten the entire skin surface (including the surface of the hands, feet, lips and inside of the mouth, and so on) without introducing massive local areal distortion obviously requires many more cuts. Rather than a homunculus, somatosensory cortex actually consists of an unfamiliar patchwork quilt of skin regions with discontinuities at the borders between these patches. For example, the representation of the glabrous surfaces (hairless under surface) of all five fingers are neatly cut out and juxtaposed in area 3b, but then the representations of the hairy upper surfaces of the same fingers are separately cut out and placed off to the side (medially and laterally) from the glabrous surface array in area 3b (Merzenich et al., 1978).

These differences between visual and somatosensory receptive surfaces are likely responsible for the fact that discontinuities of the kind that only very rarely occur in the visual system are extremely common in the somatosensory system. For example, when traversing the cortical boundary between the index finger and the middle finger in area 3b, corresponding receptive fields discontinuously jump from being entirely on one finger to entirely on the other finger. There are hundreds of discontinuities of this type in early somatosensory maps, often arranged into lines across the cortical surface. For example, the representation of the underside of the thumb is directly apposed to a representation of a portion of the chin. Many of these discontinuities are visible in the cortex as thin lines of less dense myelination (Sereno, 2005, their Figure 1; Kuehn et al., 2017), probably reflecting reduced local cortical connectivity across these map discontinuities.

Converse Cortical Map Discontinuities (in Cortical Position as Function of Receptive Field Location)

Finally, it's worth noting that the kind of discontinuity discussed above – involving jumps in receptive field location due to a small movement across a cortical map – should be distinguished from the converse kind of discontinuity – defined by a jump *on the cortex* resulting from a small movement *in the visual field*. Allman and Kaas (1975) called this converse kind of discontinuity a 'second order transformation' of the visual field. A well known example occurs at the anterior border of area V2, which represents the horizontal meridian. A small movement in the visual field from the lower visual field into the upper visual field that crosses the visual field horizontal meridian results in a sudden large jump in the corresponding location of the elicited cortical activity – from a point below the calcarine sulcus to a point above the calcarine sulcus. This converse kind of discontinuity is quite common in visual cortex, likely the end result of having to accommodate congruent borders between areas. Note that a congruent border (i.e., no discontinuity of the first kind) may be maintained at the location of this second, converse kind of discontinuity. For example, the border between lower field V2 and V3, which represents the horizontal meridian, is a congruent border between two quadrant representations (no discontinuity of the first kind), despite the fact that the horizontal meridian is the site of a discontinuity of the second, converse kind.

Similar converse discontinuities might occur in somatosensory and auditory areas. For example, is possible that

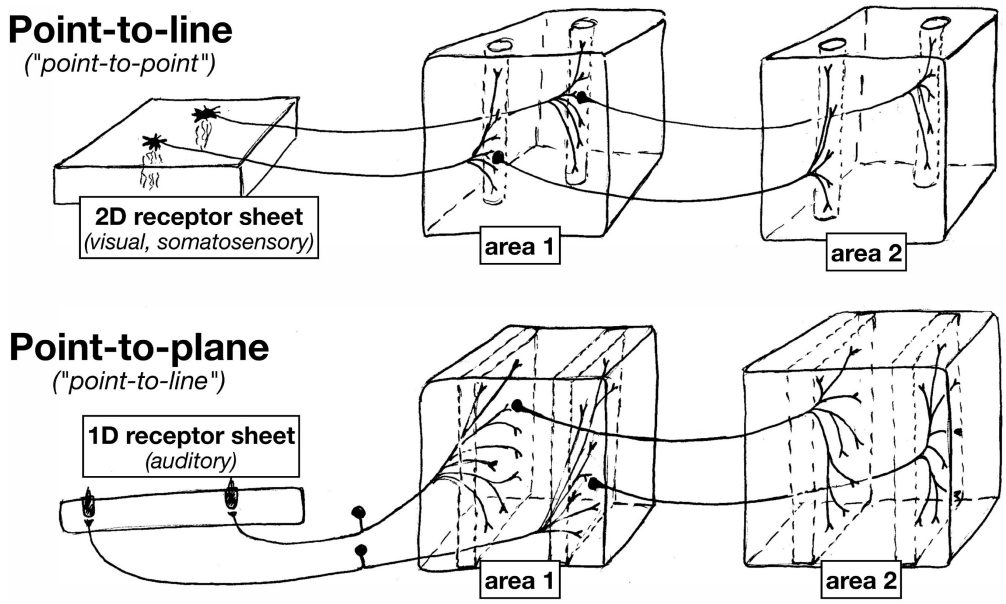

FIGURE 3 | Since auditory receptors form a 1D line, in contrast to 2D sheets of visual and somatosensory receptors, subsequent approximately topological station-to-station connections between nuclei in the auditory system have an 'extra' dimension across which to spread.

some auditory areas may have an analogous V2-like split where the representation of lower frequencies is spatially detached in the cortex from the representation of higher frequencies.

1D vs. 2D Sensory Surfaces

Despite the differences between somatosensory and visual maps (somatosensory cortical areas a 'patchwork quilt' compared to locally continuous visual areas), the receptor arrays in the visual and somatosensory system are both fundamentally arranged as *two*-dimensional surfaces. And in both systems, individual points on the sensory surfaces (retina or skin) are mapped to thin columns ('lines') by the axon terminal arbors that project to each subsequent station in the brain (e.g., different laminae in the dLGN, different cortical layers in V1) (see **Figure 3**).

Auditory system projections, however, typically exhibit characteristically different axon terminal geometry. This is because the auditory receptor array is essentially a *one*-dimensional line. At each point in the cochlea, there are three inner hair cells and one outer hair cell (Ashmore, 2008), with the latter serving as the main source of ascending tonotopic input. Along the spiral tonotopic axis of the cochlea, there is a long one-dimensional line of about 3,500 of these three-plus-one hair cell 'points.'

As a result of this 'dimensionality mismatch' (1D sensory surface vs. 2D tangential cortical map), subsequent topological station-to-station connections between nuclei in the auditory system have an 'extra' dimension across which to spread. Individual auditory projection axon terminals often form what are sometimes called 'lines' in the auditory literature, but which actually have the geometry of gently curved two-dimensional sheets. Subsequent auditory projections often exhibit a similar 'point-to-plane' morphology that contrasts with the 'point-to-line' (point-to-column) morphology typical in the visual and somatosensory systems.

The 'extra' dimension is put to good use in the auditory brainstem. For example, in barn owls (Konishi et al., 1988), there is a topological map of binaural characteristic delay that is oriented perpendicular to the tonotopic map in the nucleus laminaris (NL); it is constructed by arranging to have axonal delay lines come into the nucleus from the left and right monaural nucleus magnocellularis (NM) from opposite directions to synapse onto coincidence detecting neurons (see "NL" at upper left of **Figure 4**). Further along, a two-dimensional space map is constructed in the external nucleus of the inferior colliculus (ICx) by combining an interaural *time* difference map in the inferior colliculus, central nucleus, lateral part (ICc lat) with an interaural *amplitude* difference map in the inferior colliculus, central nucleus, medial part (ICc med, which signals elevation courtesy of the barn owl's asymmetric ears); this is accomplished by intersecting arrays of point-to-plane projections from these two sources at right angles to each other in ICx (see "ICx" at the right side of **Figure 4**). Interestingly, this constructed auditory space map is then connected to the visual system (the superior colliculus) by what look like 'standard-issue' visual system point-to-line connections, in contrast to the point-to-plane style of connections in most of the previous stations of the auditory system. The mapping of characteristic delay in ICc lat probably has uses beyond the non-frequency-selective ICx space map. For example, by inhibiting all but one characteristic delay column in ICc, sounds coming from one particular azimuth could be isolated for further analysis by the thalamus and forebrain without destroying tonotopy (i.e., auditory spatial attention).

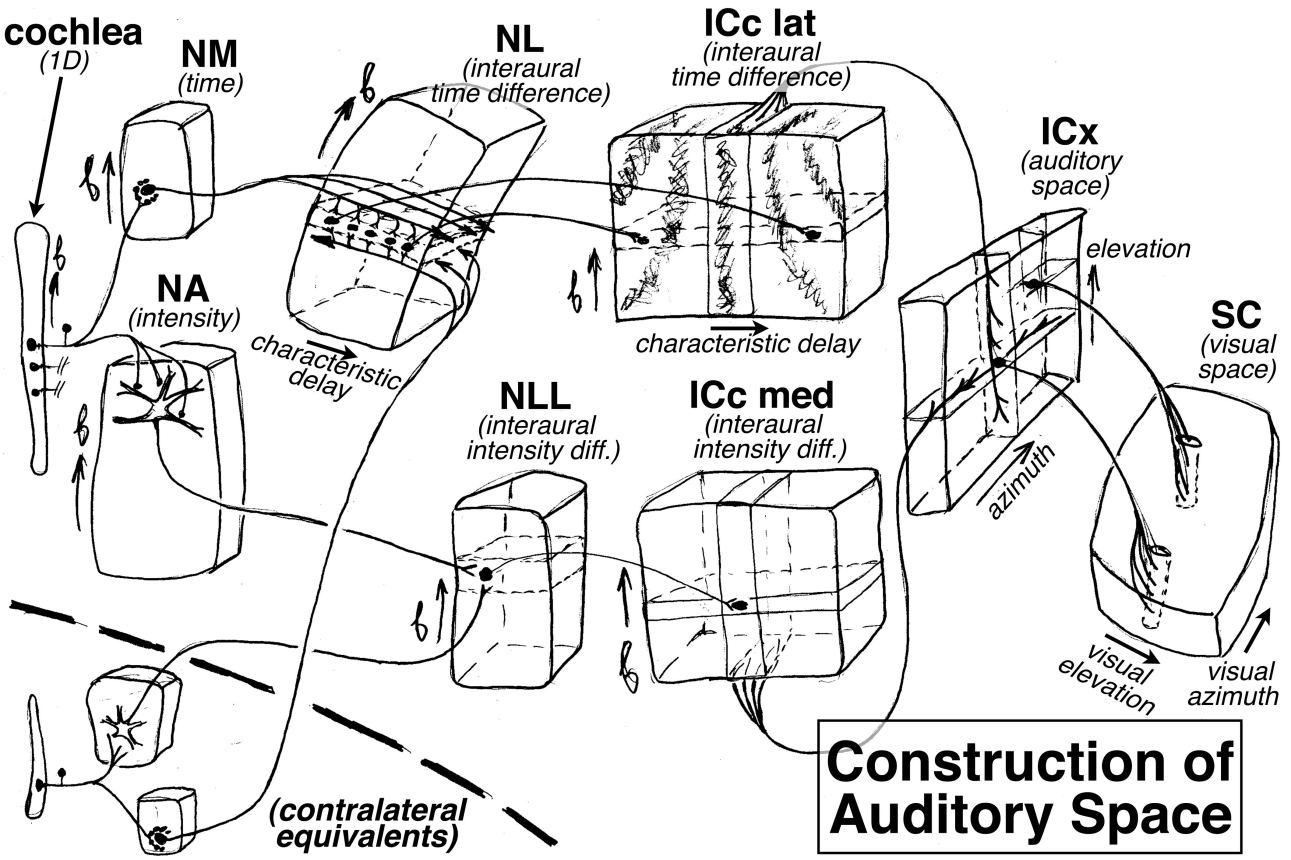

FIGURE 4 | How the auditory system plays with maps: construction of an auditory space map from two (**left** and **right**) frequency maps in the barn owl. The 'extra' dimension perpendicular to tonotopy is used to construct maps of other features, such as characteristic delay in the nucleus laminaris (NL) and the inferior colliculus central nucleus lateral part (ICc lat), and eventually an auditory map of space in the external nucleus of the inferior colliculus (ICx), which is finally sent to the superior colliculus (SC).

Finally, individual auditory areas in general have smaller surface areas than individual visual and somatosensory areas. This may be the result of the combination of a smaller total number of input receptors and the fact there is only one primary map dimension.

Comparing Phase-Encoded Maps Across Modalities

Given these substantial differences between maps in the three different modalities, we do not want to be too facile about directly comparing them. The patchwork quilt within each somatosensory cortical area differs from the more locally continuous representations in each cortical visual area. And for auditory areas, having only one primary map dimension makes finding borders perpendicular to the tonotopy gradient even more challenging; finally, what exactly is mapped in primate auditory cortex perpendicular to the tonotopic axis, if anything, remains disputed. In bats, it is known that there are higher level auditory areas that contain more complex two-dimensional auditory maps (e.g., the CF_m/CF_n areas, where CF_m and CF_n refer to different harmonics of the constant frequency part of the outgoing call and echo); individual neurons there respond to particular pairs of frequencies and are arranged into two approximately orthogonal frequency gradients for the purpose of measuring Doppler shift independent of frequency (Suga, 1988), perhaps measured by sampling along diagonal lines across these two-frequency maps.

It is currently unknown whether something similar to the bat CF_m/CF_n areas exist in human auditory areas (e.g., for identifying vowel formant patterns produced by speakers with different vocal tract sizes, a computationally similar problem to determining Doppler shift independent of outgoing frequency – in both cases, the spacing between two frequencies must be detected independent of absolute frequency); but in any case, our single bandpass stimuli would not have been optimal for revealing such a 2D map. In addition, because of constraints on scan and subject time, we were only able to map one dimension of retinotopy (polar angle, but not eccentricity); and in the somatosensory system, we have mapped one rough rostrocaudal 'axis' of main body parts from the toes to the face, without systematically interrogating the two spatial dimensions of the maps in each of these parts (e.g., in the case of the fingers, the palm to finger tip direction versus the perpendicular direction that runs from the radial to the ulnar side of each finger). Much longer experiments at higher resolution will be required to move forward from here.

Visual, Somatosensory, and Auditory Maps in the Human Cortex

With all these caveats in mind, we divided cortex containing topological maps into 117 regions (57 visual, 34 auditory, 20 somatosensory, and 6 motor – see **Table 1**). These are illustrated in **Figure 5**, which displays the FreeSurfer annotation files: lh-CsurfMaps1.annot and rh-CsurfMaps1.annot (GIFTI versions are equivalent). To help perceptually group them, visual areas were colored with different shades of blue/purple, auditory areas colored red/brown, and somatomotor areas green/yellow. These areas occupied a little under half (47%) of the total surface area of the neocortex. In a few cases, large primary areas (e.g., V1, V2, V3/VP, MT, 3b, 1, 4) were subdivided into upper/lower field or hand/face/foot.

Visual areas are grouped in **Table 1** into primary, secondary and tertiary areas (e.g., V2), lateral intermediate areas (e.g., LO1), posterior medial areas (e.g., V6), lateral temporal areas (e.g., MT), inferior intermediate areas (e.g., V8), superior parietal areas including posterior cingulate areas (e.g., LIP1), and frontal visual areas (e.g., DLPFC). The lower-case suffixes are appended to multisensory areas (e.g., VIP1v,s) to indicate the modalities involved (e.g., visual plus somatosensory).

Auditory areas are divided into primary-like areas (e.g., A1), medial and lateral belt areas (secondary), lateral parabelt areas (tertiary), and fourth and fifth tier auditory belt areas (e.g., CA4, CA5 where "C" means caudal). Several other areas include the subcentral area (Brodmann 43) representing the tympanum (43aud), several frontal auditory areas (e.g., dmFAF), and a newly recognized central sulcus area (3aud) (see below for details).

Somatosensory and motor areas are divided into primary somatosensory and motor areas (e.g., 3b, 4), superior parietal areas (e.g., 5m), lateral secondary areas (e.g., S-II), and medial secondary motor areas (e.g., SMA1).

The mapping data on which the **Figure 5** parcellation is based is illustrated in **Figure 6**, with areal borders from **Figure 5** superimposed using cyan dots. As introduced above, an intuitively similar color scale was used for each modality, where *green* indicates lower visual field, lower auditory frequency, or leg/foot; *blue* indicates horizontal meridian, middle frequency, or arm/hand; and *red* is upper field, high frequency, or face. **Figures 5**, **6** are sized and arranged identically to make it easy to blink back and forth between them in an image viewer (see also GIF animation of this[4]).

New Features of This Parcellation

For most of the areas in this new parcellation, there is no major dispute with the literature (beyond different author's conflicting nomenclature, or minor differences in boundary placement). Several comments on new or unusual features follow.

In *retinotopic* maps in the visual system, area LIP1 is 'putative human LIP' as originally defined in Sereno et al. (2001). Parietal areas posterior and anterior to LIP1 were taken from the literature, respecting priority.

[4]https://cogsci.ucsd.edu/~sereno/csurf/fsaverage-labels/CsurfMaps1-illustrations/CsurfMaps1-areas,maps.gif

TABLE 1 | Cortical area abbreviations by modality (annotation file order).

Visual areas	
Primary, secondary, and tertiary areas	
V1–	Striate cortex, lower field
V1+	Striate cortex, upper field
V2–	Second visual area, lower
V2+	Second visual area, upper
V3	Third visual area, lower
VP	Ventroposterior (=V3v)
Lateral intermediate areas	
DI	Dorso intermediate area
V3A	Visual area 3, accessory
V3B	Visual area 3, accessory B
OPA	Occipital place area
LO1	Lateral occipital area, 1
LO2	Lateral occipital area, 2
LO3	Lateral occipital area, 3
PGp	Parietal ang. area G, post.
Posterior medial areas	
V6	Visual area 6
V6A	Visual area 6 accessory
aPOS	Ant. parieto-occipital sulc.
POm	Parieto-occipital medial
ProS1	Area prostriata, 1
ProS2	Area prostriata, 2
Lateral temporal areas	
MT–	Middle temporal, lower
MT+	Middle temporal, upper
MTc	MT crescent (=V4t, DLa)
MSTd	Med sup. temporal, dorsal
MSTv	Med sup temporal ventral
FSTd	Fundus of STS, dorsal
STV1	Sup. temp. visual, area 1
STV2	Sup. temp. visual, area 2
7b-PICv	Area 7b parietal insular ctx
7b-PICv,s	Area 7b par. ins., vis/som
Inferior intermediate areas	
V4v	Visual area 4, ventral
hV4	Human V4
V8	Visual area 8
PITd	Post. inferotemp. dorsal
PH	Basal parietal area H
FFC	Fusiform face complex
VVC	Ventral visual complex
VO1	Ventral occipital area 1
VO2	Ventral occipital area 2
Superior parietal areas	
V7	Visual area 7
cIPS	Caudal intraparietal sulc.
LIP0	Lateral intraparietal zero
LIP1	Lateral intraparietal area
PEc	Parietal area E, caudal
IPS4	Intraparietal sulcus area 4
IPS5	Intraparietal sulcus area 5
aPCu1	Ant. pre-cuneus visual 1
aPCu2	Ant. pre-cuneus visual 2

(Continued)

TABLE 1 | (Continued)

Superior parietal areas	
VIP1v	Ventral intraparietal 1, vis
VIP1v,s	VIP1, visual and somato.
VIP2v	Ventral intraparietal 2, vis
VIP2v,s	VIP2, visual and somato.
Frontal visual areas	
dmFEF	Dorsomedial FEF
FEF	Frontal eye fields
6a	Area 6, part a
DLPFC	Dorsolateral prefontal ctx
DLPFCa	Dorsolateral PFC, part a
Auditory areas	
Auditory core (primary)	
A1	Primary auditory area
R	Rostral auditory area
RT	Rostro-temporal area
Auditory caudal/medial belt (2°)	
MM	Middle medial belt
RM	Rostromedial belt
CM	Caudomedial belt
Auditory lateral belt (secondary)	
CL	Caudolateral belt
ML	Middle lateral belt
AL	Anterior lateral belt
RTL	Rostrotemporal lateral belt
Auditory para belt (tertiary)	
CP	Caudal parabelt
MPc	Middle parabelt, caudal
MPr	Middle parabelt, rostral
RP	Rostral parabelt
TA2	Temporal area A, part 2
TA3	Temporal area A, part 3
Auditory belt areas, 4th tier (A4)	
CA4	Caudal 4th tier auditory
MA4	Middle 4th tier auditory
RA4	Rostral 4th tier auditory
Auditory belt areas, 5th tier (A5)	
CA5	Caudal 5th tier auditory
MA5	Middle 5th tier auditory
RA5	Rostral 5th tier auditory
Subcentral area (tympanum)	
43aud	Area 43, subcentral area
Posterior sylvian areas	
PSaud1	Posterior sylvian aud. 1
PSaud2	Posterior sylvian aud. 2
Central sulcus auditory area	
3aud	Area 3 auditory area
Medial frontal auditory areas	
dmFAF	Dorsomed front. aud field
p32aud	Area p32, auditory part
Lateral frontal auditory areas	
PZa,v,s	Polysensory zone, all 3
PZa,s	Polysensory zone, au/som
DLPFCaud	Dorsolateral PFC, aud.
IFSp	Infer. front. sulcus, post.
45aud	Area 45, auditory
FOPaud	Frontal operculum aud.
Somatosensory areas	
Primary somatosensory areas	
3b-fa	Area 3b, face and mouth
3b-ha	Area 3b, arm and hand
3b-ft	Area 3b, leg and foot
3a-fa	Area 3a, face and mouth
3a-ha	Area 3a, arm and hand
3a-ft	Area 3a, leg and foot
1-fa	Area 1, face and mouth
1-ha	Area 1, arm and hand
1-ft	Area 1, leg and foot
2	Area 2, face/hand/foot
Higher somatosensory areas	
5m	Area 5, medial
pCl	Post. cing. sulc., vis./som.
5L	Area 5, lateral
PFt	Parietal inf. F, tenuicortic.
AIPv,s	Anter. intrapar., vis./som.
Lateral sulcus somatosensory areas	
S-II	Secondary somatosensory
PV	Parietal ventral somato.
Ig	Insular granular field
FOP2	Frontal operculum, area 2
PHt	Bas. par. H, temporal entr.
Motor areas	
Primary motor cortex	
4-fa	Area 4, face and mouth
4-ha	Area 4, arm and hand
4-fo	Area 4, leg and foot
Medial secondary motor areas	
6d	Area 6, dorsal
SMA1	Supplementary mot. area
SMA2	Supplementary mot. area

(Continued)

We outlined VIP1 and VIP2 using retinotopy, but then further distinguished their anterior halves (VIP1v,s and VIP2v,s), which have multisensory (visual plus somatomotor) maps (visual maps shown in **Figure 6**). However, since our coverage of the visual field was much better than our coverage of the body surface, it is likely that more complete stimulation of the skin surface would have extended the multisensory overlap somewhat posteriorly (see Huang et al., 2017, for a higher resolution investigation of multisensory overlap and variation in the VIP's). We include both V4v and hV4 (sometimes contrasted), a third LO area (LO3), and another area adjoining V3A (OPA, occipital place area, Huang and Sereno, 2013). On the medial surface anterior to V6 and V6A and the periphery of V1 and V2, we define four areas; moving superior to inferior, these are: an anterior parietal-occipital sulcus area (aPOS), the medial parieto-occipital area (POm), and two retinotopic subdivisions of area prostriata (ProS1 and ProS2). Further anterior on the midline (after a small gap without a visual map) are two retinotopic anterior precuneus visual areas (aPCu1 and aPCu2). 7b-PIC in the posterior lateral

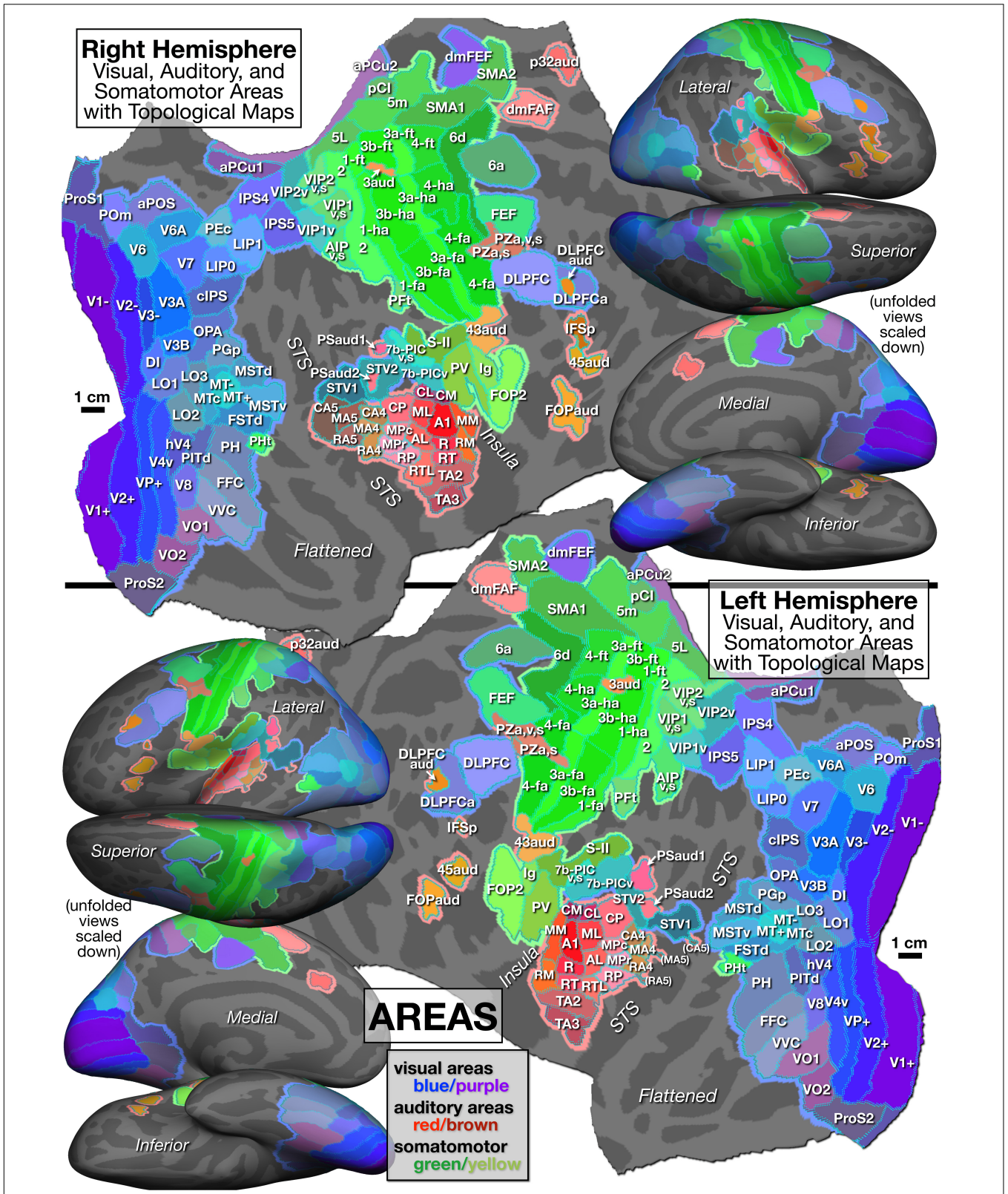

FIGURE 5 | Parcellation of cortical areas containing topological sensorimotor maps as defined by significant amplitude response and significant phase spread to phase-encoded visual (blue/purple), auditory (red/brown), and somatomotor (green) mapping stimuli. See identically arranged **Figure 6** for supporting mapping data and **Table 1** for abbreviation definitions.

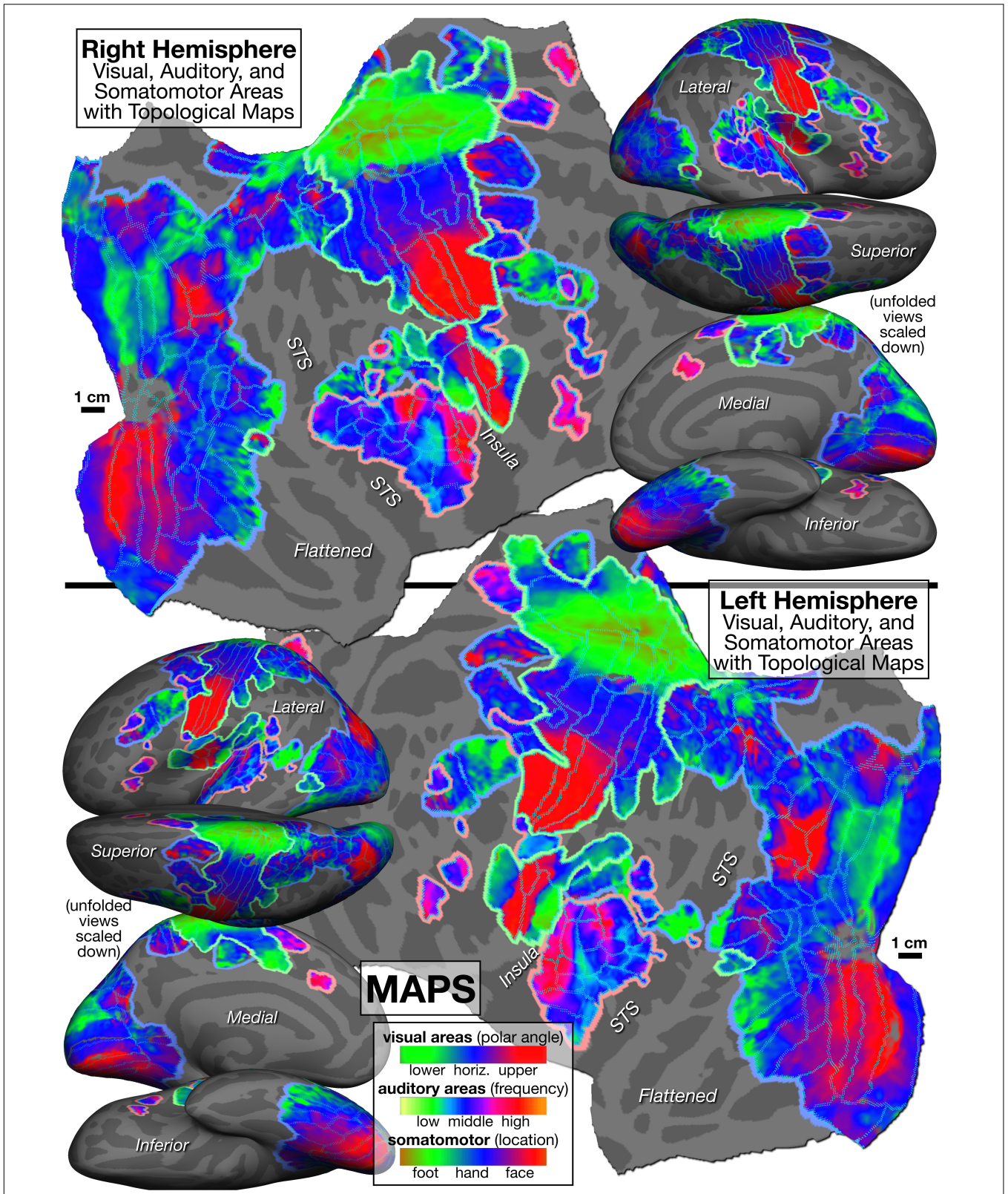

FIGURE 6 | Topological cortical maps defined by periodic response to phase-encoded mapping stimuli (*visual*: clockwise/counter-clockwise rotating polar angle wedges; *auditory*: ascending/descending bandpass-filtered non-verbal vocalizations; *somatomotor*: face-to-foot/foot-to-face bilateral, cued voluntary movements of individual body parts). *Green* is lower field, low freq, or leg/foot; *blue* is horizontal meridian, mid freq, or arm/hand; *red* is upper field, high freq, or face.

sulcus is predominantly visual, but the anterior-superior part also has somatosensory input from the foot; these areas are distinguished as unimodal 7b-PICv and multisensory 7b-PICv,s.

In frontal cortex, we have labeled area CSv (cingulate sulcus visual area), an area anterior to the central sulcus, with its prior name from the non-human primate literature, dmFEF (dorsomedial frontal eye fields) (review: Tehovnik, 1995; also known as the supplementary eye fields).

In *tonotopic* maps in the auditory system, we placed the core areas A1, R, and RT along the highly myelinated crown (Dick et al., 2012) of Heschl's gyrus with nearly parallel tonotopic gradient directions (see Leaver and Rauschecker, 2016, for a different proposed orientation of the auditory core relative to Heschl's gyrus). We then defined four additional tiers of areas moving posteriorly and inferiorly from the core, using conventional abbreviations for the second and third tier areas (Kaas and Hackett, 2000). The second tier includes the medial (M) and lateral (L) belt, and the third tier is the parabelt (P), where within-belt subdivisions are indicated by a C/M/R prefix for caudal/middle/rostral. The fourth tier was named caudal/middle/rostral A4. The strong tonotopic responses in the right hemisphere in the fifth tier, caudal/middle/rostral A5 (CA5, MA5, and RA5), were weak in the left hemisphere. See Rauschecker and Scott (2009) and Rauschecker (2018) for a different, functionally-based definition of A4 and A5 by analogy with the functions of V4 and V5/MT as opposed to their distance from primary cortex; their A4 areas, by contrast, are the anterior auditory "what" stream, and their A5 areas, the posterior "how/action" stream. Finally, the most rostral temporal auditory area (TA2 and TA3) have higher numbers moving rostrally (following Jones and Burton, 1976, but in contrast to the foundational core-and-belt study of Pandya and Sanides, 1973, where Ts1 is the most rostral of Ts1, Ts2, and Ts3).

There was a small (2 mm) auditory/somatomotor overlap between a region at the border between the middle medial belt (MM) and the caudal medial belt (CM), and the foot representation in the parietal ventral somatosensory area (PV) (not subdivided here, auditory-somatosensory multisensory region included in PV).

Most unusually, we found a small bilateral superior central sulcus auditory area (low to high frequencies from anterior-lateral to posterior-medial) embedded within Brodmann area 3a/3b (3aud). It occupies about half of a small no-response gap in our somatomotor mapping data between the representation of the 'hand' (which includes the arm and stomach) and the 'foot' (which includes the thigh and leg) that likely corresponds to the representation of the genitalia (Knop et al., 2021) and/or respiratory muscles (McKay et al., 2003), both of which we did not specifically stimulate. Auditory responses in this region are not unprecedented (see Tierney et al., 2012, their Figure 2). We also describe a subcentral sulcus auditory area (43aud) lateral to the face S1/M1 face representation in Brodmann area 43 (low to high frequencies moving inferior to superior) (Job et al., 2011).

We outline seven tonotopic frontal auditory areas. Moving inferior to superior, these include two frontal opercular areas (FOPaud, 45aud), a small inferior frontal sulcus area (IFSp), a small area embedded within the anterior of two retinotopic dorsolateral prefrontal cortical areas (DLPFCaud), two tonotopic multisensory areas that intrude posteriorly into area 3a and 4, near the junction between the hand and face representations (PZa,s and PZa,v,s; both areas contain a face somatomotor representation, while the second also has a visual map; "PZ" is for polysensory zone, from Cooke and Graziano, 2004), a dorsomedial frontal auditory field that rounds onto the medial wall (dmFAF) adjoining the opposite side of the supplementary motor cortical areas from dmFEF, and a small auditory area further inferior within the cingulate sulcus (p32aud). Finally, there were two small posterior sylvian auditory regions (PSaud1,2) adjoining (in one case embedded within) superior temporal visual areas 1 and 2 (STV1,2).

In *somatomotor* maps, in the central sulcus and adjoining gyri, we subdivided areas 4, 3a, 3b, and 1 into "face," "hand," and "foot" (Kuehn et al., 2017; for finer subdivisions of the somatomotor "face" areas, see Carey et al., 2017). We distinguished five areas in the lateral sulcus moving posterior to anterior: a multisensory area in posterior insular cortex (7b-PICv,s), secondary somatosensory cortex (S-II), parietal ventral somatosensory (PV), insular granular (Ig), and a frontal opercular area (FOP2). Lateral to VIP1v,s and VIP1v, we illustrate a multisensory (visual and somatomotor) anterior intraparietal area (AIPv,s) containing a full body representation (**Figure 6** shows somatosensory, not visual, representation), and further laterally, there is another hand and foot area, PFt (von Economo and Koskinas, 1925; Triarhou, 2007; the "PF" is for "parietal, inferior" and the "t" is for "tenuicortical") that is posterior to the central sulcus face representations that protrudes posteriorly and inferiorly from area 1. Much further posteriorly, directly bordering temporal visual areas, there is a small somatosensory map, PHt (von Economo and Koskinas, 1925), at the anterior boundary between visual areas FSTd and PH (the posterior third of PHt also has visual responses, not subdivided here; the "PH" is for "parietal, basal" and this "t" is for "temporal entrance"). Finally, on the medial wall, between visual aPCu2 and somatosensory 5m, we delineated a visual plus somatomotor multisensory area, pCI (posterior cingulate sulcus multisensory area: Serra et al., 2019). Further anterior on the midline, we distinguish two supplementary motor areas joined at a representation of the upper body and face (SMA1 and SMA2).

An Atlas of Maps and Map Coordinate Gradients in Individual Areas

One of the difficulties that arises when averaging small topological maps across subjects is that slight map misalignments between subjects tend to compress the range of map coordinates within an area ('regression toward the horizontal meridian' in the visual system, 'regression to mid frequencies' in the auditory system), overemphasizing map coordinates in the middle of the maps. That can make it more difficult to discern the direction of the map coordinate gradient; the gradient can also be harder to see with partial representations of the sensory surface (e.g., visual hemifield versus quadrant versus other partial hemifield divisions – for the last case, see Gattass et al., 1988). Another set of difficulties for the reader's visual understanding of these maps arises from just how many close-packed areas there are. This causes visual crowding from surrounding areas and partial map

occlusion by border annotations (cyan border dots were used to allow some of the map data to show through).

Therefore, to provide a more user-friendly atlas for the new parcellation, we made a movie for the left and right flattened hemispheres (see **Supplementary Videos 1, 2**) that sequentially shows the mapping data from each of the 117 areas individually (234 Figures). We used a white arrow to indicate the average direction of the map coordinate gradient for each area, $\nabla\phi(\mathbf{r})$, where $\phi(\mathbf{r})$ is the response phase at cortical position $\mathbf{r}$ (the gradient is the local steepest uphill direction in phase along the cortical surface; local phase gradient vectors are perpendicular to isophase lines). To annotate the map direction of the gradient, we used "lower/horiz/upper" for visual maps, "low f./high f." (frequency) for auditory maps, and "foot/hand/face" for somatosensory maps. To aid interhemispheric comparison, we cropped the two movies and put them side by side (see **Supplementary Video 3**) so that the similarities in areal position, but especially, similarities in gradient direction across hemispheres (after mentally left-right mirror-imaging the gradient vector) were easier to appreciate. Each area is displayed for 1 s to make it easier to page through the atlas. Finally, the parcellation and map data have been displayed more traditionally on rotating folded surfaces (see **Supplementary Video 4**) and inflated surfaces (see **Supplementary Video 5**); the first rotations in each movie show the parcellation and the second, the map data (videos also at https://cogsci.ucsd.edu/~sereno/csurf/fsaverage-labels/CsurfMaps1-atlas-movies/).

Maps/Cognition Overlap

The fraction of the cortex that contains topological maps (here approximately 47%) is larger than has usually been appreciated in the cognitive neuroscience literature. This suggests that areas with maps might be directly involved with many higher level 'cognitive' operations. To directly address the question as to whether areas containing topological maps participate in higher level 'cognitive' processes, we had subjects: (1) imagine navigating (eye closed) through familiar environments contrasted with imagining staying still (Huang and Sereno, 2013), or (2) naturalistically read short paragraphs contrasted with reading (same saccades) over paragraphs of unfamiliar (Hindi) characters (Sood and Sereno, 2016), or (3) have their gaze directed over scenes in a wordless picture story contrasted with the same saccade sequence over scrambled versions of the scenes (Sood and Sereno, 2018). In all three cases, well over half of all the 'higher level' activity (after the 'low level' subtractions) was situated in visual and auditory areas containing topological maps (see also Rauschecker and Scott, 2009). There was less overlap with non-eye movement related somatomotor areas; but perhaps this is not surprising given the general immobility of the body during the three 'cognitive' tasks.

Maps in Action

The conditions under which we mapped topological areas – with unchanging central fixation for visual mapping, with eyes closed in the case of auditory stimuli, and with the great majority of the body virtually immobile for somatomotor mapping, is obviously highly artificial. For one thing, these simple mapping experiments conflate receptotopy and 'attention-o-topy,' which can be distinguished with more elaborate paradigms (e.g., for visual maps see Saygin and Sereno, 2008; for auditory maps see Dick et al., 2017). But in both of these cases (receptotopy and attention-o-topy) the maps are fixed. However, under even moderately more naturalistic conditions, a number of these maps have been shown to be dynamic and moveable.

Shifting Maps

For example, it is known that in area VIP, from both microelectrode experiments as well as fMRI experiments in humans (Avillac et al., 2005; Sereno and Huang, 2006) that the visual maps there are moveable relative to the cortex; the visual map is shifted using information from eye position to align the visual map with the essentially fixed-to-the-cortex somatosensory map of the face and axial body.

Movements of visual maps of a related kind have been found in area LIP (and a number of other parietal areas), where the retinotopic map (and much of its contents) temporarily moves just before a saccade to the position it will be in *after* the saccade (and then snaps back into alignment with the retina immediately after the saccade) using information from the deep superior colliculus about the planned eye movement (Duhamel et al., 1992; Heiser and Colby, 2006). This predictive movement may be preparing the system for how the world will look after the saccade; if nothing changes in the scene during the saccade, there will be no surprise at the new retinotopic map locations of all the stimuli after the saccade. These experiments in the cortex followed up on earlier experiments on double-step saccades in the superior colliculus that showed that the positions of salient targets are updated in retinotopic coordinates after each saccade so that even when a target has become invisible or camouflaged, the system is prepared to be able to make a saccade to its expected location (Mays and Sparks, 1980; Sparks and Hartwich-Young, 1989) by activating the corresponding location in the underlying saccade map in the deep colliculus (see below on the nature of the deeper map).

Auditory (spatial) maps can be shifted, too. As already noted above, experiments in the superior colliculus have shown that intermediate layer auditory spatial maps there, constructed from binaural comparisons, can be moved, despite a fixed head and thus a fixed interaural time delay and interaural amplitude difference, in order to dynamically keep the auditory spatial map in line with the retinotopic map that is being used to calculate which location in the deep colliculus saccade vector map should be activated for each successive saccade (Jay and Sparks, 1984).

Note that this auditory map shifting differs from the kind of map shifting that we previously described in VIP – auditory maps in the intermediate colliculus are moved to keep them in line with a fixed retinotopic map, while in VIP, retinotopic maps are moved to keep them in line with a fixed somatosensory face map. This difference reflects different goals. A major goal of the colliculus is to get the retinotopic *fovea* to a target (whether the target is visual or auditory or somatosensory) using the underlying *retinotopically*-organized saccade vector map; by contrast, a goal of VIP may be to avoid getting hit in the face by an object (or to help the face accurately bite a target), whether the target is somatosensory or visual, and independent of current retinotopic position.

Deep Cross-Modal Map Interactions

Multisensory interactions have often been studied in higher areas near the boundary between modalities, such as area VIP, situated at the border between visual and somatosensory cortex. Nevertheless, map-based multisensory interactions may be more ubiquitous than our simple division of areas into visual, auditory, and somatosensory would seem to imply. By touching one or another finger of a human subject with sand paper in the dark and then comparing somatotopic cortical responses (7T imaging) to responses from a second experiment where the same subjects simply viewed one or another finger of a hand being touched (in a first-person view), it was shown that merely observing touches results in a detectable amount of activity in the corresponding finger representation in primary somatosensory areas 3b and 1 (Kuehn et al., 2018). Remarkably, the visual signal somehow penetrated all the way back to the correct/corresponding finger representation in primary somatosensory cortex; and finger-specific, observation-related activation even generalized to an experiment using a third-person view of observed touch. Finally, there was evidence that the top-down observed-touch signal in areas 3b and 1 elicited activity in different cortical lamina outside those receiving direct ascending input from the ventrobasal nucleus (Kuehn and Sereno, 2018). The pathway by which the visual information got to area 3b and area 1 is currently obscure, but this data suggests that even low level maps can be 'cognitive' – or more precisely, single cortical columns within an area can contain map-coordinate-indexed information from markedly different levels of processing.

Traveling Waves and Bumps Across Maps

By applying the phase-encoded method to a more naturalistic reach-to-eat movement, it was possible to visualize the spatiotemporal unfolding of activity across map-containing areas. The unexpected result was that there was a spatially coherent traveling wave and bump activity that began in early visual areas and then swept over parietal cortex to the hand areas of somatomotor cortex eventually closing in on face somatomotor cortex (Chen et al., 2018). This is strongly reminiscent of similar (though much faster) coherent waves of activity visualized in the barrel cortex of awake rodents during active whisking using voltage sensitive dyes (Moldakarimov et al., 2018; see also Wu et al., 2008, who describe similar waves visualized in slices). This suggests that the numerical dominance of extremely local connections in the cortex illustrated in **Figure 1** together with the presence of topological maps in the cortex more strongly shapes activity during naturalistic actions than is usually appreciated.

Motor Output Maps – Superior Colliculus and Frontal Eye Fields

Perhaps the best characterized motor output map is the retinotopically organized saccade vector map that is constructed in the deeper layers of the superior colliculus. The saccade vector generated by electrical stimulation at different 2D map locations in the deep colliculus results in a saccade appropriate to fixate a stimulus situated in the peripheral location of receptive field in the overlying superficial retinotopic map. The saccade vector is coded by the position of activity in the deep colliculus map, not by the strength of activity (or stimulation intensity) there. By contrast, the final motor output commands in the brainstem take the form of three positive-only Cartesian (lateral, up, and down) coordinates (firing rate variables to drive oculomotor muscles). Both the saccade burst pattern generators [*lateral*: paramedian pontine reticular formation (PPRF), *vertical* (*up, down*): rostral interstitial nucleus of the medial longitudinal fasciculus (riMLF)] as well as the oculomotor efference copy monitoring of eye position [*lateral*: prepositus hypoglossi, *vertical* (*up/down*): interstitial nucleus of Cajal] are coded by firing rate, *not* map position within these nuclei. The conversion from colliculus map position to firing rate is called the "spatio-temporal transformation" in the eye movement literature (with 'temporal' referring to firing rate). A simple way to implement it would be to have deep colliculus neurons from different map locations vary the strength of their connection to the horizontal and vertical (up and down) burst centers (Sereno, 1985; Sereno and Ulinski, 1985).

A similar kind of topological (retinotopic) saccade vector map is implemented in the frontal eye fields. The frontal eye fields have direct access to the horizontal and vertical saccade burst pattern generators in the brain stem (PPRF and riMLF), in parallel with the deep colliculus, and in communication with it.

But in order for efference copy eye position information to be able to shift 2D maps in the colliculus and cortex (as described above), these Cartesian firing-rate coordinates must somehow be converted back into positions within a 2D neural map. This is the much less well-understood "temporo-spatial" transformation. A possible implementation in the colliculus might involve axons from eye position centers synapsing across the colliculus in lines (e.g., see mediolateral-oriented tectal afferent axons from profundus mesencephali: Dacey and Ulinski, 1986b, their Figures 17, 18) contacting tectal cells with local axonal arbors that are systematically offset from the position of their dendritic arbors (e.g., see Dacey and Ulinski, 1986a, their Figures 7–9, 11–13; Sereno, 1985, their Figure 27). This shifting operation has been studied in the most detail in the intermediate and deep layers of the superior colliculus. But it must also be occurring independently in the cortex because brainstem-originating Cartesian eye position signals – that are known to transit through several thalamic nuclei (Tanaka, 2007) on the way to frontal oculomotor regions – have been shown to be critical for shifting retinotopic maps in posterior parietal cortex (LIP) during preemptive retinotopic map updating (Sommer and Wurtz, 2006). Finally, moveable spatial maps at many different levels in the brain must be coordinated; for example, the same eye position signals must somehow get to VIP in order to shift retinotopic maps into alignment with fixed somatotopic maps.

Motor Output Maps – Motor Cortex and Spinal Cord

Experiments in which multiple points were stimulated in the gray matter of the spinal cord in frogs have found that simultaneous stimulation of two sites results in the vector summation of the endpoint forces generated by simulating each site separately (Mussa-Ivaldi et al., 1994). More recently, similar results have been demonstrated in the primate spinal cord (Yaron et al.,

2020). These results are quite reminiscent of what happens upon stimulating two sites in the deep colliculus, or one site in the deep colliculus and one site in the frontal eye fields (Schiller and Sandell, 1983), which both result in an eye movement that is a vector sum of the eye movements elicited by stimulating each site individually. The stability and repeatability of these spinal cord maps (Giszter et al., 2000) suggests that topological motor maps like the one in the deep colliculus may be the rule rather than the exception.

Finally, a series of experiments in which long stimulus trains were used in the motor cortex have suggested that topological maps of movement vectors are present there, too (see Aflalo and Graziano, 2007, for review and Kohonen model; see also Stepniewska et al., 2009, for similar results from stimulating primate posterior parietal cortex). The topological maps of movements in motor cortex are quite different than the patchwork quilt of skin regions described above in somatosensory cortical areas, though there is a rough match between main body part somatotopy in area 4 and that in areas 3a, 3b, and 1. In particular, these stimulation studies have found maps of nearby limb endpoints in particular regions of extrapersonal space. There are also different subregions that elicit different classes of ethologically relevant movements (e.g., acquisitive hand-to-mouth movements *versus* a defensive arm and hand movements). Because motor cortex controls a wider range of movements than the deep colliculus, it may consist of a patchwork quilt of multiple 2D vector maps. These results are broadly consistent with our finding of traveling waves and traveling bumps observed also in parietal and motor cortex in the phase-encoded reach-to-eat experiment (Chen et al., 2018).

CONCLUSION AND SPECULATION

The evidence presented above has concentrated on the half of the cortex that we have shown contains relatively straightforward visual, auditory, somatosensory, and motor maps. So what's going on in the other half of cortex? Does it work entirely differently from the topologically mapped parts? We have seen that the strongly local connectivity found in areas with sensorimotor maps is also found in cortical areas without obvious maps. In early areas, there is no question that the exact spatial shape of an activation pattern across the cortex – e.g., activity due to a particular individual's face – is crucial to recognition of that individual. A natural extension of this idea is that some of the apparently non-mapped regions may support moving, spatially localized disturbances with specific shapes similar to what regularly occurs in areas with maps, but detached from any fixed sensory map. We start by first drawing out the implications of the moveable maps reviewed above.

A number of the maps described were moveable, for example, as a mechanism of keeping maps from different modalities in register as the eyes move around relative to the head, body, and limbs. Map shifting has mostly been demonstrated to occur in areas that are several synapses beyond primary sensory areas (or in the case of the colliculus, in 'higher level' collicular layers that are anatomically below the direct retinal-recipient layers). Of course, in our phase-encoded mapping experiments, we were doing our best to *prevent* map shifting in order to be able to measure the coordinates of the maps under 'neutral' conditions (e.g., straight ahead gaze). Given how boring and long-drawn-out phase-encoded mapping paradigms are, it is possible that the apparently more 'messy' maps in **Figure 6** in some of the higher areas could partly reflect poorer experimental control of map shifting in those areas.

It has generally been assumed that map shifting takes place within the bounds of a single cortical or subcortical area. In several cases, however, it is obvious that activity in maps can be shifted longer distances, namely, to the other hemisphere or other colliculus. For example, a brief target presented to the near right hemifield with central fixation will cause activity in the left colliculus. Before the eyes can move to it, a location in the left colliculus that causes a saccade to the far right hemifield is electrically stimulated. By using eye position information generated by electrical-stimulation-induced saccade, it is known that the original target will be shifted into the opposite colliculus from the one that originally viewed the target in order to generate the appropriate corrective saccade (Sparks, 1986). A similar target transfer to the opposite hemisphere has been demonstrated to occur in human LIP (Merriam et al., 2003), and can even occur when callosal connections have been severed (Berman et al., 2007).

Now re-consider the visualization of spatiotemporal activity during a naturalistic reach-to-eat task described above (Chen et al., 2018), which showed coherent traveling waves of activity sweeping across multiple topological maps, several of which have been demonstrated to be capable of map shifting. Given that the strong local connectivity present in the half of the cortex that contains maps is *also* present in the remaining half of the cortex without obvious sensory maps, this suggests an intriguing picture where spatially coherent activity might be able to 'escape' from sensorimotor maps and be injected into surrounding cortical areas that lack fixed maps. Since this activity would be even less tied to specific cortical locations than, say, visual activity in VIP that is being shifted around *within* VIP by eye position, it would be more difficult to visualize and average using standard low temporal resolution fMRI methods; however, it might be detectable with dense electrode arrays, dynamic optical imaging, or time-resolved echo-planar MRI (e.g., Wang et al., 2021).

But why might we want some soliton-like waves or localized attractor bumps (Wilson and Cowan, 1972; Zhang, 1996; Samsonovich and McNaughton, 1997; Baker and Cruz, 2021) to 'escape?' If we consider the computational problem of scene comprehension, it fundamentally involves a serial assembly process whereby information about different objects, actors, affordances, paths, and locations is built up over time for the purpose of controlling behavior. One can view other characteristically human cognitive operations such as language comprehension in a similar way – as code-directed serial assembly of fictive scenes (Sereno, 1991, 2014; Sood and Sereno, 2018). In both cases, there is the need to load chunks of isolated content – in the case of a scene, a glance at another monkey, at a branch, at a leaf, or in the case of language, a string of isolated word meanings – into working memory to allow these chunks to interact with each other. This process is often visualized as a buildup of persisting, spatially distributed activity.

Instead, we might think of each glance or word as initiating a localized cortical disturbance that 'escapes' into non-sensorimotor mapped cortex, and which can then be attached to other localized disturbances there to create a temporary, spatially extended 'molecular' pattern that is capable of propagating across parts of the cortical sheet while retaining its spatial topological structure. This initially might seem a strange picture; but it would not be out of place with the picture of spatially coherent, soliton-like traveling waves and bumps that we observed in during the reach-to-eat task, and with the partial overlap between cortex with maps and cortex involving in language and scene integration in temporal, parietal, and frontal cortex (Huang and Sereno, 2013; Sood and Sereno, 2016, 2018; Popham et al., 2021; Groen et al., 2022).

In the end, the goal would be to eventually inject some of that 'escaped' activity back into motor maps at various levels in order to manipulate arrays of muscles, or in the case of eye movements, to manipulate activity in the saccade vector map in the frontal eye fields and the deep layers of the superior colliculus, both of which require spatially localized bump shifting. Given the precedent of targets being able to be shifted into the opposite hemisphere, it might be possible to inject part of a temporarily 'escaped' pattern back into a spatially distant area in the cortex via corticocortical, cortico-thalamo-cortical, or other subcortical loop back connections. Earlier sensory maps represent objects and actions by the shape and movement of activation patterns there; rather than 'maps all the way up,' perhaps it's 'moving shapes all the way up.'

Existing theories of traveling waves or bumps typically start with a sheet with local excitation and slightly less local inhibition [both typically circularly symmetric and arranged similarly across the sheet (Wilson and Cowan, 1972; Zhang, 1996)]. With some form of input/output non-monotonicity (e.g., rapid habituation), traveling waves (rather than merely static bumps) can emerge. An early locally connected 'neural network' (cellular automaton) with a non-monotonic update rule is Conway's Game of Life (too few neighbors → die, enough → birth/persist, too many → die). This simple architecture can nevertheless support myriad complex, composite propagating patterns of arbitrary sizes[5] ("gliders," "spaceships"). The idea above of building up moveable 'molecular' patterns that contain multiple localized attractor-like bumps that are temporarily bonded together is no more (or less) than an idea for a new theory of cortical computation. It goes beyond existing well-worked out theoretical frameworks, but it is a natural extension of how object shape, articulation, and actions are represented across early sensory and motor maps.

DATA AVAILABILITY STATEMENT

The datasets presented in this study can be found in online repositories here: https://cogsci.ucsd.edu/~sereno/csurf/fsaverage-labels and https://mri.sdsu.edu/sereno/csurf/fsaverage-labels.

[5] http://conwaylife.com

ETHICS STATEMENT

The studies involving human participants were reviewed and approved by UCSD Human Subject Committee, University College London Ethics Committee. The patients/participants provided their written informed consent to participate in this study. The animal study was reviewed and approved by Caltech Institutional Review Board.

AUTHOR CONTRIBUTIONS

MIS conceived of the study, wrote the software, analyzed the data, made illustrations, and wrote the manuscript. MRS conceived of the study, collected data, wrote the software, and analyzed the data. R-SH conceived of the study, constructed stimulus devices, wrote the software, collected the data, and analyzed the data. All authors contributed to the article and approved the submitted version.

FUNDING

This research was supported by NIH MH47035 (microelectrode retinotopic mapping); NSF BCS 0224321 (fMRI visual mapping); NIH Grant R01 MH081990 (fMRI multisensory mapping); and UK Royal Society Wolfson Fellowship (fMRI auditory mapping, theory). An earlier version was presented as a keynote lecture at Human Brain Mapping 2013.

SUPPLEMENTARY MATERIAL

The Supplementary Material for this article can be found online at: https://www.frontiersin.org/articles/10.3389/fnsys.2022.787737/full#supplementary-material

Supplementary Video 1 | The visual, auditory, and somatomotor maps in each of the 117 individual cortical areas in the parcellation are shown for 1 s each on the flattened left hemisphere of the FreeSurfer average subject, fsaverage. Major sulci are annotated at the beginning, and all areal borders are indicated by cyan dots. White arrows indicate the average gradient of the map coordinate for each area ("lower/horiz/upper" for visual maps, "low f./high f." for auditory maps, and "foot/hand/face" for somatosensory maps). The color scale for the map data is: green for lower visual field, low frequency, or leg/foot; blue for horizontal meridian, mid frequency, or arm/hand, and red for upper field, high frequency, or face.

Supplementary Video 2 | The visual, auditory, and somatomotor maps in each of the 117 individual cortical areas in the parcellation are shown on the flattened right hemisphere, using the same annotations and color scales as the left hemisphere (**Supplementary Video 1**).

Supplementary Video 3 | The first two videos (**Supplementary Videos 1, 2**) have been cropped and juxtaposed so that similarities in areal position and gradient direction across the two hemispheres are easier to appreciate (after mentally left-right mirror-imaging them across a vertical axis).

Supplementary Video 4 | The parcellation and map data are more conventionally displayed on the rotating folded surfaces of the left and right hemisphere of the

FreeSurfer average subject, fsaverage (surface: white). The first rotation around a vertical axis shows the parcellation, and the second rotation shows the topological map data. After each vertical-axis rotation, the brain is rotated around a horizontal axis to expose superior and then inferior areas. The color scale for the map data is the same as in **Figure 6** and **Supplementary Video 1**.

Supplementary Video 5 | The parcellation and map data from **Supplementary Video 4** are displayed on the rotating inflated surfaces of the left and right hemisphere of FreeSurfer average subject, fsaverage (surface: inflated_avg) in the same order, using the same color scales, and at the same magnification as in **Supplementary Video 4**.

REFERENCES

Aflalo, T. N., and Graziano, M. S. A. (2007). Possible origins of the complex topographic organization of motor cortex: reduction of a multidimensional space onto a two-dimensional array. *J. Neurosci.* 26, 6288–6297.

Albright, T. D. (1984). Direction and orientation selectivity of neurons in visual area MT of the macaque. *J. Neurophysiol.* 52, 1106–1130. doi: 10.1152/jn.1984.52.6.1106

Allman, J. M., and Kaas, J. H. (1975). The dorsomedial cortical visual area: a third tier area in the occipital lobe of the owl monkey (*Aotus trivirgatus*). *Brain Res.* 100, 473–487. doi: 10.1016/0006-8993(75)90153-5

Amano, K., Wandell, B. A., and Dumoulin, S. O. (2009). Visual field maps, population receptive field sizes, and visual field coverage in the human MT+ complex. *J. Neurophysiol.* 102, 2704–2718. doi: 10.1152/jn.00102.2009

Angelucci, A., and Rosa, M. G. P. (2015). Resolving the organization of the third tier visual cortex in primates: a hypothesis-based approach. *Vis. Neurosci.* 32:E010. doi: 10.1017/S0952523815000073

Ashmore, J. (2008). Cochlear outer hair cell motility. *Physiol. Rev.* 88, 173–210. doi: 10.1152/physrev.00044.2006

Avillac, M., Deneve, S., Olivier, E., Pouget, A., and Duhamel, J. R. (2005). Reference frames for representing visual and tactile locations in parietal cortex. *Nat. Neurosci.* 8, 941–949. doi: 10.1038/nn1480

Baker, V., and Cruz, L. (2021). Traveling waves in quasi-one-dimensional neuronal minicolumns. *Neural Comput.* 34, 78–103. doi: 10.1162/neco_a_01451

Berman, R. A., Heiser, L. M., Dunn, C. A., Saunders, R. C., and Colby, C. L. (2007). Dynamic circuitry for updating spatial representation. III. From neurons to behavior. *J. Neurophysiol.* 98, 105–121. doi: 10.1152/jn.00330.2007

Born, R. T., and Tootell, R. B. H. (1992). Segregation of global and local motion processing in primate middle temporal visual area. *Nature* 357, 497–499. doi: 10.1038/357497a0

Brodmann, K. (1909). *Vergleichende Lokalisationslehre Der Großhirnrinde In Ihren Prinzipien Dargestellt Auf Grund Des Zellenbaues*. Leipzig: Verlag von Johann Ambrosius Barth.

Campbell, A. W. (1905). *Histological Studies on the Localisation of Cerebral Function*. Cambridge: Cambridge University Press.

Carey, D., Krishnan, S., Callaghan, M. F., Sereno, M. I., and Dick, F. (2017). Functional and quantitative MRI mapping of somatomotor representations of human supralaryngeal vocal tract. *Cereb. Cortex* 27, 265–278. doi: 10.1093/cercor/bhw393

Carreira-Perpin, M. A., and Goodhill, G. J. (2004). Influence of lateral connections on the structure of cortical maps. *J. Neurophysiol.* 92, 2947–2959. doi: 10.1152/jn.00281.2004

Caspers, S., Eickhoff, S. B., Geyer, S., Scheperjans, F., Mohlberg, H., Zilles, K., et al. (2008). The human inferior parietal lobule in stereotaxic space. *Brain Struct. Funct.* 212, 481–495. doi: 10.1007/s00429-008-0195-z

Chen, C.-F., Kreutz-Delgado, K., Sereno, M. I., and Huang, R.-S. (2018). Unraveling the spatiotemporal brain dynamics during a simulated reach-to-eat task. *Neuroimage* 185, 58–71. doi: 10.1016/j.neuroimage.2018.10.028

Cooke, D. F., and Graziano, M. S. A. (2004). Sensorimotor integration in the precentral gyrus: polysensory neurons and defensive movements. *J. Neurophysiol.* 91, 1648–1660. doi: 10.1152/jn.00955.2003

Dacey, D. M., and Ulinski, P. S. (1986b). Optic tectum of the eastern garter snake, thamnophis sirtalis. v. morphology of brainstem afferents and general discussion. *J. Comp. Neurol.* 245, 423–453. doi: 10.1002/cne.902450402

Dacey, D. M., and Ulinski, P. S. (1986a). Optic tectum of the eastern garter snake, *Thamnophis sirtalis*. III. Morophology of intrinsic neurons. *J. Comp. Neurol.* 245, 283–300. doi: 10.1002/cne.902450302

Dale, A. M., and Sereno, M. I. (1993). Improved localization of cortical activity by combining EEG and MEG with MRI cortical surface reconstruction: a linear approach. *J. Cogn. Neurosci.* 5, 162–176. doi: 10.1162/jocn.1993.5.2.162

Dale, A. M., Fischl, B., and Sereno, M. I. (1999). Cortical surface-based analysis I: segmentation and surface reconstruction. *NeuroImage* 9, 179–194. doi: 10.1006/nimg.1998.0395

Dick, F., Lehet, M., Callaghan, M. F., Keller, T., Sereno, M. I., and Holt, L. (2017). Extensive tonotopic mapping across auditory cortex is recapitulated by spectrally-directed attention and systematically related to cortical myeloarchitecture. *J. Neurosci.* 37, 12187–12201. doi: 10.1523/JNEUROSCI.1436-17.2017

Dick, F., Tierney, A. T., Lutti, A., Josephs, O., Sereno, M. I., and Weiskopf, N. (2012). In vivo functional and myeloarchitectonic mapping of human primary auditory areas. *J. Neurosci.* 32, 16095–16105. doi: 10.1523/jneurosci.1712-12.2012

Ding, S.-L., Royall, J. J., Sunkin, S. M., Ng, L., Facer, B. A. C., Lesnar, P., et al. (2016). Comprehensive cellular-resolution atlas of the adult human brain. *J. Comp. Neurol.* 524, 3127–3481.

Diogo, A. C. M., Lima, B., Soares, J. G. M., and Gattass, R. (2020). Tangential distributin of cell type and reiction selectiviy in monkey area MT. *An. Acad. Bras. Cienc.* 92:e20190564. doi: 10.1590/0001-3765202020190564

Duhamel, J. R., Colby, C. L., and Goldberg, M. E. (1992). The updating of the representation of visual space in parietal cortex by intended eye movements. *Science* 255, 90–92. doi: 10.1126/science.1553535

Engel, S. A., Rumelhart, D. E., Wandell, B. A., Lee, A. T., Glover, G. H., Chichilnisky, E.-J., et al. (1994). fMRI of human visual cortex. *Nature* 369:525.

Felleman, D. J., and Van Essen, D. C. (1991). Distributed hierarchical processing in the primate cerebral cortex. *Cereb. Cortex* 1, 1–47. doi: 10.1093/cercor/1.1.1-a

Filimon, F., Nelson, J., Huang, R.-S., and Sereno, M. I. (2009). Multiple parietal reach regions in humans: cortical representations for visual and proprioceptive feedback during online reaching. *J. Neurosci.* 29, 2961–2971. doi: 10.1523/JNEUROSCI.3211-08.2009

Fischl, B., and Sereno, M. I. (2018). Microstructural parcellation of the human brain. *Neuroimage* 182, 219–231. doi: 10.1016/j.neuroimage.2018.01.036

Fischl, B., Sereno, M. I., Tootell, R. B. H., and Dale, A. M. (1999a). High-resolution inter-subject averaging and a coordinate system for the cortical surface. *Hum. Brain Mapping* 8, 272–284. doi: 10.1002/(sici)1097-0193(1999)8:4<272::aid-hbm10>3.0.co;2-4

Fischl, B., Sereno, M. I., and Dale, A. M. (1999b). Cortical surface-based analysis II: inflation, flattening, and a surface-based coordinate system. *NeuroImage* 9, 195–207. doi: 10.1006/nimg.1998.0396

Frank, S. M., and Greenlee, M. W. (2018). The parieto-insular vestibular cortex in humans: more than a single area? *J. Neurophysiol.* 120, 1438–1450. doi: 10.1152/jn.00907.2017

Fritsch, G., and Hitzig, E. (1870). Über die elektrische Erregbarkeit des Grosshirns [On the electrical excitability of the cerebrum]. *Arch. Anat. Physiol. Wiss. Med.* 37, 300–332. doi: 10.1007/bf01759916

Fukushima, K. (1980). Neocognitron: a self-organizing neural network model for a mechanism of pattern recognition unaffected by shift in position. *Biol. Cybern.* 36, 193–202. doi: 10.1007/bf00344251

Ganepola, T., Lee, Y., Alexander, D. C., Sereno, M. I., and Nagy, Z. (2021). Multiple b-values improve discrimination of cortical gray matter regions using diffusion MRI: an experimental validation with a data-driven approach Magnetic Resonance Materials in Physics. *Biol. Med.* 34, 677–687. doi: 10.1007/s10334-021-00914-3

Ganepola, T., Nagy, Z. N., Ghosh, A., Papadopoulo, T., Alexander, D. C., and Sereno, M. I. (2018). Using diffusion MRI to discriminate areas of cortical grey matter. *Neuroimage* 182, 456–468. doi: 10.1016/j.neuroimage.2017.12.046

Garrett, M. E., Nauhaus, I., Marshel, J. H., and Callaway, E. M. (2014). Topography and areal organization of mouse visual cortex. *J. Neurosci.* 34, 12587–12600. doi: 10.1523/JNEUROSCI.1124-14.2014

Gattass, R., Sousa, A. P. B., and Gross, C. G. (1988). Visuotopic organization and extent of V3 and V4 of the macaque. *J. Neurosci.* 8, 1831–1845. doi: 10.1523/JNEUROSCI.08-06-01831.1988

Giszter, S. F., Loeb, E., Mussa-Ivaldi, F .A., and Bizzi, E. (2000). Repeatable spatial maps of a few force and joint torque patterns elicited by microstimulation applied throughout the lumbar spinal cord of the spinal frog. *Hum. Mov. Sci.* 19, 597–626. doi: 10.1016/S0167-9457(00)00029-4

Glasser, M. F., Coalson, T. S., Robinson, E. C., Hacker, C. D., Harwell, J., Yacoub, E., et al. (2016). A multi-modal parcellation of human cerebral cortex. *Nature* 536, 171–178. doi: 10.1038/nature18933

Groen, I. I. A., Dekker, T. M., Knapen, T., and Silson, E. H. (2022). Visuospatial coding as ubiquitous scaffolding for human cognition. *Trends Cogn. Sci.* 26, 81–96. doi: 10.1016/j.tics.2021.10.011

Hagler, D. J. Jr., Riecke, L., and Sereno, M. I. (2007). Pointing and saccades rely on common parietal and superior frontal visuospatial maps. *Neuroimage* 35, 1562–1577. doi: 10.1016/j.neuroimage.2007.01.033

Haynes, W. I. A., and Haber, S. N. (2013). The organization of prefrontal-subthalamic inputs in primates provides an anatomical substrate for both functional specificity and integration: implications for basal ganglia models and deep brain stimulation. *J. Neurosci.* 33, 4804–4814. doi: 10.1523/JNEUROSCI.4674-12.2013

Heiser, L. M., and Colby, C. L. (2006). Spatial updating in area LIP Is independent of saccade direction. *J. Neurophysiol.* 95, 2751–2767. doi: 10.1152/jn.00054.2005

Huang, R.-S., and Sereno, M. I. (2013). Bottom-up retinotopic organization supports top-down mental imagery. *Open Neuroimaging J.* 7, 58–67. doi: 10.2174/1874440001307010058

Huang, R.-S., and Sereno, M. I. (2018). "Chapter 7. multisensory and sensorimotor maps. in: the parietal lobe," in *Neurological and Neuropsychological Deficits (Handbook of Clinical Neurology)*, 3rd Edn, Vol. 151, eds G. Vallar and H. B. Coslett (Amsterdam: Elsevier), 141–161. doi: 10.1016/b978-0-444-63622-5.00007-3

Huang, R.-S., Chen, C.-F., and Sereno, M. I. (2017). Mapping the complex topological organization of the human parietal face area. *Neuroimage* 163, 459–470. doi: 10.1016/j.neuroimage.2017.09.004

Huang, R.-S., Chen, C.-F., Tran, A. T., Holstein, K. L., and Sereno, M. I. (2012). Mapping multisensory parietal face and body areas in humans. *Proc. Natl. Acad. Sci. U.S.A.* 109, 18114–18119. doi: 10.1073/pnas.1207946109

Janssens, T., Zhu, Q., Popivanov, I. D., and Vanduffel, W. (2014). Probabilistic and single-subject retinotopic maps reveal the topographic organization of face patches in the macaque cortex. *J. Neurosci.* 34, 10156–10167. doi: 10.1523/jneurosci.2914-13.2013

Jay, M., and Sparks, D. L. (1984). Auditory receptive fields in primate superior colliculus shift with changes in eye position. *Nature* 309, 345–347. doi: 10.1038/309345a0

Job, A., Paucod, J.-C., O'Beirne, G. A., and Delon-Martin, C. (2011). Cortical representation of tympanic membrane movements due to pressure variation: an fMRI study. *Hum. Brain Mapping* 32, 744–749. doi: 10.1002/hbm.21063

Jones, E. G., and Burton, H. (1976). Areal differences in the laminar distribution of thalamic afferents in cortical fields of the insular, parietal and temporal regions of primates. *J. Comp. Neurol.* 168, 197–247. doi: 10.1002/cne.901680203

Kaas, J. H., and Hackett, T. A. (2000). Subdivisions of auditory cortex and processing streams in primates. *Proc. Natl. Acad. Sci. U.S.A.* 97, 11793–11799. doi: 10.1073/pnas.97.22.11793

Knight, P. L. (1977). Representation of the cochlea with the anterior auditory field (AAF) of the cat. *Brain Res.* 130, 447–467.

Knop, A. J. J., Spengler, S., Bogler, C., Forster, C., Brecht, M., Haynes, J.-D., et al. (2021). Sensory-tactile functional mapping and use-associated structural variation of the human female genital representation field. *J. Neurosci.* 42, 1131–1140. doi: 10.1523/JNEUROSCI.1081-21.2021

Kohonen, T. (1982). Self-organized formation of topologically correct feature maps. *Biol. Cybern.* 43, 59–69. doi: 10.1007/bf00337288

Kolster, H., Janssens, T., Orban, G. A., and Vanduffel, W. (2014). The retinotopic organization of macaque occipitotemporal cortex anterior to V4 and caudoventral to the middle temporal (MT) cluster. *J. Neurosci.* 34, 10168–10191. doi: 10.1523/JNEUROSCI.3288-13.2014

Kolster, H., Peeters, R., and Orban, G. A. (2010). The retinotopic organization of the human middle temporal area MT/V5 and its cortical neighbors. *J. Neurosci.* 30, 9801–9820. doi: 10.1523/JNEUROSCI.2069-10.2010

Konishi, M., Takahashi, T. T., Wagner, H., Sullivan, W. E., and Carr, C. E. (1988). "Neurophysiological and anatomical substrates of sound localization in the the owl," in *Auditory Function: Neurobiological Bases of Hearing*, eds G. M. Edelman, W. E. Gall, and W. M. Cowan (Hoboken NJ: John Wiley and Sons), 721–745.

Krubitzer, L., Clarey, J., Tweedale, R., Elston, G., and Calford, M. (1995). A redefinition of somatosensory areas in the lateral sulcus of macaque monkeys. *J. Neurosci.* 15, 3821–3839. doi: 10.1523/JNEUROSCI.15-05-03821.1995

Kuehn, E., and Sereno, M. I. (2018). Modeling the human cortex in three dimensions. *Trends Cogn. Sci.* 22, 1073–1075. doi: 10.1016/j.tics.2018.08.010

Kuehn, E., Dinse, J., Jakobsen, E., Long, X., Schafer, A., Bazin, P.-L., et al. (2017). Body topography parcellates human sensory and motor cortex. *Cereb. Cortex* 27, 3790–3805. doi: 10.1093/cercor/bhx026

Kuehn, E., Haggard, P., Villringer, A., Pleger, B., and Sereno, M. I. (2018). Visually-driven maps in area 3b. *J. Neurosci.* 38, 1295–1310. doi: 10.1523/JNEUROSCI.0491-17.2017

Kusmierek, P., and Rauschecker, J. P. (2009). Functional specialization of medial auditory belt cortex in alert Rhesus monkey. *J. Neurophysiol.* 102, 1606–1622. doi: 10.1152/jn.00167.2009

Larsson, J., and Heeger, D. J. (2006). Two retinotopic visual areas in human lateral occipital cortex. *J. Neurosci.* 26, 13128–13142. doi: 10.1523/JNEUROSCI.1657-06.2006

Leaver, A. M., and Rauschecker, J. P. (2016). Functional topography of human auditory cortex. *J. Neurosci.* 36, 1416–1428. doi: 10.1523/JNEUROSCI.0226-15.2016

LeCun, Y., Bengio, Y., and Hinton, G. (2015). Deep learning. *Nature* 521, 436–444.

Lim, H., Wang, Y., Xiao, Y., and Felleman, D. J. (2009). Organization of hue selectivity in macaque V2 thin stripes. *J. Neurophysiol.* 102, 2603–2615. doi: 10.1152/jn.91255.2008

Linsker, R. (1986). From basic network principles to neural architecture: Emergence of orientation-selective cells. *Proc. Natl. Acad. Sci. U.S.A.* 83, 8390–8394. doi: 10.1073/pnas.83.21.8390

Lund, J. S., Yoshioka, T., and Levitt, J. B. (1993). Comparison of intrinsic connectivity in different areas of macaque monkey cerebral cortex. *Cereb. Cortex* 3, 148–162. doi: 10.1093/cercor/3.2.148

Mays, L. E., and Sparks, D. L. (1980). Dissociation of visual and saccade-related responses in superior colliculus neurons. *J. Neurophysiol.* 43, 207–232. doi: 10.1152/jn.1980.43.1.207

McClelland, J. L., and Rumelhard, D. E. (1986). *Parallel Distributed Processing: Psychological And Biological Models*. Cambridge: MIT Press.

McKay, L. C., Evans, K. C., Frackowiak, R. S. J., and Corfield, D. R. (2003). Neural correlates of voluntary breathing in humans. *J. Applied Physiol.* 95, 1170–1178 doi: 10.1152/japplphysiol.00641.2002

Meier, J. D., Aflalo, T. N., Kastner, S., and Graziano, M. S. A. (2008). Complex organization of human primary motor cortex: a high-resolution fMRI study. *J. Neurophsyiol.* 100, 1800–1812. doi: 10.1152/jn.90531.2008

Merriam, E. P., Genovese, C. R., and Colby, C. L. (2003). Spatial updating in human parietal cortex. *Neuron* 39, 361–373. doi: 10.1016/s0896-6273(03)00393-3

Merzenich, M. M., Kaas, J. H., Sur, M., and Lin, C.-S. (1978). Double representation of the body surface within architectonic areas 3b and 1 in "SI" in the owl monkey (*Aotus trivirgatus*). *J. Comp. Neurol.* 181, 41–74. doi: 10.1002/cne.901810104

Moerel, M., De Martino, F., and Formisano, E. (2014). An anatomical and functional topography of human auditory cortical areas. *Front. Neurosci.* 8:225. doi: 10.3389/fnins.2014.00225

Moldakarimov, S., Bazhenov, M., Feldman, D. E., and Sejnowski, T. J. (2018). Structured networks support sparse traveling waves in rodent somatosensory cortex. *Proc. Natl. Acad. Sci. U.S.A.* 115, 5277–5282. doi: 10.1073/pnas.1710202115

Mussa-Ivaldi, F. A., Giszter, S. F., and Bizzi, E. (1994). Linear combinations of primitives in vertebrate motor control. *Proc. Natl. Acad. Sci. U.S.A.* 91, 7534–7538. doi: 10.1073/pnas.91.16.7534

Nagy, Z., Alexander, D. C., Thomas, D. L., Weiskopf, N., and Sereno, M. I. (2013). Using high angular resolution diffusion imaging data to discriminate cortical regions. *PLoS One* 8:e63842. doi: 10.1371/journal.pone.0063842

Nakashima, A., Ihara, N., Ikegaya, Y., and Takeuchi, H. (2021). Cell type-specific patterned neural activity instructs neural map formation in the mouse olfactory system. *Neurosci. Res.* 170, 1–5. doi: 10.1016/j.neures.2020.06.007

Padberg, J., Franca, J. G., Cooke, D. F., Soares, J. G. M., Rosa, M. G. P., Fiorani, M. Jr., et al. (2007). Parallel evolution of cortical areas involved in skilled hand use. *J. Neurosci.* 27, 10106–10115. doi: 10.1523/JNEUROSCI.2632-07.2007

Pandya, D. N., and Sanides, F. (1973). Architectonic parcellation of the temporal operculum in rhesus monkey and its projection pattern. *Z. Anat. Entwicklungsgesch.* 139, 127–161. doi: 10.1007/BF00523634

Parent, A., and Hazrati, L.-N. (1994). Multiple striatal representation in primate substantia nigra. *J. Comp. Neurol.* 334, 305–320. doi: 10.1002/cne.903440211

Pitzalis, S., Sereno, M. I., Committeri, G., Fattori, P., Galati, G., Patria, F., et al. (2010). Human V6: the medial motion area. *Cereb. Cortex* 20, 411–424. doi: 10.1093/cercor/bhp112

Popham, S. F., Huth, A. G., Bilenko, N. Y., Deniz, F., Gao, J. S., Nunez-Elizalde, A. O., et al. (2021). Visual and linguistic semantic representations are aligned at the border of human visual cortex. *Nat. Neurosci.* 24, 1628–1636. doi: 10.1038/s41593-021-00921-6

Press, W. A., Brewer, A. A., Dougherty, R. F., Wade, A. R., and Wandell, B. A. (2001). Visual areas and spatial summation in human visual cortex. *Vis. Res.* 41, 1321–1332. doi: 10.1016/s0042-6989(01)00074-8

Pylyshyn, Z. (1984). *Computation and Cognition*. Cambridge, MA: MIT Press.

Rauschecker, J. P. (2011). An expanded role for the dorsal auditory pathway in sensorimotor control and integration. *Hear. Res.* 271, 16–25. doi: 10.1016/j.heares.2010.09.001

Rauschecker, J. P. (2018). Where, when, and how: are they all sensorimotor? Towards a unified view of the dorsal pathway in vision and audition. *Cortex* 98, 262–268. doi: 10.1016/j.cortex.2017.10.020

Rauschecker, J. P., and Scott, S. K. (2009). Maps and streams in the auditory cortex: nonhuman primates illuminate human speech processing. *Nat. Neurosci.* 12, 718–724. doi: 10.1038/nn.2331

Rauschecker, J. P., Tian, B., and Hauser, M. (1995). Processing of complex sounds in the macaque nonprimary auditory cortex. *Science* 268, 111–114. doi: 10.1126/science.7701330

Samsonovich, A., and McNaughton, B. L. (1997). Path integration and cognitive mapping in a continuous attractor neural network model. *J. Neurosci.* 17, 5900–5920. doi: 10.1523/JNEUROSCI.17-15-05900.1997

Saygin, A. P., and Sereno, M. I. (2008). Retinotopy and attention in human occipital, temporal, parietal, and frontal cortex. *Cereb. Cortex* 18, 2158–2168. doi: 10.1093/cercor/bhm242

Schiller, P. H., and Sandell, J. H. (1983). Interactions between visually and electrically elicited saccades before and after superior colliculus and frontal eye field ablations in the rhesus monkey. *Exp. Brain Res.* 49, 381–392. doi: 10.1007/BF00238780

Schoenfeld, T. A., Marchand, J. E., and Macrides, F. (1985). Topographic organization of tufted cell axonal projections in the hamster main olfactory bulb: an intrabulbar associational aystem. *J. Comp. Neurol.* 235, 503–518. doi: 10.1002/cne.902350408

Seelke, A. M. H., Padberg, J. J., Disbrow, E., Purnell, S. M., Recanzone, G., and Krubitzer, L. (2011). Topographic maps within Brodmann's area 5 of macaque monkeys. *Cereb. Cortex* 22, 1834–1850. doi: 10.1093/cercor/bhr257

Sereno, M. I. (1985). Tectoreticular pathways in the turtle, *Pseudemys scripta*. I. Morphology of tectoreticular axons. *J. Comp. Neurol.* 233, 48–90. doi: 10.1002/cne.902330105

Sereno, M. I. (1991). Four analogies between biological and cultural/linguistic evolution. *J. Theor. Biol.* 151, 467–507. doi: 10.1016/s0022-5193(05)80366-2

Sereno, M. I. (2005). Plasticity and its limits. *Nature* 435, 288–289. doi: 10.1038/435288a

Sereno, M. I. (2014). Origin of symbol-using systems: speech, but not sign, without the semantic urge. *Philos. Trans. R. Soc. B* 369:20130303. doi: 10.1098/rstb.2013.0303

Sereno, M. I., and Allman, J. M. (1991). "Cortical visual areas in mammals," in *The Neural Basis of Visual Function, Vol 4, Vision and Visual Dysfunction*, eds A. Leventhal and J. Cronly-Dillon (London: Macmillan), 160–172.

Sereno, M. I., and Huang, R.-S. (2006). A human parietal face area contains aligned head-centered visual and tactile maps. *Nat. Neurosci.* 9, 1337–1343. doi: 10.1038/nn1777

Sereno, M. I., and Sereno, M. E. (1991). "Learning to see rotation and dilation with a Hebb rule," in *Advances in Neural Information Processing Systems 3*, eds R. P. Lippmann, J. E. Moody, and D. S. Touretzky (Burlington MA: Morgan Kaufmann Publishers), 320–326.

Sereno, M. I., and Ulinski, P. S. (1985). Tectoreticular pathways in the turtle, *Pseudemys scripta*. II. Morphology of tectoreticular cells. *J. Comp. Neurol.* 233, 91–114. doi: 10.1002/cne.902330106

Sereno, M. I., Dale, A. M., Reppas, J. B., Kwong, K. K., Belliveau, J. W., Brady, T. J., et al. (1995). Borders of multiple visual areas in human revealed by functional magnetic resonance imaging. *Science* 268, 889–893. doi: 10.1126/science.7754376

Sereno, M. I., Diedrichsen, J., Tachrount, M., Testa-Silva, G., d'Arceuil, H., and De Zeeuw, C. (2020). The human cerebellum has almost 80% of the surface area of the neocortex. *Proc. Natl. Acad. Sci. U.S.A.* 117, 19538–19543. doi: 10.1073/pnas.2002896117

Sereno, M. I., Lutti, A., Weiskopf, N., and Dick, F. (2012). Mapping the human cortical surface by combining quantitative T1 with retinotopy. *Cereb. Cortex* 23, 2261–2268. doi: 10.1093/cercor/bhs213

Sereno, M. I., McDonald, C. T., and Allman, J. M. (1994). Analysis of retinotopic maps in extrastriate cortex. *Cereb. Cortex* 4, 601–620. doi: 10.1093/cercor/4.6.601

Sereno, M. I., McDonald, C. T., and Allman, J. M. (2015). Retinotopic organization of extrastriate cortex in the owl monkey – dorsal and lateral areas. *Vis. Neurosci.* 32:E021. doi: 10.1017/S0952523815000206

Sereno, M. I., Pitzalis, S., and Martinez, A. (2001). Mapping of contralateral space in retinotopic coordinates by a parietal cortical area in humans. *Science* 294, 1350–1354. doi: 10.1126/science.1063695

Serra, C., Galletti, C., Di Marco, S., Fattori, P., Galati, G., Sulpizio, V., et al. (2019). Egomotion-related visual areas respond to active leg movements. *Hum. Brain Mapping* 40, 3174–3191. doi: 10.1002/hbm.24589

Shambes, G. M., Gibson, J. M., and Welker, W. (1978). Fractured somatotopy in granule cell tactile areas of rat cerebellar hemispheres revealed by micromapping. *Brain Behav. Evol.* 15, 94–140. doi: 10.1159/000123774

Sincich, L. C., and Horton, J. C. (2005). The circuitry of V1 and V2: integration of color, form, and motion. *Annu. Rev. Neurosci.* 28, 303–326. doi: 10.1146/annurev.neuro.28.061604.135731

Sommer, M. A., and Wurtz, R. H. (2006). Influence of the thalamus on spatial visual processing in frontal cortex. *Nature* 444, 374–377. doi: 10.1038/nature05279

Sood, M., and Sereno, M. I. (2016). Areas activated during naturalistic reading comprehension overlap topological visual, auditory, and somatotomotor maps. *Hum. Brain Mapping* 37, 2784–2810. doi: 10.1002/hbm.23208

Sood, M., and Sereno, M. I. (2018). Estimating the cortex-wide overlap between wordless narrative scene comprehension, reading comprehension, and topological visual, auditory, and somatomotor maps. *bioRxiv* [Preprint] bioRxiv: 264002, doi: 10.1101/264002

Sparks, D. L. (1986). Translation of sensory signals into commands for control of saccadic eye movements: role of primate superior colliculus. *Physiol. Rev.* 66, 118–171. doi: 10.1152/physrev.1986.66.1.118

Sparks, D. L., and Hartwich-Young, R. (1989). "The deep layers of the superior colliculus," in *The Neurobiology of Saccadic Eye Movements*, eds R. H. Wurtz and M. E. Goldberg (Amsterdam: Elsevier), 213–255.

Stepniewska, I., Fang, P.-C., and Kaas, J. H. (2009). Microstimulation reveals specialized subregions for different complex movements in posterior parietal cortex of prosimian galagos. *Proc. Natl. Acad. Sci. U.S.A.* 102, 4878–4883. doi: 10.1073/pnas.0501048102

Striem-Amit, E., Hertz, U., and Amedi, A. (2011). Extensive cochleotopic mapping of human auditory cortical fields obtained with phase-encoding fMRI. *PLoS One* 6:e17832. doi: 10.1371/journal.pone.0017832

Suga, N. (1988). "Auditory neuroethology and speech processing: complex-sound processing by combination-sensitive neurons," in *Auditory*

Function: Neurobiological Bases of Hearing, eds G. M. Edelman, W. E. Gall, and W. M. Cowan (Hoboken NJ: John Wiley and Sons), 679–720.

Swindale, N. V., Shoham, D., Grinvald, A., Bonhoeffer, T., and Hubener, M. (2000). Visual cortex maps are optimized for uniform coverage. *Nat. Neurosci.* 3, 822–826. doi: 10.1038/77731

Swisher, J. D., Halko, M. A., Merabet, L. B., McMains, S. A., and Somers, D. C. (2007). Visual topography of human intraparietal sulcus. *J. Neurosci.* 27, 5326–5337. doi: 10.1523/JNEUROSCI.0991-07.2007

Talavage, T. M., Sereno, M. I., Melcher, J. R., Ledden, P. J., Rosen, B. R., and Dale, A. M. (2004). Tonotopic organization in human auditory cortex revealed by progressions of frequency sensitivity. *J. Neurophysiol.* 91, 1282–1296. doi: 10.1152/jn.01125.2002

Tanaka, M. (2007). Spatiotemporal properties of eye position signals in the primate central thalamus. *Cereb. Cortex* 17, 1504–1515. doi: 10.1093/cercor/bhl061

Tehovnik, E. J. (1995). The dorsomedial frontal cortex: eye and forelimb fields. *Behav. Brain Res.* 67, 147–163. doi: 10.1016/0166-4328(94)00151-5

Tierney, A., Dick, F., Deutsch, D., and Sereno, M. I. (2012). Speech versus song: multiple pitch-sensitive areas revealed by a naturally cccurring musical illusion. *Cereb. Cortex* 23, 249–254. doi: 10.1093/cercor/bhs003

Tootell, R. B. H., Mendola, J. D., Hadjikhani, N. K., Ledden, P. J., Liu, A. K., Reppas, J. B., et al. (1997). Functional analysis of V3A and related areas in human visual cortex. *J. Neurosci.* 17, 7060–7078. doi: 10.1523/JNEUROSCI.17-18-07060.1997

Triarhou, L. C. (2007). A proposed number system for the 107 cortical areas of Economo and Koskinas, and Brodmann area correlations. *Stereotact. Funct. Neurosurg.* 85, 204–215. doi: 10.1159/000103259

von Economo, C. F., and Koskinas, G. N. (1925). *Die Cytoarchitektonik Der Hirnrinde Des Erwachsenen Menschen*. Berlin: Julius Springer Verlag.

Wandell, B. A., and Winawer, J. (2011). Imaging retinotopic maps in the human brain. *Vis. Res.* 51, 718–737. doi: 10.1016/j.visres.2010.08.004

Wandell, B. A., Brewer, A. A., and Dougherty, R. F. (2005). Visual field map clusters in human cortex. *Philos. Trans. R. Soc. Lond. B* 36, 693–707. doi: 10.1098/rstb.2005.1628

Wang, F., Dong, Z., Reese, T. G., Rosen, B., Wald, L. L., and Setsompop, K. (2021). 3D Echo Planar Time-resolved Imaging (3D-EPTI) for ultrafast multi-parametric quantitative MRI. *bioRxiv* [Preprint] doi: 10.1101/2021.05.06.443040

Wang, L., Mruczek, R. E. B., Arcaro, M. J., and Kastner, S. (2015). Probabilistic maps of visual topography in human cortex. *Cereb. Cortex* 25, 3911–3931. doi: 10.1093/cercor/bhu277

Wang, Q., and Burkhalter, A. (2007). Area map of mouse visual cortex. *J. Comp. Neurol.* 502, 339–357. doi: 10.1002/cne.21286

Wang, Y., Xiao, Y., and Felleman, D. J. (2007). V2 thin stripes contain spatially organized representations of achromatic luminance change. *Cereb. Cortex* 17, 116–129. doi: 10.1093/cercor/bhj131

Wilson, H. R., and Cowan, J. D. (1972). Excitatory and inhibitory interactions in localized populations of model neurons. *Biophys. J.* 12, 1–24. doi: 10.1016/S0006-3495(72)86068-5

Wu, J. Y., Xiaoying, H., and Chuan, Z. (2008). Propagating waves of activity in the neocortex: what they are, what they do. *Neuroscientist* 14, 487–502. doi: 10.1177/1073858408317066

Yaron, A., Kowalski, D., Yaguchia, H., Takeia, T., and Sekia, K. (2020). Forelimb force direction and magnitude independently controlled by spinal modules in the macaque. *Proc. Natl. Acad. Sci. U.S.A.* 117, 27655–27666. doi: 10.1073/pnas.1919253117

Yu, H., Farley, B. J., Jin, D. Z., and Sur, M. (2005). The coordinated mapping of visual space and response features in visual cortex. *Neuron* 47, 267–280. doi: 10.1016/j.neuron.2005.06.011

Yu, H.-H., Rowley, D. P., Price, N. S. C., and Rosa, M. G. P. (2020). A twisted visual field map in the primate dorsomedial cortex predicted by topographic continuity. *Sci. Adv.* 6:eaaz8673. doi: 10.1126/sciadv.aaz8673

Zeharia, N., Hofstetter, S., Flash, T., and Amedi, A. (2019). A whole-body sensory-motor gradient is revealed in the medial wall of the parietal lobe. *J. Neurosci.* 39, 7882–7892. doi: 10.1523/JNEUROSCI.0727-18.2019

Zhang, K. (1996). Representation of spatial orientation by the intrinsic dynamics of the head-direction cell ensemble: a theory. *J. Neurosci.* 16, 2112–2126. doi: 10.1523/JNEUROSCI.16-06-02112.1996

Zhu, Q., and Vanduffel, W. (2019). Submillimeter fMRI reveals a layout of dorsal visual cortex in macaques, remarkably similar to New World monkeys. *Proc. Natl. Acad. Sci. U.S.A.* 116, 2306–2311. doi: 10.1073/pnas.1805561116

Conflict of Interest: The authors declare that the research was conducted in the absence of any commercial or financial relationships that could be construed as a potential conflict of interest.

Advantages of publishing in Frontiers

OPEN ACCESS
Articles are free to read for greatest visibility and readership

FAST PUBLICATION
Around 90 days from submission to decision

HIGH QUALITY PEER-REVIEW
Rigorous, collaborative, and constructive peer-review

TRANSPARENT PEER-REVIEW
Editors and reviewers acknowledged by name on published articles

Frontiers
Avenue du Tribunal-Fédéral 34
1005 Lausanne | Switzerland

Visit us: www.frontiersin.org
Contact us: frontiersin.org/about/contact

REPRODUCIBILITY OF RESEARCH
Support open data and methods to enhance research reproducibility

DIGITAL PUBLISHING
Articles designed for optimal readership across devices

FOLLOW US
@frontiersin

IMPACT METRICS
Advanced article metrics track visibility across digital media

EXTENSIVE PROMOTION
Marketing and promotion of impactful research

LOOP RESEARCH NETWORK
Our network increases your article's readership